Research Group

The International Journal of **Research on Engineering Structures and Materials (RESM**) is a peer-reviewed open access journal (p-ISSN: 2148-9807; o-ISSN: 2149-4088) published by MIM Research Group. It is published in February, June, September, and December.

The main objective of RESM is to provide an International academic platform for researchers to share scientific results related to all aspects of mechanical, civil, and material engineering areas.

RESM aims the publication of original research articles, reviews, short communications technical reports, and letters to the editor on the latest developments in the related fields.

All expenditures for the publication of the manuscripts are most kindly reimbursed by *MIM Research Group*. Thus, authors do not need to pay for publishing their studies in the journal.

The scope of the journal covers (but not limited to) behavior of structures, machines and mechanical systems, vibration, impact loadings and structural dynamics, mechanics of materials (elasticity, plasticity, fracture mechanics), material science (structure and properties of concrete, metals, ceramics, composites, plastics, wood, etc.,), nano-materials performances of new and existing buildings and other structural systems, design of buildings and other structural systems, seismic behavior of buildings and other structural systems, repair and strengthening of structural systems, case studies and failure of structural systems, safety and reliability in structural and material engineering, use of new and innovative materials and techniques in energy systems and mechanical aspects of biological systems (biomechanics and biomimetics).

The topics covered in JRESM include:

- Structural Engineering
- Mechanical Engineering
- Material Engineering
- Earthquake Engineering
- Nano-technology
- Energy Systems (Focus on Renewable)
- Biomechanics and Biomimetics
- Environment (Material and Engineering System Related Issues)
- Computer Engineering and Data Science (Material and Engineering System-Related Issues)

Abstracting and Indexing
Please visit http://www.jresm.org for more information.

Graphics and Design

Yunus Demirtaş   ydemirtas@jresm.net

The International Journal of **Research on Engineering Structures and Materials (RESM**) is a peer-reviewed open access journal (p-ISSN: 2148-9807; o-ISSN: 2149-4088) published by MIM Research Group. It is published in February, June, September, and December.

The main objective of RESM is to provide an International academic platform for researchers to share scientific results related to all aspects of mechanical, civil, and material engineering areas.

RESM aims the publication of original research articles, reviews, short communications technical reports, and letters to the editor on the latest developments in the related fields.

All expenditures for the publication of the manuscripts are most kindly reimbursed by *MIM Research Group*. Thus, authors do not need to pay for publishing their studies in the journal.

The scope of the journal covers (but not limited to) behavior of structures, machines and mechanical systems, vibration, impact loadings and structural dynamics, mechanics of materials (elasticity, plasticity, fracture mechanics), material science (structure and properties of concrete, metals, ceramics, composites, plastics, wood, etc.,), nano-materials performances of new and existing buildings and other structural systems, design of buildings and other structural systems, seismic behavior of buildings and other structural systems, repair and strengthening of structural systems, case studies and failure of structural systems, safety and reliability in structural and material engineering, use of new and innovative materials and techniques in energy systems and mechanical aspects of biological systems (biomechanics and biomimetics).

The topics covered in JRESM include:

- Structural Engineering
- Mechanical Engineering
- Material Engineering
- Earthquake Engineering
- Nano-technology
- Energy Systems (Focus on Renewable)
- Biomechanics and Biomimetics
- Environment (Material and Engineering System Related Issues)
- Computer Engineering and Data Science (Material and Engineering System-Related Issues)

Abstracting and Indexing
Please visit http://www.jresm.org for more information.

Graphics and Design

Yunus Demirtaş   ydemirtas@jresm.net

RESEARCH on
ENGINEERING STRUCTURES &
MATERIALS

Research Group

RESEARCH on ENGINEERING STRUCTURES & MATERIALS

Editorial Board

Editorial Office

Mohammad Saleh Baradaran	Islamic Azad University of Mashhad	Iran
Peyman Beiranvand	Razi University	Iran
Hadj Bekki	University Ibn Khaldoun of Tiaret	Algeria
Abdelhalim Bensaada	University of Yahia Fares of Medea	Algeria
Mohammed Bentahar	Tahar Moulay University of Saida	Algeria
H. Alperen Bulut	Erzincan University	Türkiye
Esitake Cebolina		Iraq
Halit Cetiner	Isparta University	Türkiye
Kamel Chaoui	Badji Mokhtar University	Algeria
Venkatesh Chava	CVR College of Engineering	India
Maheswaran Chellapandian	Mepco Schlenk Engineering College	India
Xinrong Chengil	Tongji University	China
Sonali Sri Durga Chereddy	CVR College of Engineering	India
Anna Chiaradonna	DICEAA, University of L'Aquila	Italy
Ajay Chourasia	Central Building Research Institute	India
Daniel Cruze	Mohamed Sathak A J College of Engineering	India
Zhaoyan Cui	Nanjing Forestry University	China
Ashish Kumar Dash	Indian Institute of Technology	Indian
Cengiz Görkem Dengiz	Ondokuz Mayıs University	Türkiye
Arindam Dey	Indian Institute of Technology Guwahati	India
Marwan Effendy	Universitas Muhammadiyah Surakarta	Indonesia
Ashraf El-Shamy	National Research Centre	Egypt
Ali Ercetin	Bandırma Onyedi Eylül University	Türkiye
Kemal Ermis	Sakarya University of Applied Science	Türkiye
Uchechi Eziefula	University of Agriculture and Environmental Sciences, Umuagwo	Nigeria
Mingjing Fang	Wuhan University of Technology	China
Christopher Fapohunda	Federal University Oye-Ekiti	Nigeria
Abdelkader Fidjah	University of Djelfa	Algeria
Saeid Foroughi	Konya Technical University	Türkiye

Sharanabasava V. Ganachari	KLE Technological University	India
Zhong Ge	Yunnan University	China
Gökhan Gece	Bursa Teknik University	Türkiye
Mahesh Gopal	College of Engineering and Technology	Ethiopia
Chandrasekhar G L Gotur	Atria Institute of Technology	India
Mert Göksüzoğlu	SAMPA	Türkiye
Layachi Guelmine	B.B.A University	Algeria
Kadir Günaydın	GE Aviation, Marmara Technology Center	Türkiye
Endalkachew Mosisa Gutema	College of Engg and Tech	Ethiopia
Ahmet Güral	Gazi University	Türkiye
Hussein Hamada	University Malaysia Pahang	Malaysia
Taihao Han	Missouri University of Science and Technology	USA
Md. Zia Ul Haq	Panjab University	India
Md. Naimul Haque	East West University	India
Noor Sheena Herayani Harith	University Malaysia Sabah	Malaysia
Shrikant Harle	Ram Meghe College of Engineering and Management	India
Catur Harsito	Universitas Sebelas Maret	Indonesia
Muttaqin Hasan	Syiah Kuala University	Indonesia
Maboud Hekmatifar	Islamic Azad University	Iran
Mohammad Heydari Vini	Islamic Azad University	Iran
Qing Hong	Midwestern University	USA
Oleksii Hrechanyi	Zaporizhzhia National University	Ukraine
Md. Saiful Islam	University Putra Malaysia	Malaysia
Mehmet Zerrakki Işık	Batman University	Türkiye
Ghassan Subhi Jameel	University of Anbar	Iraq
Saifulnizan Jamian	University Tun Hussein Onn Malaysia	Malaysia
Girish M. Joshi	VIT University	India
Bhuria Jyothi		Nepal

Arunkumar K		India
Hossein Kabir	University of Illinois	USA
Pulitha Kavitri		Sri Lanka
Mehmet Kaya	Bozok University	Türkiye
Emre Kemer	Usak University	Türkiye
Pallavi Pradeep Khobragade	Rungta College of Engineering and Technology	India
Cemal Kochan	Dokuz Eylul University	Türkiye
Ali Koçak	Yıldız Technical University	Türkiye
Nitin Kumar	University of California Davis	USA
A. Suresh Kumar	Kalasalingam Academy of Research and Education	India
Sanjeev Kumar	Sanjeev Agrawal Global Educational University	India
Josephine Chang Hui Lai	University Malaysia Sarawak	Malaysia
Ravichandran M	K. Ramakrishnan College of Engineering	India
Uma Mageshwari		India
Lomesh Mahajan	Dr. Babasaheb Ambedkar Technological University	India
Natt Makul	Phranakhon Rajabhat University	Thailand
Anirban Mandal	National Institute of Technology	India
Tahara Ramadzan Md Kassim	International Islamic University Malaysia	Malaysia
Priyansha Mehra	Manipal University	India
Adamah Messan	Laboratoire Eco Matériaux de Construction (LEMC)	France
Suruchi Mishra		Malaysia
Khairul Anwar Mohamad Said	UNIMAS	Malaysia
Fadzli Mohamed Nazri	University Sains Malaysia	Malaysia
Mohsin Talib Mohammed	Kufa University	Iran
Noor Azline Mohd Nasir	University Putra Malaysia	Malaysia

Mohd Syahrul Hisyam Mohd Sani	University Teknologi MARA (UiTM) Cawangan Pahang	Malaysia
Mahmoud Mokhtar	Housing & Building National Research Center	Egypt
Alaa M. Morsy	Arab Academy for Science	Egypt
Rini Mulyani	Senior Lecturer at University Bung Hatta, Padang, Indonesia	Indonesia
Yasmin Murad	University of Jordan Amman	Jordan
Nahida Nazim Musayeva	Azerbaijan National Academy of Sciences	Azerbaijan
Arslan Mushtaq	NUST Institute of Civil Engineering	Pakistan
Maheswaran Muthiah	Kalasalingam Academy of Research and Education	India
Madeva Nagaral	Aircraft Research and Design Centre, Hindustan Aeronautics Limited	India
Salem Nawel	University of Gabes	Tunisia
Amarachi Nkwoada	Federal University of Technology Owerri	Nigeria
Mehrab Nodehi	University of California	USA
Samson Olalekan Odeyemi	Kwara State University	Nigeria
Hayri B. Ozmen	Usak University	Türkiye
İbrahim Öz	Ahi Evran University	Türkiye
Gurusamy P	Chennai Institute of Technology	India
Partheeban Pachaivannan	Chennai Institute of Technology	India
Chitaranjan Pany	Vikram Sarabhi Space Center	India
Rajesh Kumar Paswan	National Institute of Technology Jamshedpur	India
Vikas Patel	National Council for Cement and Building Materials	India
Hiteshkumar Patil	Dr. Babasaheb Ambedkar Technological University	India
Zühtü Onur Pehlivanlı	Kırıkkale University	Türkiye
Amin Moslemi Petrudi	Tehran University	Iran
Hemadri Prasad Raju	Sree Vidyanikethan Engineering College	India

Kalappa Prashantha	Adichunchanagiri University	India
Harris Priya	Kurukshetra University	India
Kavendra Pulkit		India
Helogi Putin		India
Ajibola Ibrahim Quadri	Federal University of Technology	Nigeria
Md. Mijanur Rahman	Military Institute of Science and Technology	Bangladesh
Azida Rashidi	UNIMAS	Malaysia
Badrinarayan Rath	Wollega University	Ethiopia
T.V. Reshma		India
Pier Paolo Rossi	University of Catania	Italy
Md Jalal Uddin Rumi	Military Institute of Science and Technology	Bangladesh
Abbasali Sadeghi	Islamic Azad University	Iran
Mohammed A. Sakr	Tanta University	Egypt
M.Helen Santhi	Vellore Institute of Technology	India
Tamer Saraçyakupoğlu	Istanbul Gelişim University	Türkiye
Divya Sharma	NITTTR Chandigarh	India
Fatheali Shilar	Jain College of Engineering Belgaum	India
Lenganji Simwanda	Stellenbosch University	South Africa
Brijesh Singh	National Council for Cement and Building Materials	India
Navdeep Singh	Dr B R Ambedkar National Inst. of Tech.	India
Rami Sldozian	University of Technology	Iraq
M. Somasundaram	PSG College of Technology	India
Rajkumar Srinivasan	SRM TRP Engineering College Irungalur	India
Rianti Dewi Sulamet-Ariobimo	Universitas Trisakti	Indonesia
Marthin Dody Josias Sumajouw	Sam Ratulangi University	Indonesia
Gülsah Susurluk	Beykent University	Türkiye
Jumrik Taipodia	NIT Arunachal Pradesh	India
Aykut Tamer	Imperial College London	England
Chan Sin Tan	University Malaysia Perlis	Malaysia
Hamide Tekeli	Süleyman Demirel University	Türkiye

Delsye Ching Lee Teo	Melbourne Polytechnic	Australia
Mehmet Topuz	Van Yüzüncü Yıl University	Türkiye
Tuan Norhayati Tuan Chik	University Tun Hussein Onn	Malaysia
Hasan Ulus	Selcuk University	Türkiye
Dilay Uncu	Celal Bayar University	Türkiye
Prem Kumar V	VIT Chennai	India
Harinadh Vemanaboina	Sri Venkateswara College of Engineering and Technology	India
Tadesse Gemeda Wakjira	University of British Columbia	Canada
Gustavo Bosel Wally	Federal University of Rio Grande do Sul	Brazil
Narong Wichapa	Kalasin University	Thailand
I Wiryadi	Mahasaraswati Denpasar University	Indonesia
Omid Aminoroayai Yamani	K. N. Toosi University of Technology	Iran
Guney Guven Yapici	Ozyegin University	Türkiye
Salih Hakan Yetgin	Kütahya Dumlupınar University	Türkiye
Sevim Yolcular Karaoğlu	Ege University	Türkiye
Ana Sakura Zainal Abidin	UNIMAS	Malaysia

In This Issue

ABSTRACTING / INDEXING

The international journal of Research on Engineering Structures and Materials (RESM) is currently Abstracted/Indexed by Asos Indeks, CiteFactor, Cosmos, CrossRef, Directory of Research Journal Indexing, Engineering Journals (ProQuest), EZB Electronic Journal Library, Global Impact Factor, Google Scholar, International Institute of Organized Research (I2OR), International Scientific Indexing (ISI), Materials Science & Engineering Database (ProQuest), Open Academic Journals Index, Publication Forum, Research BibleScientific Indexing Service, Root Indexing, Scopus, Ulakbim TR Index (Tubitak), Universal Impact Factor and under evaluation by many other respected indexes.

Check web site for current indexing info, www.jresm.org

Research Article

Precast concrete wall-raft connectors for increasing the lateral load capacity: An experimental and analytical approach

P. SenthilKumar[1,a], D. Tensing[1,b], G. Hemalatha[1,c], S. Vivekananda Sharma[*,1,d], C. Daniel[2]

[1]*Department of Civil Engineering, Karunya Institute of Technology and Sciences, India*
[2]*Department of Civil Engineering, Hindustan Institute of Technology and Science, India*

Article Info	Abstract
	Precast structural walls and rafts commonly resist lateral load in structures owing to improved traits and faster construction. The behavior of five different types of precast reinforced concrete structural wall and raft connection systems is evaluated in this study. In all five configurations, the cyclic load is applied in the wall systems to observe the lateral load-carrying capacity and hysteretic characteristics. The damage and failure patterns were assessed. To confirm and contrast the behavior of the proposed precast structural wall and raft connection systems with the experimental findings, FEM analysis was used. Only shear and flexural cracks were observed. The specimen with 12 mm dia rods has the maximum load carrying capacity of 10.23 kN in the negative cycle, which is 57% more than the specimen without grouting and connector. The suggested connection can improve the resistance behavior in all key directions by absorbing more energy than precast walls under dynamic load.

1. Introduction

Precast concrete buildings are frequently used to construct structures in developed nations, particularly urbanized regions. Precast concrete structures are superior to traditional cast-in-place concrete structures in design and construction, including better structural components, faster construction, and lower noise. To protect the integrity of the structure of precast concrete buildings during lateral loads like wind or earthquakes, precast concrete structures in many countries have been restricted to buildings of less than ten stories. Arthi et al. conducted experimental research to examine the dowel connection's shear capacity under reverse cyclic loading. The investigation entailed comparing the findings of the real experiments with the numerical analysis of the dowel connection between the precast shear wall and slab. According to the study, the ultimate strength of the dowel connection in the push and pull directions of loading was 11.17 kN and 11.03 kN, respectively[1]. Arthi et al. employed ABAQUS to simulate a dowel connection between the precast shear wall and slab to examine joint failure, damage, and hysteresis. The studied specimen showed a failure pattern consistent with the "Strong joint-Weak member." The findings of the finite element analysis were 11% higher than the outcomes of the actual tests. Using scaled-down models that were one-third the size of the actual connection. According to the study, the precast specimen's ductility factor and cumulative ED were higher than those of the monolithic specimen by 128.95% and

74.34%, respectively [2,3]. The importance of connecting zones in structural systems, particularly in buildings situated in seismic zones, was emphasized by Bannan in his research. He conducted a study to determine how seismic load combinations affected the behaviour of slabs at the points connected to shear walls. The parts of reinforced concrete buildings where the slabs meet the walls are considered the most important [4]. Precast concrete shear walls with low reinforcing, frequently utilized in Dutch residential structures of intermediate height, were the focus of Brunesi's research. Push and pull tests on precast wall connections were also conducted following the asymmetric approach as part of the study, and the results were used to illustrate how these joint systems behave cyclically under the influence of simulated seismic loads. Brunesi tested a 2-story precast concrete wall-slab-wall structure with minimal reinforcement in the Groningen area, where recent seismic occurrences brought on by gas extraction reservoir depletion have occurred. This building was picked to symbolize a common type of house in the region. Brunesi studied five specimens' monotonic and cyclic response curves, and the resulting damage patterns showed that the reported flexural failure mechanism was extremely stable and closely matched that shown in full-scale building tests. A mock-up of a building was tested using a shake table by Brunesi, who ran it through five iterations of increasing test intensity. Steel connectors used to connect the longitudinal and transverse walls finally failed, causing the structure to collapse [5-8]. Using fibre-reinforced polymer (FRP), Chalot studied the mechanical performance of full-scale reinforced concrete (RC) wall-slab connections under cyclic loading. It was found that Composite reinforcement increased joint strength by 80% and ductility by 33%. Reinforcement changed the failure mode from wall bending to joint shear. The composite strengthening also led to a 385% increase in the joint's ability to dissipate energy by relocating the failure zone [9]. Devine performed 20 tests to examine the relationship between connections' capacity for horizontal shear and their vertical uplift. Findings from three specimens are given, including reverse cyclic shear with 50 mm uplift, monotonic uplift, and cyclic uplift. It was found that the existing welding procedure utilized to connect the steel angle embedded in the concrete slab to the plate installed in the wall caused the weld to fail after just a few uplift cycles. Devine also created a nonlinear analytical model for wall-to-slab connectors to provide nonlinear dynamic analysis for assessing deformation needs during extreme seismic events [10]. Guo tested the seismic performance of a revolutionary precast structural system using a shaking table on a scaled-down, three-story model. The system was discovered to have a high collapse margin ratio, rigidity, and load capacity. There were created fragility curves for both the structural and nonstructural elements [11]. Hamicha performed a nonlinear finite element analysis of a reinforced concrete external shear wall-slab connection subjected to cyclic loading using the ABAQUS software package. The study examined structural reactions, including load-bearing capability, Energy Dissiaption, ductility, and stiffness deterioration. To assess their impact on the structural response of the connection, study characteristics included connection type, the aspect ratio of slab thickness to shear wall thickness, the aspect ratio of shear wall height to the effective width of the slab, and concrete strength [12]. According to Hemamalini, the connections are a crucial element in the precast wall system's ability to resist lateral loads because they are the weakest point. The most significant difficulty is the connections' behaviour and potential failure when subjected to intense lateral loads and natural hazards. The article briefly examines shear walls' horizontal and vertical connections and their performance under various loading patterns [13]. Henry's study uses a wall-to-floor connection for a rigid cast-in-place connection to protect the floor from serious damage. This method isolates the floor from the vertical displacement and rotation of the wall. Rocking walls are only one effect of the wall-to-floor contact on a building's seismic response. It can be much more crucial for typical reinforced concrete walls, increasing their vulnerability to shear or axial failure [14]. The construction of computational models to validate the stress levels of structural components was made possible by Krentowski's assessment of the physical and

mechanical characteristics of the materials used to make connections. A suggestion for effectively strengthening weak connections was developed based on the research, computations, and analyses. Also, suggestions for efficient interlayer connection testing methods for challenging interlayer connections were suggested [15]. Lu created a novel structural method for precast concrete wall panels that connects using bolts for low-rise structures in rural areas. The ground-breaking technique enables dispersed bolt connections between permanent foundation walls, floors, and connecting columns. This capability makes it possible to disassemble and rebuild the complete system as necessary. However, the bolted joints displayed an unfavourable punching shear failure, as they could not exploit the strength of the wall panels completely, according to the findings of the prior quasi-static cycle push-over test[16]. Pavel examined Bucharest's 12-story reinforced concrete structure's seismic performance. Many new city office buildings use a flat slab supported by columns and strong, reinforced concrete core walls [17]. Through a significant experimental effort, Pavese investigated the behaviour of prefabricated reinforced concrete sandwich panels (RCSPs) under simulated seismic loading. Full-scale panels were used in tests to simulate the behaviour of fixed-end and cantilever walls that resist lateral forces. Moreover, tests were performed on a two-story, full-scale H-shaped structure of individually linked panels [18]. Rossley's study concentrated on using loop bars to connect precast concrete walls on the exterior and inside of a building. A transverse bar is inserted to guarantee continuity between the looping bars, resulting in a gap between the walls filled with concrete to create a firm connection. Analyzing the behaviour of the loop bar connection under shear force was the main goal of the experimental inquiry. [19]Shen proposed using slotted floor slabs, which have spaces close to the wall limbs and are filled with polystyrene, to improve the independent deformation of the limbs. The study's primary goal was to understand better how the limbs of shear walls and slotted floors interact. Three reinforced concrete prefabricated shear wall samples with shear keys were created to accomplish this. The study discovered that by adding slots to the floor slabs, concentrated deformation could be eased, and the slabs would be better protected. Shen conducted an experimental investigation to examine how a novel connection between walls and slabs that used high-performance concrete (HPC) post-casted in the core region responded to a fire. For comparison, three full-scale specimens—two completed connections and one cast-in-place connection underwent monotonic static loading testing before and after the fire [20-21]. The efficacy and durability of connections between precast panel joints are essential considerations, according to Singhal's study on the seismic behaviour of precast buildings. The total seismic performance of precast structures is significantly influenced by the transmission of loads and the ductility of the joint connections. Correct connection design is also required to transmit seismic forces between the precast panels effectively.

Singhal researched the seismic behaviour of a cast-in-place concrete hollow core precast reinforced concrete shear wall. The wall was under lateral stress and assessed for seismic characteristics, damage patterns, and lateral load capacity. Because of its ductile reaction, the wall demonstrated competent deformation properties. Precast RC wall connections, codal provisions, a study of experimental results, and the impact of post-tensioning on precast RC walls were all reviewed by Singhal. The precast wall-column system and the precast double-leaf system are two different kinds of precast reinforced concrete structural wall systems whose performance is evaluated by Singhal. The former uses loop bars to connect a precast wall to precast hollow columns, while the latter uses two precast panels with an in-situ concrete-filled hollow core. The hysteretic characteristics that resulted from applying lateral loads to both wall systems in a displacement-controlled cyclic mode were carefully evaluated regarding the damage pattern and numerous seismic properties. Singhal looked at the seismic behaviour of a full-scale precast reinforced

concrete wall exposed to in-plane cyclic loading and out-of-plane loading simulated by sand backfill.

The tested wall showed substantial out-of-plane movement and flexural fractures because of the high aspect ratio and lateral pressure from the backfill [22-26]. Tatsambon's study concentrated on the connections between slabs and walls because these components are frequently extended to the connection axis, assuming complete rotation [27]. Vaghei proposed a novel method for joining two adjacent precast wall panels utilizing two steel U-shaped channels. To provide a solid connection, these channels are fastened to the sides of the walls and joined together as male and female joints using bolts and nuts. A U-shaped rubber piece is fitted between the two channels to reduce any vibration impact within the structure. Vaghei looked into how well a precast concrete structure with a novel connection performed. The study concentrated explicitly on connections between precast concrete panels in industrial structures that used a unique U-shaped steel channel connector. The examination covered crack propagation, plastic strain trends in the concrete panels and connections, the primary stress distribution, and deformation of concrete panels and welded wire mesh reinforcements (BRC) [28-29]

Wang suggested the concept of equivalent cross-sectional area, in which the flexural strength of the horizontal part of the interior wall-slab joints is estimated using a coefficient known as the equivalent cross-sectional area ratio. These joints are essential in constructions with strong walls and thick slabs [30]. According to Xia, the precast specimens showed a flexural collapse at the end of the beam with no severe damage to the joint or shear wall. The four specimens' hysteresis curves revealed a pinching behaviour. The energy dissipation capacities of the precast specimens were on par with those of the cast-in-place specimens [31]. Three samples of precast slabs and monolithic walls subjected to quasi-static loads were compared in a study by Zenunovic. Mathematical models were created using displacement and FEM techniques to examine the connection types of both specimens. The stiffness matrix was modified by adding a semi-rigid parameter to the connection. [32]

The current investigation examines the wall-raft connectors' performance in precast structural elements under cyclic loading conditions. The specimens are designed and modelled using six different configurations in the Ansys tool for numerical simulation. The results obtained from the simulation are then validated through experimental investigation, with a focus on load-carrying capacity and energy dissipation. There are six configurations to consider in this study. These configurations include i) a wall raft without a connector and no grouting, ii) a wall raft without a connector but with grouting, iii) a wall raft with a shear connector of 8mm, iv) a wall raft with a shear connector of 10mm, v) a wall-raft with a shear connector of 12mm, and vi) a wall-raft with a shear connector of 12mm subjected to earthquake loading.

2. Simulation of Pre-Cast Model Using Finite Element Analysis (FEA)

Modeling is one of the important features in Finite Element Analysis. It takes around 40% to 60% of the total solution time. Improper modeling of the structures leads to the unexpected errors in the solution. Hence, proper care should be taken for modeling the structures. A good idealization of the geometry reduces the running time of the solutioNThe raft and wall are modelled using ANSYS software, considerably. In many situations, a three dimensional structure can easily be analyzed by considering it as a two dimensional structure without any loss of accuracy. Creative thinking in idealizing and meshing of the structure helps not only in reducing considerable amount of time but also in reducing the memory requirement of the system. Flow plasticity theory has been widely used for nonlinear simulation of RC structures. Constitutive reations of flow plastic theory

in CAE software are refered to as material model.In the current modelling Menetrey-Willam model is used.The Menetrey-William constitutive model can well capture important mechanical behaviours of concrete such as tensile strength,compressive strength,nonlinear hardening,softening and dilantacy.

Finite Element modeling of Raft and wall assembly in ANSYS consist of three stages, which are listed as (a)Selection of element type(b)Assigning material properties (C)Modeling and meshing the geometry

Table 1. Details of Element and material properties

S.No	Name	Material	ANSYS Element
1	Concrete	M20	SOLID 185
2.	Steel Reinforcement	Fe550	BEAM 188
3.	Connecting rod	Fe550	BEAM 188

To create the finite element model in ANSYS WORKBENCH 2022 there are multiple tasks that have to be completed for the model to run properly for this model, ANSYS DESIGN MODELER environment was utilized to create the model the reinforcement (1D model) using concept tool and concrete model (3D model) by using extrude tool as shown in the figure below. Properties of concrete and reinforcements used in the development of model is presented in Table 1 and Table 2 respectively.

Table 2. Details of concrete element

Property	Values	Property	Values
Young's Modulus	31623N/mm²	Plastic strain at uniaxial compressive strength	0.001
Poisson's ratio	0.15	Plastic strain at transition from power law to exponential softening	0.002
Bulk Modulus	1.5×10^5 N/mm²	Relative stress at start of nonlinear hardening	0.33
Shear Modulus	1.37×10^5 N/mm²	Residual relative stress at transition from power law to exponential softening	0.85
Uniaxial Compressive strength	20N/mm²	Residual compressivestress	0.2
Uniaxial tensile strength	2.2	Mode 1 area specific fracture energy	50
Biaxial Compressive strength	25	Residual tensile relative stress	0.1
Dilantancy Angle	30		

Table 3. Details of steel element

Property	Values
Density	7850 kg/m^3
Young's Modulus	2x10^{11} N/mm^2
Poisson's ratio	0.3
Bulk Modulus	1.66x10^5 N/mm^2
Shear Modulus	7.69x10^4 N/mm^2
Yield Strenght	550 N/mm^2
Tangent Modulus	0

As per the designed scaled model, the wall and raft are modelled seperately with reinforcement, as shown in Figure 1 and the assemble model with and without connector rod is shown in Figure2.
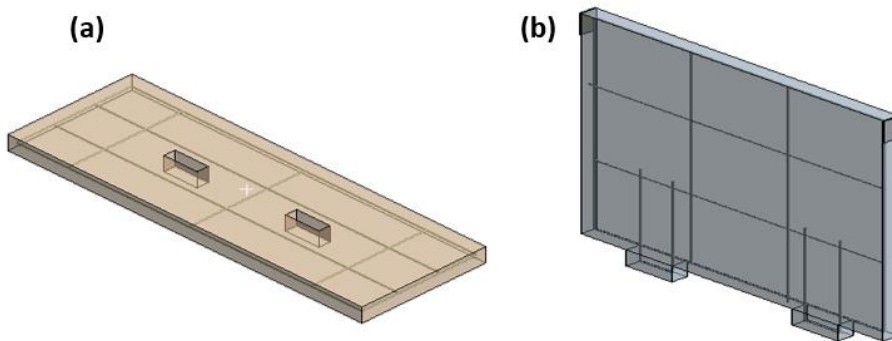
Fig. 1 Modelling of a) Raft b) Wall
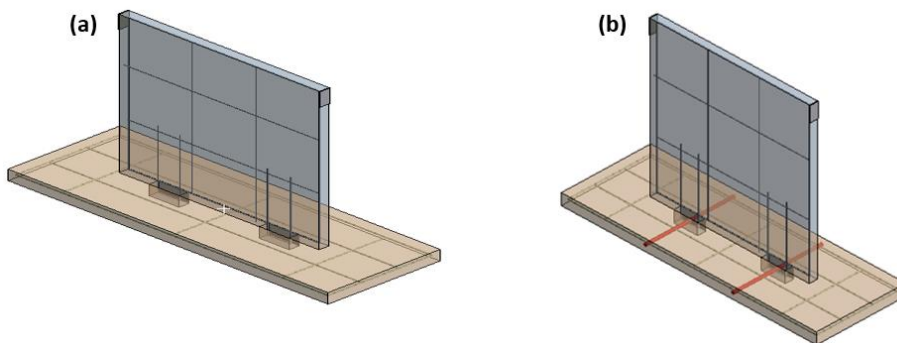
Fig. 2 Assembly of Raft and Wall a) with connector, b) without connector

The FEA of the raft and wall connection is carried out in ANSYS software. The material properties and meshing fineness was generated appropriately, for shell elements of 10 mm size were used for meshing. In the precast raft and wall connection study, five different configurations are studied, namely i) without connector, ii) with grouting, iii) raft and wall connection with 8 mm rod, iv) raft and wall connection with 10 mm rod v) raft and wall

connection with 12 mm rod. The specimens' models have been elaborated per IS 456:2021. ANSYS was employed to model and examine the specimens to confirm the experimental test results. The modelling tool highlights the specimen's meshing and the rod in red, as shown in Figure 3. The model needs boundary conditions for restriction to have a unique solution. Boundary conditions must be imposed on the faces to guarantee that the model performs similarly to the experiment. The bottom of the raft is fully constrained in all DOF, and reverse cyclic loading in the displacement-controlled method is applied on the top face of the wall. The maximum deflection occurs at 37.94 mm. The simulated raft and wall connection without connection is shown in Figure 4.
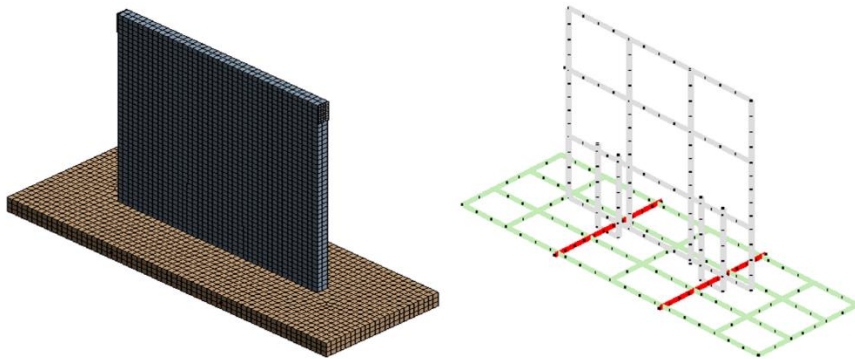
Fig. 3 Mesh of Raft and wall
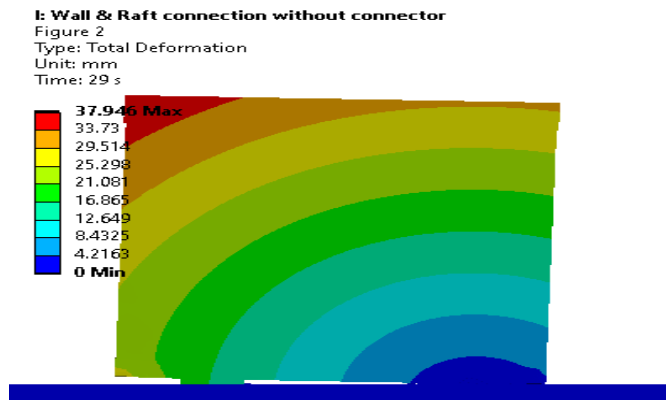
Fig. 4 Deflection for the wall without connector

3. Experimental Investigation on The Precast Specimen

3.1 Properties of Materials Used For Casting of Precast Specimen

Materials are all in compliance with Indian standards. Portland Pozzolana Cement(PPC), per IS 1489 (part 1): 1991, was the cement used in the specimens [33]. The coarse and fine aggregate utilized in the mix design satisfies Zone-III requirements in IS 383-1970 [34] and has a fineness modulus 2.34. The study used two kinds of crushed coarse aggregates, one with a nominal size of 20 mm and a specific gravity of 2.62. Tables 4-8 provide information on the characteristics of several materials utilized in the experiment.

Table 4. Physical characteristics of PPC

Characteristics	Obtained values	Value as per IS:1489 (Part 1) – 1991
Standard Consistency(%)	31	
Fineness Of Cement	0.78	≯ 10%
Setting Time Initial	43 min	≮30 min
Setting Time Final	285 min	≯ 600 min
7 days Compressive Strength (MPa)	24.5	≮ 22.0
28 days Compressive Strength (MPa)	35.5	≮ 33.0

Table 5. Physical characteristics of coarse aggregate

Characteristics	Values
Form	crushed
Max.Nominal size (mm)	20
Specific Gravity	2.65
Water Absorption (%)	2.03
Fineness Modulus	6.79

Table 6. Physical characteristics of fine aggregate

Characteristics	Values
Specific Gravity	2.7
Bulk Modulus (kg/l)	1.35
Fineness Modulus	2.28
Water Absorption (%)	2.40
Grading zone as per IS: 383–1970	III

Table 7. Properties of rebars

Size	Yield Strength(N/mm^2)	Ultimate Strength(N/mm^2)	Elongation (%)
8mm	554.65	670.69	20.53
10mm	557.26	676.84	25.81
12mm	561.32	702.71	31.25

Table 8. M20 mix design

Materials	Quantity(kg)
Cement	396.62
Fine Aggregates	572.69
Coarse Aggregates	1172.86
Water	189.91

3.2 Description of precast specimens

Table 9 shows the five raft-wall connections used in this study's experimental study: RW1, RW2, RW3, RW4, RW5, and RW6. Two of these specimens are made from standard individuals with no connections. The other two are made from 8 mm and 10 mm shear

connectors, and the final two specimens are made with 12mm rods as shear connectors. The shear connections are used to ensure the joint's shearing capability. The components of the wall-raft specimens were designed and detailed per IS 456-2021. To reinforce all specimens longitudinally and transversally, high-yield strength Fe-550 steel bars were used. As indicated in Table 7, the longitudinal steel's yield and ultimate strengths were 554.65 and 670.69 for 8 mm, 557.26 N/mm^2 and 676.84 N/mm^2 for 10 mm diameter rods, and 561.32 and 702.71 for 12mm. The only difference between the 5 specimens is the diameter of the shear connector rods. Figures 5 and 6 show schematics of the longitudinal and transverse reinforcing details for the 6 specimens' walls and rafts. The cross-section chosen is 77 x 1000 mm for the entire wall, with a height of 1000 mm. The concrete connector's dimensions are 100 x 50 mm and 110 x 560 mm for the raft, for a total length of 1600 mm. Figure 7 represents the overall reinforcements of the precast wall and raft specimen. Specimens RW3, RW4, and RW5 are connected to the raft without grouting using 8mm, 10mm, and 12mm rods as shear connectors. RW6 is also connected to a raft without grouting with a 12 mm rod shear connector for earthquake loading.
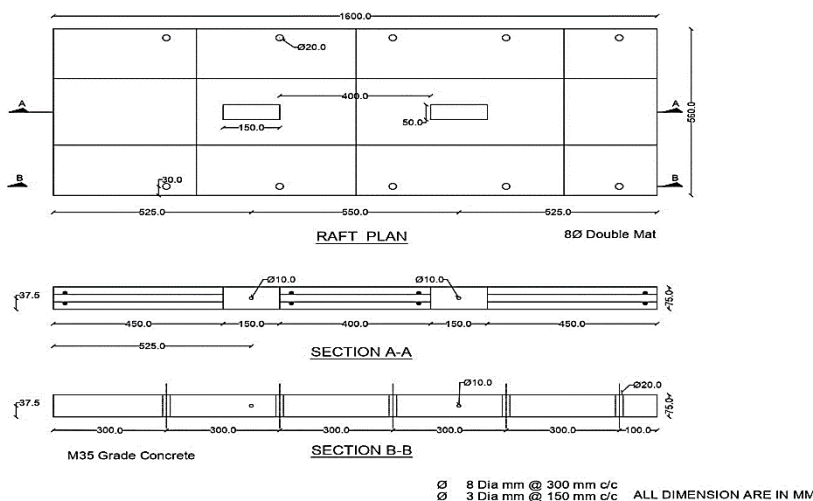
Fig. 5 Schematic representation of raft

Table 9. Casted specimens

Specimen	Representation
RW1	Wall raft without connector and no grouting
RW2	Wall raft without connector and with grouting
RW3	Wall-raft with shear connector 8mm
RW4	Wall-raft with shear connector 10mm
RW5	Wall-raft with shear connector 12mm
RW6	Wall-raft with shear connector 12mm and earthquake loading

WALL ELEVATION   WALL SECTION
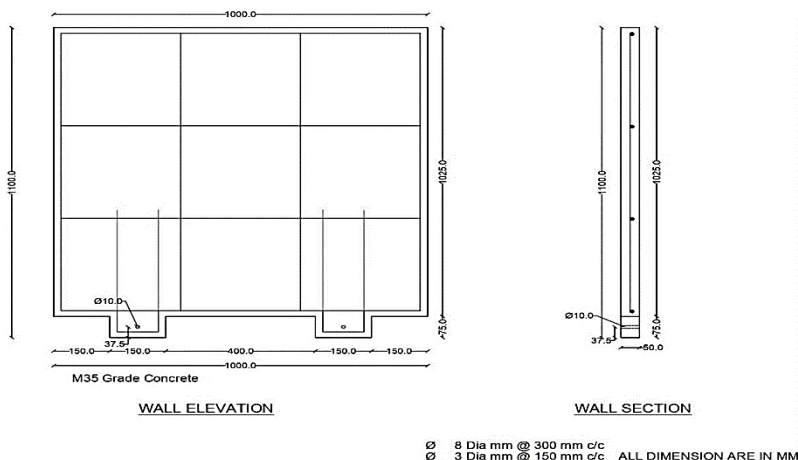
Fig. 6 Schematic representation of the wall
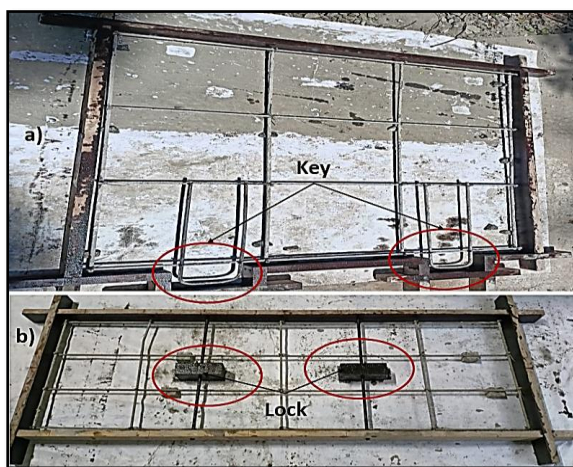
Fig. 7 Reinforcement detailing for a) wall, b) raft

3.3 Setup for the Experimental Investigation

The experimental work aims to examine the wall and raft connection behaviour under lateral loading by implementing cyclic load tests. An experimental arrangement was established to achieve this objective, consisting of loading devices, base fixtures, lateral supports, and instrumentation. Figure 8 shows a schematic of the loading test configuration used on the Raft-wall connection. The raft is mounted horizontally and is held in place by a fixed support.

Figure 9 depicts the instrumentation that included a data-collecting system utilised to observe the load-deformation behaviour. However, applying axial loads on the columns was not feasible in this study due to limitations in the available testing equipment and challenges associated with real-time force control. The experimental setup employed in this investigation is elucidated in the subsequent section.

Fig. 8 Experimental setup of the raft and wall connection
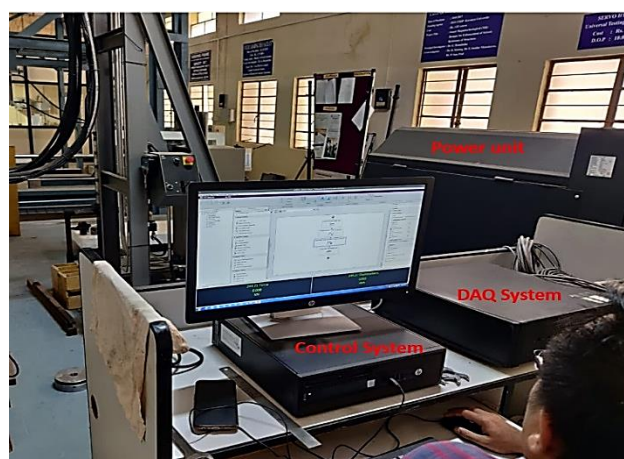
Fig. 9 Control system with DAQ

The experiment is being conducted at the Department of Civil Engineering's structural Engineering lab at the Karunya Institute of Technology and Sciences in Coimbatore, India. A servo-hydraulic system controls the actuator that is employed in the experiment. The actuator has a maximum stroke length of 125 mm in both directions and a capacity of 500kN (in tension and compression). The load cell and displacement transducer previously integrated inside the actuator made measuring the force and displacement produced by the actuator's piston easier.

On the other hand, the transverse wall is oriented vertically, and the wall tip is maintained in place by the actuator. This study's test methodology is similar to that utilized by Roy et al. [35], Park and Paulay [36], and Hakuto et al. [37] and differs where no axial force was applied to the raft throughout the testing. Each specimen is subjected to cyclical loading based on displacement. Figure 3 illustrates the control system and the DAQ system for data collection. ACI 374 states that for each level of increasing deformation, the number of cycles required to create damage equal to the number of cycles at a specific drift level must be doubled by at least two, and thus the applied displacement was repeated for 2 cycles throughout the experiment. The displacement was steadily increased during this study to obtain realistic inter-story drift-ratio of 0.5 percent, 0.7 percent, 1.0 percent, 1.5 percent, 2.0 percent, 3 percent, 4 percent, 5 percent, 6 percent, and 7 percent. Figure 10 shows the

displacement histories that were applied to all of the specimens similar to the loading pattern of Ebanesar et.al[38].
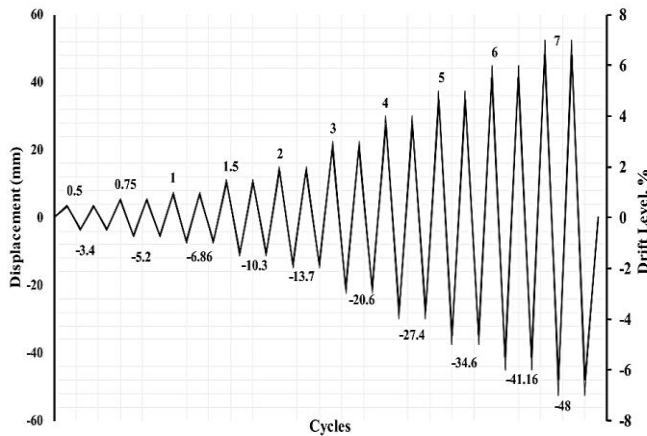
Fig. 10 Cyclic loading pattern for experimental purpose

3.4 Observation During The Experimental Investigation

While experimenting, some interesting observations concerning the various RW specimens emerged. The first cracks appeared at the key and lock interface of specimen RW1 at a drift-ratio of 0.7% (0.57 kN) of the third forward cycle. With increased loading, shear cracks are developed mainly in the key of the wall. No flexural cracks were observed on the RW joining faces during the experiment. The shearing in the joint and the raft caused degradation of the key in the specimen leading to failure. In the forward and reverse directions, the maximum lateral load was 1.22 kN and 2.27 kN, respectively.

Fig. 11 Observation from RW1 specimen   Fig. 12 Failure from RW1 specimen

The wall uplift can be seen in Figure 11, which was created because no grouting or connectors were used. This one exhibited significantly less restraint on its uplift movement than other specimens. It is observed that the wall is uplifted back and forth. The RW1 specimen experiences complete failure at the key, which was used for connection to the

raft footing. This failure occurs as the displacement increases. It was observed that the key had been completely distorted, as shown in Figure 12.

Fig. 13 Observation from RW2 specimen

Grouting is done in the gap between the wall panel and raft. The area grouted has been circled and presented in Fig 13 . As a high-strength, non-shrink, cementitious precision grout, Fosroc Conbextra GP2 is used as grouting material. In numerous industries, including construction and civil engineering, it is frequently employed for precise grouting and anchoring applications. Conbextra GP2 is renowned for its superior flow characteristics, high early and ultimate strengths, and chemical resistance.

For grouted specimen RW2, Cracks were observed all over the connecting face of the wall and the raft footing, which is depicted in Figure 13, which also shows the initial crack pattern. Because the damage was confined to the grouting mortar only, the specimen did not appear to have suffered any significant losses. The first cracks appeared in specimen RW1 during the first cycle, with drift-ratio of 0.7% (0.65kN) in the grouted area. With increased loading, these cracks spread throughout the grouted region. Under the applied load, there is a lack of confinement, and thus the shear cracks are visible in the key and lock region, causing structural deformation. The specimen's shear failure was caused by decreasing concrete strength in the joint core of the lock and key. The maximum lateral load in the forward and reverse directions was 1.72 kN and 3.95 kN, respectively.

The observations made by RW3, RW4, RW5, and RW6 were entirely dissimilar to those made by RW1 and RW2. For the specimens RW3, RW4, Rw5, and RW6, where connectors were used, the connector rod restricted the rocking movement as the displacement increased. In general, for specimens RW3, RW4, RW5, and RW6, hairline shear cracks were formed perpendicular to the key and lock joint region. The formation of shear cracks form whenever there is an increase in displacement, as shown in Figure 14. Figure 15 illustrates the initial failure of joints in the wall's key area and the raft footing's lock area. This phenomenon was observed for specimens that contained connector rods. It has been found that the initial shear cracks are always accompanied by the initial failure at the joints of the wall and the raft, which is later followed by the complete failure of the specimen, as shown in Figure 16.

Fig. 14 Shear crack from the specimen with connector

Fig. 15 Initial failure of RW joints with connector

Fig. 16 Complete failure of RW joints with connector

Shear cracks were produced at 2% drift-ratio for RW3 at a displacement of 13.69mm (forward first cycle). Hairline shear cracks were discovered in the raft footing face perpendicular to the joint region. The pinching length steadily rose until it reached a drift-ratio of 4%. Further cracks formed after the 5% DR and substantial damage was noticed in the joint area. After 5% drift, the raft wall interface widened, and concrete failure mode developed within the joint area. This specimen's maximum lateral load was 4.98 kN in the forward direction and 5.96 kN in the reverse direction. The specimen failed due to degeneration of the joint core, which was caused by deterioration of the lock-key joint region. For specimen RW4, under a load of 6.35 kN (3.5% drift-ratio), the first shear crack manifested itself in the third forward cycle. After increasing the load, cracks in the RW interface joint were found. Hairline shear cracks were seen on the face of the raft footing perpendicular to the joint region at a drift level of 3.5% (reversed first cycle) and a displacement of 20.78 mm. At the lock-key interface, the cracks widened at the same drift-ratio. A progressive increase followed the DR of 3.5% in the pinching length. After a drift-ratio of 4%, new cracks in the lock-key joint area appeared. After 5% drift-ratio, the RW join interface damage grew severely. This specimen could withstand a lateral force of up to 8.17 kN going forward and 8.04 kN backwards.

Ultimately, the specimen failed because the lock-key joint region of the concrete had failed. The initial shear crack appeared in the fourth forward cycle of specimen RW5 with a load of 7.59 kN (4.5% drift-ratio). Cracks in the RW joint contact were discovered after increasing the tension. At a drift-ratio of 4.5% (reversed fourth cycle) and a displacement of 26.88 mm, the raft footing face perpendicular joint region revealed hairline diagonal cracks. With the same drift-ratio, the fissures grew at the lock-key interface. A steady rise in pinching length after 4.5% drift-ratio. Severe cracks in the lock-key joint area were discovered after a 5% drift-ratio.

The RW joint interface damage increased significantly after 5% drift-ratio. This specimen could bear lateral forces of up to 9.82 kN in the forward direction and 10.23 kN in the reverse direction. Finally, the specimen failed because the concrete's lock-key joint region collapsed. To better understand the RW behaviour, specimen RW6 was subjected to data from the El Centro earthquake. During the process of installing the system, the time-history data for El-Centro was supplied by the MTS corporation. The specimen achieved a maximum load of 3.65 kN when moving in a forward direction and 6.36 kN when moving in a backward direction. The maximum displacement that the specimen goes through is 9.27 mm in the forward direction and 12.92 mm in the reversed direction. It was found that the lock-key interface region had sustained considerable damage comparable to the damage sustained by the earlier specimens that contained the connector rod.

Under the experimental results, using steel rods as shear connectors in RW joints significantly increased the load-deflection behaviour. All specimens outperform the control specimens in RW1 and RW2. The specimens RW1 and RW2 fail with complete deterioration of the key but minor damage to the lock region. In contrast, the specimens with steel rods of any diameter as shear connectors fail with initial shear cracks perpendicular to the key-lock joint on the face of the raft footing and complete failure due to severe deterioration of both the key-lock and the region around the joints. Two significant findings were observed: (a) a delay in key-lock joint deterioration in specimens with connector rods compared to specimens without connectors. (b) When the diameter of the connector rod is increased, shear fracture formation is delayed, resulting in the complete deterioration of the lock-key joint. Figure 16 depicts the generalized failure of the specimens RW3, RW4, RW5, and RW6. More micro fractures are found in these specimens in the early stage as the drift-ratio increases by 3.5%. The cracks in the RW joint interface become severe and waste more energy.

4. Results and Discussion

Figure 17-Figure 21 compares the performance of RW joints in terms of force-displacement curves and the hysteresis curves acquired from experimental observations and FEA analysis for all specimens. It is evident from the hysteresis plots that the experimental and FEA models agree with each other with an error lesser than 10%, which is acceptable in comparison[4-6][13][24]. The values obtained from the FEA model are presented in the table for comparison purposes. This strengthening technique improves the ultimate load-carrying capacity of RW with shear connectors strengthened specimens over reference specimens while also lowering shear demand. RW5 was found to yield the maximum performance. The maximum load-carrying capacity of the strengthened RW5 specimen was 9.82 kN in the forward direction and 10.23 kN in the reversed direction. It is inferred from Figure 9 that after a displacement of 42mm in the opposite direction, the load begins to fall. It is possible to conclude that lock-key joint failure occurs later in strengthened specimens than in specimens without connectors.
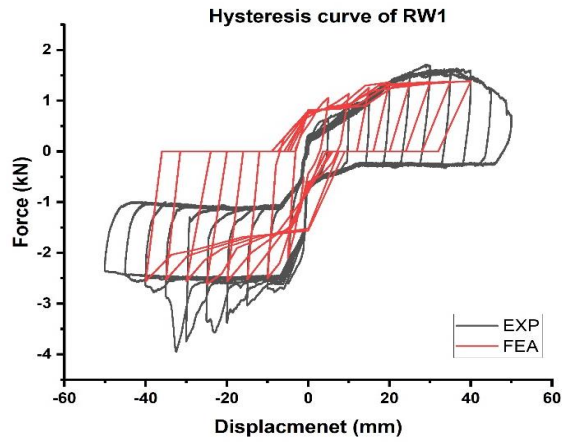
Fig. 17 Hysteresis plot for RW1(no connector)
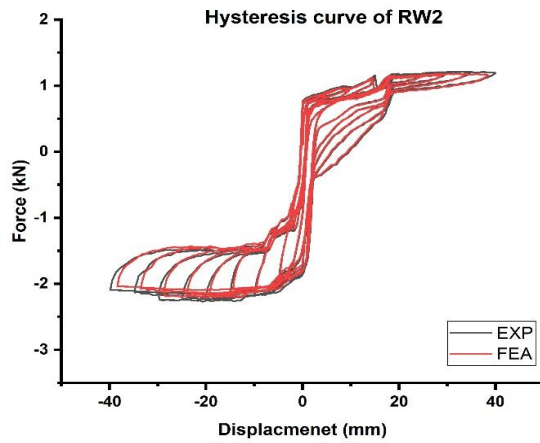
Fig. 18 Hysteresis plot for RW2(with Grouting)
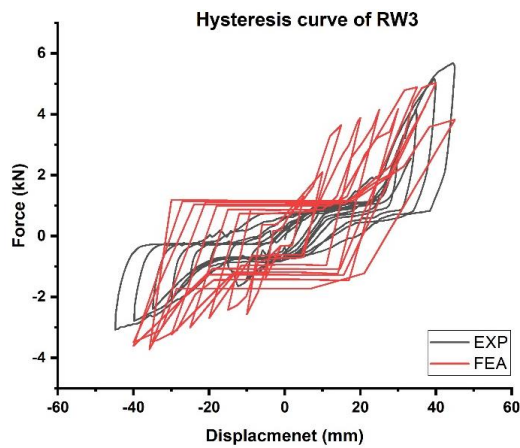
Fig. 19 Hysteresis plot for RW3(8mm connector)
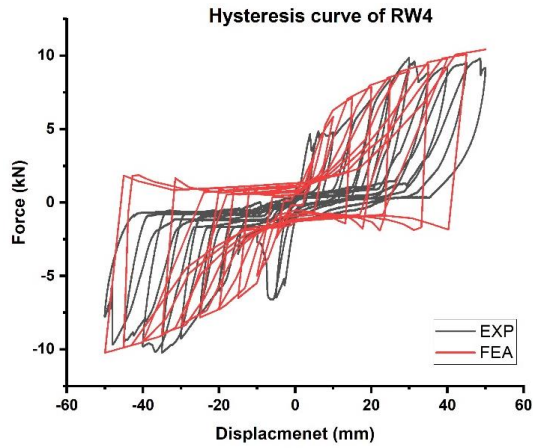
Fig. 20 Hysteresis plot for RW4(10mm connector)
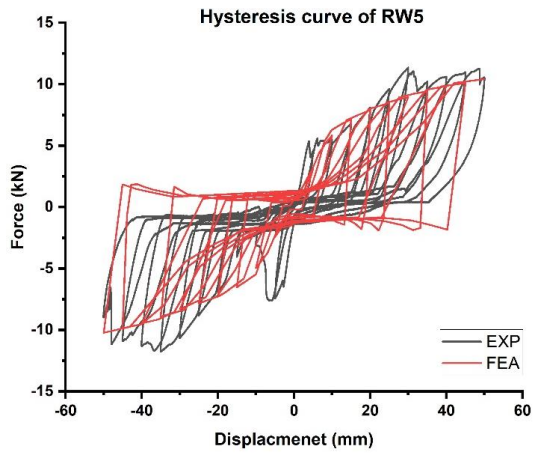
Fig. 21 Hysteresis plot for RW5(12mm connector)
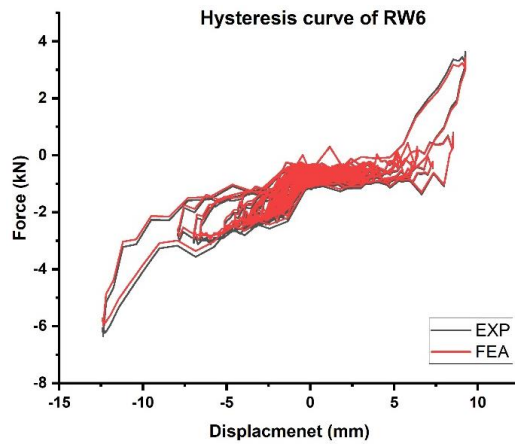
Fig. 22: Hysteresis plot for RW6(12mm connectors)

The grouted specimen RW2 and specimens with steel rod connectors, RW3, RW4, RW5, and RW6, have a load-carrying capacity increase of 39.32%,67.42%,78.77%,82.84%, and 65.63% over the specimens without grouting or any connector rods (RW1). According to the test results, adding steel rods as shear connector reinforcement significantly increases the load-bearing ability. Therefore, shear connectors in RW joint-strengthened specimens would suit RC constructions in seismically active regions. The results from the study discussed above have been tabulated in Table 10 for a clear view of the change in the load-carrying capacity of the RW under cyclic loading.

Table 10. Capacity for lateral loads

Spec.	Initial Shear crack (kN)	Initial Shear crack disp. (mm)	Experimental Model		FEA Model		Percentage Varition	
			Max load+ve (kN)	Max load-ve (kN)	Max load+ve (kN)	Max load-ve (kN)	Max load+ve (%)	Max load-ve (%)
RW1	0.52	5.23	1.22	2.27	1.19	2.15	2.45	5.28
RW2	0.96	8.36	1.72	3.95	1.68	3.88	2.32	1.77
RW3	1.24	13.69	4.98	5.66	4.55	5.21	8.63	7.93
RW4	1.58	20.78	8.17	8.04	8.25	8.12	0.96	0.98
RW5	1.63	26.88	9.82	10.23	9.98	10.63	1.60	3.76
RW6	1.91	12.92	3.65	6.36	3.55	6.45	2.73	1.39

The energy dissipation capability of a structure is a crucial factor to consider when assessing how well it performs when subjected to seismic excitations. The utilisation of transverse shear reinforcement as a shear connector resulted in a notable increase in the peak load-carrying capacity of the specimen. This increase was directly proportional to the more excellent energy dissipation exhibited by the specimen[39]. Consequently, energy dissipation without a considerable loss of stiffness or strength indicates the structure's capability. A structure can release more energy by supplying enough inelastic deformation in a key area or enough ductility in its connections. The energy dissipation capacity is defined as the region under the hysteresis loop for each load cycle.
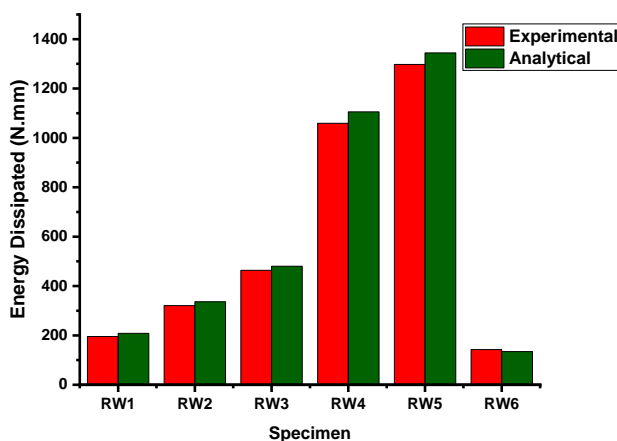
Fig. 23 Energy dissipation plot

Cumulative energy dissipation may be computed by adding the load-displacement loop throughout the test. Fig. 23 shows the usual cumulative energy determined from the area under the force-displacement curves of test specimens. The following equation was used to calculate how hysteretic energy dissipation was standardized to the area of an elastic perfectly-plastic rectangular block at each load cycle[40,41]:

$ED = \frac{A}{4*Vmax.\delta max}$ or normalized ED. A = region encircled by the hysteresis loops, V_{max} = maximum load, and δ_{max} = maximum displacement in positive and negative directions during the ultimate cycle.

Maximum ED observed from the experimental and FEA model findings is tabulated in Table 11 for a clear understating.

Table 11. Energy dissipated by the specimens

Specimen	Energy Dissipation (N-mm)		Percentage Varition(%)
	Experimental	FEA Model	
RW1	195.41	208.43	6.24
RW2	320.65	336.29	4.65
RW3	463.78	480.23	3.42
RW4	1059.23	1105.64	4.19
RW5	1297.48	1344.43	3.49
RW6	142.49	134.28	5.76

It can be inferred that with an increment in the diameter of the steel rod connector, the energy dissipating capacity of the raft wall connection increases and, thus, resistance to seismic forces.

5. Conclusions

The present study examines the precast reinforced concrete walls using the grouting technique and steel rods as shear connectors subjected to cyclic loading conditions. A total of six RW joint specimens were developed following the stipulations outlined in Indian codal provisions(IS 456:2021). The specimens subjected to cyclic loadings were equipped with grouting and shear connectors. The testing parameters of the study encompass load-carrying capacity, hysteresis responses, and crack patterns. The analysis conducted in this study yielded the subsequent conclusions:

- The hysteresis behaviour and energy dissipation capacity of the Finite Element Analysis (FEA) model are verified through experimental validation with a variation of less than 10%.
- The Finite Element Analysis (FEA) and experimental testing findings demonstrate a direct correlation between the addition of shear connector rod diameter and the corresponding enhancement in load-carrying capacity.
- The load-carrying capacity of the specimen utilising a 12mm steel rod as a shear connector (RW5) exhibited a maximum increase of 82.84% when compared to the standard specimen. The reinforced specimens (RW2, RW3, RW4, and RW6) exhibited notable performance improvements, with gains of 39.32%, 67.42%, 78.77%, and 65.93%, respectively.
- In the specimens where shear connectors were employed, shear cracks were observed perpendicular to the wall key. An increase in shear connectors' diameter leads to a reduction in the width of shear cracks. Typically, the failure of specimens featuring shear connectors can be ascribed to the degradation of the wall key inserted within the raft footing.

- In conclusion, the steel rod connector proposed for the RW joint presents an alternative configuration that exhibits improved performance when subjected to cyclic and seismic loads. Moreover, the proposed utilisation of steel rods as shear connections represents an innovative approach to enhance the structural integrity of the existing RW precast connection. Furthermore, when comparing the specimen utilising a steel rod as a shear connection to the reference specimen, it is observed that the former exhibits a relatively less substantial level of damage.

- The results obtained from this study can be utilised as a foundation for subsequent verification and enhancement of the suggested method for strengthening. Future research may consider conducting theoretical approaches to validate the obtained results and evaluate the performance of the RW joint under different loading conditions. To ascertain the sustained efficacy of the proposed reinforcement method, it is imperative to conduct a comprehensive assessment of its long-term durability. Subsequent investigations could potentially prioritise evaluating the durability of the grouting material and shear connectors concerning various environmental influences, including moisture, corrosion, and ageing. This would be done to guarantee the long-term effectiveness of the RW joint when implemented in practical scenarios.

Acknowledgement

References

[1] Arthi S, Jaya KP. Experimental study on shear behaviour of precast shear wall-slab dowel connection. Asian J Civ Eng. 2020;21(4):663-76. https://doi.org/10.1007/s42107-020-00229-z

[2] Arthi S, Jaya KP. Hysteresis behaviour of precast shear wall-slab connection under reverse cyclic loading. In: IOP Conference Series. IOP Conf Ser.: Mater Sci Eng (Vol. 936, No. 1, p. 012039). 2020, September;936(1). https://doi.org/10.1088/1757-899X/936/1/012039

[3] Arthi S, Jaya KP. Seismic performance of precast shear wall-diaphragm connection: a comparative study with monolithic connection. Int J Civ Eng. 2020;18(1):9-17. https://doi.org/10.1007/s40999-019-00444-z

[4] Soleimani-Abiat MR, Banan M. Seismic behavior of RC building by considering a model for shear wall-floor slab connections. Comput Concr. 2015;16(3):381-97. https://doi.org/10.12989/cac.2015.16.3.381

[5] Brunesi E, Nascimbene R. Experimental and numerical investigation of the seismic response of precast wall connections. Bull Earthquake Eng. 2017;15(12):5511-50. https://doi.org/10.1007/s10518-017-0166-y

[6] Brunesi E, Peloso S, Pinho R, Nascimbene R. Cyclic testing of a full-scale two-storey reinforced precast concrete wall-slab-wall structure. Bull Earthquake Eng. 2018;16(11):5309-39. https://doi.org/10.1007/s10518-018-0359-z

[7] Brunesi E, Peloso S, Pinho R, Nascimbene R. Cyclic tensile testing of a three-way panel connection for precast wall-slab-wall structures. Struct Concr. 2019;20(4):1307-15. https://doi.org/10.1002/suco.201800280

[8] Brunesi E, Peloso S, Pinho R, Nascimbene R. Shake-table testing of a full-scale two-story precast wall-slab-wall structure. Earthquake Spectra. 2019;35(4):1583-609. https://doi.org/10.1193/072518EQS184M

[9] Chalot A, Roy N, Michel L, Ferrier E. Mechanical behavior of a full-scale RC wall-slab connection reinforced with frp under cyclic loading. Eng Struct. 2021;239:112146. https://doi.org/10.1016/j.engstruct.2021.112146

[10] Devine F, Olund O, Elwood K, Adebar P. Seismic performance of concrete tilt-up buildings: current wall-to-slab connections. In: Proceedings of the 14th. Beijing, China: World Concrete on Earthquake Engineering; 2008. p. 12-7.

[11] Guo W, Zhai Z, Cui Y, Yu Z, Wu X. Seismic performance assessment of low-rise precast wall panel structure with bolt connections. Eng Struct. 2019;181:562-78. https://doi.org/10.1016/j.engstruct.2018.12.060

[12] Hamicha A, Kenea G. Investigation on the effect of geometric parameter on reinforced concrete exterior shear wall-slab connection using finite element analysis. Adv Civ Eng. 2022;2022:1-17. https://doi.org/10.1155/2022/4903650

[13] Hemamalini S, Vidjeapriya R, Jaya KP. Performance of precast shear wall connections under monotonic and cyclic loading: A state-of-the-art review. Iran J Sci Technol Trans Civ Eng. 2021;45(3):1307-28. https://doi.org/10.1007/s40996-020-00530-6

[14] Henry RS, Ingham JM, Sritharan S. Wall-to-floor interaction in concrete buildings with rocking wall systems. In: Proceedings of the NZSEE Annual Conference. Christchurch, New Zealand; 2012, April.

[15] Krentowski JR, Knyziak P, Mackiewicz M. Durability of interlayer connections in external walls in precast residential buildings. Eng Fail Anal. 2021;121:105059. https://doi.org/10.1016/j.engfailanal.2020.105059

[16] Lu Y, Chen W, Xiong F, Yan H, Ge Q, Zhao F. Seismic performance of a full-scale two-story bolt-connected precast concrete composite wall panel building tested on a shake table. J Struct Eng. 2021;147(12):04021209. https://doi.org/10.1061/(ASCE)ST.1943-541X.0003183

[17] Pavel F, Vacareanu R, Marcu D. Seismic performance assessment and rating for a flat-slab RC core wall structure in Bucharest, Romania. Structures. 2021, June;31. https://doi.org/10.1016/j.istruc.2021.02.036

[18] Pavese A, Bournas DA. Experimental assessment of the seismic performance of a prefabricated concrete structural wall system. Eng Struct. 2011;33(6):2049-62. https://doi.org/10.1016/j.engstruct.2011.02.043

[19] Rossley N, Aziz FNAA, Chew HC. Behaviour of precast walls connection subjected to shear load. J Eng Sci Technol. 2014;10:142-50.

[20] Shen SD, Cui Y, Pan P, Gong RH, Miao QS, Li WF. Experimental study of RC prefabricated shear walls with shear keys affected by a slotted floor slab. J Aerosp Eng. 2019;32(3):04019013. https://doi.org/10.1061/(ASCE)AS.1943-5525.0001000

[21] Shen Y, Ni Z, Ai T, Dai M, Jiang B. Experimental study on postfire behavior of a novel assembled wall-slab joint. Adv Struct Eng. 2023;26(6):1142-58. https://doi.org/10.1177/13694332231153939

[22] Singhal S, Chourasia A. Joint connections for precast structural concrete components. In: 16th Symposium on Earthquake Engineering; 2018, December.

[23] Singhal S, Chourasia A. Seismic resistance of precast reinforced concrete shear wall: experimental and analytical study. In: Proceedings of the 8th int engineering symp. Kumamoto, Japan. Kumamoto University; 2019, March.

[24] Singhal S, Chourasia A, Chellappa S, Parashar J. Precast reinforced concrete shear walls: state of the art review. Struct Concr. 2019;20(3):886-98. https://doi.org/10.1002/suco.201800129

[25] Singhal S, Chourasia A, Kajale Y, Singh D. Behaviour of precast reinforced concrete structural wall systems subjected to in-plane lateral loading. Eng Struct. 2021;241:112474. https://doi.org/10.1016/j.engstruct.2021.112474

[26] Singhal S, Chourasia A, Panigrahi SK, Kajale Y. Seismic response of precast reinforced concrete wall subjected to cyclic in-plane and constant out-of-plane loading. Front Struct Civ Eng. 2021;15(5):1128-43. https://doi.org/10.1007/s11709-021-0753-5

[27] Tatsambon L, Massé N, Hervé-Secourgeon E, Hervé-Secourgeon G, Théodore CÉ. Impact of a hybrid modelling for wall/wall and wall/slab connections on the constructability of reinforced concrete nuclear building; 2022.

[28] Vaghei R, Hejazi F, Firoozi AA, Jaafar MS. Performance of loop connection in precast concrete walls subjected to lateral loads. Int J Civ Eng. 2019;17(3):397-426. https://doi.org/10.1007/s40999-018-0366-0

[29] Vaghei R, Hejazi F, Taheri H, Jaafar MS, Ali AAA. A new precast wall connection subjected to monotonic loading. Comput Concr. 2016;17(1):1-27. https://doi.org/10.12989/cac.2016.17.1.001

[30] Wang J, Kusunoki K. Study on the flexural strength of interior thick wall-thick slab joints subjected to lateral force using finite-element analysis. Buildings. 2022;12(5):535. https://doi.org/10.3390/buildings12050535

[31] Xia K, Hu X, Xue W. Experimental studies on in-plane connections of composite beam-precast concrete shear wall under reversed cyclic loading. Structures. 2021, December;34. https://doi.org/10.1016/j.istruc.2021.08.127

[32] Zenunović D, Folić R. Models for behaviour analysis of monolithic wall and precast or monolithic floor slab connections. Eng Struct. 2012;40:466-78. https://doi.org/10.1016/j.engstruct.2012.03.007

[33] IS: 1489 (Part 1)-1991. Portland-Pozzolana Cement specification Part 1, Fly ash based. New Delhi: Bureau of Indian Standards.

[34] IS: 383-1970. Specification for coarse and fine aggregates from natural sources concrete. New Delhi: Bureau of Indian Standards.

[35] Park R, Paulay T. Reinforced concrete structures. New York: John Wiley & Sons; 1975. https://doi.org/10.1002/9780470172834

[36] Hakuto S, Park R, Tanaka H. Retrofitting of reinforced concrete moment resisting frame. Res Reprod. 1995;95-4:1.

[37] Roy B, Laskar AI. Cyclic behavior of in-situ exterior beam- column subassemblies with cold joint in column. Eng Struct. 2017;132:822-33. https://doi.org/10.1016/j.engstruct.2016.12.001

[38] Ebanesar A, Gladston H, Farsangi EN, Sharma SV. Strengthening of RC beam-column joints using steel plate with shear connectors: Experimental investigation. Structures 2022; 35: 1138-1150. https://doi.org/10.1016/j.istruc.2021.08.042

[39] Rath, B., Garoma, S., Kudama, R. et al. Effect of different width ratio and transversal link pattern on the load carrying capacity of partially encased composite column. Asian J Civ Eng. 2023; 24: 205-218. https://doi.org/10.1007/s42107-022-00498-w

[40] Shannag MJ, Abu-Dyya N, Abu-Farsakh G. Lateral load response of high performance fiber reinforced concrete beam-column joints. Constr Build Mater. 2005;19(7):500-8. https://doi.org/10.1016/j.conbuildmat.2005.01.007

[41] Siva Chidambaram R, Agarwal P. Seismic behavior of hybrid fiber reinforced cementitious composite beam-column joints. Mater Des. 2015;86:771-81. https://doi.org/10.1016/j.matdes.2015.07.164

Research Article

Evaluating the SWS bolted connection strength of Bitis wood

Erwan Sukarman[1,a], Abdul Razak Abdul Karim[*1,b], Norazzlina M.Sa'don[1,c], Abdul Azim Abdullah[1,d], Siti Hanim Sahari[2,e], Nur Liza Rahim[3,f], Pierre Quenneville[4,g]

[1]Faculty of Engineering, Universiti Malaysia Sarawak (UNIMAS), Malaysia
[2]Research, Development and Innovation Division, Forest Department Sarawak (FDS), Malaysia
[3]Faculty of Civil Engineering Technology, Universiti Malaysia Perlis (UniMAP), Malaysia
[4]Faculty of Engineering, The University of Auckland (UoA), New Zealand

Article Info	Abstract
	The current study was conducted to evaluate the strength of the steel-wood-steel (SWS) bolted connections of Bitis wood. The wood was chosen because it is commonly used as the structural elements of the as-built floor and roof diaphragms in Malaysian unreinforced masonry (URM) buildings. This present work was performed to continue the initiation of the wood database development for the purpose of retrofitting the wall-diaphragm connections of the URM building. The bolted connection testing was the main experimental investigation, where a total of eighteen groups of different connection configurations were tested, each consisting of ten specimens. The embedding strength tests, moisture content and density tests were also conducted to determine the wood's basic properties. The results obtained from this experimental study were utilized for verifying the prediction effectiveness of the existing design equations, namely the Malaysian Timber Standard (MS544-5), the European Yield Model (EYM), and the Row Shear Model (RSM). From the comparison made between the prediction values and the experimental results, the MS544-5 was found to be too conservative, whereas a combination of the EYM and RSM is recommended for predicting the bolted connection strength of the Bitis wood.

1. Introduction

It has long been recognized that the main issue with the as-built characteristic of an unreinforced masonry (URM) building is the discontinuity between its vertical and horizontal structural elements. An absence of the connection between the masonry walls and the timber floor diaphragms was found to be the main weakness causing the building to perform poorly in resisting the lateral load from earthquakes [1, 2, 3]. Thus, all countries over the world that still have this type of buildings must seriously confront retrofitting interventions due to the locality of these buildings that can be easily found in the main city areas, which typically use as commercial or residential purposes. Many reconnaissance reports [4, 5, 6] on damaging earthquakes show various catastrophic failures of masonry construction, supporting the claim that the unreinforced masonry buildings are not only dangerous to the occupants but also to the nearby pedestrians, including the neighboring public and private properties. All major collapses of masonry walls are mainly caused by the lack of wall-diaphragm connections. Therefore, this present study was carried out to continue the initiation of [7, 8, 9] in developing the wood database for the design of wall-

diaphragm connections to retrofit the URM buildings. The wall-diaphragm connections are comprised of two major parts, which are the wall anchorages and the diaphragm connections [10, 11, 12, 13]. The former can be in the form of a through-bolt anchor connected with an external bearing plate or a dowel-type anchor drilled into the wall. The latter is typically a bolted steel cleat to the timber floor joists or to the timber roof rafters. Because the design details of the latter part are not provided by [12, 13], the next discussion focuses on the existing Malaysian timber code, in particular the bolted joint design procedures.

Referring to the Malaysian Timber Standard (MS544-5) [14] under clause 11.2.3, it outlines an equation to determine the permissible load, F_{adm}, of a bolt system loaded parallel to grain. The equation is given by:

$$F_{adm} = k_1 k_2 k_{16} k_{17} F \tag{1}$$

where, k_1: Factor of duration of load given in Table 4 of [14], k_2: Factor of 1.0 for dry timber or 0.7 for wet timber, k_{16}: Factor of 1.25 for the bolts that transfer load through metal side plates of adequate strength and the bolts are a close fit to the holes in these plates provided that $b/d > 5$ (where b denotes the effective timber thickness and d is the bolt diameter) or 1.0 otherwise, k_{17}: Factor for multiple bolted connections given in Table 15 of [14], F: Basic working load as derived in clause 11.2.2 of [14]. From clause 11.2.2 of [14], it can be seen that the design method considers only a ductile failure mode. The standard only reflects a brittle failure mode by applying the k_{17} value of less than one for connections with five bolts and more. This is not in agreement with the international timber engineering community because the criteria in the timber standards to determine the capacity of bolted joints shall be from an established mechanical model that is capable of identifying each conceivable failure mechanism [15]. Many published works [16, 17, 18, 19, 20] found that the geometric configurations of the bolted joints, such as the end distance, e_t, and spacing between bolts, s_b, can significantly control the mode of failure. From [7, 8, 9, 21, 22], the standard was identified as providing a very conservative design capacity for bolted joints in local hardwoods like Meraka and Nyatoh. Thus, this present experimental work continues the bolted connection study on the Bitis wood evaluation.

Besides utilizing the experimental data of the bolted connection on the Bitis wood for evaluating the effectiveness of the existing timber standard of the MS544-5 [14], this current study also examines the efficiency of the European Yield Model (EYM) and Row Shear Model (RSM). The EYM represents the mechanical models of the ductile failure mode developed by Johansen [23], whereas the RSM demonstrates the mechanical models of the brittle failure mode established by Quenneville [15]. Details of both design equations of the EYM and RSM can be found in [9], but herein the authors highlight and discuss the important parameters involved in both theories. In each possible failure mode as per EYM theory, the most important parameter in the design equation for determining the resistance of bolted timber joints, R, is the embedding strength of the wood, denoted as f_h. The absence of this parameter in the existing code of MS544-2 [24] makes the efficacy valuation of the EYM theory to estimate the bolted connection strength on local hardwood is impossible to be assessed. Besides providing the test data on bolted connection strength of local hardwood that was also found to be very limited, this present study conducted the embedding strength test on Bitis wood using the ISO/DIS 10984-2 [25] for the use of the EYM efficiency verification.

For the design equation in the RSM theory, the authors focus the discussion on the parameters of the wood shear strength parallel to the grain, f_v, and the calibration factor, CF. From [8], it was identified that the f_v value can be taken directly from Table 4 of [24]. However, it makes the prediction capacity of RSM became unacceptably under-designed. The use of the correlation of the f_v equivalent to $17.8G^{1.24}$, which can be obtained from Table

4-11a of the Wood Handbook [26], was recommended. Thus, this present study provides the density of Bitis in accordance with AS/NZS 1080.3 [27]. Note that G in the f_v correlation is the specific gravity of the wood. The calibration factor is another parameter to consider in the RSM design equations. From [9] and [22], it can be seen that different woods have a specific CF in order to optimize the design strength of timber bolted connections. Because of that, this present study also recommends a specific CF to be used for the bolted timber joints of Bitis wood.

From the above discussion, this present study is not only providing the design parameters of Bitis Wood and adding its bolted connection results to the database as per the prior works of [7, 8, 9, 21, 22], but also recommending a set of enhanced design equations for the timber bolted connections of local hardwoods to assist the engineers in designing an optimized retrofit solution of wall-diaphragm connections for the URM buildings. The readers of this article should also be informed that this current study considers the critical part of the wall-diaphragm connections to be the diaphragm connection, which is the bolted joint on the timber floor and roof diaphragms. Therefore, it is assumed to fail before the masonry brick wall and the timber floor or roof diaphragms.

2. Selection of Wood Material and Wood Identification

Since the focus of this current study is on the bolted joint design of the structural components of joists or rafters of floor and roof diaphragms in URM buildings, respectively, the selection of wood materials to be tested in the experimental works is crucial. From Table 3 of MS544-2 [24], it can be seen that Bitis is categorized under the strength group SG1, which is commonly used as structural components such as joists and rafters, as stated by the Malaysian Timber Industry Board [28]. From Table B1 of MS544-2 [24], there are common cross-sectional sizes of structural timbers in Malaysia. Also, to select the typical domestic rafters and joists sizing, a cross-checked was done by referring to [29] and [30], respectively. Based on the above findings, a Bitis wood measuring 50 mm in breadth, b, and 100 mm in depth, d, was chosen for this present study. Table 1 below provides an extract of the information on Bitis obtained from Table A1 of MS544-2 [24].

Table 1. Information on Bitis wood [24]

Class	Std. Name	Other Common Name	Species yielding the timber	Density at 19% Moisture Content (kg/m³)	Specific Gravity	Color
Heavy Hardwood	Bitis	Nyatoh batu	Madhuca utilis, Palaquium ridleyi and P. stellatum	1100	0.98	Red-brown or purple brown

To ensure the right wood specimen was tested in this study, a wood genus verification was conducted using the end-grain microscopic examination technique. The similar steps of the specimen preparation outlined in [21] were adopted in this current study for obtaining the wood sample end-grain at a magnification of 20 times (20x), as shown in Fig. 1(a). From Fig. 1(a), the microscopic anatomical characteristics of the wood sample can be identified. It can be seen that the pore size is small (< 50 μm) with a pore frequency of very few (< 5 pores/mm²) to few (5-20 pores/mm²). The pore arrangement is in multiples of 2-6 pores and oriented in the vertical (radial) direction. A growth of tyloses, which sometimes closes off the pores completely, is common. The wood parenchyma is separated from the

pores (apotracheal), which are identified as being in a joined parenchyma (diffuse-in-aggregates). This can be clearly seen by the formation of thin lines oriented in the horizontal (tangential) direction. The radial cells (rays), which are more-or-less straight lines, can be observed at a close (14-20 rays/mm) spacing. The presence of thin lines formed by both parenchyma and rays in a closely spaced pattern is also very apparent. This is known as a reticulate (net-like or grid-like) pattern. All readers are suggested to refer to [31] for definitions of some terms used in this article to describe the microscopic anatomical characteristics, as this article does not provide those definitions. A summary of the terms used can also be found in [21].

From the above descriptions of the microscopic anatomical characteristics of the wood sample, similar characteristic details can be found in [32] as shown in Fig. 1(b). The characteristic descriptions of the wood sample can also be similarly gathered from the genus of *Madhuca* outlined by [33]. From this comparison, the wood sample used in the present study was verified as Bitis wood from the genus of *Madhuca* spp. under the family of *Sapotaceae*. The reader of this article should be aware that the wood identification conducted herein was only confirmed to the genus level, which is specified by the spp. abbreviation that indicates species in plural form. In other words, more than one or some species falls under the same genus. The identification of the particular species is beyond the scope of this present research work.

| (a) wood sample | (b) Bitis |
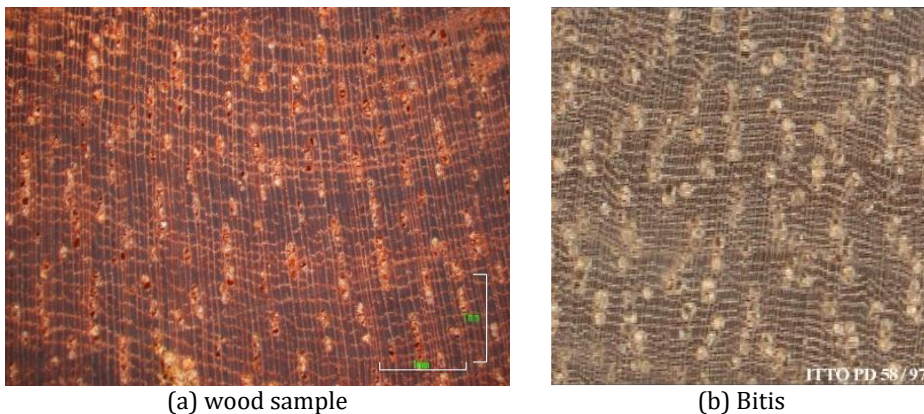
Fig. 1. End-grain sections (20x) (a) from this present study, and (b) from [32]

3. Testing Program

This section describes the main bolted connection testing conducted to determine the strength of bolted connections in Bitis wood. The explanation includes specimen preparation and configuration details, as well as the experimental setup and procedures. The tests for determining the wood properties, such as embedding strength, f_h, and density, are also included as both are very important parameters for EYM and RSM predictions as per mentioned in Section 1 of this article, respectively. The wood density test was performed as per requirement of AS/NZS 1080.3 [27]. For the monitoring of water contents in all wood specimens, the moisture content test was also conducted in accordance with the procedures given in AS/NZS 1080.1 [34].

3.1. Bolted Connection Test

3.1.1 Specimen Preparation and Configuration Details

For the bolted connection testing, a total of eighteen groups of bolted connection specimens were prepared, with each group consisting of ten replicates. The supply of wood

was in the form of rough-sawn timber planks with a cross-sectional area of 50 mm in width and 100 mm in height. All specimens in each group were ensured to be prepared from a different plank of timber supply so as to reduce the possibility of extracting the specimen from the same tree. Even a different timber plank can be from the same tree, but by applying this precautionary measure during the specimen preparation, it can at least increase the variations of the wood samples to be tested. Every specimen was fabricated with duplicated connection details at both extremities, with l_4 (refer to Fig. 2) not to be less than 30×d as per requirement stated in [25]. Because a 13-mm-diameter mild steel bolt was used in this present study, the distance to ensure two independent connections at both ends of each specimen, l_4, must not be less than 390 mm. However, the authors decided to round the l_4 into 400 mm for all specimens. Since the height of the timber plank used was 100 mm, a single row bolted connection was applied to all specimens because the a_1 must not be less than 3×d (39 mm) in accordance to [25]. Due to the focus of the study was on the one row bolted connection, only the row shear failure was considered to be the critical brittle failure mode in comparison to other failures such as group tear-out, splitting, and net tension specified in [15]. The specimen configuration details of each connection group tested can be obtained from Table 2. An illustration of the variables used in the specimen preparation of bolted connections is provided in Fig. 2.

Table 2. Bolted connection specimen configuration details

Group	End distance, e_t (mm)	Spacing of bolts, s_b (mm)	Number of bolt, n_f
1	150	-	1
2	125	-	1
3	100	-	1
4	75	-	1
5	50	-	1
6	150	100	2
7	125	100	2
8	100	100	2
9	75	100	2
10	50	100	2
11	150	50	2
12	125	50	2
13	100	50	2
14	75	50	2
15	50	50	2
16	100	50	3
17	75	50	3
18	50	50	3
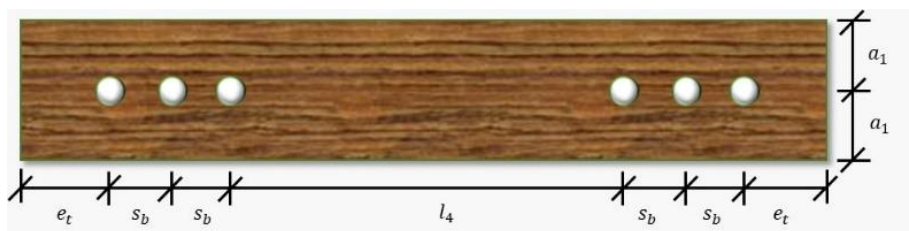
Fig. 2. Illustration of variables used

3.1.2 Experimental Setup and Procedures

Each bolted connection specimen was tested in the form of a steel-wood-steel (SWS) arrangement, in which this double shear connection sandwiched the timber specimen with two mild steel plates on both sides. The plates used were 16 mm thick and made from mild steel with a 400 MPa ultimate tensile strength in order to ensure a rigid test rig can be achieved. A mild steel bolt and nut graded 4.6, which varies in number for each connection group tested, was used to fasten the SWS specimen by applying only a finger-tight force to the nut. All specimens were loaded in tension parallel to the timber grain direction using a 300 kN universal testing machine. Through the side steel plate at both connection ends that were attached to the testing machine, a static force with a displacement rate of approximately 1 mm per minute was applied until any of the extremities reached their ultimate capacity as per the recommendation of ISO 6891 [35]. A force-displacement data set collected for each specimen was recorded to obtain the maximum strength of the tested bolted connection specimen. A failure mode observed on every tested specimen of bolted connections was also identified. The failure pattern on the tested specimen was clearly marked and photographed.

3.2. Tests of Wood Properties

3.2.1 Embedding Strength Test

The test specimens for the embedding strength determination were extracted from the timber bolted connection strength tested specimens. In ISO/DIS 10984-2 [25], the minimum height of the embedding test specimen must not less than 7×d (91 mm). Thus, all specimens were prepared with 100 mm height as shown in Fig. 3. In order to ensure the test piece was uniformly loaded, a 13-mm-diameter bar with 70 mm length made from stainless steel was used.
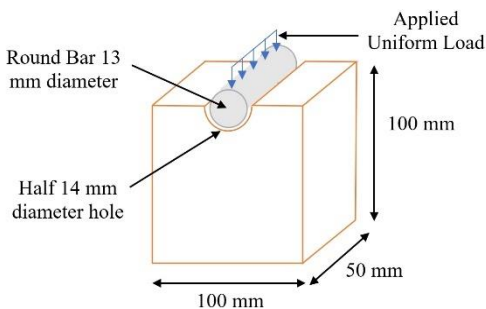
Fig. 3 Illustration of the test piece   Fig. 4 Embedding strength test setup

A static compression load with a rate of 1 mm per minute was applied in this test until the wood specimen fails. If the bar is fully compressed into the half 14-mm-diameter hole of the test piece, the load was observed to keep on continue to increase. This occurrence was due to the surface of the loading plate was in contact with the surface of the wood test piece. The loading of the universal testing machine was stopped for some specimens that exhibited this behavior. For this condition, one should note that the maximum force should only be taken up to the bearing failure of the wood that in contact with the bar. A typical setup for the embedding strength test can be seen in Fig. 4. All load-displacement data were

collected and the embedding strength of Bitis wood was calculated by using the following equation:

$$f_h = F_{max}/A_b \tag{2}$$

where, F: Maximum force, A_b: Bearing area of contact between bolt diameter (d) and wood test piece thickness (t).

3.2.2 Moisture Content and Density Tests

As per recommended by [27] and [34], the specimens for both wood density and moisture content tests were extracted from the bolted connection test piece. All extracted specimens were cut into 20 mm (width) x 50 mm (length) x 10 mm (thick) size. An initial mass of each specimen was measured to an accuracy of 0.01 g before placing all of the wood samples in an oven for a drying process with 103°C ± 2°C of temperature. After 24 hours of the oven-dry process, all specimens were taken out from the oven and each wood sample was weighed to determine the oven-dry mass of the first day. The 24-hour oven-dry step was repeated until a constant mass on each wood specimen was achieved. From this present study, it was found out that the constant mass of each wood sample was achieved in three days, which was then taken as the final mass. The difference between the initial mass and the final mass of each specimen was used to calculate the moisture content of Bitis wood. The oven-dry density value was also computed using the mass difference dividing by the volume of the wood test piece.

4. Results and Discussion

This section describes the test results of Bitis wood properties such as embedding strength, f_h, density, ρ, and moisture content, MC, as well as the strength of the bolted connection. An average value, designated as an abbreviation of avg in a subscript form, was calculated based on the total number of specimens tested. Due to the specimen preparation of the wood properties testing was done by extracting from the main bolted connection test piece, both embedding strength and density tests should have the same total of 180 specimens. However, it should be noted that due to some of the tested specimens of the bolted connection were failed in splitting for its entire length, the total specimens that can be prepared for the embedding strength test was only 137 pieces. A 5th percentile value, designated as an acronym of 5th% in a subscript form, was also computed for all results obtained, including the bolted connection strength results. The 5th percentile value was calculated based on an assumption that the results obtained is in the variation of the normal data distribution curve. The 5th percentile embedding strength, $f_{h,5th\%}$, was used in EYM and the 5th percentile density, $\rho_{5th\%}$, was used in RSM to estimate the bolted connection strength in ductile and brittle failure modes, respectively. These were then enabling a comparison to be made between the bolted connection characteristic strength estimation given by the Malaysian timber code of MS544-5, which typically provides the bolted connection capacity in the 5th percentile value [9]. One should note that the present study was carried out to investigate the Malaysian local timber, namely the Bitis wood. Thus, in order to ensure a realistic comparison of results was made in this article, the specific former studies of Meraka wood [7, 8, 9] and Nyatoh wood [21, 22] were selected. This is due to the comparable geometrical configuration details of bolted connections and the moisture content of wood specimens during the execution of the testing. Both factors are very important to be considered because of the significant influences in the timber bolted connection failure modes as well as its strength.

4.1 Wood Properties

The results of embedding strength of Bitis wood are tabulated in Table 3. Both average embedding strength, $f_{h,avg}$, and 5th percentile embedding strength, $f_{h,5th\%}$, values are determined from a total of 137 wood samples. From the statistical analysis of the embedding strength data, the coefficient of variation, CoV, shows an acceptable dispersion of data obtained in relation to the mean. Due to the lack of this embedding strength of Bitis wood in the existing MS544-5 [14], this present study initiates this important parameter determination for the use of an efficiency evaluation of the EYM equation in predicting the bolted connection capacities. The results of density of Bitis wood are presented in Table 4. The value of the average oven-dry density, ρ_{avg}, was computed using a total of 180 wood samples. The 5th percentile oven-dry density value, $\rho_{5th\%}$, was also obtained from the similar total of wood samples. In the statistical analysis of the density results, he coefficient of variation, CoV, shows the experimental results obtained are acceptably clustered around the average value. As per discussion made in the fourth paragraph of Section 1 in this article, the oven-dry density obtained was use to find the wood shear strength parallel to the grain using the correlation given by $17.8G^{1.24}$ [26]. This allows an assessment of RSM equation effectiveness in estimating the bolted connection strength of Bitis wood to be performed. Because of the wood moisture content can significantly affects the bolted connection capacity, it is essential to monitor the condition of the wood samples either in green or dry. From the average moisture content calculated from 180 wood samples, it can be seen that the wood samples were tested in dry condition, which in compliance with the MS544-2 [24]. Thus, the effect of moisture content to the bolted connection strength of Bitis wood was not a concern in this present study.

Table 3. Embedding strength of Bitis wood

Hardwood	No. of Specimens	$f_{h,avg}$ (MPa)	CoV (%)	$f_{h,5th\%}$ (MPa)
Bitis	137	42.21	25.23	24.69

Table 4. Moisture content and density of Bitis wood

Hardwood	No. of specimens	ρ_{avg} (kg/m³)	CoV (%)	$\rho_{5th\%}$ (kg/m³)	MC_{avg} (%)
Bitis	180	800	14.95	603	19

4.2. Bolted Connection

4.2.1 Observation on Ductile Failure Mode

Referring to the bolted connections of Groups 1-4 and Groups 6-9, with end distance, e_t, and bolt spacing, s_b, equal and more than 75 mm, it can be seen that the failure of the tested specimens was predominantly exhibited in ductile mode. This can be identified from the initial bearing failure observed in the wood part that directly in contact with the steel bolt, which caused the diameter of the pre-drilled hole to enlarge (see Fig. 5). At this stage, the embedding strength of the wood was mainly utilized. The bending of steel fasteners can be observed, which the bending strength of the steel bolts was triggered when the wood embedding strength exceeds the fastener bending resistance. The brittle failure, either row shear (Fig. 5a) or splitting (Fig. 5b), can be finally observed in the wood test piece of the bolted connection when the bending capacity of the bolt surpasses either the wood shear strength parallel to the grain or the wood embedding strength, respectively. However, this brittle failure, which can be seen from Fig. 6 as a sudden drop in loading, was identified as a secondary failure mode that did not control the bolted connection capacity. From Fig. 6,

it can be seen that the load-displacement curves of the bolted connection that failed in this ductile mode show an occurrence of a strain hardening. This can be spotted from the development of a plateau of the load-displacement curves of the bolted connection system. One should note that an alphabetical tagging system from a to j was implemented to represent the running number of the ten replicate specimens in each group of the bolted connection tested, as shown in the legend of Fig. 6.

(a) Group 4 with e_t = 75 mm

(b) Group 7 with e_t = 125 mm and s_b = 100 mm

Fig. 5 Tested bolted connection specimen that showing initial wood bearing failure with secondary brittle failure
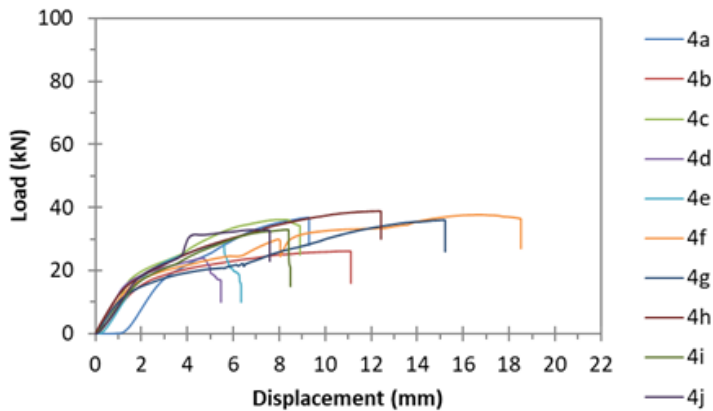
(a) Group 4 with e_t = 75 mm
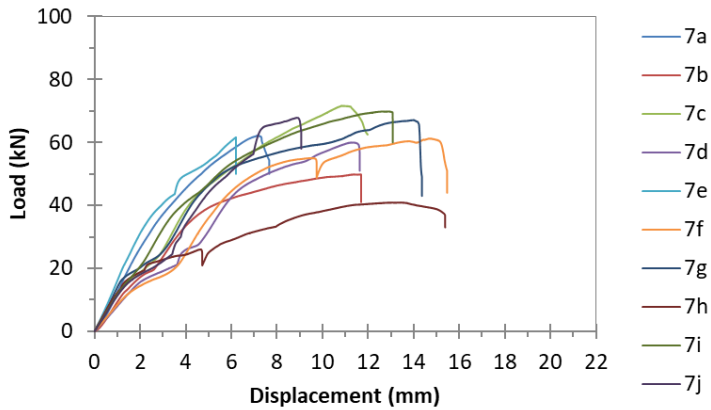
(b) Group 7 with e_t = 125 mm and s_b = 100 mm

Fig. 6 Typical load-displacement curves of bolted connections that exhibit the ductile failure mode

4.2.2 Observation on Brittle Failure Mode

In the bolted connection of Group 5 and Groups 10-18, with a minimum of 50 mm either e_t or s_b, majority of the specimens were primarily failed in brittle mode. No visible expansion of pre-drilled hole diameter was found, whereas the row shear failure parallel to the grain of the wood test piece was evident (see Fig. 7). At this point, only the shear strength parallel to the wood grain was fully utilized as the embedding strength of the wood is prominently greater than the wood shear parallel capacity.
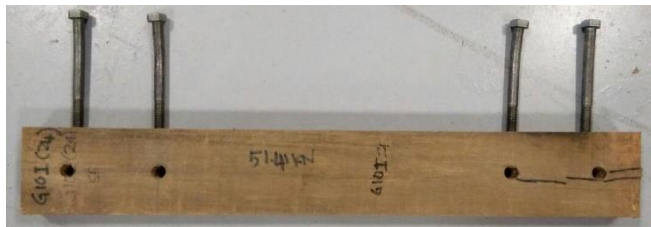
(a) Group 10 with e_t = 50 mm and s_b = 100 mm

(b) Group 15 with e_t = 50 mm and s_b = 50 mm

Fig. 7 Tested bolted connection specimen that showing row shear parallel to the wood grain failure

No significant bending can be observed on the steel bolts used translates that the steel fastener bending resistance is also very high in comparison to both embedding and shear strengths of the wood. From these observations, the bolted connection specimens of the above-mentioned groups can be concluded to fail mainly in row shear parallel to the wood grain due to no utilization of the wood embedding strength and the steel bolt bending

capacity. The row shear failure was the brittle mode that governs the capacity of the bolted connection system. Also, it should be noted that the geometrical configuration of the e_t and s_b are extremely important parameters in the design considerations. The failure of this brittle mode can be obviously spotted from the sudden drop of loading at a low displacement value with no establishment of plateau in the load-displacement curves shown in Fig. 8. A similar alphabetical labelling mentioned in the previous section was also used as per shown in the legend of Fig. 8.
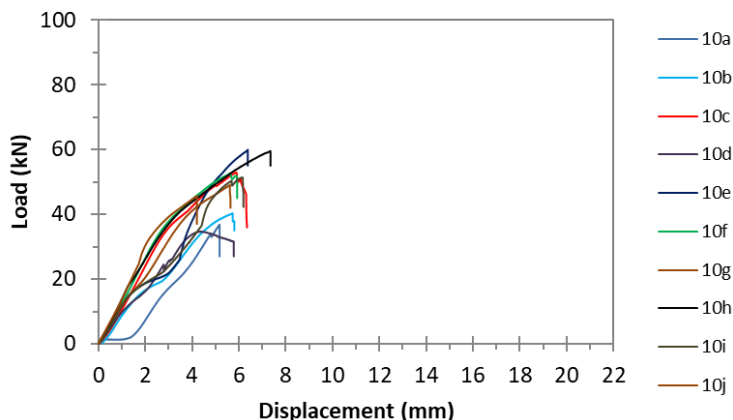
(a) Group 10 with e_t = 50 mm and s_b = 100 mm
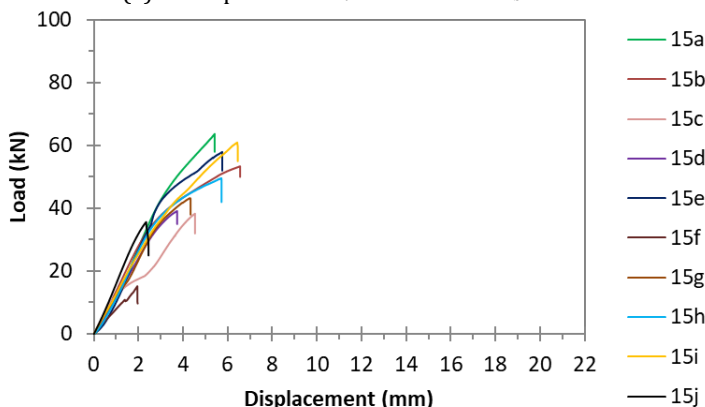
(b) Group 15 with e_t = 50 mm and s_b = 50 mm

Fig. 8 Typical load-displacement curves of bolted connections that exhibit the brittle failure mode

4.2.3 Strength Prediction Effectiveness of Ductile Failure Mode - EYM versus MS544-5

The test results of this present study, specifically for the bolted connections that failed in wood bearing (i.e. Groups 1-4 and Groups 6-9) are summarized in the Table 5. It should be noted that the experimental results were analyzed using the ultimate capacity of each bolted connection specimen. The CoV values show a satisfactorily dispersion of data obtained that were calculated based on ten specimens in each bolted connection group. The bolted connection strength estimation of EYM was calculated using equations of the four possible failure modes for a double shear joint type that can be found in [7, 9, 21]. It should be noted that the EYM estimation for each bolted connection group tabulated in Table 5 was taken from the minimum strength value out of the four possible failure mode capacities. The MS544-5 prediction on bolted connection capacity was computed using

Table 12 of [14] by taking the effective timber thickness, b, equal to 50 mm, and the bolt diameter, d, equal to 13 mm. In bolted joint design using MS544-5, it is required to perform a joint group classification for a specific timber species. From Table 1 of [14], one can see that there are five joint groups from J1 to J5 where the particular wood species are clustered to the specific joint group. For the prediction of bolted connection capacity using MS544-5, the Bitis wood used in this present study can be classified as J1 in accordance with Table 1 of [14]. Thus, from Table 12 of [14], the dry basic load for one bolt in a single shear can be obtained. It should be noted that for this present study, the double shear connection was tested, therefore, the capacity value gathered from Table 12 of [14] was multiplied by two. Also, for connections more than one fastener, a multiplication is required depending on the number of bolts used. From the comparison made between the predicted values and the experimental results, a ratio of EYM/$R_{5th\%}$ and MS544-5/$R_{5th\%}$ for each bolted connection group was calculated to show their effectiveness. It was found that, for the bolted connections of the Bitis wood that failed in ductile mode, the EYM strength predictions better than the MS544-5 with an average efficacy of 70%, whereas the code provides an average efficiency of 43%.

Table 5. EYM predictions vs experimental results of connection groups that failed in ductile

Group	Experimental			Predictions		Ratio	
	R_{avg} (kN)	CoV (%)	$R_{5th\%}$ (kN)	EYM (kN)	MS544-5 (kN)	EYM $R_{5th\%}$	MS544-5 $R_{5th\%}$
1	34.37	13	26.78	16.05	9.88	0.60	0.37
2	33.21	14	25.62	16.05	9.88	0.63	0.39
3	34.50	11	28.34	16.05	9.88	0.57	0.35
4	33.12	15	24.74	16.05	9.88	0.65	0.40
6	63.81	22	40.70	32.10	19.76	0.79	0.49
7	59.78	22	37.75	32.10	19.76	0.85	0.52
8	63.80	14	49.44	32.10	19.76	0.65	0.40
9	61.86	23	38.37	32.10	19.76	0.84	0.52
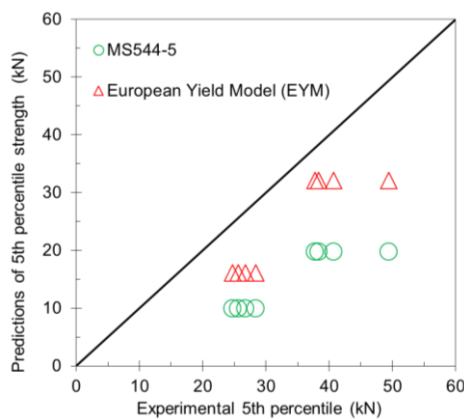
Fig. 9 Effectiveness of MS544-5 and EYM in predicting the strength of bolted connections that failed in ductile

The efficiency of both EYM and MS544-5 can be obviously seen in the plotting of predictions versus the experimental results (see Fig. 9). A one-to-one ratio line was drawn to show the efficacy of both predictions of EYM and MS544-5. The farther below the plotting from the one-to-one ratio line indicate that the estimation of the strength provided

is too conservative. This finding is in agreement with the previous published articles that investigating the bolted connection for Meraka wood [7] and Nyatoh wood [21].

4.2.4 Strength Prediction Effectiveness of Brittle Failure Mode - RSM versus MS544-5

Referring to the bolted connections that failed in row shear, Group 5 and Groups 10-18, the connection strength results obtained from the experiment are tabulated in Table 6. The average and 5th percentile strength values shown in Table 6 were analyzed using the maximum resistance of ten specimens for each group of connections. From the calculated CoV, one can see that the test data obtained show an acceptable data distribution. To get the RSM equation to predict the strength of the bolted connections, which is not included in this article, one can obtain from [8, 9, 15, 16, 22]. As per discussion in Section 1 of this article, the shear strength parallel to the wood grain was calculated using the correlation with the wood density which is equal to $17.8G^{1.24}$ as per recommendation of [8]. It should be noted that the factor of 0.6 to convert the average to 5th percentile, as per mentioned in [15] and [16], was not applied in the connection resistance calculation. This is because the 5th percentile of oven-dry wood density was used when performing the capacity estimations of the bolted connections for Bitis wood. Also, due to the average moisture content of Bitis wood obtained was 19%, the $17.8G^{1.24}$ was used instead of $21.9G^{1.13}$ because the former correlation is suitable to the local dry timber condition compared to the latter correlation that based on wood condition at 12% moisture content [26]. Another important item to highlight in the bolted connection capacity prediction using RSM equation is the calibration factor as discussed in Section 1 of this paper. The details of the calibration factor identification are described in the next section, whereas the analysis was performed in considerations of the failure mode of the connection groups to be selected in the calibration factor determination. For the MS544-5 strength predictions in the bolted connection of Bitis wood, a similar approach was implemented as per explained in the previous Section 4.2.3. In evaluating the effectiveness of both strength predictions of RSM and MS544-5 against the experimental data obtained, the calculated ratios of RSM/$R_{5th\%}$ and MS544-5/$R_{5th\%}$ show that the RSM provides better efficacy to predict the connection capacity of Bitis wood with an average of 82% efficiency.

Table 6. RSM predictions vs experimental results of connection groups that failed in brittle

Group	Experimental			Predictions		Ratio	
	R_{avg} (kN)	CoV (%)	$R_{5th\%}$ (kN)	EYM (kN)	MS544-5 (kN)	RSM $R_{5th\%}$	MS544-5 $R_{5th\%}$
5	26.02	23	16.14	11.88	9.88	0.74 (0.67)	0.61
10	48.60	18	33.83	23.77	19.76	0.70 (0.64)	0.58
11	55.19	21	36.23	23.77	19.76	0.66 (0.60)	0.55
12	52.93	26	30.45	23.77	19.76	0.78 (0.71)	0.65
13	59.38	27	33.31	23.77	19.76	0.71 (0.65)	0.59
14	55.72	29	29.14	23.77	19.76	0.82 (0.74)	0.68
15	45.74	32	21.73	23.77	19.76	1.09 (0.99)	0.91
16	84.97	30	43.67	35.65	29.64	0.82 (0.74)	0.68
17	72.37	31	35.75	35.65	29.64	1.00 (0.91)	0.83
18	59.84	19	41.38	35.65	29.64	0.86 (0.78)	0.72

The MS544-5 was found to only provide 68% of prediction effectiveness. From Fig. 10, one can see clearly the effectiveness comparisons between the timber code of MS544-5 and the RSM. It should be noted that the RSM shows 9% of over-predicted strength in Group 15. This is mainly due to the variation of the experimental data obtained because the failure of all specimens in Group 15 was thoroughly inspected to confirm that the strength was not

influenced by any of the strength affecting factors like the slope of grain and moisture content. Also, the wood defects such as pre-cracked or knot occurrence on the specimens of Group 15 were not visibly evident. The designers should take note that this over-prediction issue can be resolved by applying a higher calibration factor value, which is further discussed in the next Section 4.2.5.
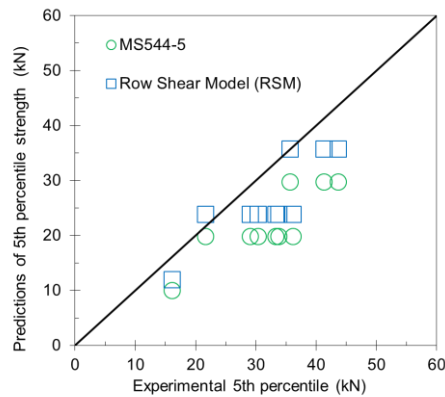
Fig. 10 Effectiveness of MS544-5 and RSM in predicting the strength of bolted connections that failed in brittle

4.2.5 Calibration Factor Determination for Bitis Wood

In the calibration factor identification, only groups of bolted connections that failed in the row shear mode were included in the analysis, they are Group 5 and Groups 10-18. These groups were fabricated with 50 mm, either the end distance or bolt spacing. In general, a linear regression technique was used to obtain the calibration factor for Bitis wood. To start the analysis, a graph of the average predicted strength by RSM versus the experimental average plotting was developed with a trial-and-error calibration factor value. The graph is also equipped with a reference one-to-one ratio line shown in Fig. 11. A linear regression line was then drawn for the plotting as shown in Fig.11 as the thick line. The calibration factor can be determined by repeating the trial-and-error process with a different calibration factor value until the regression line is comparably matched the reference line. For Bitis wood, a calibration factor of 4 with 66% similarities of regression model was suggested to achieve an acceptable prediction of the 5th percentile strength by the RSM equation. One can see that the coefficient of determination, R^2, of 0.98 obtained from the analysis shows a good data fit was achieved with respect to the proposed regression model. To provide a remedial solution of the over-predicted value by RSM in Group 15 as per mentioned in the previous section, a higher calibration factor of 4.4 is recommended with 60% regression model relationships can be achieved as shown in Fig.12. This application of 4.4 calibration factor makes the preceding over-predicted ratio of 1.09 to drop to 0.99 (see figures in parentheses) as given in Table 6. By using the new 4.4 calibration factor for Bitis wood, the effectiveness of RSM predictions was still identified to be better than the timber code of MS544-5 estimations as per calculated ratios of RSM/$R_{5th\%}$ shown in parentheses of Table 6. In average, the RSM was found to give 74% efficacy for the recommended calibration factor of 4.4. From this finding, one can see even the selection of the calibration factor for the particular wood species is based on the decision of designers to obtain their intended optimized strength prediction. However, it is strongly recommended the designers to establish the regression model of the 5th percentile strength predictions as shown in Fig.13. This was to cross-check that the

plotting data of the 5th percentile strength estimations to be below the one-to one ratio line for ensuring a safe strength prediction can be obtained from the RSM.
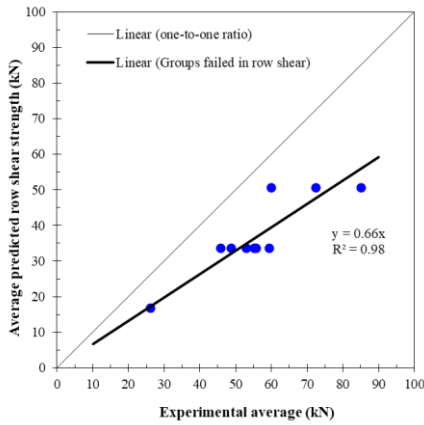
Fig. 11 Calibration factor of 4   Fig. 12 Calibration factor of 4.4
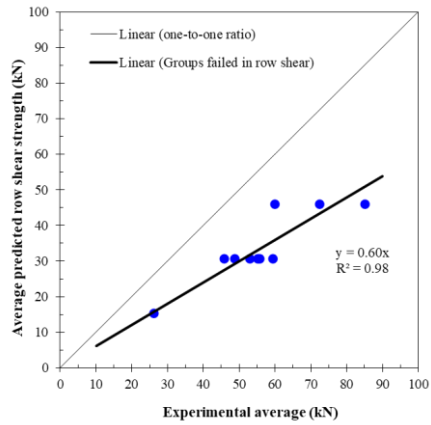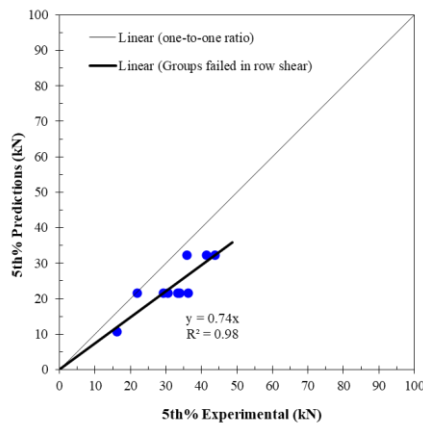
Fig. 13 Regression model of 5th pecentile strength

5. Conclusions

The addition of the bolted connection findings on the Bitis wood obtained from this present experimental work was not only to enrich the wood database of the preceding works done by Abdul Karim et al. [9] on the Meraka wood and Ujan et al. [22] on the Nyatoh wood, but the design parameters for optimizing the strength are proposed. The geometrical parameters of both the end distance, e_t, and bolt spacing, s_b, were identified to affect significantly the strength of the connections as they are the main cause to govern the failure mode of the bolted connection parallel to the wood grain. For the Bitis wood, it was recognized that either end distance or bolt spacing that equal or than 50 mm can cause the bolted connection to behave in the brittle failure of the row shear. This is very crucial to be avoided in the fabrication of the connection configuration unless a significant number of fasteners are required to be used due to the strength demand, which consequently a small distance of the geometrical parameters could not be avoided. The embedding strength of the Bitis wood, which is not provided by the timber code of MS544-2 [24], was determined

in this present study. The proposed embedding strength value was validated to offer 70% efficiency (in average) of the European Yield Model (EYM) in estimating the bolted connection capacity for the ductile failure mode, whereas the timber standard of MS544-5 [14] only 43% of efficacy. On the use of the calibration factor, CF, for predicting the strength of bolted connections using the Row Shear Model (RSM), a value of 4.4 for the Bitis wood is proposed due to neither to provide an over-predicted strength nor a too conservative strength. The calibration factor recommended herein offers 74% of average effectiveness, whereas the MS544-5 provides 38% of efficiency.

Acknowledgement

References

[1] Griffith MC. Performance of Unreinforced Masonry Buildings during the Newcastle Earthquake, Australia. Research Report No. R86, The University of Adelaide, Adelaide, Australia, 1991.

[2] Blaikie EL, Spurr DD. Earthquake vulnerability of existing unreinforced masonry buildings. Works Consultancy Services, Wellington, New Zealand, 1992.

[3] Bruneau M. State-of-the-art report on seismic performance of unreinforced masonry buildings. Journal of Structural Engineering 1994;120(1):230-251. https://doi.org/10.1061/(ASCE)0733-9445(1994)120:1(230)

[4] Evans N. The earthquake's impacts on buildings and infrastructure. In: Shaken Up, proceedings of a workshop on Recovery following the Gisborne Earthquake (Vol. 7), 2009.

[5] Dizhur D, Lumantarna R, Ismail N, Ingham JM, Knox C. Performance of unreinforced and retrofitted masonry buildings during the 2010 Darfield earthquake. Bulletin of the New Zealand Society for Earthquake Engineering 2010;43(4):321. https://doi.org/10.5459/bnzsee.43.4.321-339

[6] Dizhur D, Ingham J, Moon L, Griffith M, Schultz A, Senaldi I, Magenes G, Dickie J, Lissel S, Centeno J, Ventura C, Leite J, Lourenco P. Performance of masonry buildings and churches in the 22 February 2011 Christchurch earthquake. Bulletin of the New Zealand Society for Earthquake Engineering 2011;44(4):279-296. https://doi.org/10.5459/bnzsee.44.4.279-296

[7] Abdul Karim AR, Quenneville P, MSa'don N, Yusof M. Investigating the Meraka Hardwood Failure in Bolted Connections Parallel to the Timber Grain. International Journal of Engineering & Technology 2018;7(3.18):62-65. https://doi.org/10.14419/ijet.v7i3.18.16675

[8] Abdul Karim AR, Quenneville P, Sa'don N M. Shear failure of the Meraka hardwood in bolted connections loaded parallel to the timber grain. In: IOP Conference Series: Materials Science and Engineering 2021;1101(1):012005. https://doi.org/10.1088/1757-899X/1101/1/012005

[9] Abdul Karim AR, Quenneville P, Sa'don N M. Design Optimization of the Bolted Connection Loaded Parallel to the Timber Grain for Masonry Building Retrofits.

International Journal of Mechanics 2022;16:6-14. https://doi.org/10.46300/9104.2022.16.2

[10] Abdul Karim AR, Quenneville P, MSa'don N, Ingham J. Assessment Guidelines of Wall-Diaphragm Connections for Masonry Buildings. In: Yazdani S, Singh A, eds. New Developments in Structural Engineering & Construction. Research Publishing, Singapore, 2013. https://doi.org/10.3850/978-981-07-5354-2_St-136-427

[11] Abdul Karim AR. Seismic Assessment of Wall-Diaphragm Connections in New Zealand Unreinforced Masonry Buildings. PhD thesis The University of Auckland, New Zealand, 2012.

[12] New Zealand National Society for Earthquake Engineering. Draft Guidelines for Assessing and Strengthening Earthquake Risk Buildings, New Zealand National Society for Earthquake Engineering, Wellington, New Zealand, 1995.

[13] Federal Emergency Management Agency. Techniques for the Seismic Rehabilitation of Existing Buildings. FEMA 547, Federal Emergency Management Agency, Washington, D.C., 2006.

[14] Department of Standards Malaysia. Code of Practice for Structural Use of Timber: Part 5: Timber Joints. MS544-5, Department of Standards Malaysia, 2001.

[15] Quenneville P. Design of Bolted Connections: A Comparison of a Proposal and Various Existing Standards. Journal of the Structural Engineering Society (SESOC) New Zealand Inc. 2009;22(2):57-62.

[16] Quenneville JHP, Jensen J. Validation of the Canadian Bolted Connection Design Proposal. CIB-W18 meeting Proceedings 2008.

[17] Jockwer R, Fink G, Köhler J. Assessment of the failure behaviour and reliability of timber connections with multiple dowel-type fasteners. Engineering Structures 2018;172:76-84. https://doi.org/10.1016/j.engstruct.2018.05.081

[18] Yurrita M, Cabrero JM. New design model for brittle failure in the parallel-to-grain direction of timber connections with large diameter fasteners. Engineering Structures 2020;217:110557. https://doi.org/10.1016/j.engstruct.2020.110557

[19] Lokaj A, Dobes P, Sucharda O. Effects of loaded end distance and moisture content on the behavior of bolted connections in squared and round timber subjected to tension parallel to the grain. Materials 2020;13(23):5525. https://doi.org/10.3390/ma13235525

[20] Cao J, Xiong H, Liu Y. Experimental study and analytical model of bolted connections under monotonic loading. Construction and Building Materials 2021;270:121380. https://doi.org/10.1016/j.conbuildmat.2020.121380

[21] Ujan XL, Karim ARA, Sa'don NM, Teng XY, Quenneville P, Rahim NL. Effectiveness Validation on Existing Design Equations for the Sustainable Design of Masonry Building Retrofits. Journal of Sustainability Science and Management 2022;17(6):79-91. https://doi.org/10.46754/jssm.2022.06.007

[22] Ujan XL, Karim ARA, Sa'don NM, Sahari SH, Rahim NL, Quenneville P. Validation of Shear Failure on Bolted Connection for Nyatoh Hardwood. Journal of Engineering Science and Technology 2023;18(5):2398-2410.

[23] Johansen KW. Theory of timber connections. Publications of International Association for Bridge and Structural Engineering 1949;9:249-262.

[24] Department of Standards Malaysia. Code of Practice for Structural Use of Timber: Part 2: Permissible Stress Design of Solid Timber (First Revision). MS544-2, Department of Standards Malaysia, 2001.

[25] International Organization for Standardization. Draft International Standard ISO/DIS 10984-2 Timber structures - Dowel-type fasteners - Part 2: Determination of embedding strength and foundation values. International Organization for Standardization, Geneva, Switzerland, 2008.

[26] Forest Products Laboratory. Wood Handbook: Wood as an Engineering Material. Forest Service U.S. Department of Agricultural, Washington, D.C, 1987.

[27] Australian/New Zealand Standard. Timber - Methods of Test - Method 3: Density. AS/NZS 1080.3, Standards New Zealand (electronic copy), 2000.

[28] Malaysian Timber Industry Board. Strength Groups of Timber and Their Applications. [Date of update: 28/09/2020] https://www.mtib.gov.my/en/wisdec?view=article&id=64:specifying-timber-for-building-construction&catid=2

[29] Malaysian Standard. MS 544: Part 11: 2001 Code of Practice for Structural Use of Timber: Part 11: Recommendations for the Calculation Basis for Span Tables - Section 4: Domestic Rafters. Department of Standards Malaysia, 2001.

[30] Malaysian Standard. MS 544: Part 11: 2001 Code of Practice for Structural Use of Timber: Part 11: Recommended Span Tables and Their Calculations: Section 1: Domestic Floor Joists. Department of Standards Malaysia.

[31] Meier E. The Wood Database: Hardwood Anatomy. [Date of access: 06/04/2023] https://www.wood-database.com/wood-articles/hardwood-anatomy/

[32] Universiti Putra Malaysia. Laboratory Report of Wood Properties: Wood Anatomy (Bitis) by Universiti Putra Malaysia Kampus Bintulu Sarawak. [Date of report: 14/09/2021] http://histaf.upm.edu.my/upload/inovasi/2021/20211130163926LAB_2_WOOD_ANATOMY_compressed-2.pdf

[33] PlantUse English contibutors. Madhuca (PROSEA Timbers). [Date of update: 05/08/2017] https://uses.plantnet-project.org/e/index.php?title=Madhuca_(PROSEA_Timbers)&oldid=326801

[34] Australian/New Zealand Standard. Timber - Methods of Test - Method 1: Moisture content. AS/NZS 1080.1, Standards New Zealand (electronic copy), 1997.

[35] International Organization for Standardization. International Standard ISO 6891 Timber structures - Joints made with mechanical fasteners - General principles for the determination of strength and deformation characteristics. International Organization for Standardization, Geneva, Switzerland, 1983.

Research Article

Self-sensing concrete with recycled coarse aggregates and multi-walled carbon nanotubes: A sustainable and effective method

C. Arvind Kumar [1*,a], Panga Narasimha Reddy[2,b], S.A. Aejaz [3,c], Prathik Kulkarni[4,d]

[1]Department of Civil Engineering, Matrusri Engineering College, Hyderabad, India
[2]Department of Civil Engineering, Sri Venkateswara College of Engineering & Technology (A), Chittoor, India
[3]Department of Civil Engineering, National Institute of Technology, Srinagar, Jammu and Kashmir, India
[4]Department of Civil Engineering, Bajaj Institute of Technology, Wardha, Nagpur, India

Article Info	Abstract
	This study explores the production of self-sensing concrete using recycled coarse aggregates and Multi-walled Carbon Nanotubes (MWCNTs) in varying dosages. The objective is to reduce the usage of natural coarse aggregates and to develop an environmentally friendly and sustainable material for the future generation. The self-sensing concrete was also self-compacting (SCC), which enhances its ability to fill complicated molds without the need for external vibration. The fresh properties of the self-sensing concrete were tested, and the mix proportions with varying dosages of MWCNTs were within the prescribed limit as per European Federation of National Associations Representing for Concrete (EFNARC) code. The mechanical properties of the self-sensing concrete were also evaluated, and it was observed that incorporating MWCNTs into the concrete enhanced its strength. Incorporating MWCNT into concrete increased its strength, seen in higher compressive and split tensile strengths. Adding 0.05%, 0.1%, and 0.15% of MWCNT resulted in compressive strength increases of 1.51%, 3.21%, and 4.72%, respectively. Likewise, the inclusion of 0.05%, 0.1%, and 0.15% of MWCNT led to split tensile strength increases of 1.54%, 3.31%, and 4.82%, respectively. The SEM images of specimens with different MWCNT dosages show a random yet uniform dispersion within the concrete matrix. The initial electrical resistance plot demonstrates the transformation from conventional to self-sensing concrete, with the resistance dropping significantly from 400k-ohms to 37k-ohms. This plot establishes the critical threshold level for self-sensing at 0.10% MWCNTs. Furthermore, the study examined the stress sensing ability and crack detection properties of the self-sensing concrete, and it was found that during cyclic loading, the concrete's stress sensing ability improves with increasing MWCNT dosage. The most favorable similarity plot between stress and FCR is seen at 0.15% MWCNT. However, considering economic reasons, a dosage of 0.1% MWCNT can be considered the best option since it doesn't show a significant difference for both stress and crack detection property.

1. Introduction

Throughout the world, there is a huge demand for concrete, and the current structures are often referred to as "concrete jungles." This demand is considered a sign of development, but from a sustainability point of view, the materials such as coarse aggregate and fine aggregate used to produce concrete are continuously depleting as they are naturally occurring resources. On the other hand, some buildings are continuously being dismantled

*Corresponding author: arvind.cholker@gmail.com
[a] orcid.org/0000-0003-3980-9088, [b]orcid.org/0000-0001-8856-9741, [c] orcid.org/0000-0000-2304-210X, [d]orcid.org/0000-0002-4004-9330

due to various reasons, and disposing of the demolished waste can be challenging. Therefore, using recycled aggregate from this waste can help solve the problem of depleting natural resources and disposing of the waste. In this study, recycled concrete was utilized to produce self-sensing concrete instead of using new coarse aggregate.

The seismic event that recently occurred at the boundary of Turkey and Syria had devastating effects, claiming the lives of more than 40,000 individuals. While natural disasters like earthquakes are beyond human control, utilizing structural health monitoring (SHM) techniques can be effective in mitigating the loss of both life and property. SHM involves the use of different methods to detect potential weaknesses in structures, enabling preventive measures such as repairs or demolition to be taken within time. This can help prevent the structures from being easily compromised during earthquakes, consequently reducing casualties. Embedding sensors in concrete or attaching them to the external surface are among the different techniques available for SHM [1]–[4], where they are used to measure parameters such as strains, deflections, and stresses. It is clear that there is an urgent need to implement SHM to minimize the losses that may result from such events in the future. On the other hand, the conventional SHM approach using external or internal sensors provides information only for the specific locations where the sensors are attached and not for the entire structure. To overcome this limitation, a new technique called SHM using self-sensing concrete (SSC) has been developed. This innovative method involves turning the concrete into a sensor itself, rather than relying on attaching external or internal sensors.

The concept of SSC was discovered by DDL Chung in the early 1990s, who found that the addition of electrically conductive carbon fibers to cement enabled the resulting material to sense external loads[5]–[8]. The sensing ability of the material was measured by monitoring the electrical resistance of the specimen. This groundbreaking technique offers the potential to monitor the entire structure continuously, allowing for timely interventions that could save lives and property during natural disasters like earthquakes. DDL Chung's discovery of the sensing ability of electrically conductive carbon fibers added to cement marked the birth of self-sensing concrete. Since then, a plethora of studies have been carried out to further explore this concept. Researchers have experimented with various materials to enhance the sensing capabilities of self-sensing concrete. The various materials like carbon fibers [9], [10], single walled nano tubes [11] multi-walled carbon nanotubes (MWCNT). [12]–[15], carbon black[16], [17], combined carbon fibers with MWCNT[18]–[20]. Dehghani and Aslani [21] also conducted a study using a blend of steel fibers and carbon fibers. These various studies have contributed significantly to the development and potential applications of self-sensing concrete.

In their research, Suchorzewski, et al. [22] discovered that adding multi-walled carbon nanotubes (MWCNT) to high-performance concrete (HPC) improves both its mechanical and self-sensing properties. The researchers studied the concrete's ability to detect stress during cyclic compression and found that even a small amount of MWCNT (0.05% and 0.10%) improved stress detection and allowed for the monitoring of micro cracking. This study highlights the potential benefits of using MWCNT in HPC to improve the sensing capabilities of the material, which could lead to more effective and accurate monitoring of structures for potential damage or failure. Song, Niu, and Zhong conducted a study to investigate the dynamic mechanical properties of carbon nanotube reinforced concrete when subjected to freeze-thaw cycles. Their results revealed that, with an increase in freeze-thaw cycles, the peak stress of the concrete sample gradually decreased under the same impact pressure, while the corresponding strain increased slightly. Furthermore, the stress-strain curve shifted downwards and to the right as a whole. These findings suggest that the addition of carbon nanotubes to concrete may have a positive effect on its dynamic

mechanical properties and ability to withstand environmental stressors like freeze-thaw cycles.

The addition of multi-walled carbon nanotubes (MWCNT) to recycled aggregate concrete (RAC) has been the subject of several studies. One such study by Gao [23]. showed that adding 0.1% MWCNT by weight of cement to RAC, made from various waste cementitious materials, and replacing natural aggregates with recycled concrete aggregates (RCA) at rates of 50%, 70%, and 100%, significantly increased the compressive strength of treated RAC samples by approximately 42% compared to untreated RAC samples. In contrast, another study by Song [24] examined the impact of different levels of MWCNT on the interfacial mechanical properties of RAC. They found that the highest shear strength was achieved with the addition of 0.2% MWCNT, resulting in a 53% improvement compared to free-nano mixtures. These studies suggest that the addition of MWCNT to RAC can lead to significant improvements in its mechanical properties and provide insights into the optimal levels of MWCNT for achieving the desired outcomes. Further I. Murali et al. [25] evaluated the impact response of fibrous concrete that incorporated expanded clay aggregate in combination with MWCNT and steel fibers at 0.2% and 2.5% by cement weight, respectively. The study found that 0.2% MWCNT significantly filled nanopores, resulting in a denser concrete matrix.

After conducting a literature review, it was discovered that previous research on self-sensing concrete has been limited to cement, mortar specimens, and conventional concrete. As such, further investigation is required to understand the behavior of concrete with conductive fibers when used in actual site conditions. Furthermore, in the present era, self-compacting concrete (SCC) is being utilized widely in various applications. In the current study, self-sensing concrete was produced by incorporating multi-walled carbon nanotubes (MWCNT) into self-compacting concrete (SCC), which uses recycled coarse aggregate. The aim was to investigate the potential of self-sensing concrete in addressing sustainability concerns. A range of SCC specimens containing varying dosages of MWCNT were produced and tested to assess their mechanical properties, stress-sensing capabilities, crack detection ability under cyclic loading.

2. Experimental Work

2.1. Material Used

For production of self-sensing concrete in present study, Multi Walled Carbon Nano Tubes (MWCNT) obtained from Sun Young Industry, South Korea was used. The MWCNT were completely electrically conductive with an average diameter of 10-20 nm, average length of 5-20 μm, and purity greater than 95%. The properties of the MWCNT used in the study are shown in Table 1.

To ensure adequate dispersion of the MWCNT and produce self-compacting concrete (SCC), a high-range water-reducing super plasticizer with a density of 1.08 g/ml and based on polycarboxylate ether (PCE) was used. Tap water with a pH of 7.2 was used for mixing and curing the concrete. The coarse aggregate used in the study was obtained by screening and cleaning concrete waste from nearby demolished structures, with a size of 10 mm and a specific gravity of 2.75 after cleaning and sieving. River sand with a specific gravity of 2.65 and a fineness modulus of 2.8 was used as the fine aggregate. Cement with a specific gravity of 3.14 and a grade of 43 was used to produce the SCC. The Physical properties and Chemical composition of cement are shown in Table 2.

Table 1. Properties of MWCNT's

Property	Value
Purity	>94%
Colour	Black
Length	6-16 μm
Inner Diameter	5-10 nm
Outer Diameter	40-60 nm
True Density	~2.2 g/cm3
Bulk Density	~0.12 g/cm3
Specific Surface Area	45-600 m2/g
Pore Volume	081cm3/g

Table 2. Physical properties and Chemical composition of cement

Physical Characteristics	Values
Fineness	9%
Density	3080.2 kg/m3
Specific Gravity	3.13
Normal Consistency	31%
Chemical Composition	Values in %
CaO	61.2
SiO2	21.5
Al2O3	5.45
SO3	3.21
Fe2O3	3.57
MgO	2.54

2.2. Mix Proportion

In this study, self-compacting concrete (SCC) mixes were produced using different dosages of MWCNT ranging from 0% to 0.15% by weight of cement, with increments of 0.05%. The mix proportions of materials used are presented in Table 3.

Table 3. Material proportions and slump flow results

Specimen ID	Materials used in kg/m³							Slump flow test in mm	
	MWCNT		Cement	Fine aggregate	Coarse aggregate	Water	Super Plasticizer (1.55%)	Experimental	Range as per EFNARC
	%	kg							
Ref.	0	0	460	950	880	186	7.13	760	600-850
SCC-0.05	0.05	0.26	460	950	880	186	7.13	732	600-850
SCC-0.1	0.1	0.52	460	950	880	186	7.13	706	600-850
SCC-0.15	0.15	0.78	460	950	880	186	7.13	690	600-850

A compressive strength of 40N/mm2 was chosen for the SCC mix after conducting several trials to ensure that both the fresh and hardened properties satisfied the code European Federation of National Associations Representing for Concrete (EFNARC) [26] requirements.

The European Guidelines for Self-Compacting Concrete. The material proportions for the SCC without MWCNT, which was used as the reference mix after conducting adequate trials, are shown in Table 3 with the label "Reference". The table also shows the flow properties of the different mixes after adding MWCNT. The slump flow of all mixes fell within the prescribed limits and was measured using the slump flow test specified by the EFNARC code

2.3. Specimen Preparation

In order to disperse the MWCNTs in water, initially a solution was prepared by mixing 50% of the water required for concrete preparation with Sodium Dodecylbenzene Sulfonate (SDBS) powder, in a concentration of 0.18% by weight of the nano tubes. The MWCNT were added to this solution, and the mixture was agitated using a mechanical churner for 15 minutes to ensure proper dispersion of the nano tubes in water. This dispersed solution was then added to the concrete mixer containing dry cement, fine aggregate (FA), and coarse aggregate (CA), along with a solution containing the remaining 50% of the water and the superplasticizer. The mixture was further mixed in the concrete mixer until self-compacting concrete was obtained. The complete mix procedure is depicted in Fig. 1.
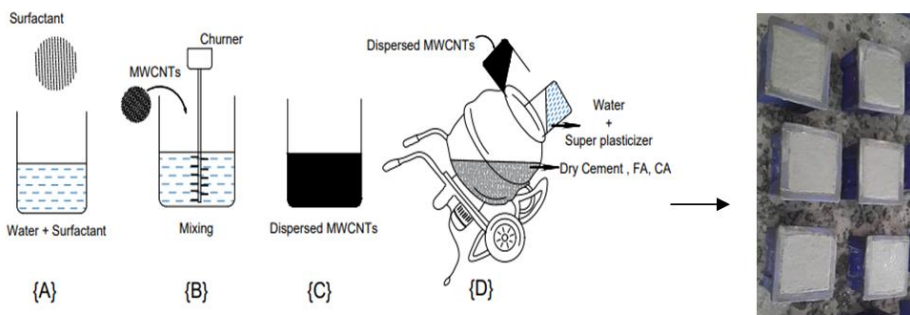
Fig. 1. Mixing procedure for production of self sensing concrete

The freshly prepared self-compacting concrete (SCC) mix was evaluated for its fresh properties using the slump flow test [26]. Subsequently, the mix was poured into steel molds of cubes and cylinders. The cube molds had dimensions of 150 x 150 x 150 mm3, while the cylinder molds had a diameter of 150 mm and a length of 300 mm. The filled molds were then allowed to dry at room temperature for 24 hours. After the drying period, the molds were carefully demoded, and the specimens were placed in fresh water for curing over a period of 28 days. Each SCC mix was used to create five cubes and three cylinders.

2.4. Testing Procedure

2.4.1. Compressive and Split Tensile Strength

After 28 days of curing, the self-sensing concrete specimens were removed from the water and underwent testing to determine their load carrying capacity under both compression and tension using a Universal Testing Machine (UTM). To determine the ultimate load carrying capacity in compression, a set of three cubes were loaded gradually using the UTM

until failure occurred. The average stress value of the three specimens was then calculated and recorded. Similarly, the split tensile strength of the SSC was evaluated by subjecting the cylinders to a transverse load using the UTM until they reached failure. The split tensile strength value was then calculated using the codal formula and included in the results section.

2.4.2. Electrical Resistivity Measurements

In order to achieve consistent and reliable measurements of electrical resistance in the specimens, an electrically conductive paint is used to coat the periphery of each cube, and copper wire is wrapped over the paint at a distance of 10mm from the top and bottom edges, as depicted in Fig. 2. A digital multimeter (DMM) is used to measure the electrical resistance at the top and bottom ends of the copper wires, both during non-loading and loading situations. Prior to any loading, the sensor's sensing capability is tested by measuring the initial electrical resistance. The stress sensing ability is then evaluated by measuring the resistance during both loading and unloading in a cyclic manner.
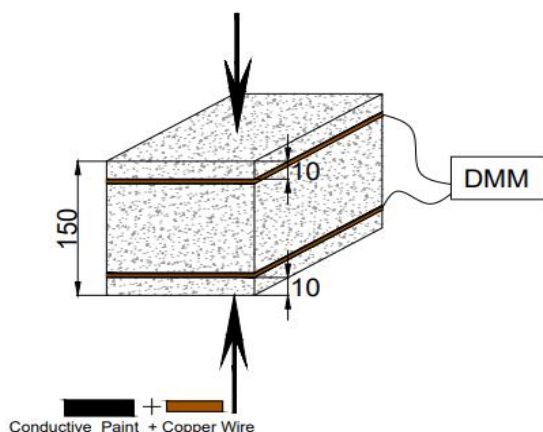
Fig. 2. Specimen details for stress sensing test

3. Results and Discussion

3.1. Dispersion of MWCNT's

Various samples, each containing different dosages of Multi-Walled Carbon Nanotubes (MWCNT's), underwent testing using a Hitachi 3600 N Scanning electron microscope (SEM) with a 5 axis motorized stage. These tests involved examining the SEM images of hardened concrete powder obtained from broken cube specimens after 28 days of curing during compressive testing.

In Fig. 3, the SEM images depict the concrete with varying dosages of MWCNTs. All the sample dimensions were almost kept uniform of 16.2mm with zooming of X150 resolution for SEM imaging. From the obtained images SEM images, it becomes evident that as the dosage of nano-tubes increases within the concrete, their visibility improves. Additionally, the images reveal that the nanotube fibers have been uniformly and randomly dispersed throughout the concrete matrix.

(a) No MWCNT's

(b) 0.05% MWCNT's

(c) 0.1% MWCNT's

(d) 0.15% MWCNT's
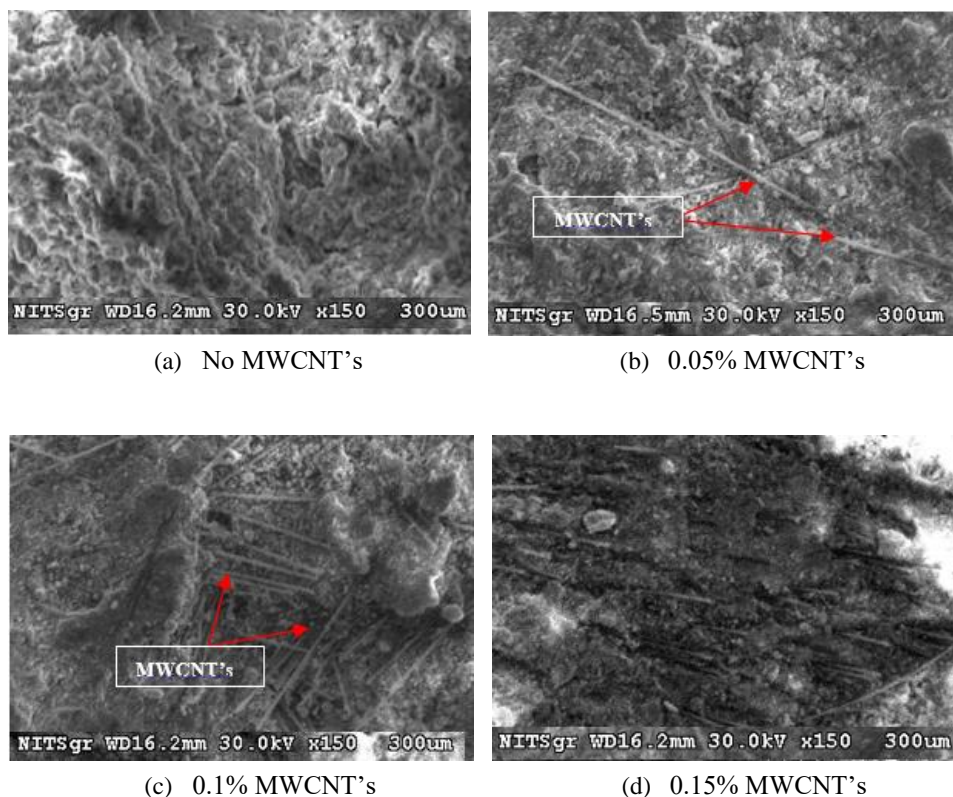
Fig. 3. SEM images of hardened samples

3.2. Mechanical Properties

3.2.1. Compressive Strength

To evaluate the influence of MWCNT on concrete strength, the ultimate load carrying capacity was determined. For each MWCNT dosage, three sets of cubes were subjected to a Universal Testing Machine (UTM) with a 1000kN capacity, and gradually loaded at a constant speed of 5.2kN/sec until failure. The maximum load carrying capacity was recorded for each set, and the average value for each MWCNT dosage was presented in Table 4 for both compressive and split tensile strength.

Table 4. Compressive and Split tensile strength results

Specimen ID	Compressive Strength			Split Tensile Strength		
	Ultimate Load (kN)	Compressive Stress (N/mm^2)	% Increase in stress	Ultimate Load (kN)	Stress (N/mm^2)	% Increase in stress
Ref.	733.95	32.62	-	200.06	2.83	-
SCC-0.05	745.21	33.12	1.51	202.86	2.87	1.54
SCC-0.1	757.35	33.66	3.21	206.40	2.92	3.31
SCC-0.15	768.37	34.15	4.72	209.23	2.96	4.82

From these results, it can be inferred that the MWCNT dosage plays an important role in enhancing the compressive strength of self-compacting concrete. The increase in compressive strength for sample containing 0.05% of MWCNT's is 1.51% when compared to reference sample. Similarly, the increase in compressive strength for samples congaing 0.01% and 0.15 % MWCNT's is 3.21 and 4.72% respectively when compared to reference samples.

In a parallel investigation conducted by Ali Naqi and Naseem Abbas[27], which focused on cement paste blended with silica fume, the inclusion of 0.01% Multi-Walled Carbon Nanotubes (MWCNTs) led to notable enhancements in compressive strength. Compared to the reference specimens, the concrete samples with 0.01% MWCNTs exhibited 4.4%, 9.7%, and 12.4% higher compressive strengths at 1, 3, and 7 days, respectively. Also Morsy et al. [28] demonstrated an 11% improvement in compressive strength by adding 0.02 wt.% CNT and 6 wt.% nano metakaolin. Similarly, Cwirzen et al. [29] achieved a significant 50% increase in compressive strength by adding 0.045% MWCNTs compared to the reference samples. It is important to note that in present study, there is a limit to the increase in compressive strength, and the dosage of MWCNT cannot be increased indefinitely. The optimal dosage range for MWCNT addition appears to be between 0.1% and 0.15% by weight of cement. Beyond this range, the increase in compressive strength may not be significant or may even decrease due to issues related to agglomeration of the nano tubes. Overall, the results indicate that the addition of MWCNT in self-compacting concrete can lead to an improvement in the compressive strength, which can result in the production of more durable and long-lasting structures.

(a) Compressive strength   (b) Increase in compressive strength
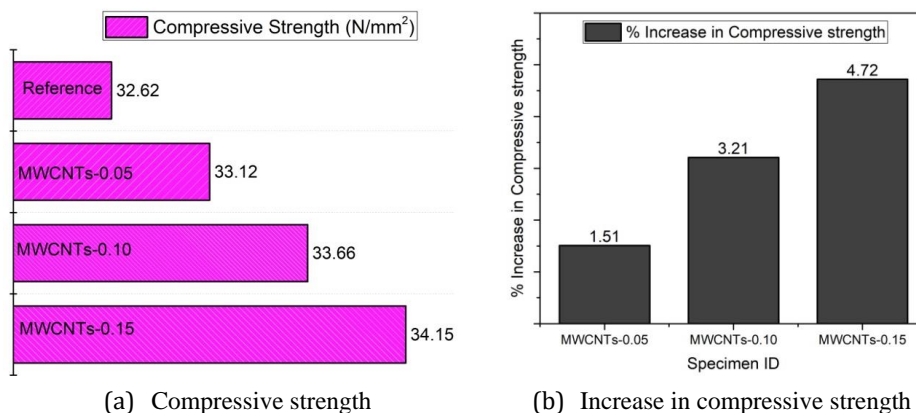
Fig. 4. Increase in compressive strength

The figure presented in Fig. 4 (a) graphically represents the compressive strength and Fig.4 (b) represent shows increase in compressive strength resulting from the addition of MWCNT to the concrete mix. The increase in compressive strength is attributed to the ability of MWCNT to fill pores within the concrete structure, making it denser due to its small size. Furthermore, the fibers contribute to bridging small cracks in the concrete, which ultimately increases the strength of the material. However, it is worth noting that the increase in strength is relatively small despite the positive impact of MWCNT on concrete strength.

3.2.2. Split Tensile Strength

Based on the results of split tensile strength shown in Fig. 5, it is observed that the addition of MWCNT has a positive impact on split tensile strength, and the increase in strength is proportional to the dosage of MWCNT added to the mix. The increase in split tensile

strength for 0.05, 0.1 and 0.15% dosage of MWCNT's is 1.51, 3.21 and 4.72% respectively. Similar research conducted by Baban Singh and Sushmita[31], observed that incorporating Multi-Walled Carbon Nanotubes (MWCNTs) into concrete resulted in significant improvements in split tensile strength. Concrete specimens containing 0.015%, 0.030%, and 0.045% MWCNT content demonstrated higher values of split tensile strength compared to conventional concrete. The enhancement in split tensile strength was measured at 30.83%, 45.38%, and 66.3%, respectively, for the mentioned MWCNT content levels. The increase in split tensile strength can be attributed to the bridging effect of the MWCNT in the concrete matrix, which enhances the tensile strength. Moreover, the smaller size of MWCNT compared to traditional fibers enables them to penetrate and fill the small voids in the concrete, making it denser and hence more resistant to cracking as said earlier.

(a) Split tensile strength   (b) Increase in split tensile strength
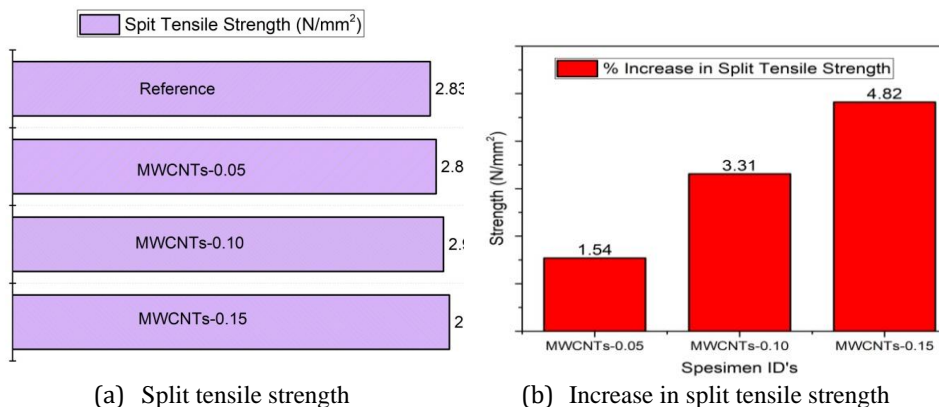
Fig. 5. Split tensile strength

It is noteworthy that the split tensile strength showed higher improvement compared to the compressive strength for the same dosage of MWCNT. This indicates that the addition of MWCNT can significantly enhance the tensile behavior of concrete, making it more durable and resistant to cracking, especially under tensile stresses. Therefore, the use of MWCNT can potentially improve the durability and longevity of concrete structures, especially those subject to heavy loads and harsh environmental conditions. The results suggest that the addition of MWCNT improves the tensile strength of concrete to a greater extent than its compressive strength, even when the same dosage is used. This can be attributed to the fact that the concrete tends to develop cracks and separate from each other during tensile loading, whereas the presence of MWCNT acts as a bridge, holding the concrete together and improving its strength.

3.3 Electrical Properties

3.3.1 Initial Resistance

To evaluate the conversion of normal concrete to sensing concrete and its sensing ability, the initial resistance of all specimens with varying dosages of MWCNT was measured by assessing the initial resistance in a dry condition before loading the specimens. Fig. 6 illustrates the measured values of initial resistance for different dosages of MWCNT for all the specimens. It is observed that as the dosage of MWCNT increases, the electrical resistance decreases, indicating that the concrete becomes more sensitive compared to the reference concrete. The initial resistance of the reference concrete was 332 k-ohms, while for 0.05% of MWCNT, it drastically reduced to 48k-Ohms. However, beyond the 0.05% dosage of MWCNT, the change was relatively small. Thus, the addition of MWCNT to the reference concrete converted it to a sensor. In a study conducted by D'Alessandro et al.

[30], it was discovered that the introduction of multi-wall carbon nanotubes (MWCNTs) and carbon fibers (CFs) into concrete led to a significant reduction in the initial electrical resistance. Specifically, when the MWCNT dosage varied between 0% and 1.5%, the initial electrical resistance experienced a remarkable decrease at the 0.75% MWCNT concentration.
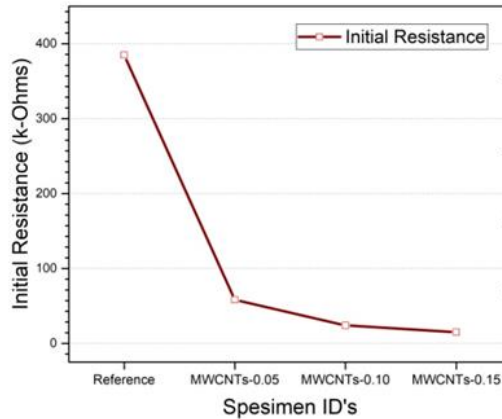
Fig. 6. Initial electrical resistance

3.3.2 Stress Sensing Test

As previously stated, in order to assess the stress sensing capability of the specimen, it underwent 5 cycles of cyclic loading at a peak load of 382kN. This specific load was selected based on 40% of the maximum load-carrying capacity of the reference sample, and the cyclic load was kept within the elastic limit. Throughout the testing process, the electrical resistance and load were recorded, and a graphical representation of the stress and fractional change in resistance (FCR) was produced which us shown in Fig. 7 The stress was calculated using the load, while the FCR was determined using the equation shown below as Eq. 1.

$$FCR = \frac{\Delta R}{R} = \frac{R_x - R_0}{R_0} \tag{1}$$

In the previously provided equation, Rx denotes the electrical resistance of the sample at any point in time during the loading process, whereas R0 signifies the initial resistance of the sample.

The plot depicted in Fig. 7 portrays time on the x-axis and FCR and stress on the y-axis (2 YY axis plot). Throughout the cyclic loading process, both the stress and FCR were computed and graphed. As demonstrated by the results presented in Fig. 7 (a), there was no significant fluctuation in FCR measurements during the cyclic loading of the reference sample. In addition, Fig. 7 (a) demonstrates that the FCR readings steadily rise without any correlation with stress. This is due to the lack of MWCNT in the specimen, which prevented it from transforming into a sensor and exhibiting any sensing capabilities under external loading. Conversely, Fig. 7 (b) showcases the specimen containing 0.05% MWCNT, revealing an enhancement in the FCR plot when compared to the reference specimen. The FCR plot depicted in Fig. 7 (b) displays fluctuations both during the increase and decrease in loading, indicating that the addition of MWCNT induces sensing capabilities to external loading. Although the variation observed is not as precise as that of cyclic stress, it is still

noticeable. Additionally, the correlation between stress and FCR improves as the amount of MWCNT added increases. As the loading increases, the FCR tends to rise, whereas it decreases with a decrease in load. Galao[31] and Chung [32] observed a similar trend in cement cubes, varying the dosage of carbon nano fibers (CNF) from 0 to 2% by weight of the cement. As the CNF percentage increased, the cubes exhibited enhanced self-sensing, detecting structural changes. In contrast, cement composites without conductive admixtures lack self-sensing behavior, and any observed behavior is non-reversible and non-repeatable. The findings highlight the importance of incorporating conductive materials like carbon nano fibers for improved structural health monitoring and concrete durability. This is because the MWCNT dispersed in the concrete specimen move closer to each other during loading, which in turn reduces the electrical resistance and increases conductivity.

a) 0% MWCNT   b) 0.05% MWCNT

c) 0.10% MWCNT   d) 0.15% MWCNT
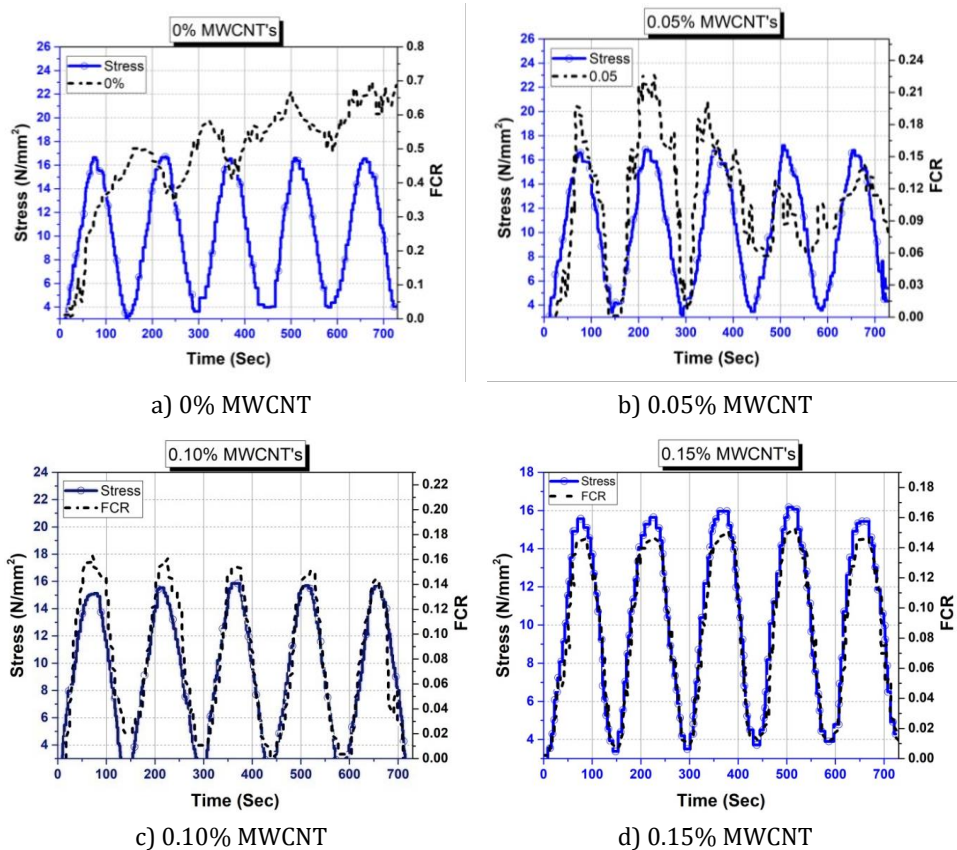
Fig. 7. Plot of Stress and FCR against time

Likewise, when the specimen is unloaded, the fibers move apart due to the decrease in load, leading to a reduction in ion flow and an increase in resistance. For a dosage of 0.1%, Fig. 7 (c) illustrates that the FCR plot displays even greater enhancement in stress sensing when compared to the reference and 0.05% MWCNT specimens. This is due to the increased sensing ability caused by the greater dispersion of nanotubes within the concrete specimen as more MWCNT is added. Additionally, the FCR plot fluctuates in a very similar manner to the stress plot and overlaps with it. The stress sensing ability of the specimen improves with the addition of 0.15% MWCNT, as indicated by the plot Fig.7 (d), but it is not considerably distinct from the plot for 0.1% MWCNT, as depicted in Fig. 7 (c).

As a result, for economic considerations, it can be inferred that a dosage of 0.1% MWCNT would be sufficient for the production of self-sensing concrete.

It can be concluded that self-sensing concrete has the potential to transform the approach to stress and damage monitoring of structures. Real-time stress measurement without requiring the dismantling of structures can contribute to enhanced infrastructure safety and maintenance. Self-sensing concrete can facilitate continuous Structural Health Monitoring (SHM) across the entire structure, eliminating the necessity for attaching or inserting sensors at specific locations. This could potentially enhance the overall safety and durability of structures by enabling the timely detection and addressing of any stress or damage.

3.3.3 Crack Detection Test

This test aims to determine the effectiveness of self-sensing concrete in detecting crack formation in a concrete specimen. The test involves subjecting the specimen to cyclic loading, where the stress is incrementally increased to 4N/mm² for each cycle. Initially, the load is applied until the specimen reaches a stress level of 15kN and is then unloaded back to zero stress. In the next cycle, the load is increased to reach a stress level of 19kN (15+4), and in the subsequent cycle, the stress level is raised to 23N/mm2 (19+4). The stress level is increased to 27 N/mm² in the following cycle, and after that, the load is applied until the specimen fails. In this test, the load was measured using a data logger, while changes in resistance were recorded using a DMM, as was done in the stress sensing test. The load measurements were used to calculate stress, and a plot of FCR and stress was generated, as shown in Fig. 8.
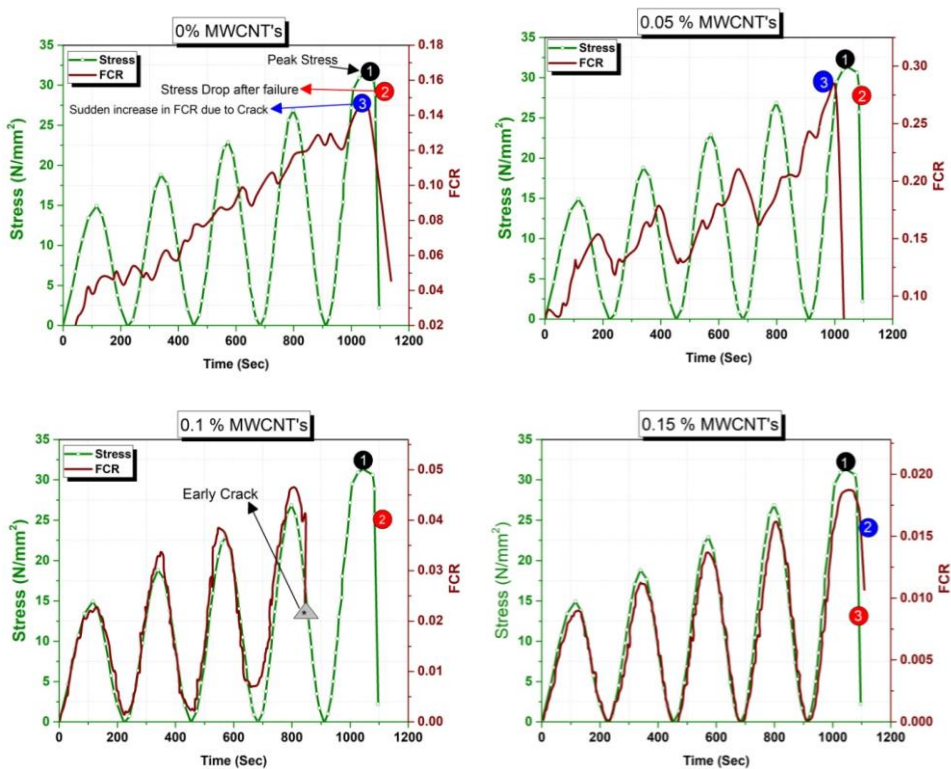
Fig. 8. Results of crack detection test

The results indicate that all specimens exhibited crack detection properties. However, it is important to note that the stress sensing ability improved with increasing dosages of MWCNTs. The sudden drop in the FCsR plot observed in all graphs indicates the formation of cracks within the specimens. The sudden drop in FCR is due to the formation of cracks in the concrete specimen at the peak load. Galao's[31] research investigated the impact of incorporating carbon nano fibers (CNF) at a 2% dosage in cement paste. The study revealed that this addition made the cement paste highly sensitive to its own structural damage, enabling successful crack detection. On a similar note, Arvind[33] conducted a study involving self-compacting concrete (SCC) reinforced with CNF. Their findings indicated that the damage sensing capacity of SCC increased proportionally with the CNF content, ranging from 0 to 2%. Both studies highlight the promising potential of carbon nano fibers in enhancing the structural health monitoring of cement-based materials, leading to the development of more durable and self-aware construction elements. The crack creates a gap between the specimen, which interrupts the flow of electrons and discontinues the FCR measurements, resulting in a drop in FCR.

In all graphs Fig.7, the value "1" indicates the peak stress capacity, "2" indicates stress drop due to failure, while the value "3" indicates the sudden drop in FCR plot due to crack formation in the specimen. The specimen with 0.1% MWCNTs showed an early drop in FCR before reaching the peak load level, indicating the presence of cracks in the specimen at an earlier stage. The results suggest that whenever there is a crack in the specimen, the FCR plot drops suddenly, indicating the formation of cracks. Therefore, it can be concluded from the results that self-sensing concrete can be used for both stress sensing and crack detection in concrete.

4. Conclusions

From the results of this study, the following conclusions can be drawn:

- The maximum critical buckling load was achieved in specimen having 0o rowing orientation angle.
- The specimens having small cutout diameter were showed the maximum strength against to buckling. So that, the maximum critical buckling load was achieved in specimen with 2 mm cutout diameter.
- The utilization of recycled coarse aggregate in the manufacturing of self-sensing concrete can lessen the requirement for natural coarse aggregate. Additionally, the addition of MWCNT did not have a significant impact on the fresh characteristics of self-compacting concrete.
- Incorporating MWCNT into concrete resulted in an enhancement of its strength, as demonstrated by the elevation of both compressive and split tensile strength. The addition of 0.05%, 0.1%, and 0.15% of MWCNT resulted in an increase of 1.51%, 3.21%, and 4.72%, respectively, in compressive strength. Similarly, incorporating 0.05%, 0.1%, and 0.15% of MWCNT led to an increase of 1.54%, 3.31%, and 4.82%, respectively, in split tensile strength.
- The SEM images of specimens containing varying dosages of MWCNTs provide evidence of a random yet uniform dispersion of MWCNTs within the concrete matrix. Additionally, the initial electrical resistance plot clearly illustrates the transformation of conventional concrete into self-sensing concrete, as the initial resistance of the sample significantly decreases from 400k-ohms to 37k-ohms. Moreover, this plot establishes that the critical threshold level of MWCNTs required for creating a self-sensing sample is 0.10%.
- During cyclic loading, the stress sensing ability of concrete improves as the dosage of MWCNT increases. The best similarity plot between stress and FCR is observed

at 0.15% MWCNT. However, for economic reasons, a dosage of 0.1% MWCNT can be considered the best option as it does not show a significant difference.

- During the crack detection test, it was observed that the specimen containing MWCNTs was able to detect crack formation within the specimen at any point of loading, regardless of the dosage of MWCNTs, all the specimens have shown the damage sensing property with improved sensing ability with dosage increase of MWCNTs.

- In comparison to the current methods used for structural health monitoring (SHM), the self-sensing concrete developed using recycled aggregate has shown more efficient stress-sensing capabilities. This new material has the potential to revolutionize the field of SHM by providing real-time and continuous monitoring of structures, leading to better safety and maintenance practices.

References

[1] Gómez J, Casas JR, Villalba S. Structural Health Monitoring with Distributed Optical Fiber Sensors of tunnel lining affected by nearby construction activity. Automation in Construction. 2020 Sep; 117: 103261. https://doi.org/10.1016/j.autcon.2020.103261

[2] Reddy PN, Kavyateja BV, Jindal BB. Structural health monitoring methods, dispersion of fibers, micro and macro structural properties, sensing, and mechanical properties of self-sensing concrete—A review. Structural Concrete. 2021 Apr;22(2):793-805. https://doi.org/10.1002/suco.202000337

[3] Cholker AK, Kavyateja BV, Reddy PN. Influence of Carbon Fibers on Strain and Damage Sensing of Self Compacting Concrete under External Applied Forces. I2M. 2019 Dec 30;18(6):559-65.https://doi.org/10.18280/i2m.180607

[4] Di Nuzzo F, Brunelli D, Polonelli T, Benini L. Structural Health Monitoring System with Narrowband IoT and MEMS Sensors. IEEE Sensors J. 2021 Jul 15;21(14):16371-80. https://doi.org/10.1109/JSEN.2021.3075093

[5] Chen, P. W., & Chung, D. D. Carbon fiber reinforced concrete for smart structures capable of non-destructive flaw detection. Smart Materials and Structures, 1993; 2(1); 22. https://doi.org/10.1088/0964-1726/2/1/004

[6] Fu X, Chung D. Self-monitoring of fatigue damage in carbon fiber reinforced cement. Cement and Concrete Research. 1996 Jan;26(1):15-20. https://doi.org/10.1016/0008-8846(95)00184-0

[7] Chung D. Self-monitoring structural materials. Materials Science and Engineering: R: Reports. 1998 Mar;22(2):57-78. https://doi.org/10.1016/S0927-796X(97)00021-1

[8] Fu X, Ma E, Chung D, Anderson W. Self-monitoring in carbon fiber reinforced mortar by reactance measurement. Cement and Concrete Research. 1997 Jun;27(6):845-52. https://doi.org/10.1016/S0008-8846(97)83277-2

[9] Cholker AK, Tantray MA. Strain-sensing characteristics of self-consolidating concrete with micro-carbon fibre. Australian Journal of Civil Engineering. 2020 Jan 2;18(1):46-55. https://doi.org/10.1080/14488353.2019.1704206

[10] Cholker AK, Tantray M. Electrical resistance-based health monitoring of structural smart concrete. Materials Today: Proceedings. 2021; 43: 3774-9. https://doi.org/10.1016/j.matpr.2020.10.991

[11] Kang J, Al-Sabah S, Théo R. Effect of Single-Walled Carbon Nanotubes on Strength Properties of Cement Composites. Materials. 2020 Mar 13;13(6):1305. https://doi.org/10.3390/ma13061305

[12] Guo Y, Li W, Dong W, Luo Z, Qu F, Yang F, et al. Self-sensing performance of cement-based sensor with carbon black and polypropylene fibre subjected to different loading conditions. Journal of Building Engineering. 2022 Nov; 59: 105003. https://doi.org/10.1016/j.jobe.2022.105003

[13] Li GY, Wang PM, Zhao X. Mechanical behavior and microstructure of cement composites incorporating surface-treated multi-walled carbon nanotubes. Carbon. 2005 May;43(6):1239-45. https://doi.org/10.1016/j.carbon.2004.12.017

[14] Xu S, Liu J, Li Q. Mechanical properties and microstructure of multi-walled carbon nanotube-reinforced cement paste. Construction and Building Materials. 2015 Feb;76:16-23. https://doi.org/10.1016/j.conbuildmat.2014.11.049

[15] Nochaiya T, Chaipanich A. Behavior of multi-walled carbon nanotubes on the porosity and microstructure of cement-based materials. Applied Surface Science. 2011 Jan;257(6):1941-5. https://doi.org/10.1016/j.apsusc.2010.09.030

[16] Dong W, Li W, Wang K, Guo Y, Sheng D, Shah SP. Piezoresistivity enhancement of functional carbon black filled cement-based sensor using polypropylene fibre. Powder technology. 2020;373:184-194. https://doi.org/10.1016/j.powtec.2020.06.029

[17] Li H, Xiao HG, Ou JP. Effect of compressive strain on electrical resistivity of carbon black-filled cement-based composites. Cement and Concrete Composites. 2006;28(9):824-828. https://doi.org/10.1016/j.cemconcomp.2006.05.004

[18] Zuo J, Yao W, Wu K. Seebeck effect and mechanical properties of carbon nanotube-carbon fiber/cement nanocomposites. Fullerenes, Nanotubes and Carbon Nanostructures. 2015;23(5):383-391. https://doi.org/10.1080/1536383X.2013.863760

[19] Hunashyal AM, Tippa SV, Quadri SS, Banapurmath NR. Experimental investigation on effect of carbon nanotubes and carbon fibres on the behavior of plain cement mortar composite round bars under direct tension. International Scholarly Research Notices. 2011. https://doi.org/10.5402/2011/856849

[20] Armoosh SR, Oltulu M, Alameri I, Mohammed HM, Karacali T. The combined effect of carbon fiber and carbon nanotubes on the electrical and self-heating properties of cement composites. Journal of Intelligent Material Systems and Structures. 2022;33(18):2271-2284. https://doi.org/10.1177/1045389X221077447

[21] Dehghani A, Aslani F. The effect of shape memory alloy, steel, and carbon fibres on fresh, mechanical, and electrical properties of self-compacting cementitious composites. Cement and Concrete Composites. 2020;112:103659. https://doi.org/10.1016/j.cemconcomp.2020.103659

[22] Suchorzewski J, Prieto M, Mueller U. An experimental study of self-sensing concrete enhanced with multi-wall carbon nanotubes in wedge splitting test and DIC. Construction and Building Materials. 2020;262:120871. https://doi.org/10.1016/j.conbuildmat.2020.120871

[23] Gao C, Huang L, Yan L, Jin R, Chen H. Mechanical properties of recycled aggregate concrete modified by nano-particles. Construction and Building Materials. 2020;241:118030. https://doi.org/10.1016/j.conbuildmat.2020.118030

[24] Song XB, Li CZ, Chen DD, Gu XL. Interfacial mechanical properties of recycled aggregate concrete reinforced by nano-materials. Construction and Building Materials. 2021; 270: 121446. https://doi.org/10.1016/j.conbuildmat.2020.121446

[25] Murali G, Abid SR, Karthikeyan K, Haridharan MK, Amran M, Siva A. Low-velocity impact response of novel prepacked expanded clay aggregate fibrous concrete produced with carbon nano tube, glass fiber mesh and steel fiber. Construction and Building Materials. 2021;284:122749. https://doi.org/10.1016/j.conbuildmat.2021.122749

[26] EFNARC, "Specification and Guidelines for Self-Compacting Concrete," Rep. from EFNARC, vol. 44, no. February, 2002.

[27] Naqi A, Abbas N, Zahra N, Hussain A, Shabbir SQ. Effect of multi-walled carbon nanotubes (MWCNTs) on the strength development of cementitious materials. Journal of Materials Research and Technology. 2019;8(1):1203-1211. https://doi.org/10.1016/j.jmrt.2018.09.006

[28] Morsy MS, Alsayed SH, Aqel M. Hybrid effect of carbon nanotube and nano-clay on physico-mechanical properties of cement mortar. Construction and Building Materials. 2011;25(1):145-149. https://doi.org/10.1016/j.conbuildmat.2010.06.046

[29] Cwirzen A, Habermehl-Cwirzen K, Penttala V. Surface decoration of carbon nanotubes and mechanical properties of cement/carbon nanotube composites. Advances in cement research. 2008;20(2):65-73. https://doi.org/10.1680/adcr.2008.20.2.65

[30] D'Alessandro A, Ubertini F, Materazzi AL, Laflamme S, Cancelli A, Micheli L. Carbon cement-based sensors for dynamic monitoring of structures. In 2016 IEEE 16th International Conference on Environment and Electrical Engineering (EEEIC) (pp. 1-4). 2016; IEEE. https://doi.org/10.1109/EEEIC.2016.7555628

[31] Galao O, Baeza FJ, Zornoza E, Garcés P. Strain and damage sensing properties on multifunctional cement composites with CNF admixture. Cement and concrete composites. 2014;46:90-98. https://doi.org/10.1016/j.cemconcomp.2013.11.009

[32] Chen PW, Chung DDL. Concrete as a new strain/stress sensor. Composites Part B: Engineering. 1996;27(1):11-23. https://doi.org/10.1016/1359-8368(95)00002-X

[33] Cholker A, Tantray M. Strain and damage sensing property of self-compacting concrete reinforced with carbon fibers. International Journal of Engineering. 2019;32(11):1577-1583. https://doi.org/10.5829/ije.2019.32.11b.09

Research Article

Utilization of textile and tannery sludges in cement mortar

Md. Adnan Haque Chowdhury[a], Md. Shariful Alam[b], Bayzid Ahmed[c], Rakibul Islam[d], Md. Naimul Haque[*,e]

Department of Civil Engineering, East West University, A/2, Aftabnagar, Dhaka-1212, Bangladesh

Article Info	Abstract
	The aim of this study is to investigate the characteristics of Textile ETP and Tannery sludges and strength characteristics of cement-sludge mortar. The textile Effluent Treatment Plant (ETP) and tannery sludges have the potential to become a serious environmental burden for Bangladesh in the future because of their high rate of generation, with a very limited safe disposal option. On the other hand, day by day the demand and price of cement are increasing. This study was devoted to evaluate the technical feasibility of utilizing textile ETP and tannery sludges in cement mortar both as separate and mixed modes. An attempt was taken to replace 5%, 10%, 15% and 20% by weight of cement in mortar with textile ETP and tannery sludges both as a separate and mixed modes. To evaluate the characteristics of the textile ETP and tannery sludges, the pH, moisture content, organic matter content, chemical composition (XRF), TCLP (Heavy Metal) tests were studied. The initial and final setting time, compressive strength, tensile strength, and water absorption of mortar by partial replacement of cement by textile ETP and tannery sludges both as separate and mixed modes were studied to evaluate the properties of cement-sludge mortar. It was found that the textile ETP and tannery sludges both as separate and mixed modes can be a replacement of cement up to 10% in cement mortar and can be used for the purposes of S-type of mortar. The textile ETP sludge as a separate and mixed modes of the sludges can be a replacement of cement up to 20% and can be used for the purposes of N-type of mortar.

1. Introduction

Cement mortar is a hardening material used to bind building blocks such as stones, bricks, and concrete masonry units together which is developed by mixing cement, sand, and water. Mainly sand and binding materials are responsible for the strength and durability of the mortar. Cement mortars are used for plastering the exposed surface of masonry and one of the largest used materials in the construction industry of Bangladesh. The consumption rate of cement mortar in Bangladesh is rapidly increasing due to the construction boom. As the cost of construction materials, especially cement is gradually increasing day by day, therefore, a cheaper solution for cement mortar is required. The Textile and clothing industry have a large contribution to Bangladesh's economy. In 2002, the total commodities exported by Bangladesh out of which 77% was textile clothing and ready-made garments (RMG) [1]. Everyday textile industries in Bangladesh generate around 2.82 million m^3 wastewater, which generates 1.14 kg of solid sludge per m^3 of wastewater [2].

Similar to the textile, the leather industry also produces a huge amount of wastewater and solid waste, which is known as tannery waste [3]. Normally 100-150 kg of sludge is created

after processing per ton of hides/skins [4]. The government of Bangladesh established a large Common Effluent Treatment Plant (CETP), to treat the wastewater generated from this industry which is situated in BSCIC Tannery Industrial Estate, Hemayetpur. BSCIC Tannery Industrial Estate's CETP also generates approximately 20,000 m^3 of tannery effluent and 232 tons of solid waste per day [5].

Based on the discussion above, this is evident that both industries have a very high sludge generation rate. Several options are available to manage these sludges. In Bangladesh, landfill is the only option to manage these sludges, however, landfill has serious adverse environmental effect and there is also scarcity of land. Therefore, it is required to find an alternate path to consume these sludges to save the environment from pollution and recycling could be a promising way. Both sludges can be used in making concrete block, preparing brick, generating biogas, and can also be used for composting [6 ,7]. Balasubramania et al. [8] explored the possibility of using textile ETP in different non-structural building materials such as flooring titles, hollow bricks, solid bricks etc. It was concluded that cement in these building materials can be replaced up to a quantity of 30% by the textile ETP. The chemical sludge generated from the treatment of textile dyeing wastewater was reused in cement blocks as a partial replacement of cement by Patel and Pandey [9]. It was shown that the compressive strength of the cement decreases as the proportion of the sludge increases. The structural and non-structural application by partial substitution of concrete by fly ash up to 30%, and ETP sludge was replaced by fine aggregate up to 20% by Mariappan et al. [10]. The research found that ETP sludge-based concrete performs and fulfills the basic properties of conventional concrete and addition of textile sludge more than 20% reduces the strength of the block noticeably. Goyal et al. [11] investigated the effect of replacement of cement by textile sludge on the properties of mortar and paste. Cement was replaced by textile sludge up to 20% by weight. Results indicated no adverse effect of introducing textile sludge in place of cement up to 5% replacement level. However, there was a considerable loss in strength for higher replacement levels. Jeevanandam et al. [12] reused textile effluent treatment plant (ETP) sludge in substituting cement in conventional cement mortar. Cement in the mortar was replaced by sludge from 0% to 60% with an interval of 10%. They concluded that textile ETP sludge has a potential to be reused up to 20% replacement of cement in cement mortar and can be used as construction materials of different applications. An attempt was taken to investigate the behavior of concrete and its mechanical properties with replacement of cement with textile sludge by Arul et al. [13]. From their experimental investigations, it was found that there is a possibility of utilization of textile industry sludge up to 15% without adding any admixtures.

Similar to the aforementioned works, a group of other researchers focused on tannery sludge to replace cement in various civil engineering applications. Juel et al. [14] prepared clay bricks with different proportions of sludge varying between 10% to 40% by dry weight in both laboratory-controlled and field conditions. The applicability of sludge brick was assessed based on their mechanical and physical properties. Results from that study indicated that it is possible to produce good quality bricks by incorporating tannery sludge that can satisfy all the required mechanical and physical properties as per ASTM and BDS standards. The utilization of tannery sludge by producing a ceramic product was explored by Basegio et al. [15]. The tannery sludge and clay were mixed together in different proportions, and the quality of the ceramic product was characterized in terms of water absorption, porosity, linear shrinkage and transverse rupture strength. Their experimental investigation concluded that in a ceramic product, 10% tannery sludge can be used safely. Malaiskiene et al. [16] recycled tannery sludge in cement mortar for partial replacement of cement by weight. The percentage of cement replacement by the tannery sludge was gradually varied from 3–12%. Results of their study indicated that it is feasible to use

tannery sludge in construction mortars by replacing 6% of cement. In addition to the tannery and textile sludges, other researchers devoted their studies to other types of sludges as well. For example, Brotons et al. [17] and Mandlik and Karale [18] utilized sewage sludge; Ching et al. [19] and Kaish et al. [20] explored the possibility of using alum sludge; Allam et al. [21] used granite sludge, Lima and Zulanas [22] utilized hazardous sludge and Ahmad et al. [23] utilized wastepaper sludge in various cementitious products.

From the above works, it is evident that both the textile ETP and tannery sludges have potential to utilize in civil construction, however, a very limited studies were carried out for partial replacement of cement in mortar. Further, from above studies this is not possible to recommend an optimum value for the sludges available in Bangladesh to replacement cement in mortar as the properties of Bangladeshi sludges could be different from other countries. Therefore, further studies are required based on the textile and tannery sludges available in Bangladesh as a partial replacement of cement in mortar to find an optimum percentage of cement replacement in mortar. Furthermore, this is also necessary to know when the textile and tannery sludges are used in combine mode to partially replace the cement in mortar, how the results differ from the separate mode (only textile or tannery sludge). This kind of mixed mode usage of sludges to replace cement in mortar is also absent in past investigations. Knowing their effect on cement mortar performance will give great flexibility to the users i.e., where there is scarcity of one type of sludge, they can combine the textile and tannery sludges to replace the cement partially in mortar. Therefore, the aim of this study is to utilize the textile ETP and tannery sludges in cement mortar to replace cement partially both as a separate and mixed modes.

2. Working Procedure

The textile ETP sludge was collected from an effluent treatment plant known as Integrated Textile Resources Ltd. (Network Group) and the tannery sludge sample was collected from the Common Effluent Treatment Plant (CETP) of BSCIC Tannery Industrial Estate (Fig. 1). Portland composite cement (PCC) (Type II) and river sand were used in the experimental tests. The textile ETP and tannery sludges were oven dried for 24 hours at 105° C. After 24-hours heating, the color of the textile ETP sludge remained the same, yet the color of the tannery sludge changed to ash color from the black (Fig. 2). Then the oven dried sludges were hammered and turned into powder so that it can be mixed with the mortar (Fig. 3). The characteristics of textile and tannery sludges were evaluated using several experimental tests, it includes the moisture content and pH of the sludges (both as separate and mixed modes) (Fig. 4). The Organic Matter Content, Chemical Composition, and TCLP (Heavy Metal) tests were also carried out for the textile ETP and tannery sludges in combine mode.

| (a) Textile sludge dumping zone | (b) Tannery sludge dumping zone |

Fig. 1 Dumping zones of textile and tannery sludges

(a) Colour of textile ETP sludge before oven dry

(b) Colour of textile ETP sludge after oven dry

(c) Colour of tannery sludge before oven dry

(d) Colour of tannery sludge after oven dry

Fig. 2 Colour of textile ETP and tannery sample before and after the oven dry process

Fig. 3 Hammering of oven dry sludge to make it powder

The cement and sand that were used to prepare the mortar, all the basic tests such normal consistency of cement and sieve analysis of sand were carried out. Three different types of cement mortar with sludges were prepared as summarized in Table 1. The basic ratio for cement and sand were set to 1:2.75 and a water-cement ratio was set to 0.485 by following the guideline of ASTM C109 and C307. The portion of the cement was gradually replaced by the sludges by weight. For all three types of mortar, the cement was replaced by weight of sludge for 5%, 10%, 15% and 20%. Around 72 cement mortar cubes and 36 briquet samples of sludge-cement-sand mixture of varying proportion (5%, 10%, 15%, 20%, replacement by weight) was prepared (Fig. 4). To quantify the quality of the cement-sludge mortar, the initial and final setting time, compressive strength, tensile strength and water absorption tests were carried out by following appropriate codes and standards (Fig. 4).
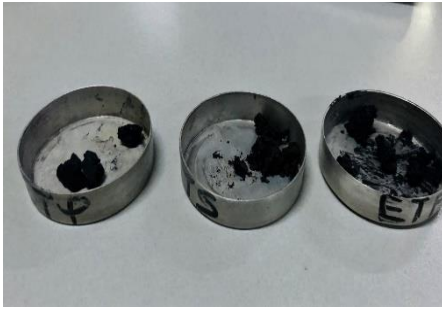
(a) Moisture content test

(b) pH determination

(c) Cement-sludge mortar preparation

(d) Mortar cubes and briquet under water curing

(e) Initial and final setting time test

(f) Compressive strength test of mortar

(g) Tensile strength test of mortar

(h) Water absorption test

Fig. 4 Testing of Cement-Sludge mortar

3. Results and Discussion

3.1. Characteristics of Textile ETP and Tannery Sludges

3.1.1 Moisture Content and pH

The moisture content and pH for textile ETP and tannery sludges were determined both as separate and mixed modes. The moisture content test was conducted based on ASTM

Table 1. Composition of Cement Mortar

Sludge Used	Materials Used	0% Replacement by Weight (kg/m^3)	5% Replacement by Weight (kg/m^3)	10% Replacement by Weight (kg/m^3)	15% Replacement by Weight (kg/m^3)	20% Replacement by Weight (kg/m^3)
Textile ETP Sludge (TETPS)	Cement	384.00	365.00	345.50	326.00	307.00
	Sand	1170.00	1170.00	1170.00	1170.00	1170.00
	Water	187.00	187.00	187.00	187.00	187.00
	TETPS	0.00	19.00	38.50	58.00	77.00
Tannery Sludge (TS)	Cement	384.00	365.00	345.50	326.00	307.00
	Sand	1170.00	1170.00	1170.00	1170.00	1170.00
	Water	187.00	187.00	187.00	187.00	187.00
	TS	0.00	19.00	38.50	58.00	77.00
Textile ETP Sludge (TETPS) + Tannery Sludge (TS)	Cement	384.00	365.00	345.50	326.00	307.00
	Sand	1170.00	1170.00	1170.00	1170.00	1170.00
	Water	187.00	187.00	187.00	187.00	187.00
	TETPS	0.00	9.50	19.25	29.00	38.50
	TS	0.00	9.50	19.25	29.00	38.50

D2216 standard and the electrometric method was used to carry out pH test. For moisture content test, 2.5 gm sample was taken for separate and mixed modes (for mixed mode 50% of each sludge was mixed). The moisture contents of raw textile ETP and tannery sludges in separate mode were 59% and 67%, respectively, whereas in mixed mode it was 64%. The pH of dry textile ETP sludge was 6.07 at a temperature 27.7° C. Therefore, it can be classified as acidic. The dry tannery sludge had a pH value of 8.10 at 28° C, which seems that the dry tannery sludge is basic. The pH in mixed mode of textile ETP and tannery sludges was 6.98 at a temperature of 27.1° C. Therefore, the sludges in the mixed mode can be classified as neutral.

Table 2. Chemical Composition of a Mixed Mode of Textile ETP and Tannery Sludge

Analyte	Sludge Sample Result (%)	Expected concentration for Portland Composite Cement (PCC) According to (Md. Alhaz Uddin, et al., 2013)
CaO	33.0355	64.82
SiO_2	13.6849	20.60
Cr_2O_3	10.7118	-
Al_2O_3	10.2913	4.74
TiO_2	8.4906	-
MgO	7.0763	1.84
SO_3	5.8915	2.4
Fe_2O_3	4.7440	3.28
Na_2O	2.1392	0.21
P_2O_5	1.4806	-
Cl	0.9586	-
ZnO	0.7905	-
K_2O	0.5052	0.38
ZrO_2	0.1189	-
SrO	0.0811	-
LOI	-	1.73

3.1.2. Organic Matter Content and Chemical Composition

The organic matter content in the mixed mode of textile ETP and tannery sludge was found 53.76% based on the dry combustion method. The chemical composition of mixed mode of textile ETP and tannery sludges was determined using X-Ray Fluorescence (XRF-1800, Shimadzu) method. The chemical composition results of the combined textile ETP and tannery sludges were summarized as percentage of major oxides as shown in Table 2. The expected concentration [24] of oxide components for Portland Composite Cement (PCC) was also compared in Table 2. It was found that the slurry in mixed mode has similar chemical components as the Portland composite cement (PCC) yet the proportion is different.

3.1.3. TCLP Test (Heavy Metal Determination)

Toxicity Characteristics Leaching Procedure (TCLP) test results of the combined textile ETP and tannery sludges are shown in Table 3. As can be seen the concentration of all the metals in the sludge is lower than the USEPA guideline values which indicates the lower risk of surface and ground water pollution and less hazardous.

Table 3. Heavy Metals of a Mixed Mode of Textile ETP and Tannery Sludge

	Heavy Metal Concentration (mg/L)							
	As	Cd	Cr	Cu	Hg	Ni	Pb	Zn
Sludge Sample	0	0	0.726	0	0	3.86	0.039	2.33
USEPA Guideline Values	5	1	5	-	0.2	-	5	150

From the above TCLP test results, it can be concluded that the textile ETP and tannery sludges both as separate and mixed modes can be incorporated in cement mortar and at the end-of-life cycle, this mortar waste will not cause any environmental hazard.

3.2. Characteristics of Cement-Sludge Mortar

3.2.1. Initial and Final Setting Time

The initial and final setting time of sludge-cement mortar where cement was replaced by 5%, 10%, 15%, and 20% textile ETP and tannery sludges as separate and mixed modes. The normal consistency of cement was 30% which is within the recommended value of 22 to 30 percent by weight of dry cement according to ASTM C187 for 10 mm penetration. According to ASTM C150, the minimum initial setting time for Portland composite cement has to be 45 minutes and the final setting time should be lower than 375 minutes.
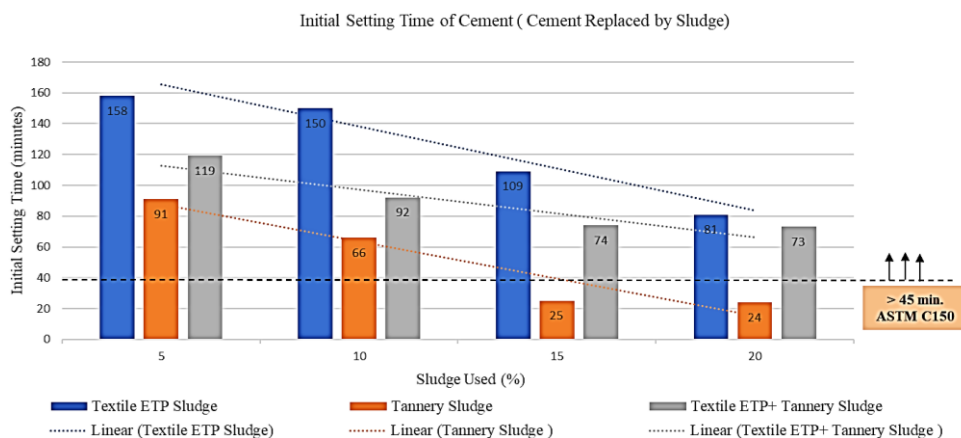
Fig. 5 Initial setting time of cement-sludge mortar
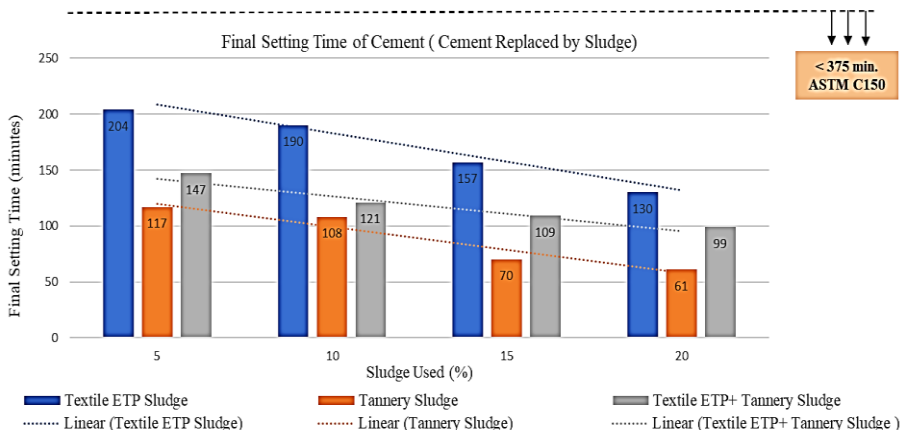
Fig. 6 Final setting time of cement-sludge mortar

The initial setting time results of cement-sludge mortars are plotted in Fig. 5. It was found that the initial setting time of cement-sludge mortars decreases when the amount of sludge inclusion increases. Similar findings were also reported by Goyal et a. [11] and Jeevandam et al. [12]. The initial setting time of cement-sludge mortars with 15% and 20% replacement of cement by tannery sludge are settling earlier than the ASTM standard recommended value. However, for other cases, the cement-sludge mortar's initial setting

time is more than the ASTM standard recommended value. In the case of final setting time, it can be seen that the final setting times of cement-sludge mortars are also decreasing with the increase in sludge inclusion as shown in Fig. 6. As can be seen, all the sludge mortar has a final setting time less than 375 minutes and following the ASTM standard.

3.2.2. Compressive and Tensile Strength of Cement-Sludge Mortar

The 3 days, 7 days and 28 days compressive strengths of cement-sludge mortars are summarized in Fig. 7. From the plot, it is evident that the compressive strength of the cement-sludge mortar decreases with the increase in sludge amount in the mortar which has good agreement with earlier findings [13,16]. According to ASTM C270-14a, the S-type and N-type of mortar should have a minimum compressive strength of 1800 Psi or 12.4 N/mm^2 and 750 Psi or 5.2 N/mm^2 at 28 days, respectively. The 5% and 10% replacement of cement with the textile ETP and tannery sludges both as separate and mixed modes have more than 1800 Psi or 12.4 N/mm^2 compressive strength at 28 days which fulfils the requirement of S-type of cement mortar. For higher percentage of replacement (15% and 20% cases), the cement-sludge mortar fulfils the requirement of N-type mortar. Therefore, the textile ETP and tannery sludges can be utilized in cement-sludge mortar by replacing 5% and 10% of cement in mortar by its weight to produce code recommended S-type of mortar. However, with a higher percentage, the cement-sludge mortar can be used to produce N-type of mortar.

According to ASTM 307-03, usually cement mortar doesn't experience any tension during its service life and tension test is not recommended for mortar, therefore, lower or higher tension will not produce any impact on mortar during its service life. The tensile strength of cement mortar is tested only for research purposes and further information by following the ASTM C307-03 standard. The 3 days, 7days, and 28 days tensile strengths of cement-sludge mortar are plotted in Fig. 8. The tensile strength of cement-sludge mortar decreases with the increase in sludge amount in the mortar. As compared to the textile ETP sludge, the tannery sludge mortar has comparatively lower tensile strength.
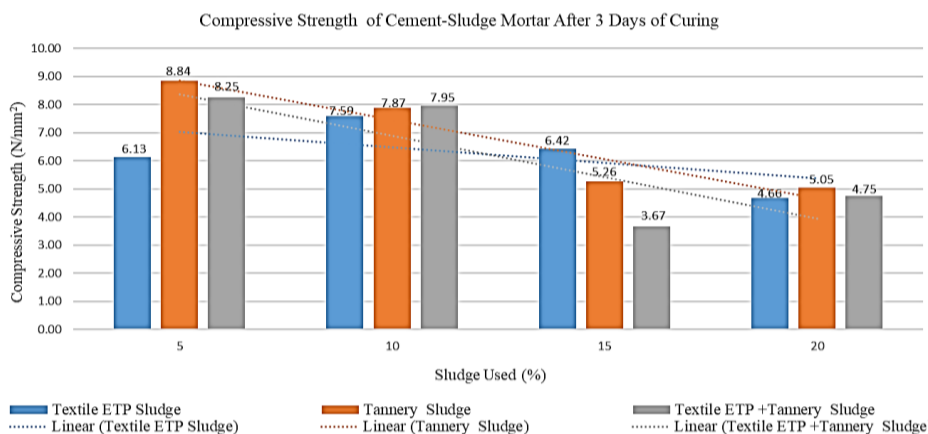
(a) Compressive strength of prepared samples after 3 days of curing
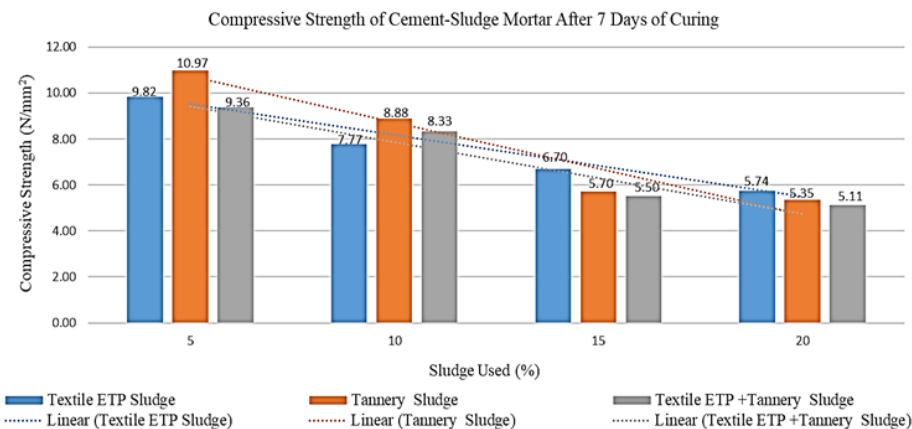
(b) Compressive strength of prepared samples after 7 days of curing
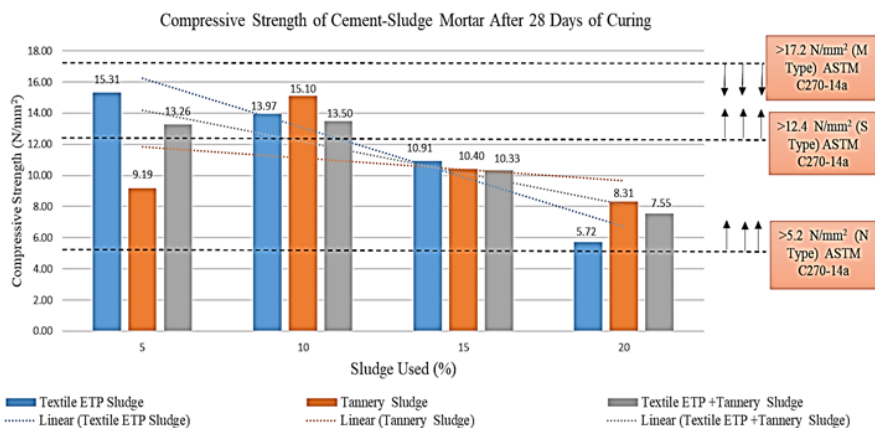
(c) Compressive strength of prepared samples after 28 days of curing

Fig. 7 Compressive Strength test of Cement-Sludge Mortar

(a) Tensile strength of prepared samples after 3 days of curing
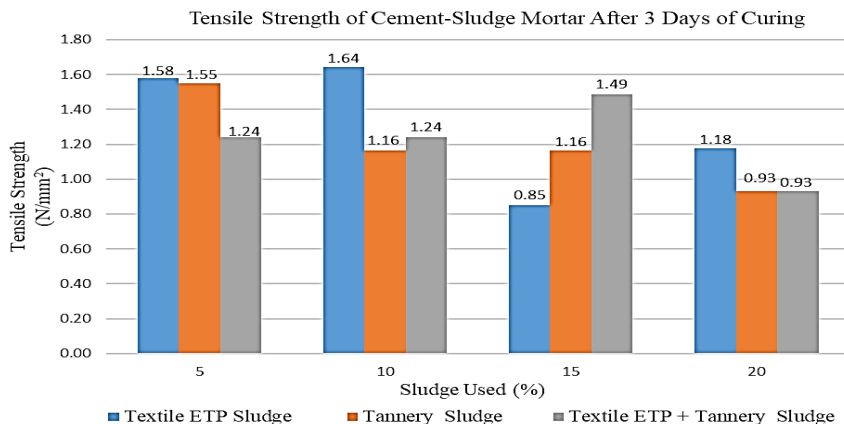
Tensile Strength of Cement-Sludge Mortar After 7 Days of Curing

(b) Tensile strength of prepared samples after 7 days of curing
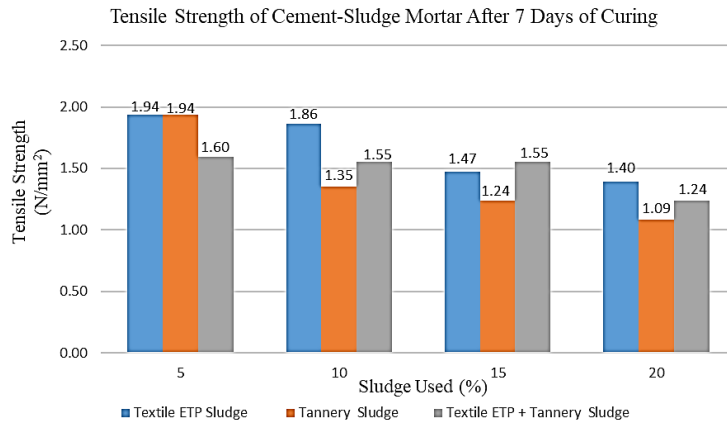
Tensile Strength of Cement-Sludge Mortar After 28 Days of Curing
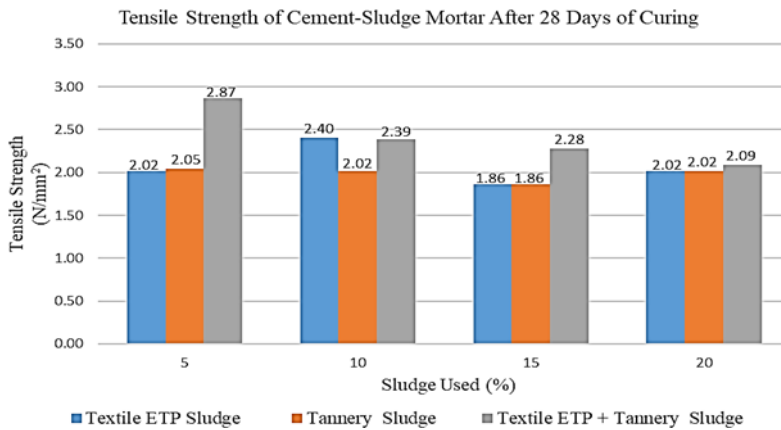
(c) Tensile strength of prepared samples after 28 days of curing

Fig. 8 Tensile Strength test of Cement-Sludge Mortar

3.2.3. Water Absorption Capacity of Cement-Sludge Mortar

The water absorption test of cement-sludge mortar was carried out only for 28 days cured mortar. The water absorption values of cement-sludge mortar are shown in Fig. 9. In general, the water absorption quantity gradually decreases with the increase in sludge quantity in the mortar. In addition to that, textile sludge mortar absorbs more water than the tannery sludge-mortar. Though there is no recommended value for water absorption quantity of cement mortar, however, a good mortar should have a water absorption capacity less than 10%. In the present study, all the cement-sludge mortars have a water absorption capacity less than or very close to the desired value of 10%.
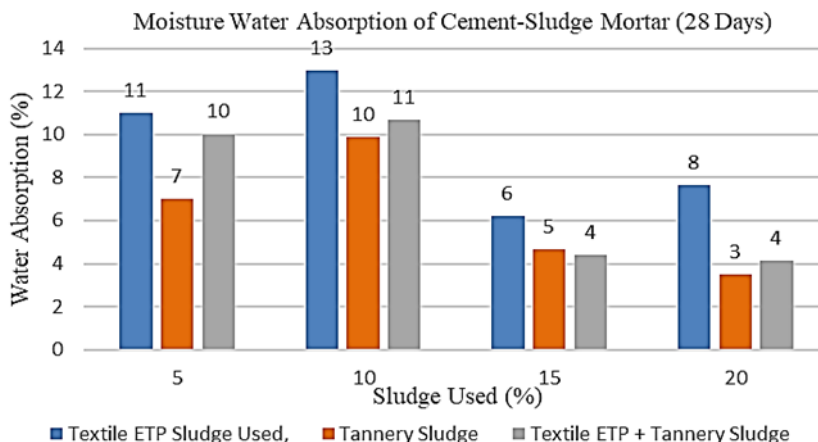
Fig. 9 Water absorption of cement-sludge mortar

4. Conclusions

In this study, textile ETP and tannery sludges are utilized in cement mortar as a partial replacement of cement. Important physical and chemical tests of sludges were carried out. The cement mortars were prepared by replacing 5%, 10%, 15% and 20% (by dry weight) of cement by textile and tannery sludges both as separate and mixed modes and the performance of sludge-cement mortars were evaluated.

The major findings of this study are follows:

- Based on the pH value, the dry textile ETP and tannery sludges can be classified as acidic and basic, respectively. However, in mixed mode, the sludge becomes neutral. The organic matter content percentage in the mixed mode of textile ETP and tannery sludges is 53.76%. The combined mode of textile ETP and tannery sludges has a chemical composition, similar to the Portland Composite Cement (PCC) with different quantities. The heavy metals concentration like As, Cd, Cr, Cu, Hg, Ni, Pb, and Zn in the combined mode of sludges are also within the allowable limit as per the guideline of USEPA. Therefore, the textile ETP and tannery sludges can be utilized safely in cement mortar for partial replacement of cement due to its less hazardous behavior.
- The addition of sludge, in general decreases both the initial and final setting time of cement-sludge mortar and the tannery sludge-cement mortar has comparatively lesser initial and final setting time. The initial setting times for all the cement-sludge mortars both as separate and mixed modes were more than 45 minutes, except for 15% and 20% replacement of cement by tannery sludge cases. In case of final setting time, for any value of cement replacement, the cement-sludge mortar had final setting time less than the codal recommendation.
- Textile ETP and tannery sludges both as separate and mixed modes, up to 10% replacement of cement, fulfilled the compressive strength requirement at 28 days for S type of mortar which can be used for masonry structures with normal to moderate loading such as foundation walls, manholes, sewers, and pavements walks etc. Up to 20% partial replacement of cement by the textile ETP and tannery sludges both as separate and mixed modes fulfilled the compressive strength requirement at 28 days for N-type of mortar which can be utilized for unimportant masonry structures such as partition and parapet walls. For all the cement-sludge mortars, both as separate and mixed modes, the water absorption capacity was near about or less than 10%.

Finally, it can be said that textile ETP and tannery sludges are safe to use in cement mortar and a combination of textile ETP and tannery sludges has better performances as compared to the separate cases in all aspects.

Acknowledgement

References

[1] Garmentsarena. Textile industry in Bangladesh, Garments Arena. June 11, 2017. https://garmentsarena.wordpress.com (Dec. 11,2021).

[2] Anwar TB, Behrose B, Ahmed S. Utilization of textile sludge and public health risk assessment in Bangladesh. Sustainable environment research, 2018; 28(5): 228-233. https://doi.org/10.1016/j.serj.2018.04.003

[3] Hashem M, Islam A, Mohsin S. Green environment suffers by discharging of high-chromium-containing wastewater from the tanneries at Hazaribagh, Bangladesh. Sustainable Water Resources Management, 2018; 1(4): 343-347. https://doi.org/10.1007/s40899-015-0033-4

[4] UNIDO. Solidification and Stabilization of Tannery Sludge. United Nations Industrial Development Organization, South - East Asia. 2018.

[5] Alamgir A, Debnath K, Hossain D, Jalil DMA. Solid Waste Management of Tannery Industrial Estate Dhaka. Sixteenth International Waste Management and Landfill Symposium, 2 -6 October, 2017.

[6] Morshed MN, Guha AK. Production of Biogas from Textile Sludge by Anaerobic Digestion, a Sustainable Ecofriendly Sludge Management Method. Bangladesh Textile Today, 2014.

[7] Hammadi MA, Trabelsi M, Hanchi B. Comparison of Specific Nutrients of Tunisian Textile Sludge and Produced Composts. International Journal of Soil Science, 2007; 2(3):230-234. https://doi.org/10.3923/ijss.2007.230.234

[8] Balasubramanian J, Sabumon PC, Lazar JU, Ilangovan R. Reuse of textile effluent treatment plant sludge in building materials. Waste management, 2006; 26(1): 22-28. https://doi.org/10.1016/j.wasman.2005.01.011

[9] Patel H, Pandey S. Evaluation of physical stability and leachability of Portland Pozzolona Cement (PPC) solidified chemical sludge generated from textile wastewater treatment plants. Journal of hazardous materials, 2012; 207:56-64. https://doi.org/10.1016/j.jhazmat.2011.05.028

[10] Mariappan C, Natarajan M, Sathanandham T. Utilization of flyash and ETP sludge in concrete with addition of Banana fiber. International Journal of Civil Engineering Technology, 2018; 9:398-406.

[11] Goyal S, Siddique R, Jha S, Sharma D. Utilization of textile sludge in cement mortar and paste. Construction and Building Materials, 2019; 214: 169-177. https://doi.org/10.1016/j.conbuildmat.2019.04.023

[12] Jeevanandam S, Ravikumar K, Das A, Goel M. Comprehensive study on textile dyeing sludge as a substitute for cement in cement-mortar. International Journal of Technology, 2015; 5(2):24-35. https://doi.org/10.5958/2231-3915.2015.00024.3

[13] Arul M N, SenthilKumar S, Velumani MP. Studies on behaviour of concrete with ETP sludge. Int. J. Appl. Eng. Res, 2015; 10(38): 28182-28185.

[14] Juel MAI, Mizan A, Ahmed T. Sustainable use of tannery sludge in brick manufacturing in Bangladesh. Waste Management, 2017; 60: 259-269. https://doi.org/10.1016/j.wasman.2016.12.041

[15] Basegio T, Berutti F, Bernardes A, Bergmann CP. Environmental and technical aspects of the utilisation of tannery sludge as a raw material for clay products. Journal of the European Ceramic Society, 2002; 22(13): 2251-2259. https://doi.org/10.1016/S0955-2219(02)00024-9

[16] Malaiškienė J, Kizinievič O, Kizinievič V. A study on tannery sludge as a raw material for cement mortar. Materials, 2019; 12(9): 1562. https://doi.org/10.3390/ma12091562

[17] Brontons F, Garces P, Paya J Saval J. Portland cement systems with addition of sewage sludge ash. Application in concretes for the manufacture of blocks. Journal of Cleaner Production, 2014; 82(1), 112-124. https://doi.org/10.1016/j.jclepro.2014.06.072

[18] Mandlik AD, Karale SA. Sludge use in concrete as a replacement of cement. International Journal for Research in Engineering Application & Management, 2018, 3(10), 22-27.

[19] Ching CY, Bashir MKJ, Aun NC, Aldahdood MAA. Sustainable production of concrete with treated alum sludge. Construction and Building Materials, 2021, 282, 122703. https://doi.org/10.1016/j.conbuildmat.2021.122703

[20] Kaish ABMA, Odimegwu TC, Zakaria I, Abood MM, Nahar L. Properties of concrete incorporating alum sludge in different conditions as partial replacement of fine aggregate. Construction and Building Materials, 2021, 284, 122669. https://doi.org/10.1016/j.conbuildmat.2021.122669

[21] Allam ME, Bakhoum ES, Garas GL. Re-Use of granite sludge in producing green concrete. APRN journal of Engineering and Applied Sciences, 2014, 9(12), 2731-2737.

[22] Lima DA, Zulanas C. Use of contaminated sludge in concrete. Procedia Engineering, 2016, 145, 1201-1208. https://doi.org/10.1016/j.proeng.2016.04.155

[23] Ahmad S, Malik MI, Wani MB, Ahmad R. Study of Concrete Involving Use of Waste Paper Sludge Ash as Partial Replacement of Cement. IOSR Journal of Engineering, 3(11), 6-15. https://doi.org/10.9790/3021-031130615

[24] Uddin MA, Jameel M, Sobuz HR, Islam M, Hasan NM. Experimental study on strength gaining characteristics of concrete using Portland Composite Cement. KSCE Journal of Civil Engineering, 2013; 17(4): 789-796. https://doi.org/10.1007/s12205-013-0236-x

Research Article

Performance of high strength concrete containing locust bean pod ash as cement replacement

Felix Nkapheeyan Isa[*,1,a], Megat Azmi Megat Johari[1,b], Iorwuese Anum [2,c], Julius Lananzakan Agabus [2,d], Solomon Maxwell Soji[2,e], Changlia Hassan Salihu[1,2,f]

[1]School of Civil Engineering, Engineering Campus, Universiti Sains Malaysia, Nibong Tebal 14300, Malaysia
[2] Department of Building, Modibbo Adama University, Yola, Nigeria

Article Info	Abstract
	High-strength concrete (HSC) is becoming popular as a result of its great strength and superior durability. Despite the fact that several supplementary cementitious materials (SCMs) have been explored in HSC, the use of locust bean pod ash (LBPA) as an SCM has not been considered. This study evaluated the use of LBPA as an SCM in HSC. The locust bean pod (LBP) underwent a two-hour calcination process in a furnace at a temperature of 600 °C. At 5%, 10%, 15%, and 20% by weight of cement, LBPA was used in place of cement. The slump, strength (compressive: 100 × 100 × 100 mm cubes; flexural: 100 × 100 × 400 mm beam, and splitting tensile: 100 × 200 mm cylinder at 28 days), water absorption, resistance to sulfate and the effects of elevated temperatures were assessed. Mechanical properties of the concrete were statistically analyzed and optimized using linear Regression. The results showed that 5% LPBA replacement improved compressive, flexural and tensile strengths by 13.14%, 6.42% and 7.08% respectively over the control samples. Additionally, LBPA improved the performance of concrete against water absorption, sulphate attack, and elevated temperatures. The optimized model of 15% LBPA had the highest accuracy with percentage errors of 5.89% and 2.78% for compressive and flexural strengths respectively, while 5% had the highest accuracy for tensile strength with percentage error of 3.08%. The study concludes that LBPA can be successfully used as an SCM in HSC, with a 10% recommended optimum replacement amount.

1. Introduction

Due to urbanization, population expansion, and infrastructure development, concrete production has steadily increased over the past few decades; thus, concrete remains the most extensively utilized building material on the planet [1], [2]. Hence, the manufacturing of cement, which is the most crucial component of concrete which has increased to 3,500 million tons in 2020 and is anticipated to hit 3,700–4,400 million tons by 2050 [3]. This increase in cement production has a corresponding negative effect on the environment. The production of cement alone produces 1,350 million tons of greenhouse emissions annually according to estimates [4]. Also, around 110kWh of energy and 1,500 kg of primary ingredients are needed to produce one ton of cement [5]. Moreso, the construction industry alone contributes to 50% global CO_2 emission [6]. This environmental concern coupled with high cost of cement has led to the development of alternative construction materials. The shift from conventional to alternative materials is aimed principally at conservation of the environment, energy and natural resources associated with cement

production as well as cost reduction [7]–[10]. To achieve the above objectives, SCMs have been consistently used to reduce cement consumption in concrete production [11], [12]. Agricultural wastes and industrial byproducts have been utilized as SCMs in concrete production with resultant positive effects [12]–[17].

Concrete that has a defined compressive strength of 55 MPa or more is termed high strength concrete (HSC) [18]. It is characteristically used in applications where high strength and/or durability are required, such as high-rise buildings and bridges. It is advantageous over normal concrete due to better workability, greater strength and improved durability [19]. Pozzolans, such as fly ash and silica fume, are commonly employed as SCMs in HSC. These compounds enhance the strength of concrete by interacting with the hydration products of Portland cement, resulting in the production of more C-S-H gel, which is the constituent responsible for providing concrete with its strength [20]. For instance, in their study, [19] included rice husk ash (RHA) as a replacement for cement in HSC.

(a)   (b)   (c)   (d)

(e)   (f)   (g)
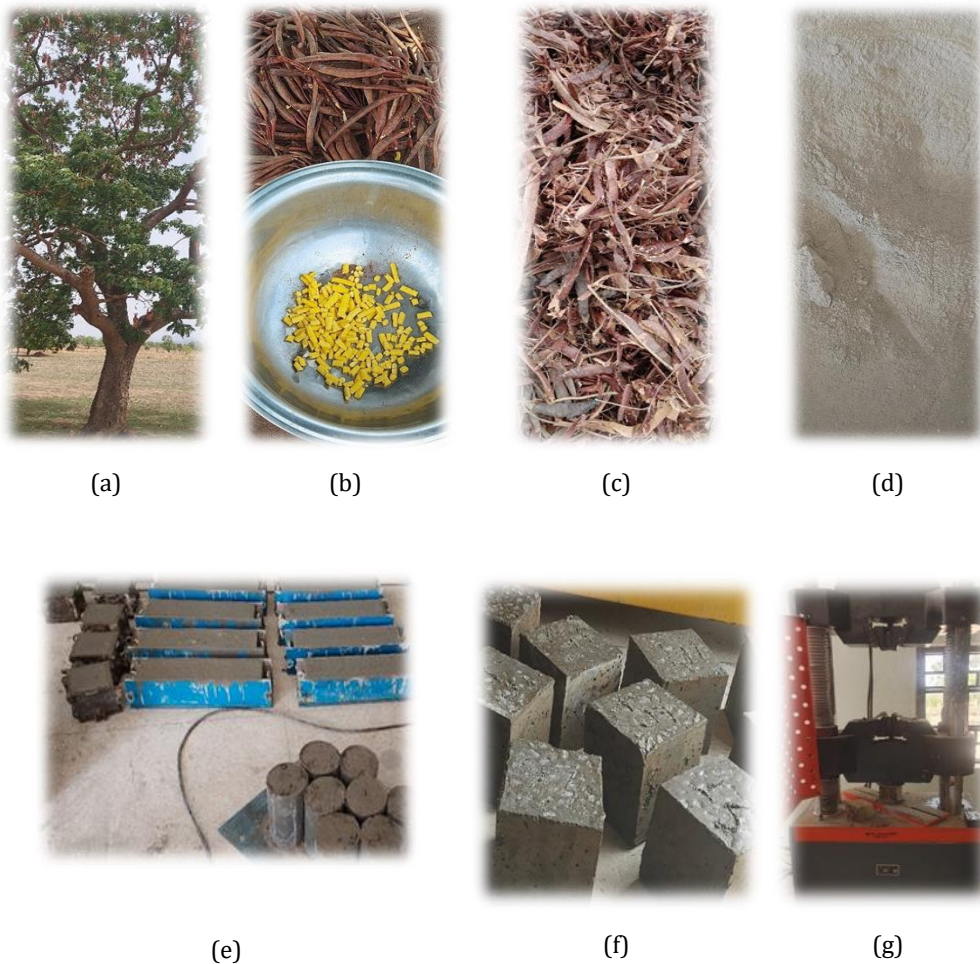
Fig. 1. Locust bean tree with ripe fruits (a), harvested locust bean fruit (b), locust bean pod (c), locust bean pod ash (d), cast concrete cubes, beams and cylinders (e), 'demoulded' concrete cubes (f), and a cube on a universal testing machine (g)

The varying percentages of rice husk ash used were 0%, 5%, 10%, 15%, and 20%. They obtained a cylindrical compressive strength of 56.2 MPa at 28 days of curing and concluded that 10% RHA was the optimum replacement level. Also, the effectiveness of Metakaolin (MK), Fly Ash (FA), and Silica Fume (SF) as SCMs on HSC was assessed by [21]. Under compression, the combinations outperformed the control mix.

Table 1. Summary of nominated previous studies using LPBA as reported in literature

No.	Authors	% Replacement	HSC	Compressive Strength	Flexural Strength	Tensile Strength	Sulphate Resistance	Thermal Resistance	Water Absorption	Remarks
					Summary of Findings					
1	[16]	0, 5, 10 and 15%	X	√	X	X	X	X	X	Decreased compressive strength.
2	[27]	0, 10, 15, 20 and 30%	X	√	X	X	X	X	X	Increased compressive strength up to 15% replacement.
3	[24]	0, 5, 10, 15 and 20%	X	X	√	X	X	X	X	Increased flexural strength with curing time.
4	[33]	0, 5,10,15 and 20%	X	X	X	X	X	X	X	Increased consistency.
5	[34]	0, 5, 10 and 15%	X	√	X	X	X	X	X	Reduction in compressive strength with increase in curing age.
6	[28]	0, 40, 50 and 60%	X	√	X	√	X	X	√	Increased strength.
7	[35]	0, 2.5, 5, 7.5, and 10%	X	√	√	X	X	X	X	Increased strength with curing age.
8	Current Research	0, 5,10,15, and 20%	√	√	√	√	√	√	√	Presented in this paper.

LBPA obtained from calcination of the African Locust Bean (Parkia biglobosa); a perennial tree species native to the west African Savannah has been utilized in production of concrete and mortar [22]–[24]. Figure 1 shows locust bean tree, ripe locust bean fruit, LBP, LBPA, LBPA concrete and Universal Testing Machine.

The utilization of LBPA as SCM has been examined in numerous studies aimed at ensuring effective waste management, construction cost reduction and conservation of the environment [22], [24], [25]. Available literature reveals that concrete made with LBPA exhibits an appreciable level of strength and durability hence, it can be used to produce structural light weight concrete. In their study, [26] observed a progressive rise in strength with curing time. They found that the highest compressive strength of 28.44 N/mm^2 was realized at 28 days when using 5% of LBPA, compared with the control mix which had a strength of 22.27 N/mm^2. Similarly, [27] found an increase in strength of LBPA mortar up to 15% and thence a decline. In the same vein, [28] also discovered that the tensile strengths of 20 and 40% LBPA concrete were higher than that of OPC concrete. The observed increase in strength can be attributed to the substantial surface area of LBPA, which facilitates the pozzolanic reaction leading to the formation of C-S-H gel. Additionally, [29] reported an improvement in flexural strength as the curing period progressed. Some blends had greater strength than the control. Similarly, the utilization of LBPA has been demonstrated to enhance the performance of concrete in various aspects, including water absorption, sulphate resistance, shrinkage, and chloride permeability [28], [30]–[32]. A summary of selected works utilizing LBPA are in Table 1.

Despite its vast potential and the extensive experimental work carried out to determine the properties of LBPA concrete, there is paucity of literature on the performance of LBPA in HSC as well as prediction models. This study is an attempt to assess the performance of LBPA on the properties of HSC. The impact of LBPA on properties of HSC comprising slump, compressive, tensile and flexural strengths as well as water absorption, resistance to sulphate attack and elevated temperatures were examined. Furthermore, the mechanical properties of the concrete were statistically modelled using Regression analysis. This study is expected to cause a reduction in construction cost, greenhouse gases, and cement consumption while ensuring efficient agricultural waste management and sustainability.

2. Materials and Methods

2.1. Materials

The ordinary Portland cement (BUA brand, Nigeria, specific gravity: 3.15) conforming to BS EN 197 [36] was used in this research. The LBP was obtained from Makurdi, Benue state, Nigeria and thermally processed to ash (LBPA, specific gravity: 2.18, bulk density: 875 kg/m^3 and moisture content: 1.58%) in a furnace (600°C for 2 hours) and allowed to cool to room temperature before being sieved (75μm). The chemical compositions of OPC and LBPA was determined via XRF analysis (RaynyEDX-700/800, Shimadzu Corporation, Tokyo, Japan) at Umaru Musa Yar'Adua University, Katsina, Nigeria (Table 2). Sand collected from Benue River in Yola, Nigeria (passing through 4.75mm sieve, specific gravity: 2.67, bulk density: 1,626.04kg/m^3 and moisture content: 2.48%) was used as fine aggregate. Crushed granite (maximum size 12.5 mm, specific gravity: 2.70, moisture content: 1.31% and bulk density: 1883.0 kg/m^3) was used as coarse aggregate. SIKAMENT NNR which conforms to ASTM C494 [37] was the superplasticizer used.

Table 2. Chemical composition of OPC and LBPA

Chemical Composition	OPC	LBPA
SiO_2	20.05	37.03
Al_2O_3	5.27	3.11
Fe_2O_3	3.54	2.67
CaO	61.18	5.10
MgO	0.93	5.85
Na_2O	1.01	0.00
K_2O	0.07	9.94
SO_3	1.24	2.99
P_2O_5	-	3.53
TiO_2	-	-

2.2. Methods

Table 3 displays the mix design and slump values for the concrete. The LBPA as cement replacement material was evaluated (control mix, L00: 0%, L05: 5%, L10: 10%, L15: 15%, L20: 20%). The slump test was conducted on the freshly mixed concrete to determine its workability (BS EN 12350) [38].

Table 3. Mix design for LBPA concrete

Mix No.	OPC (kg/m³)	LBPA (kg/m³)	FA (kg/m³)	CA (kg/m³)	Water (kg/m³)	SP (kg/m³)	Slump (mm)
L00	350	-	525	875	105	10.5	105
L05	332.5	17.5	525	875	105	10.5	97
L10	315	35	525	875	105	10.5	85
L15	297.5	52.5	525	875	105	10.5	45
L20	280	70	525	875	105	10.5	26

2.2.1. Mechanical Properties

2.2.1.1. Compressive Strength

An evaluation of the concrete's compressive strength was carried out (BS EN 12390-4) [39]. Forty-five samples were cast in 100 mm steel cube moulds and cured in water (3, 7, and 28 days). Three samples were crushed at the conclusion of each curing procedure using the Civit Test Hydraulic Universal Testing Machine of 1000 kN capacity and at constant rate of 15 kN/s and the average taken.

2.2.1.2. Flexural Strength

The flexural strength of the concrete was evaluated (BS EN 12390-5) [40]. A total of forty-five concrete specimens were cast in steel beam moulds (100 x 100 x 400mm long) and kept in water (3,7, and 28 days). Three samples were crushed at the conclusion of each curing regime.

2.2.1.3. Splitting Tensile Strength

Splitting tensile strength was determined (BS EN 12390-2) [41]. Forty-five concrete samples were cast in cylindrical moulds of 100mm diameter by 200mm long and cured in water (3, 7, and 28 days).

2.2.2. Durability of LBPA Concrete

The durability of concrete is its ability to withstand deterioration caused by physical, mechanical or chemical factors during its service life in the form of acid attack, carbonation, alkali-aggregate reaction, freezing-thawing, leaching, sulphate attack among others [42]. To ensure that the HSC will be able to withstand the environmental conditions that it will be exposed to, the durability of the concrete was determined in terms of water absorption, resistance to sulfate and elevated temperatures.

2.2.2.1. Water Absorption

The standards of ASTM C642 [43] were followed in order to conduct the water absorption test for the concrete. After 28 days at a temperature of $25 \pm 2°C$, the concrete cubes (15) were cured. After heating the specimens in an oven at $110°C$ for twenty-four hours, their weights (W1) were determined, and then they were immersed in water for twenty-four hours. After the specimens were brought out, the surfaces of the specimens were dried, and their weights were measured once more (W2). The formula for calculating the proportion of water absorbed was:

$$WA\ (\%) = \left| \frac{W2 - W1}{W1} \times 100\% \right|$$

(1)

2.2.2.2. Resistance to Sulphate Attack

The cubes (60) underwent a curing process in water at ambient temperature (28 days). The sample cubes were thereafter soaked in 10% Magnesium sulphate ($MgSO_4$) solution, adopted from works by [44]–[46]. At 7, 14, 21, and 28 days, samples' compressive strength was evaluated.

2.2.2.3. Effect of Elevated Temperature

The concrete specimens (90) were cured in water at $25 \pm 2°C$ (28 days). The samples were brought out of water and allowed to dry for 24 hours before being subjected to various elevated temperatures. Three concrete cubes were exposed for 2 hours to temperatures of $100°C, 200°C, 300°C, 400°C, 500°C,$ and $600°C$ in a furnace, adopted from previous works by [47], [48]. After exposure to the required temperature range, the concrete samples were permitted to settle to room temperature before crushing them to determine their residual compressive strength.

2.3. Model Optimization

Concrete's compressive strength is regarded as the foremost significant mechanical characteristic, typically ascertained subsequent to a curing period of 28 days [49]–[51]. Because the widely used compressive strength factor is only available after 28 days, determining the strength of concrete requires time, preparation, and resources [52]. The development of a strength prediction model was based on the experimental findings depicted in Figure 2, utilizing the Statistical Package for Social Sciences (SPSS) Version 29. Multiple regression analysis is a statistical technique used to predict the value of a dependent variable based on a set of known independent variables. Multiple regression analysis provides evidence that the dependent variable Y is influenced by one or more independent variables (x_1, x_2, x_k) [53]. The association between the anticipated dependent variable (Y) and the independent predictor variables ($x_1, x_2, ..., x_k$) is expressed as:

$$Y = \alpha + \beta_1 x_1 + \beta_2 x_2 +......... \beta_k x_{k + E}.........$$

(2)

Where:

α = constant on Y axis

Y = dependent variable

x_1 and x_2 = independent variables

α is the intercept, representing the value of Y on the regression plane when are both zero. β_1, β_2, and β_k are the regression coefficients representing marginal change in Y associated with a unit change in the corresponding x variable, if the other x variable remains unchanged. For validation of the models, the percentages of error between experimental and predicted values of response variables were evaluated using Equation 3.

$$Error\ (\%) = \left| \frac{Experimental\ Value - Predicted\ Value}{Experimental\ Value} \times 100\% \right| \qquad (3)$$

3. Results and Discussion

3.1.1. Slump

The slump values of the LBPA concrete exhibited a decline as the LBPA content increased. This finding is consistent with [22]. Because LBPA particles have a wide surface area, it is possible that their absorption of some water contributed to the decrease in workability. The decrease in workability can also be ascribed to the permeable characteristics of LBPA resulting from the existence of macro and meso-pores situated both internally and externally on the material, hence contributing to its substantial specific surface area [27]. During the process of mixing, the LBPA undergoes water absorption on its surface, resulting in a decrease in the amount of free water and a corresponding decrease in the slump value [54]. This is not only attributed to the particle size distribution of the LBPA, but also to its mean particle size and geometric shape.

3.1.2. Compressive Strength

The result presented in Figure 2 illustrates the compressive strength of LBPA HSC. The compressive strength improved with inclusion of LBPA and curing age. Concrete containing 5% LBPA was the strongest at 3-, 7- and 28-days having strength of 7.8%, 11.1%, and 13.1% better than the control respectively.
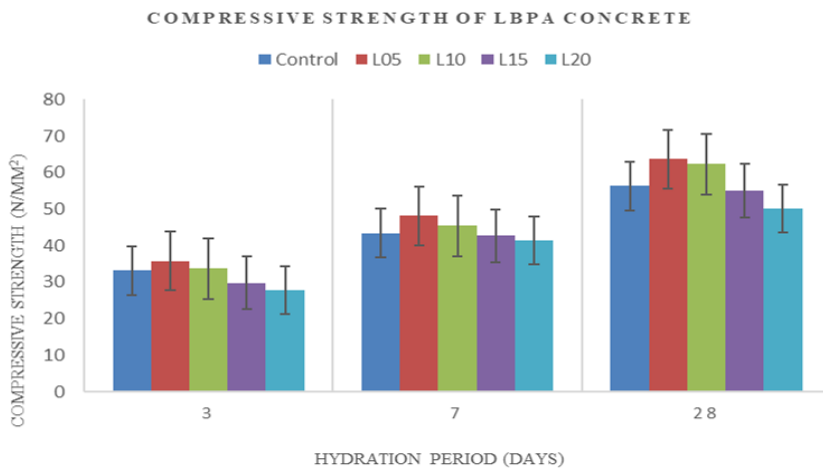
Fig. 2. Compressive strength of LBPA concrete

The aforementioned outcome aligns with the discoveries made by [55] and [56] who stated that pozzolan mixes develop higher strength with curing age. The change in strength gains

between the LBPA concrete and the control is due to the pozzolanic interaction between LBPA and Ca (OH)$_2$, which results in the creation of more C-S-H gel [42]. The strength declined beyond 10% replacement. The 28-day compressive strength of L15 and L20 were 5.7 and 10.8 % lower than that of the OPC concrete with L20 having the lowest strength. The reduction in compressive strength at higher level of LBPA may be as a result of clinker dilution effect [57]. The optimum replacement level is 10% in agreement with [19] and [58] who utilized RHA and (MK) in HSC respectively.

3.1.3. Flexural Strength

The flexural strength behavior of LBPA HSC is similar to that of compressive strength (Figure 3). The result indicates that flexural strength increased with curing age consistent with [24], [29]. The flexural strength of L05 and L10 were 6.4 and 5.2% higher than control concrete at 28 days with L05 showing the best performance. The observed improvement in low-level LBPA substitution can perhaps be attributed to the heightened pozzolanic reaction and enhanced particle packing capacity of LBPA particles [59]. Beyond 10% substitution, the flexural strength declined. The lower flexural strength at higher LBPA content could be attributed to low pozzolanic reaction of LBPA. The observed reduction in flexural strength as the LBPA content increases can be attributed to two factors: the diluting effect of OPC and the poorer formation of C-S-H gel due to the pozzolanic reaction of LBPA [60].
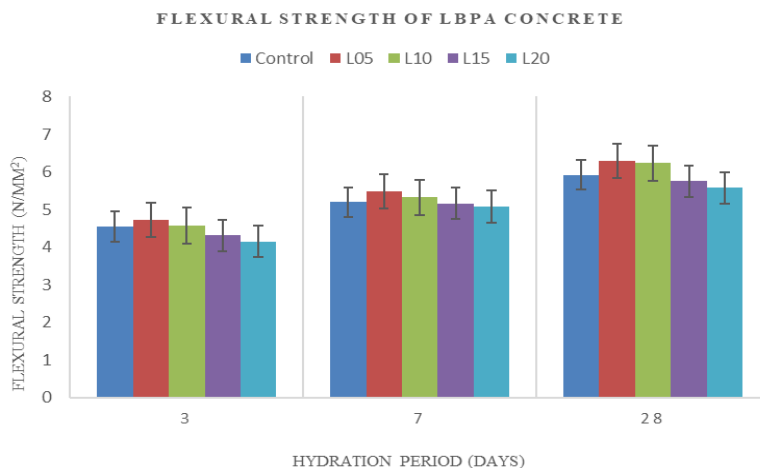
Fig. 3. Flexural Strength of LBPA concrete

3.1.4. Splitting Tensile Strength

Both the curing age and the LBPA content contributed to an increase in the splitting tensile strength. It was observed that at 28 days, the tensile strength of L05 and L10 were 7.1 and 5.9% higher than the control concrete. [28] obtained similar result. The 28-day tensile strength of the reference sample was 4.24 N/mm^2 whereas that of LBPA concrete ranged between 94 and 106% of the control with concrete containing 5% and 20% LBPA content having the highest and least strengths, respectively. The observed improvement in low-level LBPA substitution can perhaps be attributed to the heightened pozzolanic reaction and enhanced particle packing capacity of LBPA particles [59]. The optimum substitution was found to be 10%, same reported by [58] using MK blended mix.
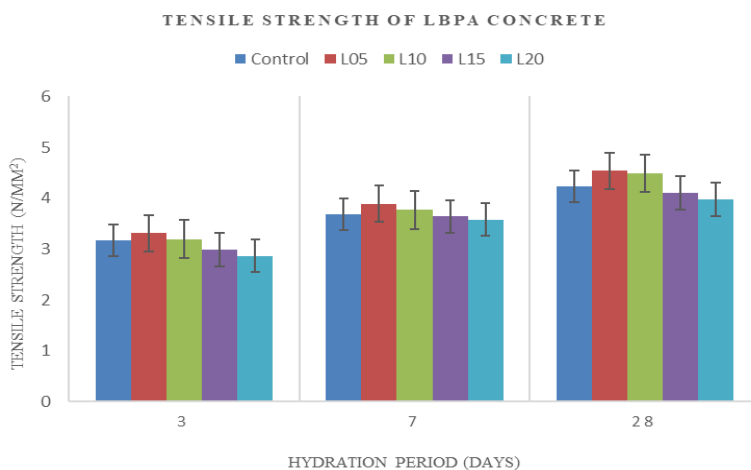
Fig. 4. Tensile Strength of LBPA Concrete

3.2. Durability Properties

3.2.1. Water Absorption

The water uptake of LBPA concrete is between 2.2% and 3.8% with 5% LBPA contributing to the lowest water absorption (Table 4). The rise in LBPA level was accompanied by an increase in the water absorption. However, given that the quantity of water consumed is less than 10%, all of the concretes fall within the category of high-quality concrete [2]. The inclusion of LBPA content led to a reduction in water migration into the concrete, resulting in a decrease in porosity and an increase in impermeability compared to the control sample. This was accomplished by the process of infilling the spaces, resulting in a decrease in potential pathways for the intrusion of water [28]. The resistance to water intrusion is due to the secondary C-S-H gel that develops during the pozzolanic reaction and covers the gaps within the LBPA structure, resulting in denser and more impermeable concrete. The decreased water absorption value reflects the diminished porosity and restricted pore connectivity of the LBPA concrete [61]. [62] also reported less water absorption in ternary concrete containing MK and FA. Similarly, [63] found that concrete made from palm oil fuel ash (POFA) and MK concrete absorbs less water than OPC concrete. Thus, inclusion of pozzolans reduces the water uptake of concrete.

Table 4. Water Absorption of LBPA Concrete

Mix Designation	Water Absorption (%)
L00	3.2
L05	2.2
L10	2.6
L15	3.3
L20	3.8

3.2.2. Resistance to Sulphate Attack

The LBPA concrete showed better resistance to $MgSO_4$ than the control concrete (Figure 5) with LB05 demonstrating the highest resistance. The compressive strength decreased by 18.12%, 11.46%, 14.45%, 13.94%, and 16.53 % for L00, L05, L10, L15 and L20 respectively after 28 days' immersion $MgSO_4$ solution. The resistance may be attributed to

the silicate gel produced during hydration processes which coats and binds the matrix together and prevents the detrimental effects of sulphate on the concrete construction [28]. Another reason could be that the pozzolanic reaction caused by LBPA results in the production of extra binding gel, which leads to the formation of concrete that is more compact. The pozzolanic reaction may have been responsible for the consumption of calcium hydroxide, which may have led to the formation of ettringite, which ultimately had an effect on the concrete [64]. This is because pozzolans are known to enhance concrete's resistance against Sulphate attack [65].
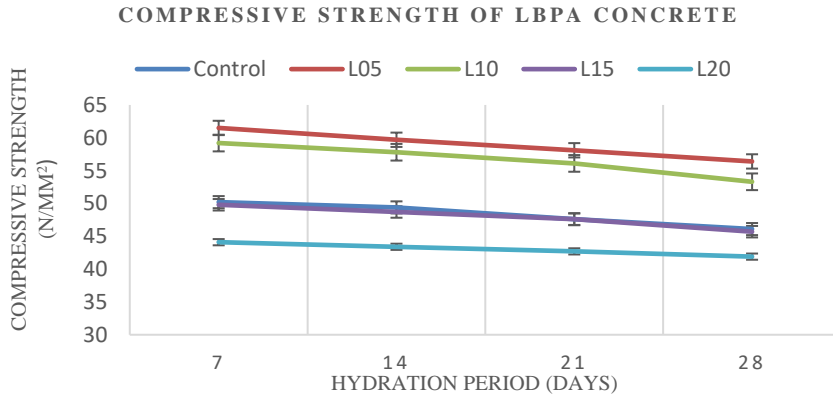
Fig. 5. Compressive strength of LBPA Concrete after Immersion in $MgSO_4$.

3.2.3. Performance Against Elevated Temperature

The correlation between compressive strength and temperature is illustrated in Figure 6. There was a variable change in the compressive strength of LBPA concrete as the temperature increased. The study observed a sharp decline in compressive strength at 100℃, thence an increase at 200 ℃. As temperatures rise, water in the concrete dissipates, exposing a greater proportion of the cementitious components and resulting in a decrease in binding strength between the binder and aggregates.
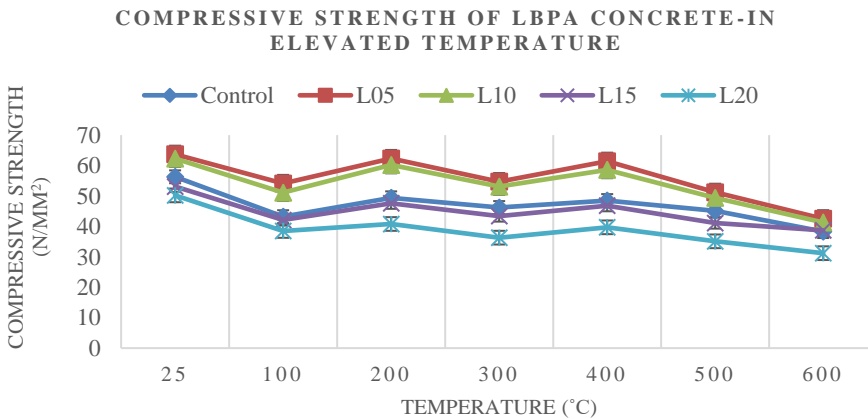
Fig. 6. Compressive Strength of LBPA concrete at elevated temperature

During the dehydrating process, there is an initial decrease in compressive strength followed by an increase [66]. Generally, it was observed that the specimens had better performance at 200 and 400°C with increase in strength while the worst performance was recorded at 600°C. L05 had the best performance at temperature of 400°C with a 68.21% increase in compressive strength from 300°C. This observation is consistent with the one made by [47] who had the best performance at 200°C and 400°C with a drastic strength loss at 800°C when they subjected MK blended cement paste to elevated temperatures. The low content of the LBPA was responsible for the thermal stability of the composite. This may be attributed to the chemical decomposition of the already depleted C-S-H in the blends [67]. The specimens recorded lower compressive strength at 100°C and 600°C. Therefore, the thermal stability of LBPA concrete could be achieved at 10% replacement respectively.

3.3.1. Evaluation of Statistical Model

Equations 4, 5, and 6 show the regression equations for the compressive, flexural, and splitting tensile strengths of LBPA concrete models.

$$F_{CS} = 36.665 - 0.329\,(x_1) + 0.875\,(x_2) \tag{4}$$

$$F_{FS} = 4.774 - 0.020\,(x_1) + 0.051\,(x_2) \tag{5}$$

$$F_{TS} = 3.345 - 0.015\,(x_1) + 0.040(x_2) \tag{6}$$

Where:

F_{cs}= concrete compressive strength the concrete

F_{FS} = flexural strength

F_{TS} = concrete splitting tensile strength

x_1 = percentage replacement of cement by LBPA

x_2 = curing age

The multiple regression analysis findings are presented in Table 5. According to the coefficient of determination (R^2) values of 82.2, 80.1, and 80.6% for the compressive, flexural, and tensile strengths, respectively, the differences in LBPA content and curing age have a considerable impact on the variation in concrete strengths indicating a strong correlation.

Table 5. Results of the multiple regression analysis.

Strength Property	Model	R	R-squared	Adjusted R-squared	Std. error of the estimate
Compressive	1	0.907	0.822	0.792	5.1376
Flexural	2	0.895	0.801	0.768	0.32256
Tensile	3	0.898	0.806	0.773	0.24814

The p-value presented in Table 6 provides an assessment of the overall statistical significance of the model. At a significance level of 0.05, the P-value is less than 0.001 for both LBPA content and age of curing of concrete. This indicates that both variables are

highly significant (P < 0.05), suggesting that the variation in the concrete compressive, splitting tensile, and flexural strengths can be attributed to the LBPA content and age of curing. The emerged model indicates that 82.2, 80.1, and 80.6% of the variation in compressive, flexural and tensile strengths of LBPA concrete can be explained by the two variables (LBPA content and curing age).

Table 6. Analysis of variance (ANOVA) showing the significance of the regression model.

	Model		Sum of squares	df	Mean Square	F	Sig.
Compressive	1	Regression	1461.314	2	730.657	27.681	< 0.01
		Residual	316.742	12	26.395		
		Total	1778.056	14			
Flexural	2	Regression	5.021	2	2.511	24.130	< 0.001
		Residual	1.249	12	0.104		
		Total	6.270	14			
Tensile	3	Regression	3.064	2	1.532	24.883	< 0.001
		Residual	0.739	12	0.062		
		Total	3.803	14			

The coefficients of the independent variables in the regression equation are shown in the B-column of Table 7. The statistical analysis of the Table reveals that both the LBPA content and curing age have a substantial impact on the anticipated strengths. This is supported by the fact that the p-value for curing age is less than 0.001. The t-values quantify the degree of influence that each variable has on the projected strengths. Hence, the t-values and corresponding p-values provide evidence about the statistical significance of the effects of LBPA content and curing age on the predictive capability of LBPA concrete strength.

Table 7. Coefficients of the independent variables in the regression equation.

			B	Std. error	Beta	T	p-value
Compressive	1	Constant	36.665	2.762		13.276	< 0.001
		% Replacement	-0.329	0.188	-0.23	-1.752	0.105
		Curing Age	0.875	0.121	0.881	7.231	< 0.001
Flexural	2	Constant	4.774	0.173		27.532	< 0.001
		% Replacement	-0.020	0.012	-0.219	-1.698	0.115
		Curing Age	0.051	0.008	0.868	6.736	< 0.001
Tensile	3	Constant	3.345	0.133		25.080	< 0.001
		% Replacement	-0.015	0.009	-0.217	-1.707	0.114
		Curing Age	0.040	0.006	0.871	6.845	< 0.001
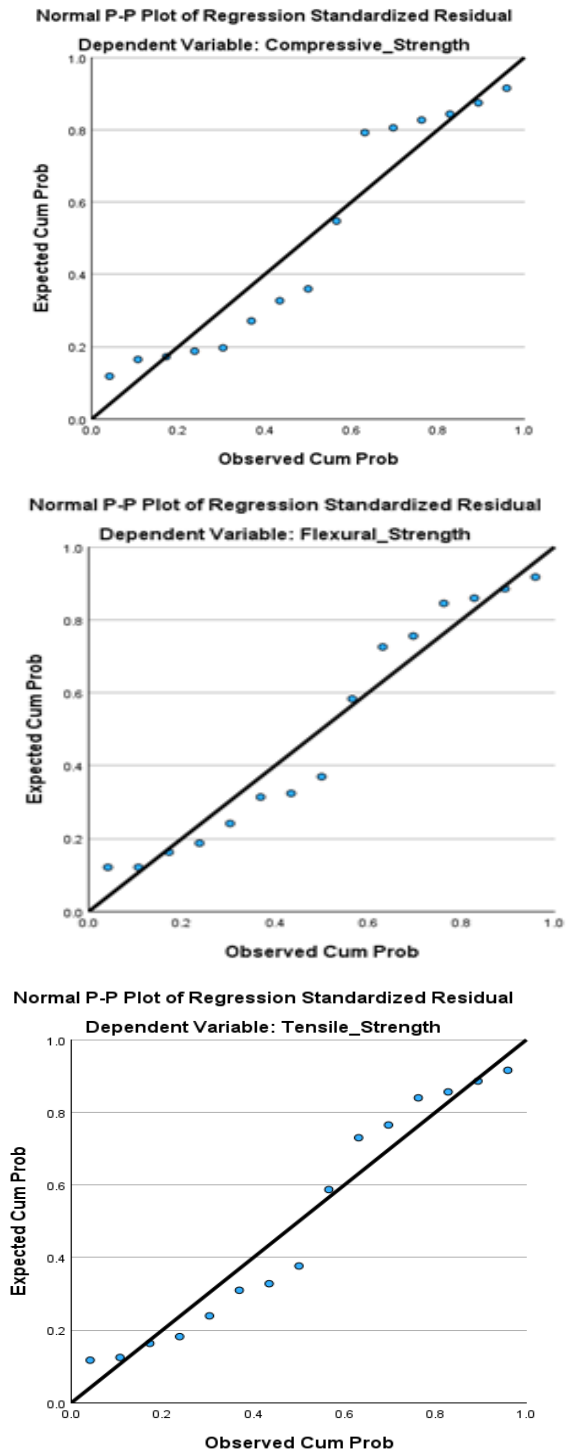
Fig. 7. Normal probability plot for a. Compressive strength b. Flexural strength c. Tensile strength

Figure 7 is the Normal Probability plot for the strength (compressive, flexural and tensile) models of LBPA concrete. The data points exhibit a close proximity to the linear regression line, suggesting that the residuals follow an approximated normal distribution.

3.3.2. Validation of the Model

The optimized model's validity is displayed in Table 8. In engineering contexts, a 20% margin of error is considered to be acceptable [68], [69]. From the table, all the response variable are within the acceptable limits with L15 having the best accuracy for compressive and flexural strengths respectively while L05 had the highest accuracy for tensile strength. This shows that all the optimized prediction models in relation to percentages of LBPA are adequate for design prediction.

Table 8. Validation of optimized models.

Replacement Level	Compressive Strength (N/mm²)		Percentage Error (%)	Flexural Strength (N/mm²)		Percentage Error (%)	Tensile Strength (N/mm²)		Percentage Error (%)
	Experimental	Predicted		Experimental	Predicted		Experimental	Predicted	
0	56.3	61.17	8.65	5.92	6.20	4.73	4.24	4.47	5.42
5	63.7	59.52	6.56	6.30	6.10	3.17	4.54	4.40	3.08
10	62.3	57.88	7.10	6.23	6.00	3.69	4.49	4.32	3.77
15	53.1	56.23	5.89	5.75	5.91	2.78	4.11	4.24	3.16
20	50.2	54.59	8.75	5.58	5.80	3.94	3.98	4.17	4.77

4. Conclusions

The performance of HSC containing LBPA as cement replacement was investigated in this study. The LBPA was obtained by thermal digestion of LBP at 600°C for 2 hours. The slump, strengths, water absorption, resistance to sulphate, and the effects of elevated temperatures were assessed, after initial curing in water for 28 days. Results from the study revealed that slump values decrease with increase in LBPA content in the HSC with the lowest value of 26mm for the 20% replacement. The strength (compressive, flexural and tensile) of concrete improved by 13.14%, 6.42% and 7.08% respectively over the control samples at 5% replacement level. Additionally, LBPA improved the durability of concrete in terms of water absorption, resistance to sulphate action and elevated temperatures. Water absorption decreased with increase in LBPA content recording the lowest value of 2.2% over control samples at 5% replacement level. The compressive strength decreased by 18.12%, 11.46%, 14.45%, 13.94%, and 16.53% for L00, L05, L10, L15, and L20 respectively after 28 days' immersion in MgSO4; implying that LBPA improves the resistance of concrete against MgSO4. The compressive strength of LBPA concrete fluctuated with increase in temperature; providing a better resistance at temperatures of 200°C and 400°C compared to OPC concrete as a result of low pozzolanic activity. The optimized model of L15 had the highest accuracy with percentage errors of 5.89% and 2.78% for compressive and flexural strengths respectively while L05 had the highest accuracy for tensile strength with percentage error of 3.08%. The study concludes that LBPA can be used successfully as an SCM in HSC. Thus, 10% optimum replacement amount is recommended. The findings of the study are comparable with previous work carried out by [70], [71] utilizing POFA and bamboo leaf ash in HSC respectively. The study further recommends that the effect of the use of additional pozzolans together with LBPA in HSC be studied. Additionally, the performance of LBPA in geopolymer and self-compacting concrete should be studied. Finally, the environmental impacts and the economic aspects of using LBPA should be investigated.

Acknowledgement

References

[1] Faraj RH, Mohammed AA, Omer KM. Self-compacting concrete composites modified with nanoparticles: A comprehensive review, analysis and modeling. Journal of Building Engineering. 2022; 50:104170. https://doi.org/10.1016/j.jobe.2022.104170

[2] Neville AM. Properties of Concrete. Prentice Hall; 2012.

[3] Madeleine R. Emissions from the Cement Industry. Earth Institute, Columbia University, Columbia. 2012.

[4] Cleetus A, Shibu R, Kurian Paul V, Jacob B. Analysis and Study of the Effect of GGBFS on Concrete Structures. International Research Journal of Engineering and Technology. 2018. 5(3):3033-7.

[5] Ahmad W, Ahmad A, Ostrowski KA, Aslam F, Joyklad P, Zajdel P. Sustainable approach of using sugarcane bagasse ash in cement-based composites: A systematic review. Case Studies in Construction Materials. 2021 Dec 1;15. https://doi.org/10.1016/j.cscm.2021.e00698

[6] Arrigoni A, Panesar DK, Duhamel M, Opher T, Saxe S, Posen ID, et al. Life cycle greenhouse gas emissions of concrete containing supplementary cementitious materials: cut-off vs. substitution. J Clean Prod. 2020; 263:121465. https://doi.org/10.1016/j.jclepro.2020.121465

[7] Alabadan B, Olutoye M, Abolarin MS. Partial replacement of ordinary Portland cement (OPC) with bambara groundnut shell ash (BGSA) in concrete. Leonardo Electronic Journal of Practices and Technologies. 2005; (6):43-8.

[8] Ramlochan T, Thomas M, Gruber KA. Effect of metakaolin on alkali-silica reaction in concrete. Cem Concr Res. 2000; 30(3):339-44. https://doi.org/10.1016/S0008-8846(99)00261-6

[9] Ahsan MB, Hossain Z. Supplemental use of rice husk ash (RHA) as a cementitious material in concrete industry. Constr Build Mater. 2018; 178:1-9. https://doi.org/10.1016/j.conbuildmat.2018.05.101

[10] Rashad AM. An exploratory study on high-volume fly ash concrete incorporating silica fume subjected to thermal loads. J Clean Prod. 2015; 87(1):735-44. https://doi.org/10.1016/j.jclepro.2014.09.018

[11] Pacewska B, Wilińska I. Usage of supplementary cementitious materials: advantages and limitations: Part I. C-S-H, C-A-S-H and other products formed in different binding mixtures. J Therm Anal Calorim. 2020; 142(1):371-93. https://doi.org/10.1007/s10973-020-09907-1

[12] Patil S, Patel TH. Performance of rice husk ash, silica fume, and quarry dust-based glass fibre reinforced concrete subjected to acid attack. Mater Today Proc. 2022; 66:2315-21. https://doi.org/10.1016/j.matpr.2022.06.231

[13] Zeyad AM, Khan AH, Tayeh BA. Durability and strength characteristics of high-strength concrete incorporated with volcanic pumice powder and polypropylene fibers. Journal of Materials Research and Technology. 2020; 9(1):806-18. https://doi.org/10.1016/j.jmrt.2019.11.021

[14] Tayeh BA, Alyousef R, Alabduljabbar H, Alaskar A. Recycling of rice husk waste for a sustainable concrete: A critical review. J Clean Prod. 2021; 312:127734. https://doi.org/10.1016/j.jclepro.2021.127734

[15] Nwofor T, Sule S. Stability of groundnut shell ash (GSA)/ordinary Portland cement (OPC) concrete in Nigeria. Advances in Applied Science Research. 2012; 3(4):2283-7.

[16] Ochola AB, Ahmadu AM, Balarabe Bala A. Sugarcane Bagasse Ash and Locust Beans Waste Ash as a Replacement for Cement in Concrete. International Journal of African Sustainable Development. 2021;16(2):301-8.

[17] V. M. Malhotra, V. S. Ramachandran, R. F. Feldman, and P. C. A'itcin, Condensed silica fume in concrete. CRC Press, 2018. https://doi.org/10.1201/9781351070843

[18] ACI Committee (ACI 363R). High-Strength Concrete. Special Publication. 2010; 228:79-80.

[19] Nursyamsi N, Aruan AF. Application of rice husk ash in high strength concrete. IOP Conf Ser Mater Sci Eng. 2021; 1122(1):012013. https://doi.org/10.1088/1757-899X/1122/1/012013

[20] Fernando A, Selvaranjan K, Srikanth G, Gamage JCPH. Development of high strength recycled aggregate concrete-composite effects of fly ash, silica fume and rice husk ash as pozzolans. Materials and Structures/Materiaux et Constructions. 2022; 55(7):1-22. https://doi.org/10.1617/s11527-022-02026-3

[21] Banjare A, Jaiswal SK. Influence of Supplementary Cementitious Materials on High Strength Concrete. IJSRD-International Journal for Scientific Research & Development. 2017; 5:2321-0613.

[22] Afolayan JO, Oriola FOP, Sani JE. Experimental Investigation of the Effect of Partial Replacement of Cement in Concrete with Locust Bean Waste Ash. International Journal of Engineering and Applied Sciences. 2018; 5(12):42-7.

[23] Akpenpuun TD, Akinyemi B, Olawale O, Aladegboye OJ, Adesina OI. Mechanical and Structural Characteristics of Cement Mortars Blended with Locust Bean Pod Ash. Agricultural Engineering International: CIGR Journal. 2019; 21(4):48-55.

[24] Auta SM, Anthony AI, Amadi AA. Flexural Strength of Reinforced and Revibrated Concrete Beams Using Locust Bean Pod Epicarp Ash as Replacement for Cement. Journal of Civil Engineering, A Publication of NICE. 2020;12(2).

[25] Aliyu SD, Ma'aruf A, Farouq MM, Dawusu SU. Stabilization of Lateritic Soil Using Powdered Locust Bean Pod 'Makuba'. In: International Journal of Engineering & Science Research. 2018; 249-55.

[26] Auta SM, Kabiru A. Effect of Locust Bean Pod Epicarp Ash (Lbpea) on the Compressive Strength of Revibrated Concrete. Construction of Unique Buildings and Structures. 2020; 90(9002).

[27] Akpenpuun TD, Akinyemi BA, Olawale O, Aladegboye OJ, Adesina OI. Physical, mechanical and microstructural characteristics of cement-locust bean pod ash mortar blend. Journal of Applied Sciences and Environmental Management. 2019; 21(4):377. https://doi.org/10.4314/jasem.v23i3.1

[28] Yalley PP. Mechanical and Durability Properties of Engineered Cementitious Composite Containing High Volume of Pozzolanic admixture. American Journal of Engineering Research. 2019; 8(4):229-35.

[29] Olubajo OO, Jibril A, Osha OA. Effect of Locust Bean Pod Ash and Eggshell Ash on the Mortar Compressive and Flexural Strengths of Cement Blends. Path of Science. 2020; 6(3):4001-16. https://doi.org/10.22178/pos.56-2

[30] Ikumapayi C. Optimisation of Selected Pozzolanic Concrete Mixes for Improved Strength and Durability of Concrete. Federal University of Technology Akure Information Repository. 2016.

[31] Ikumapayi CM, Akingbomire SL. Effects of Bamboo Leaf and Locust Beans Pod Ashes on Autogenous Shrinkage Strain and Compressive Strength of Mortar. FUTA Journal of Engineering and Engineering Technology. 2018; 12(1):49-53.

[32] Ikumapayi CM, Akingbonmire SL, Oni O. The Influence of Partial Replacement of Some Selected Pozzolans on the Drying Shrinkage of Concrete. Guigoz Sci Rev. 2019; (511):189-97. https://doi.org/10.32861/sr.511.189.197

[33] Ja'e IA, Sulaiman TA, Abdurrahman AA. Evaluation of Pozzolanic Materials and Their Influence Cement and Workability Retention of Concrete. Nigerian Journal of Scientific Research. 2019; 18.

[34] Ali H, Babatunde RI, Adejoh BO. Investigation of Locus Beans Waste Ash as Partial Replacement for Cement in Concrete Structures. International Journal of Advances in Scientific Research and Engineering. 2019; 5(4):149-53. https://doi.org/10.31695/IJASRE.2019.33133

[35] Olu OO, Osha OA, Jibril A. Setting Times of Portland Cement Blended with Locust Bean Pod and Eggshell Ashes. American Journal of Chemical Engineering. 2020; 8(5):103. https://doi.org/10.11648/j.ajche.20200805.11

[36] BS EN 197-1. Cement. Composition, specifications and conformity criteria for common cements. British Standards Institution. 2019; 56.

[37] ASTM C494/C494M. Standard Specification for Chemical Admixtures for Concrete. American Society for Testing and Materials. 2022

[38] BS EN 12350. Testing fresh concrete. British Standards Institution. 2019.

[39] BS EN 12390-4. Testing hardened concrete Compressive strength. Specification for testing machines. European Standards; 2019.

[40] BS EN 12390-5. Testing hardened concrete. Flexural strength of test specimens. British Standards Institution. 2019.

[41] BS EN 12390-6. Testing hardened concrete. Tensile splitting strength of test specimens. British Standards Institution. 2019.

[42] Neville AM, Brooks JJ. Concrete technology. 2nd ed. London: Prentice Hall; 2010.

[43] ASTM C642. Standard Test Method for Density, Absorption, and Voids in Hardened Concrete. American Society of Testing and Materials. 2021.

[44] Ambrose EE, Ogirigbo OR, Ekop IE. Compressive Strength and Resistance to Sodium Sulphate Attack of Concrete Incorporated with Fine Aggregate Recycled Ceramic Tiles. Journal of Applied Sciences and Environmental Management. 2023 ;27(3):465-72. https://doi.org/10.4314/jasem.v27i3.9

[45] Tang Z, Li W, Ke G, Zhou JL, Tam VWY. Sulfate attack resistance of sustainable concrete incorporating various industrial solid wastes. J Clean Prod. 2019; 218:810-22. https://doi.org/10.1016/j.jclepro.2019.01.337

[46] Mohammadhosseini H, Lim NHAS, Tahir MM, Alyousef R, Samadi M, Alabduljabbar H, et al. Effects of Waste Ceramic as Cement and Fine Aggregate on Durability Performance of Sustainable Mortar. Arab J Sci Eng. 2020; 45(5):3623-34. https://doi.org/10.1007/s13369-019-04198-7

[47] Wang W, Liu X, Guo L, Duan P. Evaluation of Properties and Microstructure of Cement Paste Blended with Metakaolin Subjected to High Temperatures. Materials. 2019; 12(6):941. https://doi.org/10.3390/ma12060941

[48] Tanyildizi H, Şahin M. Application of Taguchi method for optimization of concrete strengthened with polymer after high temperature. Constr Build Mater. 2015; 79:97-103. https://doi.org/10.1016/j.conbuildmat.2015.01.039

[49] Krishnya S, Yoda Y, Elakneswaran Y. A two-stage model for the prediction of mechanical properties of cement paste. Cem Concr Compos. 2021; 115:103853. https://doi.org/10.1016/j.cemconcomp.2020.103853

[50] Nithurshan M, Elakneswaran Y. A systematic review and assessment of concrete strength prediction models. Case Studies in Construction Materials. 2023;18. https://doi.org/10.1016/j.cscm.2023.e01830

[51] Saloma, Nasution A, Imran I, Abdullah M. Improvement of Concrete Durability by Nanomaterials. Procedia Eng. 2015; 125:608-12. https://doi.org/10.1016/j.proeng.2015.11.078

[52] Ma S, Shi X, Yu C, Wang W, Ren Y, Tian X. Research on Improved BP Neural Network Gangue Powder Concrete Compressive Strength Prediction Model. 2020;419-23. https://doi.org/10.1109/ITAIC49862.2020.9339112

[53] Blaikie NWH. Analyzing quantitative data: from description to explanation. SAGE Publications; 2003. https://doi.org/10.4135/9781849208604

[54] Cordeiro GC, Toledo Filho RD, Tavares LM, Fairbairn EMR. Experimental characterization of binary and ternary blended-cement concretes containing ultrafine residual rice husk and sugar cane bagasse ashes. Constr Build Mater. 2012; 29:641-6. https://doi.org/10.1016/j.conbuildmat.2011.08.095

[55] Aquino W, Lange DA, Olek J. The influence of metakaolin and silica fume on the chemistry of alkali-silica reaction products. Cem Concr Compos. 2001; 23(6):485-93. https://doi.org/10.1016/S0958-9465(00)00096-2

[56] Ahmadi M, Alidoust O, Sadrinejad I, Nayeri MD. Development of Mechanical Properties of Self Compacting Concrete Contain Rice Husk Ash. International Journal of Computer, Information, and Systems Science and Engineering. 2007;1(4):259-262.

[57] Ramezanianpour AA, Bahrami JH. Influence of metakaolin as supplementary cementing material on strength and durability of concretes. Constr Build Mater. 2012; 30:470-9. https://doi.org/10.1016/j.conbuildmat.2011.12.050

[58] Dinakar P, Sahoo PK, Sriram G. Effect of Metakaolin Content on the Properties of High Strength Concrete. Int J Concr Struct Mater. 2013;7(3):215-23. https://doi.org/10.1007/s40069-013-0045-0

[59] Siddique R, Klaus J. Influence of metakaolin on the properties of mortar and concrete: A review. Appl Clay Sci. 2009; 43(3-4):392-400. https://doi.org/10.1016/j.clay.2008.11.007

[60] Prasanphan S, Sanguanpak S, Wansom S, Panyathanmaporn T. Effects of ash content and curing time on compressive strength of cement paste with rice husk ash. thaiscience. 2010; 7(3).

[61] Jindal BB, Jangra P, Garg A. Effects of ultra fine slag as mineral admixture on the compressive strength, water absorption and permeability of rice husk ash based geopolymer concrete. Mater Today Proc. 2020; 32:871-7. https://doi.org/10.1016/j.matpr.2020.04.219

[62] Güneyisi E, Gesoğlu M, Algin Z, Mermerdaş K. Optimization of concrete mixture with hybrid blends of metakaolin and fly ash using response surface method. Compos B Eng. 2014; 60:707-15. https://doi.org/10.1016/j.compositesb.2014.01.017

[63] Ismail MH, Megat Johari MA, Ariffin KS, Jaya RP, Wan Ibrahim MH, Yugashini Y. Performance of High Strength Concrete Containing Palm Oil Fuel Ash and Metakaolin as Cement Replacement Material. Advances in Civil Engineering. 2022; 2022:1-11. https://doi.org/10.1155/2022/6454789

[64] Muthusamy K, Wan Ahmad S, Hashim MH, Mohamad N, Kirgiz MS, Kamarudin MAA, et al. Sulphate resistance of lightweight aggregate concrete comprising sieved palm oil fuel ash as fine aggregate replacement. Mater Today Proc. 2022; 66:2536-40. https://doi.org/10.1016/j.matpr.2022.07.077

[65] Ahmad Zawawi MNA, Muthusamy K, P.P. Abdul Majeed A, Muazu Musa R, Mokhtar Albshir Budiea A. Mechanical properties of oil palm waste lightweight aggregate concrete with fly ash as fine aggregate replacement. Journal of Building Engineering. 2020; 27. https://doi.org/10.1016/j.jobe.2019.100924

[66] Shen J, Xu Q. Effect of elevated temperatures on compressive strength of concrete. Constr Build Mater. 2019; 229:116846. https://doi.org/10.1016/j.conbuildmat.2019.116846

[67] Nwankwo PO, Achuenu E. Effects of Fibre Treatment on the Properties of Sisal Fibre Reinforced Ternary Concrete. Int J Sci Eng Res. 2014; 5(8).

[68] Manan TSBA, Kamal NLM, Beddu S, Khan T, Mohamad D, Syamsir A, et al. Strength enhancement of concrete using incinerated agricultural waste as supplementary cement materials. Sci Rep [Internet]. 2021; 11(1). https://doi.org/10.1038/s41598-021-92017-1

[69] Baji H. The effect of uncertainty in material properties and model error on the reliability of strength and ductility of reinforced concrete members. Material Science. 2014.

[70] Tangchirapat W, Jaturapitakkul C, Chindaprasirt P. Use of palm oil fuel ash as a supplementary cementitious material for producing high-strength concrete. Constr Build Mater. 2009; 23(7):2641-6. https://doi.org/10.1016/j.conbuildmat.2009.01.008

[71] Odeyemi SO, Atoyebi OD, Kegbeyale OS, Anifowose MA, Odeyemi OT, Adeniyi AG, et al. Mechanical properties and microstructure of High-Performance Concrete with bamboo leaf ash as additive. Clean Eng Technol. 2022; 6. https://doi.org/10.1016/j.clet.2021.100352

Research Article

Effect of sea sand in the behaviour of fresh concrete partially replaced with M-sand

Neethu S[*,a], Tensing D[b], Vincent Sam Jebadurai S[c]

Department of Civil Engineering, Karunya Institute of Technology and Sciences, Coimbatore

Article Info	Abstract
	The research paper aims to address the environmental challenges caused by uncontrolled river sand mining in various regions of the country. Indiscriminate mining has led to multiple issues, necessitating restrictions on river sand extraction, but these restrictions have also affected the building industry's stability. As a solution, exploring cost-effective alternative materials for cement production becomes essential to promote resource utilization and efficiency in the construction sector. The study focuses on using excavated marine sand as a fine aggregate to develop enduring and resilient concrete. Partial replacement of river sand and manufactured sand (MS) with dredged sea sand (DSS) is conducted to understand the benefits of the proposed concrete in terms of strength and durability compared to traditional concrete made of river sand (RS). This investigation is significant in the current scenario to assess the potential of DSS as a building material. The methodology employed includes grading analysis, assessment of flexural and compressive strength, evaluation of water absorption, alkalinity testing, rapid chloride penetration test, bond strength examination, and sorptivity assessment. The research aims to determine the behavior of fresh concrete with sea sand as a partial replacement for traditional sands, ultimately contributing to more eco-friendly and resource-efficient construction practices. The gradation has been done in three different proportions say 10, 20, and 30%. The results indicate that for all the mixes the compressive strength of the cylinder shows an average value of 0.83 times the strength of the cubes, while the flexural strength value ($K\sqrt{fck}$) shows an average of 0.69 times the strength of the cubes for all the mixes. RCPT and Water Absorption results show an average value of 1775 and 3.96 respectively which is within the limit specified. The addition of MS improves the alkalinity of concrete and the result was in accordance with ASTM D 4262. The bond strength increases with an increase in the replacement of sea sand and sorptivity decreases with an increase in the replacement of sea sand. This is indeed a study of the strength of concrete and toughness using MS as a partial replacement for dredged sand. The analysis shows that a 30% replacement of dredged sea sand with MS does not impact the overall strength of concrete, ensuring satisfactory strength and durability.

1. Introduction

Uncontrolled river sand mining in India for construction causes severe environmental challenges, including river bank erosion, biodiversity loss, lowered water tables, groundwater contamination, flooding, sedimentation, siltation, altered landscapes, social

---

conflicts, and illegal activities. Sustainable alternatives and stringent regulations are vital to address these impacts and promote responsible mining practices. It is seen nowadays that there is a scarcity of river sand (RS) due to an increase in the construction industry and other major environmental issues. Because of its readiness, ease of mining, ample source, and price benefits, marine sand is considered an effective alternative to other sands [1 & 2]. The corrosion impact caused by chloride ions and the stability of reinforced concrete members has been a major concern while making sea-sand concrete. [3–6].

On the other hand, how would dredge sea sand (DSS) affect the output of the concrete? Various research has indicated different findings [7-10]. Liu et al. discovered that the workability of concrete, compressive strength, elastic modulus, and flexural strength with marine sand possessing fewer sodium and shells were unaffected [11]. If Cl-induced rust is not a concern, both cleaned and unclean marine sand should be used in place of river sand in concrete. According to Chandrakeerthy et al [12], Marine sand concrete has a compressive strength lower than that of conventional concrete. Limeira et al [13–15] demonstrated that marine sand could be effectively used as a fine aggregate for construction purposes because of the similar mechanical and physical properties of marine sand concrete compared to standard concrete. Various researchers [16-18], on the other hand, discovered that the compressive strength of marine sand concrete was lower than that of normal concrete after 28 days. Jau et al. [21] concluded that after investigating 35 weeks of accelerated corrosion tests under wet-dry cycles on marine sand concrete, the cylinder compressive strength was found to show enhancement in strength during the initial phase and reached a maximum value at the age of 21 weeks. However, the strength was found to decrease by about 5%–8% at the age of 35 weeks.

According to Shuai Wu's research [22], on the crust of beach sand, there may be microfilm that includes chemical substances and organic compounds which are constituents of marine water. The appearance of a film on such sand will affect the mechanical properties of marine sand concrete. Other studies [23–29] have discovered that the particle size of sea sand influences the interlocking characteristics of cement thereby the strength of concrete. Saeed Moradi et al [30] used dredged marine sediments (DMS) to replace sands obtained from quarries with different percentages and discovered that replacing DMS material enhanced the particle packing density of a cementitious system, which was due to the particles obstruction of capillary pores. Under pressure, the availability of pores, sorptivity, and water penetration depth was maintained or decreased when raw sand was replaced with DMS. According to Matthew Zhi Yeon Ting et al. [31], incorporating silicomanganese slag with sea sand reduced the compressive and tensile strengths of concrete by 9.2% and 17.5%, respectively. In terms of sorptivity and chloride penetration, however, sea sand enhanced concrete's durability by at least 42.3 percent and 11.5 percent, respectively. Norpadzlihatun Manap et al [32] investigates that, the strength of concrete made with sediments (sand) from Sungai Bebar replacing % of sand and aggregate components is 30.6 N/mm2 after 28 days of curing, while the strength of concrete made with silt from Kuala Perlis as an additive is 48.8 N/mm2 after 28 days of curing.

The most commonly used fine aggregate in concrete is river sand, but extensive processing of stream sand and gravel causes river degradation. The stream bottom is lowered by in-stream mixing, which can contribute to bank erosion. As a result, the government imposed some restrictions on river sand mining. Today Manufactured sand (MS) is used as fine aggregate in concrete. MS unlike natural sand is not smooth and round; hence more water and cement are required to sustain the workability of concrete. The use of dredged marine sand to make green and robust concrete may be a perfect remedy to the engineering industry's problems.

2. Need and Scope of the Study

The dredged sea sand has been collected from the Puthuvypeen beach area after getting special permission from Cochin Port Trust. The Port is now dumping around 21 million cubic meters per annum of dredging material in the permitted dumping zone in the sea, 20 kilometers from the beach [35]. Previously, attempts were attempted to utilize the waste in landfills or as bio-fertilizers. However, attempts have so far achieved no beneficial results due to the presence of heavy metals on one hand, and difficulties in removing the material from the Port's following suction hopper dredgers on the other. The Port has decided to focus its efforts in the Puthuvypeen area, where land is accessible. Every year, it is estimated that 4 million cubic meters of sand are dredged from an area of around 8 kilometers in the shipping channel for smooth ship movement and thrown in the open sea. The government has been looking into ways to cut the net cost of maintenance dredging. The use of dredge material was one of the recommendations made in this regard.

3. Materials Used and Properties

3.1. Cement

Cement is a substance used in construction that sets, hardens, and adheres to other materials in order to bind them together. Cement is seldom used on its own; rather, it is utilized to hold sand and aggregate together. The properties of Ordinary Portland Cement (OPC) 53-grade cement with a specific gravity of 3.14 were tested according to IS: 12269-2013 [38], and IS 4031- 4:1988 [39] regulations, as shown in Table 1.

3.2. Fine Aggregates

3.2.1. Dredged Sea Sand

The foreseeable need for river sand and M-sand as fine aggregate in the construction sector is almost fulfilled by sea sand. The sea sand samples were taken from the Puthuvypeen area, which lies close to the Arabian Sea coast. The sand samples were collected from the seabed which is approximately 7 – 8km away from the seashore by using the method of dredging. Also, the sea sand samples were subjected to rainfall for roughly a year and practically all the chlorine content was washed out because sand is an inert material. Dredged sea sand (DSS) used as a substitute for MS was in accordance with Zone IV. Specific gravity and water absorption of DSS were 2.28 and 5.9 percent respectively.

3.2.2. Manufactured Sand

In the construction industry, Manufactured sand (MS) is a substitute for river sand in concrete, and it is made from hard granite stones crushed in a quarry. Crushed sand from cubical rocks or stones with grounded edges is washed and processed for use as a construction material. The MS used for the concrete contains crushed powder and granite grains with a size of less than 4.75 mm. MS with a specific gravity of 2.59 and water absorption of 3.4% conforming to IS 383-2016 [36] was used as a partial replacement for sea sand. MS was partially replaced with 10%, 20%, and 30% of DSS.

3.3. Coarse Aggregates

In concrete, crushed granite stone coarse aggregate with a size of less than 20 mm is used as the major matrix component. According to IS 383–2016 [36], the aggregate size used in the concrete mix should be retained on a sieve having a 4.75 mm size. The coarse aggregate (CA) used in this investigation was found to have a specific gravity of 2.76 and water absorption of 1.2 percent. M sand used for the research work has been collected from S K Traders and M Sand Supplier, Coimbatore. MS features angular/cubical particles with consistent gradation, controlled moisture content (2-6%), minimal fines content (0-15%),

and absence of organic impurities, it has a density of 1850 kg/m^3 and adheres to construction standards IS 383-2016 [36] for optimal workability, strength, and durability in concrete.

Table 1. Outlines the properties of all materials

Properties		Cement	Fine Aggregate		Coarse aggregates
			MS	DSS	
Normal consistency		28.60%	-	-	-
setting time (min)	Initial	161	-	-	-
	Final	259	-	-	-
Specific gravity		3.24	2.59	2.28	2.76
Impact factor		-	-	-	23.1%
Crushing value		-	-	-	19.4%
Water absorption		-	3.4%	5.9%	0.7%
Zone		-	II	IV	-

4. Methodology

4.1. Grading

The Sea sand was classified into the appropriate zone by means of sieving using a standard set of sieves as per IS 383-2016 [36]. The grading of sea sand indicates that they are very fine and hence need to go for gap grading with the replacement of MS which helps to maintain the particle size distribution curve lies within the boundary of zone III. Gap grading improves particle distribution, workability, and aggregate packing when mixing dredged sea sand with M sand, resulting in better concrete or mortar properties, including higher strength and durability, reduced risk of segregation, and optimized use of materials for a more sustainable construction process. M sand and Sea sand were taken and the samples were allowed to pass through standard sieves 4.75mm to 0.75micron size. After drawing the particle size distribution curve of Sea sand, a major portion of samples goes outside zone 4, according to IS 383 – 2016 [36] Table 9, Note 4: It is recommended that fine aggregate conforming to Grading Zone IV should not be used in reinforced concrete. Hence gap grading was done, i.e., samples passing through 4.75 to 600 microns of sea sand were taken in different proportions, 10, 20, and, 30% and the portion was filled with samples retained in 300 microns, 150 microns, and 75 microns sieve in different proportions say 10, 20 and 30% respectively.

4.2. Flexural Strength

Beams of size 100 x 100 x 500mm were cast, cured, and tested for 28 days in accordance with IS 516-2021 [37] in the Universal Testing Machine for flexure.

4.3. Compressive Strength

Cubes are the most common shape used for compressive strength testing because they are easy to manufacture and handle. Cylinders are also used for compressive strength testing which helps to ensure a comprehensive evaluation of concrete made with sea sand, considering material variability and different stress distributions during compressive strength testing. In accordance with IS 516-2021[37], Cubes of size 150 x 150 x 150mm and cylinders of size 150 x 300mm were cast, cured, and tested for 28 days in the Compression Testing Machine.

Fig. 1. Compressive strength test arrangement for Cylinder and cube

4.4. Water Absorption

According to ASTM C 140 [40], 100mmx100mmx100mm size cubes were cast and cured for 28 days. For testing, it was oven-dried at 100°C for 24 hours and the dry weight of the specimen was taken. The specimen was then immersed in the water for 24 hours and then the wet weight was taken.

$$\% \ water \ absorption = \left(\frac{wet \ weight - dry \ weight}{dryweight} \right) \times 100 \qquad (1)$$

4.5. Alkalinity Test

The sample for the test was obtained by crushing the concrete cube from which a portion of the cement mortar was collected in accordance with ASTM D 4262 [41]. The cement mortar passing through a 50 microns sieve was collected as a sample for the test. 10g of the obtained material was taken in a glass beaker and mixed with 50 ml of distilled water and stirred in a Jar test apparatus till the particles settle down at the bottom. Then Alkalinity of surface water was determined using a pH meter.

4.6. Rapid Chloride Penetration Test

According to ASTM C 1202 [42], Concrete samples were cast using standard 100 mm x 50 mm x 50mm size moulds. The samples were stored for a period of time in vacuum desiccators until it is submerged in water and the sample is inundated. The samples were then secured within the two chambers of the diffuser cell. A solution of NaCl was used in the first chamber, a and NaOH solution was used in the second. 60V electrical current was connected to the diffuser cells. The readings were taken at 30-minute intervals for 6 hours.

4.7. Bond Strength

To determine the pullout strength of concrete made with partial replacement of MS with dredged sea sand, a steel rod is inserted into the concrete cube at the time of casting itself. After curing for 28 days, the specimens were tested for their pullout strength according to IS 2770 (Part 1): 1967 [43]

4.8. Sorptivity Test

The water sorptivity test is conducted to determine the rate of water movement under capillary suction through the concrete. It is highly sensitive with respect to the

microstructural properties of the concrete near-surface region and thus represents the nature and efficacy of the curing process. The sorptivity can be determined by the measurement of the absorption rate due to capillary rise on reasonably homogeneous material. Sorptivity test based on ASTM C 642: 2021 [44] codes. In addition to the water sorptivity test, surface wettability can also be performed to estimate the durability of cementitious systems [33] [34]. Surface wettability refers to how readily the concrete's surface allows water to spread and penetrate. A surface with high wettability may indicate reduced durability and potential issues with water ingress and subsequent deterioration. Together, the water sorptivity test and surface wettability evaluation provide valuable insights into the concrete's quality, curing effectiveness, and potential long-term durability.

4.9. Mixture Design

It has been discovered that coastal sand comprises about 50% of particles that are smaller than 300 microns, which become unsuitable for concrete production. The particles were finer than 300 microns were separated from sea sand using sieves. Instead of discarded sea sand particles, MS passing through 300 microns was mixed in 10, 20, and 30 percentages to study the possible improvement of the properties of fine aggregate in concrete. M20, M25, and M30 grades of concrete mixes adopted in this investigation were designed as per IS 10262-2009 [45]. According to the results obtained from the mix design, the water-cement ratio was calculated as 0.55, 0.5, and 0.45 for M20, M25, and M30 grades respectively. The identification details of the specimens are given in Table 2.

Table 2 Details for Sample Identification

Sl No	Specimen ID	Label	Sl No	Specimen ID	Label
1	20(100% DSS)	SP1	15	25(30% MS + 70% DSS)	SP15
2	20(100% MS)	SP2	16	25(10% RS+ 90% DSS)	SP16
3	20(100% RS)	SP3	17	25(20% RS + 80% DSS)	SP17
4	20(10% MS+ 90% DSS)	SP4	18	25(30% RS + 70% DSS)	SP18
5	20(20% MS + 80% DSS)	SP5	19	30(100% DSS)	SP19
6	20(30% MS + 70% DSS)	SP6	20	30(100% MS)	SP20
7	20(10% RS+ 90% DSS)	SP7	21	30(100% RS)	SP21
8	20(20% RS + 80% DSS)	SP8	22	30(10% MS+ 90% DSS)	SP22
9	20(30% RS + 70% DSS)	SP9	23	30(20% MS + 80% DSS)	SP23
10	25(100% DSS)	SP10	24	30(30% MS + 70% DSS)	SP24
11	25(100% MS)	SP11	25	30(10% RS+ 90% DSS)	SP25
12	25(100% RS)	SP12	26	30(20% RS + 80% DSS)	SP26
13	25(10% MS+ 90% DSS)	SP13	27	30(30% RS + 70% DSS)	SP27
14	25(20% MS + 80% DSS)	SP14			

5. Results and Discussions

5.1. Sea Sand Grading

The sieve analysis was carried out for dredged sea sand and an attempt was made to compare the obtained grading with the grading zones specified by IS 383-2016 [36] for the Zones III and IV. Figures 2a and 2b show the comparison of the grading of dredged sea sand with Zone III and Zone IV separately. While observing the graphs, it was found that the grading of sea sand falls closer to the Zone IV classification of sand. However, the grading line obtained for sea sand while sieving through 300 microns sieve was found to fall outside the boundaries of Zone IV classification according to the IS Code.
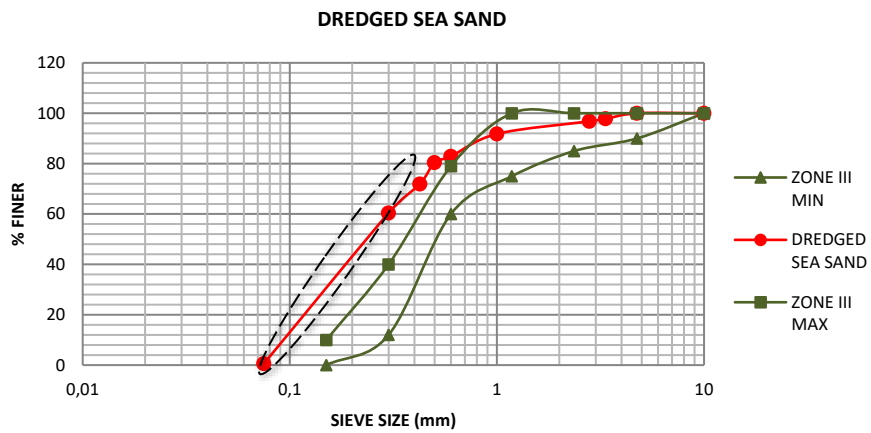
Fig. 2a Particle size distribution curve for sea sand in comparison with Zone III grading limits
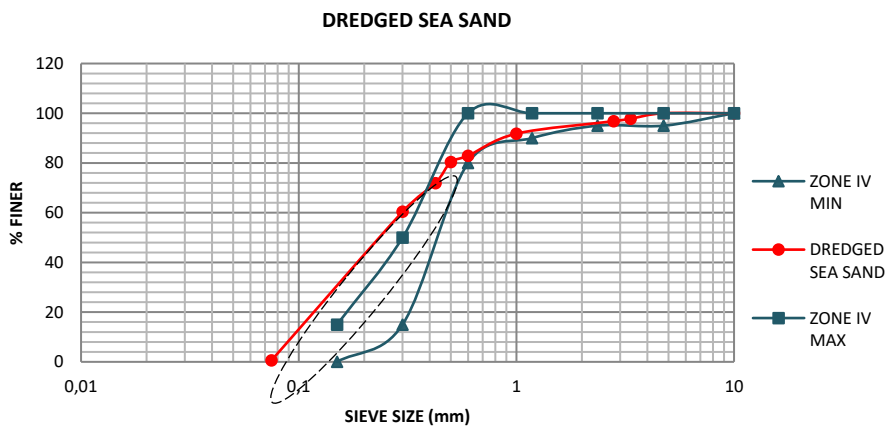
Fig. 2b Particle size distribution curve for sea sand in comparison with Zone IV grading limits

Sieve analysis was also carried out for MS that was used in this investigation and it was found that the grading curve of MS was well within the lower and upper limits of Zone III as per IS Code. This is depicted in Figure 3.
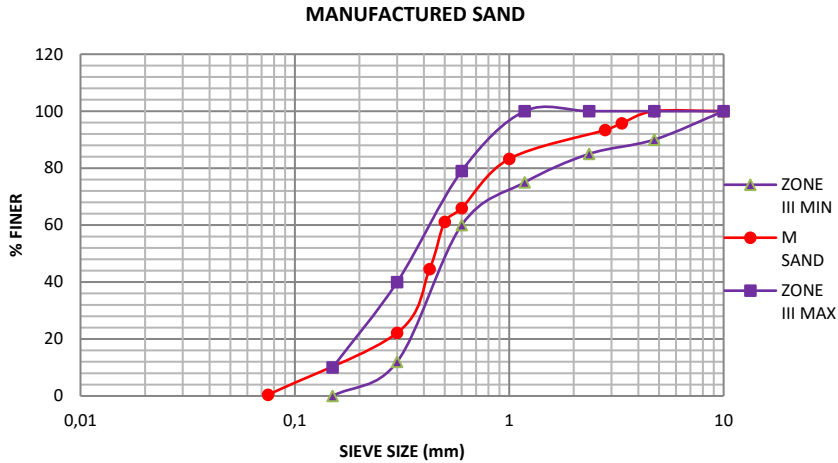
Fig. 3 Particle size distribution curve for MS in comparison with Zone III grading limits

5.2. Gap Grading of Sea Sand with MS

In this investigation, MS was taken as a partial replacement for sea sand. The too-fine portion of sea sand i.e., the sand particles passing through 300 microns sieve were replaced with MS passing through the same sieve. M sand and Sea sand were taken and the samples were allowed to pass through standard sieves 4.75mm to 0.75micron size. After drawing the particle size distribution curve of Sea sand, a major portion of samples goes outside zone 4, according to IS 383 – 2016 [36] Table 9, Note 4: It is recommended that fine aggregate conforming to Grading Zone IV should not be used in reinforced concrete.
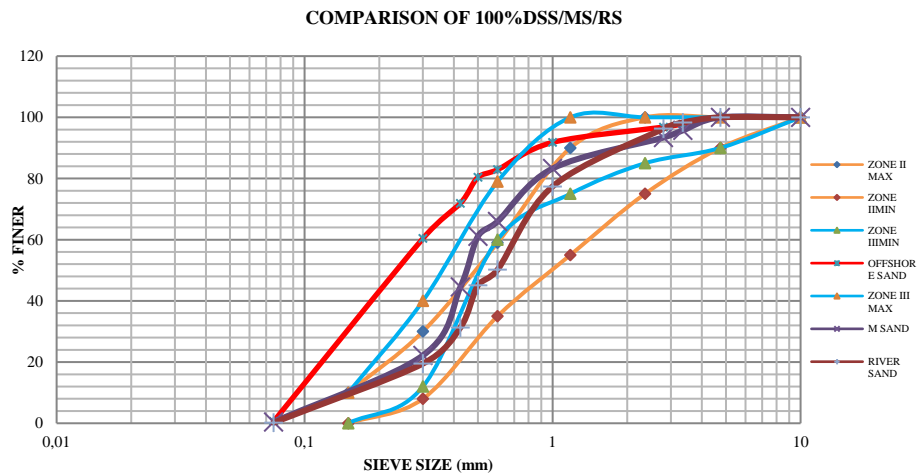
Fig. 4 Particle size distribution curve for 100% DSS/MS/RS in comparison with Zone II & III grading limits

COMPARISON OF 90%DSS + 10% MS/RS
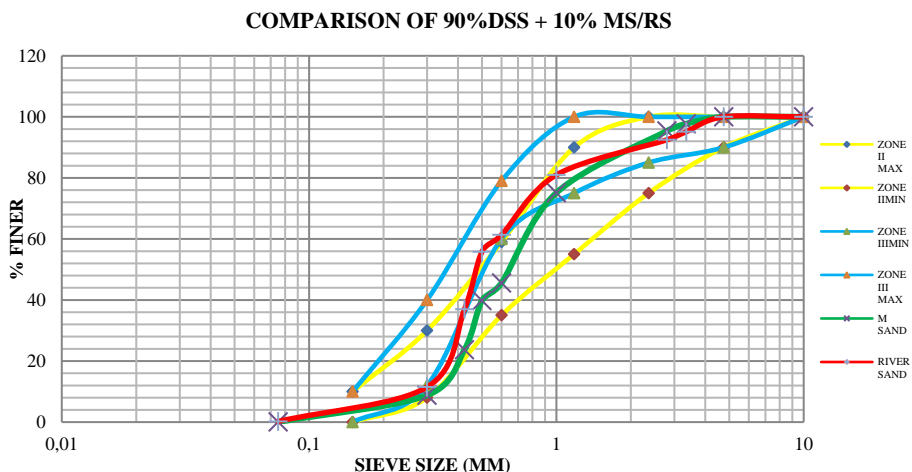
Fig. 5 Particle size distribution curve for 90% DSS + 10%MS/RS in comparison with Zone II & III grading limits

COMPARISON OF 80%DSS + 20% MS/RS
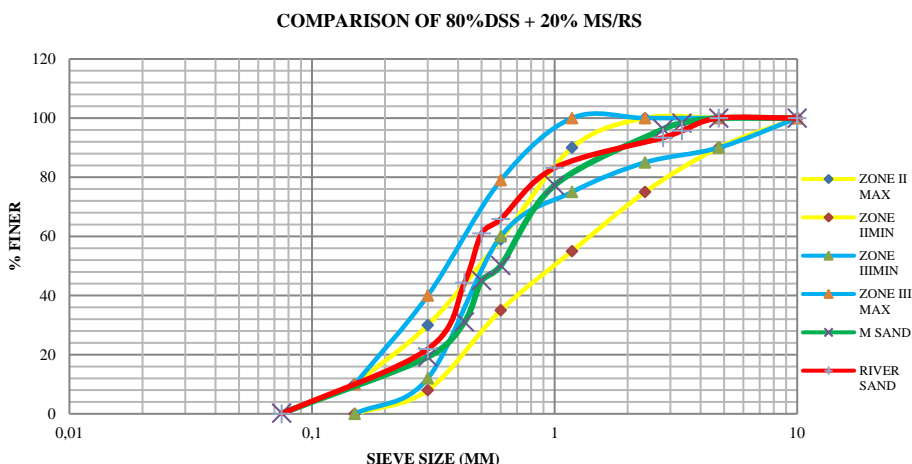
Fig. 6 Particle size distribution curve for 80% DSS + 20%MS/RS in comparison with Zone II & III grading limits

Hence gap grading was done, i.e., samples passing through 4.75 to 600 microns of sea sand were taken in different proportions, 10, 20, and 30% and the portion was filled with samples retained in 300 microns, 150 microns, and 75 microns sieve in different proportions say 10, 20 and 30% respectively.

To understand the comparison between 100% DSS, 100% MS, and 100% RS clearly, a particle size distribution curve has been drawn in comparison with Zone II & III grading limits which is depicted in Fig 4. Fig 5, 6, and 7 show the comparison of gap-graded DSS with MS as well as RS in different proportions say 10%, 20%, and 30% respectively.

COMPARISON OF 70%DSS + 30% MS/RS
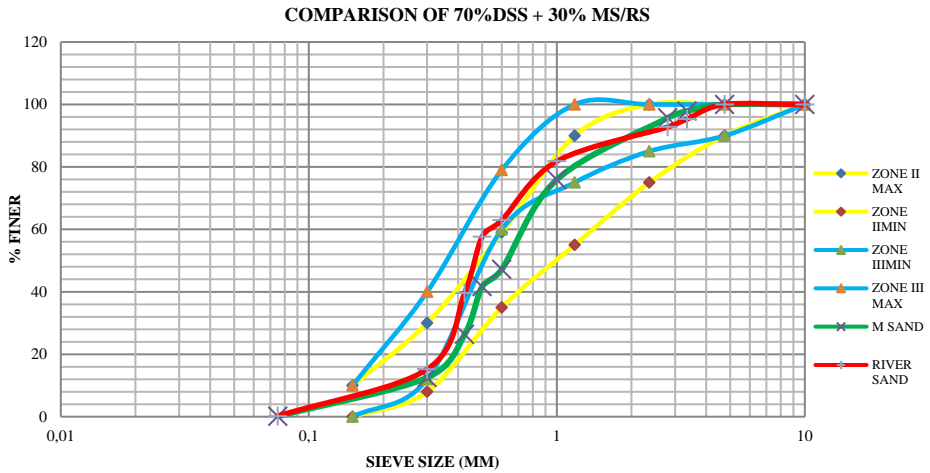
Fig. 7 Particle size distribution curve for 70% DSS + 30%MS/RS in comparison with Zone II & III grading limits

5.3. Compressive Strength

Cube and cylinder specimens were cast, cured, and evaluated for 28-day compressive strength to investigate the compressive strength of concrete specimens while DSS was replaced with MS. Figure 8 and 9 shows the comparison of various specimens' cube and cylinder compressive strengths.
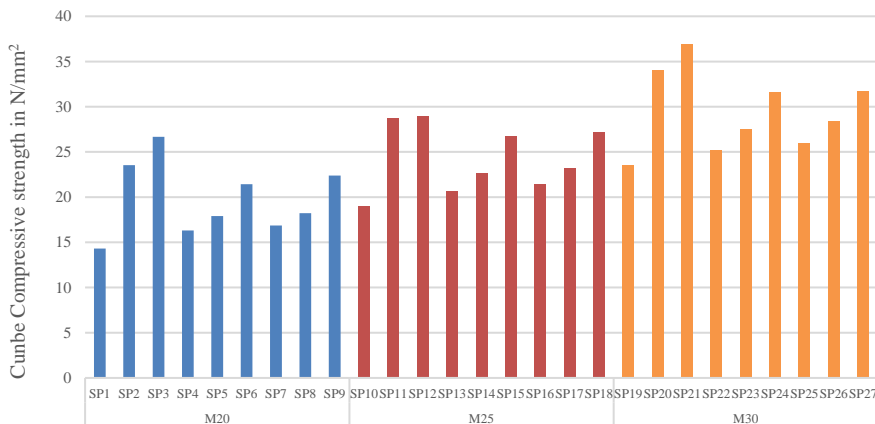
Fig. 8 28 days Cube Compressive Strength

From Figure 9, it was found that the concrete made of DSS with 10%, 20%, and 30% of MS as a partial replacement was closely equal to the design target strength of M20, M25, and M30 grade concrete. On the same line, Deepak et al. [17] discovered that there is almost a 44% reduction in the compressive strength of concrete mixed with 40% river sand and 60% river sand.
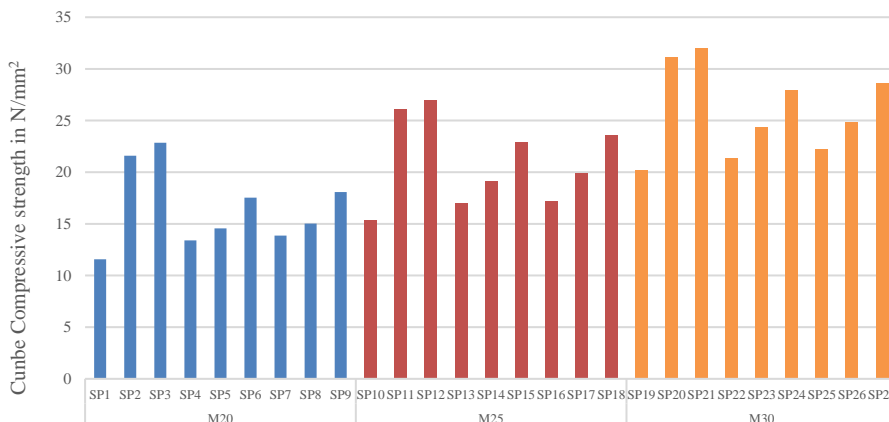
Fig. 9 28 days Cylinder Compressive Strength.

5.3.1. The Ratio Between Cube Compressive Strength and Cylinder Compressive Strength

The compressive strength of cylinder specimens with DSS partially replaced with or without MS was found to be around 0.85 times the compressive strength of cube specimens. This is in accordance with BS 1881: Part 120:1983 [46] i.e., the Strength of the cylinder is equal to 0.8 times the strength of cubes. Table 3 shows the details of the obtained ratios.

Table 3. Ratio between the strength test on cubic and cylindrical sample

Ratio Between the strength test on cubic and cylindrical sample			
Sample	Ratio	Sample	Ratio
SP1	0.81	SP15	0.86
SP2	0.92	SP16	0.81
SP3	0.86	SP17	0.86
SP4	0.82	SP18	0.87
SP5	0.81	SP19	0.86
SP6	0.82	SP20	0.91
SP7	0.82	SP21	0.87
SP8	0.82	SP22	0.85
SP9	0.81	SP23	0.89
SP10	0.81	SP24	0.89
SP11	0.91	SP25	0.86
SP12	0.93	SP26	0.88
SP13	0.82	SP27	0.90
SP14	0.84		

5.3.2. The Effect of The Grade of Concrete on The Strength Parameters

Overall, the concrete specimens with DSS demonstrated lower cube and cylinder compressive strength compared to the specified target strength. However, it was observed that as the grade of concrete increased, the extent of this reduction in compressive strength in relation to the design target strength gradually decreased. The specific data regarding this reduction for different grades of concrete and the DSS mix can be found in Table 4.

Table 4. Details of the reduction in Cube and Cylinder Strength

Specimens	SP1	SP10	SP19
Cube with 100% DSS	28.45%	24.00%	21.67%
Cylinder with 100% DSS	42.15%	38.64%	32.63%

5.4. Flexural Strength

By carrying out two-point loading, the flexural strength of different samples was calculated. The flexural resistance represents the strongest tension within the material and its moment of rupture.
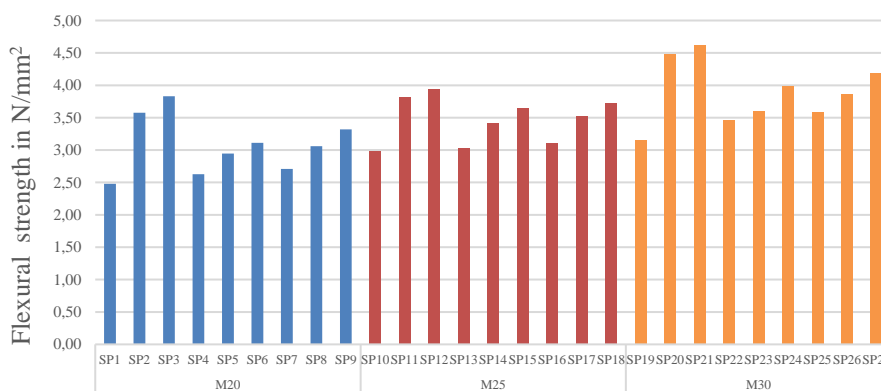
Fig. 10 Flexural Strength after 28 days

5.4.1. Flexural strength and compressive strength relation

Fig 10 shows the flexural strength of different concrete specimens. In accordance with IS 516-2021 [37], the flexural strength of concrete beam specimens with dredged sea sand partially replaced with or without MS was calculated as per IS 456-2000 [47]. S. Pranavan [18] observed that the percentage of flexural strength results increases on the addition of MS in concrete. Table 5 shows the details of the obtained values.

Table 5. K values for dredged sea sand with partial replacement of MS

Indirect tensile strength due to bending, f_t in terms of fck ($f_t = K\sqrt{(f_{ck})}$)			
Sample	Ratio	Sample	Ratio
SP1	0.66	SP15	0.71
SP2	0.74	SP16	0.67
SP3	0.74	SP17	0.73
SP4	0.65	SP18	0.72
SP5	0.70	SP19	0.65
SP6	0.67	SP20	0.77
SP7	0.66	SP21	0.76
SP8	0.72	SP22	0.69
SP9	0.70	SP23	0.69
SP10	0.68	SP24	0.71
SP11	0.71	SP25	0.71
SP12	0.73	SP26	0.73
SP13	0.67	SP27	0.74
SP14	0.72		

5.5. Rapid Chloride Penetration Test

The average current passing various samples were calculated. The outcomes of various models are shown in Figure 11.
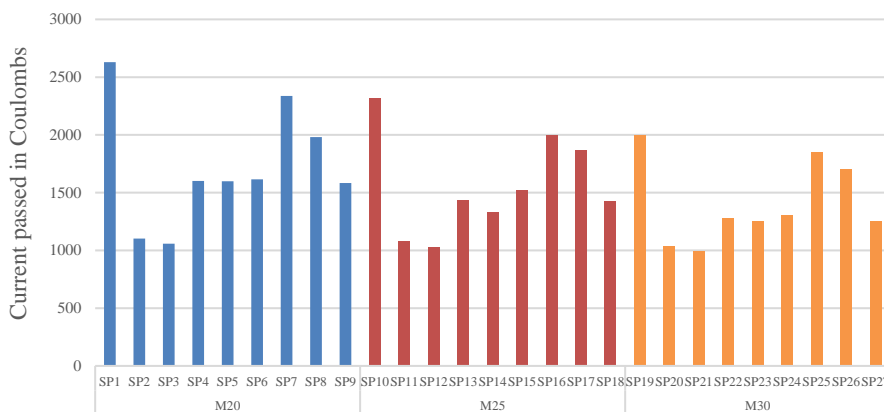
Fig. 11 Chloride penetration in Coulombs

According to ASTM C 1202 [42], the average current that flows through the Conventional concrete sample of concrete ranges between 1000 & 4000 coulombs. From the experimental investigation, it was found that the average chloride penetration through the specimens made with DSS partially replaced with or without MS is 1791 which is well within the limit specified by ASTM C 1202 [42]. The presence of MS as a partial replacement of DSS was found to improve the resistance to Chloride penetration. This is owing to the reason that the quality of DSS while partially replaced with MS improves the quality of the sand by filling the finer side of the fine aggregate. It is worth mentioning that B S Dhanya et al [28] found similar results that, as the Supplementary cementitious material dosage increases, the charge passed gets decreased, thereby improvement in the concrete quality.

5.6. Water Absorption

Figure 12 displays the results of calculating the proportions for water absorbed by various specimens.
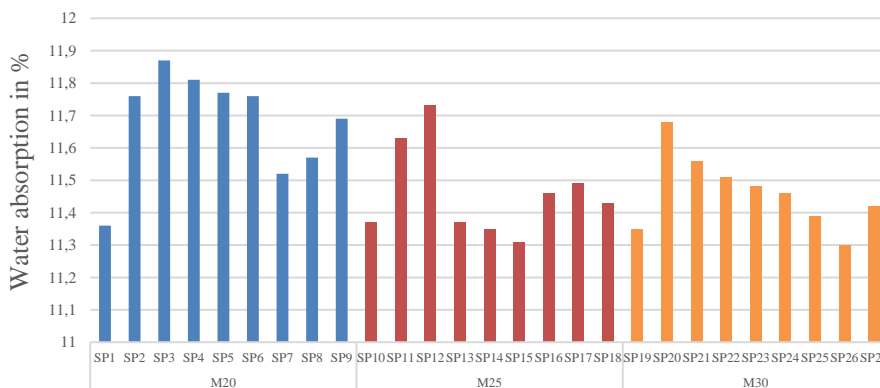
Fig. 12 Percentage of water absorption

5.7. Alkalinity Test

The alkalinities of different samples were calculated and are shown in Figure 9.
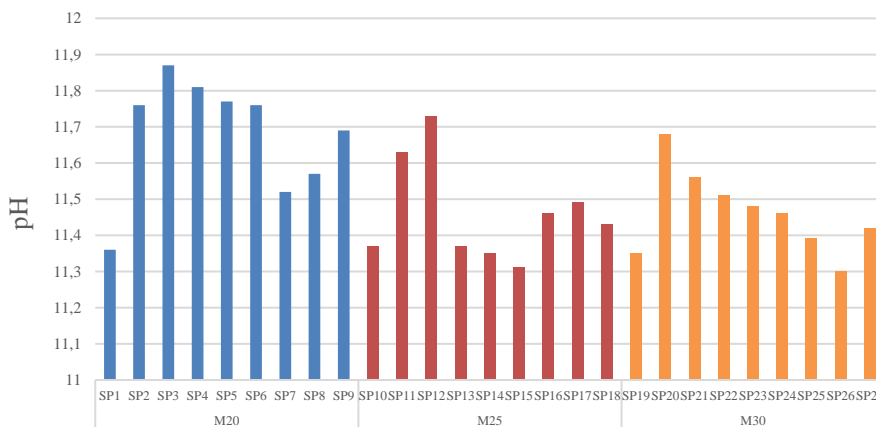
Fig. 13 Alkalinity test result after 28 days

The DSS has been collected from a dumping area near Puthuvypeen, also a major portion of the chloride content has been washed out because the sand samples were subjected to rainfall for roughly a year. According to ASTM D 4262 [41], healthy concrete has a high pH of 12 – pH 13.3 whereas in newly cured concrete it is expected to be between 11 and 13.5. The Alkalinity of concrete specimens made with DSS partially replaced with or without MS was found to be an average of 11.47. It was found that the addition of MS as a partial replacement for dredged sea sand improves the alkalinity of concrete.

5.8. Bond Strength

The bond strength of all mixtures was tested on specimens with reinforcement bars having 16 mm diameter. A pull-out test was done to find out bond strength. According to Adarsh M S [26] concrete specimens covered with mortar made with 15% dredged marine sand showed better results with higher bond strength when compared to concrete made with mortar composed of fine aggregate only. Table 6 displays the test results of the bond strength of specimens.

Table 6. Pull-out test results of specimens

Bond strength of Corroded specimen							
Mix	Specimen	Maximum load (kN)	Bond strength N/mm²	Mix	Specimen	Maximum load (kN)	Bond strength N/mm²
M20	SP1	13.98	0.27	M30	SP19	16.03	0.38
	SP2	22.79	0.51		SP20	32.60	0.64
	SP3	23.39	0.54		SP21	34.01	0.67
	SP4	15.21	0.31		SP22	17.45	0.44
	SP5	16.39	0.38		SP23	19.61	0.51
	SP6	19.98	0.42		SP24	23.42	0.58
	SP7	15.62	0.34		SP25	18.55	0.47
	SP8	17.03	0.39		SP26	20.39	0.56
	SP9	20.23	0.45		SP27	24.69	0.61

	SP10	14.70	0.32
	SP11	24.10	0.56
	SP12	25.81	0.60
	SP13	15.99	0.38
M25	SP14	16.78	0.43
	SP15	20.86	0.50
	SP16	16.30	0.40
	SP17	17.99	0.47
	SP18	22.20	0.53

5.9. Sorptivity Result

The Sorptivity expresses the tendency of a material to absorb and transmit water and other liquids by capillarity. The greater the absorption and flowability, the more corrosion of steel rods may happen fast which weakens the structural component. The sorptivity values of various mixes are shown in Table 7. The result shows a decrease in sorptivity with an increase in the sea sand proportion.

Table 7(a) Sorptivity results for M20 Grade Concrete

Time (Min)	Specimen of M20 grade (mm/m)								
	SP1	SP2	SP3	SP4	SP5	SP6	SP7	SP8	SP9
0	197.56	144.41	142.12	185.72	181.38	175.90	184.32	179.78	174.10
5	197.56	144.41	142.12	185.76	181.45	175.86	184.36	179.85	174.06
10	197.56	144.42	142.13	185.82	181.39	175.80	184.42	179.79	174.00
20	197.56	144.42	142.14	185.82	181.45	175.83	184.42	179.85	174.03
30	197.57	144.39	142.16	185.81	181.43	175.81	184.41	179.83	174.01
60	197.57	144.40	142.16	185.84	181.43	175.79	184.44	179.83	173.99
120	197.58	144.40	142.18	185.87	181.45	175.78	184.47	179.85	173.98
180	197.59	144.42	142.18	185.95	181.42	175.74	184.55	179.82	173.94
240	197.61	144.44	142.18	185.97	181.44	175.79	184.57	179.84	173.99
300	197.61	144.45	142.20	185.97	181.44	175.90	184.57	179.84	174.10

Table 7(b) Sorptivity results for M25 Grade Concrete

Time (Min)	Specimen of M25 grade (mm/m)								
	SP10	SP11	SP12	SP13	SP14	SP15	SP16	SP17	SP18
0	189.03	142.37	139.45	174.23	158.05	152.57	172.73	156.25	150.47
5	189.03	142.37	139.46	174.24	158.13	152.54	172.74	156.33	150.44
10	189.03	142.38	139.48	174.24	158.07	152.48	172.74	156.27	150.38
20	189.19	142.38	140.88	174.26	158.15	152.53	172.76	156.35	150.43
30	189.19	142.38	142.03	174.26	158.12	152.50	172.76	156.32	150.40
60	189.27	142.41	144.74	174.27	158.13	152.49	172.77	156.33	150.39

120	189.27	142.41	147.66	174.29	158.16	152.49	172.79	156.36	150.39
180	189.27	142.42	147.98	174.32	158.15	152.47	172.82	156.35	150.37
240	189.39	142.42	148.01	174.32	158.15	152.50	172.82	156.35	150.40
300	189.40	142.43	149.23	174.32	158.15	152.61	172.82	156.35	150.51

Table 7(c): Sorptivity results for M30 Grade Concrete

	Specimen of M30 grade (mm/m)								
Time (Min)	SP19	SP20	SP21	SP22	SP23	SP24	SP25	SP26	SP27
0	173.82	120.67	118.87	161.98	145.80	140.32	160.28	144.20	138.52
5	173.82	120.67	118.87	162.02	145.91	140.32	160.32	144.31	138.52
10	173.82	120.68	118.88	162.08	145.91	140.32	160.38	144.31	138.52
20	173.82	120.68	118.88	162.08	145.97	140.35	160.38	144.37	138.55
30	173.87	120.69	118.89	162.11	145.97	140.35	160.41	144.37	138.55
60	173.87	120.70	118.90	162.14	146.00	140.36	160.44	144.40	138.56
120	173.88	120.70	118.90	162.17	146.04	140.37	160.47	144.44	138.57
180	173.88	120.71	118.91	162.24	146.07	140.39	160.54	144.47	138.59
240	173.88	120.71	118.91	162.24	146.07	140.42	160.54	144.47	138.62
300	173.88	120.72	118.92	162.24	146.07	140.53	160.54	144.47	138.73

From the tables 7(a), 7(b), and 7(c) it was found that the Sorptivity is of lower value in the case of concrete made with 100% MS. In the case of concrete with 100% dredged sea sand, the sorptivity value was higher by about 44%. By the addition of MS in Concrete as a partial replacement to dredged sea sand, the sorptivity value was found to be 24% lower than the specimens made with MS. From the observation by Davoud Vafae et al [19] replacing fresh water and normal sand with sea water and dredged sea sand results in a significant reduction in sorptivity parameters.

6. Conclusions

This paper investigates the behavior of dredged sea sand partially replaced with manufactured sand in concrete.

- According to the literature review, practically all prior studies were carried out by replacing fine aggregate directly into concrete in varied proportions. Hence, the method gap grading is adopted in the present experimental investigation which helps to maintain the particle size distribution curve lies within the boundaries of Zone III as per IS 383- 2016 [36].
- After partially substituting dredged sea sand with 10%, 20%, and 30% MS, the grade of dredged sea sand was found to be improved and the grading curve of the composition lies within the boundaries of Zone III. 28 days Cube Compressive Strength of 100% dredged sea sand was 46% lesser than that of MS, however partial replacement of dredged sea sand with 10, 20, and 30% of MS has shown improvement in the strength of concrete. Additionally, the compressive strength of the cube and cylinder specimens was in accordance with BS 1881: Part 120:1983 [46] (i.e., the cylinder strength is roughly 0.83 times that of the cubes).

- The flexural strength of concrete made of dredged sea sand was significantly lower than that of MS. The flexural strength of each concrete beam specimen made with dredged sea sand partially replaced with or without MS was determined to be 0.69 times the compressive strength of cube specimens in accordance with IS 516-2021 [37].
- The results of the Rapid Chloride Penetration Test were well within the limit specified by ASTM C 1202 [42]. By filling the finer side of the fine aggregate with MS, the grade of dredging sea sand improves, and hence the degree of the risk of corrosion is therefore lower.
- The water absorption rate for concrete made from sea sand was higher. After partially replacing dredged sea sand with 10, 20, and 30% shows better results in accordance with ASTM C 140 [40].
- The alkalinity of concrete specimens created with dredged sea sand partially replaced with or without MS was determined to be within the ASTM D 4262 [41] standard as the collected dredged sea sand samples were exposed to rainwater for nearly a year. Also, the addition of MS improves the alkalinity of concrete compared to the 100% replacement of MS with dredged sea sand.
- The bond strength increases with an increase in the replacement of sea sand, however, the 30% replacement of sea sand with MS gives a closer result than the 100% replacement with MS.
- The sorptivity which is greater for concrete with dredged sea sand was found to decrease as the portion of dredged sea sand was partially replaced with MS.

On the basis of the above results, it can be concluded that dredged sea sand can be used as a partial replacement for fine aggregate in concrete. As a future research direction, further investigations can be carried out to explore the incorporation of fiber-reinforced concrete with dredged sea sand. Fiber reinforcement has gained prominence in recent times for enhancing the mechanical properties and durability of concrete structures. Incorporating fibers in concrete mixtures with dredged sea sand can offer significant advantages, particularly in terms of eliminating the corrosion risks caused by steel reinforcements. Recommendations for future studies include evaluating the mechanical properties, crack resistance, and long-term performance of fiber-reinforced concrete containing dredged sea sand. Moreover, examining the effects of different types and dosages of fibers on the concrete's behavior can provide valuable insights for optimizing the mix design. By exploring the potential of fiber-reinforced concrete with dredged sea sand, researchers and practitioners can contribute to the development of sustainable and corrosion-resistant construction materials, thus fostering a more resilient and eco-friendly infrastructure for the future.

References

[1] Ojhaa PN, Singh B, Kaurac P, Singhd A. Lightweight geopolymer fly ash sand: an alternative to fine aggregate for concrete production. Research on Engineering Structures and Materials. 2021; 375-391. https://doi.org/10.17515/resm2021.257ma0205

[2] Lijuan L, Bin H, Zhongyu L, Feng Liu. Fatigue behavior of sea sand concrete beams reinforced with basalt fiber-reinforced polymer bars. Construction and Building Materials. 2018 ; 160-171. https://doi.org/10.1016/j.conbuildmat.2018.05.218

[3] Xing F, Liu J, Dong B, Huo Y. Combination procedure and mechanism of sea sand type chlorine ions with cement materials. Journal of Southeast University (Natural Science Edition). 2006; S2: 167-172.

[4] Ustabas I. The effect of capillarity on chloride transport and the prediction of the accumulation region of chloride in concretes with reinforcement corrosion.

Construction and Building Materials. 2012; 28(1); 640-647. https://doi.org/10.1016/j.conbuildmat.2011.10.043

[5] Lan C, Jang H, Jay K, Seong-Tae Y. Bond strength prediction for reinforced concrete members with highly corroded reinforcing bars. Cement and concrete composites. 2008 ; 30(7) ; 603-611. https://doi.org/10.1016/j.cemconcomp.2008.03.006

[6] Yoon S C, Seong-Tae Y, Myung Y K, Woo Y J, Eun I Y. Effect of corrosion method of the reinforcing bar on bond characteristics in reinforced concrete specimens. Construction and Building Materials. 2014; 4: 180-189. https://doi.org/10.1016/j.conbuildmat.2013.12.065

[7] Jianzhuang X, Chengbing Q, Antonio N,Kaijian Z. Use of sea-sand and seawater in concrete construction : Current status and future opportunities. Construction and Building Materials. 2017; 155: 1101-1111. https://doi.org/10.1016/j.conbuildmat.2017.08.130

[8] Feng B, Liu J, Wei J, Zhang Y. Research on Properties and durability of desalinated sea sand cement modified with fly ash. Case Studies in Construction Materials. 2021 ; e00675 https://doi.org/10.1016/j.cscm.2021.e00675

[9] Azzam A, Shuaicheng G, Zuhua Z, Caijun S. A review on durability of fiber reinforced polymer (FRP) bars reinforced seawater sea sand concrete. Construction and Building Materials. 2020 https://doi.org/10.1016/j.conbuildmat.2020.119484

[10] Branavan A, Chaminda K. Pertinence of alternative fine aggregates for concrete and mortar: a brief review on river sand substitutions. Australian Journal of Civil Engineering. 2021 https://doi.org/10.1080/14488353.2021.1971596

[11] Liu W, Xie Y J, Dong B Q, Xing F. Study on characteristics of dredged marine sand and the mechanical properties of concrete made with dredged marine sand. Bulletin of the Chinese ceramic society. 2014; 33(1); 15-22.

[12] Chandrakeerthy S. Suitability of sea sand as a fine aggregate for concrete production, Transactions. Institution of Engineers Sri Lanka. 1994; 93-114.

[13] Limeir J, Agullo L, Etxeberria M. Dredged marine sand as construction material. European journal of environmental and civil engineering. 201; 16(8); 906-918. https://doi.org/10.1080/19648189.2012.67637 6

[14] Limeira J, Etxeberria M, Agullo L, Molina D. Mechanical and durability properties of concrete made with dredged marine sand. Construction and building materials. 2011 ; 25(11) ; 4165-4174. https://doi.org/10.1016/j.conbuildmat.2011.04.053

[15] Limeira J, Agullo L, Etxeberria M. Dredged marine sand in concrete: An experimental section of a harbor pavement. Construction and Building Materials. 2010 ; 24(6) ; 863-870. https://doi.org/10.1016/j.conbuildmat.2009.12.011

[16] Girish C G, Tensing D, Priya K L. Dredged Sea sand as a replacement for fine aggregate in concrete. International Journal of Engineering Sciences & Emerging Technologies. 2015 ; 8(3) ; 88-95.

[17] Deepak W S, Naidu G T. Effect on compressive strength of concrete using sea sand as a partial replacement for fine aggregate. International Journal of Research in Engineering and Technology. 2015; 4(6); 180-183. https://doi.org/10.15623/ijret.2015.0406030

[18] Pranavan S , Srinivasan G.Investigation on behaviour of M-Sand based concrete. Materials Today : Proceedings. 2021; 45; 7079 - 7085 https://doi.org/10.1016/j.matpr.2021.01.930

[19] Davoud V, Reza H, Xing M, Jinming D, Yan Z. Sorptivity and mechanical properties of fiber-reinforced concrete made with seawater and dredged sea-sand. Construction and Building Materials. 2020 https://doi.org/10.1016/j.conbuildmat.2020.121436

[20] Sidhardhan S , Sheela S J , Meylin J S. Study on sea sand as a partial replacement for fine aggregate. Journal of Advances in Chemistry. 2017; 6166-6171.

[21] Jau W, Tan J C, Yang C T. Effect of sea sand on concrete durability and its management. Journal of Southeast University (Natural Science Edition). 2006; 36(2); 161-166.

[22] Shuai W. Research about the detection method of the content of the content of chloride ion in the sea sand. China Building Materials Academy. 2016.

[23] Hasdemir S, Tugrul , Yılmaz M. The effect of natural sand composition on concrete strength. Construction and Building Materials. 2016; 112; 940-948. https://doi.org/10.1016/j.conbuildmat.2016.02.188

[24] Katz A, Baum H. Effect of high levels of fines content on concrete properties. ACI Materials Journal. 2006 ; 103(6) ; p.474. https://doi.org/10.14359/18226

[25] Safiuddin M, Raman S N, Zain M F M. Utilization of quarry waste fine aggregate in concrete mixtures. Journal of Applied Sciences Research. 2007; 3(3); 202-208.

[26] Adarsh M S. Experimental Investigations on Partial Replacement of Fine Aggregate by Onshore Marine Sand using Corossion Inhibitor. International Journal of Engineering Research & Technology. 2016 ; Volume 4 ; Issue 08.

[27] Kim D G, Cho M S and Lee J S. The effects of chloride on durability of concrete mixed with sea sand. US-China Education Review A. 2013; 3(5) ;25-331.

[28] Dhanya B S , Manu S. Performance evaluation of rapid chloride permeability test in concretes with supplementary cementitious materials. Materials and Structures. 2017; 50-67 https://doi.org/10.1617/s11527-016-0940-3

[29] Dora F, Michela L, Maria F S, Vitantonio V. Mechanical Characteristics and Water Absorption Properties of Blast-Furnace Slag Concretes with Fly Ashes or Microsilica Additions. Applied sciences. 2019 ; 1-13 https://doi.org/10.3390/app9071279

[30] Saeed M, Shore S. Eco-friendly mix for Roller-Compacted Concrete: Effects of Persian-Gulf-Dredged marine sand on durability and resistance parameters of concrete. Construction and Building Materials. 2021; 281; 122555 https://doi.org/10.1016/j.conbuildmat.2021.122555

[31] Matthew Z Y T, Kwong S W, Muhammad E R, Meheron S J. Mechanical and durability performance of marine sand and seawater concrete incorporating silicomanganese slag as coarse aggregate. Construction and Building Materials. 2020; 254; 119195 https://doi.org/10.1016/j.conbuildmat.2020.119195

[32] Norpadzlihatun M, Stanleyster P, Kavitha S, Md Asrul N M, Goh K C, Mohd Y Y. Strength of concrete made from dredged sediments. Jurnal Teknologi. 2016; 111-116

[33] Lee J B, Derome D, Carmeliet J.Drop impact on natural porous stones. Journal of colloid and interface science. 2016; 469, 147-156. https://doi.org/10.1016/j.jcis.2016.02.008

[34] Kabir, H., & Garg, N. Rapid prediction of cementitious initial sorptivity via surface wettability. npj Materials Degradation. 2023; 7(1), 52. https://doi.org/10.1038/s41529-023-00371-4

[35] The Economic Times, Cochin Port to explore use of dredged sand for construction Jan 21, 2016 https://economictimes.indiatimes.com/industry/transportation/shipping-/-transport/cochin-port-to-explore-use-of-dredged-sand-for-construction

[36] IS 383-2016 Coarse and Fine Aggregate for Concrete - Specification (Third Revision)

[37] IS 516 (Part-1 Sec-I) - 2021 Compressive, Flexural and Split Tensile Strength

[38] IS 12269-2013 Ordinary Portland Cement, 53 grade -Specification

[39] IS 4031 - 4: 1988 Methods of Physical Tests Hydraulic Cement, part 4: Determination of consistency of standard cement paste.

[40] ASTM C 140 Standard Test Methods for Sampling and Testing Concrete Masonry Units and Related Units

[41] ASTM D 4262 Standard Test Method for pH of Chemically Cleaned or Etched Concrete Surfaces

[42] ASTM C 1202 Standard Test Method for Electrical Indication of Concrete's Ability to Resist Chloride Ion Penetration

[43] IS 2770 (PART 1): 1967 Methods of Testing Bond in Reinforced Concrete, Part 1 - Pull out Test

[44] ASTM C 642: 2021 Standard Test Method for Density, Absorption, and Voids in Hardened Concrete

[45] IS 10262 - 2009 Concrete Mix Proportioning - Guidelines

[46] BS 1881: Part 120: 1983 Method for determination of the compressive strength of concrete cores.

[47] IS 456 - 2000 Plain and Reinforced Concrete - Code of practice

Research Article

Response surface methodology use in optimization of concrete properties using blast furnace slag aggregate and recycled concrete sand

Poonam[*, a], VP Singh[b]

Department of Civil Engineering, National Institute of Technology, Kurukshetra, (Haryana) India

Article Info	Abstract
	The utilization of waste materials in concrete plays a crucial role in sustainable construction by contributing to environmental conservation and enhancing concrete properties. However, waste management and sustainable construction present significant challenges within the construction industry. This study specifically focuses on the optimization of concrete properties by utilizing Blast furnace slag aggregate (BFSA) as coarse aggregate (CA) and recycled concrete sand (RCS) as fine aggregate (FA). To assess the impact of BFSA and RCS replacement parameters, response surface methodology (RSM) based on central composite design (CCD) was employed. The RSM regression equations generated in this study demonstrated high R2 values (>0.8), indicating their capability to explain the variability observed in the responses. To assess the impact of BFSA and RCS replacement parameters, response surface methodology (RSM) based on central composite design (CCD) was employed. In conclusion, the implementation of RSM enables the incorporation of waste materials into concrete, resulting in waste reduction without significant effects on concrete properties.

1. Introduction

Rapid urbanization and industrialization have led to an increase in construction and demolition (C&D) waste generation, resulting in a higher demand for natural resources [1]. The disposal of C&D waste through dumping and landfilling causes environmental issues and land occupation. Reclaiming C&D waste is crucial for reducing end-of-life impacts and minimizing the extraction of natural resources [2–4]. Recycling C&D waste into aggregates, particularly as sustainable building materials, has been extensively studied, and it has been accepted that recycled coarse aggregates (RCAs) can replace natural coarse aggregates by up to 30% without sacrificing concrete performance [5–7]. However, a significant portion of concrete fines still cannot be recycled and reused. Recycled concrete powder (RCP) has been investigated as a replacement for fine aggregate in mortar or concrete. Studies have shown that RCP mortar exhibits inferior properties due to higher porosity and water absorption [8,9]. The inclusion of RCP affects the particle packing status of aggregates in mortar, primarily due to changes in particle size distribution after adding different contents and sizes of RCP particles. The packing status of granular materials can be characterized by the particle packing density, which is defined as the absolute volume to bulk volume ratio of the packed material.

Various industrial by-products, including red mud, fly ash, silica fume (SF), metakaolin, B flexural strength, and rice husk ash, have been used as cement replacements to enhance

---

concrete strength [9–13]. These by-products possess latent hydraulic properties, leading to improved compressive strength (CS) at an early stage and flexural strength at a later age. Incorporating these by-products into concrete helps conserve natural resources. The utilization of ground granulated blast furnace slag (GBFS), a by-product of the iron-making process, has gained significant attention. Blast furnace slag is a versatile material with a structure similar to conventional building materials such as cement and natural stone. It can be recycled and used in a variety of ways, such as replacing cement, improving concrete, and even making bricks. The cooling method during production affects how we can use it. When a molten slag is rapidly cooled with water, the result is a granular aggregate. This granular material is mainly processed as ground granulated blast furnace slag aggregate which is known as Granulated Blast furnace slag Aggregate (BFSA), which is commonly used in various construction projects, including mixed and precast concrete, masonry, floor level materials, and high temperature resistant building manufacturing processes. GBFS has high glass content and potential hydration activity when rapidly cooled by water quenching [14]. It has been widely used in the cement and concrete industry, as well as in other applications [15].

The utilization of solid wastes for the production of composite ground granulated blast furnace slag (GBFS) as an alternative to natural coarse has been investigated in previous studies [16,17]. The promotion of GBFS hydration is facilitated by the synergistic effects of solid wastes and flexural strength, which encompass alkali, sulphate, and particle filling effects. Composite GBFS not only caters to the need for superior quality GBFS, but also facilitates the efficient usage of many other solid waste materials, hence fostering collaboration across different industries. Several research works have investigated the utilization of GBFS and Recycled Concrete Aggregate (RCA) in the context of concrete. The utilization of self-compacting concrete (SCC) with GBFS as a substitute for natural coarse aggregate resulted in a significant decrease in compressive strength, surpassing 20% as reported in previous studies [18,19].

Previous research conducted on blast furnace slag aggregate concrete has demonstrated the potential for enhancing the compressive strength, flexural strength, and split tensile strength of the concrete. Qasrawi [20] did a study on the utilization of furnace slags as coarse aggregate in concrete constructions. The findings indicated that including furnace slag as a coarse aggregate in concrete has the potential to enhance the mechanical characteristics of the concrete. Maslehuddin et al. [21] conducted an assessment of the mechanical properties and durability characteristics of furnace slag aggregate concrete and normal aggregate concrete. The experimental findings demonstrated that the durability properties of concrete containing furnace slag aggregate surpassed those of concrete containing normal aggregate. Additionally, certain mechanical attributes of furnace slag aggregate concrete, including compressive strength, flexural strength, and split tensile strength, exhibited improvements in comparison to normal aggregate concrete. The authors Yu et al. [22] undertook a series of experiments to investigate the properties of concrete with steel slag and waste glass. The findings of the study suggest that the substitution of coarse aggregate with steel slag and/or waste glass is a viable option. BFSA concrete exhibits considerable potential as a feasible alternative to concrete including natural aggregate within the building sector [23]. Nevertheless, a significant portion of the prior research has mostly concentrated on the application of BFSA as the fine aggregate. Several studies [24-26] have examined the behavior of coarse aggregate with a significant volume replacement of natural aggregates. Some of these studies [27] have specifically focused on determining the behavior in question. Multiple studies have demonstrated that the physical properties of concrete with BFS aggregates closely resemble those of concrete incorporating naturally occurring aggregates [11].

1.1. Response Surface Methodology

An efficient method is required for optimizing the properties of concrete containing waste materials, as it is an important step towards sustainable construction that reduces the depletion of natural resources and promotes cleaner neighborhoods [28]. RSM has been used to generate models for independent variable optimization, which is a statistical, theoretical, and numerical technique [45,46]. The effect of independent parameters on one or numerous responses is considered by RSM, which employs partial factorial designs like CCD to generate response surfaces for second-order mathematical models [29]. Mathematical models generated using RSM have been observed to be efficient in predicting the properties of concrete containing waste materials [30].

Several researchers have applied the use of RSM in the optimization of concrete containing waste materials, and it has been found to be an effective method for identifying mixtures that yield the best compromises among the responses [31,32]. Regression analysis, experimental designs, and recommended statistical tests are generated by RSM employing design of experiment (DOE) software packages such as Minitab and Design Expert [33]. Partial factorial designs used by RSM reduce the number of experiments required compared to full factorial designs, making it a practical method for researchers with limited time and resources [34].

Numerous investigations have been undertaken to examine the mechanical characteristics of concrete by substituting natural resources with various waste materials [35]. Additionally, diverse contemporary methodologies have been employed for the purpose of optimization [36]. Although there have been research investigations examining the substitution of river sand with WFS in regular concrete mixtures [37], there is a lack of statistical modeling and optimization of concrete mixtures that incorporate WFS. Based on the extant study data, it can be inferred that Response Surface Methodology (RSM) has the potential to serve as a valuable tool for determining the optimal proportion of Waste Foundry Sand (WFS) to be utilized as a replacement for natural sand in concrete. This may be achieved by employing a design matrix that incorporates relevant parameters and corresponding responses. In order to address the existing research gap, the present study aimed to examine the slump and mechanical properties of a concrete mixture. This was achieved by partially replacing the fine aggregate with varying percentages of WFS. The experimental design matrix was built using the CCD function of RSM. During the experimental design, the factors chosen were the WFS percentage and number of curing days, while the responses picked were the CS, STS, and FS. The water-to-fly ash ratio incrementally increased from 0% to 40% in intervals of 10%, while the duration of the curing process ranged from 7 to 56 days. The concrete mixtures were formulated based on the recommended proportions of water, fine aggregate, and coarse aggregate. The corresponding characteristics of the concrete were assessed at designated time intervals, as specified by the experimental design matrix [38]. The statistical models were afterwards constructed through the utilization of ANOVA analysis, allowing for the examination of the combined impacts of various factors on the specified responses. Ultimately, the process of multi-objective design optimization was undertaken in accordance with predetermined design criteria in order to ascertain the optimal proportion of WFS and the duration of curing days that would yield the highest levels of slump and mechanical properties. The optimal outcomes that were acquired were then validated using further experimental procedures.

A solution to cost-effective conventional concrete production is provided by this study using waste materials such as BFSA (0-50%) as coarse aggregate and RCS (0-100%) as sand replacement in concrete. The performance of concrete containing these waste materials is predicted by mathematical models generated in this study, which optimize

their contents split tensile strength and flexural strength [39]. The response surface models generated in this research are distinct from those developed by other researchers and validate the practicability of the generated models. Overall, an efficient method that can bring about a revolution in sustainable construction is the use of RSM in optimizing the properties of concrete containing waste materials [40,41].

1.2. Optimization Process

The optimization process for the RSM based on CCD involves finding the optimal values of BFSA and RCS replacement percentages to achieve the desired response variable while considering any constraints that may exist. The first step is to generate a mathematical model using experimental data and validate it through ANOVA [41,42] . Once the model is validated, optimization techniques can be employed to determine the optimal values of the input variables (BFSA and RCS) for the desired response variable. Various optimization techniques can be used, such as RSM, gradient-based optimization, or genetic algorithms. Response surface plots can help visualize the relationship between the input variables and the response variable, aiding in the identification of optimal values. Constrained optimization techniques consider any constraints, such as cost limitations or specific strength requirements. These techniques find optimal values that satisfy the constraints while achieving the desired response [30,36]. To verify the optimal values, experiments can be conducted at the predicted values, and the results can be compared to the model predictions. If the experimental results align with the model predictions, the optimal values are considered the final solution. If discrepancies occur, the model may require refinement or additional experiments for improved accuracy. Over the last decade, there has been a growing trend towards employing optimal experimental designs as opposed to traditional methods. This shift is attributed to their enhanced flexibility and capacity to address a broader spectrum of challenges compared to conventional designs [39].

The study presents significant opportunities for sustainable construction through the utilization of Blast furnace slag aggregate (BFSA) and recycled concrete sand (RCS). However, it exhibits certain gaps. Firstly, the investigation into the long-term durability and performance of concrete mixes incorporating BFSA and RCS is lacking, requiring future exploration. Additionally, a comprehensive environmental assessment, involving life cycle analysis, is necessary to holistically evaluate the sustainability impact of these materials in concrete. Moreover, to effectively scale up the adoption of waste materials in concrete construction, bridging the divide between research findings and practical implementation, while addressing industry standards and regulations, remains a vital challenge. The study aims to optimize concrete properties by incorporating Blast Furnace Slag Aggregate (BFSA) as coarse aggregate and Recycled Concrete Sand (RCS) as fine aggregate. This involves utilizing Response Surface Methodology (RSM) and Central Composite Design (CCD) to assess how different levels of BFSA and RCS replacements impact split tensile strength, flexural strength, and bond strength. The research demonstrates that this approach enables the integration of waste materials into concrete, promoting sustainable construction practices by reducing waste while maintaining concrete quality, as evidenced by high R^2 values in regression equations.

2. Materials and Methods

2.1. Materials

In this study, the researchers used 43-grade OPC cement that complied with the IS: 8112 [43] standard. The BFSA used in the study was obtained from Ambala city, India. Various laboratory tests were conducted to determine the properties of both the cement and BFSA. These tests included measurements of normal consistency (28%), soundness (2.5mm), fineness (2%), initial setting time (126 minutes), final setting time (243 minutes), specific

gravity SG (3.19), and CS. The compressive strength of the cement was found to be 26.6, 34.23, and 45.60 MPa at 3, 7, 28 days respectively. Specifications for the mechanical behavior of ordinary coarse aggregate and BFSA has been shown in table 1. For fine aggregate and CAs, natural aggregates were sourced from local markets and underwent grading analysis following the Indian standard IS: 383 [44]. The BFSA used in the study was processed into coarse aggregate shape using a jaw crusher. Additionally, RCS was obtained for the study by manually crushing 5 to 7-month-old uncontaminated concrete cubes (150 mm^3) with a hammer. During the concrete casting process, tap water was utilized after purification to eliminate any harmful substances, adhering to the guidelines specified in IS: 10500-2012 [45].

The comparison of properties between BFSA and normal coarse aggregate revealed some noteworthy differences. These comparisons provide valuable insights into the distinctive characteristics and properties of the two types of aggregates. Such knowledge can aid in the appropriate selection of materials for various construction applications.

Table 1. Specifications for the mechanical behavior of ordinary coarse aggregate and BFSA

Property	Normal coarse aggregate	Blast furnace slag aggregate
Fineness modulus	7.38	7.25
Flakiness index (%)	15.39	7.35
Bulk density(compact) (kg/m3)	1565	1417
Los Angeles abrasion resistance (%)	22.56	35.45
Impact value (%)	9.60	17.30
Bulk density(loose) (kg/m3)	1485	1310
Crushing value (%)	20.10	12.53
Elongation index (%)	10.31	18.65
Specific gravity	2.67	2.58

3. Experimental Design

To optimize the concrete mixture and analyze the experimental data, a CCD of RSM was employed. This design enables the generation of precise optimum values and a comprehensive explanation of the experimental data. The CCD is a well-known experimental design that offers flexibility in selecting the number of center points and axial distances. In this study, Design Expert-13 software was used for 25 mixes experimental runs were conducted using the CCD. In this study, we used 3 center points for a balance of accuracy and efficiency. For more complex systems or higher precision, you can opt for 4 or 5 center points. These runs involved varying amounts of cement, sand, RCS, BFSA, and CA, as detailed in Table 1. The mixture proportions were based on the M25 concrete mix design specified in IS 456:2000 [46]. The independent parameters considered in the study were BFSA and RCS shown in table 2.

Table 2. Independent parameters

Factor	Name	Minimum	Maximum	Coded Low	Coded High	Mean	Std. Dev.
A	RCS (%)	0	100.00	-1	+1	52.00	33.32
B	BFSA(%)	0	50.00	-1	+1	26.00	15.94

Table 3. Mix design with replacement

Level	S No.	RCS(%)	BFSA(%)	Cement (kg/m³)	fine aggregate (kg/m³)	RCS (kg/m³)	CA (kg/m³)	BFSA (kg/m³)	Water (kg/m³)	Extra water (%)
0	0R0B	0	0	342	711.4	0	1174	0	153.9	0
1	10R5B	10	5	342	640.26	71.14	1115.3	58.7	153.9	1
2	25R5B	25	5	342	533.55	177.85	1115.3	58.7	153.9	1
3	50R5B	50	5	342	355.7	355.7	1115.3	58.7	153.9	1
4	75R5B	75	5	342	177.85	533.55	1115.3	58.7	153.9	1
5	100R5B	100	5	342	0	711.4	1115.3	58.7	153.9	1
1	10R15B	10	15	342	640.26	71.14	997.9	176.1	153.9	2
2	25R15B	25	15	342	533.55	177.85	997.9	176.1	153.9	2
3	50R15B	50	15	342	355.7	355.7	997.9	176.1	153.9	2
4	75R15B	75	15	342	177.85	533.55	997.9	176.1	153.9	2
5	100R15B	100	15	342	0	711.4	997.9	176.1	153.9	2
1	10R25B	10	25	342	640.26	71.14	880.5	293.5	153.9	5
2	25R25B	25	25	342	533.55	177.85	880.5	293.5	153.9	5
3	50R25B	50	25	342	355.7	355.7	880.5	293.5	153.9	5
4	75R25B	75	25	342	177.85	533.55	880.5	293.5	153.9	5
5	100R25B	100	25	342	0	711.4	880.5	293.5	153.9	5
1	10R35B	10	35	342	640.26	71.14	763.1	410.9	153.9	6
2	25R35B	25	35	342	533.55	177.85	763.1	410.9	153.9	6
3	50R35B	50	35	342	355.7	355.7	763.1	410.9	153.9	6
4	75R35B	75	35	342	177.85	533.55	763.1	410.9	153.9	6
5	100R35B	100	35	342	0	711.4	763.1	410.9	153.9	6
1	10R50B	10	50	342	640.26	71.14	587	587	153.9	8
2	25R50B	25	50	342	533.55	177.85	587	587	153.9	8
3	50R50B	50	50	342	355.7	355.7	587	587	153.9	8
4	75R50B	75	50	342	177.85	533.55	587	587	153.9	8
5	100R50B	100	50	342	0	711.4	587	587	153.9	8

Ranking: 1 (Very Low), 2 (Low), 3 (High), 4 (Very High), 5 (Extreme)

The mix design for M25 grade concrete followed the Indian Standard, as indicated in the provided table 3. These parameters were carefully adjusted to analyze their effects. The response parameters, denoted as R1, R2 and R3 corresponded to split tensile strength flexural strength and bond strength after 28 days of curing, respectively.

The study involved manipulating specific factors within defined ranges to assess their impact on the concrete's performance. The two factors, RCS (Recycled Concrete Sand) and BFSA (Blast Furnace Slag Aggregate), were varied systematically. RCS ranged from 0% to 100%, while BFSA ranged from 0% to 50%, with both factors assigned coded values of -1 (low) and +1 (high). The mean and standard deviation for RCS were 52.00 %and 33.32%, respectively, while for BFSA, they were 26.00% and 15.94%.

These carefully selected parameters enabled the analysis of their influence on response parameters (R1, R2, and R3) representing split tensile strength, flexural strength, and bond strength after a 28-day curing period.

4. Experimental Procedure

The experimental designs for all 25 runs, including the control mix, were generated using Design Expert 13, as depicted in Table 3. Each individual run involved the manual mixing of concrete with waste materials and water to ensure a homogeneous mixture. The C, fine aggregate, and coarse aggregate were mixed slowly for two minutes, and water was added gradually to achieve the desired workable consistency. Once the suitable mixture was obtained, it was transferred into lubricated molds and uniformly compacted using a table vibrator.

| (a) Split Tensile Test setup | (b) Flexural test setup | (c) Prepared sample for bond test |
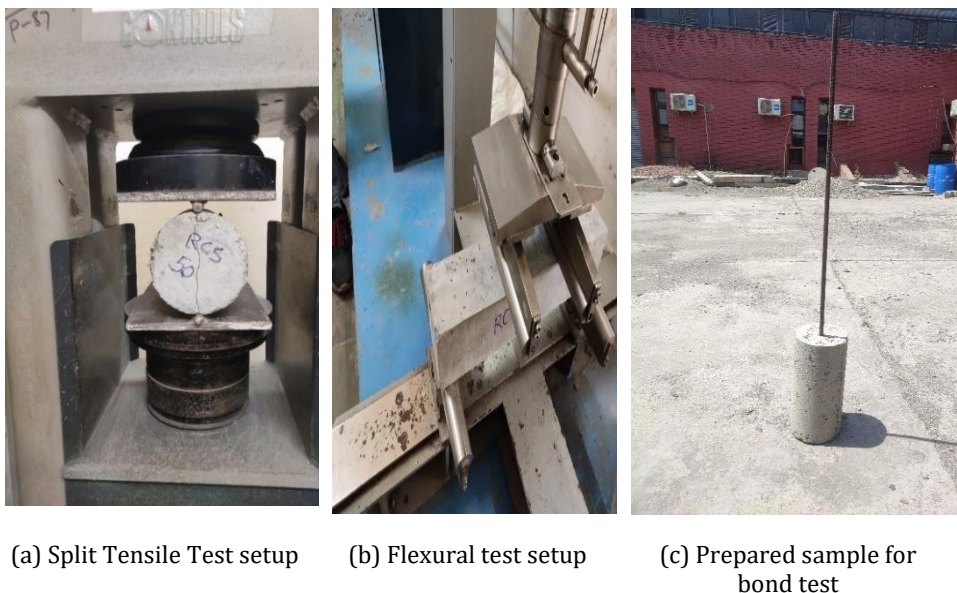
Fig. 1. Experimental setup

The freshly mixed concrete specimens were then subjected to testing according to the relevant Indian standard codes of practice. The tests included measuring the CS, split tensile strength flexural strength, and concrete-steel tensile bond after 28 days of submersion in water at 27°C. The cube specimens were tested for compressive strength using a Compression Testing Machine (CTM) at the age of 28 days. The testing was conducted without impacts or jerks, applying a uniform load, and recording the failure load

for each specimen. The results obtained from these tests are presented in Figure 1. For the ST and flexural strength test, the same CTM machine was used, as the hydraulic arrangement for the flexural test was attached to the CTM. Additionally, a Universal Testing Machine (UTM) was utilized for the tensile bond test.

5. Results And Discussion

This section presents the results and discussion of the experimental data and mathematical models for various properties, split tensile strength flexural strength, and bond strength. The models were validated using ANOVA, and the coefficients and response surface plots were interpreted to gain insights into the relationships between variables. The results and discussion shed light on the impact of BFSA and RCS replacement parameters on the properties of construction materials. Furthermore, the effectiveness of RSM based on CCD for modeling and optimizing construction materials is demonstrated throughout the analysis.

5.1. Models Fitting

The regression coefficients in the model are estimated by minimizing the sum of squared errors between the predicted values and the actual values of the response variable. The significance of the model and its individual terms is determined using the F-test and t-test, respectively. Once the model is fitted and validated, it becomes useful for predicting the response variable at any combination of BFSA and RCS replacement percentages within the range of the experiments. Additionally, the model can be utilized to identify the optimal combination of BFSA and RCS replacement percentages that maximize or minimize the desired outcome. The Table 4 provides statistical data for various properties of a material, specifically the coefficient, split tensile strength flexural strength, and bond strength.

Table 4. Fit Statistics split tensile strength flexural strength and bond strength

Coefficient	Split tensile strength	Flexural Strength	Bond strength
Std. Dev.	0.0563	0.1455	0.2493
Mean	4.01	4.40	7.84
C.V. %	1.40	3.30	3.18
R^2	0.9935	0.9718	0.9444
Adjusted R^2	0.9852	0.9359	0.9131
Predicted R^2	0.9534	0.8317	0.8291
Adeq Precision	38.6985	18.2110	19.0167

The standard deviation (SD) for these properties is presented as 0.0563, 0.1455, and 0.2493, respectively. The mean values are 4.01, 4.40, and 7.84 for split tensile strength flexural strength, and bond strength, respectively. The coefficient of variation (CV) is 1.40, 3.30, and 3.18% for the corresponding properties. The Table 4 also includes R^2 values, indicating the degree of correlation between the variables, with high values of 0.9935, 0.9718, and 0.9444. Adjusted R^2 values are provided as 0.9852, 0.9359, and 0.9131, representing a measure of the quality of the model fit. Additionally, predicted R^2 values are given as 0.9534, 0.8317, and 0.8291, indicating the predictive power of the model. Finally, precision values are provided as 38.6985, 18.2110, and 19.0167, which represent the precision of the model's predictions for the respective properties.

5.2 Coded Factors

Tables 5 and 6 present the regression equations in terms of coded factors for all responses. The equations express the relationship between the coded factors (represented as A and B) and the dependent variable (denoted as C). The coefficients assigned to the coded

factors determine their impact on the dependent variable. The final equation in Table 5 is derived from the analysis and showcases how the values of the coded factors are combined to determine the value of the dependent variable. It is important to note that for a linear interaction between variables and responses, at least one regression coefficient in the model should not be zero. The experimental data suggests that the relationships between factors and response variables are different for the three strength measures. Split Tensile Strength and Flexural Strength share similar factors, indicating consistent effects across these two measures, while Bond Strength is characterized by cubic terms, suggesting a more intricate and nonlinear relationship with the experimental factors.

The specific reasons for these patterns would likely be influenced by the nature of the materials, the experimental design, and the physical phenomena being studied. The notable observation is that Split Tensile Strength and Flexural Strength exhibit shared factors, signifying a coherent impact across these two measures. In contrast, Bond Strength presents itself with cubic terms, signifying a more complex and nonlinear connection with the experimental factors.

Table 5: Final equation in terms of coded factors

Factors	Split Tensile Strength	Flexural Strength	Bond Strength
	4.03	4.24	8.46
A	-0.0256	0.1114	0.4279
B	6.2	7.97	-4.18
AB	-0.1481	-0.8407	0.2634
A^2	-0.3402	-0.1536	-0.8318
B^2	41.13	52.11	-6.61
A^2B	-0.0597	0.1005	-0.1088
AB^2	-0.5976	-2.73	-0.0669
A^3	0.1891	-0.0087	0.1688
B^3	66.76	81.76	-1.35
A^2B^2	-0.0486	0.0617	
A^3B	-0.0041	-0.0193	
AB^3	-0.414	-1.93	
A^4	-0.0319	0.0104	

Table 6. Actual equation in terms of coded factors

Factor	Split Tensile Strength	Flexural Strength	Bond Strength
	3.18485	3.36335	6.38704
RCS	0.052185	0.020932	0.082
BFSA	-0.02874	0.03658	0.089552
RCS * BFSA	-0.00023	-0.00094	0.000492
RCS^2	-0.00176	-0.00026	-0.00197
$BFSA^2$	0.011599	0.010551	-0.00099
$RCS^2 * BFSA$	1.59E-06	1.11E-06	-3.48E-06
$RCS * BFSA^2$	0.000012	0.000047	-1.07E-06
RCS^3	0.000021	-2.00E-06	0.000011
$BFSA^3$	-0.00047	-0.00052	-1.1E-05
$RCS^2 * BFSA^2$	-3.11E-08	3.95E-08	
$RCS^3 * BFSA$	-5.29E-09	-2.46E-08	
$RCS * BFSA^3$	-1.32E-07	-6.16E-07	
RCS^4	-8.17E-08	2.67E-08	
$BFSA^4$	5.04E-06	5.93E-06	

5.3. Splitting tensile Strength (STS) Optimization

5.3.1. Linear Model Fit Summary and ANOVA Evaluation for Split Tensile Strength

The identification of the response surface model was assisted by the model statistics summary and ANOVA for the linear model for split tensile strength as presented in Table 6, respectively. A perfect correlation in the split tensile strength response was observed. The Table 7 includes the sources of variation, the sum of squares, degrees of freedom, mean square, F-value, and p-value for each factor.

The model is found to be significant with a sum of squares of 5.30, 14 degrees of freedom, a mean square of 0.3787, an F-value of 119.54, and a p-value of less than 0.0001. Among the individual factors, B-BFSA has a significant effect on the split tensile strength with a sum of squares of 0.1628, a mean square of 0.1628, an F-value of 51.38, and a p-value of less than 0.0001. A^2 and B^2 also show significant effects on the split tensile strength with corresponding sum of squares, mean squares, F-values, and p-values indicating their significance.

The remaining factors and interactions do not show significant effects on the split tensile strength as indicated by their non-significant F-values and p-values. The residual sum of squares is 0.0348, and the total sum of squares is 5.34.

Table 7. ANOVA for split tensile strength

Source	Sum of Squares	df	Mean Square	F-value	p-value	
Model	5.30	14	0.3787	119.54	< 0.0001	significant
A-RCS	0.0006	1	0.0006	0.1865	0.6742	
B-BFSA	0.1628	1	0.1628	51.38	< 0.0001	
AB	0.0007	1	0.0007	0.2179	0.6498	
A^2	0.0513	1	0.0513	16.19	0.0020	
B^2	0.2766	1	0.2766	87.31	< 0.0001	
A^2B	0.0006	1	0.0006	0.1756	0.6833	
AB^2	0.0025	1	0.0025	0.7759	0.3972	
A^3	0.0373	1	0.0373	11.76	0.0056	
B^3	0.2738	1	0.2738	86.43	< 0.0001	
A^2B^2	0.0008	1	0.0008	0.2665	0.6159	
A^3B	0.0001	1	0.0001	0.0213	0.8866	
AB^3	0.0027	1	0.0027	0.8522	0.3757	
A^4	0.0266	1	0.0266	8.41	0.0145	
B^4	0.2260	1	0.2260	71.36	< 0.0001	
Residual	0.0348	11	0.0032			
Cor Total	5.34	25				

5.3.2. Model Graphs and Diagnostic Findings of Split Tensile Strength

Diagnostic findings in design expert typically include statistical tests and numerical measures that assess the model's quality and predictive accuracy. The lack of fit test determines if the model adequately fits the data, while the residual plot identifies patterns or outliers that may indicate problems with the model. Additional measures like RMSE and R-squared assess the model's predictive accuracy.

Figure 2(a) presents a normal plot of residuals for diagnosing model problems. Figure 2(b) compares predicted and actual values, identifying discrepancies and indicating misspecification or missing predictors. Figure 2(c) identifies systematic bias or non-linear relationships, while Figure 2(d) identifies influential observations and evaluates model robustness. Adjustments can be made based on these findings to enhance accuracy and

predictive power. The ANOVA summary for split tensile strength can be found in Appendix 1.

(a) Normal plot of residual

(b) Predicted vs actual
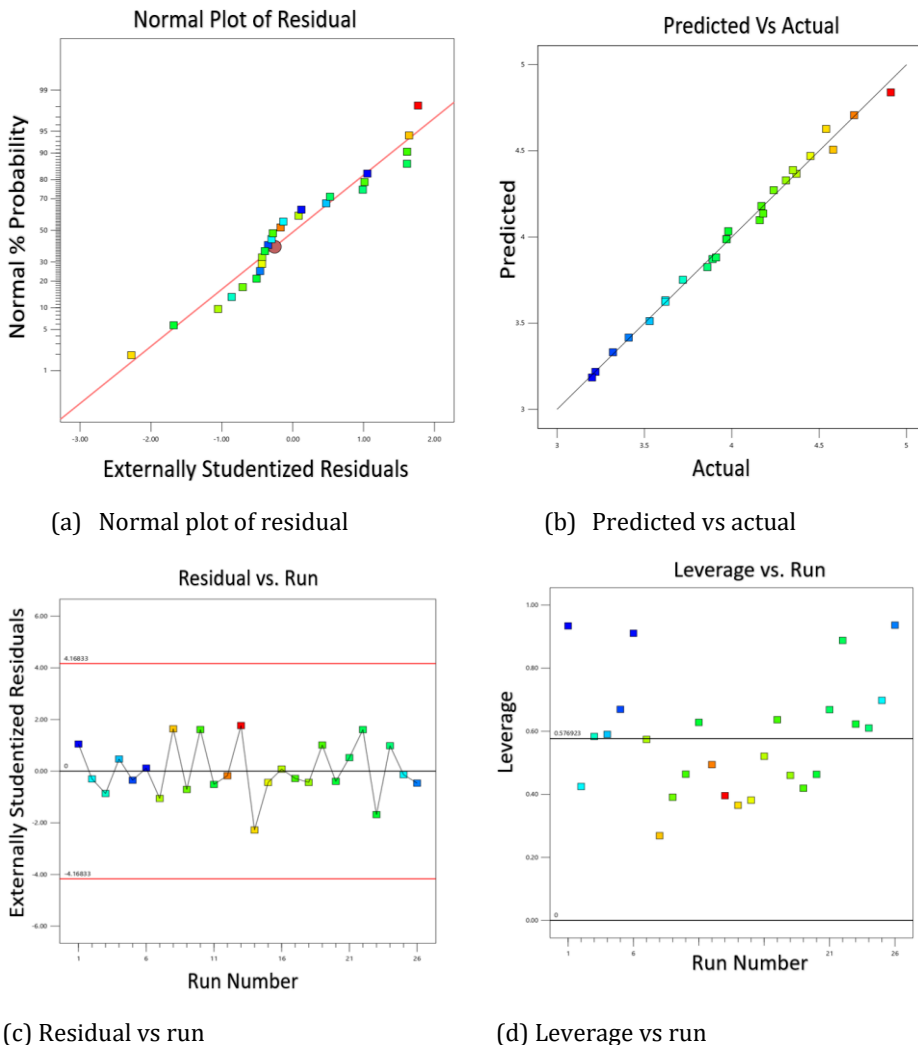
(c) Residual vs run

(d) Leverage vs run

Fig. 2. Model graphs and diagnostic findings of split tensile strength

5.3.3. Model Graphs of STS

Model graphs typically include graphical representations of the model, such as contour plots or surface plots, that allow the user to visualize the relationship between the input variables and the response variable. These plots can help identify any nonlinear relationships between the variables and can also help identify any interactions between the variables that may be important for the model.

The relationship between split tensile strength BFSA, and RCS is visualized in Figure 3(a) and 3(b) through contour and 3D plots. The contour plot depicts lines of constant split tensile strength on a grid of BFSA and RCS, while the 3D plot represents split tensile strength on the z-axis and BFSA and RCS on the x and y axes, respectively. By analyzing the contours or the plot's surface, specific regions in the input space can be identified where

split tensile strength is highly responsive to variations in BFSA or RCS. This information facilitates the identification of optimal BFSA and RCS values that minimize split tensile strength or enables an examination of the model's sensitivity to changes in the input variables.
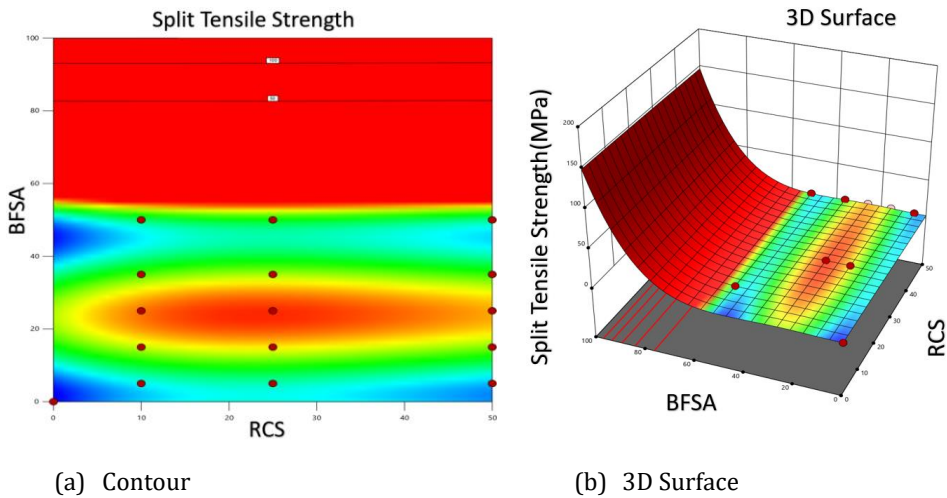

(a) Contour   (b) 3D Surface

Fig. 3. Model graphs of split tensile strength

From the above figure 3 its clear that the minimum split tensile strength observed in the dataset is 3.22 MPa, which occurs when there is 100% BFSA replacement and 5% RCS replacement. Conversely, the maximum split tensile strength is 4.91 MPa, observed when there is 25% BFSA replacement and 25% RCS replacement.
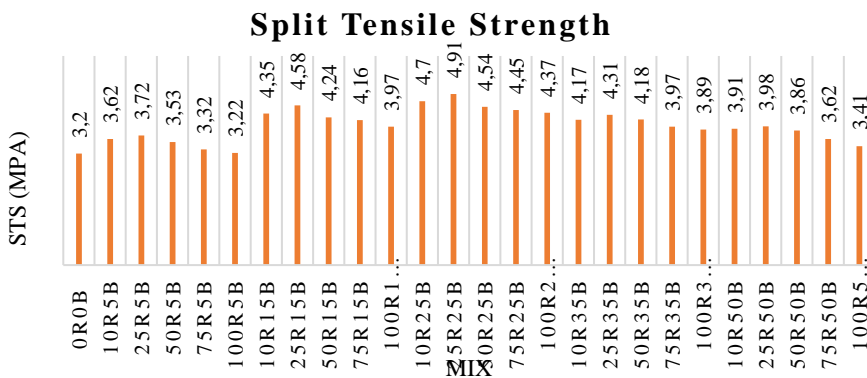

Fig. 4 Split tensile strength values for different concrete mixtures

Figure 4 compares the split tensile strength values of concrete mixtures with varying replacements of fine aggregate by RCS and coarse aggregate by BFSA. The mix labelled "0R0B" represents no replacement of fine aggregate or CA, with a split tensile strength of 3.2 MPa. The Figure reveals the relationship between replacement percentages and split tensile strength values. When both fine aggregate and coarse aggregate replacements are kept constant at 5%, split tensile strength values range from 3.22 (Mix "100R5B") to 3.72 MPa (Mix "25R5B"). This suggests that higher replacement of fine aggregate by RCS does not necessarily lead to a significant decrease in split tensile strength when the coarse

aggregate replacement remains consistent. In terms of coarse aggregate replacement by BFSA, an increase in the replacement percentage from 5 to 25% generally results in higher STS. For example, split tensile strength increases from 4.35 MPa (Mix "10R15B") to 4.91 MPa (Mix "25R25B"). However, when the replacement percentage of coarse aggregate by BFSA reaches 35 and 50%, there is a noticeable decreasing trend in STS. As the coarse aggregate replacement increases, the split tensile strength gradually decreases, with values dropping from 4.18 MPa (Mix "50R35B") to 3.41 MPa (Mix "100R50B").

5.4 Flexural Strength Optimization

5.4.1. Linear Model Fit Summary and ANOVA Evaluation for Flexural Strength

Table 8 presents the results of an ANOVA (Analysis of Variance) model for flexural strength on different sources of variation, including the sum of squares, degrees of freedom (df), mean squares, F-values, and p-values. The objective is to determine the significance of each factor in influencing the FS. The model is found to be significant, with a sum of squares of 8.03, 14 degrees of freedom, a mean square of 0.5734, an F-value of 27.09, and a p-value of less than 0.0001. The table 7 further breaks down the sources of variation, including the factors and their interactions. The factors considered in this analysis are denoted as A-RCS (fine aggregate replacement by RCS) and B-BFSA (coarse aggregate replacement by BFSA). The interactions between these factors are denoted as AB.

Table 8. ANOVA model for flexural strength

Source	Sum of Squares	df	Mean Square	F-value	p-value	
Model	8.03	14	0.5734	27.09	< 0.0001	significant
A-RCS	0.0112	1	0.0112	0.5296	0.4820	
B-BFSA	0.2694	1	0.2694	12.73	0.0044	
AB	0.0222	1	0.0222	1.05	0.3274	
A^2	0.0105	1	0.0105	0.4942	0.4967	
B^2	0.4441	1	0.4441	20.98	0.0008	
A^2B	0.0016	1	0.0016	0.0746	0.7899	
AB^2	0.0512	1	0.0512	2.42	0.1480	
A^3	0.0001	1	0.0001	0.0038	0.9523	
B^3	0.4107	1	0.4107	19.40	0.0011	
A^2B^2	0.0014	1	0.0014	0.0645	0.8042	
A^3B	0.0015	1	0.0015	0.0692	0.7973	
AB^3	0.0584	1	0.0584	2.76	0.1250	
A^4	0.0028	1	0.0028	0.1346	0.7207	
B^4	0.3139	1	0.3139	14.83	0.0027	
Residual	0.2328	11	0.0212			
Cor Total	8.26	25				

It indicates whether each factor or interaction is statistically significant based on the corresponding p-values. It can be observed that the factor B-BFSA has a significant effect on flexural strength, as it has a sum of squares of 0.2694, a mean square of 0.2694, an F-value of 12.73, and a p-value of 0.0044. In summary, the Table 7 provides a comprehensive analysis of the ANOVA model for flexural strength, indicating the significance of the overall model and the effects of different factors and interactions on the flexural strength of the tested samples. interactions do not show significant effects on flexural strength, as their p-values are higher than the significance level (typically 0.05).

5.4.2. Model Graphs and Diagnostic Findings

Design expert provides diagnostic findings that assess the quality of statistical models. These include statistical tests and numerical measures. For instance, the lack of fit test determines if the model adequately fits the data, while the residual plot identifies patterns or outliers that may indicate model issues. Other findings assess predictive accuracy, such as RMSE and R-squared. Users can analyze these diagnostic findings to evaluate model performance, adjust, and enhance accuracy and predictability.

(a) Normal plot of residual

(b) Predicted vs actual

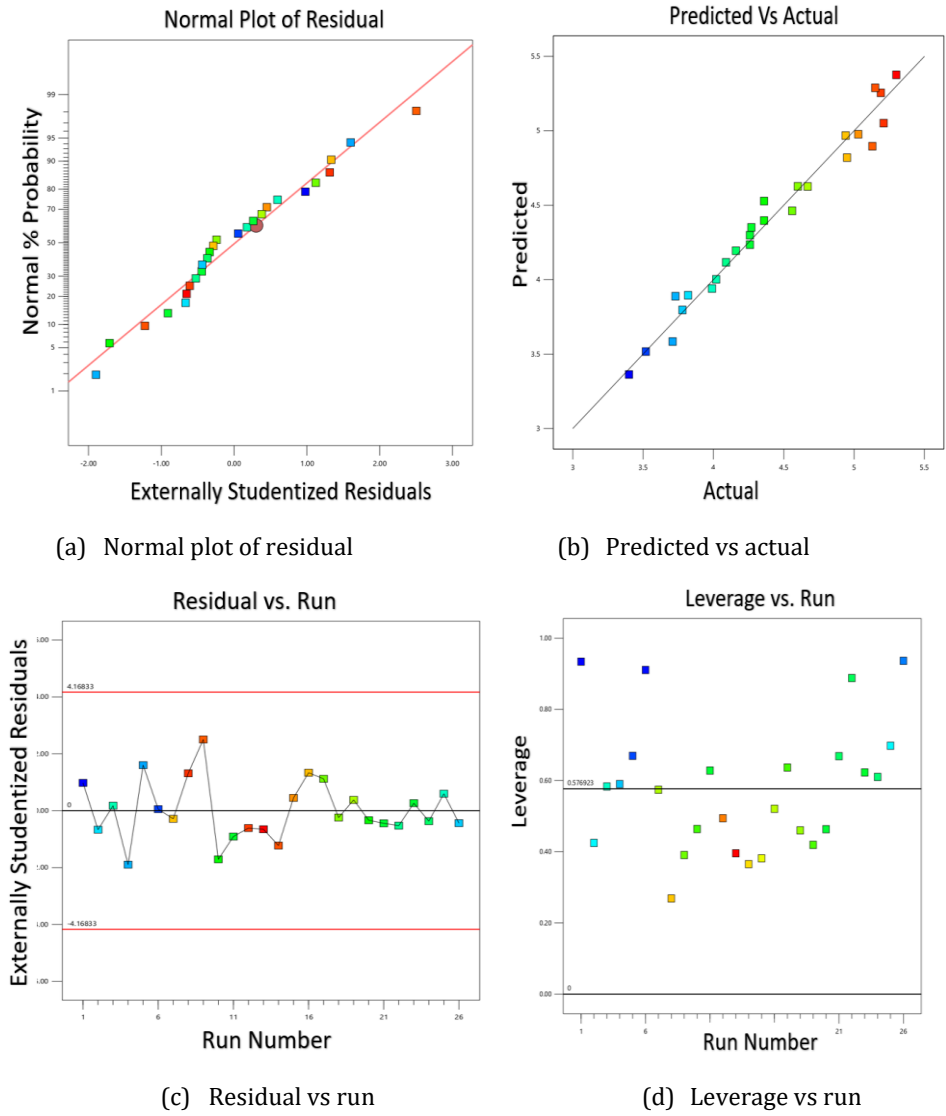(c) Residual vs run

(d) Leverage vs run

Fig. 5. Model graphs and diagnostic findings of flexural strength

Figure 5(a) presents a normal plot of residuals, allowing for the diagnosis of problems in a statistical model. Departures from normality in the plot suggest potential issues such as a mis specified model or missing predictors. In Figure 5(b), a predicted vs actual plot compares predicted values to actual values. Deviations from the diagonal line indicate

discrepancies between predicted and actual values, indicating potential model misspecification or missing predictors. Figure 5(c) demonstrates how a predicted vs actual plot can identify systematic bias or non-linear relationships. Figure 5(d) utilizes a leverage vs run plot to identify influential observations and assess model robustness over time or other variables. If influential observations are detected, the model may require re-evaluation or the exclusion of those observations. Additionally, a residual vs run plot can identify trends or cycles in residuals, indicating the need for additional predictors to update the model. These plots contribute to improving the accuracy and predictive power of the model.

5.4.3. Model Graphs of Flexural Strength

Model graphs typically include graphical representations of the model, such as contour plots or surface plots, that allow the user to visualize the relationship between the input variables and the response variable. These plots can help identify any nonlinear relationships between the variables and can also help identify any interactions between the variables that may be important for the model.
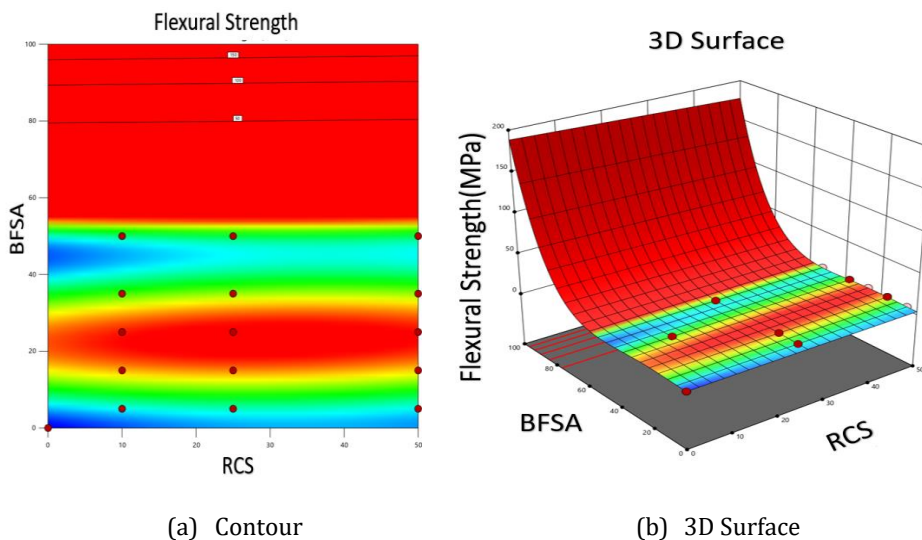

(a) Contour   (b) 3D Surface

Fig. 6. Model graphs of Flexural Strength

Contour plots and 3D plots offer visualizations of the relationship between flexural strength, BFSA, and RCS in figure 6(b). In a contour plot, constant flexural strength lines are displayed on a 2D grid representing BFSA and RCS in figure 6(a). Each contour line represents a different flexural strength level, and the spacing between lines indicates the rate of change in F as BFSA and RCS vary. In a 3D plot Figure 6(b), flexural strength values are plotted on the z-axis, while BFSA and RCS are plotted on the x-axis and y-axis. It can be observed that as the percentage of fine aggregate replacement by RCS increases, flexural strength tends to decrease. For example, at 0% RCS replacement, flexural strength is 3.4 MPa, whereas at 100% RCS replacement, flexural strength decreases to 3.52 MPa similarly, flexural strength is affected by the percentage of coarse aggregate replacement by BFSA.

The plot's surface shape depicts the relationship between the variables, with higher flexural strength values corresponding to higher elevations. These plots provide a visual representation of the relationship between flexural strength, BFSA, and RCS. By examining the contours or surface, regions where flexural strength is sensitive to BFSA or RCS changes can be identified. This information aids in determining optimal BFSA and RCS

values to minimize flexural strength or exploring the model's sensitivity to input variable changes.
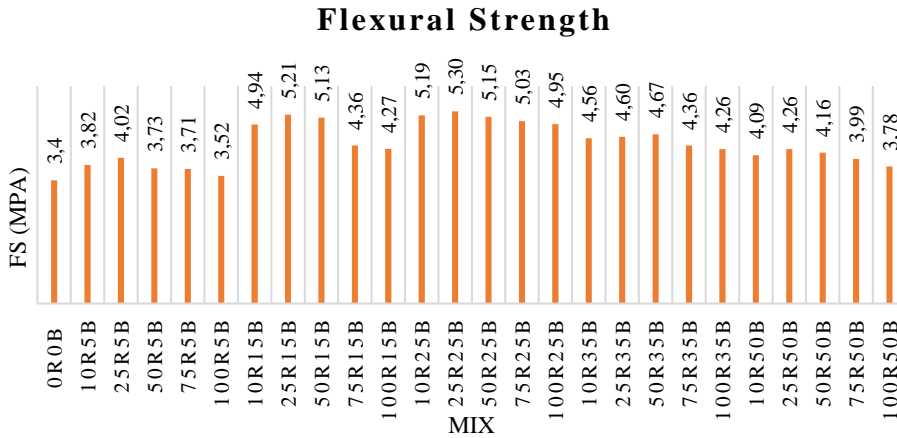
Flexural Strength

Fig. 7. Flexural strength with different levels of concrete mixture

The Figure 7 provided compares the flexural strength with different levels of fine aggregate replacement by RCS (%) and coarse aggregate replacement by BFSA (%). For each combination of fine aggregate replacement by RCS and coarse aggregate replacement by BFSA, the corresponding flexural strength value is given. It can be observed that as the percentage of fine aggregate replacement by RCS increases, flexural strength tends to decrease. For example, at 0% RCS replacement, flexural strength is 3.4 MPa, whereas at 100% RCS replacement, flexural strength decreases to 3.52 MPa similarly, flexural strength is affected by the percentage of coarse aggregate replacement by BFSA. As the BFSA replacement percentage increases, the flexural strength shows some variations. For instance, at 0% BFSA replacement, the flexural strength is 3.4 MPa, while at 50% BFSA replacement, the flexural strength decreases to 3.73 MPa. The Figure 7 provides a comparison of flexural strength values with different combinations of fine aggregate replacement by RCS and coarse aggregate replacement by BFSA. It helps in understanding the relationship between these replacement percentages and the resulting flexural strength, assisting in the evaluation of suitable aggregate replacement proportions to achieve desired flexural strength levels.

5.5. Bond Strength Optimization

5.5.1. Linear Model Fit Summary and ANOVA Evaluation for Bond Strength

Table 9 displays the analysis of variance (ANOVA) for bond strength, presenting various sources of variation with their sum of squares, degrees of freedom, mean squares, F-values, and p-values. The "Model" row indicates the overall significance of the model, with a sum of squares of 16.88, 9 degrees of freedom, a mean square of 1.88, and an F-value of 30.17. The p-value for the model is less than 0.0001, highlighting its significance. The ANOVA reveals that the overall model fit, represented by the "Model" row, is significant with a small p-value (< 0.0001). The individual factors of fine aggregate replacement by RCS ("A-RCS") and coarse aggregate replacement by BFSA ("B-BFSA") are also found to be significant, with p-values of 0.0462 and 0.0073, respectively. However, the interaction term "AB" and some higher-order terms (A^2B, AB^2, A^3, B^3) are not significant as their p-values are relatively high. The "residual" row captures the unexplained variability in bond

strength after accounting for the factors in the model, while the "Cor Total" row represents the total sum of squares, measuring the overall variability in the bond strength data.

Table 9. ANOVA for bond strength

| Source	Sum of Squares	df	Mean Square	F-value	p-value	
Model	16.88	9	1.88	30.17	< 0.0001	significant
A-RCS	0.2904	1	0.2904	4.67	0.0462	
B-BFSA	0.5868	1	0.5868	9.44	0.0073	
AB	0.0171	1	0.0171	0.2753	0.6070	
A^2	1.65	1	1.65	26.58	< 0.0001	
B^2	0.2071	1	0.2071	3.33	0.0867	
A^2B	0.0580	1	0.0580	0.9329	0.3485	
AB^2	0.0017	1	0.0017	0.0267	0.8722	
A^3	1.19	1	1.19	19.17	0.0005	
B^3	0.0176	1	0.0176	0.2832	0.6019	
Residual	0.9947	16	0.0622			
Cor Total	17.88	25				

A more flexible model for capturing non-linear relationships in bond strength data can be achieved by introducing a quadratic term in ANOVA. However, careful consideration of the trade-offs and challenges linked to model complexity and interpretation is necessitated by this approach.

5.5.2. Model Graphs and Diagnostic Findings

Diagnostic findings in Design Expert involve statistical tests and measures to assess model quality. These include the lack of fit test, which evaluates model adequacy, and the residual plot, which detects patterns or outliers that may indicate model issues. Additionally, measures of predictive accuracy like RMSE and R-squared are considered. By examining these findings, users can evaluate model performance, adjust, and enhance accuracy and predictive power. Figure 8(a) provides a normal plot of residuals for diagnosing statistical model problems. In Figure 8(b), a predicted vs actual plot compares predicted values to actual values, highlighting discrepancies that indicate model misspecification or missing predictors. Figure 8(c) identifies systematic bias or non-linear relationships using a predicted vs actual plot. Figure 8(d) uses a leverage vs run plot to identify influential observations and assess model robustness.

(a) Normal plot of residual   (b) Predicted vs actual
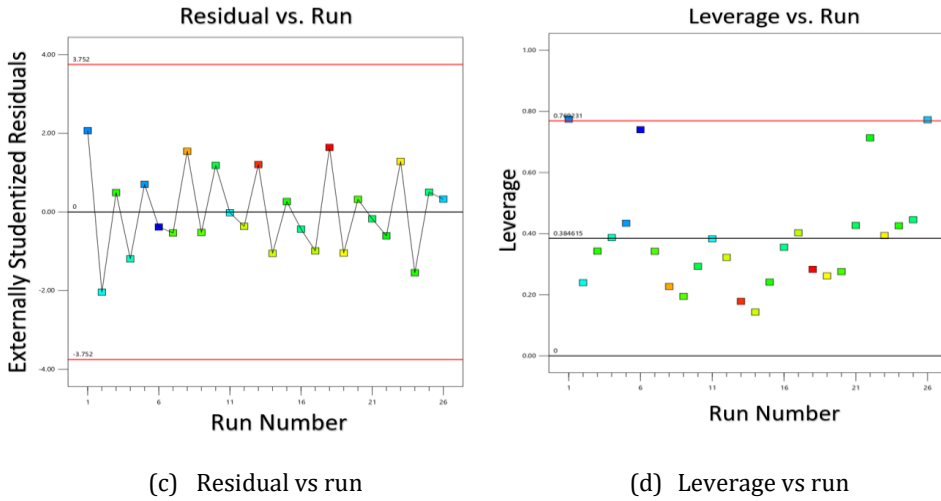
(c) Residual vs run

(d) Leverage vs run
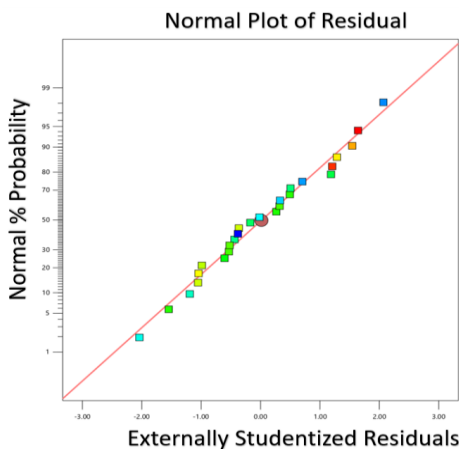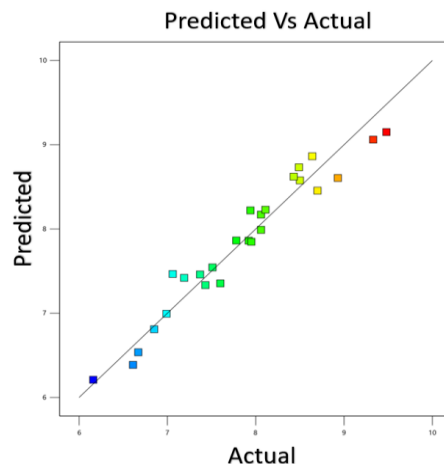
Fig. 8. Model graphs and diagnostic findings of bond strength

If influential observations are found, the model may require re-evaluation or exclusion. A residual vs run plot can detect trends or cycles in residuals, indicating the need for additional predictors. These plots enhance model accuracy and predictive power.

5.5.3. Model Graphs of Bond Strength

Model graphs typically include graphical representations of the model, such as contour plots or surface plots, that allow the user to visualize the relationship between the input variables and the response variable. These plots can help identify any nonlinear relationships between the variables and can also help identify any interactions between the variables that may be important for the model.

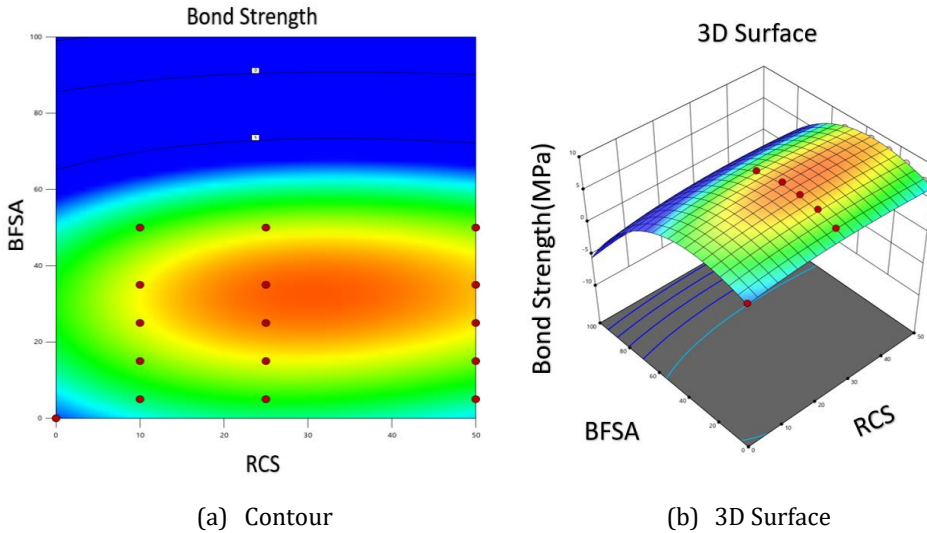

(a) Contour

(b) 3D Surface

Fig. 9 Model graphs of bond strength

Figure 9. (a) shows a contour plot and a 3D plot visualize the relationship between bond strength, BFSA, and RCS. Figure 9 (b) shows, lines of constant bond strength are shown on

a grid of BFSA and RCS values. Each contour line represents a different bond strength level, with the spacing indicating the rate of change with varying BFSA and RCS. In a 3D plot, bond strength is plotted on the z-axis, while BFSA and RCS are on the x-axis and y-axis. The plot's surface shape illustrates the relationship, with higher bond strength values corresponding to higher elevations. The minimum bond strength observed in the data is 6.16, which occurs when RCS is replaced by 100% and BFSA by 5%. This suggests that using a higher percentage of replacement for RCS and a lower percentage for BFSA results in a weaker bond strength between the concrete components.

The maximum bond strength recorded is 9.48, occurring when RCS is replaced by 25% and BFSA by 35%. This indicates that a balance between the replacement percentages of both RCS and BFSA can lead to the highest bond strength between the components of the concrete mixture. These plots help identify regions where bond strength is sensitive to BFSA or RCS changes. Optimal BFSA and RCS values can be determined to minimize bond strength or explore sensitivity to input variables.
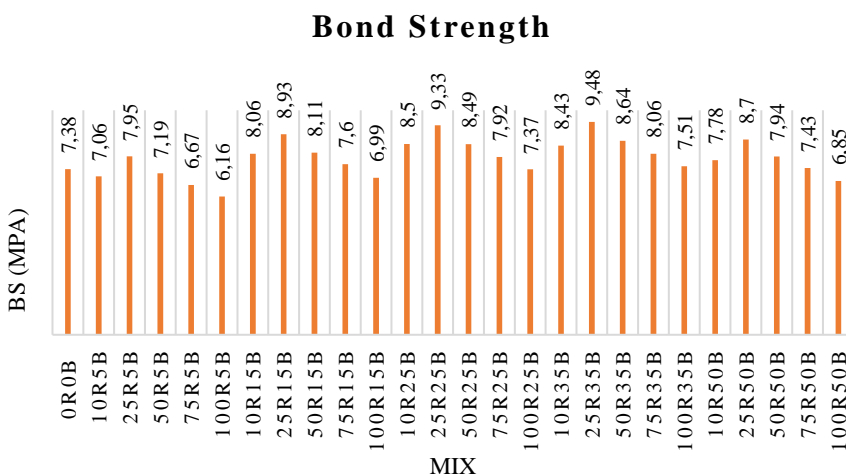
Bond Strength

Fig. 10. Bond strength values for different mixes

Figure 10 provides bond strength values for different concrete mixes, indicating the percentages of fine aggregate replacement by RCS and coarse aggregate replacement by BFSA. Each mix is identified by a code consisting of the RCS and BFSA percentages, along with a mix number. The bond strength values represent the strength of the bond between components in each mix. Higher values indicate stronger bonds, while lower values indicate weaker bonds. Increasing the percentage of fine aggregate replacement by RCS generally leads to a decrease in bond strength. For example, comparing mix 0R0B (no replacement) with mix 100R5B, the bond strength decreases from 7.38 to 6.85 MPa. The percentage of coarse aggregate replacement by BFSA does not follow a consistent pattern in relation to bond strength. For instance, mix 10R5B and mix 10R35B both have a 5% BFSA replacement, but their bond strength values differ 7.06 and 8.43 MPa, respectively. Varying the coarse aggregate replacement while keeping the fine aggregate replacement constant can result in different bond strength values. For example, in mix series 10R15B, the bond strength increases as the BFSA replacement increases from 5 to 35%. Figure 10 allows for comparing bond strength values across mixes with varying percentages of RCS and BFSA replacements, providing insights into the impact of these replacements on overall bond strength. therefore, the combination of 25% fine aggregate replacement by RCS and 25% coarse aggregate replacement by BFSA results in the highest bond strength

value of 9.33. This composition seems to offer the optimal balance between the materials, leading to enhanced bond strength in the concrete mixture.

Certain concrete mixtures incorporating Blast Furnace Slag Aggregate and Recycled Concrete sand excel due to BFSA enhancing bonding, countering strength reduction from increased replacements, and enabling properties like traditional concrete. While higher RCS content increased voids and water absorption, BFS helped manage these effects by enhancing bonding. This showcases the potential of thoughtful mixture design with BFSA and RCS to optimize concrete quality and performance[47].

6. Conclusion

In the conclusion, specified limits play a vital role in determining the permissible ranges for various parameters involved in the assessment of construction materials. These limits provide essential guidelines for evaluating the values of parameters such as split tensile strength flexural strength, and bond strength. By defining lower and upper limits for each parameter, these limits ensure that the values fall within acceptable ranges and adhere to specific criteria or desired standards. Adhering to these limits is crucial for maintaining the quality, durability, and overall performance of construction materials.
The Alternate split tensile strength parameter, with a lower limit of 3.2 MPa and an upper limit of 4.91 MPa. The desired range for the flexural strength value is represented by the flexural strength parameter, which has a lower limit of 3.4 MPa and an upper limit of 5.3 MPa. Similarly. The bond strength parameter signifies the acceptable range for the bond strength value, with a lower limit of 6.16 MPa and an upper limit of 9.48 MPa. These limits establish the boundaries within which each parameter should ideally fall, ensuring compliance with specific criteria and desired standards. A similar decreasing trend is observed in the split tensile strength as the percentage of coarse aggregate replacement with BFSA increases. The split tensile strength gradually decreases with a higher coarse aggregate replacement. For example, the split tensile strength decreases from 4.18 in mix "50R35B" to 3.41 in mix "100R50B". Likewise, the flexural strength is influenced by the percentage of coarse aggregate replacement with BFSA. As the BFSA replacement percentage increases, variations in the flexural strength are observed. For instance, at 0% BFSA replacement, the flexural strength is 3.4, while at 50% BFSA replacement, the flexural strength decreases to 3.73.

Furthermore, the bond strength values differ when comparing mixes with the same fine aggregate replacement by RCS but varying coarse aggregate replacement by BFSA. For instance, mix 10R5B and mix 10R35B both have a BFSA replacement of 5%, but their bond strength values differ (7.06 and 8.43, respectively). In mix series 10R15B, the bond strength increases as the BFSA replacement increases from 5 to 35%, indicating the impact of coarse aggregate replacement on bond strength values. These observations highlight the influence of replacing coarse aggregate with BFSA on the mechanical properties of the concrete mixes, such as, split tensile strength flexural strength, and bond strength. It is essential to consider the percentage of coarse aggregate replacement carefully to achieve the desired properties and performance in concrete applications.

Declaration of Competing Interest

The author declares that he has no known competing financial interests or personal relationships that could have appeared to influence the work reported in this paper.

References

[1] Pradhan B, Chand S, Chand S, et al. Emerging groundwater contaminants: A comprehensive review on their health hazards and remediation technologies. Groundwater for Sustainable Development. 2023;20:100868. https://doi.org/10.1016/j.gsd.2022.100868

[2] McAllister J. Factors influencing solid-waste management in the developing world. A Plan B Report Submitted. Degree of Master of Science in Geography. 2015;299:1-95.

[3] Evangelista L, de Brito J. Mechanical behaviour of concrete made with fine recycled concrete aggregates. Cement and Concrete Composites. 2007;29:397-401. https://doi.org/10.1016/j.cemconcomp.2006.12.004

[4] Escalante-García JI, Magallanes-Rivera RX, Gorokhovsky A. Waste gypsum-blast furnace slag cement in mortars with granulated slag and silica sand as aggregates. Construction and Building Materials. 2009;23:2851-5. https://doi.org/10.1016/j.conbuildmat.2009.02.032

[5] Russo N, Lollini F. Effect of carbonated recycled coarse aggregates on the mechanical and durability properties of concrete. Journal of Building Engineering. 2022;51:104290. https://doi.org/10.1016/j.jobe.2022.104290

[6] Pacheco-Torgal F. Introduction to the recycling of construction and demolition waste (CDW). In: Pacheco-Torgal F, Tam VWY, Labrincha JA, et al., editors. Woodhead Publ. Ser. Civ. Struct. Eng., Woodhead Publishing; 2013, 1-6. https://doi.org/10.1533/9780857096906.1

[7] Ulubeyli GC, Artir R. Properties of Hardened Concrete Produced by Waste Marble Powder. Procedia - Social and Behavioral Sciences. 2015;195:2181-90. https://doi.org/10.1016/j.sbspro.2015.06.294

[8] Grazia M De, Trottier C, Dantas SRA, et al. Influence of Recycled Concrete Aggregate Type on Rheological Behaviour of Mixtures Proportioned Using the Equivalent Volume Method. Recent Progress in Materials. 2022;4:1-1. https://doi.org/10.21926/rpm.2203017

[9] Zhu F, Yang C, Miao M. Experimental study on the properties of polyvinyl alcohol fiber reinforced cementitious composites with super early strength. Materials Letters. 2023;330:133264. https://doi.org/10.1016/j.matlet.2022.133264

[10] Latif SD. Concrete compressive strength prediction modeling utilizing deep learning long short-term memory algorithm for a sustainable environment. Environmental Science and Pollution Research. 2021;28:30294-302. https://doi.org/10.1007/s11356-021-12877-y

[11] Pulkit K. Effect of stone slurry & recycled aggregate on properties of concrete Waste management. LAP LAMBERT Academic Publishing (2018-10-12). 2018.

[12] Pulkit K, Saini B, Chalak HD. Factors Affecting the Bond Between Substrate-Overlay Material. A Review. Journal of Engineering Science and Technology Review. 2022;15:55-69. https://doi.org/10.25103/jestr.156.08

[13] Pulkit K, Saini B, Chalak H. The influence of interfacial bond between substrate and overlay concrete by Bi-surface Shear Test and Split prism test. Asia-Pacific Journal of Science and Technology,. 2023.

[14] Koelmel J, Prasad MN V, Velvizhi G, et al. Chapter 15 - Metalliferous Waste in India and Knowledge Explosion in Metal Recovery Techniques and Processes for the Prevention of Pollution. In: Prasad MN V, Shih KBT-EM and W, editors., Academic Press; 2016, 339-90. https://doi.org/10.1016/B978-0-12-803837-6.00015-9

[15] Horii K, Tsutsumi N, Kitano Y, et al. Processing and reusing technologies for steelmaking slag. Nippon Steel Technical Report. 2013;805:123-9.

[16] SALIH MA. New geo-polymerization process for high strength alkali-activated binder with palm oil fuel ash and ground granulated blast furnace slag. 2015. https://doi.org/10.1016/j.conbuildmat.2015.05.119

[17] Owaid HM, Hamid RB, Taha MR. A review of sustainable supplementary cementitious materials as an alternative to all-portland cement mortar and concrete. Australian Journal of Basic and Applied Sciences. 2012;6:287-303.

[18] Abhishek P, Ramachandra P, Niranjan PS. Use of recycled concrete aggregate and granulated blast furnace slag in self-compacting concrete. Materials Today: Proceedings. 2020;42:479-86. https://doi.org/10.1016/j.matpr.2020.10.239

[19] Cao Q, Nawaz U, Jiang X, et al. Effect of air-cooled blast furnace slag aggregate on mechanical properties of ultra-high-performance concrete. Case Studies in Construction Materials. 2022;16:e01027. https://doi.org/10.1016/j.cscm.2022.e01027

[20] Qasrawi H. The use of steel slag aggregate to enhance the mechanical properties of recycled aggregate concrete and retain the environment. Construction and Building Materials. 2014;54:298-304. https://doi.org/10.1016/j.conbuildmat.2013.12.063

[21] Maslehuddin M, Sharif AM, Shameem M, et al. Comparison of properties of steel slag and crushed limestone aggregate concretes. Construction and Building Materials. 2003;17:105-12. https://doi.org/10.1016/S0950-0618(02)00095-8

[22] Yu X, Tao Z, Song T-Y, et al. Performance of concrete made with steel slag and waste glass. Construction and Building Materials. 2016;114:737-46. https://doi.org/10.1016/j.conbuildmat.2016.03.217

[23] Ríos JD, Vahí A, Leiva C, et al. Analysis of the utilization of air-cooled blast furnace slag as industrial waste aggregates in self-compacting concrete. Sustainability (Switzerland). 2019;11. https://doi.org/10.3390/su11061702

[24] Akaözolu S, Ati CD. Effect of Granulated Blast Furnace Slag and fly ash addition on the strength properties of lightweight mortars containing waste PET aggregates. Construction and Building Materials. 2011;25:4052-8. https://doi.org/10.1016/j.conbuildmat.2011.04.042

[25] Habert G. Assessing the environmental impact of conventional and "green" cement production. Eco-Efficient Constr. Build. Mater. Life Cycle Assess. (LCA), Eco-Labelling Case Stud., 2013, 199-238. https://doi.org/10.1533/9780857097729.2.199

[26] Shi J, Tan J, Liu B, et al. Experimental study on full-volume slag alkali-activated mortars: Air-cooled blast furnace slag versus machine-made sand as fine aggregates. Journal of Hazardous Materials. 2021;403. https://doi.org/10.1016/j.jhazmat.2020.123983

[27] Verian KP, Panchmatia P, Olek J, et al. Pavement concrete with air-cooled blast furnace slag and dolomite as coarse aggregates: Effects of deicers and freeze-thaw cycles. Transportation Research Record. 2015;2508:55-64. https://doi.org/10.3141/2508-07

[28] Ahmed T, Ray S, Haque M, et al. Optimization of properties of concrete prepared with waste glass aggregate and condensed milk can fiber using response surface methodology. Cleaner Engineering and Technology. 2022;8:100478. https://doi.org/10.1016/j.clet.2022.100478

[29] Seetharaman R, Seeman M, Kanagarajan D, et al. A statistical evaluation of the corrosion behaviour of friction stir welded AA2024 aluminum alloy. Materials Today: Proceedings. 2020;22:673-80. https://doi.org/10.1016/j.matpr.2019.09.066

[30] Chong BW, Othman R, Jaya RP, et al. Meta-analysis of studies on eggshell concrete using mixed regression and response surface methodology. Journal of King Saud University - Engineering Sciences. 2021.

[31] Manohar DR, Anbazhagan P. Shear strength characteristics of geosynthetic reinforced rubber-sand mixtures. Geotextiles and Geomembranes. 2021;49:910-20. https://doi.org/10.1016/j.geotexmem.2020.12.015

[32] Shi J, Zhao L, Han C, et al. The effects of salinized rubber and nano-SiO2 on microstructure and frost resistance characteristics of concrete using response surface methodology (RSM). Construction and Building Materials. 2022;344:128226. https://doi.org/10.1016/j.conbuildmat.2022.128226

[33] Guo L, Guo Y, Zhong L. Research on the back analysis and failure mechanism of recycled concrete aggregate meso-parameters based on Box-Behnken Design response surface model. Journal of Building Engineering. 2022;51:104317. https://doi.org/10.1016/j.jobe.2022.104317

[34] Ali M, Kumar A, Yvaz A, et al. Central composite design application in the optimization of the effect of pumice stone on lightweight concrete properties using RSM. Case Studies in Construction Materials. 2023;18:e01958. https://doi.org/10.1016/j.cscm.2023.e01958

[35] Mala AA, Sherwani AFH, Younis KH, et al. Mechanical and fracture parameters of ultra-high performance fiber reinforcement concrete cured via steam and water: Optimization of binder content. Materials. 2021;14. https://doi.org/10.3390/ma14082016

[36] Ahmed HU, Mohammed AA, Rafiq S, et al. Compressive strength of sustainable geopolymer concrete composites: A state-of-the-art review. Sustainability (Switzerland). 2021;13. https://doi.org/10.3390/su132413502

[37] Nafees A, Javed MF, Musarat MA, et al. FE Modelling and Analysis of Beam Column Joint Using Reactive Powder Concrete. Crystals. 2021;11. https://doi.org/10.3390/cryst11111372

[38] Peng Y, Ghahnaviyeh MB, Ahamd MN, et al. Analysis of the effect of roughness and concentration of Fe3O4/water nanofluid on the boiling heat transfer using the artificial neural network: An experimental and numerical study. International Journal of Thermal Sciences. 2021;163. https://doi.org/10.1016/j.ijthermalsci.2021.106863

[39] Saboo N, Nirmal Prasad A, Sukhija M, et al. Effect of the use of recycled asphalt pavement (RAP) aggregates on the performance of pervious paver blocks (PPB). Construction and Building Materials. 2020;262:120581. https://doi.org/10.1016/j.conbuildmat.2020.120581

[40] Sinkhonde D. Generating response surface models for optimization of CO2 emission and properties of concrete modified with waste materials. Cleaner Materials. 2022;6:100146. https://doi.org/10.1016/j.clema.2022.100146

[41] Sinkhonde D, Onchiri RO, Oyawa WO, et al. Response surface methodology-based optimisation of cost and compressive strength of rubberized concrete incorporating burnt clay brick powder. Heliyon. 2021;7:e08565. https://doi.org/10.1016/j.heliyon.2021.e08565

[42] Madani T, Boukraa M, Aissani M, et al. Experimental investigation and numerical analysis using Taguchi and ANOVA methods for underwater friction stir welding of aluminum alloy 2017 process improvement. International Journal of Pressure Vessels and Piping. 2023;201:104879. https://doi.org/10.1016/j.ijpvp.2022.104879

[43] IS 8112 - 1989, Specification for 43 grade Ordinary Portland Cement. Bureau of Indian Standards, New Delhi. 2013:17.

[44] IS 383-1970. Specification for coarse and fine aggregates from natural sources for concrete. Bureau of Indian Standard. Published online 1970.

[45] IS 10500. Indian Standard Drinking Water Specification (Second Revision). Bureau of Indian Standards. May 2012;IS 10500:1-11

[46] IS 456. Plain and Reinforced Concrete. Bureau of Indian Standards. Published online 2000.

[47] Lin SK, Wu CH. Improvement of bond strength and durability of recycled aggregate concrete incorporating high volume blast furnace slag. Materials. 2021;14. https://doi.org/10.3390/ma14133708

Research Article

An investigation on optimizing the carbonation resistance of coal bottom ash concrete with its carbon footprints and eco-costs

Nitin Ankur[a], Navdeep Singh*[,b]

Department of Civil Engineering, Dr BR Ambedkar National Institute of Technology, Jalandhar, India

Article Info	Abstract
	Energy from coal-fed thermal power plants is provided at the cost of the generation of coal ash. Coal bottom ash (CBA) is an ash generated in coal-fed power plants which is landfilled. Existing literature reports the potential of CBA as a replacement for Portland cement (PC) and natural fine aggregates (NFA) in concrete. Carbonation is an important durability parameter of concrete having fatal consequences at later ages if not estimated and controlled as it leads to corrosion in reinforcement. In the present study, experimental, microstructural, and statistical analysis along with life cycle assessment was performed to investigate the combined effect of two-hour grinded CBA (GCBA) as PC (10-30%) and raw CBA as NFA replacement (0-50%) on compressive strength and carbonation resistance. Accelerated carbonation tests were performed at an exposure of four weeks after 28 and 90 days of curing. Among CBA-based concrete mixes, concrete with 20% GCBA and 25% CBA (G20C25) reported higher compressive strength and carbonation depth owing to pozzolanic reactivity and filler effect of fine CBA particles. However, G20C25 resulted in comparable performance in comparison with the control mix in terms of strength and carbonation resistance. The findings of X-ray diffraction spectroscopy, scanning electron microscopy and Fourier transform infrared spectroscopy also validate the trends. The mathematical models derived for the carbonation resistance and strength were well-fitted. Multi-objective optimization recommended 21.5% GCBA and 29.8% CBA as the optimum amount that resulted in 20.08% and 19.40% lower carbon footprints and eco-costs compared to control mix.

1. Introduction

The durability and sustainability assessment of concrete are key aspects in the production of concrete as it is the most consumed building material around the world. The majority of the constituents of concrete are dependent on natural resources for procurement [1]. Concrete is being utilized at a very rapid pace hence, the rate at which natural resources are depleted is much higher than the rate at which they are being replenished. The construction of new infrastructure is not only a concern, as poor durability performance of concrete also demands repair and retrofitting which also increases the demand for concrete. The need of the hour is to reduce the overburden on the natural resources and alternative constituents of concrete must be explored that can perform in tandem with concrete prepared with conventional ingredients. Numerous industrial waste has been investigated for the potential replacement of cement, fine aggregates, and coarse aggregates in concrete [2–12]. Recently, many industrial wastes like fly ash, silica fumes,

slag, recycled concrete aggregates, etc. have been discovered as alternative cement and aggregates in concrete, and promising results have been stated worldwide [2,4–12]. The rise in the global population results in increasing demand for concrete as well. Hence, it is important to develop alternatives that are not only durable but also sustainable.

With the rise in population, the energy demand especially electricity is also rising. The majority of the world depends on coal-fed thermal power plants for electricity generation. It has been estimated that 47% of global electricity will be provided by coal-fed thermal power plants by 2030 [13,14]. It has also been expected that despite the world's focus on renewable energy resources, the dependency on coal-fed power plants will persist for the coming decades. The cost effective and surplus energy from coal-fed thermal power plants is provided at the cost of the generation of coal ash that pollutes the environment. Coal bottom ash (CBA) is one such ash that is generally landfilled and unlike fly ash is yet to be developed as a potential replacement for building materials. The CBA particles are heavy and settle at the foot of the combustion chamber. It constitutes around 20-30% of overall coal ash. Also, the concentration of heavy metals like Arsenic, Barium, Nickel, etc. is three to four times higher than permissible limits that make it unsafe for landfill. It has been estimated that around 100 million tons of CBA are annually dumped into various dumpsites [15]. Attempts have been made in recent years to develop CBA as a replacement of natural fine aggregate (NFA) and cement in concrete [16–24]. The CBA resembles the size of NFA due to its coarser size and has been studied as NFA replacement. Few studies also reported CBA as cement replacement after grinding CBA to obtain size similar to the cement particle [25–34].

The replacement of aggregates and cement with industrial waste is common practice now a day. However, satisfactory performance in terms of mechanical as well as durability parameters must be ensured. Durable and environment sustainable products is the need of hour not only in construction industry but other industries also [1,35]. The durability of concrete is also related to environmental impacts of concrete as less durable concrete demands more repair and retrofitting those further aids in to enhancement of impacts associated with the concrete. Among the durability of concrete, carbonation is an important property as carbonation poses serious threat to reinforcement of the structures [9,36,37]. Carbonation may have fatal consequences if not rectified on time. Carbonation tends to lower the pH of concrete resulting in decreasing the alkalinity of concrete and making reinforcing bars prone to corrosion. Carbonation is one of the key aspects that leads to deterioration of concrete structures. Extensive research has been carried out to study the influence of industrial waste based concretes on the carbonation resistance [37–41], however, research carried out on the carbonation behavior of CBA-based concrete is scarce.

It has been revealed that when CBA has been used as NFA replacement, the carbonation is not governed by diffusion theory i.e. carbonation depth depends on square root of exposure period, as porous CBA particles provides easy permeability to diffusing gases [42]. It has also been stated that the carbonation depth increases with increase in CBA content. Existing literature revealed that due to pore size densification by the fine particle of CBA, using 10% CBA as NFA replacement yields similar carbonation depth in CBA-based concrete when compared to conventional concrete [19,42–46]. At higher replacement levels, the presence of porous CBA leads to poor interlocking between the particles consequently increasing the carbonation depth. Also, CBA as PC replacement in CBA concrete resulted in better performance in terms of carbonation resistance than fly ash-based concrete. However, there is very limited research available of the carbonation resistance of CBA concrete where CBA has been used as cement replacement [33]. Also, the effect of combined replacement of grinded CBA and raw CBA as cement and NFA replacement respectively on carbonation resistance is yet to be explored.

1.1. Research Objectives and Significance

The brief review of the existing studies has been presented in the above sections and it can be interpreted that carbonation resistance and environmental impacts of CBA-based concrete where CBA has been used as joint replacement of cement and NFA is yet to be explored. Therefore, the prime objectives of the present investigations are:

- Investigating the potential of CBA to be use as dual replacement i.e. as PC replacement in grinded form (GCBA) and as NFA in raw form (CBA) in concrete.

- Maximizing the utilization of GCBA and CBA so as to attempt reduction in environmental impacts and the consumption of natural resources in concrete without significant reduction/compensation in compressive strength, microstructural characteristics and carbonation resistance of the designed concrete mixes.

- Determining the carbon footprints and eco-cost associated with the CBA based concrete so as to determine its sustainability potential and reduction in environmental impacts in comparison with the conventional concrete.

Based on the outcomes of the abovementioned objectives, a design mix for concrete prepared with GCBA and CBA can be proposed that will not only satisfy the structural requirements of a concrete but will also minimize the detrimental effects of conventional concrete on people and the environment.
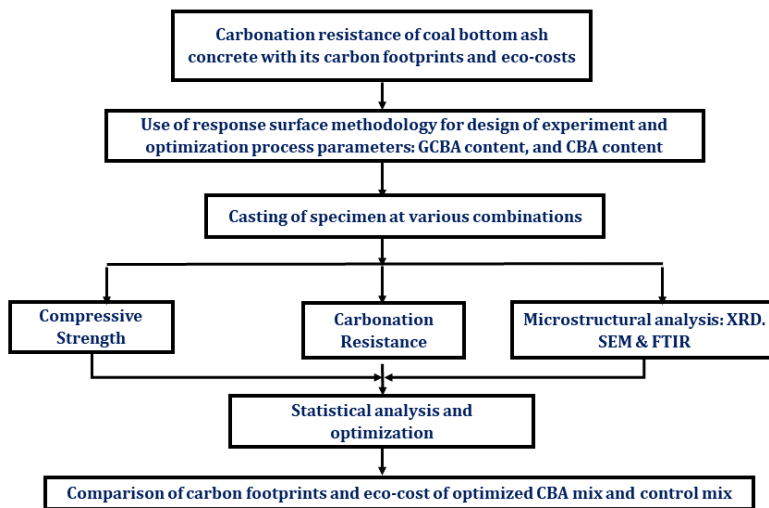

Fig. 1. Overview of the objectives and experimental program in the present study

The present research article can be divided in 4 parts where Part 1 contains present day scenario of coal combustion products along with a brief review of the existing literature on CBA based concrete. Part 2 contains materials and methods that are used in the present investigation for development of CBA based concrete. Part 3 contains results and discussions and provides in depth analysis of trends observed in compressive strength, carbonation depth, microstructural characteristics. Statistical analysis and optimization part has also been discussed in Part 3 along with the environmental impacts of CBA based concrete mixes. The research article concludes with key findings of the study in Part 4.

2. Materials and Methods

Fig.1 represents the overview of the objectives and experimental program of the present study. The present study focuses on investigating the effect of grinding CBA (2 hours), grinded CBA (GCBA) as Portland cement (PC) replacement and CBA as NFA replacement on carbonation resistance and environmental impacts of concrete. Accelerated carbonation tests along with compressive strength tests have been conducted to study the combined effect. Microstructure analysis like X-ray diffraction spectroscopy (XRD), scanning electron microscopy (SEM) and Fourier transform infrared spectroscopy (FTIR) were also performed to determine the influence of GCBA and CBA on microstructural characteristics. Statistical analysis was also performed to determine the significance of the GCBA, CBA and their interactions on the compressive strength as well as carbonations resistance. In addition, carbon footprints and eco-costs associated with CBA concrete were also calculated so as to determine the sustainability potential of CBA-based concrete.

2.1. Material

The present study used ordinary Portland cement (OPC) grade 43 for preparing concrete that conforms to IS 8112-2013 [47]. The natural coarse aggregate (NCA) of two different sizes i.e. 20 mm and 10 mm were used in 40:60 proportion conforming to IS 383 2016 [48]. The coarse sand conforming to zone II as per IS 383 2016 was used as natural fine aggregate (NFA). The physical properties of NFA and CBA are presented in Table 1.

Table 1. Chemical and Physical properties of PC, CBA, GCBA and NFA

Chemical composition of PC, CBA and GCBA			
Compounds	PC	CBA	GCBA
SiO_2	20.89	56.4	56.5
Al_2O_3	5.88	29.13	26.6
Fe_2O_3	3.99	8.31	10.8
MgO	0.93	0.42	0.318
CaO	60.58	0.78	1.24
SO_3	2.83	0.21	0.555
K_2O	1.12	1.27	1.48
Na_2O	0.81	0.07	0.24
TiO_2	0.22	0.22	1.67
Loss of Ignition	2.01	0.87	-
Physical properties of NFA, CBA and GCBA			
Property	NFA	CBA	GCBA
Fineness Modulus (FM)	2.43	2.23	-
Water Absorption (%)	1.52	9.5	-
Specific Gravity	2.6	2.38	2.62
Specific Surface Area (m^2/g)	-	-	1.41
Average Pore Width (nm)	-	-	8.07
Pore Volume (cm^3/g)	-	-	0.0024

Coal bottom ash (CBA) was acquired from Ropar thermal power plant and was utilized in two discrete ways i.e in grinded form (GCBA) as a PC replacement and in raw form (CBA) as NFA replacement (Fig. 2). The CBA was grinded for 2 hours so as to obtain CBA at different specific surface area. A ball mill of 20 Kg capacity with 15 kg steel balls of varying diameter was used for grinding CBA at 55rpm.

(a)   (b)

Fig. 2. Coal bottom ash in (a) grinded form (b) raw form

The chemical composition of CBA along with the physical characteristic of GCBA are presented in Table 1. It is evident from Table 1 that the grinding of CBA has minimal effect on the chemical composition of CBA however, the particle size of CBA decreases significantly with grinding (Fig. 3). Table 1 also represents the specific surface area, average pore width, and pore volume for GCBA as obtained from Brunauer, Emmett and Teller (BET) test. Fig. 3 represents the particle size distribution curve for PC, GCBA, CBA and NFA and it can be interpreted that the particles of GCBA and CBA are finer than PC and NFA respectively. CBA also reported higher water absorption (9.5%) and lower specific gravity (2.38) than the NFA.
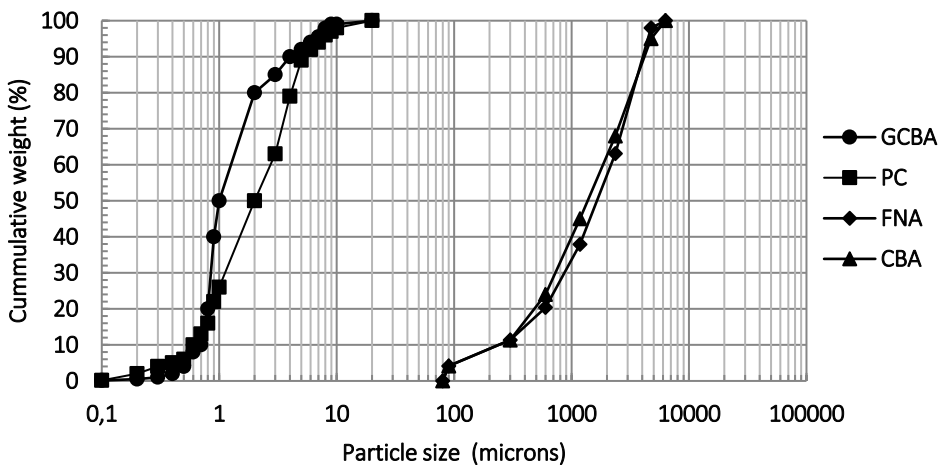

Fig. 3. Particle size distribution curves of GCBA, PC, CBA and NFA

2.2. Experimental Program

A two factor three level central composite design was adopted to study the combined effect of CBA as simultaneous replacement of PC and NFA in concrete. GCBA grinded for two hours was varied over the range of 10-20-30% replacement of PC whereas the effect of CBA was investigated over range of 0-25-50% replacement of NFA. A total of 9 concrete mixes of M 25 grade were cast as per IS 10262-2019 [49] and detailed mix proportion has been presented in Table 2.

Table 2. Mix proportions adopted for various CBA-based concretes

Mix	Grinding Period (Hours)	PC (kg/m³)	GCBA (%)	GCBA (kg/m³)	NFA (kg/m³)	CBA (%)	CBA (kg/m³)	NCA (kg/m³)
Control	-	395	-	-	732	-	-	1068
G10C0	2	355.5	10	39.5	732	0	0	1068
G10C25	2	355.5	10	39.5	549	25	183	1068
G10C50	2	355.5	10	39.5	366	50	366	1068
G20C0	2	316	20	79	732	0	0	1068
G20C25	2	316	20	79	549	25	183	1068
G20C50	2	316	20	79	366	50	366	1068
G30C0	2	276.5	30	118.5	732	0	0	1068
G30C25	2	276.5	30	118.5	549	25	183	1068
G30C50	2	276.5	30	118.5	366	50	366	1068

A total of 4 responses were investigated i.e. 28 day and 90-day compressive strength, and carbonation depth after 28 day and 90 day of curing after 4 week of exposure to accelerated carbonation and are presented in Table 3. Compressive strength tests were performed on 100 mm cubes after 28 days and 90 days of curing conforming to IS 516:2006 [50]. After 28 days and 90 days of water curing, accelerated carbonation test were performed on concrete mixes. Carbonation tests were performed on 500x100x100 mm beams that were split in two parts and covered with epoxy from 5 sides keeping one side exposed to accelerated carbon dioxide (CO_2). The samples were kept in accelerated carbonation chamber as present in Fig. 4. For the present study, the concentration of CO_2 was kept at 4% and the samples prepared were exposed to CO_2 for 4 weeks as per CPC-18, RILEM: 1988, EN 14360-2006 [51]. A solution containing 1% phenolphthalein in 70% ethyl alcohol was prepared and sprinkled on the slices. The colorless area represents the extent of carbonated area whereas pink color represents the non-carbonated area. Statistical analysis of these responses was also performed using analysis of variance (ANOVA). The microstructure characterization was performed using microstructure techniques such as X-ray diffraction (XRD), Scanning Electron Microscopy (SEM) analysis and Fourier Transform Infrared Spectroscopy (FTIR). Panalytical X'pert Pro (NDP) diffractometer was used for performing XRD analysis with 2θ in the range 5-80 degrees. Zeiss Sigma 500VP was used to study the SEM of the concrete mixes. FT-IR analysis was conducted on Bruker Tensor 27 FT-IR instrument.

The fast-track Life cycle assessment method was used to determine and compare the environmental impacts of optimized CBA concrete with conventional concrete. This innovative method was developed by Delft University of Technology and is an innovative and practical method for performing LCA [52]. The method is best suited for comparing the two different scenarios of a same product to determine the sustainability impacts metrics as this method generally focus on 'what to calculate' instead 'how to calculate' [52]. Carbon footprints and eco-costs were eco indicator selected for performing the LCA of optimized CBA concrete mix. The amount of greenhouse gases resulting from the production of material are represented in terms of carbon footprints and are calculated in kg CO_2 equivalent [52–57]. Eco-costs is monetized eco indicator that represents a virtual cost that need to be sustained so as to make the production of material sustainable and decrease the natural resource depletion and pollution to a level that resembles the carrying potential of Earth [52].

(a) Casted beams
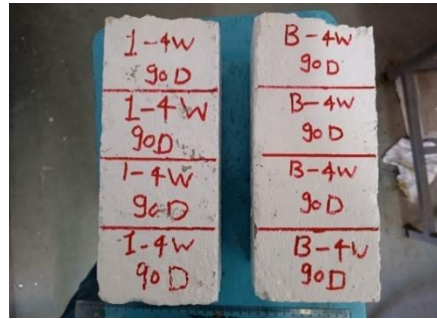
(b) Beams painted with epoxy

(c) Beams placed in accelerated
carbonation chamber

(d) Tested specimen

Fig. 4. Steps in determining the carbonation resistance of concrete

Table 3. Results of 28 and 90-day compressive strength and carbonation depth after 4 weeks of exposure

Std	Run	Mix	Factor 1 A: GCBA (%)	Factor 2 B: CBA (%)	Response 1 28 Day Compressive strength (MPa)	Response 2 90 Day Compressive strength (MPa)	Response 3 28 Day-4 Week Carbonation Depth (mm)	Response 4 90 Day-4 Week Carbonation Depth (mm)
-	-	Control	-	-	29.34	33.94	5	3
7	1	G20C0	20	0	25.87	33.09	5	1
6	2	G30C25	30	25	23.5	30.57	15	8
1	3	G10C0	10	0	23.04	28.774	14	6
9	4	G20C25	20	25	26.01	34.01	2	0
3	5	G10C50	10	50	20.14	27.12	7	5
2	6	G30C0	30	0	24.01	31.04	18	8
8	7	G20C50	20	50	24.29	32.01	8	5
5	8	G10C25	10	25	22.6	29.11	4	3
4	9	G30C50	30	50	21.57	27.6	29	14

3. Results and Discussion

3.1. Compressive Strength

The influence of 2-hour grinding, GCBA, and CBA on the compressive strength development of concrete has been presented in Fig. 5. It can be revealed that all the CBA-based concrete mixes yielded lower 28-day compressive strength than the control mix. This may be attributed to the inactive pozzolanic reactivity of GCBA particles that does not contribute in strength development in concrete at an early age. However, G20C25 reported a lower strength of 26.01 MPa in comparison with the control mix (29.34 MPa). Among CBA-based mixes, the 28-day compressive strength has been increased with an increase in GCBA content up to 20% and then decreased with a further increase in GCBA content to 30%. G20C0 yielded 12.25% and 7.7% higher compressive strength than G10C0 and G30C0. The compressive strength development tends to decrease with the increase in the GCBA (30%) due to the porous CBA particles that absorb the moisture and deters the hydration process. However, at 20% CBA, fine GCBA particles imparts pore filling effect that lead to increase in compressive strength after 28 days of curing [26,32].
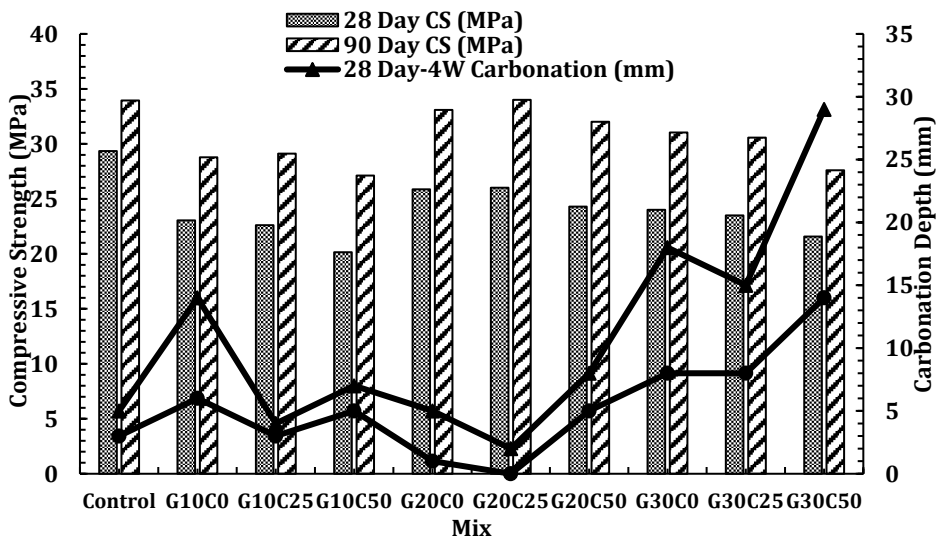

Fig. 5. Trends observed in 28-day compressive strength, 90-day compressive strength, 28 days- 4-week carbonation and 90 days-4-week carbonation

The increasing CBA percentage overall decrease the compressive strength development as shown in Fig. 5. For mixes prepared at 10 and 30% GCBA content, the compressive strength after 28-day curing decreased gradually with increase in CBA percentage as Mix G10C25 (22.6 MPa), G10C50 (20.14 MPa), G30C25 (23.5 MPa) and G30C50 (21.57) reported lower 28-day compressive strength than G10C0 (23.01 MPa) and G30C0 (24.0 MPa). However, Mix G20C25 reported higher but comparable 28-day compressive strength (26.01 MPa) as that of G20C0 (25.87 MPa). CBA as an NFA replacement imparts two distinctive effects; the refinement of pore size owing to fine CBA particles and the high porosity due to porous CBA particles. The pore size refinement effect dominates the effect of imparting high porosity up to 25% replacement resulting in higher compressive strength whereas, at a higher replacement level porous CBA particles result in the development of excess voids, thus, resulting in the drop in the 28-day compressive strength [17,58–63].

However, after 90 days of curing, the strength development in G20C25 was higher than the control mix. The compressive strength in G20C25 was 34.01 MPa in comparison with the

control mix that yielded a 90-day compressive strength of 33.91 MPa. The pozzolanic reactivity of GCBA particles along with the pore size refinement effect of CBA particles resulted in the formation of excess of calcium silicate hydrate (CSH) gel and dense microstructure in G20C25 that further resulted in enhancement in compressive strength. The overall behavior in CBA-based concrete was similar to 28-day strength wherein, the increase in GCBA and CBA replacement up to 20% and 25% respectively resulted in increase in compressive strength followed by gradual decrease in compressive strength with further increase in replacement.

3.2. Carbonation

Fig. 5 represents the trends observed in the carbonation depth of concrete mixes prepared with various replacement levels of GCBA and CBA. Fig. 6 illustrates the samples tested for carbonation after 28 day-4week and 90 day-4week exposure. It can also be revealed from Fig. 5 that after 28 days of curing and 4 week of exposure the carbonation depth in CBA-based concrete mixes was higher than the control mix. From Fig. 6, it can be interpreted that carbonated depth as shown by colorless region in the tested specimens was more in case of G10C0, G20C25 and G30C50 than the control mix. However, after 90 days of curing and 4 weeks of exposure, G20C25 yielded lower carbonation depth than the control mix. The lower carbonation depth in G20C25 can be revealed by comparing the carbonated depths as illustrated in Fig. 6. The pozzolanic reactivity of GCBA becomes active at the later stages and hence contribute in the production of CSH along with formation of dense microstructure that inhibits the moment of water and CO_2 in concrete.

Mix	28 Day – 4 Week Carbonation	90 Day – 4 Week Carbonation
Control		
G10C0		

Fig. 6. Carbonation depth as observed in various specimen of different concrete mix after 28 day-4-week carbonation and 90 day-4-week carbonation

Also, among the CBA-based concrete, the rate of carbonation decreased with increase in GCBA content at 20% and then further increased with increase in GCBA content after 28 and 90-day curing. Mix G20C0 yielded 2 mm carbonation and 1mm carbonation after 28 day-4week and 90 day-4week exposure respectively in comparison with G10C0 and G30C0 in which the carbonation depth was 5-1 mm and 8-5 mm after 28 day and 90-day 4 week of exposure. This may be due to pore densification by finer CBA particles and pozzolanic action of CBA that results in limiting the air permeability and hence, reduction in the carbonation depth. At lower percentage of GCBA (10%), the carbonation depth decreases with increase in CBA content as G10C25 (4-3mm) and G10C50 (7-5mm) reported lower carbonation depth than G10C0 (14-6mm) after 28 day-4 Week and 90 day-4-week exposure to accelerated carbonation. However, at higher replacement of GCBA (20%), the carbonation depth at 25% CBA is lower than 0% and 50% CBA content as G20C25 reported yielded 2 and 0 mm carbonation depth in comparison with G20C0 (5-1mm) and G20C50 (8-5mm) after 28 day-4 weeks and 90 day-4 week exposure. At 30% GCBA, the carbonation depth increases with increase in CBA content, though, the carbonation depth in G30C0 and G30C25 was almost comparable, whereas G30C50 yielded significant higher carbonation depth (29-14 mm) than G30C0 (18-8mm) and G30C25 (15-8mm) after 28 day-4 Week and 90 day-4 week exposure. The carbonation rate in CBA concrete increases due to porous CBA particles that increases the permeability of gases and accelerates the CO_2 diffusion into concrete. Poor interlocking between the particles of CBA and cement matrix may also lead to increase in carbonation depth.

3.3. Microstructural Analysis

3.3.1 X-Ray Diffraction (XRD) Analysis

The four concrete mixes i.e. D10C0, D20C25, D30C50 and control mix were analyzed for hydrated mineral phases using XRD analysis after 90 days of curing using Xpert high score. Several characteristics peaks of Portlandite (Ca(OH)2), Calcium silicate hydrate (CSH), and Ettringite (Aft) were identified at various d spacing and are plotted in Fig. 7. As the total count of Portlandite in G20C25 at d spacing 4.90 Å, 2.62 Å, 1.92 Å was 2589 lowest among control (2784), G10C0 (3463) and G30C50 (3538), therefore, it can be interpreted that Portlandite consumption was highest in the G20C25 and conversion of Portlandite to CSH was highest consequently resulting in higher compressive strength and lowest carbonation with respect to other mixes.
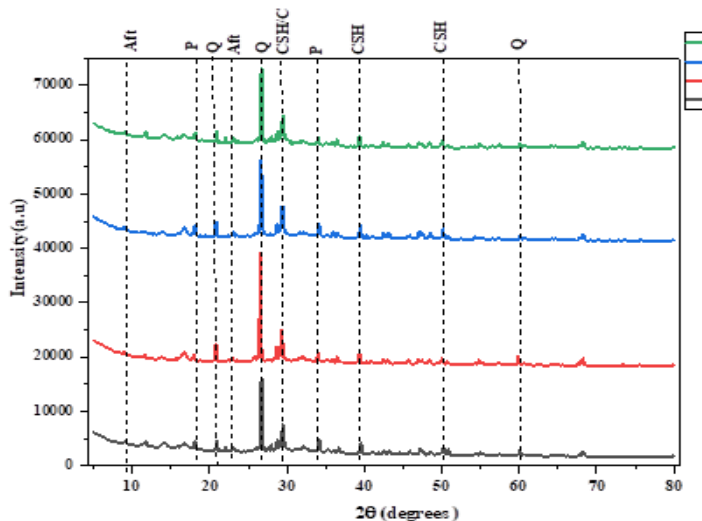

Fig. 7. XRD Spectrum for different concrete mix after 90 day of curing

Also, higher counts of CSH d spacing 3.04 Å, 2.72 Å, 1.82 Å in G20C25 than control mix, D10C0 and D30C25 further validated the trend observed in compressive strength and carbonation depth in CBA-based concretes. The presence of Ettringite (Aft) has also been detected in XRD spectrum and intensity was highest in G30C50 (875) followed by G10C0 (819), control mix (735) and G20C25 (702). The higher intensity of Aft in G30C50 also justified the lowest strength and maximum carbonation in the respective mix. The lean peaks of calcite were also detected that attributes to filler effect in cementitious matrix [64]. The existing literature also revealed the existence of these peaks in XRD spectrum analysis [9,65].

3.3.2 Scanning Electron Microscopy (SEM)

The microstructure of various concrete mixes was visualized and studied using SEM analysis. Fig. 8 represents the micrographs obtained for different concrete mixes after 90 days of curing. The presence of dense CSH can be revealed in micrographs of G20C25 as illustrated in Fig. 8 (c) which corroborated the attainment of highest compressive strength after 90 days and no carbonation after 4 weeks of exposure. The dense CSH gel offers higher resistance to compressive loads as well as ingression agents like water and CO_2, hence results in excellent performance of concrete. The presence of excess of Ettringite has been revealed from micrograph presented in Fig. 8 (d) that validates the presence of high

intensity Aft peak in XRD spectrum as well as the lowest compressive strength and maximum carbonation in G30C50. Fig. 8 (b) represents the micrographs for G10C0 and the presence of voids, cracks and Ettringite revealed lower compressive strength and higher carbonation depth in comparison with G20C25. These voids make concrete porous and provides easy passage to incoming water and CO_2 consequently leading to excessive carbonation. The micrographs of control mix are presented in Fig. 8 (a) shows the existence of dense CSH gel along with few traces of Ettringite as well as cracks along the ITZ that lead to lower but comparable strength in comparison with G20C25.

### 3.3.3 Fourier Transform Infrared Spectroscopy (FT-IR)

FT-IR analysis was performed to identify various functional groups present in different concrete mixes and presented in Fig. 9. The characteristics peak around wavenumber 3680 cm^{-1}, 2861 cm^{-1}, 1424 cm^{-1}, 1075 cm^{-1}, 955 cm^{-1}, and 887 cm^{-1} were produced in FTIR spectrum. The characteristic peak around 3680 cm^{-1} reveals the occurrence of Portlandite $(Ca(OH)_2)$ that originates from O-H stretching. The presence of CSH can be detected due to characteristic peak of Si-O originating from asymmetric bending around 955 cm^{-1}. The reaction between Portlandite and atmospheric carbon dioxide results in formation of intense peak around 1424 cm^{-1} and 887 cm^{-1} and confirmed the presence of carbonate (CO_3^{2-}). The sulphate group in ettringite has been observed around 1075 cm^{-1}.
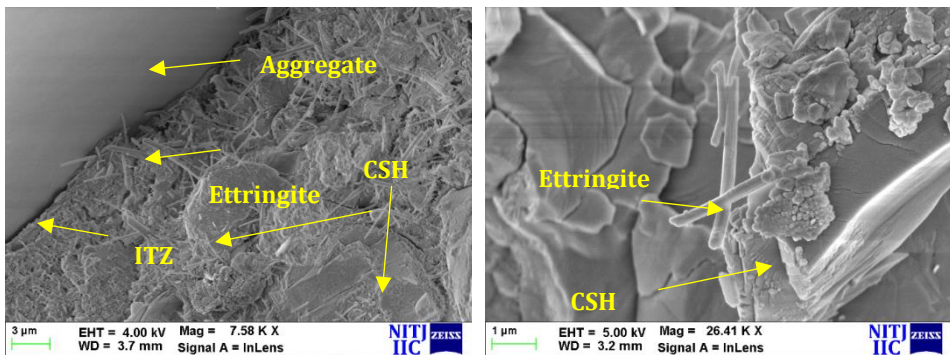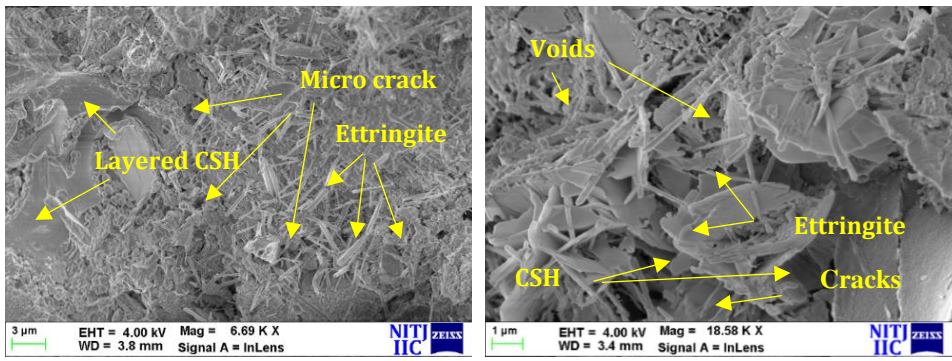

(a) Control mix
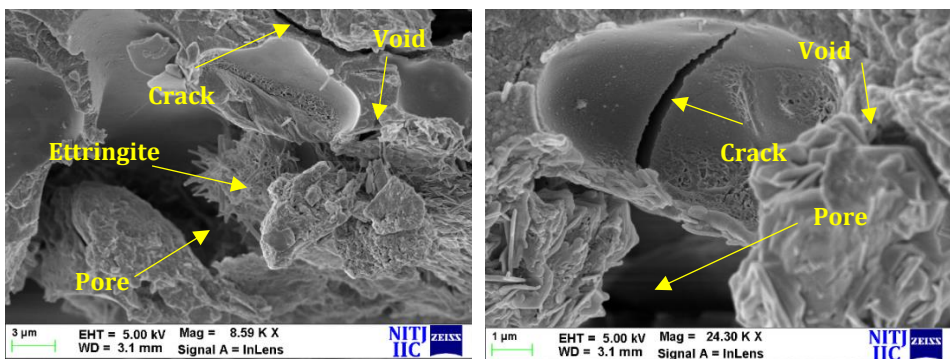
(b) G10C0
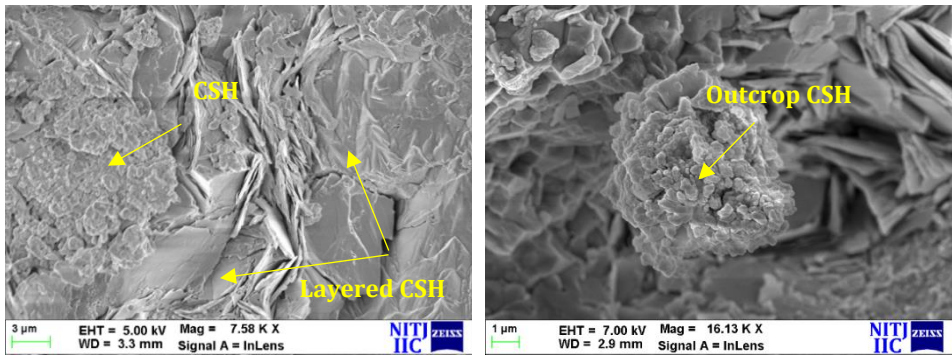
(c) G20C25

(d) G30C50

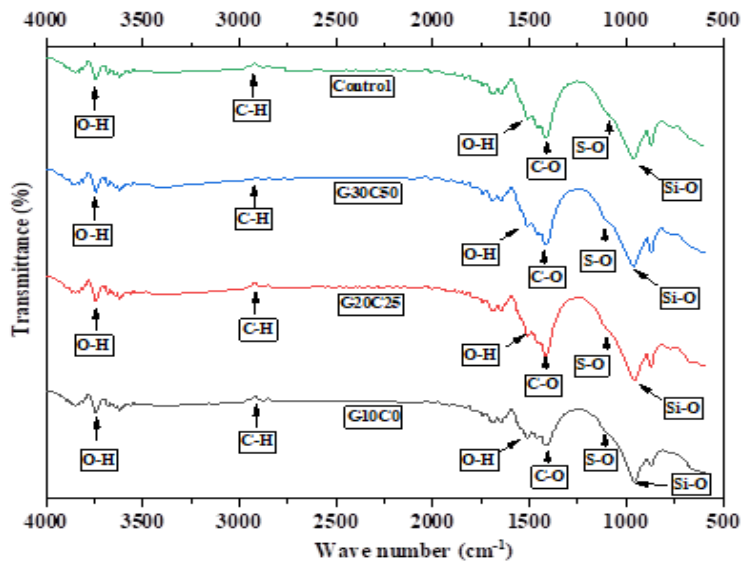Fig. 8. Micrographs for various concrete mix after 90 days of curing

Fig. 9. FTIR spectrum for various concrete mix after 90 days of curing

From Fig. 9, it can be interpreted that the G20C25 exhibit a sharp and intense peak of Si-O as compared to other concrete mixes that further validates the formation of excess of CSH in the mix. The presence of dense CSH in G20C25 was also revealed in XRD and SEM analysis. More consumption of Portlandite in G20C25 has also been confirmed due to broader peak of O-H in comparison with control, D10C0 and D30C50. A steep bend in S-O as observed in G30C50 revealed the existence of higher amount of Ettringite than other mixes that resulted in significant reduction in compressive strength and increase in carbonation depth in the mix. The characteristics bands in the range 400-4000 cm^{-1} are in good agreement with the previous papers [11,66–70].

3.4. Statistical Analysis

Statistical analysis was done using regression analysis to analyze the compressive strength after 28 and 90 days of curing along with the carbonation depth after 4 weeks of exposure to accelerated carbonation in 28 and 90-day water cured specimen. Quadratic models were the best-found models for all the responses where p value lies below 0.05. Quadratic models were well fitted and no transformation was required. ANOVA was further used to check the significance of the models. Table 4 represents the results of ANOVA as obtained for 28-day compressive strength, 90-day compressive strength, 28 day–4-week carbonation depth and 90 day-4-week carbonation depth. Equations 1-4 represents the regression equations as obtained for the various responses investigated.

$$28 \text{ Day Compressive Strength} = +25.98 + 0.5480 \text{ A} - 1.15 \text{ B} + 0.1145 \text{ AB} - 2.91 \text{ A}^2 - 0.8813 \text{ B}^2 \tag{1}$$

$$90 \text{ Day Compressive Strength} = +33.90 + 0.7010 \text{ A} - 1.03 \text{ B} - 0.4465 \text{ AB} - 4.00 \text{ A}^2 - 1.29 \text{ B}^2 \tag{2}$$

$$28 \text{ Day-4 Week Carbonation Depth} = + 0.6667 + 6.17 \text{ A} + 1.17 \text{ B} + 4.50 \text{ AB} + 9.50 \text{ A}^2 + 6.50 \text{ B}^2 \tag{3}$$

$$90 \text{ Day-4 Week Carbonation Depth} = + 0.1111 + 2.67 \text{ A} + 1.50 \text{ B} + 1.75 \text{ AB} + 5.33 \text{ A}^2 + 2.83 \text{ B}^2 \tag{4}$$

The statistical significance of the model is determined using the F values which are generally the ratio of mean squares and reflect the ratio of explained variance to the unexplained variance. The F values for the 28-day compressive strength, 90-day compressive strength, 28 day–4-week carbonation depth and 90 day-4-week carbonation depth were 39.86, 36.43, 61.66, and 98.50 respectively, representing there are only 0.6%, 0.69%, 0.32% and 0.16% chance that larger F values than these in models can occur due to unexplained variations. The models are fitted satisfactorily as the R^2(adj) values of 0.96, 0.956, 0.974, and 0.983 for 28-day compressive strength, 90-day compressive strength, 28 day–4-week carbonation depth and 90 day-4-week carbonation depth respectively revealed that only 4%, 4.4%, 2.6%, 1.7% of the total variation that cannot be explained by the models. From the results of adequacy precisions, it can be concluded that design space can be navigated using the fitted models as the value were greater than 4 for all the responses. It can be revealed from Table 4 that A, B, A^2, and B^2 are significant model terms for 28 days compressive strength as well as the 90 days compressive strength as p-values for these model terms were less than 0.05.

Table 4 also revealed that A, AB, A^2, B^2 are significant model terms (p value < 0.05) for 28 day – 4 week carbonation depth whereas for 90 day-4 week carbonation the significant model terms were A, B, AB, A^2, B^2. Actual vs. Predicted plots were also found to determine the goodness of fit of the models and variations in the predicted values from the regressed diagonal line obtained from the actual values. It can be concluded from Fig. 10 (a and c)

and Fig. 11 (a and c) that residual points fall on regressed diagonal line throughout the range of actuals and hence, the adequacy of models can be established. Response surface plots were used to study the influence of GCBA and CBA along with their interactions on various responses studied. It can be revealed from slopes of response surface in Fig. 10 (b and d) that the compressive strength increases with the increase in GCBA and CBA content and then gradually decrease with further addition in replacement level. On contrary, slopes of response surface in Fig. 11 (b and d) validated that the carbonation depth decreases with the increase in GCBA and CBA content followed by gradual rise in carbonation depth with further addition of GCBA and CBA. The results in the current study are in good agreement with the existing studies that revealed similar pattern in compressive strength and carbonation depth in CBA-based concrete [19,21,26,30,32,33,71–75].

3.4.1 Optimization

A multi-objective optimization technique has been adopted in which response surface methodology serves as the base to find the optimal solution. Optimum setting of factors and responses were discovered using face central composite design method. The importance and weight along with the objective of optimization of factors as well as responses were defined so as to perform the objective based optimization. The optimization was carried out in Design expert software, that uses 'Desirability function' approach for executing optimization. In this method, desirability function for each response is constructed for carrying out the optimization. As presented in Table 5,'Importance' is also assigned to individual factors and responses that can vary from 1 to 5. Value '5' is assigned for critical goals or goals having very high importance; value '3' is assigned for goals with medium or equal importance whereas value '1' is assigned for the goal with lowest importance. Since, the goals of maximising the replacement level of GCBA and CBA, maximising the compressive strength and minimising the carbonation depth as defined in multi-objective optimisation were considered to be equally important, hence a 'value of 3' was assigned by the authors. The 'value of 3' is also preferable as assigning any one goal the importance 'value of 5 or 1' makes the optimisation biased towards the assigned value of the goal. So, for practical point of view, the 'value of 3' delivers optimised results that further gives almost equal desirability to all the selected goals.

Each response is transformed into a dimensionless value called Individual desirability scale (di). The scale varies from 0 to 1, where 0 represents completely undesired response and 1 represents completely desired response. These individual transformations are combined using geometric mean that assists in examining the outcomes of various responses to form overall desirability (D). The method was first introduced by George Derringer & Ronald Suich in 1980 [76]. Though there are many other advanced methods that have been developed for multi objective optimization [77,78], the desirability function method has been widely used in existing studies [79–82] and hence the same methodology has been adopted in the present study.

Multiobjective optimization with desirability as mentioned in Table 5 has been performed in order to find the optimal combination of GCBA and CBA that would yield maximum compressive strength and minimum carbonation depth. The optimal solution as suggested by optimization revealed 21.51% GCBA and 29.82% CBA content as the best combination that will yield maximum strength with minimum carbonation. The desirability of factors and responses along with the total desirability of the optimization solution has been provided in Fig. 12. It can be revealed from Fig. 12 that the factors GCBA and CBA have the individual desirability of 0.57 and 0.58 whereas individual desirability for responses varied from 0.92 to 0.98.

Table 4. Results of ANOVA for 28-day compressive strength, 90-day compressive strength, 28 days-4-week carbonation and 90 days-4-week carbonation

	28 Day Compressive Strength						90 Day Compressive Strength					
Source	Sum of Squares	df	Mean Square	F-value	p-value		Sum of Squares	df	Mean Square	F-value	p-value	
Model	28.34	5	5.67	39.86	0.0060	significant	45.45	5	9.09	36.43	0.0069	significant
A-GCBA	1.80	1	1.80	12.67	0.0378		2.95	1	2.95	11.82	0.0413	
B-CBA	7.98	1	7.98	56.11	0.0049		6.35	1	6.35	25.46	0.0150	
AB	0.0524	1	0.0524	0.3689	0.5865		0.7974	1	0.7974	3.20	0.1718	
A^2	16.95	1	16.95	119.24	0.0016		32.02	1	32.02	128.33	0.0015	
B^2	1.55	1	1.55	10.93	0.0455		3.33	1	3.33	13.36	0.0354	
Residual	0.4265	3	0.1422				0.7484	3	0.2495			
Cor Total	28.76	8					46.20	8				

Adjusted R^2 = 0.960; Predicted R^2 = 0.819; Adequacy Precision = 19.09   Adjusted R^2 =0.956; Predicted R^2 = 0.805; Adequacy Precision = 16.12

	28 Day-4 Week Carbonation						90 Day-4 Week Carbonation					
Source	Sum of Squares	df	Mean Square	F-value	p-value		Sum of Squares	df	Mean Square	F-value	p-value	
Model	582.33	5	116.47	61.66	0.0032	significant	141.36	5	28.27	98.50	0.0016	significant
A-GCBA	228.17	1	228.17	120.79	0.0016		42.67	1	42.67	148.65	0.0012	
B-CBA	8.17	1	8.17	4.32	0.1291		13.50	1	13.50	47.03	0.0063	
AB	81.00	1	81.00	42.88	0.0072		12.25	1	12.25	42.68	0.0073	
A^2	180.50	1	180.50	95.56	0.0023		56.89	1	56.89	198.19	0.0008	
B^2	84.50	1	84.50	44.74	0.0068		16.06	1	16.06	55.94	0.0050	
Residual	5.67	3	1.89				0.8611	3	0.2870			
Cor Total	588.00	8					142.22	8				

Adjusted R^2 = 0.974; Predicted R^2 = 0.914; Adequacy Precision = 24.8   Adjusted R^2 = 0.983; Predicted R^2 = 0.927; Adequacy Precision = 32.19

Cor Total: Corrected Total Sum of Squares, df : degree of freedom

(a) Actual vs predicted for 28-day compressive strength

(b) Response surface for 28-day compressive strength

(c) Actual vs predicted for 90-day compressive strength

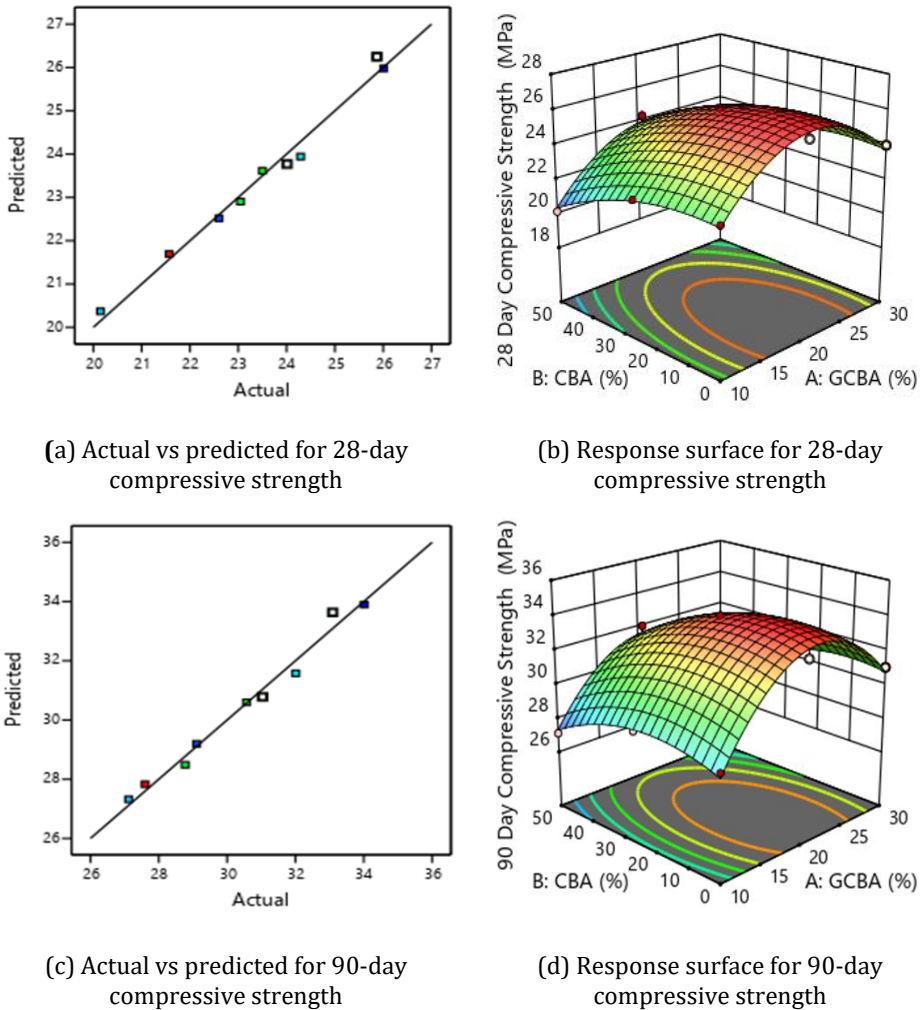(d) Response surface for 90-day compressive strength

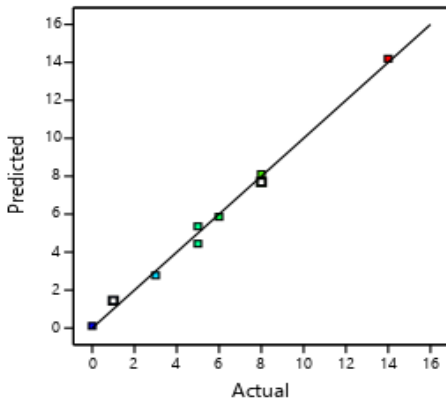Fig. 10. Actual vs predicted and response surface graph for compressive strength after 28 days and 90 days curing

The contour plots for the responses were also obtained and are presented in Fig. 13. The suggested optimum combination of the GCBA and CBA was cast to validate the predicted values. The optimum combination yielded a 28-day compressive strength of 26.03 MPa in comparison with the predicted value of 25.773 MPa. The experimental result of the optimized combination correlated well with the predicted result and can be adopted as optimum mix combination while using CBA as a potential replacement of PC and NFA in concrete.
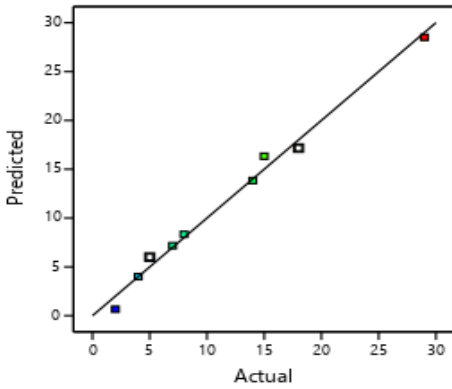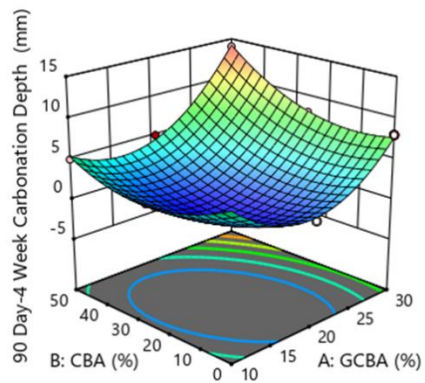
(a) Actual vs predicted for 28 day- 4 week carbonation
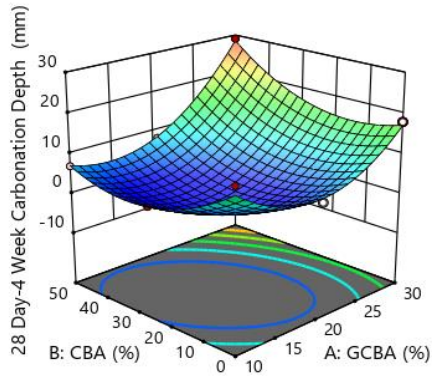
(b) Response surface for 28 day- 4 week carbonation

(c) Actual vs predicted for 90 day- 4-week carbonation

(d) Response surface for 90 day- 4-week carbonation

Fig. 11. Actual vs predicted and response surface graph for carbonation depths after 4 weeks of exposure to accelerated carbonation after 28 days and 90 days curing

Table 5. Desirability criteria adopted for optimization, and importance assigned to each investigated factor and response

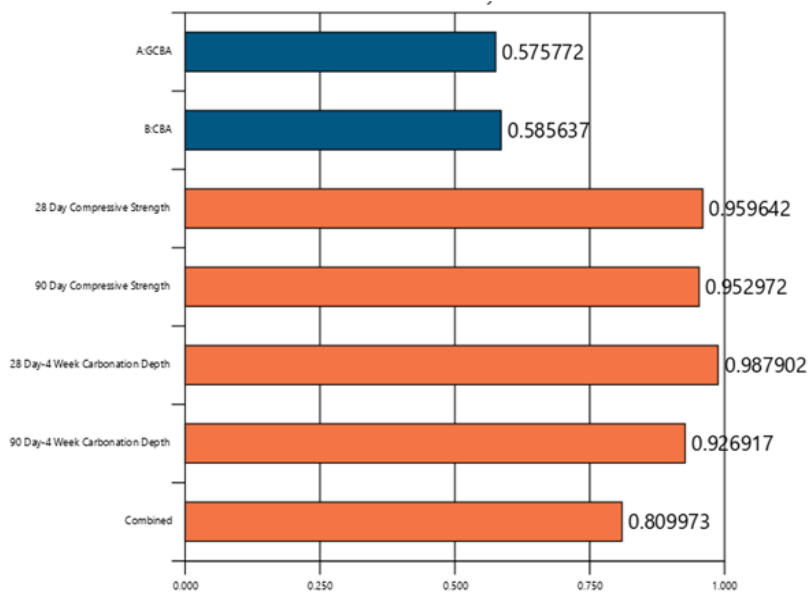| Name	Goal	Lower Limit	Upper Limit	Lower Weight	Upper Weight	Importance
A:GCBA	maximize	10	30	1	1	3
B:CBA	maximize	0	50	1	1	3
28 Day Compressive Strength	maximize	20.147	26.01	1	1	3
90 Day Compressive Strength	maximize	27.12	34.01	1	1	3
28 Day-4 Week Carbonation Depth	minimize	2	29	1	1	3
90 Day-4 Week Carbonation Depth	minimize	0	14	1	1	3

Fig. 12. Desirability of individual factors and responses along with overall combine desirability as obtained using desirability function approach

3.5. Life Cycle Assessment

The environmental impacts in terms of carbon footprints and eco-costs were calculated in order to compare the impacts associated with optimized concrete mix with conventional concrete mix. The optimization suggested 21.51% GCBA and 29.82% CBA content as the optimum content which is really encouraging in transforming traditional engineering design criteria considering function, cost and safety to more sustainable engineering design criteria that also considers impact on people and planet. Fast track life cycle assessment has been used to determine and compare the environment impacts of optimized CBA concrete with conventional concrete mix. The methodology adopted for performing Fast track LCA was in accordance with ISO 140040, 140044, and the LCA handbook of the ILCD [52,83–85].

3.5.1 Goal and Scope

The goal of conducting Fast track LCA was to determine the environmental impacts associated with optimized CBA-based concrete and compare it with conventional concrete mix so as to validate the benefits of utilizing the CBA in concrete over conventional concrete. An attempt has been made to enhance the environmental impacts of traditional concrete with the upcycling of CBA as a resource in concrete and reduce the burden on the natural resources from where majority of ingredients of concrete are acquired. 1 m^3 of concrete was considered as the functional unit for performing the LCA. Fig. 14 represents the system boundaries adopted for performing 'Gate to Gate' LCA of optimized CBA concrete and control mix. The data sets compiled by Delft University of Technology were used to perform the LCA. Idemat 2023 database was referred for determining the eco impacts of various materials and processes involved in production of concrete [52].

(a) Desirability

(b) 28 Day compressive strength

(c) 90 Day compressive strength

(d) 28 Day 4 Week Carbonation

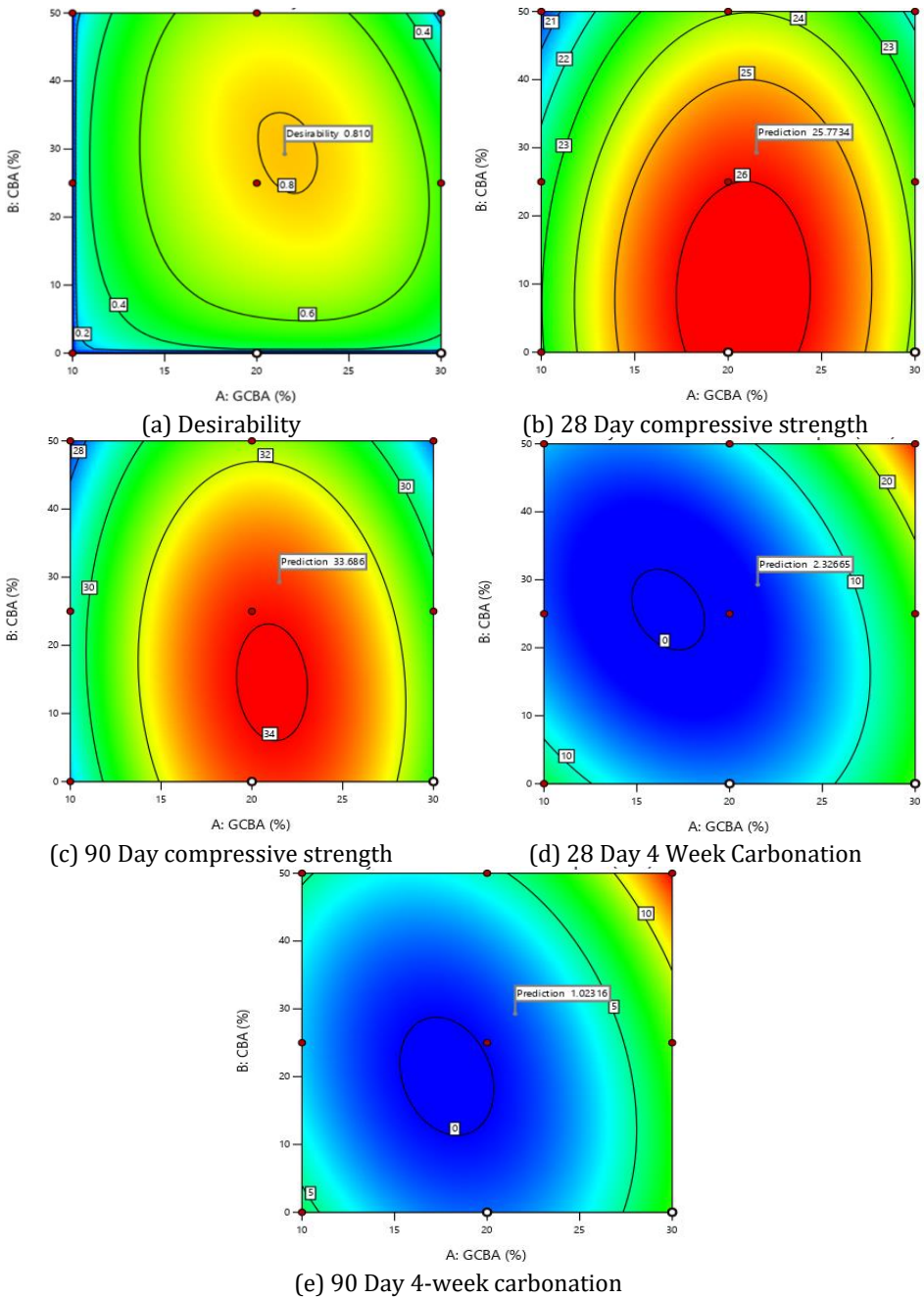(e) 90 Day 4-week carbonation

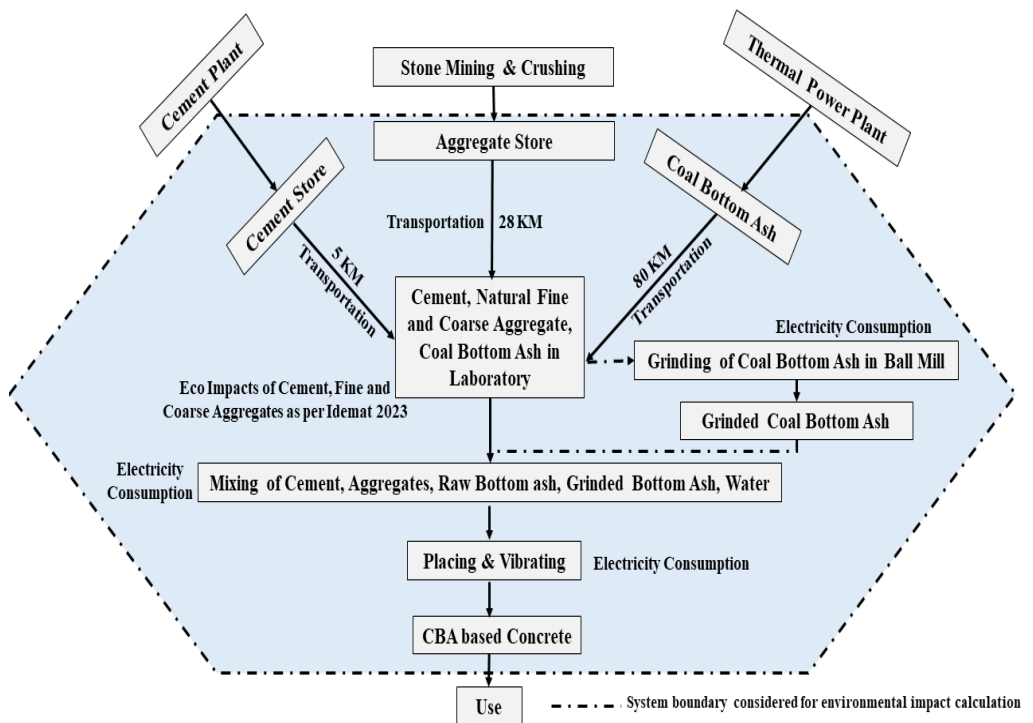Fig. 13. Contour plots for optimized solutions

Fig. 14. System boundary considered in Gate-to-Gate life cycle assessment

3.5.2 Life Cycle Inventory Analysis

Inventory analysis was done under three broad categories as mentioned in the methodology of Fast track LCA i.e. Materials, Transportation, and Energy use. Since, the LCA in the present study considered only 'Gate to Gate' scenario, hence 'End of life' category was excluded from the inventory analysis. Table 6 compiled the various materials, transportation and energy use processes considered along with the life cycle inventory source. The 21.51% GCBA as PC replacement curtailed the cement content to 310 Kg per m^3 from 395 Kg per m^3. The cement in both the scenario were purchased from same vendor and were transported over a distance of 5 KM. Similarly, the content of NFA was curtailed from 732 Kg/m^3 to 517 Kg/m^3 with 29.82% replacement of fine aggregate with CBA. The coarse aggregate content was 1068 in both the scenarios. The aggregates (NCA and NFA) were procured from same crusher and that required transportation over 28 KM. A total of 1800 Kg and 1585 Kg aggregates were transported over the specified distance. CBA was acquired from Ropar Thermal power plant and a total of 310 kg of CBA was transported over a distance of 80 KM. The impacts associated with transportation of CBA were only considered in optimized CBA concrete. GCBA was grinded for 2 hours in a ball mill in case of CBA-based optimized concrete mix, hence electricity consumption for grinding CBA was also included. The calculations and units' conversions adopted for determining the inventory analysis has been presented in Table 6.

3.5.3 Life Cycle Assessment

The excel sheet available on 'Sustainability Impact Metrics' website was used to perform the life cycle assessment and calculate carbon footprints as well as eco-costs associated with each step in manufacturing of conventional and optimized CBA concrete. Fig. 15 illustrates the total carbon footprints and eco-costs obtained from fast track LCA. A total

reduction of 21.519 % have been achieved in cement consumption in optimized CBA concrete as it yielded carbon footprint of 282.1 kg CO_2 equiv. in comparison with control mix that yielded carbon footprint of 359.45 kg CO_2 equiv. Also, carbon footprint associated with NFA in control mix is 1.464 kg CO_2 equiv. which was 29.317% higher than optimized CBA concrete (1.034 kg CO_2 equiv.). A total reduction of 21.645% has been reported in material stage of optimized CBA concrete mix as compared to normal control mix (Fig. 15). The reduction in cement content also reduced the carbon footprints associated with the transportation of cement wherein, cement transportation in optimized CBA concrete resulted in 21.229% lower carbon footprints (Fig. 15). The optimized concrete mix requires CBA which includes additional carbon footprints of 2.178 kg CO_2 equiv. with respect to control mix. Also, it can be revealed from Fig. 15 that lower aggregate content in optimized CBA concrete reduced the carbon footprints associated with transportation of aggregates. Total carbon footprints associated with transportation of aggregates reduced from 11.259 in case of control mix to 9.985 kg CO_2 equiv. in case of optimized CBA concrete. The carbon footprints associated with transportation stage increased by 7.57% in case of optimized concrete mix when compared with the control mix (Fig. 15). Similarly, optimized CBA concrete requires grinding of CBA that results in additional carbon footprints in comparison with the control mix. Control mix resulted in 0.283 kg CO_2 equiv. in energy use stage which was lower than the carbon footprints associated with optimized CBA concrete (1.0393 kg CO_2 equiv.). Overall, the carbon footprints associated with optimized CBA concrete was 303.06 kg CO_2 equiv. which were 20.08% lower than control mix (379.22 kg CO_2 equiv.).

Similarly, the eco-costs associated with cement consumption in optimized concrete mix was €49.6 which was 21.51% lower than the eco-costs of cement consumption in control mix (€63.2). Also, the lower consumption of fine aggregates resulted in 29.37% reduction in eco-costs associated with optimized CBA concrete (Fig. 15). A total reduction of 21.01% in eco-costs has been observed in material stage of optimized CBA concrete in comparison with control mix. In transportation stage, the transportation of CBA is an additional process that resulted in €0.717 more eco-costs in optimized concrete mix. Lower cement and fine aggregate content in optimized CBA concrete resulted in 22.03% and 11.32% lower eco-costs in comparison with the control mix. Grinding of CBA also resulted in additional eco-costs of €0.717 in optimized CBA concrete in comparison with control mix. Overall, the eco-costs associated with optimized CBA concrete was €55.415 which was 19.40% lower than control mix (€68.759).

Table 6. Life cycle inventory analysis for comparing the impacts associated with control mix and optimized CBA concrete

S No	Stage	Description	Impact Factor Considered	Unit	Eco-Impacts		LCI Source	Amount	
					Carbon Footprint (kg CO_2 equiv./unit)	Eco-costs (€/unit)		Control Mix	Optimized CBA Concrete
1.	Materials	Cement	Idemat2023 Cement (Portland CEM I 52.5 N)	Kg	0.91	0.16	European reference Life Cycle Database (ELCD)	395.00	310
		Fine Aggregate	Idemat2023 Sand	Kg	0.002	0.001	Delft University of Technology based thesis (JG Vogtlander 2001)	732.00	517
		Coarse Aggregate	Idemat2023 Gravel	Kg	0.006	0.0016	Delft University of Technology based on Dutch Industry	1068.0	1068.00
		Water	Idemat2023 Drinking water Europe	Kg	0.001	0.0001	European reference Life Cycle Database (ELCD)	180.00	180.00
2.	Transport	Aggregates (From Quarry to Lab)	Idemat2023 Tractor (240 pk)	tkm	0.225	0.06	ELCD	1800 Kg transported for 28 Km = 50.04	1585 Kg transported for 28 Km = 44.380
		Cement (From Distributor to Lab)	Idemat2023 Truck+trailer 24 tons net (min weight/volume ratio 0.32 ton/m³) (tkm)	tkm	0.091	0.03		395 Kg transported for 5 Km = 1.97	310 Kg transported for 5 Km = 1.550
		Coal bottom ash (From Thermal Power Plant to Lab)		tkm	0.091	0.03	Idemat Database	-	299.28 Kg transported for 80 Km = 23.942
3.	Use	Electricity (Concrete Mixing, Vibrating and other Operations)	Idemat2023 Electricity General Industry	MJ	0.141	0.02	Idemat Database	3 HP motor run for 15 min = 2.01	3 HP motor run for 15 min = 2.01
		Electricity (Grinding of CBA)		MJ	0.141	0.02		-	1 HP motor run for 2 hours = 5.364

Adopted Unit Conversions: 1HP = 0.745 Kwh; 1Kwh = 3.6 MJ; 1 Kg for 1 Km = 0.001 tkm

3.5.4 Interpretation

The prime objective of the research was to obtain at comparable or at least at par performance of CBA-based concrete with respect to control mix in terms of compressive strength and carbonation resistance. Herein, it is important to mention that more concern was in maximizing utilization of coal ashes/bi-products (in form of GCBA and CBA) so as to reduce environmental impacts and the consumption of natural resources without significant reduction/compensation in strength and durability of the designed concrete mixes. It is further important to mention that GCBA/CBA mixes (5 out of 9 in total i.e., mixes G20C0, G20C25, G20C25, G30C0, and G30C25) made in this study resulted in compressive strength more than 30 MPa (as original mix was designed for a target strength of at least 25 N/mm^2). Such grades of concrete can be successfully used for both structural and non-structural construction works.

Since considerable reductions in carbon footprints (20.08%) and eco-costs (19.40%) were observed as per the fast-track LCA, it can be inferred that the use of CBA as a potential cement and NFA substitute is an environmentally friendly sustainable alternative. Lack of significant impact on compressive strength has been rewarded with added advantage of significant reduction in the environmental impacts of CBA based concrete on comparing with the control mix. In comparison to the control mix, the CBA-based ideal concrete mix produced comparable mechanical and durability performance in terms of strength and carbonation resistance, and had less negative environmental effects. However, utilizing more effective milling parameters, such as increasing ball mill revolutions, ball mill feed, and shortening the optimal time for grinding CBA, can reduce the increased carbon footprints and eco-costs related to grinding CBA.

4. Conclusions and Future Work

The present investigation studied and optimized the compressive strength and carbonation resistance in CBA-based concrete wherein the effect of 2-hour grinding of CBA, GCBA as PC and CBA as NFA replacement was considered. The GCBA as PC replacement lead to increase in compressive strength and carbonation resistance at 20% replacement followed by a reduction in strength at 30% replacement. The pozzolanic reactivity of GCBA becomes active at later stages that leads to development of excess CSH and dense microstructure, consequently leading to enhancement in strength at later stages. The CBA as NFA replacement resulted in an enhancement in compressive strength and carbonation resistance till 25% replacement owing to the ascendency of the pore size refinement effect. At higher replacement (beyond 25%), the porous CBA particles resulted in excess water absorption as well as porous microstructure leading to the formation of excess voids in concrete, consequently resulting in a reduction in the strength as well as carbonation resistance. XRD spectrum revealed higher count intensity of Portlandite and calcium silicate hydrate gel in G20C25. SEM analysis revealed dense cement matrix and interfacial transition zone (ITZ) formation in G20C25. FT-IR spectroscopy also governed the higher strength development and carbonation resistance at 20% GCBA and 25% CBA content, as broader peak of O-H bending and sharp-intense peak of Si-O was observed in G20C25 when compared to control and CBA-based concrete. The mathematical models obtained for compressive strength and carbonation depth strength are well fitted and are in good agreement with experimental as well as predicted values. 21.51% GCBA and 29.82% CBA are the optimum values of the factors that have combined desirability of 0.80 in achieving the desired compressive strength and carbonation resistance.

A reduction of 20.08% and 19.40% in carbon footprints and total eco-costs with the inclusion of 21.51 % GCBA and 29.82% CBA as PC and NFA replacement in concrete has been revealed in fast-track life cycle assessment.
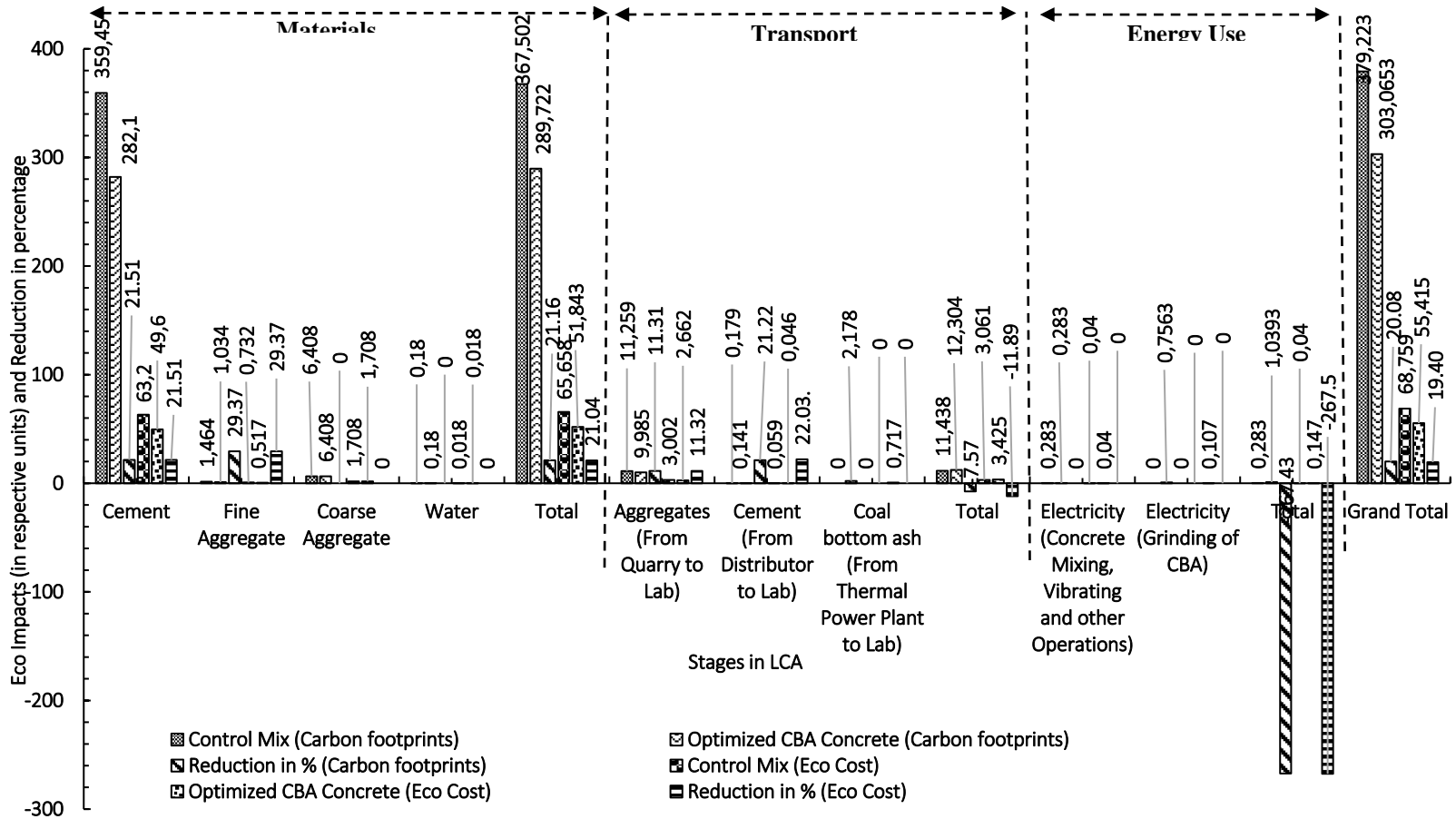
Fig. 15. Results of fast track life cycle assessment at various stages in production of CBA-based concrete and control mix

Based on the optimized values of the factors studied, a design mix for concrete prepared with GCBA and CBA can be proposed that will not only satisfy the structural requirements of a concrete but will also minimize the detrimental effects of conventional concrete on people and the environment. However, the grinding period of GCBA can be optimized further using more efficient milling factors like increase in revolutions of ball mill, increase in ball mill feed, etc. Also, reducing the water absorption of CBA is still a major concern and various chemical and physical treatment must be investigated to overcome the excessive water absorption. With these improvements, higher replacement of PC and NFA can be targeted without compromising the mechanical, durability and environmental aspects of CBA-based concrete.

Acknowledgement

References

[1] Ankur N, Singh N. A review on the life cycle assessment phases of cement and concrete manufacturing. In: Role of Circular Economy in Resource Sustainability. Springer, Cham; 2022. p. 85–96.

[2] Boubekeur T, Boulekbache B, Aoudjane K, Ezziane K, Kadri EH. Prediction of the durability performance of ternary cement containing limestone powder and ground granulated blast furnace slag. Constr Build Mater . 2019;209:215–21. https://doi.org/10.1016/j.conbuildmat.2019.03.120

[3] Singh N, Singh A, Ankur N, Kumar P, Kumar M, Singh T. Reviewing the properties of recycled concrete aggregates and iron slag in concrete. J Build Eng . 2022;60(May):105150. https://linkinghub.elsevier.com/retrieve/pii/S2352710222011573

[4] Baite E, Messan A, Hannawi K, Tsobnang F, Prince W. Physical and transfer properties of mortar containing coal bottom ash aggregates from Tefereyre (Niger). Constr Build Mater . 2016;125:919–26. http://dx.doi.org/10.1016/j.conbuildmat.2016.08.117

[5] Lau CK, Rowles MR, Parnham GN, Htut T, Ng TS. Investigation of geopolymers containing fly ash and ground-granulated blast-furnace slag blended by amorphous ratios. Constr Build Mater. 2019;222:731–7.

[6] Corinaldesi V, Mazzoli A, Siddique R. Characterization of lightweight mortars containing wood processing by-products waste. Constr Build Mater . 2016;123:281–9. http://dx.doi.org/10.1016/j.conbuildmat.2016.07.011

[7] Muthusamy K, Hafizuddin RM, Yahaya FM, Sulaiman MA, Syed Mohsin SM, Tukimat NN, et al. Compressive strength performance of OPS lightweight aggregate concrete containing coal bottom ash as partial fine aggregate replacement. In: IOP Conference Series: Materials Science and Engineering. 2018. p. 012099.

[8] Dash MK, Patro SK, Rath AK. Sustainable use of industrial-waste as partial replacement of fine aggregate for preparation of concrete – A review. Int J Sustain Built Environ . 2016;5(2):484–516. http://dx.doi.org/10.1016/j.ijsbe.2016.04.006

[9] Singh N, Nassar RUD, Kaur S, Bhardwaj A. Microstructural characteristics and carbonation resistance of coal bottom ash based concrete mixtures. Mag Concr Res. 2020;

[10] Singh R, Patel M. Strength and durability performance of rice straw ash-based concrete: an approach for the valorization of agriculture waste. Int J Environ Sci Technol. 2022

[11] Meena A, Singh N, Singh SP. High-volume fly ash Self Consolidating Concrete with coal bottom ash and recycled concrete aggregates: Fresh, mechanical and microstructural properties. J Build Eng. 2023;63(PA):105447. https://doi.org/10.1016/j.jobe.2022.105447

[12] Rodríguez-Álvaro R, González-Fonteboa B, Seara-Paz S, Rey-Bouzón EJ. Masonry mortars, precast concrete and masonry units using coal bottom ash as a partial replacement for conventional aggregates. Constr Build Mater. 2021;283.

[13] Muthusamy K, Rasid MH, Jokhio GA, Budiea AMA, Hussin MW, Mirza J. Coal bottom ash as sand replacement in concrete: A review. Constr Build Mater . 2020;236:1–12. https://doi.org/10.1016/j.conbuildmat.2019.117507

[14] Yao ZT, Ji XS, Sarker JK, Tanga JH, Ge LQ, Xia MS, et al. A comprehensive review on the applications of coal fly ash. Earth Sci Rev. 2015;141:105–21.

[15] Abdullah MH, Rashid ASA, Anuar UHM, Marto A, Abuelgasim R. Bottom ash utilization: A review on engineering applications and environmental aspects. IOP Conf Ser Mater Sci Eng. 2019;527(1).

[16] Basheer PAM, Bai Y. Strength and durability of concrete with ash aggregate. In: Proceedings of the Institution of Civil Engineers Structures & Buildings. 2005. p. 191–9.

[17] Aggarwal P, Aggarwal Y, Gupta SM. Effect of bottom ash as replacement of fine aggregates in concrete. Asian J Civ Eng (Building Housing). 2007;8(1):49–62.

[18] Andrade LB, Rocha JC, Cheriaf M. Influence of coal bottom ash as fine aggregate on fresh properties of concrete. Constr Build Mater . 2009;23(2):609–14. http://dx.doi.org/10.1016/j.conbuildmat.2008.05.003

[19] Siddique R, Aggarwal P, Aggarwal Y. Mechanical and durability properties of self-compacting concrete containing fly ash and bottom ash. J Sustain Cem Mater. 2012;1(3):67–82.

[20] Abubakar AU, Baharudin KS. Potential Use Of Malaysian Thermal Power Plants Coal Bottom Ash In Construction. Int J Sustain Constr Eng Technol. 2012;3(2):25–37.

[21] Al-fasih MYM, Ibrahim MHW, Basirun NF, Jaya RP, Sani MSHBM. Influence of partial replacement of cement and sand with coal bottom ash on concrete properties. Int J Recent Technol Eng. 2019;8(3S3):356–62.

[22] Zhou H, Bhattarai R, Li Y, Si B, Dong X, Wang T, et al. Towards sustainable coal industry: Turning coal bottom ash into wealth. Sci Total Environ. 2022;804:149985.

[23] Jaturapitakkul C, Cheerarot R. Development of bottom ash as pozzolanic material. J Mater Civ Eng. 2003;15(1):48–53.

[24] Kim HK. Utilization of sieved and ground coal bottom ash powders as a coarse binder in high-strength mortar to improve workability. Vol. 91, Construction and Building Materials. 2015. p. 57–64.

[25] Mangi SA, Ibrahim MHW, Jamaluddin N, Arshad MFa, Jaya RP. Short-term effects of sulphate and chloride on the concrete containing coal bottom ash as supplementary cementitious material. Eng Sci Technol an Int J . 2019;22(2):515–22. https://doi.org/10.1016/j.jestch.2018.09.001

[26] Mangi SA, Wan Ibrahim MH, Jamaluddin N, Arshad MF, Memon SA, Shahidan S. Effects of grinding process on the properties of the coal bottom ash and cement paste. J Eng Technol Sci. 2019;51(1):1–13.

[27] Mangi SA, Wan Ibrahim MH, Jamaluddin N, Arshad MF, Memon FA, Putra Jaya R, et al. A Review on Potential Use of Coal Bottom Ash as a Supplementary Cementing Material in Sustainable Concrete Construction. Int J Integr Eng. 2018;10(9):28–36.

[28] Mangi SA, Ibrahim MHW, Jamaluddin N, Arshad MF, Memon SA, Shahidan S, et al. Coal bottom ash as a sustainable supplementary cementitious material for the concrete exposed to seawater. AIP Conf Proc. 2019;2119(July):1–8.

[29] Argiz C, Moragues A, Menéndez E. Use of ground coal bottom ash as cement constituent in concretes exposed to chloride environments. J Clean Prod. 2018;170(January):25–33.

[30] Brás A, Faustino P. Repair mortars and new concretes with coal bottom and biomass ashes using rheological optimisation. Int J Environ Res. 2016;10(2):203–16.

[31] Khan RA, Ganesh A. The effect of coal bottom ash (CBA) on mechanical and durability characteristics of concrete. J Build Mater Struct. 2016;3(1):31–42. http://journals.oasis-pubs.com

[32] Bajare D, Bumanis G, Upeniece L. Coal combustion bottom ash as microfiller with pozzolanic properties for traditional concrete. Procedia Eng . 2013;57:149–58. http://dx.doi.org/10.1016/j.proeng.2013.04.022

[33] Martins IM, Gonçalves A. Durability and strength properties of concrete containing coal bottom ash. In: International RILEM Conference on Material Science . 2010. p. 6–10. http://eprints.whiterose.ac.uk/76421/

[34] Ankur N, Singh N. Performance of cement mortars and concretes containing coal bottom ash: A comprehensive review. Renew Sustain Energy Rev. 2021;149(January):111361. https://doi.org/10.1016/j.rser.2021.111361

[35] Behara NSR, Rao PS. Vibration energy harvesting using telescopic suspension system for conventional two-wheeler and EV. Res Eng Struct Mater. 2023;(March).

[36] Singh N, Mithulraj M, Arya S. Influence of coal bottom ash as fine aggregates replacement on various properties of concretes: A review. Resour Conserv Recycl. 2018;138(July):257–71.

[37] Singh N, Singh SP. Carbonation resistance of self-compacting recycled aggregate concretes with silica fume. J Sustain Cem Mater. 2018;7(4):214–38.

[38] Cheah CB, Ramli M. Mechanical strength, durability and drying shrinkage of structural mortar containing HCWA as partial replacement of cement. Constr Build Mater . 2012;30:320–9. http://dx.doi.org/10.1016/j.conbuildmat.2011.12.009

[39] Batt AS, Garg A. Partial Replacement of Wood Ash with Ordinary Portland Cement and Foundry Sand as Fine Aggregate. J Civ Environ Eng. 2017;07(02).

[40] Singh N, Singh SP. Validation of Carbonation Behaviour of Self Compacting Concrete made with Recycled Aggregates using Microstructural and Crystallization Investigations. Eur J Environ Civ Eng. 2018;

[41] Singh N, Shehnazdeep, Bhardwaj A. Reviewing the role of coal bottom ash as an alternative of cement. Constr Build Mater. 2020;233:117276. https://doi.org/10.1016/j.conbuildmat.2019.11727

[42] Bai Y, Basheer PAM. Influence of furnace bottom ash on properties of concrete. In: Proceedings of the Institution of Civil Engineers: Structures and Buildings. 2003. p. 85–92.

[43] Basheer PAM. Permeation analysis. In: Handbook of analytical technology: principles, techniques and applications (Ramachandran V S and Beaudoin J J (eds)). Noyes Publications, NJ,; 2001. p. 658–737.

[44] Hussain M, Tufa LD, Yusup S, Zabiri H. Characterization of coal bottom ash &its potential to be used as catalyst in biomass gasification. In: Materials Today: Proceedings. 2019. p. 1886–93.

[45] Kasemchaisiri R, Tangtermsirikul S. Properties of self-compacting concrete incorporating bottom ash as a partial replacement of fine aggregate. ScienceAsia. 2008;34(1):87–95.

[46] Siddique R, Kunal. Design and development of self-compacting concrete made with coal bottom ash. J Sustain Cem Mater. 2015;4(3):225–37.

[47] IS:8112-2013. IS 8112: 2013, Ordinary Portland Cement, 43 Grade — Specification, Bureau of Indian Standards, New Delhi. Bureau of Indian Standards,New Delhi. 2013.

[48] IS 383: 2016. Coarse and fine aggregate for concrete - specification (third revision). Vol. third edit, Indian Standard. 2016.

[49] IS 10262. Concrete Mix Proportioning Guidelines IS 10262. 2019.

[50] Indian Standard. IS 516 - 1959 Methods of Tests for Strength of Concrete. 2006.

[51] RILEM. CPC-18 Measurement of hardened concrete carbonation depth. Mater Struct. 1988 Nov;21(6):453–5.

[52] Delf University of Technology. Sustainability Impact Metrics. https://www.ecocostsvalue.com/

[53] Ali B, Qureshi LA, Khan SU. Flexural behavior of glass fiber-reinforced recycled aggregate concrete and its impact on the cost and carbon footprint of concrete pavement. Constr Build Mater. 2020;262:120820. https://doi.org/10.1016/j.conbuildmat.2020.120820

[54] Momotaz H, Rahman MM, Karim MR, Zhuge Y, Ma X, Levett P. Comparative study on properties of kerb concrete made from recycled materials and related carbon footprint. J Build Eng. 2023;72(March).

[55] Wang C, Chen B, Vo TL, Rezania M. Mechanical anisotropy, rheology and carbon footprint of 3D printable concrete: A review. J Build Eng . 2023;76(June):107309. https://doi.org/10.1016/j.jobe.2023.107309

[56] Li XJ, Xie WJ, Jim CY, Feng F. Holistic LCA evaluation of the carbon footprint of prefabricated concrete stairs. J Clean Prod. 2021;329(August):129621. https://doi.org/10.1016/j.jclepro.2021.129621

[57] Elkhaldi I, Roziere E, Turcry P, Loukili A. Towards global indicator of durability performance and carbon footprint of clinker-slag-limestone cement-based concrete exposed to carbonation. J Clean Prod. 2022;380(P1):134876. https://doi.org/10.1016/j.jclepro.2022.134876

[58] Yüksel I, Genç A. Properties of concrete containing nonground ash and slag as fine aggregate. ACI Mater J. 2007;104(4):303–9.

[59] Balasubramaniam T, Thirugnanam GS. An experimental investigation on the mechanical properties of bottom ash concrete. Indian J Sci Technol. 2015;8(10):992–7.

[60] Kou SC, Poon CS. Properties of concrete prepared with crushed fine stone, furnace bottom ash and fine recycled aggregate as fine aggregates. Constr Build Mater. 2009;23(8):2877–86. http://dx.doi.org/10.1016/j.conbuildmat.2009.02.009

[61] Kim HK, Lee HK. Use of power plant bottom ash as fine and coarse aggregates in high-strength concrete. Constr Build Mater. 2011;25(2):1115–22. http://dx.doi.org/10.1016/j.conbuildmat.2010.06.065

[62] Raju R, Paul MM, Aboobacker KA. Strength performance of concrete using bottom ash as fine aggregate. Int J Res Eng Technol. 2014;2(9):111–22.

[63] Singh M, Siddique R. Effect of low-calcium coal bottom ash as fine aggregate on microstructure and properties of concrete. ACI Mater J. 2015 Sep 1;112(5):693–703.

[64] Silva LA, Nahime BO, Lima EC, Akasaki JL, Reis IC. XRD investigation of cement pastes incorporating concrete floor polishing waste. Ceramica. 2020;66(380):373–8.

[65] Aggarwal Y, Siddique R. Microstructure and properties of concrete using bottom ash and waste foundry sand as partial replacement of fine aggregates. Constr Build Mater . 2014;54:210–23. http://dx.doi.org/10.1016/j.conbuildmat.2013.12.051

[66] Yasipourtehrani S, Strezov V, Bliznyukov S, Evans T. Investigation of thermal properties of blast furnace slag to improve process energy efficiency. J Clean Prod. 2017;149:137–45.

[67] Saleh HM, El-Sheikh SM, Elshereafy EE, Essa AK. Mechanical and physical characterization of cement reinforced by iron slag and titanate nanofibers to produce advanced containment for radioactive waste. Constr Build Mater. 2019;200:135–45.

[68] Govindarajan D, Gopalakrishnan R. Spectroscopic Studies on Indian Portland Cement Hydrated with Distilled Water and Sea Water. Front Sci. 2012;1(1):21–7.

[69] Kontoleontos F, Tsakiridis P, Marinos A, Katsiotis N, Kaloidas V, Katsioti M. Dry-grinded ultrafine cements hydration. Physicochemical and microstructural characterization. Mater Res. 2013;16(2):404–16.

[70] Lo FC, Lee MG, Lo SL. Effect of coal ash and rice husk ash partial replacement in ordinary Portland cement on pervious concrete. Constr Build Mater. 2021;286:122947.

[71] Hamzah AF, Ibrahim MHW, Jamaluddin N, Jaya RP, Arshad MF, Abidin NEZ. Nomograph of self-compacting concrete mix design incorporating coal bottom ash as partial replacement of fine aggregates. J Eng Appl Sci. 2016;11(7):1671–5.

[72] Singh M, Siddique R. Strength properties and micro-structural properties of concrete containing coal bottom ash as partial replacement of fine aggregate. Constr Build Mater . 2014;50:246–56. http://dx.doi.org/10.1016/j.conbuildmat.2013.09.026

[73] Singh M, Siddique R. Compressive strength, drying shrinkage and chemical resistance of concrete incorporating coal bottom ash as partial or total replacement of sand. Constr Build Mater. 2014;68:39–48. http://dx.doi.org/10.1016/j.conbuildmat.2014.06.034

[74] Rafieizonooz M, Mirza J, Salim MR, Hussin MW, Khankhaje E. Investigation of coal bottom ash and fly ash in concrete as replacement for sand and cement. Constr Build Mater . 2016;116(July):15–24. http://dx.doi.org/10.1016/j.conbuildmat.2016.04.080

[75] Majhi RK, Nayak AN. Properties of concrete incorporating coal fly ash and coal bottom ash. J Inst Eng Ser A . 2019;100(3):459–69. https://doi.org/10.1007/s40030-019-00374-y

[76] Derringer G, Suich R. Simultaneous Optimization of Several Response Variables. 2018;4065.

[77] Luesak P, Pitakaso R, Sethanan K, Golinska-Dawson P, Srichok T, Chokanat P. Multi-Objective Modified Differential Evolution Methods for the Optimal Parameters of Aluminum Friction Stir Welding Processes of AA6061-T6 and AA5083-H112. Metals (Basel). 2023;13(2).

[78] To-on P, Wichapa N, Khanthirat W. A novel TOPSIS linear programming model based on response surface methodology for determining optimal mixture proportions of lightweight concrete blocks containing sugarcane bagasse ash. Heliyon. 2023;9(7):e17755. https://doi.org/10.1016/j.heliyon.2023.e17755

[79] Hamada HM, Al-attar A, Shi J, Yahaya F, Al MS, Yousif ST. Optimization of sustainable concrete characteristics incorporating palm oil clinker and nano-palm oil fuel ash using response surface methodology. Powder Technol. 2023;413(August 2022):118054. https://doi.org/10.1016/j.powtec.2022.118054

[80] Dahish HA, Almutairi AD. Case Studies in Construction Materials Effect of elevated temperatures on the compressive strength of nano-silica and nano-clay modified concretes using response surface methodology. Case Stud Constr Mater. 2023;18(January):e02032. https://doi.org/10.1016/j.cscm.2023.e02032

[81] Waheed H, Hamcumpai K, Nuaklong P. Effect of graphene nanoplatelets on engineering properties of fly ash-based geopolymer concrete containing crumb rubber and its optimization using response surface methodology. J Build Eng. 2023;75(March):107024. https://doi.org/10.1016/j.jobe.2023.107024

[82] Peng Q, Chen B, Lu Q, Li K, Jin W. Effect of steel-waste PET hybrid fiber on properties of recycled aggregate concrete based on response surface methodology. Constr Build Mater . 2023;397(26):132448. https://doi.org/10.1016/j.conbuildmat.2023.132448

[83] ISO 14044. Environmental management - Life Cycle Assessment: Requirements and Guidelines. Geneva, Switzerland; 2006.

[84] ISO 14040. Environmental management - Life Cycle Assessment: Principles and Framework. Geneva, Switzerland; 2006.

[85] European Commission-Joint Research Center. ILCD Handbook International Reference Life Cycle Data System. Constraints. 2010. 1–393 p.

Research Article

Influence of alumina and zinc oxide nanoparticles on microstructure and electro-mechanical properties of aluminum metal matrix composites fabricated by customized two-step stir casting method

Md Jalal Uddin Rumi[*1, a], Muhammad Muzibur Rahman[2,b]

[1]*Dept. of Aeronautical Eng., Military Institute of Science and Technology, Bangladesh*
[2]*Dept. of Mechanical Eng., Sonargaon University, Bangladesh*

Article Info	Abstract
	The present paper reports the influence of Alumina (Al_2O_3) and Zinc Oxide (ZnO) nanoparticles on the microstructure and electro-mechanical properties of aluminum metal matrix composites (Al MMCs) fabricated by a customized two-step stir casting method. Two types of Al MMCs were developed, (i) Al MMC-01 having 97.5 wt. % of Al and 2.5 wt. % of Al_2O_3 and (ii) Al MMC-02 having 95 wt. % of Al, 2.5 wt. % of Al_2O_3 and 2.5 wt. % of ZnO. The microstructures of Al MMC-1 and Al MMC-2 observed in a Scanning electron microscope (SEM) have affirmed the uniform distribution of Al_2O_3 and ZnO in the metal matrix composites. It has been observed that the addition of 2.5% Al_2O_3 has improved the hardness, flexural strength, and impact toughness of Al composite significantly compared with pure Al. Furthermore, both bulk and micro hardness of Al MMC-02 have also increased significantly. However, impact strength, flexural strength, modulus of elasticity, and electrical conductivity of Al MMC-02 have been reduced by 12%, 52.5%, 60.8%, and 9.81% respectively in comparison with Al MMC-01 as it becomes brittle in nature for the presence of cleavage cracks, deep shear dimples, and crystallographic planes than that of Al MMC-01 as revealed by fractured surface analysis through SEM.

1. Introduction

Aluminum (Al) has been becoming increasingly popular across a variety of industries, including aerospace, automotive, space, etc. due to their superior strength-to-weight ratio, cost-effectiveness, and ample supply of Al on a worldwide scale [1-2]. However, pure Al cannot be used directly in aforesaid industries as many of its properties do not meet the requirements and concerned industries are looking for those composites which are having enhanced electro-mechanical properties. In this regard, researchers around the world are continuously applying different innovative techniques to develop aluminum-based metal matrix composites with the inclusion of various reinforcement particles in nano and micro sizes.

Al MMCs can be fabricated using a variety of processing methods, including stir casting, ultrasonic assisted casting, compo-casting, powder metallurgy, etc. [3-5]. Among these techniques, stir casting is relatively easy to use and inexpensive for the production of Al composites. Up to 30% volume fractions of reinforcement, aluminum composites can be developed using the stir casting method [6-7]. However, the wettability of the reinforcement with the matrix, porosity, and homogeneous reinforcement dispersion are

---

the technical difficulties in stir casting. When creating Al MMCs by stir casting, these problems must be resolved in order to get the necessary characteristics [8-11]. The non-homogeneous dispersion of reinforcement particles in the matrix reduces the material properties of the composite in many aspects. Few techniques, such as two-step stir casting, can mitigate or at least reduce the drawbacks of single stir-casting [12-13]. These criteria led to the two-step stir casting method being chosen as the fabrication method to develop Al composites.

The stir-casting process and parameters such as stirring speed, stirring duration, casting temperature, preheating temperature, the effect of squeeze pressure, reinforcement size, etc. can have effects on developed Al composites, which need to be identified and addressed. Numerous studies have examined the creation of metal matrix composites using the stir-casting method while varying various process variables. However, it is still unclear how stirrer blade angle and rpm affect the uniform dispersion of reinforcement particles in the molten matrix. Research on the dispersion of reinforcement particles during the stir-casting process to create MMCs has been conducted by Hashim et al. [14–16]. Mehta and Sutaria [17] looked at the effects of stirrer geometry, position, and speed on particle dispersion into the molten matrix. They investigated the effects of stirrer speed and geometry and discovered a strong association with the outcomes of the experiments. Singh et al. [18] demonstrated that the stirring speed, duration, and angle of the stirrer's blade are crucial factors in ensuring uniform dispersion of reinforcement particles. The effect of stirring speed on the homogenous dispersion of particles in a comparable Al-SiC composite has been simulated by Naher et al. [19].

Literature survey also indicates that relentless efforts are being made to improve the electro-mechanical properties of Al composites by adding different reinforcement particles such as Alumina (Al_2O_3), Silicon Carbide (SiC), Graphite (Gr), Boron carbide (B_4C), and Titanium Carbide (TiC) [20-25]. Among them, Al_2O_3 is the most frequently utilized reinforcement material due to its superior interfacial affinity and resistance to chemical degradation by molten aluminum alloys [26-27]. Aybarç et al. [27] observed that aluminum composites with nano- Al_2O_3 particles exhibited higher mechanical properties than the ones with micro- Al_2O_3 particles. Akbari et al. [28] investigated TiC-reinforced Al matrix composite developed via friction stir processing (FSP) and found uniform particle distribution of TiC particles in the Al matrix resulted in higher mechanical and wear properties. Kandpa et al. [29] developed an aluminum composite using the stir casting method and observed the clustering of Al_2O_3 particles in a few places through SEM for higher wt. % of reinforcement particles.

To improve further on the mechanical qualities and wear characteristics of Al composites, Jasim et al. [30] added different wt. % of ZnO and observed an increase in compressive strength and wear characteristics. They also exhibited a progressive rise of the hardness of Al composites reinforced with a higher percentage of ZnO particles. As per the literature review, ZnO received very rare attention in making hybrid Al-based composites. Moreover, the combined effect of using Al_2O_3 and ZnO in aluminum composites is yet to be investigated. Therefore, there is a prospective research scope of developing a novel hybrid Al composite reinforced with Al_2O_3 and ZnO particles together. As such, two aluminum composites: (i) one having 2.5 wt. % of Al_2O_3 nano-particles and (ii) another having 2.5 wt. % of Al_2O_3 and 2.5 wt. % of ZnO nano-particles in the aluminum matrix. The current research has focused on the selection processes and parameters for customization of stir casting technique and characterization of a few mechanical properties like hardness, impact strength, flexural strength, and electrical conductivity of the developed two Al composites so that their significant usefulness in the aerospace and automotive industries can be explored.

2. Material Under Study

The base metal used for the casting of composites is aluminum ingots collected from RUSAL of Russia. The reinforcement particles used for the fabrication of composites are nanoparticles such as Alumina (Al_2O_3) and Zinc Oxide (ZnO) provided by Hebei Suoyi New Material Technology Co. Ltd. in China. The details of these components/ingredients used for the present study are briefly described below.

2.1 Pure Aluminum

The chemical composition analysis of the pure aluminum has been done by the XRF Analyzer of Olympus, Model: Vanta C Series and the results are presented in Table 1.

Table 1. Composition of Pure Aluminum

Element	Al	Si	Fe	Cu	Zn	Zr	Pb
Percentage (%)	99.052	0.614	0.323	0.002	0.008	0.0007	0.0009

2.2 Alumina (Al_2O_3)

Aluminum oxide commonly named as Alumina is a chemical compound of aluminum and oxygen with the chemical formula Al_2O_3. It has significant uses to produce Al metal matrix composite, as it has an abrasive owing to its hardness, and has a refractory material owing to its high melting point. As per the maker's manual of Al_2O_3, the Melting point is 2072^0C, Boiling point is 2977^0C, Limit of application is 1175^0C, Hardness as per Moh's Scale is 7.5, the Linear coefficient of expansion is 4.5 $\mu m/m^0C$, the Molecular weight is 101.96 g/mol, Bulk Density is 0.1-0.3 g/cm^3 and Thermal conductivity is 30 $W.m^{-1}-K^{-1}$. Fig. 1 shows the SEM image of Al_2O_3 collected for the study.

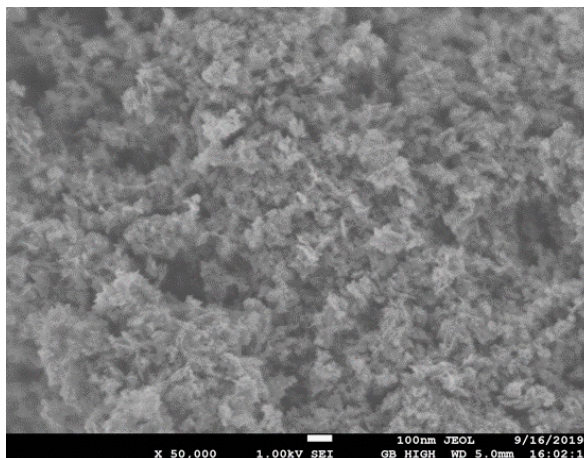Fig. 1. SEM of Reinforcement particles Al_2O_3 with grain size of 20 nm

2.3 Zinc Oxide (ZnO)

ZnO is a white powder that is essentially water-insoluble. To customize the mechanical properties of several materials, ZnO is employed as reinforcement. As per the maker's manual of ZnO, the Melting point is 1974^0C, the Flashpoint is 1436^0C, the Hardness as per Moh's Scale is 4.5, the Linear coefficient of expansion is 4.5 $\mu m/m^0C$, the Molecular weight

is 81.406 g/mol, Bulk Density is 0.15-0.3 g/cm^3 and Thermal conductivity is 50 W.m^{-1}-K^{-1}. Fig. 2 shows the SEM image of ZnO collected for the study.
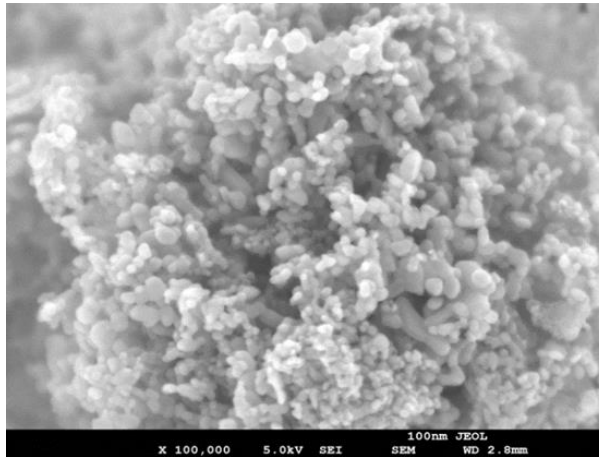

Fig. 2. SEM of Reinforcement particles ZnO with grain size of 30 nm

3. Experimental Details

3.1 Selection Criteria for Process and Parameters of Stir Casting

The stir-casting process and associated parameters such as stirring speed, stirring duration, casting temperature, preheating temperature, the effect of squeeze pressure, reinforcement size, etc. have a variety of effects on developed Al composites which will be discussed here sequentially. In the case of stirring speed, there is no room for the reinforcement particles (dispersed phase) to scatter evenly throughout the matrix due to reduced shearing force [31]. With a faster stirring speed, there is a potential that the matrix's porosity will increase as the gas particles move around inside it. Therefore, an optimum stirring speed of 400 RPM has been chosen to avoid such circumstances. The duration of stirring is crucial in ensuring that the dispersed phase is distributed evenly throughout the matrix. The clustering of reinforcement particles is brought on by shorter stirring times [32]. Therefore, stirring of 5 minutes in two steps has been selected to avoid such agglomeration.

The casting temperature is one of the factors that have the biggest impact on the stir casting process. The viscosity of the matrix metal reduces as the temperature rises, and the particle distribution is also impacted. By raising the melt temperature, the chemical reaction between the metal matrix and the reinforcing particles is sped up [33]. According to the microstructure analysis of numerous study articles, the reinforcing particles were discovered to be evenly distributed between 750°C and 800°C for casting. Due to variations in the viscosity of the liquid Al matrix, the particle agglomerations were seen at processing temperatures of 700°C, 850°C, and 900°C [34]. To keep the optimum viscosity and minimum chemical reaction between the metal matrix and reinforcement particles, 800°C has been selected as the casting temperature.

Preheating the base metal and reinforcing material is essential to reducing porosity [35]. Base metal is preheated at 500^{0}C for an hour and reinforcing particles at 300^{0}C for two hours because preheating is needed to release the trapped gases from the metal and reinforcing particles. The MMC strength is impacted by the size of the reinforcement. The size of the reinforcement has an inverse relationship with strength. Strength improves as

reinforcement size decreases [36]. With the heat being dissipated from various dies, the squeeze pressure accelerates cooling [34]. Additionally, it reduces the nucleation of gas bubbles, which decreases porosity [37].

On the basis of the notable factors and their parameters on the effects of stirring casting after studying the various research works [31-37], the finalized parameters for the development of Al composites are shown in Table 2.

Table 2. Selection of Stir Casting Parameters with Arrangements

SL No	Casting Arrangement	Casting parameter
1	Base Metal	99% pure Al
2	Casting Method	Two Step Stir Casting
3	Base Metal Preheat	500°C
4	Base Metal Preheat Time	60 minutes
5	Casting Temperature	800°C
6	Reinforcement	Al_2O_3 and ZnO
7	Reinforcement Particle Size	Al_2O_3: 20 nm and ZnO: 30 nm
8	Reinforcement Preheat	300°C
9	Reinforcement Preheat Time	120 minutes
10	Stirrer RPM	400 RPM
11	Stirring Time	05 minutes in two steps

3.2 Design and Development of Customized Stirring Mechanism

A dedicated small version of the stirring mechanism has been designed and developed to apply the effects of selected casting parameters such as stirring speed, stirring time, Squeeze Pressure, etc. during the fabrication of Al composites for the present research purpose. The stirring mechanism was developed using two major parts, i.e., a power drive and a stirring rod with an impeller (mixer head).
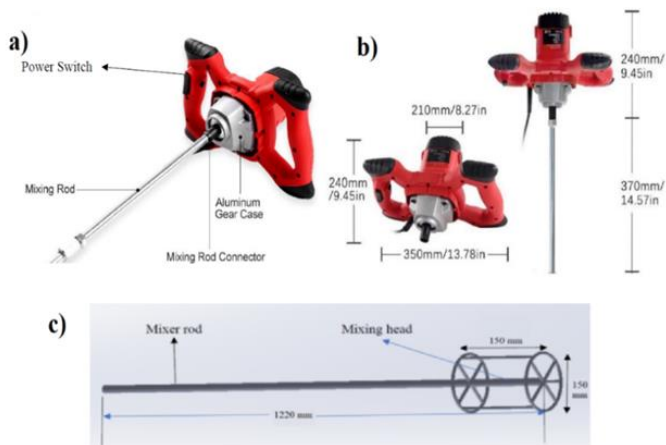

Fig. 3. (a) Component details of Stirrer (b) Dimensions of Stirrer machine (c) Dimension of mixer rod & head

For the power drive part, one multi-speed handheld mixer machine motor was used having a rated voltage of 220V, power of 2100w, frequency of 50/60 Hz and for the stirring part, a rod of about 1220 mm length was connected with an impeller of 150 mm diameter. This

mixer machine had 6 gears to operate at different rotational speeds, i.e., 100 rpm to 600 rpm with an interval of 100 rpm for each gear. For the present work of the fabrication process, the 4th gear having 400 rpm was selected as the optimum one after a few trials with speed variations. A detachable arrangement was made to remove the mixer head from the motor part for cleaning purposes.

Since the crucible furnace was supposed to be set at 800°C for casting the metal matrix composite, the materials were selected in such a way that the stirring rod and mixer head could sustain at such an elevated temperature. Therefore, the mixer head was made of stainless steel (SS) and the mixer rod was made of mild steel (MS) as their melting point are about 1500°C and 1300°C, respectively. Fig.3 shows the driving part and the stirring part along the dimensions of the developed stirring gear used for casting purposes in the crucible furnace.

3.3 Fabrication Procedure of Al Composites

The stir casting was done in a gas-fired crucible furnace which could sustain very high temperatures even more than 3500°C. An external air blower was used to supply a sufficient amount of air for maintaining a steady temperature during gas burning. The step-by-step process of Stir casting is shown in Fig. 4. Firstly, Al metal was kept in the crucible and fired up the furnace without activating the blower which generates heat at the temperature of about 300°C heat. After 15 minutes, an electric blower was activated and maintained a temperature of 500°C for preheating the base metal for 60 minutes. Simultaneously the preheating of reinforcement particles is done in the oven at 300°C for 120 minutes. It takes nearly 60 minutes to melt the metal completely at a casting temperature of 800°C. Then, the stirring machine was used for 05 minutes in two steps to mix the molten metal properly with Al_2O_3. When the metal is ready, it was poured into the empty sand mold. After pouring 1st mold with Al composite reinforced Al_2O_3 (Al MMC-01) into the 1st mold, the 2nd reinforcement particle ZnO was added in the crucible and mixed similarly with a two-step stirring mechanism for 05 minutes. When the metal is ready again, Al composite reinforced with Al_2O_3 and ZnO (Al MMC-02) was poured into another sand mold. Mixing of Al_2O_3 and ZnO in the crucible was maintained 20 gm/minute.
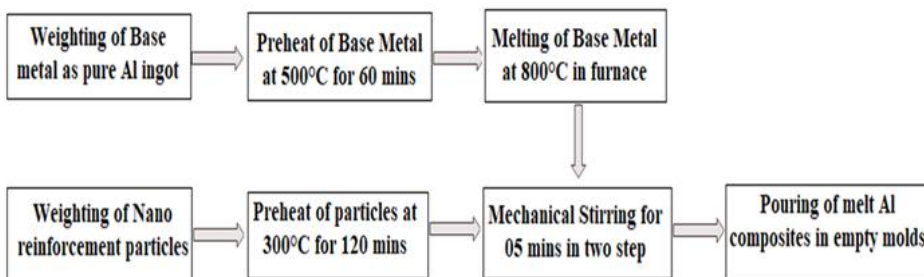

Fig. 4. Flowchart of the Stir casting process

3.4 Preparation of Test Specimens

Test specimens were prepared by a CNC machine, Model VF-2 type as shown in in Fig. 5(a). The cutting tools used for surfacing and machining were respectively 12 mm and 6mm coated with bronze as shown in Fig. 5(b). The finished smooth surface of the Al composite is shown in Fig. 5(c). Test specimens for Impact Charpy and flexural were prepared respectively as per ASTM standards E23-18 and D790-10 as shown in Fig. 5(d)-5(e). The dimension of Impact Charpy and flexural test specimens are respectively 55 mm×10

mm×10 mm and 80 mm×10 mm×04 mm. Test specimens for hardness (Rockwell and Vickers micro) and electrical conductivity were prepared respectively as per ASTM standards E10-18, E18-20, E92-17, and E1004-17 with the dimensions of 20 mm×20 mm×08 mm. The specimens are demonstrated sequentially in Fig. 5(f).
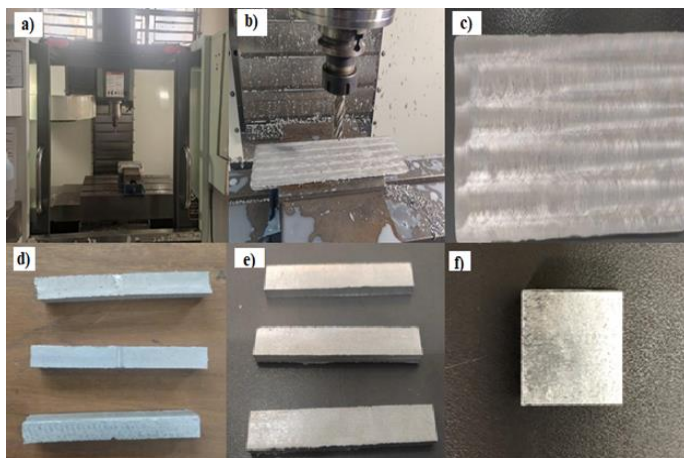

Fig. 5. (a) CNC machine set up (b) End Mill cutter (c) Finished Al composite, Sample specimens for (d) Impact (Charpy) (e) Flexural (f) Hardness and Electrical Conductivity

3.5 Surface Roughness of Test Specimens

The cutting speed, feed rate, and depth of cut for the CNC machining were maintained as 375m/min, 400m/min, and 1 mm respectively during facing and preparation of test specimens for hardness, flexural & impact strength and electrical conductivity. The surface roughness of a test specimen is the prediction factor for mechanical performance. Mainly surface irregularities contribute to the breakage and initial formation of corrosion. A sample of test specimen from Al MMC-01 has been taken to conduct the surface roughness test by a Mitutoyo roughness tester, Model SJ-210 to identify the possible imperfection and obtained an overall Ra of 0.492 μm. The evaluation profile of measured surface roughness is shown in Fig. 6(a).

The microstructure of the same test specimen from Al MMC-01 was also observed by Scanning Electron Microscope (SEM), Model: TESCAN VEGA 4 from the Czech Republic. As shown in Fig. 6 (b), a sample of test specimen with a dimension of 05mm×05mm×05mm was observed in SEM with FoV: 109 μm, WD:11.57 mm, Speed: 7:19, Energy: 30KeV, Mag: 2.56Kx, Pixel Size: 107 nm, DoF: 74.1 μm. As shown in Fig. 06 (b), we identified a few discontinuities and a few holes with elliptical sizes of 2.09 μm & 1.28 μm.
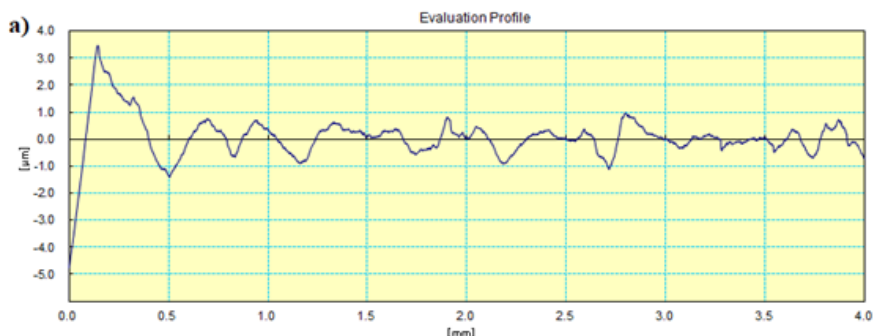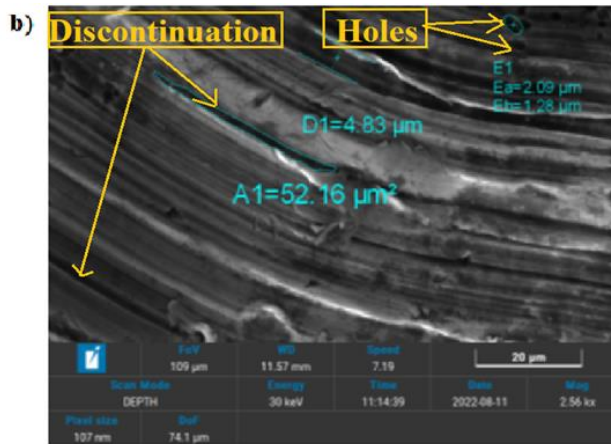
Fig. 6. (a) Evaluation profile of Surface roughness (b) Microstructure observation by SEM of a test specimen from Al MMC-01

4. Microstructure Observation

After the preparation of the aluminum metal matrix composite by two-step stir casting, microstructure observation was carried out by SEM in order to confirm the mixing of reinforcement particles (Al_2O_3) and (ZnO) into a base material (99% Al). A sample of Al-Al_2O_3 (Al MMC-01) and Al-Al_2O_3-ZnO (Al MMC-02) with a dimension of 05mm×05mm×05mm prepared for microstructure observation by Scanning Electron Microscope (SEM), Model: TESCAN VEGA 4.
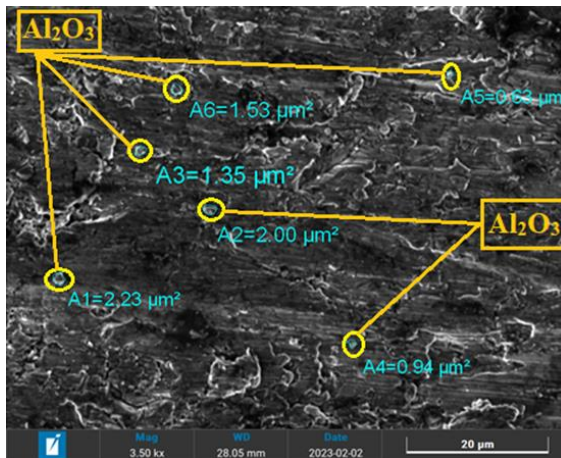

Fig. 7. Microstructure observation by SEM of Al composite having 97.5% of Al and 2.5% of Al_2O_3 (Al MMC-01)

For Al MMC-01, the morphology of Al_2O_3 particles is mainly irregular or nearly elliptical shown in Fig. 7. The Al_2O_3 particles were uniformly distributed in the Al/ Al_2O_3 as casted-condition. The elliptical area immersed by the reinforcements (Al_2O_3) in Al MMC-01 are approximately 5.45 μm^2 and 6.29 μm^2 which is investigated through image processing as shown in Fig. 7. Also, a few clustering or agglomerations of Al_2O_3 particles were perceived in Al MMC-01.
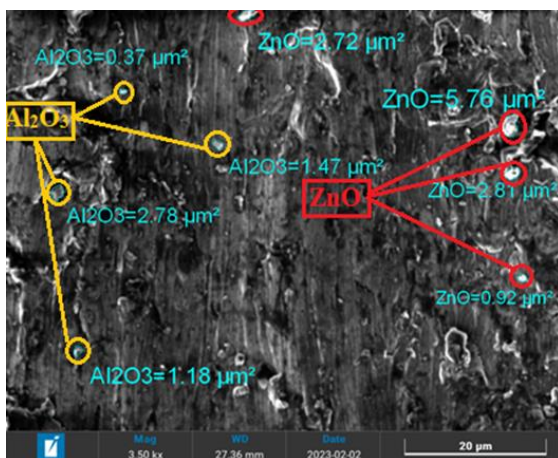
Fig. 8. Microstructure observation by SEM of Al composite having 95% of Al, 2.5% of Al_2O_3, and 2.5% of ZnO (Al MMC-02)

Fig. 8 exhibits the distribution of Al_2O_3 and ZnO particles in Al MMC-02 where the morphology of both nanoparticles is also irregular or nearly elliptical in shape. As shown in Fig. 8, both nanoparticles were also uniformly distributed in Al MMC-02 as a casted condition. The elliptical area immersed by the reinforcements Al_2O_3 and ZnO in Al MMC-02 are respectively 0.37 to 2.78 μm^2 and .92 to 5.76 μm^2 which was investigated through image processing. We also observed a few agglomerations of Al_2O_3 and ZnO particles perceived in Al MMC-02.

Singla et al. [38] applied a two-step stirring technique during the fabrication of Al composite reinforced with SiC particles by the stir casting method. This experimental method had an effective contribution to the improvement of the strength and hardness of fabricated Al MMCs for the uniform dispersion of SiC particles in the matrix. The uniform dispersion of Al_2O_3 in Al MMC-01 and Al_2O_3 and ZnO in Al MMC-02 was achieved by the selection of process and parameters of two-step stir casting which goes in line with Singla et al. [38].

The introduction of Al_2O_3 nanoparticles in Al MMC-01 and Al_2O_3 and ZnO nanoparticles in Al MMC-02 leads to a decrease in the grain size of primary Al as shown in the microstructure of both MMC as per Fig. 7 and Fig.8. This decrease in grain size of primary Al was highly observed in both Al MMC-01 and Al MMC-02 at high concentrations of nanoparticles. Wazery et al. [39] observed similar microstructure during the investigation of mechanical properties for Al composites reinforced with 3 wt.% of ZnO nanoparticles.

5. Investigation Procedure

5.1 Rockwell Hardness

Rockwell hardness test was carried out by a hardness tester from Brooks Inspection Equipment Ltd, United Kingdom at a room temperature of 26^0C. The test specimens were prepared as per ASTM standard E10-18 with dimensions of 20 mm×20 mm×08 mm where a 1.58 mm diameter hardened steel ball subjected to a load of 100kg was applied. The diameter of the impression is the average of five readings.

5.2 Vickers Micro Hardness

The test specimens for Vickers microhardness were prepared as per ASTM standard E92-17 with a dimension of 20 mm×20 mm×08 mm. The tests were carried out by a Vickers hardness tester model: TMHV-10MDT auto turret Vickers hardness tester with 500 gm load for 10 seconds duration. The average value of HV was taken from ten readings.

5.3 Impact Toughness

The Impact Charpy test was carried out to investigate energy being absorbed and ascertain the durability of the developed composite samples. The tests were carried out by an Impact testing machine of Model: AIT300 from Turkey at a room temperature of 26^0C. The specimens used for the Charpy test had a dimension of 55mm×10mm×10mm as per ASTM E23-18. The average value of impact toughness was taken from three readings.

5.4 Flexural Strength

The flexural test was done to determine the flexural behavior based on simple beam load-bearing capacity of developed two Al composite materials, i.e., Al MMC-01 and Al MMC-02. It was conducted using the Universal Testing Machine at a room temperature of 26^0C under three-point bending conditions. The dimension of the test specimens was 80mm×10mm×4mm as per ASTM D790-17. The flexural strength, elastic modulus, etc. were obtained on average values taken from three tests' readings.

5.5 Electrical Conductivity

The electrical conductivity of developed Al MMC-01 and Al MMC-02 are tested by Eddy Current Conductivity meter, model: 12Z from ZAPPITEC PTY LTD, Australia at a room temperature of 26^0C. The test specimens were prepared as per ASTM E1004-17 with a dimension of with dimension of 20 mm×20 mm×08 mm. The electrical conductivity of a metal depends on several factors, such as its chemical composition and the stress state of its crystalline structure. Also, the conductivity of metals changes significantly with temperature. To allow easy comparison between different metals, conductivity values were taken with a standardized temperature of 20^0C. The measurement is made in %IACS units, an acronym that means "Percent of International Annealed Copper Standard".

6. Results and Discussion

6.1 Hardness

The Rockwell hardness values (HRB) of developed Al MMC-01 were observed to be 24.33 kg/mm^2 with a standard deviation of 1.22 and Al MMC-02 was 29.2 kg/mm^2 with a standard deviation of 1.3. The diameter of the impression is the average of five readings at right angles. As per Fig. 9, there is a 20% improvement in Rockwell hardness in Al MMC-02 from that of Al MMC-01 due to the addition of 2.5% ZnO as reinforcement particles.

The Vickers mirco-hardness (HV) of Al MMC-01 was 35.72 with a standard deviation of 1.46 and that of Al MMC-02 was 50.23 with a standard deviation of 2.50. The average value of HV was taken from ten readings. As per Fig. 9, there is a 41% improvement in Vickers micro-hardness in Al MMC-02 from Al MMC-01 due to the addition of 2.5% ZnO as reinforcement particles.
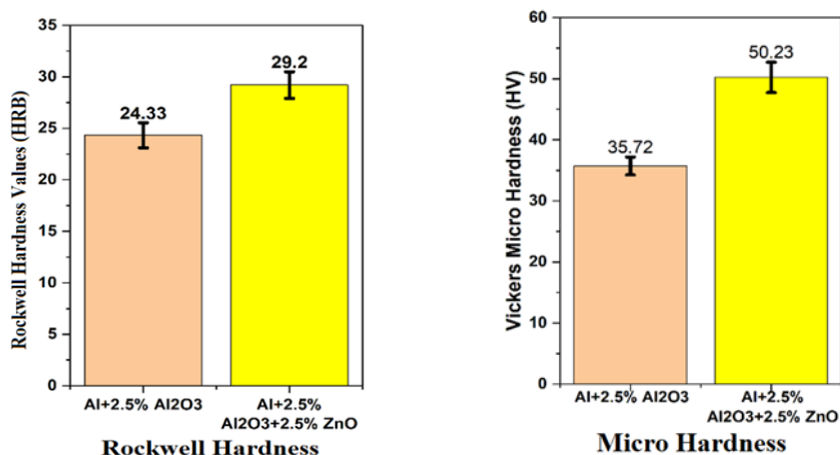
Fig. 9.   Hardness test results of Al MMC-01 (Al+2.5% Al_2O_3) and Al MMC-02 (Al+2.5% Al_2O_3+ 2.5% ZnO)

With the insertion of ZnO nanoparticles in Al MMC-02, the strength of the grain boundaries may be increased because ZnO and Al's reaction polished the microstructure can be seen in Figure 9 which contributed to the higher hardness readings of Al MMC-02. A high interfacial zone between aluminum and ZnO nanoparticles causes a strong reaction between them. The reaction reaches a high value for high ZnO nanoparticle concentrations (2.5%), leading to the sample with the highest microstructural refinement. Growth restriction factor and heterogeneous nucleation are responsible for Al refining by the addition of various elements [40-41].

More specifically, the addition of ZnO nanoparticles to an Al matrix solution at a high temperature causes the ZnO nanoparticles to break down into Zn and O. After decomposing from ZnO, almost all of the oxygen was coupled with aluminum oxide. formation is hampered by the presence of oxygen that has been broken down from ZnO at the interface between liquid and solid aluminum during the formation of the primary aluminum alloy. The diffusion of solute Zn at the interface between solid and liquid aluminum can be blamed for limiting aluminum growth during solidification. Additionally, the breakdown of Zn and oxygen yields significant amounts of Zn for the heterogeneous nucleation of primary aluminum grains. Therefore, it can be deduced that addition ZnO has the potential to increase the hardness of aluminum composites at both bulk and micro levels.

Jasim et al. [30] developed ZnO-reinforced Al MMC using the stir casting method for the investigation of mechanical properties and wear characteristics. Their investigation exhibited an increment of hardness from 23 kg/mm^2 to 30 kg/mm^2 for (2, 4, 6, 8, 10) wt.% of ZnO along with Al. In the present study, Rockwell hardness values have been found as 24.33 kg/mm^2 for Al MMC-01 and 29.2 kg/mm^2 for Al MMC-02. Therefore, the present results are quite agreeable with Jasim et al. [30] on an incremental aspect of hardness in the presence of ZnO in aluminum composites.

6.2 Impact Toughness

The effects of Al_2O_3 and ZnO on the impact strength of developed two Al MMCs are shown in Fig. 10. The average value of impact toughness energy of Al MMC-01 is 13.47J with a standard deviation of 0.64J and that of Al MMC-02 is 11.77J with a standard deviation of 0.25J respectively. The result brings forward the limitations of energy absorption capacity while ZnO is added along with Al_2O_3 in developing aluminum composites.
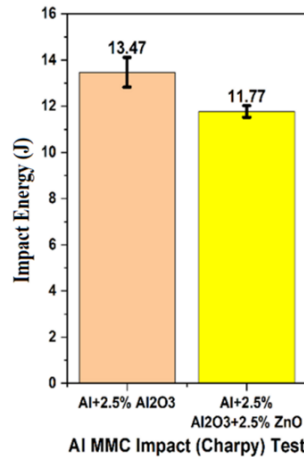
Fig. 10. Impact Toughness of Al MMC-01and Al MMC-02

Verma et al. [42] developed Al MMC reinforced with 10% Al_2O_3 and observed an impact toughness of 6.97J with a standard deviation of 0.85 [42]. The present study reveals that there is an increase in impact toughness in Al MMC-01 in comparison with pure Al due to the addition of 2.5% Al_2O_3 in the metal matrix. However, there is a decrease of 12% impact energy for Al MMC-02 in comparison to that of Al MMC-01 due to the insertion of 2.5% ZnO with 2.5% Al_2O_3 in aluminum composite. The addition of ZnO in aluminum alloy increased its hardness, thus turning it brittle in nature. As a result, the degree of plastic deformation energy for the composites is reduced. This deformation energy increases the chances of debonding during the fracture which leads to a reduction in impact strength [43]. The brittleness of the material decreases the plastic deformation energy thereby reducing the impact strength.

6.3 Flexural Strength

The flexural test results of the developed metal matrix composites, i.e., Al MMC-01 and Al MMC-02 conducted using a Universal Testing Machine on three-point bending conditions are presented in Fig.11. Fig.11 (a), show that the ultimate flexural strengths (UFS) of Al MMC-01 and Al MMC-02 are 320.06 MPa and 151.94 MPa respectively. Fig.11 (b) illustrates that the modulus of elasticity (MoE) values of Al MMC-01 and Al MMC-02 are 81.36 GPa and 31.84 GPa respectively. It is depicted that both strength and elastic modulus for the inclusion of 2.5% Al_2O_3 in Al MMC-01 have increased significantly compared to pure aluminum. This result agrees fully with the findings of Saravanakumar and Sasikumar where the flexural strength was found to be 250 MPa for the Al MMC with 3% of Al_2O_3 [44]. However, the addition of ZnO in Al MMC-02 has not shown any positive impact on UFS or MoE compared to that of Al MMC-01. Rather, the inclusion of only 2.5% ZnO in Al MMC-02 has reduced UFS and MoE from Al MMC-01 by 52.5% and 60.8% respectively. These results thus lead to limitations in specific requirements for the use of ZnO in aluminum composites.

The flexural test findings show that the flexural strength significantly changes by adding the weight % of the nanoparticles. Good particle-particle bonding, which leads to internal stress transmission, plastic deformation, and movement towards reinforcing nanoparticles, is responsible for improved strength. The nanocomposite samples' fracture is delayed and their flexural strength rises as a result of the nanoparticles' presence, high stiffness, and the high force required to break them.
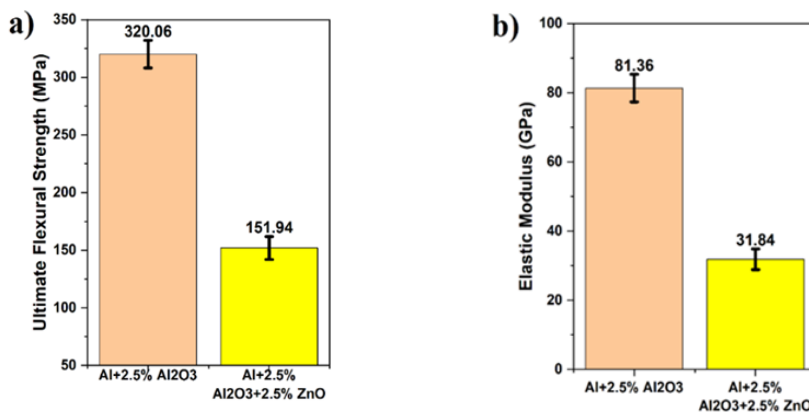
Fig. 11. (a) Ultimate Flexural Strength (UFS) and (b) Modulus of Elasticity (MoE) of
Al MMC-01and Al MMC-02

Al_2O_3 is one of the strongest reinforcing nanoparticles, and samples containing it have much higher flexural strengths than samples without it. The lowest flexural strength among all reinforced samples is provided by ZnO nanoparticles, which are weaker than other nanoparticles [45]. As a result, the presence of Al_2O_3 in Al MMC-01 improved the flexural strength of Al MMC-01. Increasing the percentage of nanoparticles results in higher local ductility because the mixing of the nanoparticles was done successfully and good distribution between the nanoparticles and Al was achieved [46]. However, adding ZnO nanoparticles along with Al_2O_3 in Al MMC-02 has reduced the flexural strength, making the metal matrix from ductile to brittle in nature. SEM imaging from the fracture cross-section of the Al MMC-01 and Al MMC-02 samples was performed to ensure the results.

6.4 SEM Observation of Fractured Surface

The fractured surfaces obtained through flexural tests of Al MMC-01 and Al MMC-02 were examined using a Scanning Electron Microscope (SEM) to identify the mode of failure. The SEM micrographs presented in Fig. 12 exhibit the characteristics of a brittleness fracture pattern.
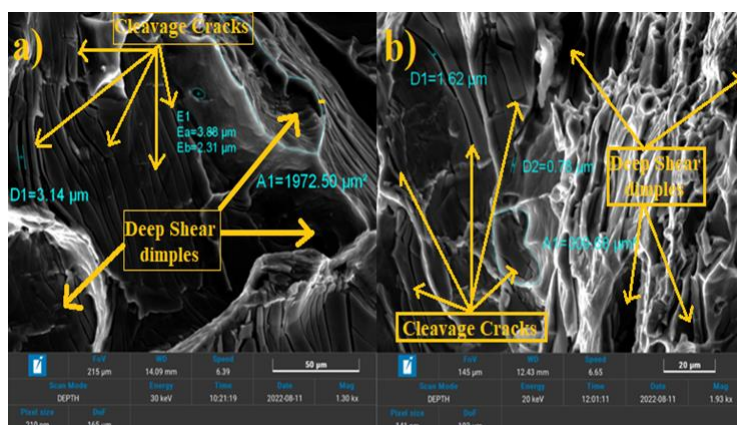

Fig. 12. SEM images of the fractured surface of: (a) Al MMC-01 & (b) Al MMC-02

The cleavage cracks and deep shear dimples of Al MMC-01 and Al MMC-02 are shown respectively in Fig. 12 (a) and 12 (b) respectively. The presence of cleavage cracks and

deep shear dimples in the fractured surface of Al MMC-02 are higher than that from the fractured surface of Al MMC-02. The existence of multiple cleavage cracks, shear dimples, and crystallographic planes within one specific grain as shown in Fig. 12 (b) in the fracture surface of Al MMC-02 is also an indication of the brittle features at the fracture surface [47].

As a whole the mechanical properties such as hardness, impact toughness, and UFS were increased a lot compared with pure Al. Bakshi et al. [48] investigated the factors which affect the strengthening mechanism of aluminum composites. According to their study, the strength mainly depends on the volume fraction of constituents and the aspect ratio of the reinforcement. In the current investigation, the findings are similar to the flexural & impact strength and Hardness of Al MMC-01 and Al MMC-02, i.e., the values have been increased in comparison to that of pure Al. However, the impact toughness, UFS, and MoE of Al MMC-02 are less than that of Al MMC-01 as shown in Fig. 10 and Fig. 11 due to the insertion of 2.5% ZnO in the metallic matrix being affirmed by SEM images shown in Fig.12.

6.5. Electrical Conductivity

The electrical conductivity of Al composite is different from pure Al. As shown in Figure 13, Al MMC-01 having a composition of 97.5% Al and 2.5% Al_2O_3 nanoparticles has an electrical conductivity of 45.15 % IACS with a standard deviation of 1.29% IACS and Al MMC-02 has a composition of 95% Al and 2.5% Al_2O_3 & 2.5% ZnO nanoparticles has an electrical conductivity of 40.72% IACS with a standard deviation of 1.97% IACS. Both Al MMC-01 and Al MMC-02 possess lower values of electrical conductivity because of the non-conducting Al_2O_3 and ZnO reinforcement materials present in MMCs.
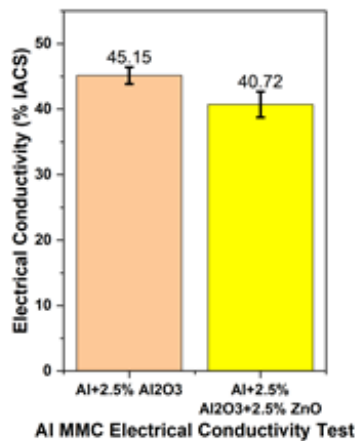

Fig. 13. Electrical Conductivity of developed two Al MMCs

As shown in Fig. 13, the electrical conductivity is observed to be reduced by 9.81% from Al MMC-01 to Al MMC-02 due to the addition of 2.5% ZnO as reinforcement particles change the crystal structure of the metal matrix. Though it is not desirable in some aerospace applications, however, there are many other applications such as heat sinks, bearings, etc.

As the Al MMCs are developed with Al_2O_3 and ZnO reinforcement particles, the electrical conductivity typically decreases. This can be attributed to several factors such as the Insulating nature of nanoparticles, increased scattering of electrons, reduced electron mobility, dilution effect etc.

Both Al_2O_3 and ZnO are ceramic materials that have inherently low electrical conductivity. When these nanoparticles are dispersed within the aluminum matrix, they act as insulating barriers, impeding the flow of electrical current through the composite. Also, the presence

of these nanoparticles creates interfaces and irregularities within the composite structure. As electrons move through the material, they scatter off these interfaces, resulting in increased resistance to the flow of current. This scattering effect further reduces the electrical conductivity of the composite. Thus, the addition of these nanoparticles also disrupts the electron mobility within the composite as these particles introduce grain boundaries, which can impede the movement of electrons. These grain boundaries act as barriers to the free flow of charge carriers, reducing the overall conductivity. It's important to note that the specific impact of nanoparticles on electrical conductivity varies depending on factors such as particle size, distribution, volume fraction, and processing techniques. Different combinations of nanoparticles and matrix materials yield different conductivity behaviors in MMCs. Babalola et al. [49] developed Al MMC with different wt. % of Al_2O_3 and investigated the electrical conductivity. As per their study, it was observed that a similar decreasing pattern of electrical conductivity of samples for each incremental wt. % of reinforcement particles in Al MMC.

6. Conclusion

In the current research, we investigated the effect of nano reinforcement particles Al_2O_3 and ZnO on microstructure and electro-mechanical properties like hardness, impact toughness, flexural strength and electrical conductivity of Al MMC fabricated by customized Two-step stir casting method. The notable outcome and findings of the investigations are summarized as follows:

- Two Al MMCs developed having compositions of 97.5% Al and 2.5% Al_2O_3 (Al MMC-1) and 95% Al, 2.5% Al_2O_3 and 2.5% ZnO (Al MMC-2) by a customized two-step stir casting method with selected process parameters.
- The microstructure observation of specimens determines an almost uniform distribution of Al_2O_3 & ZnO nano particles Al MMC-01 and Al MMC-02 with fewer agglomeration. The selection of process parameters was observed to influence the properties of developed Al MMCs.
- Al MMC-01 has displayed distinct mechanical properties such as flexural strength and impact toughness. Therefore, it can be considered for aircraft parts such as wing ribs, spars, wing-to-fuselage attachment points, control surfaces (i.e., flaps, slats, elevators, and rudders) and structural attachments such as brackets, fasteners, and joints, exposed to bending and flexing forces.
- The inclusion of 2.5% ZnO nano-particles has increased the bulk hardness (Rockwell) and surface hardness (Vickers Micro) of Al MMC-02 by 20% and 41% respectively in comparison with Al MMC-01. However, the flexural strength, impact toughness, modulus of elasticity, and electrical conductivity values of Al MMC-02 were reduced by 12%, 52.5%, 60.8%, and 9.81% in comparison to Al MMC-01 due to the presence of multiple cleavage cracks, deep shear dimples, etc. The presence of these multiple cleavage cracks and deep shear dimples indicate a mode of failure associated with brittle fracture in Al MMC-02. As these characteristics are not desirable for aerospace applications, AL MMC-02 is not getting preference to aerospace applications to meet the required high structural integrity, reliability, and fatigue resistance in aerospace applications.

Acknowledgements

References

[1] Miracle DB, Donaldson SL. Introduction to Composites. ASM Hand Book of Composite Materials. 2017;21. ASM International, USA.

[2] Mavhungu ST, Akinlabi ET, Onitiri MA, Varachia FM. Aluminum Matrix Composites for Industrial Use: Advances and Trends. Procedia Manufacturing. 2017;7:178-182. https://doi.org/10.1016/j.promfg.2016.12.045

[3] Sharma AK, Bhandari R, Bretotean CP. A systematic overview on fabrication aspects and methods of aluminum metal matrix composites. Materials Today: Proceedings. 2021;45(5):4133-4138. ISSN 2214-7853. https://doi.org/10.1016/j.matpr.2020.11.899

[4] Efzan MNE, Syazwani NS, Mustafa Al Bakri AM. Fabrication Method of Aluminum Matrix Composite (AMCs): A Review. Key Engineering Materials. 2016;700:102-110. https://doi.org/10.4028/www.scientific.net/KEM.700.102

[5] Hynes NRJ, Kumar R, Tharmaraj R, Shenbaga Velu P. Production of aluminium metal matrix composites by liquid processing methods. AIP Conference Proceedings. 2016;1728:020558. https://doi.org/10.1063/1.4946609

[6] Aynalem GF. Processing Methods and Mechanical Properties of Aluminium Matrix Composites. Advances in Materials Science and Engineering. 2020;20. https://doi.org/10.1155/2020/3765791

[7] Kumar KV, Jayahari L. Study of mechanical properties and wear behaviour of aluminium 6063 matrix composites reinforced with steel machining chips. Materials Today: Proceedings. 2018;5(9):20285-2029. https://doi.org/10.1016/j.matpr.2018.06.400

[8] Naher S, Brabazon D, Looney L. Computational and experimental analysis of particulate distribution during Al-SiC MMC fabrication. Composites Part A: Applied Science and Manufacturing. 2007;38(3):719-729. https://doi.org/10.1016/j.compositesa.2006.09.009

[9] Ayar VS, Sutaria MP. Development and Characterization of In Situ AlSi5Cu3/ TiB2 Composites. Inter Metalcast. 2020;14:59-68. https://doi.org/10.1007/s40962-019-00328-x

[10] Nirala, Soren S, Kumar N, Kaushal DR. A comprehensive review on mechanical properties of Al-B4C stir casting fabricated composite. Materials Today: Proceedings. 2020;21:1432-1435. https://doi.org/10.1016/j.matpr.2019.09.172

[11] Nirala, Soren S, Kumar N, Dwivedi VK, Kaushal DR. A comprehensive review on stir cast Al-SiC composite. Materials Today: Proceedings. 2020;21:1610-1614. https://doi.org/10.1016/j.matpr.2019.11.240

[12] Reddy R, Srinivas C. Fabrication and characterization of silicon carbide and fly ash reinforced aluminium metal matrix hybrid composites. Materials Today: Proceedings. 2018;5(2):8374-8381. https://doi.org/10.1016/j.matpr.2017.11.531

[13] Gopalakrishnan S, Murugan N. Production and wear characterisation of AA 6061 matrix titanium carbide particulate reinforced composite by enhanced stir casting method. Composites Part B: Engineering. 2012;43(2):302-308. https://doi.org/10.1016/j.compositesb.2011.08.049

[14] Hashim J, Looney L, Hashmi MSJ. Metal matrix composites: production by the stir casting method. Journal of Materials Processing Technology. 1999;92-93:1-7. https://doi.org/10.1016/S0924-0136(99)00118-1

[15] Hashim J, Looney L, Hashmi MSJ. Particle distribution in cast metal matrix composites-Part I. Journal of Materials Processing Technology. 2002;123(2):251-257. https://doi.org/10.1016/S0924-0136(02)00098-5

[16] Hashim J, Looney L, Hashmi MSJ. The enhancement of wettability of SiC particles in cast aluminium matrix composites. Journal of Materials Processing Technology. 2001;119(1-3):329-335. https://doi.org/10.1016/S0924-0136(01)00919-0

[17] Mehta VR, Sutaria MP. Investigation on the Effect of Stirring Process Parameters on the Dispersion of SiC Particles Inside Melting Crucible. Metallurgical and Materials Transactions B. 2020:1-14. https://doi.org/10.1007/s12540-020-00612-0

[18] Singh S, Singh I, Dvivedi A. Design and development of novel cost-effective casting route for production of metal matrix composites (MMCs). International Journal of Cast Metals Research. 2017;30(6):356-364. https://doi.org/10.1080/13640461.2017.1323605

[19] Naher S, Brabazon D, Looney L. Simulation of the stir casting process. Journal of Materials Processing Technology. 2003;143-144:567-571. https://doi.org/10.1016/S0924-0136(03)00368-6

[20] Sakthivelu S, Sethusundaram PP, Meignanamoorthy M, Ravichandran M. Synthesis of Metal Matrix Composites through Stir Casting Process-a Review. Mechanics and Mechanical Engineering. 2018;22(1):351-363. https://doi.org/10.2478/mme-2018-0029

[21] Surappa MK. Aluminium matrix composites: Challenges and opportunities. Sadhana. 2017;28(Parts 1 & 2):319-334. https://doi.org/10.1007/BF02717141

[22] Bhoi NK, Singh H, Pratap S. Developments in the aluminum metal matrix composites reinforced by micro/nano particles - A review. Journal of Composite Materials. 2019. https://doi.org/10.1177/0021998319865307

[23] Saravanan K, Subramanian K, Ananda Krishnan V, Sankara Narayanan R. Effect of Particulate Reinforced Aluminium Metal Matrix Composite - A Review. Mechanics and Mechanical Engineering. 2015;19(1):23-30.

[24] Yuan Z, Li F, Zhang P, Chen B, Xue F. Mechanical properties study of particles reinforced aluminum matrix composites by micro-indentation experiments. Chinese Journal of Aeronautics. 2014;27(2):397-406. https://doi.org/10.1016/j.cja.2014.02.010

[25] Kok M. Production and mechanical properties of Al2O3 particle-reinforced 2024 aluminium alloy composites. Journal of Materials Processing Technology. 2005;161:381-387. https://doi.org/10.1016/j.jmatprotec.2004.07.068

[26] Pilania G, Thijsse BJ, Hoagland RG, Laziä I, Valone SM, Liu XY. Revisiting the Al/Al2O3 interface: coherent interfaces and misfit accommodation. Scientific Reports. 2014;4:1-9. https://doi.org/10.1038/srep04485

[27] Aybarç U, Ertugrul O, Seydibeyoğlu M. Effect of Al2O3 Particle Size on Mechanical Properties of Ultrasonic-Assisted Stir-Casted Al A356 Matrix Composites.

[28] Akbari M, Asadi P, Asiabaraki HR. Investigation of Wear and Microstructural Properties of A356/TiC Composites Fabricated by FSP. Surface Review and Letters. 2022;29(10):2250130. https://doi.org/10.1142/S0218625X2250130X

[29] Kandpa BC, Kumar J, Singh H. Fabrication and characterisation of Al2O3/aluminium alloy 6061 composites fabricated by Stir casting. Materials Today: Proceedings. 2017;4(2):2783-2792. https://doi.org/10.1016/j.matpr.2017.02.157

[30] Jasim H, Joudi WM, Radhi NS, Saud AN. Mechanical Properties and Wear Characteristic of (Aluminum-Zinc Oxide) Metal Matrix Composite Prepared Using Stir Casting Process. Materials Science Forum. 2020;1002:175-184. https://doi.org/10.4028/www.scientific.net/MSF.1002.175

[31] Aqida SN, Ghazali MI, Hashim J. The effects of stirring speed and reinforcement particles on porosity formation in cast MMC. Jurnal Mekanikal. 2003;16:22-30. ISSN 0127-3396.

[32] Mathur S, Barnawal A. Effect of Process Parameter of Stir Casting on Metal Matrix Composites. International Journal of Science and Research (IJSR). 2013;2(12).

[33] Kumar R, Parshuram M. Preparation of Aluminum Matrix Composite by Using Stir Casting Method. IJEAT. 2013;Vol-3.

[34] Sozhamannan GG, Prabu SB, Venkatagalapathy VSK. Effect of Processing Parameters on Metal Matrix Composites: Stir Casting Process. Journal of Surface Engineered

Materials and Advanced Technology. 2012;2:11-15. https://doi.org/10.4236/jsemat.2012.21002

[35] Saravanakumar P, Soundararajan R, Deepavasanth PS, Parthasarathi N. A review on effect of reinforcement and squeeze casting process parameters on mechanical properties of aluminium matrix composites. Int. J. Innov. Res. Sci. Eng. Technol. 2016;5:58-63.

[36] Kumar R, Singh C, Chaudhary R. Recent progress in production of metal matrix composites by stir casting process: An overview. Materials Today: Proceedings.

[37] Seo YH, Kang CG. The effect of applied pressure on particle-dispersion characteristics and mechanical properties in melt-stirring squeeze-cast SiCp/Al composites. Journal of Materials Processing Technology. 1995;55:370-379. https://doi.org/10.1016/0924-0136(95)02033-0

[38] Singla M, Dwivedi D, Singh L, Chawla V. Development of aluminum-based silicon carbide particulate metal matrix composite. J. Miner. Mater. Character. Eng. 2009;8:455-467. https://doi.org/10.4236/jmmce.2009.86040

[39] El-Wazery MS, Elsad RA, Khafagy SM, et al. Enhancement of microstructure and mechanical properties of hypereutectic Al-16%Si alloy by ZnO nanocrystallites. Appl. Phys. A. 2018;124:736. https://doi.org/10.1007/s00339-018-2160-x

[40] Shin JH, Jeon JH, Bae DH. Microstructure refining of aluminum alloys using aluminothermic reaction with ZnO nanoparticles. Mater. Lett. 2015;151:96-99. https://doi.org/10.1016/j.matlet.2015.03.050

[41] Qasim ZS, Jabbar MA, Hassan JJ. Enhancement the mechanical properties of aluminum casting alloys (A356) by adding nanorods structures from zinc oxide. J Mater. Sci. Eng. 2017;6(2):2-5.

[42] Verma R, Sharma S, Kumar D. Analysis of Mechanical Properties of Aluminium Based Metal Matrix Composites Reinforced with Alumina and SiC. International Journal of Engineering Research & Technology (IJERT). 2017;6(03). https://doi.org/10.17577/IJERTV6IS030506

[43] Samal P, Vundavilli PR. Investigation of impact performance of aluminum metal matrix composites by stir casting. ICAMME 2019, IOP Conf. Series: Materials Science and Engineering. 2019;653:012047. https://doi.org/10.1088/1757-899X/653/1/012047

[44] Saravanakumar P, Sasikumar P. Flexural behavior and Microstructure of hybrid Metal Matrix Composites. J. Mater. Environ. Sci. 2018;9(10):2951-2955.

[45] Sadooghi A, Hashemi SJ. Investigating the influence of ZnO, CuO, Al2O3 reinforcing nanoparticles on strength and wearing properties of Aluminum matrix nanocomposites produced by powder metallurgy process. Materials Research Express.

[46] Sadeghi B, Shamanian M, Ashrafizadeh F, Cavaliere P, Rizzo A. Friction stir processing of spark plasma sintered aluminum matrix composites with bimodal micro- and nano-sized reinforcing Al2O3 particles. Journal of Manufacturing Processes. 2018;32:412-424. https://doi.org/10.1016/j.jmapro.2018.03.013

[47] Ammar HR, Samuel AM, Samuel FH, Simielli E, Sigworth GK, Lin JC. Influence of Aging Parameters on the Tensile Properties and Quality Index of Al-9 Pct Si-1.8 Pct Cu-0.5 Pct Mg 354-Type Casting Alloys. Metallurgical and Materials Transactions A. 2012;43:61-73. https://doi.org/10.1007/s11661-011-0808-7

[48] Bakshi SR, Agarwal A. An analysis of the factors affecting strengthening in carbon nanotube reinforced aluminum composites. Carbon. 2011;49:533-544. https://doi.org/10.1016/j.carbon.2010.09.054

[49] Babalola PO, Kilanko O, Banjo SO, Ogulu JO, Makinde A, Jolayemi JK, Ayara WA. Reinforcement of AA1237 with Al2O3 to form Metal Matrix Composite. International Conference on Engineering for Sustainable World, ICESW. 2020. https://doi.org/10.1088/1757-899X/1107/1/012006

Synthesis, microstructure and tensile characterization of B4C particulates reinforced Al7085 alloy aerospace composites

Hemanth Kumar M.[1,a], R. Saravanan[1,b], Madeva Nagaral[2,c], Samuel Dayanand[3,d], V. Auradi[4,e]

[1]Dept. of Mechanical Eng., University Visvesvaraya College of Engineering, Bangalore University, India
[2]Aircraft Research and Design Centre, HAL, India
[3]Dept. of Mechanical Eng., Government Engineering College, India
[4]Dept.of Mechanical Eng., Siddaganga Institute of Technology, India

Article Info	Abstract
	In the current studies microstructure and mechanical behavior of Al7085 metal alloy with 4 and 8 wt. % of B4C composites. Liquid metallurgy method was used to create composites of Al7085 alloy with 4 and 8 weight percent of B4C particles. Microstructural analysis by SEM/EDS was performed on the prepared composites. Furthermore, ASTM E8 and E10 standards were used to examine the tensile and hardness properties of Al7475 alloy reinforced with B4C composites. The SEM analysis revealed that the particles were uniformly dispersed throughout the base alloy. EDS spectrums confirmed the reinforcement particles presence in the Al7085 alloy in the form of boron and carbon elements. Moreover, the incorporation of B4C particles into Al7085 alloy has enhanced the material's mechanical behavior. The hardness and tensile strength of Al7085 alloy was improved 27.59% and 35.91% respectively with the combination of boron carbide particles. After boron carbide particles were added to Al7085, the alloy lost some of its ductility and density. The prepared composites were then subjected to tensile fractured surfaces to investigate ductile and brittle modes of fracture.

1. Introduction

Ceramic particle reinforcement of aluminium alloys is a solution to the problem that standard aluminium alloys don't give the necessary characteristics under all service situations. AMCs [1-3] are the common name for these aluminium alloys with reinforcements. The acronym "AMC" (aluminium metal composite) describes a group of aluminum-based materials that are both lightweight and high-performing. The metal matrix composites currently use aluminium as one of the most common matrices [4]. Due to their high specific strength and stiffness and outstanding wear resistance, AMCs have garnered a lot of attention over the past three decades, even among metal matrix composites. Aerospace, automotive, marine, and other industries frequently employ AMCs. Increased strength, high specific modules, improved stiffness, low thermal expansion coefficients, high thermal conductivity, tunable electrical properties, increased wear resistance, and improved damping capabilities [5] are just a few of the benefits of using particles reinforced AMC's materials rather than unreinforced ones.

*Corresponding author: madev.nagaral@gmail.com
[a] orcid.org/0009-0002-8953-7594; [b] orcid.org/0000-0001-7213-26257; [c] orcid.org/0000-0002-8248-7603; [d] orcid.org/0000-0001-5279-3522, [e] orcid.org/0000-0001-6549-6340

Improved wear resistance, high strength qualities, suitable sliding characteristics, resistance to thermal shocks and fatigue phenomena, and a decreased final product weight are all characteristics of composite materials in relation to the matrix, depending on the specific application. Therefore, the technological features of the composite, as well as the costs of its production and the ecological aspect of the product, all play a role in determining the scope of application of composites reinforced with hard ceramic particles [6, 7].

Due to their high specific strength and stiffness, aluminum alloys are a promising material among the several matrix materials now accessible. However, their usefulness is limited by their low resistance to wear. Particulate reinforced aluminum matrix composites have achieved widespread use in the automotive and aerospace industries as a result of their superior mechanical and tribological qualities compared to those of traditional alloys. Affordable Al-based MMCs with hard and soft reinforcements including SiC, Al_2O_3, B_4C, Zircon, Tungsten Carbide, Graphite, and Mica have been a primary focus of research and development [8, 9].

Reinforcement in MMCs serves primarily as a load carrier, with the matrix acting as a binding agent and a means by which external loads are transmitted and distributed to the individual reinforcement [10]. In order to transfer and distribute load from the matrix to the reinforcements without failure, good wetting is a necessary condition for the creation of a successful bond between particle reinforcements and liquid Al metal matrix during casting composites [11].

Ceramic particles have been shown to improve mechanical and other properties of aluminum alloy by serving as reinforcing materials. Ceramic reinforcements are commonly used in MMCs, and can be broadly classified into two categories: continuous and discontinuous. They are known as continuously (fibre) reinforced composites and discontinuously (fibre) reinforced composites, respectively, for the MMCs they yield [12, 13]. Continuous fibres, short fibres (chopped fibres, not always the same length), whiskers, particle, and wire (only for metal) are the five main groups into which they can be further classified. Reinforcements, with the exception of wires, are typically made of ceramics, specifically oxides, carbides, and nitrides. These are put to use because they combine excellent strength and stiffness in both cold and hot conditions.

Stir casting, squeeze casting, liquid metal infiltration, and spray co-deposition are just some of the cutting-edge manufacturing methods that were used in the production of MMC materials [14]. The simplest and most cost-effective method is the 'vortex technique' or 'stir casting technique,' which is appealing due to its simplicity, low processing cost, flexibility, and being the most cost-effective method for preparing large sized components and producing near net shaped components. Chen et al. [15] looked at the AA6061-B4C composites made with the friction stir weld technique. Mechanical characteristics and microstructure of AA6061-B4C composites were studied as well. Scanning electron microscopy was utilized to look at how the B_4C particles were distributed throughout the AA6061 matrix. Mechanical characterization of stir cast LM24-B_4C composites was investigated by Keshav Singh [16]. The ultimate tensile strength of LM24 alloys rises at 3, 5, and 7 wt.% of B4C particles. The effect of adding boron carbide particles of 40- and 90-micron size on the mechanical behaviour of A356 composites was studied by Zeeshan Ali et al. [17]. Composites of A356 alloy with 3 wt.% of 40- and 90-micron boron carbide pares were made by a standard stir casting procedure. As cast A356 combination composites with 3 wt% B_4C composites (40 & 90 μm) were also examined for their mechanical conduct. Particles in the A356 composite were found to be uniformly dispersed across the microstructure. The analysis revealed that the presence of B_4C particles in the composite increased the composite's hardness, UTS, and YS.

Moreover, the reinforcement's size and form play a crucial influence in improving the characteristics of metal matrix composites. Grain refinement and improvement of characteristics are also the result of secondary operations including rolling, shaping, and extruding.

Aluminum-boron carbide composites serve an important purpose due to the rising need for lightweight materials in cutting-edge industrial applications. In light of these findings, it is suggested that Al7085 alloy composites containing micro-particle-sized B_4C particulates and varied B_4C weight percentages be developed. Mechanical characteristics of Al7085-B_4C micro composites will be studied using ASTM protocols.

2. Materials and Methods

2.1. Materials Used

Aluminum alloy Al7085 also known as Al-Cu alloy (Procured at Fenfe Metallurgical, Bangalore) was adopted as base matrix metal because of its outstanding castability, fluidity, weldability and ability to counteract corrosion. The following image (Fig. 1) shows the Al7085 ingot procured from Fenfe Metallurgicals, Bangalore, which was used to develop composite material by melting it down and adding reinforcement.

Fig. 1. Ingot of Al7085 alloy used to prepare the composites

The Table 1 shows Al7085 alloy chemistry of selected as matrix in the current study.

Table 1. Chemical composition of Al7085 alloy

Elements (wt. %)	A7085 (actual)
Si	0.05
Fe	0.08
Cu	1.90
Mg	1.80
Cr	0.04
Zn	7.85
Ti	0.06
Mn	0.04
Al	Balance

Some important physical, mechanical and thermal properties of Al7085 alloy is listed in the Table 2.

Table 2. Properties of Al7085 alloy

Density (g/cc)	2.85
Melting point (°C)	660
Poisson's Ratio	0.33
Modulus of Elasticity (GPa)	70-80
Hardness (HV)	65
Tensile Strength (MPa)	180-190
Co-efficient of Thermal Expansion μm/m°C	24.3
Thermal Conductivity W/mK	190

Boron carbide (B_4C) is a very hard ceramic made by synthetically combining boron and carbon; it is the third hardest significant material, after cubic boron nitride (CBN) and diamond, and is used as an abrasive material and to fight wear. The material's exceptional hardness and low density make it ideal for usage as particles in aluminum matrix alloy to create composition material. In the present work B_4C particulates with 10 μm were used which was purchased from Speed Fam India Pvt. Ltd., Chennai. Fig. 2 is representing B_4C particles and Table 3 showing the typical properties of B_4C.
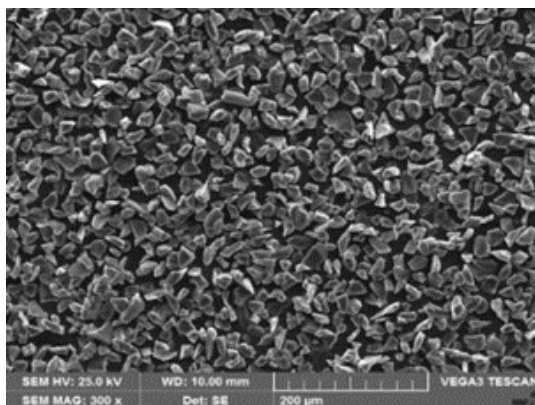

Fig. 2. Scanning electron microphotographs of 10-micron B_4C particles

Table 3. Typical properties of B_4C

Properties	Boron Carbide
Melting point	2445°C
Hardness (BHN)	2900-3580
Density (g/cm3)	2.52
Coefficient of thermal expansion (10-6 °C)	5
Fracture toughness (MPa-m1/2)	2.9 – 3.7
Poisson's ratio	0.21
Color	Black

2.2. Preparation of Composites

The stir casting process is well-known as a very promising route for producing near-net-shape hybrid metal matrix composite components at a normal cost, and it is one of the most often used liquid metallurgical route methods. In this study, we employed a stir casting technique to create Al7085 containing between 4% and 8% B_4C particulate MMCs with a size of 10 microns. In this investigation, Al7085 alloy serves as the matrix material. Composites were made using B_4C particles that were 10 microns in size. The Al7085 alloy was superheated to a temperature of 750°C in an electrical resistance furnace after being charged into a graphite crucible. Using a digital temperature controller, we were able to maintain a temperature tolerance of 10°C in the boiler.

Fig. 4. Cast iron die

Fig. 5. Al7085 alloy -B_4C composites after casting

Table 4. List of various composites prepared

Matrix	Reinforcement	Compositions of composites prepared
Al7085	B_4C	Al7085-4 wt. % of B_4C composites
Al7085	B_4C	Al7085-8 wt. % of B_4C composites

An innovative two-stage mixing procedure is used, and the reinforcing particles are preheated as well. To remove the adsorbed gases from the particle surface and to prevent a high drop in temperature after adding the particulates, ceramic B_4C particles were warmed in an oven to 300°C. After the molten alloy was effectively degassed with solid hexachloroethane (C_2Cl_6) [18], B_4C particles were injected into the vortex. A zirconia-coated steel impeller was used to create the vortex. Mechanical stirring was performed for 5 minutes at each stage before and after reinforcement was added. The stirrer, which was heated before being submerged in the molten metal, is placed about two-thirds of the way up from the bottom of the vessel and rotates at a rate of three hundred revolutions per minute. The composite material was poured into the cast iron, making it permanent.

Al7085-B$_4$C composites were prepared by using micro B$_4$C particulates and varying percentages like 4 and 8 wt. %. Cast iron die used for the study is shown in Fig. 4. Fig. 5 is showing the Al7085 ally and B$_4$C composites after casting. Table 4 indicates the various composites prepared in the current research.

2.3. Testing of Composites

The composite casting used in this study was cut into multiple pieces from various locations, and then polished at low speed using polishing materials made of abrasive particles less than 3 microns in size. Scratches on the surface of composites were eliminated through polishing. Polishing was accomplished using films composed of abrasive SiC and Al$_2$O$_3$. A fine microstructure can only be achieved with the help of high-quality abrasive films and polishing cloth. To improve the optical visibility of microstructural features including phase features and grain size, the polished material was etched using Kellar's reagent (HCl+ HF+ HNO$_3$+ H$_2$O). Kellar's reagent was applied to the cleaned and polished surface with cotton swabs soaked in etchant, employing light, rotating motions to ensure even distribution of the reagent. After drying, the etched surface was cleaned with rubbing alcohol. The features of the etched surface of the dried specimen were examined using a scanning electron microscope (SEM) and an energy dispersive spectrometer.

The ASTM D792 method is used to determine density, with standard test pieces of 12 mm in diameter and 30 mm in length (within 0.15 mm of each end). To estimate mass, we soak the sample in distilled water at room temperature and use a digital balance with a resolution of 0.001 g. The density of a composite can be evaluated empirically with the help of a physical offset and instruments that have been calibrated in line with ASTM: D792-66.

Brinell hardness testing according to ASTM E10 [19] norms is used in this research. The Brinell test is used when a material's surface is too rough for a standard hardness tester. The hardness of as cast Al7085 alloy and Al7085 alloy with B$_4$C particles reinforced composites was measured using a 5 mm ball indenter and a load of 250 kgf applied at a dwell duration of 30 seconds in different spots on each sample composite.

A universal testing machine (UTM) that complies with ASTM E8 [20] is used for the tension test. Under precise conditions, the sample is stretched to the point of failure. Tensile testing, while destructive, can reveal useful information about a material's strength and pliability. The results of this test reveal crucial details, such as the metal's tensile strength. The goal of a tension test is to locate the breaking point of a material when subjected to a high level of tension. This technique can be used to calculate the safety factor of a material and the most force that can be applied to it before it breaks. Additionally, it helps engineers choose which materials are most suited for a project.

Fig. 6. Tensile test specimen

Uni-axial tensile testing was performed on specimens that had been prepared in accordance with ASTM E8 requirements for tension testing. The 9 mm diameter circular specimen was made with a 45 mm gauge length. Fig. 6 shows a cutaway view of the tensile test specimen. Instron's servo-hydraulic machine with a cross head speed of 0.28 mm/min

was used to conduct the tensile test on the specimen. Composite samples undergo testing at room temperature.

3. Results and Discussion

3.1. Microstructural Analysis

The microstructure properties of the sample are examined by SEM. Fig. 6 (a-c) shows SEM images of Al7085 alloy and micro B_4C reinforced composite. Fig. 6 (a) shows the SEM of a pure Al7085 alloy. Figure 6 (b-c) shows Al7085-4 wt. % and Al7085-8 wt. % of boron carbide composites. These figures also show the uniformity of the composite material produced.
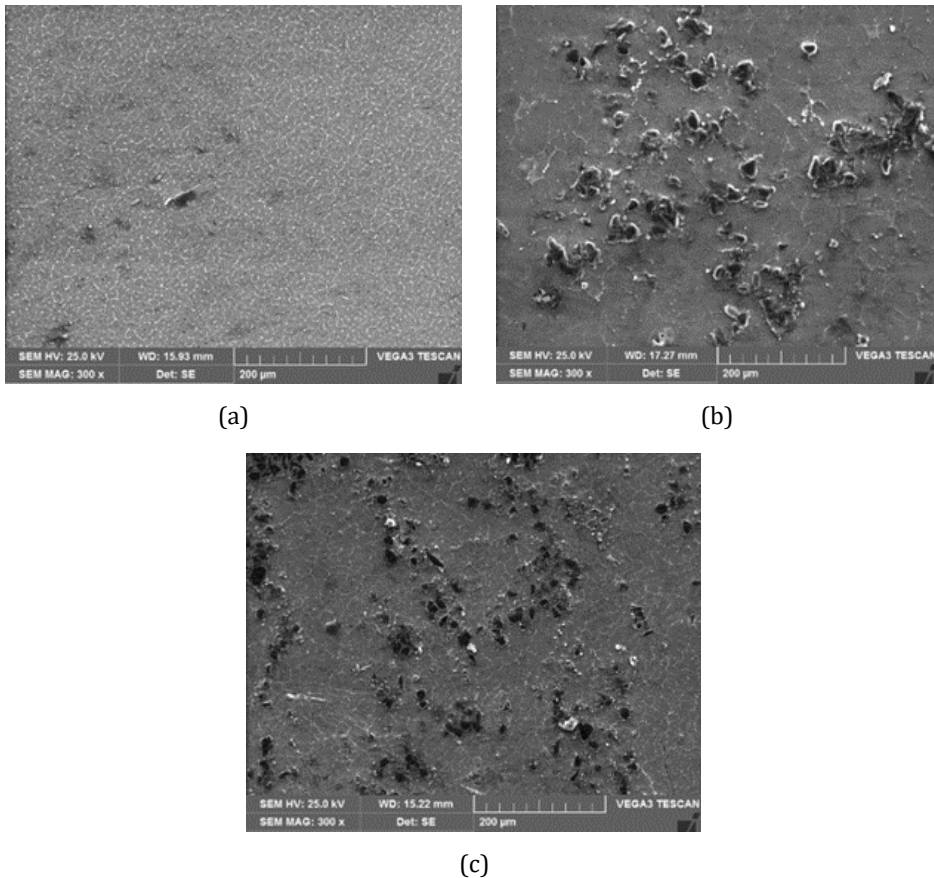

(a)   (b)

(c)

Fig. 6. Scanning electron microphotographs of (a) as cast Al7085 alloy (b) Al7085-4% B4C (c) Al7085-8% B4C composites

The scanning electron microscopy (SEM) of as cast Al7085 alloy shows that the material is completely free of particles because it is not reinforced. Given that zinc is the primary alloying component in Al7085, the matrix displays a characteristic leafy structure that is indicative of zinc's presence. Additionally, the homogeneity of the B_4C particles in the finished composites is shown in Fig. 6 (b-c). Micrographs also show how the composites of Al7085 alloys have far more reinforcement than their initial designs did. As can be observed in Fig. 6 (c), the microstructure of the composite has been greatly enhanced by the addition of 8 wt.% of 10-micron sized B_4C to the Al7085 alloy matrix in two separate

steps. Also, a close inspection of Figure 6 (b-c) reveals that the B_4C particles are easily distinguishable, indicating strong bonds between the Al7085 alloys.

EDS is one of the influential and valuable techniques for identifying elements and their relative proportion presence [21]. Although it is possible to determine which elements are present in a sample through chemical analysis, the percentages assigned to those elements cannot be determined with great precision without the help of EDS. Elements in Al7085 alloy and Al7085 with 4 and 8 wt.% of 10 µm B_4C composites are analyzed using EDS.

(a)
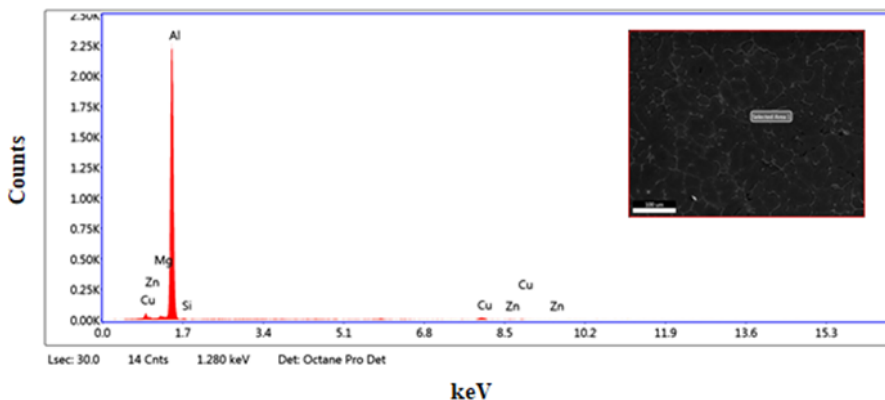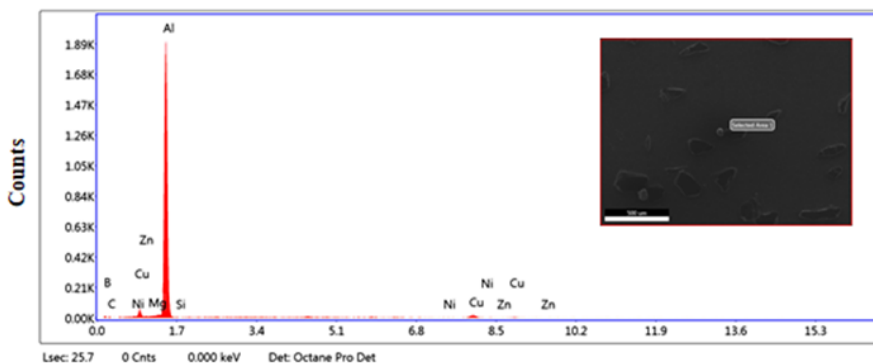
(b)

Fig. 7. EDS spectrums of (a) as cast Al7085 alloy (b) Al7085-8% B_4C composites

Figures 7 (a-b) display EDS spectrographs of Al7085 supplemented with boron carbide particles of 10 micron size, at 8 weight percent. Al and Zn are shown in Fig 7 (a); Zn is the principal alloying constituent in the Al 7XXX series alloys. The presence of boron carbide particles in the produced Al7085 with B_4C composites is further demonstrated by the presence of boron (B) and carbon (C) components alongside the Al peaks (Fig. 7b).

3.2. Density Measurements

The theoretical and experimental values obtained for of as cast Al7085 and Al7085 with varying wt. % of B_4C particles composites are detailed in Fig. 8. The calculated theoretical values are close to the values obtained via the experimental method, and it is anticipated

that the experimental values will be close to the theoretical values in this study. Due to the standardization of methods used to calculate theoretical values, it is extremely unlikely that experimental values will match those predicted by theory. If we look at Fig. 8, we can see that the density of Al7085 alloy decreases as the percentage of micron-sized B_4C increases from 4 to 8 wt.%. This decrease in density is due to presence of low density materials in the Al27085 alloy. The density of base matrix Al7085 alloy is 2.85 g/cm³, but the densities of B_4C reinforcements are 2.52 g/cm³ [22]. Due to the effect of lower densities materials addition in the Al7085 alloy contributed in decreasing the theoretical densities of the composites to 2.82 g/cm³ with the addition of 8 wt. % of boron carbide particles in the Al7085 alloy. Further, same trend has been observed in the case of experimental densities also. Both the theoretical and experimental densities are very close to each other.
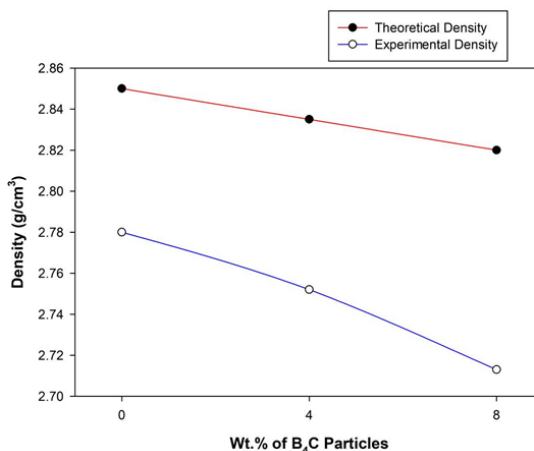

Fig. 8. Comparison of theoretical and experimental densities of Al7085 alloy and B_4C composites

3.3. Hardness Measurements

From the Fig. 9 it can be seen that the hardness of alloy Al7085 increases as the weight percent of B_4C particles increases from 4% to 8% by weight. The hardness of the cast Al7085 alloy is 67.93 BHN. The percentage of B_4C particles increased the hardness of the Al7085 alloy to 92.33 BHN. The hardness improvement of the Al7085 alloy is 35.9% with the addition of 8% by weight. % of B_4C particles. The increased hardness is due to the presence of solid B_4C particles that act as obstacles to the movement of dislocations within the Al7085 matrix. Usually, after the addition of fine particles, the strain energy at the edges of the B_4C particles increases, this increases the hardness of the composite. The same observations can be found in the studies of other researchers.

Other researchers have reported similar outcomes, and also it was determined that the improvement in hardness may be caused by the existence of reinforced particles, which make dislocation movement within the base matrix more challenging. The grain refining based on the Hall-Petch process is primarily responsible for the increase in hardness value [23]. Additionally, particles can have a particle strengthening effect, which increases hardness value while preventing dislocations from moving. The kind, size, quantity, and dispersion of ceramic hard ceramic particles all affect how hard something is. The main causes of the sample's greater hardness value are mechanical churning that breaks -Al dendrites and the use of B_4C particles as reinforcements.
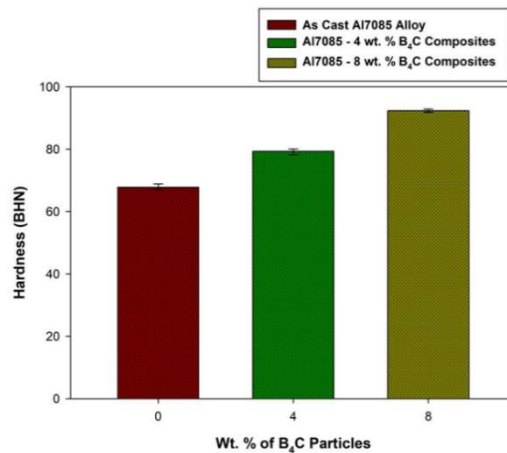
Fig. 9. Hardness of Al7085 alloy and B$_4$C composites

3.4. Tensile Properties

Tensile tests were conducted at room temperature with varying percentages of micro B$_4$C particles, and the findings are displayed in Fig. 10. Figure 10 show that when B$_4$C content in Al7085 alloy rises, so does the average UTS value. The Al7085 matrix alloy is protected from damage by the tiny B$_4$C particle. Al7085 alloy has a UTS of 211.97 MPa when cast.
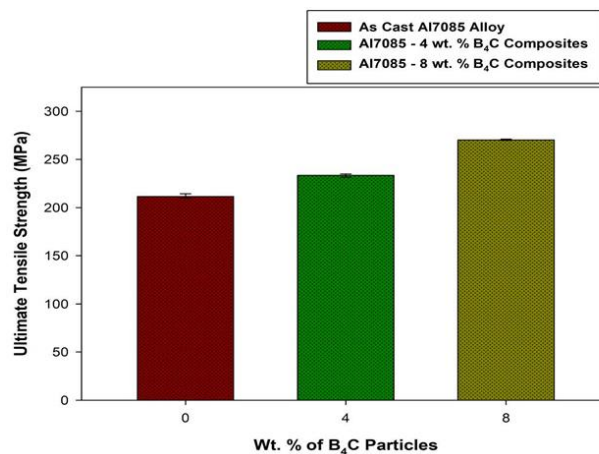
Fig. 10. Ultimate tensile strength of Al7085 alloy and B$_4$C composites

Furthermore, as shown in Fig. 10, the UTS values increased as the weight percentage of micro B$_4$C particles was increased from 4 to 8 wt.% insteps of 4 wt.%. The UTS value of B$_4$C composites in Al7085 alloy at 4 wt. % is measured to be 233.27 MPa. After 8 wt. % of micro B$_4$C particles were added to Al7085 alloy, the ultimate strength of the material increased by 27.5%. The difference in thermal co-efficient of expansion between the Al7085 matrix alloy and the uniformly dispersed micro B$_4$C particles contributes to an increase in ultimate strength of the alloy following integration of 4 and 8 wt.% of B$_4$C particles [24]. By interacting with dislocations, the addition of non-shearable tiny boron carbide particles raise the strength of Al7085 alloy from 4 to 8 wt. %.

Fig. 11. Yield strength of Al7085 alloy and B₄C composites

From the Fig. 11 the yield strength of the Al7085 alloy is enhanced with the addition of B₄C particles. As the wt. % of B4C particles increases from 4 wt. % to 8 wt. %, there is an increase in the yield strength of Al7085 alloy. The YS of as cast Al7085 alloy is 181.7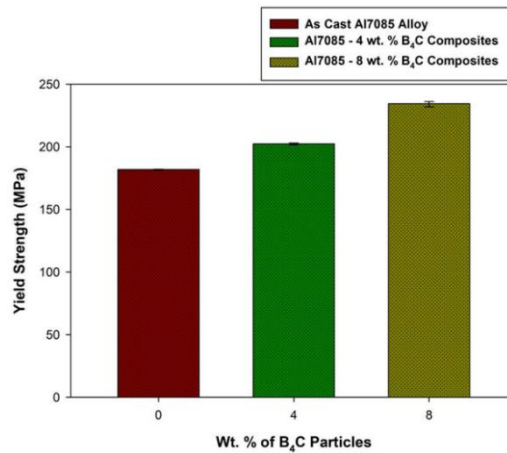7MPa, this strength is increased to 202.17 MPa and 234.03 MPa respectively in 4 and 8 weight % of B₄C reinforced composites. Similar kinds of observations were made by other authors [25] with the incorporation of B₄C particles in the Al alloy matrix. In the case of Al7085 – 8wt. % of B₄C reinforced composites, the improvement in the yield strength is 28.7%. The improvement in yield strength is demonstrated by the hard B₄C particles. This adds value to the framework mixture in this way by giving it better solid stiffness.
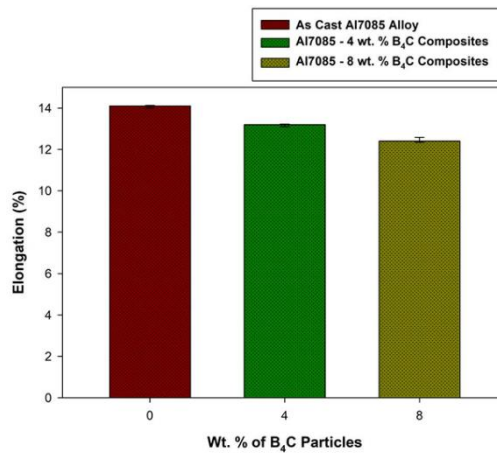
Fig. 12. Elongation of Al7085 alloy and B₄C composites

The expansion of these hard particles may have resulted in a tremendous persistent compression failure created with cementation due to the contrast of the evolving coefficients between the flexible matrix and the brittle particles. The improved quality is also due to the tight packing of the stiffeners and therefore the small spacing between the particles in the grid [26].

The influence of B₄C particles on the ductility of Al7085 alloy and its composites is shown in Fig. 12. The material tends to lengthen when an axial load is applied to a specimen.

Elongation is calculated in tensile testing by comparing the gauge length of the specimen before and after it cracks. A larger percentage of elongation indicates greater ductility, and elongation is typically represented as a percentage of the specimen's original length [27]. Tensile testing results are shown in Fig. 12 for as cast Al7085 alloy, Al7085 alloy with 4 wt.% of B_4C particulates composites, and Al7085 alloy with 8 wt.% of B_4C particulates composites. After B_4C particles are added to as cast Al7085 alloy, the percentage elongation decreases; further reductions occur as the weight percentage of reinforcement increases in Al7085 alloy.

3.5. Tensile Fractography

Fractured SEM surfaces of Al7085- B_4C composites at 800X magnification are shown in Figure 13, and broken faces of tensile test samplings of as cast Al7085 and Al7085- B_4C composites are shown in Figures 13a–13c. The purpose of this fracture analysis is to determine how B4C modifies the fracture characteristics of composites.

(a) (b)

(c)

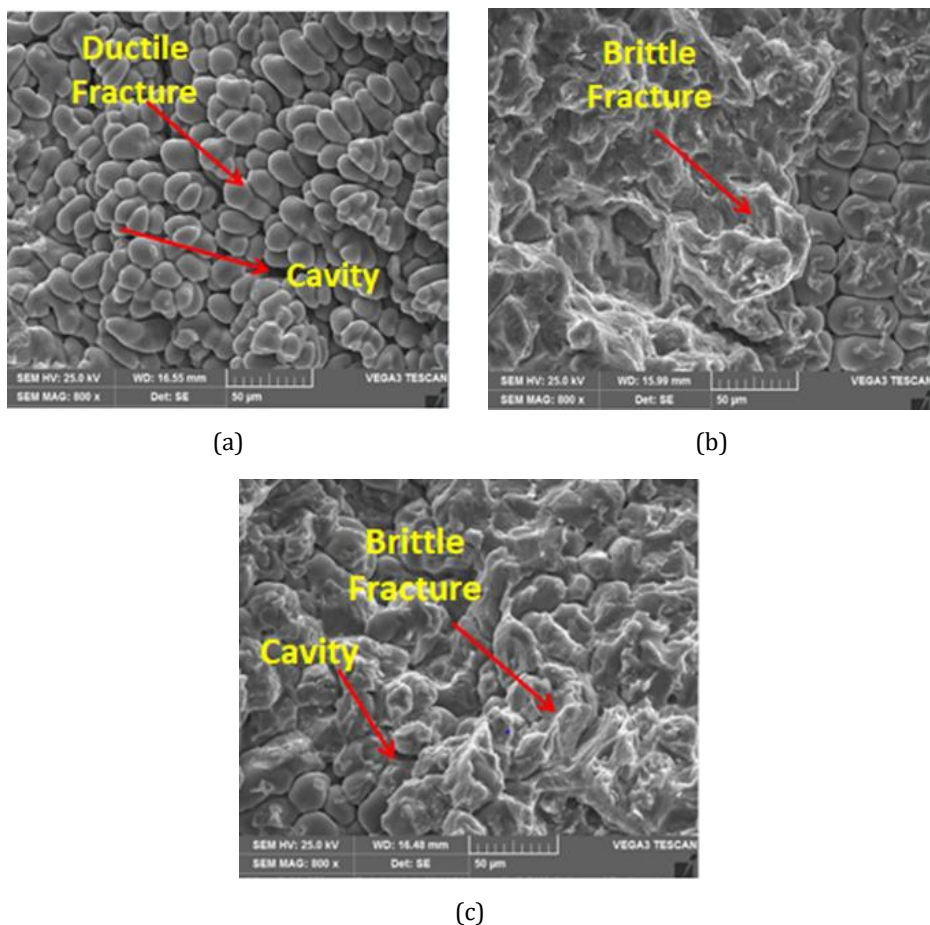Fig. 13. Tensile fractured surfaces of (a) as-cast Al7085 alloy (b) Al7085-4 wt. % B_4C (c) Al7085-8 wt. % B_4C composites

Trans granular and intergranular regions in a fracture of an Al7085 alloy (see Figure 13a) are indicative of brittle fracture. The SEM images in Figure 13 (b-c) are of Al7085- B_4C composites with 4 and 8 wt.% B_4C. Fracture zones show plastic deformation, including

ripped edges and cleavage facets. Dimples in the matrix are visible in some places along composite fracture surfaces.

These dimples may have formed as a result of void nucleation and subsequent coalescence brought on by the extreme shear distortion, fragmentation, and decohesion of B_4C. Perhaps there is some fundamental problem in the matrix. As can be shown in Fig. 13c, the particle-matrix interface functions as intended, as micro fractures did not propagate through the B_4C particle but instead to the matrix via the Al7085- B_4C contact. If dislocations build at the contact because of a load, localized high stress can result. De-bonding at the reinforcement/matrix interface, leading to cracks and dimples [28, 29], occurs when the stress exceeds the interfacial binding forces.

4. Conclusions

The stir cast method is suitable for producing Al7085 alloy with B_4C particles of 10 microns in size and MMCs of 4 and 8 wt. percent. Scanning electron microscopy images show that B_4C particles are evenly dispersed across the Al7085 alloy. This study analyzed the EDS patterns of composites made from Al7085 alloy and B_4C particles at 8 weight percent. The presence of boron and carbon elements in Al7085 alloy with B_4C composites are confirmed by EDS spectrums. The incorporation of B_4C particles reduced the density of Al7085 alloy composites. The lowest density is observed in the Al7085 alloy with 8 wt. % of boron carbide particles reinforced composites. Further, theoretical and experimental densities are very nearer to each other, which indicate the proper casting method of Al7085 alloy and B_4C composites. The hardness of Al7085 alloy has increased with the incorporation of B_4C particles. The highest hardness is observed in the case of Al7085 alloy with 8 wt. % of B_4C composites. Improvements in the hardness of Al7085 alloy with 8 wt. % of B_4C particles is 69.6%. Ultimate and yield strengths of Al7475 alloy have enhanced with the 2 to 10 wt. % of boron carbide particles reinforced addition. Improvements in the UTS and YS with 10 wt. % of B_4C particles in Al7475 alloy is 51.8% and 61.6% respectively. Further, UTS and YS values of as cast Al7475 alloy and its 2 to 10 wt. % of boron carbide composites decreased at elevated 50°C and 100°C. The ductility of Al7475 alloy has been slightly reduced with the incorporation of boron carbide particles in the Al7475 alloy matrix. The ductility has been improved in the case of elevated temperatures as compared to the room temperature experimental values.

References

[1] Sathyashankara Sharma, Achuta Kini, Gowri Shankar, Rakesh TC, Raja H. Tensile fractography of artificially aged Al6061-B4C composites. Journal of Mechanical Engineering and Sciences, 2018; 12, 3: 3866-3875.

[2] Pathalinga Prasad G, Chittappa HC, Nagaral M, Auradi V. Effect of the reinforcement particle size on the compressive strength and impact toughness of LM29 alloy B4C composites. Structural Integrity and Life-interface, 2019; 5,7:231-236.

[3] Suresh S, Shenbaga Vinayaga Moorthi, Vettivel SC, Selvakumar N, Jinu GR. Effect of graphite addition on mechanical behavior of Al6061-TiB2 hybrid composites using acoustic emission. Materials Science and Engineering A, 2014; 612: 16-27. https://doi.org/10.1016/j.msea.2014.06.024

[4] Siddesh Kumar NG, Shivashankar GS, Basavarajappa S, Suresh R. Some studies on mechanical and machining characteristics of Al2219/n-B4C/MoS2 nano hybrid metal matrix composites. Measurement, 2017; 107, 2017:1-11. https://doi.org/10.1016/j.measurement.2017.05.003

[5] Krishna UB, Vasudeva B, Virupaxi Auradi, Madeva Nagaral. Effect of Percentage Variation on Wear Behaviour of Tungsten Carbide and Cobalt Reinforced Al7075

Matrix Composites Synthesized by Melt Stirring Method. Journal of Bio-and Tribo-Corrosion, 2021; 7, 3:1-8. https://doi.org/10.1007/s40735-021-00528-1

[6] Yuling Li, Ramesh KT, Chin ESC. Comparison of the plastic deformation and failure of A359-SiC and 6061-T6-Al2O3 metal matrix composites under dynamic tension. Materials Science and Engineering A, 2004; 371:359-370. https://doi.org/10.1016/j.msea.2004.01.008

[7] Sallahauddin Attar, Madeva Nagaral, Reddappa HN, Auradi V. Effect of B4C particulates addition on wear properties of Al7075 alloy composites. American Journal of Materials Science, 2015; 5, 3C:53-57.

[8] Lu YM, Watanabe R, Miyata J, Nakamura J, Yamada H, Kato KY. Microstructures and mechanical properties of TiC particulate reinforced Ti-Mo-Al intermetallic matrix composites, Materials Science and Engineering A, 2020; 790, 14:139523. https://doi.org/10.1016/j.msea.2020.139523

[9] Clement Tom Scaria, Pugazhenthi R. Effect of process parameter on synthesizing of TiC reinforced Al7075 aluminium alloy nano composites. Materials Today Proceedings, 2021;37, 2: 1978-1981 https://doi.org/10.1016/j.matpr.2020.07.490

[10] Veeresh Kumar GB, Gude Venkatesh Chowdary, Mandadi Surya Vamsi, Jayarami Reddy K, Madeva Nagaral, Naresh K. Effects of addition of Titanium Diboride and Graphite Particulate Reinforcements on Physical, Mechanical and Tribological properties of Al6061 Alloy based Hybrid Metal Matrix Composites. Advances in Materials and Processing Technologies, 2021;1-18. https://doi.org/10.1080/2374068X.2021.1904370

[11] Zulfia A, Putro EC, Wahyudi M, Daneshwara D, Utomo BW. Fabrication and characteristics of ADC-12 reinforced nano SiC and nano Al2O3 composites through stir casting route. IOP Conference Series: Materials Science and Engineering, 2018; 432: 012032. https://doi.org/10.1088/1757-899X/432/1/012032

[12] Anjan Kumar BH, Chaithra Prasanna, Chethana CR, Chandrasekhar Singh Beekam, Latha Shankar Boluvar, Madeva Nagaral, Suresh Rangappa. Synthesis and mechanical characterization of Si3N4 reinforced copper-tin matrix composites. Journal of the Mechanical Behavior of Materials, 2021; 30, 1: 199-206. https://doi.org/10.1515/jmbm-2021-0020

[13] Siddesh Matti, Shivakumar BP, Shashidhar S, Nagaral M. Dry sliding wear behavior of mica, flyash and red mud particles reinforced Al7075 alloy hybrid metal matrix composites. Indian Journal of Science and Technology, 2021; 14,4: 310-318. https://doi.org/10.17485/IJST/v14i4.2081

[14] Pankaj RJ, Madeva Nagaral, Shivakumar Rachoti, Jayasheel IH. Impact of boron carbide and graphite dual particulates addition on wear behavior of A356 alloy metal matrix composites. Journal of Metals, Materials and Minerals, 2020; 30,4: 106-112. https://doi.org/10.55713/jmmm.v30i4.642

[15] Chen HS, Wang WX, Li L, Zhang P, Nie HH, Wu QC. The design, microstructure and tensile properties of B4C particulate reinforced 6061Al neutron absorber composites. Journal of Alloys and Compounds, 2015;632:23-29. https://doi.org/10.1016/j.jallcom.2015.01.048

[16] Keshav Singh, Rana RS, Anjaney Pandey. Fabrication and mechanical properties of aluminium alloy LM24-B4C composites. Materials Today Proceedings, 2017; 4: 701-708. https://doi.org/10.1016/j.matpr.2017.01.075

[17] Zeeshan Ali, Muthuraman V, Rathnakumar P, Gurusamy P, Madeva Nagaral. Studies on mechanical properties of 3 wt. % of 40 and 90 micron size B4C particulates reinforced A356 alloy composites. Materials Today: Proceedings, 2022; 52: 494-499. https://doi.org/10.1016/j.matpr.2021.09.260

[18] Prabhakaran K, James J, Pavithran C. Surface modification of SiC powders by hydrolysed aluminium coating. Journal of European Ceramic Society, 2003; 23: 379-385. https://doi.org/10.1016/S0955-2219(02)00172-3

[19] Ruixiao Zheng, Jing Chen, Yitan Zhang, Kei Ameyama, Chaoli Ma. Fabrication and characterization of hybrid structured Al alloy matrix composites reinforced by high volume fraction of B4C particle., Materials Science and Engineering A, 2014;601: 20-28. https://doi.org/10.1016/j.msea.2014.02.032

[20] Bharath V, Auradi V, Madeva Nagaral, Satish Babu Boppana. Experimental investigations on mechanical and wear behaviour of 2014Al-Al2O3 Composites. Journal of Bio-and Tribo-Corrosion, 2020; 6, 2:1-10. https://doi.org/10.1007/s40735-020-00341-2

[21] Sekar K, Allesu K, Joseph MA. Effect of heat treatment in tribological properties of A356 aluminium alloy reinforced with Al2O3 nano particles by combination effect of stir and squeeze casting method. Applied Mechanics and Materials, 2014; 592-594: 968-971. https://doi.org/10.4028/www.scientific.net/AMM.592-594.968

[22] Madeva Nagaral, Deshapande RG, Auradi V, Satish Babu Boppana, Samuel Dayanand, Anilkumar MR. Mechanical and wear characterization of ceramic boron carbide reinforced Al2024 alloy metal composites. Journal of Bio-and Tribo-Corrosion, 2021; 7:1-12. https://doi.org/10.1007/s40735-020-00454-8

[23] Madeva Nagaral, Auradi V, Kori SA, Reddappa HN, Jayachandran, Veena Shivaprasad. Studies on 3 and 9 wt. % of B4C particulates reinforced Al7025 alloy composites. AIP conference proceedings, 2017;1859, 1:020019. https://doi.org/10.1063/1.4990172

[24] Bharath V, Ashita DH, Auradi V, Madeva Nagaral, Influence of variable particle size reinforcement on mechanical and wear properties of alumina reinforced 2014Al alloy particulate composite. FME Transactions, 2020; 48, 4: 968-978. https://doi.org/10.5937/fme2004968B

[25] Madeva Nagaral, Shivananda BK, Virupaxi Auradi, Kori SA. Development and mechanical-wear characterization of Al2024-nano B4C composites for aerospace applications. Strength, Fracture and Complexity, 2020; 13, 1: 1-13. https://doi.org/10.3233/SFC-190248

[26] Yogesh Prabhavalkar, Chapgaon AN. Effect of volume fraction of Al2O3 on tensile strength of aluminium 6061 by varying stir casting furnace parameters: A review. International Research Journal of Engineering and Technology, 2017; 4, 10: 1351-1355.

[27] Hong SJ, Kim HM, Huh D, Suryanarayana C, Chun BS. Effects of Clustering on the Mechanical Properties of SiC Particulate -Reinforced Aluminum Alloy 2024 Metal Matrix Composites. Material Science and Engineering A, 2003; 347: 198-204. https://doi.org/10.1016/S0921-5093(02)00593-2

[28] Vijaya Ramnath B, Elanchezhian C, Jaivignesh M, Rajesh S, Parswajinan C, Siddique Ahmed Ghias. Evaluation of mechanical properties of aluminium alloy-alumina-boron carbide metal matrix composites. Materials and Design, 2014; 332-338. https://doi.org/10.1016/j.matdes.2014.01.068

[29] Madeva Nagaral, Shaivananda Kalgudi, Auradi V, Kori SA, Mechanical characterization of ceramic nano B4C-Al2618 alloy composites synthesized by semi solid state processing. Transactions of the Indian Ceramic Society, 2018; 77, 3:1-4. https://doi.org/10.1080/0371750X.2018.1506363

Technical Note

Corrosion resistant degradation of AISI 304 austenitic stainless steel exposed to simulated carburizing environments

Chaiyawat Peeratatsuwan [1,a], Suphasin Kanjanangkoonpan [2,b], Ratthakrit Reabroy [2,c], Thee Chowwanonthapunya [2,d*]

[1]Faculty of Engineering and Technology, Rajamangala University of Technology Isan, Thailand
[2]Faculty of International Maritime Studies, Kasetsart University, Sriracha, Thailand

Article Info	Abstract
	This paper aimed to evaluate the anti-corrosion performance of AISI 304 austenitic stainless steel after exposure to the simulated carburizing environment set up at 600°C, 750°C, and 900°C for 4 hrs. The microstructural alternation was investigated by Scanning electron microscopy (SEM) with energy-dispersive X-ray spectroscopy (EDS). Electrochemical Potentiokinetic Reactivation (EPR) was employed to study the anti-corrosion performance of AISI 304 austenitic stainless steel after exposure to the simulated carburizing environment. Hardness measurement was also conducted to study the role of carbon atoms released from the simulated environment. The results showed the formation of precipitated chromium carbides along grain boundaries and sensitization degree was found in ascending order: 600°C (Pa =0.23), 750°C (Pa =0.32) and finally 900°C (Pa =0.41). All carburized conditions promote carbon dissociation and diffusion through the substrate of AISI 304 austenitic stainless steel, resulting in the increased hardness and decreased corrosion resistance of AISI 304 austenitic stainless steel after exposure to the simulated carburizing environment.

1. Introduction

Austenitic stainless steels are frequently utilized in industries owing to their acceptable corrosion resistance and mechanical properties. In addition, this material shows good performance in a variety of temperature conditions. For example, it can offer good impact toughness in cryogenic conditions and good oxidation resistance in elevated temperatures up to 1,150°C [1]. Among many, AISI 304 austenitic stainless steel is a widely used material, particularly in petrochemical industries where corrosion and oxidation are a primary concern. As compared to other commercial oxidation and corrosion resistance alloys, AISI 304 austenitic stainless-steel gains the advantages of significantly lower costs with an acceptable oxidation and corrosion resistance [2]. Hence, this alloy is often used in fuel-burning systems, such as exhaust gas pipes in a furnace of petrochemical plants. It is known that fuel-burning systems, i.e., furnaces and related equipment, involve the combustion of fuels releasing not only thermal energy but also various carbonaceous gases, i.e., CO, CO_2, CO/CO_2 mixture and CH_4 [3]. This kind of environment is known as a "carburizing environment" [4], where the long-term anti-corrosion performance of materials used in the fuel-burning systems can be degraded. For instance, this hush environment can facilitate the dissociation of carbon and subsequently promote the diffusion of carbon atoms into the materials, resulting the microstructural degeneration [5]. Besides, the high

-temperature conditions induced from the combustion can also deteriorate the material, i.e., sensitization of austenitic stainless steel [6]. Both deteriorations potentially lead to the premature failure of the materials in the fuel-burning systems, negatively affecting the overall productivity and reliability of the petrochemical plants. Thus, the anti-corrosion degradation behavior of AISI 304 austenitic stainless steel exposed to such a severe environment is of great interest to study. Basically, the field exposure study of this degradation behavior of AISI 304 austenitic stainless-steel pipe encountered in the actual carburizing environment from a furnace can provide useful information. However, there are several limitations in the field exposure test. For instance, this test would take longer than one year to gain just one time of the investigation. Besides, the parameters of interest may not be precisely controlled. To overcome the drawbacks of the filed investigation, numerous studies have paid their interest in the investigation of metals in the simulated carburizing environment. Carvallho et al. [1] utilized the synthetic environment to investigate the degradation behavior of AISI 304 and AISI 430 stainless steel and they found that hematite was the predominant phase in oxide layers of AISI 304 stainless steel, leading to more oxidation resistance of this alloy. Samaras et al. [7] observed the microstructural alternation of the heat-resistant steel using the simulated carburization environment. Their results showed that $M_{23}C_6$ and M_7C_3 carbides were predominantly found in the carburization layer and the addition of Molybdenum raised the carburization resistance. Haider et al. [8] investigated the carbon diffusion of 304L stainless steel exposed to the simulated carburizing atmosphere and their results indicated that the depth of the carburization zone increased with an increase in the temperature, particularly in the temperature range of 650-750°C. Young at al. [9] found the carburization played a significant role in forming carbide particles in chromium-containing steel. Obviously, the use of the simulated carburizing environment is gaining increased attention from metallurgists. Nevertheless, there has been less work dealing with an investigation on the carburization degradation of AISI 304 austenitic stainless steel, particularly microstructural alternation observation and intergranular corrosion resistance evaluation. In response to the lack of such useful information, this work presented the investigation on the microstructural alternation using the simulated carburizing environment ranging from 600 ^{o}C,750°C, and 900°C. Besides, intergranular resistance evaluation of AISI 304 austenitic stainless steel after exposure to a simulated carburizing atmosphere was also conducted and discussed. The obtained results from this study would provide more comprehension in the carburization degradation of AISI 304 austenitic stainless steel, which can further be the significant information for the materials evaluation under other simulated carburizing conditions.

2. Experimental Procedure

The samples with a dimension of 10 mm X 10 mm X 3 mm were prepared from AISI 304 austenitic stainless steel, the chemical compositions of which were given as follows: C 0.08, Cr 17.80, Ni 8.05, Mn 1.94, and Fe. The simulated carburizing atmosphere was established in the carburized steel container and obtained from the mixture of the activated eucalyptus charcoal and catalysts (Na_2CO_3 and $CaCO_3$) with a ratio of 80:20. This ratio was prepared to ensure the occurrence of carbon dissociation and diffusion in the simulated environment [10,19-20]. The samples were then exposed to the simulated carburizing atmosphere set up at 600 ^{o}C,750°C, and 900°C with the same exposure time of 4 hrs. After exposure to the simulated carburizing atmosphere, samples were naturally cooled and subjected to microstructural observation using SEM-EDS and the hardness measurement. To evaluate the intergranular corrosion resistance, Electrochemical Potentiokinetic Reactivation (EPR) was performed. The specimen after exposure to the simulated carburizing atmosphere test was sectioned to 25 mm X 25 mm X 1 mm coupons and then mounted in cold-curing epoxy. Before the test, each sample was ground with a 120 grit SiC

abrasive paper and then polished down to 1 µm finish. The electrochemical test was performed using a three electrodes cell in a standard glass cell (1 liter). The platinum electrode was employed as a counter electrode and Ag/AgCl electrode was utilized as a reference electrode. The solution of the test was a mixed solution of 0.5 M H_2SO_4 + 0.01 M KSCN with a controlled temperature of 30^oC. To understand the intergranular resistance alternation, the normalized charge parameter (Pa) of each sample from different exposure conditions was then calculated from the resultant electrochemical curves using the following formula [11].

$$P_a = \frac{Q}{GA_s} \tag{1}$$

Where, Q is total charges consumed during the test which can be obtained by the area under curve calculation (coulomb/cm^2), G is Grain size at 100X, and A_s is Specimen areas.

Pa value can reflect the degree of sensitization of AISI 304 austenitic stainless steel. According to the ASTM G108 standard, when Pa is greater than 0.4, this means that this material is severely sensitized, and precipitation of chromium carbides occurs. Nevertheless, when Pa becomes less than 0.1, this implies that this material is not sensitized. In addition, AISI 304 austenitic stainless steel with the intermediate sensitization degree is noticed when Pa is between 0.1 and 0.4.

3. Results

3.1. Microstructure Examination

Fig.1 illustrates SEM micrographs of the reference specimen and specimens with different carburizing temperature conditions at two magnifications: 1,500X and 5,000X with the aim to differentiate the formation of carbides at grain boundaries.
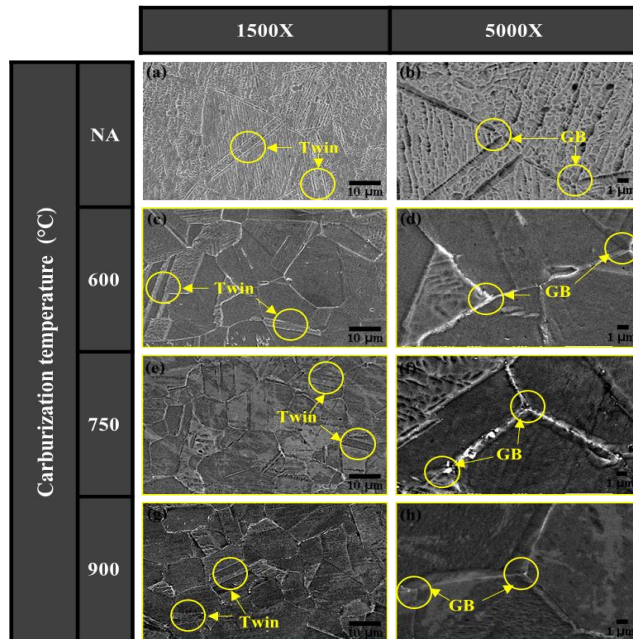

Fig. 1. SEM micrographs: (a)-(b) reference specimens, (c)-(d) 600°C, (e)-(f) 750°C and (g)-(h) 900°C

The reference specimen represents the fresh structure of AISI 304 austenitic stainless steel and its microstructure in lower magnification shows austenite grains and annealing twins as seen in Fig. 1(a). Usually, annealing twins would be formed during the recrystallization [12]. The presence of the austenitic grain boundaries of the fresh structure is clearly shown in Fig. 1(b). Fig. 1(c) reveals the microstructure of specimen exposed to the simulated carburizing atmosphere at the temperature of 600°C and its microstructure comprises of grain boundary and annealing twin. The higher magnification of its microstructure in Fig. 1(d) showed grain boundaries and some precipitated particles. Fig.1(f),(h) showed the precipitation of particles on grain boundaries of the specimens experienced the simulated carburizing atmosphere at the temperature of 750 and 900°C. Basically, the presence of the precipitated particles indicated the microstructural changes of the specimens after exposure to the simulated carburizing environment, which would subsequently affect corrosion-resistant properties. Normally, the thermal energy of this environment can facilitate the formation of particles along grain boundaries [12-13]. In addition, the dissociation of carbon atoms can occur and diffuse into the steel [14]. Thus, the elevated temperature service and the release of carbon atoms from the carburizing environment contribute to the microstructure alternation of specimens. The particles found from SEM micrograph studies were further analyzed using SEM-EDS. The details of the microstructure alternation of the sample exposed to the simulated carburizing environment at 900°C are provided in Fig.2 (a) with the magnification of 1,500X and in Fig. 2(b) with the magnification of 5,000X. The results from EDS analysis are also given. From both results, it is obvious that the particles were formed along grain boundaries, and the results from EDS analysis indicated that the major components of the particle were carbon (C) and chromium (Cr).

SEM mapping was then performed on the specimens subjected to the simulated carburizing atmosphere test set up at 900°C, aiming to obtain significant evidence of the carbide particle formation of AISI 304 austenitic stainless steel after undergoing the simulated carburizing environment. The results are shown in Fig. 3.
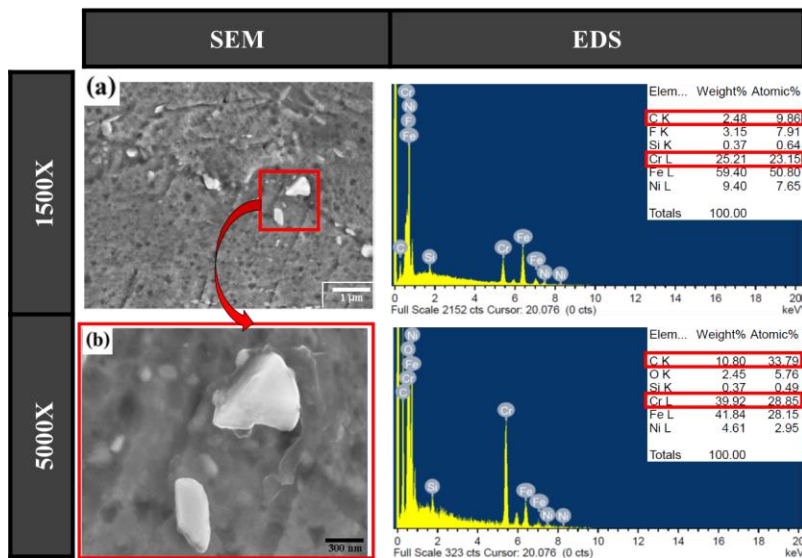
Fig. 2. SEM micrograph together with EDS analysis: (a) 1,500X and (b) 5,000X
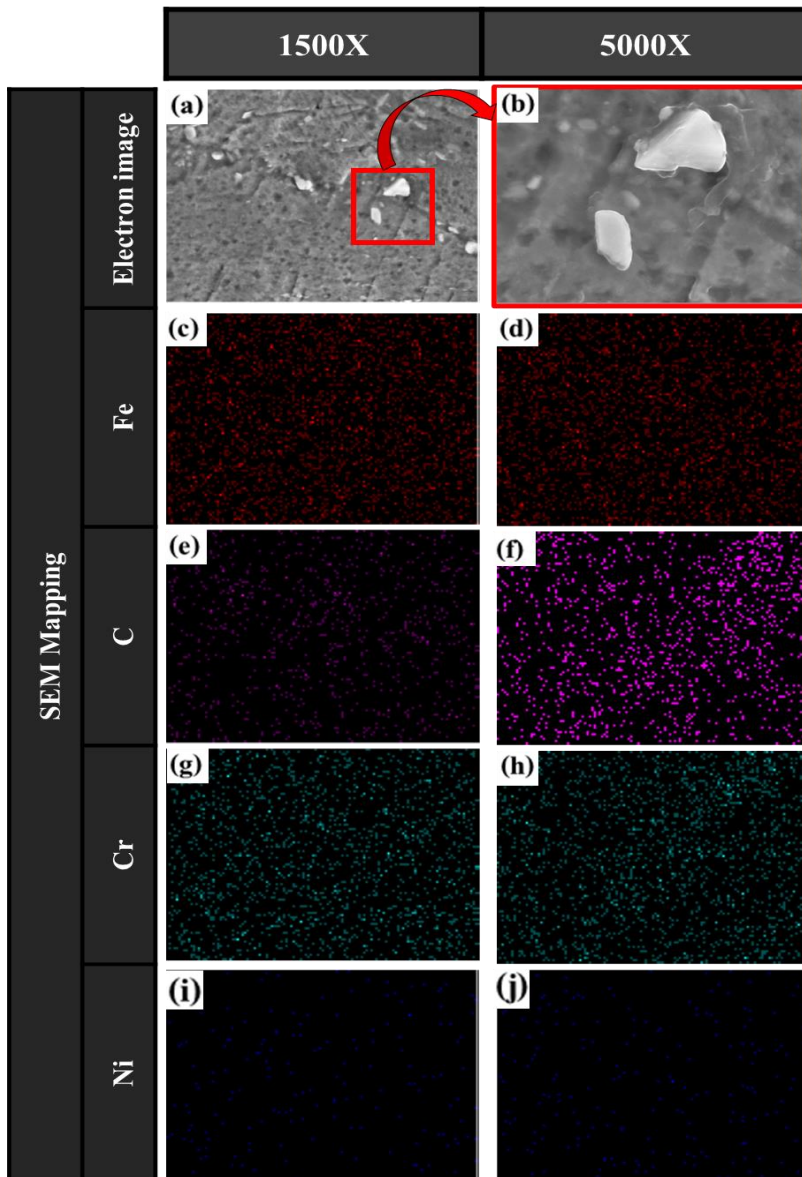
Fig. 3. SEM mapping with the magnification of 1,500X and 5,000X: (a)and(b) electron image, (c)and(d) Fe distribution, (e)and(f) carbon distribution, (g)and(h) chromium distribution and (i)and(j) nickel distribution

From the analysis, it is clear that the major elements were iron, carbon, chromium and nickel dispersed in the matrix. Iron is known as the major element in ferrous-based materials like austenitic stainless steel, but carbon and chromium are alloying elements of the material. Basically, carbon and chromium can react to form the carbide particles in grain boundaries of austenitic stainless steel. Kaewkumsai et al. [15] found the formation of chromium carbide in austenitic steel used in the failed burner pipe which was in a service temperature range of 600-900ºC. Kozuh et al. [16] reported the formation of chromium carbides in grain boundaries of austenitic stainless steel after being used in the

temperature range of 600-800°C. Thus, the results from SEM micrographs and SEM-EDS analysis point out the particles observed from the test were due to the formation of chromium carbides and this finding corresponds to the works conducted by several scientists.

3.2 Anti-Corrosion Performance Alternation Observation

Electrochemical Potentiokinetic Reactivation (EPR) was performed to obtain insight in the anti-corrosion performance alternation. The resultant electrochemical curves of specimens are given in Fig. 4. There are two types of corrosion behaviors taking place in this electrochemical test. The first corrosion behavior of the reference specimen showed non-sensitization as seen in Fig. 4(a). However, after exposure to the carburizing environment, the electrochemical curves exhibited sensitizing [17] and the maximum current density was found in ascending order: 600 °C, 750 °C and 900°C. Technically, sensitization means the carbide precipitation at grain boundaries in a stainless steel causing it vulnerable to intergranular corrosion. Usually, the ratio between the charge caused by the corrosion at grain boundaries, known as Pa value, can indicate the sensitization degree. Thus, as sensitization occurs, Pa value of each sensitized specimen should be evaluated, and the calculated results are displayed in Fig. 5. As indicated in ASTM G108 standard, Pa value is less than 1, the stainless steel is not sensitized, but the Pa value in the range between 1-4 indicates the intermediate sensitization degree [11]. The Pa value greater than 4 indicated the severely sensitized stainless steel. Clearly, the reference specimen with the fresh surface shows no sign of sensitization. However, Pa values increased with increasing the carburizing temperature and the maximum Pa value was found in specimens with the highest carburizing temperature of 900°C. This result means that increasing carburizing temperature increased the sensitization degree of AISI 304 austenitic stainless steel, especially in the carburizing temperature in 600-900°C. The higher the carburizing temperature, the higher the density of the precipitated chromium carbides. This resulted in increased sensitization and then the decreased anti-corrosion performance of AISI 304 austenitic stainless steel. To understand the role of carbon, the hardness test was conducted on specimens with varying temperatures; the Hardness result and the summarized result are shown in Fig. 6 and Table 1, respectively.

Table 1. The summarized results from the EPR and Hardness test

Carburizing temperature (°C)	NA	600	750	900
Pa (coulomb /cm^2)	0.058	0.231	0.321	0.413
Hardness (HV)	185.0	197.0	203.0	210.0

It is obvious that the higher the carburizing temperature, the higher the hardness of sample is. At the same time, the sensitization degree increased. Technically, the simulated carburizing environment promotes the dissociation of carbon atoms. It is also well known that an increase in temperature enhances the diffusion of atoms into the materials [18]. Wongtimnoi et al. [19] found the carburizing environment can increase the hardness of low carbon steel. Chowwanonthapunya et al. [20] found that carbon atoms can be diffused through the bare surface of alloys and subsequently from carbide particles. Marián Vach et al [21] reported that the second phase particles, such as $M_{23}C_6$, can be found in the austenitic stainless steel and the presence of those particles resulted in increased hardness. Treewiriyakitja et al. [22] found the formation of carbide particles resulted in the degraded corrosion resistance of austenitic stainless steel. In this experiment, microstructural analysis in Fig. 2 shows that the particle is composed of carbon and chromium. SEM-mapping exhibits the distribution of carbon atoms in the austenite matrix of AISI 304 austenitic stainless steel, as shown in Fig.3(c), (h). Thus, carbon atoms released from the

combustion in this environment transport through the substrate of samples, resulting in increasing the hardness of samples and promoting the formation of carbide particles [23-24]. As the chromium carbide particles are formed along the grain boundaries, AISI 304 austenitic stainless steel becomes harder and significantly reduces its anti-corrosion performance.
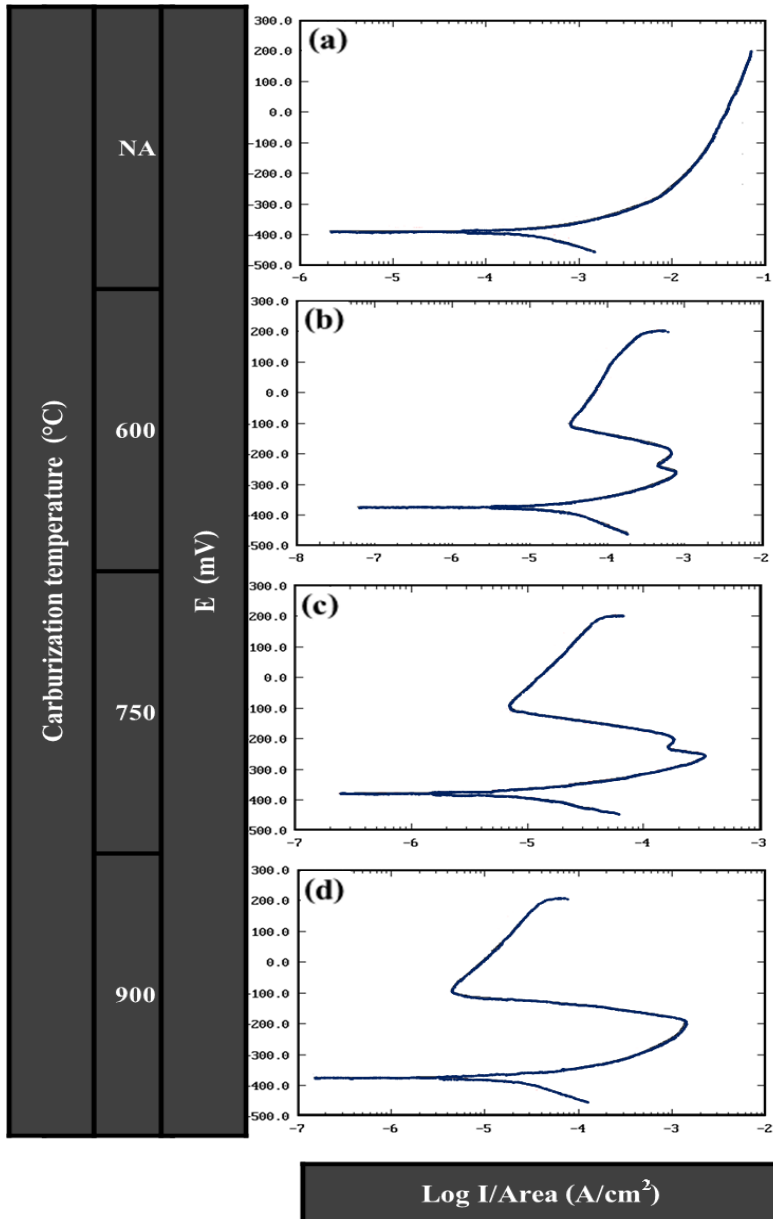
Fig. 4. Electrochemical curves of specimens: (a) reference specimen, (b) 600°C, (c) 750°C, and (d) 900°C
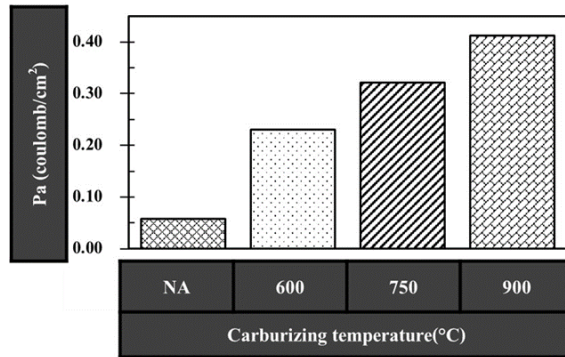
Fig. 5. The Pa value of specimens for varying temperatures.
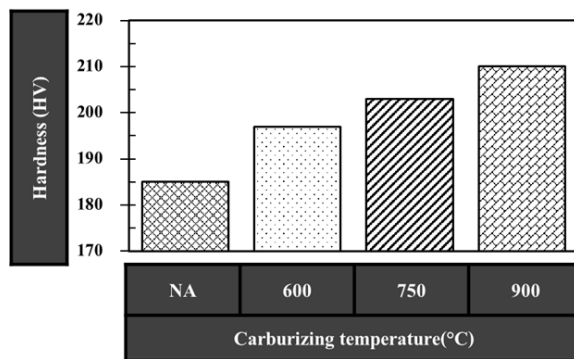
Fig. 6. Hardness of specimens for varying temperatures

4. Conclusions

The anti-corrosion performance of AISI 304 austenitic stainless steel exposed to a simulated carburizing environment set up at 600°C, 750°C, and 900°C was evaluated. In this study, the results revealed the presence of precipitated chromium carbide particles formed along grain boundaries. The formation of these particles resulted in sensitization, resulting in significantly reduced anti-corrosion performance of AISI 304 austenitic stainless steel. Sensitization degree was found in ascending order: 600°C (Pa =0.23), 750°C (Pa =0.32) and finally 900°C (Pa =0.41). Simultaneously, the hardness observation was arranged in ascending order: 600°C (197HV), 750°C (203 HV), and finally 900°C (210HV). All carburized conditions promote carbon dissociation and diffusion through the substrate of AISI 304 austenitic stainless steel, resulting in the increased hardness and decreased corrosion resistance of AISI 304 austenitic stainless steel after exposure to the simulated carburizing environment.

Acknowledgment

References

[1] Carvalho CERC, Costa GMC, Cota AB, Rossi EH. High Temperature Oxidation Behavior of AISI 304 and AISI 430 Stainless Steels. Mat. Res. 2006; 9(4): 393-397. https://doi.org/10.1590/S1516-14392006000400009

[2] Sabioni ACS, Huntz AM, Luz EC, Mantel M, Haut C. Comparative Study of High Temperature Oxidation Behaviour in AISI 304 and AISI 439 Stainless Steels. Mat. Res. 2003; 6(2): 179-185. https://doi.org/10.1590/S1516-14392003000200012

[3] Gheno T, Moneau D, Zhang J, Young D. Carburisation of ferritic Fe–Cr alloys by low carbon activity gases. Corros. Sci. 2011; 53(9): 2767-2777. https://dx.doi.org/10.1016/j.corsci.2011.05.013

[4] Tripathy DB, Yadav A, Mishra A. Applications of Petrochemicals: A Mini Review. Recent adv. Petrochem. 2017; 2(4): 67-70. https://doi.org/10.19080/RAPSCI.2017.02.555594

[5] Deuis R, Petrone S. Hot erosion wear and carburization in petrochemical furnaces. Mater. Corros. 2006; 57(2): 135-146.https://doi.org/10.1002/maco.200503900

[6] Kolli S, Javaheri V, Ohligschläger T, Kömi J, Porter D. The importance of steel chemistry and thermal history on the sensitization behavior in austenitic stainless steels: Experimental and modeling assessment. Mater. Today Commun. 2020; 24: 101088. https://doi.org/10.1016/j.mtcomm.2020.101088

[7] Samaras GF, Haidemenopoulos GN. Carburization of high-temperature steels: A simulation-based ranking of carburization resistance. Eng. Fail. Anal. 2015; 51: 29–36. https://doi.org/10.1016/j.engfailanal.2015.02.022

[8] Haider FI, Suryanto S, Mahmood MH. Carbon diffusion in 304L austenitic stainless steel at 650-750 0C in carburizing environment. Int. J. Eng. Technol. 2019; 7(6S): 76-78.

[9] Young DJ. High Temperature Corrosion in Carbon-Rich Gases. Corros. Sci. Technol, 2008; 7(2): 69-76.

[10] Kenneth GB, Michael KB. Engineering Material: Properties and Selection, Pearson Education International, Inc., USA, 2002.

[11] ASTM G108–94. ASTM International, West Conshohocken, Pensilvania,2010.

[12] Switzner N.T, Sawyer E.T, Everhart W.A, Hanlin R.L. Predicting microstructure and strength for AISI 304L stainless steel forgings. Mater. Sci. Eng. A . 2019; 745(4): 474-483. https://doi.org/10.1016/j.msea.2018.12.054

[13] Rajesh Kannan P, Muthupandi V, Devakumaran K, Sridivya C, Arthi E. Effect of grain size on self -healing behaviour of sensitized S304HCu stainless steel. Mater. Chem. Phys. 2018; 207: 203-211. https://doi.org/10.1016/j.matchemphys.2017.12.012

[14] Yae Kina A, Souza VM, Tavares SSM, Pardal JM, Souza JA. Microstructure and intergranular corrosion resistance evaluation of AISI 304 steel for high temperature service. Mater. Charact. 2008; 59(5): 651-655. https://doi.org/10.1016/j.matchar.2007.04.004

[15] Kaewkumsai S, Auampan S, Wongkinkaew K, Viyanit E. Root cause analysis for 316L stainless steel tube leakages. Eng. Fail. Anal. 2014; 37: 53–63. https://doi.org/10.1016/j.engfailanal.2013.11.008

[16] Kozuh S, Gojic M, Vrsalovic L, Ivkovic B. Corrosion failure and microstructure analysis of AISI 316L stainless steels for ship pipeline before and after welding. Kovove Mater. 2013; 51(1): 53-61. https://doi.org/10.4149/km_2013_1_53

[17] Hazarabedian MS, Lison-Pick M, Zakaria Quadir Md, Iannuzzi M. Detecting Intergranular Phases in UNS N07725: Part I. Adapting the Double-Loop Electrochemical Potentiokinetic Reactivation Test. J. Electrochem. Soc. 2021; 168: 031506. https://doi.org/10.1149/1945-7111/abe9d0

[18] Chowwanonthapunya T, Peeratatsuwan C. Experimental investigation on the carbide precipitation and mechanical property evolution of a cryogenically treated tool steel. Asia Pac J Sci Technol. 2020; 254(4): Article ID: APST-25-04-03. https://doi.org/10.14456/apst.2020.33

[19] Wongtimnoi K, Chowwanonthapunya T. Evolution of Microstructure and Wear Resistance of Carburized Low Carbon Steel. Int. J. Integr. Eng. 2022; 14(1): 66-72. https://doi.org/10.30880/ijie.2022.14.01.007

[20] Chowwanonthapunya T, Peeratatsuwan C. Study of Microstructure and Mechanical Property Degradation of SA210 A1 Boiler tube. . Int. J. Integr. Eng. 2020; 12(8): 123-132. https://doi.org/10.30880/ijie.2020.12.08.012

[21] Vach M, Kunikova T, Domankova M, Sevc P, Caplovic L, Gogola P, Janovec J. Evolution of secondary phases in austenitic stainless steels during long-term exposures at 600, 650 and 800°C. Mater. Charact. 2008; 59: 1792-1798. http://dx.doi.org/10.1016/j.matchar.2008.04.009

[22] Treewiriyakitja P , Thongyoug P, Pokwitidkul S, Tungtrongpairoj J. The Degradation of Austenitic Stainless Steel at High Temperature in Simulated Carbon Monoxide Containing Atmosphere of Biomass-to-Liquid Plants. IOP Conf. Ser.: Mater. Sci. Eng. 2021 ; 1163 : 012022. https://doi:10.1088/1757-899X/1163/1/012022

[23] Pokwitidkul S, Treewiriyakitja P, Thongyoug P, Kiatisereekul N, Kanjanaprayut N, Tungtrongpairoj J. High temperature degradation of AISI 304L stainless steel in atmospheres containing CO of biomass to liquid plants at 800 °C. Mater. Today: Proc. 2023;77: 1100-1105. https://doi.org/10.1016/j.matpr.2022.11.395

[24] Thongyoug P, Chandra-Ambhorn S, Tungtrongpairoj J. The degradation of oxide layer on Cr-containing steels in simulated atmospheres on carbothermic reduction. Mater. High Temp.2021;39:1-11. https://doi.org/10.1080/09603409.2021.1994829

Properties of modified metakaolin-based geopolymer concrete with crumbed rubber waste from damaged car tires

Nazar F. Al Obeidy [*, a], Wasan I. Khalil[b]

Civil Engineering Department, University of Technology, Baghdad, Iraq

Article Info	Abstract
	Waste rubber tires are materials that have a negative impact on the environment. Therefore, it is essential to use waste rubber recycled from damaged tires (CRWA) in geopolymer concrete (GPC) by different partial volumetric replacements to natural coarse aggregate (0, 10, 20, 25%) after preparation to a gradation similar to that for natural coarse aggregate. Calcium oxide and silica fume were substituted in metakaolin (MK) at 5 wt%. The GPC mix consisted of MK after modification, coarse aggregate, fine aggregate sodium hydroxide solution, sodium silicate solution, superplasticizer, and extra water, with quantities of 372, 911, 83, 192, 4, and 52 kg/m^3, respectively. It is clear from the experimental results that the mechanical properties of geopolymer concrete decreased with the increase in the content of the crumbed rubber waste aggregate. The compressive, splitting tensile, and flexural strengths decreased by approximately 38.6, 44.6, and 52.6%; 10.6, 15.2 and 21.2%; and 6.25, 12.75, and 16.5% when the crumbed rubber aggregate was 10, 20 and 25%, respectively. In addition to recycling the rubber waste from damaged tires, desirable properties can be obtained, starting from not using water in curing GPC and rapid strength development at early ages. There is a clear improvement in the thermal properties and weight of GPC containing CRWA by reducing the thermal conductivity and dry density by including 10, 20, and 25% CRWA compared with the reference GPC without this waste material.

1. Introduction

According to the World Commission on Environment and Development, sustainability is ensuring that the current demand of humanity can be achieved without affecting the needs of future generations. At the Earth Summit in 1992, seven principles were defined for achieving environmental efficiency, including reducing the amount of materials used in products, reducing the energy consumption of products, reducing the emissions of toxic gases, increasing the recyclability of materials, exploiting the use of renewable materials as much as possible, increasing the durability of products, and increasing the service life of products [1,2]. In 1978, Davidovits [3] developed concrete in a different way than at that time using some byproducts from the construction industry, and named it geopolymer concrete.

GPC is an inorganic composite material created by interacting strongly alkaline substances with an aluminosilicate source and aggregate. It is possible to use aluminosilicate from waste materials such as ground granulated blast furnace slag, fly ash, and natural pozzolans, such as metakaolin. Geopolymer concrete can provide many environmental advantages. Using recycled materials instead of cement, geopolymer concrete can reduce

carbon dioxide emissions by up to 80%, as well as save energy and natural resources and avoid environmental problems caused by conventional concrete. [4,5].

Tire rubber disposal has become one of the most significant environmental issues in the world today. Throughout the world, tires are routinely discarded, buried, or thrown away, posing a very serious threat to the environment[6].

The effect of the inclusion of different percentages of CRWA from damaged car and truck tires that can be used as partial replacements for fine and coarse natural aggregates (0, 10, 20, and 30%) on the properties of geopolymer concrete based on slag as a binder was studied by Aly et al. [7]. Waste rubber was divided into particle sizes passing through sieve No. 40 as fine aggregate and particle sizes from 1-4 mm as coarse aggregate. The most important of the researcher's conclusions is that the compressive strength was slightly enhanced with increasing rubber percentage up to 10%; however, an increase in rubber content higher than 10% leads to a decrease in the compressive strength by 24% and 34% for rubber percentages of 20 and 30% at 28 days and 21% and 28% at 60 days, respectively. The flexural and splitting strengths suffer reduction with the increase in the replacement of rubber content by 20, 30, and 30% for splitting strength and 34.6, 23, and 35.5% for flexural strength. The impact resistance of geopolymer concrete is greatly enhanced due to the presence of rubber, which leads to an increase in the ductility and energy absorption of approximately 50, 150, and 200% for 10, 20, and 30% rubber waste content compared with geopolymer concrete without rubber waste [7].

The use of recycled rubber in GPC was carried out by Kurek [8], fly ash was utilized as a binder activated by NaOH with a concentration of 14 M and sodium silicate with a modulus of 2.5. Rubber granules from recycling waste tires were used with a small size in the 0-0.8 mm range and a large size in the 1-4 mm range. Then, 25-50% of the sand was replaced by fly ash, and 12.5-25% of the sand was replaced in the first case with granules of waste tire rubber, once in a small size and again in a large size. The GPC specimens were cured at a temperature of 75°C for 24 hours, then left at room temperature until the test time at 7 and 28 days. The results explained that the density increases by increasing the proportion of sand from 25-50%, while it decreases when replacing sand with rubber. The highest decrease in density was obtained when using rubber of small sizes. The compressive strength of GPC increases when sand is replaced with fly ash, but decreases when rubber inclusions are added. However, a 12.5% substitution of sand with waste rubber of 1-4 mm particle size resulted in a significant increase in the compressive strength.

Yeluri and Yadav [9] reviewed the mechanical properties of using rubber tire waste as aggregate in GPC. The results demonstrated that the inclusion of rubber in geopolymer concrete enhances its workability but reduces its flow value. As the rubber content increased, the compressive strength decreased by 60% for specimens with 15% rubber in concrete and 10% in mortar. However, the rubber content had a positive effect on the splitting and flexural strengths. The highest flexural strength was achieved at 30% waste rubber, replacing the fine aggregate.

Previous local studies using local metakaolin as a base material produced GPC with a compressive strength ranging from 3 to 41 MPa. To increase the compressive strength of metakaolin-based GPC, further research is needed to improve or modify Iraqi metakaolin. One possible factor is the R-value Si/Al or molar ratio, which is the ratio of silicates to aluminates in the binder. This ratio affects the polymerization process and the mechanical properties of GPC[10–13]. Davidovits recommended that the optimal Si/Al ratio for achieving maximum strength and durability is 1:4 [3,14,15].

It was noted that few investigations are studying all the properties of concrete that use this type of geopolymer concrete with crumbed rubber aggregate wastes, and there is little research conducted for geopolymer concrete produced from other materials with rubber wastes. This research aims to improve the strength of metakaolin-based GPC by using silica-rich materials such as silica fume or calcium-rich materials such as calcium oxide as

a weight replacement for local metakaolin by changing the R-value and selecting the optimum mixture. Then, a comprehensive study was carried out to investigate the effect of the inclusion of different contents of CRWA on some properties of this GPC, so this research is considered an important addition in the field of construction.

2. Experimental Work

2.1. Materials

The kaolin clay found in Iraq's western desert was subjected to several processes, including grinding and burning at 700 degrees Celsius for two hours, to be converted into metakaolin, which conforms to the American standard ASTM C618 [16] as natural pozzolanic material class N, as a source of silica and alumina for the production of geopolymer concrete. The physical and chemical characteristics of the metakaolin utilized are shown in Tables (1) and (2), respectively.

Table 1. Physical properties of metakaolin

Physical Properties	MK	Requirements of ASTM C 618 [16]
Strength activity index at 7 days (%)	113	≥75%
Retained on 45 μm (%)	18.5	≤34%
Specific surface area (m2/kg)	14300	--
Specific gravity	2.64	--
Color	White –pinky powder	--

Table 2. Chemical properties of metakaolin

Oxide Composition	Weight (%)	Requirements of ASTM C 618 [16]
SiO_2	62.410	SiO2+ Al2O3+ Fe2O3= 98.327 ≥ 70
Al_2O_3	35.026	
Fe_2O_3	0.891	
K_2O	0.908	
TiO_2	0.531	
CaO	0.143	
SO_3	0.027	≤4%
MnO	0.002	
LO I	0.71	≤10%

LOI: Loss of ignition.

The alkaline solution used as an activator for the production of geopolymer concrete consisted of sodium hydroxide (NaOH) with a purity of 99.5% and sodium silicate (Na_2SiO_3). The natural fine aggregate used had a maximum size of 5 mm. The sieve analysis and the properties of fine aggregate are shown in Table (3), which conforms to Iraqi Standard No. 45/2016, gradation zone No. 2 [17]. The natural coarse aggregate used in this research was crushed gravel with a maximum size of 10 mm. The sieve analysis and the properties of the coarse aggregate are shown in Table (4), which is in accordance with Iraqi Standard No. 45/2016 [17].

Potable water was used for two purposes in the geopolymer concrete mixtures: to dissolve the 13 molar sodium hydroxide granules (with a molecular weight of 0.04 kg/mol) and to

provide extra water for good workability in the plastic state. The water required for dissolving sodium hydroxide was 48 kg/m³, while the extra water was 52 kg/m³.

Table 3. Properties of fine aggregate

Sieve Size (mm)	Cumulative Passing (%)	Limits of IQS No. 45 for Zone II [17]
10	100	100
4.75	94	90-100
2.36	82	75-100
1.18	68	55-90
0.6	51	35-59
0.3	27	8-30
0.15	8	0-10
Material passing from sieve 75 μm (%)	3	≤5%
Sulfate content (%)	0.085	≤0.5%
Fineness modulus	2.71	--
Absorption (%)	1.8	--
Specific gravity	2.6	--
Bulk density (kg/m³)	1744	--

Table 4. Properties of coarse aggregate

Sieve Size (mm)	Cumulative Passing (%)	Limits of IQS No. 45 [17]
10	97	85-100
5	12	0-25
2.36	--	0-5
Material passing from sieve 75 μm (%)	0.3	≥3
Dry density (kg/m3)	1627	--
Specific gravity	2.62	--
Absorption (%)	0.6	--
Sulfate content (%)		

A high-range water reducer with the commercial mark of Flocrete SP33 [18] was used. It is free from chlorides and agrees with ASTM C494 [19] types A, and F. Table (5) shows its main properties.

Silica fume from Sika Company [20], compatible with the American standard ASTM C 1240 [21], was also used in geopolymer concrete mixtures. Table (6) presents the physical and chemical properties of the silica fume used.

The calcium oxide used in this study was from the Karbala factory for the production of cement and Al Noora. The physical and chemical properties of calcium oxide are given in Table (7).

Table 5. Properties of the high-range water reducer*

Property	Description
Appearance	Dark brown liquids
Specific gravity	1.17-1.21
Chloride content	Nil
PH	6.5
Recommended dosage	0.8-2.8 L/100 kg binder

 * *According to the manufacturer [18].

Table 6. Properties of silica fume

Physical properties		
Property	Results	Requirements of ASTM C1240
Specific surface area (m²/kg)	19200	≥15000
Strength activity index with Portland cement at 7 days (%)	122	≥ 105
Retained on sieve 45 μm, max (%)	9	≤ 10
Specific gravity	2.2	--
Color	Grey	--
Chemical properties		
Oxide's composition	Results (%)	
SiO_2	88.593	≥85
Al_2O_3	--	--
Fe_2O_3	5.564	--
K2O	4.777	--
TiO2	--	--
CaO	0.666	--
SO_3	0.027	--
MnO	0.276	--

Waste tires were collected and cleaned, and the rubber from these waste tires was cut off to different sizes, starting from 0.3 to 18 mm, by the Al-Diwaniyah plant for cutting car tires in Al-Diwaniyah governorate, Iraq. The wastes were collected, washed and screened on standard sieves to obtain a gradation that matched the Iraqi specification No. 45/2016 [17], and the natural coarse aggregates used in this study. Then, the prepared crumb rubber particles were treated with a solution of 5% $Ca(OH)_2$ for 48 hours, according to previous studies [22–24]. This treatment makes the rubber particle surfaces rough and thus improves their bond strength with the geopolymer matrix. Figure 1 illustrates the preparation process for crumbed rubber waste aggregate. At the same time, Table (8) shows the properties and the sieve analysis of the rubber waste aggregate, corresponding to the sieve analysis of natural coarse aggregate based on Iraqi specification No. 45/2016 [17].

Table 7. Properties of calcium oxide

Physical properties	
Property	Results
Specific surface area (m2/kg)	16350
Specific gravity	3.3
Color	White
Chemical properties	
Oxides composition	Results (%)
SiO2	4.314
Al2O3	--
Fe2O3	0.461
K2O	1.667
TiO2	--
CaO	93.40
SO3	0.10
MnO	0.025

Table 8. Properties of the Waste Rubber Tier After Preparation

Properties	Results	Specifications
Loose bulk density (kg/m3)	--	ASTM C 29-15 [25]
Compacted bulk density (kg/m3)	494	ASTM C 29-15 [25]
Specific gravity	1.10	ASTM C127-15 [26]
Water absorption (%)	4.8	ASTM C 127-15 [26]
Sieve analysis		
Sieve size (mm)	Passing (%)	IQS No.45/2016 Limits for max. size (10 mm) [17]
14	100	100
10	97	85-100
5	12	0-25
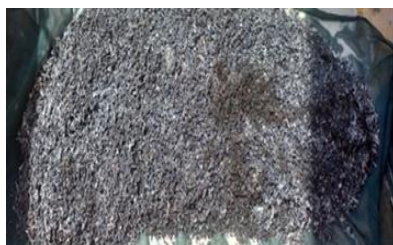
a- Collecting

b- Washing by water

c- Treatment by Ca (OH)$_2$ solutions

d- Sieving through standard sieves

Fig. 1. Rubber waste preparation process

2.2 Selection of Geopolymer Concrete Mix Proportion

The preliminary selection of the geopolymer mixture was based on previous studies [5,10,11,27,28]. First, superplasticizer (SP), extra water, and mix proportion dosages were accurately calculated. The high fineness of metakaolin requires SP and extra water 1.1, 14% by weight of metakaolin, to improve workability with slump value (180±10 mm). Many trial mixes, including modifying metakaolin as a base material in GPC by partially substituting its weight with a binary mix of silica fume and calcium oxide and selecting the optimum proportions for other materials used in the production of GPC, were carried out. Finally, the selected GPC mixture had a binder content (metakaolin) of 372 kg/m³ modified by silica fume and calcium oxide of 21 kg/m³ for both of them, sodium oxide concentration of 13 molarity, sodium silicate/sodium hydroxide of 2.5, fine and coarse aggregate of 603 kg/m³ and 911 kg/m³, SP of 4 kg/m³, extra water of 52 kg/m³, and ratio of the alkali solution/binder of 0.65 to get M50 grade of GPC with compressive strength not less than 50 MPa. The alkaline liquid used in this study was a combination of sodium hydroxide (SH) and sodium silicate (SS). After placing the water in a container (48 kg/m³), sodium hydroxide is weighed (35 kg/m³) and added to the water to achieve the appropriate molarity (13 M) in the presence of the molecular weight of NaOH to be its sum (83kg/m³) as a solution material. As the sodium hydroxide pellets dissolve in the water, they release heat. After sodium hydroxide was added and cooled, sodium silicate was added. Table (9) shows these trials and the optimum mix proportion at seven days with the curing condition at an average temperature of 46°C in the day and 29°C at night until the test age to produce GPC with a compressive strength of 58.0 MPa.

Table 9. Compressive strength of geopolymer concrete at seven days of age

Mix No.	Variables	MK*	SF	CaO	CA*	FA*	SS*	SH*	SP*	W*	Compressive strength (MPa)
							(kg/m³)				
M1	SH=12, SS/SH=2.5, AL/B= 0.55	372	21	21	955	632	162	71	8.3	85	33.4
M 2	SH=12, SS/SH=3, AL/B= 0.65	372	21	21	912	603	201	74	4	50	43.4
M 3	SH=12, SS/SH=3.5, AL/B= 0.75	372	21	21	870	575	241	75	4	28	44.0
M 4	SH=13, SS/SH=2.5, AL/B= 0.65	372	21	21	911	603	192	83	4	52	58.0
M 5	SH=13, SS/SH=3, AL/B= 0.75	372	21	21	869	575	232	84	4	30	57.3
M 6	SH=13, SS/SH=3.5, AL/B= 0.55	372	21	21	956	633	176	57	8.3	66	53.1
M 7	SH=14, SS/SH=2.5, AL/B= 0.75	372	21	21	868	574	221	95	4	32	57.0
M 8	SH=14, SS/SH=3, AL/B= 0.55	372	21	21	956	632	170	63	8.3	85	53.5
M 9	SH=14, SS/SH=3.5, AL/B= 0.65	372	21	21	913	604	209	66	4	54	57.4
R	SH=12, SS/SH=2.5, AL/B=0.55	414	--	--	911	574	193	83	4.8	50	44.4

* MK: Metakaolin, SF: Silica foam, Cao: Calcium oxide, CA: Coarse aggregate, FA: Fine aggregate, SS: Sodium silicate, SH: Sodium hydroxide, SP: Superplasticizer, W: Water, Al/B: Alkaline solution/binder.

2.3 Sample Preparation and Processing Methodology

The process of mixing and preparing GPC specimens can be summarized as follows:

- Water was used to wet the electric rotating mixer, which had a 0.1 m³ capacity.
- Calcium oxide, silica fume, and metakaolin were manually blended for two minutes.
- Dry materials, including modified metakaolin, natural fine aggregate, natural coarse aggregate for the reference mixture without wastes and crumbed rubber as a replacement to natural coarse aggregate by volume of 10, 20, and 25% for other mixes, were blended for two minutes in the mixer.
- During the mixer's rotation, the alkaline solution was added, and the mixer continued to mix all the ingredients for three minutes.
- The superplasticizer and extra water were gradually added to the mixture.
- The mixing process was stopped for one minute to give the mixture time to rest and clean the mixer arms, and then it was restarted for one minute. The total mixing duration was between 9 and 10 minutes.

Because geopolymer mixtures are more viscous than cementitious concrete, they need greater care during mixing, handling, casting, and compaction. The interior surfaces of the moulds were coated with grease to prevent concrete from sticking to the surfaces of the mould. After levelling the top surfaces of the GPC specimens, they were covered with nylon sheets and left in the laboratory for 24 hours. Then, the moulds of different sizes, based on various test methods, were opened and cured in the summer season at a temperature range of 46 °C during the day and 29 °C at night.

3. Results and Discussion

Initially, the selected crumbed rubber waste aggregate (CRWA) content as a volumetric replacement to natural coarse aggregate was 10, 20, and 30% in the geopolymeric concrete mix. Since the compressive strength of geopolymer concrete, which contains 30% replacement content of rubber waste aggregate, dropped to 15.6 MPa, the replacement percentage to a maximum value of 25% was selected to maintain an acceptable compressive strength value. Coarse aggregate is an important indicator of concrete strength. Therefore, recycled crumb rubber waste aggregate from damaged tires was substituted for natural coarse aggregate at 0, 10, 20, and 25% in the geopolymer concrete mixture in this study.

3.1 Fresh Properties

3.1.1 Workability

The slump test was used to determine the workability and consistency of concrete in accordance with ASTM C143 [29]. Figure 2 shows the slump value findings for the reference geopolymer concrete without wastes and geopolymer concrete with crumbed rubber waste aggregate with different proportions to replace the natural coarse aggregate of 10, 20, and 25% by volume. The slump decreased as the amount of crumbed rubber used to replace natural coarse aggregate in the geopolymer concrete mixtures increased. Compared with the reference mix, the slump values of the geopolymer concrete containing rubber waste aggregate decreased by 5.56%, 8.34%, and 11.11% for (CRWA) contents of 10, 20, and 25%, respectively. This decrease in the slump may be explained by the mechanically shredded crumb rubber having a rough surface and texture. As a result, there was an increase in the interparticle friction between the crumb rubber particles and the other geopolymer concrete components [30]. Additionally, the rough texture of the rubber surface may need more water to fill the void than natural aggregate with less rough

surfaces. In addition, the higher absorption of rubber with respect to natural aggregate was cited by Su Haolin [31].
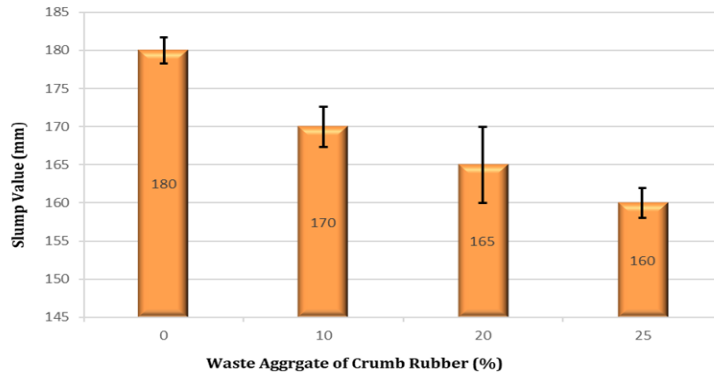

Fig. 2. Effect of crumb rubber content as a replacement to coarse aggregate on the workability of geopolymer concrete

3.1.2 Fresh Density

The fresh density of GPC was determined directly after mixing according to ASTM C138 [32]. The data in Figure 3 illustrate that using 10%, 20%, and 25% crumbed rubber waste aggregate as a volume substitute for natural coarse aggregate reduces the fresh density of geopolymer concrete. The reference mix not containing CRWA has a higher density than all GPC mixes with different contents of CRWA. The fresh density for GPC with CRWA was decreased by 2.0%, 2.6%, and 4.0% for 10, 20, and 25% crumb rubber aggregate content, respectively. This is because of the low specific gravity of the rubber waste, which is 1.1, while for natural coarse aggregate, the specific gravity is 2.62 [33,34]. Siddique and Naik reported similar findings about the density of rubber concrete [35]. They hypothesized that since rubber particles are nonpolar in nature, they may have the capacity to deflect the flow of water and entrap air on the surface of the rubber. This would lead to an increase in the number of air voids and cause a reduction in the density of the geopolymer concrete.
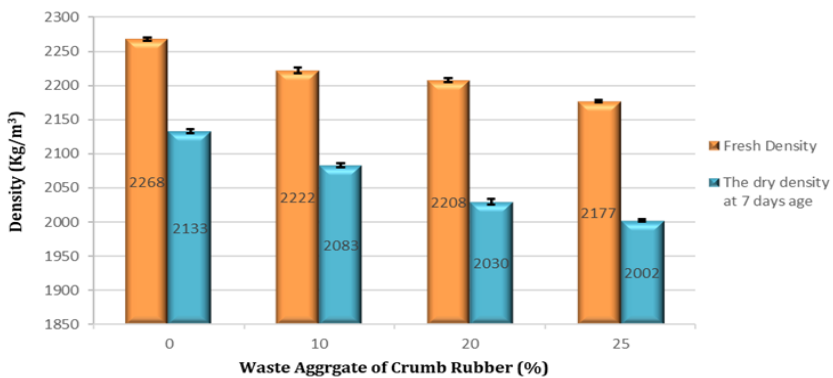

Fig. 3. Effect of crumb rubber content as a replacement to coarse aggregate on the density of geopolymer concrete

3.2 Hardened Properties

3.2.1 Dry Density

The oven dry density of GPC was determined according to ASTM C642[36]. Figure 3 shows a decrease in geopolymer concrete dry density at seven days of age as CRWA content increases. This is attributed to the lower specific gravity of crumbed rubber waste aggregate (1.1) than the specific gravity of natural coarse aggregates (2.62).

3.2.2 Compressive Strength

The compressive strength is the most significant indicator when assessing geopolymer concrete. The compressive strength of every mixture was determined using the average of three cubic samples with dimensions of 100×100 mm according to BS1881:part116. Compressive strength data for different GPC mixtures at seven days of age are shown in Table (10) and Figure 4.
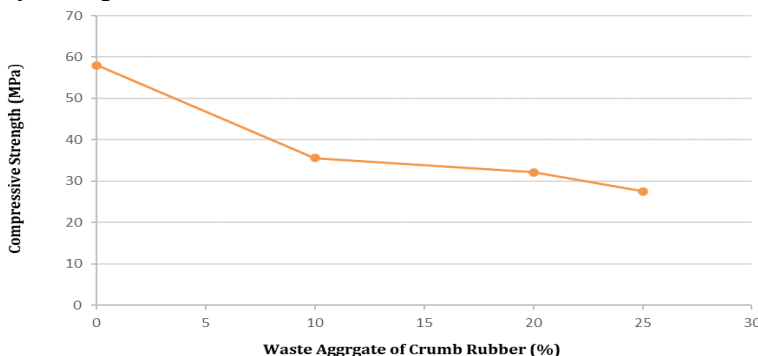

Fig. 4. Influence of crumbed rubber waste aggregate on the compressive strength of geopolymer concrete

Table 10. Mechanical properties of different geopolymer concrete mixtures

Mix Symbol	Comp. Strength (MPa)	Change Perc. in Comp. Strength (%)	Splitting Tensile Strength (MPa)	Change Perc. in Splitting Tensile Strength (%)	Flexural Strength (MPa)	Change Perc. in Flexural Strength (%)	Absorption (%)	Change Perc. In absorption (%)
R	58	--	3.3	--	4	--	4.99	--
10%T	35.6	- 38.6	2.95	-10.6	3.75	- 6.25	5.07	+ 1.60
20%T	32.1	-44.6	2.8	-15.2	3.49	- 12.75	5.62	+ 12.6
25%T	27.5	- 52.6	2. 6	-21.2	3.34	- 16.5	6.23	+ 24.8

Most of the reasons behind the negative effect on the mechanical properties of geopolymer concrete are (1) the large difference in modulus of elasticity between natural aggregate and CRWA, resulting in a large incompatibility between geopolymer paste and CRWA; (2) the weak bond between the rubber aggregate and geopolymer paste, resulting in the formation of weak areas in the interfacial transition zone (3), the CRWA has an inhomogeneous distribution due to its low weight relative to the natural aggregate, which causes inhomogeneity due to compaction. (4) the water-repellent property of the CRWA,

which leads to the trapping of air bubbles within the mixture and the creation of weak zones, loss of stiffness owing to the inclusions of crumb rubber waste aggregate, and lower density as the crumbed rubber content increased [7,31,37]. All these factors contribute to the loss of the mechanical properties of geopolymer concrete containing crumbed rubber waste aggregate.

3.2.3 Ultrasonic Pulse Velocity

The UPV test is used to assess the uniformity, quality, and existence of voids in geopolymer concrete using the average of three cubic specimens 100 mm according to ASTM C 597 [38]. Figure 5 depicts the relationship between ultrasonic pulse velocity and varying proportions of CRWA. According to this Figure, the pulse transmission of the investigated specimens decreases linearly as the content of CRWA increases. Incorporating crumb rubber waste aggregate by 10%, 20%, and 25% reduces the UPV results to 8.8%, 17.4% and 19.7% at 7 days of age, respectively.

$$UPV=-0.0009C^2+0.0963C+0.6949$$
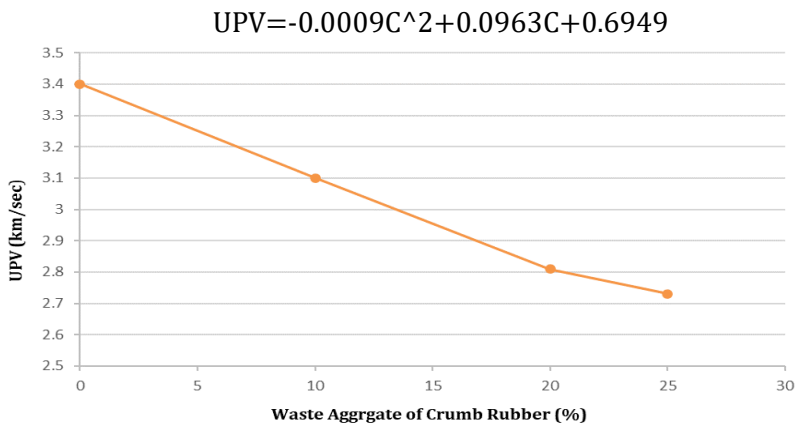
Fig. 5. Effect of crumb rubber waste aggregate recycling on the upv of geopolymer concrete
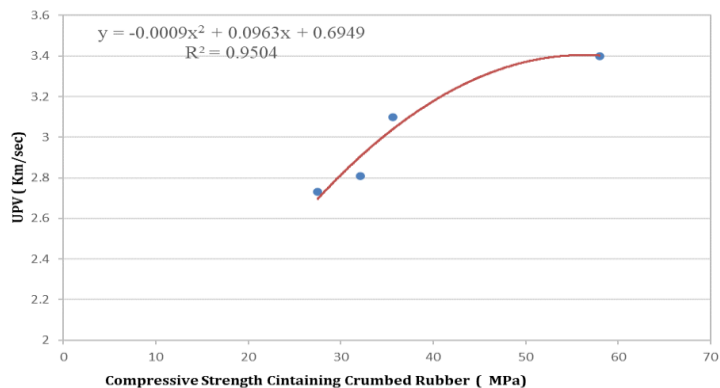
Fig. 6. The Relationship between the Compressive Strength and UPV for GPC with Crumbed Rubber Waste Aggregate

This reduction is attributed to the porous structure of geopolymer concrete containing rubber and the lower wave conductivity of rubber compared to natural aggregate, thus delaying the time required for waves to travel through the geopolymer concrete matrix

[39,40]. There is a strong correlation with R2=0.9504 between the compressive strength (C) of geopolymer concrete containing crumbed rubber waste aggregate and the ultrasonic pulse velocity (UPV), as shown in Figure 6. The following equation can illustrate these two essential properties:

3.2.4 Splitting Tensile Strength

Figure 7 and Table (10) display the results of the splitting tensile strength for different geopolymer concrete mixtures at seven days of age using the average of three cylindrical specimens 100 mm in diameter and 200 mm in height according to ASTM C 496[41]. The results illustrate that the splitting tensile strength for GPC decreases by about 10.6%, 15.2%, and 21.2% for GPC with 10%, 20%, and 25% CRWA, respectively. This is due to the reduction in the bond between the geopolymer matrix and rubber aggregate surfaces and the low stiffness of the CRWA compared with the natural coarse aggregate [33,42,43].
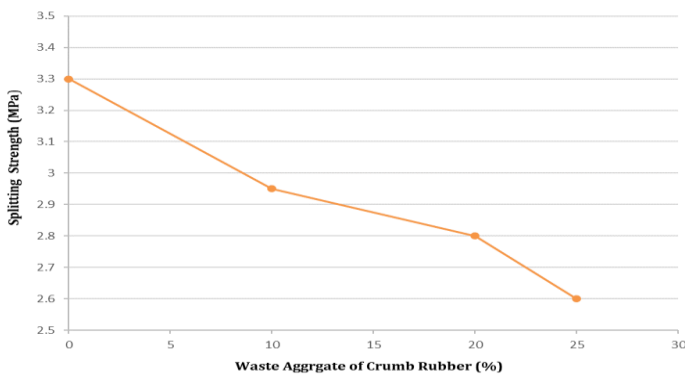
Fig. 7. Effect of recycled crumb rubber waste aggregate on the splitting tensile strength of geopolymer concrete

3.2.5 Flexural Strength

The flexural strength of every mixture at seven days of age was determined using the average of three prismatic samples with dimensions of 100*100*400 mm according to ASTM C 78 [44]. The results of GPC without and with different contents of crumbed rubber waste aggregate are shown in Figure 8 and Table (10).
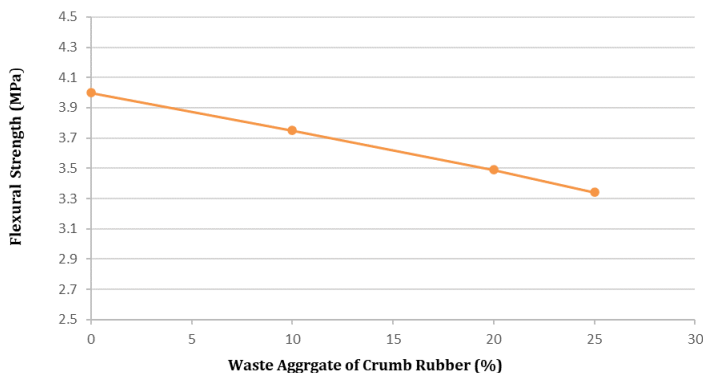

Fig. 8. Influence of crumb rubber waste aggregate recycling on the flexural strength of geopolymer concrete

The flexural strength of GPC decreases marginally, with crumb rubber aggregate waste increasing the flexural tensile strength decreased by 6.25%, 12.75% and 16.5% for the10%, 20% and 25% crumb rubber substitutions, respectively. The reason for the low flexural strength is due to the weak bond strength between the rubber surface and the geopolymer paste and as a result of the high Poisson's ratio, which is approximately 0.5, and the low stiffness of rubber compared to natural coarse aggregate [33,45]. The high value of Poisson's ratio gives a clear indication that as soon as internal tensile stresses occur in the concrete, the rubber will compress in the perpendicular direction to those stresses faster than the concrete itself and the aggregates and thus increase the bond failure [46,47].

3.2.6 Water Absorption

Table (10) shows the water absorption capability of different GPC mixes with or without crumb rubber waste aggregate at seven days of age. The average of three cubic specimens 100 mm in size was used according to ASTM C 642[36]. It can be concluded that the water-absorption capacity of rubberized geopolymer concrete increases with increasing crumb rubber content. This is because the number and size of voids in the geopolymeric concrete microstructure increased [48]. The evaporation of water content and the lower degree of mix compaction due to the light weight of rubber lead to the formation of more voids in the interfacial transition zone between the geopolymer matrix and the rubber waste aggregate compared with the geopolymer concrete mix not containing crumbed rubber waste aggregate. All concrete mixes have a water absorption rate of less than 10%, considered good concrete [49].

3.2.7 Permeability (Depth of Penetration Water Under Pressure)

Water penetration was applied according to BSEN12390-8:2000[50] on cubic geopolymer concrete specimens (150 mm) under pressures of 500-+50 kPa for 72-+2 hr. The permeability results for geopolymer concrete mixes at seven days of age, including crumb rubber waste aggregate, are shown in Figure 9.
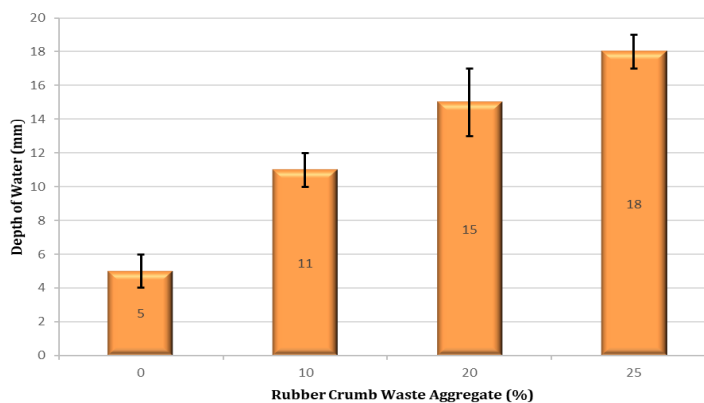
Fig. 9. Effect of crumb rubber waste aggregate recycling on the permeability of geopolymer concrete

It can be shown that the inclusion of crumb rubber waste increases the water penetration depth from 5 mm for the reference mix without rubber waste to 11, 15, and 18 mm for GPC with crumb rubber waste aggregate as a substitute for the natural coarse aggregate of 10, 20, and 25%, respectively. The detrimental effect created by the inclusion of rubber waste is due to the initiation of more pores and microcracks in the microstructure of the geopolymer matrix. The increase in pores is due to the poor workability of the mixtures

containing a larger volume fraction of rubber waste, which made the compaction process difficult and caused low bonding between the geopolymer matrix and rubber, thus producing more voids in the interfacial transition zone between the geopolymer matrix and the surfaces of the crumbed rubber waste aggregate and increasing the permeability of the geopolymer concrete [33,51]. In all cases, the average water penetration depth is less than 50 mm (5-18 mm) for all specimens, consistent with what was mentioned by Skutnik [52]; therefore, the geopolymer concrete tested is considered impermeable.

3.2.8 Thermal Conductivity

The thermal conductivity of any material is influenced by a wide variety of characteristics, such as its structure, the elements' proportion in the mixture, the aggregate type, density, and porosity [53]. Previous studies have shown that the type of aggregate has a significant impact on the thermal conductivity of the material [54]. According to ASTM C1113[55], the average thermal conductivity of three 100 mm cubic samples was determined. Figure 10 shows the experimental thermal conductivity values for the geopolymer concrete with different crumbed rubber waste aggregate contents measured under dry conditions at seven days of age. It has been discovered that including rubber particles in a geopolymer concrete matrix decreases the heat conductivity of geopolymer concretes. The values declined from 0.9229 W/m. K for the reference mix without rubber waste to 0.6153 W/m. K for a specimen with 25% rubber particles as a volume substitute for natural coarse aggregate with a reduction of 33.3% relative to the reference GPC. The reduction in the heat conductivity of the composite is due to the insulating effect of the rubber particles, which have lower thermal conductivity than the geopolymer matrix and natural coarse aggregate [56].
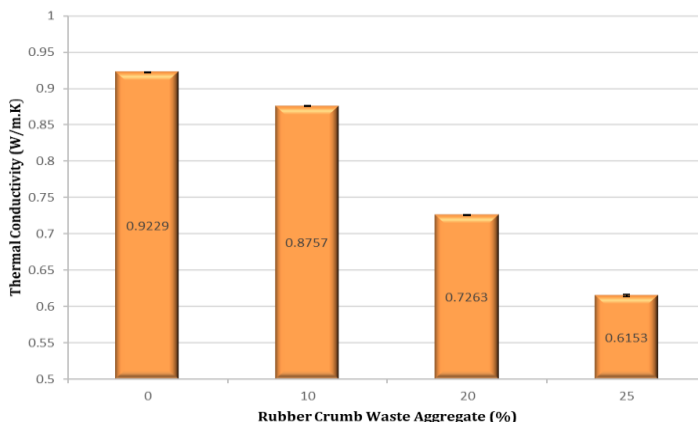
Fig. 10. Effect of the crumbed rubber waste aggregate content on the thermal conductivity of geopolymer concrete

3.2.9 SEM for GPC with Crumbed Rubber Waste Aggregate

A compacted dense geopolymer paste with tiny holes and a limited number of microcracks is observed in the GPC microstructure with 10% crumbed rubber waste aggregate, as illustrated in Figure 11. The microscopic images with different magnifications show a weak bond between the geopolymer matrix and the rubber waste aggregate particle. It is clear from these images that there is a continuous gap between the geopolymer matrix and the rubber waste aggregate. This enhances the experimental results obtained in this investigation, including the reduction in the strength and thermal conductivity and the

increase in the water absorption and permeability of GPC-containing crumbed rubber waste aggregate.

However, Figure 12 (a-f) show various (6) microscopic scales of the SEM micrographs of the fracture surface of hardened GPC specimens with natural coarse aggregate. The GPC matrix in Figure 12 (GPC without wastes) has a fairly uniform distribution of well-adhered aggregates; in contrast, Figure 11 (GPC with rubber) exhibits less uniformity and slightly more pore matrices with wider cracks. This is to be anticipated since the addition of CRWA often decreases concrete's mechanical strengths [7,57,58]. At increased magnification, the aggregate/matrix interaction may be seen in more detail in Figure 11 and 12 (d, e, f). It can be seen that cracks propagated throughout the microstructure of the samples. However, GPC without wastes exhibited fewer and narrower fractures, while GPC with rubber had greater propagation and broader cracks.
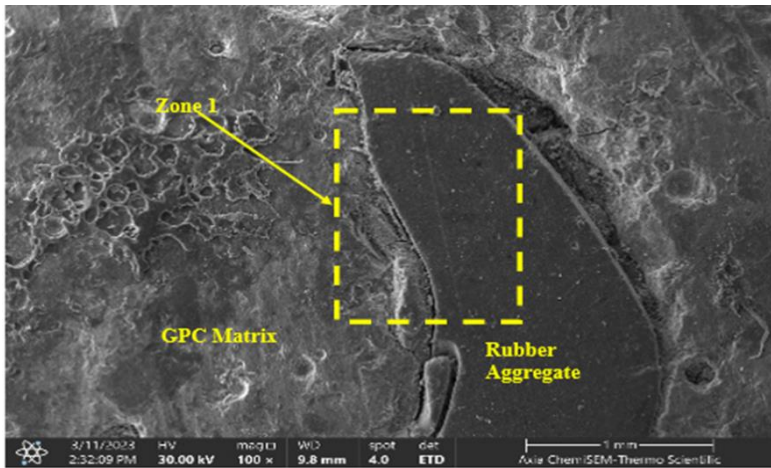
a- SEM for GPC with Crumbed Rubber waste Aggregate
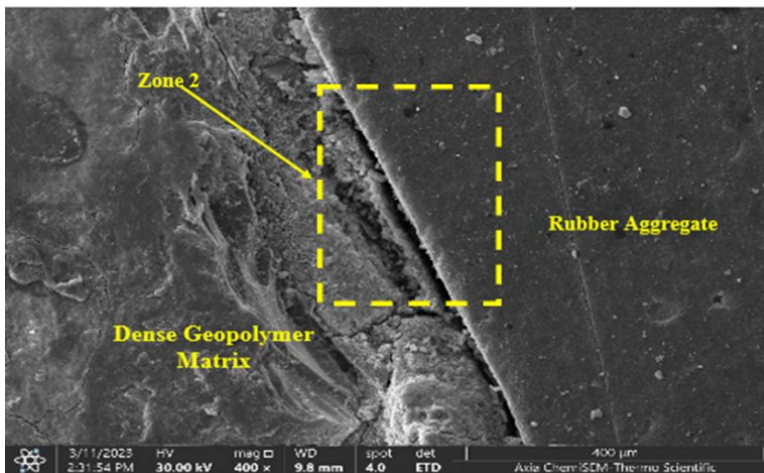
b- SEM for GPC with Crumbed Rubber waste Aggregate (Zone 1)
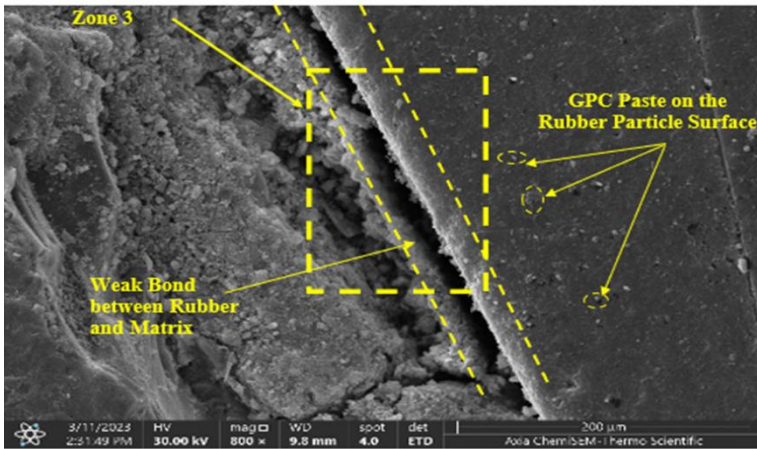
c- SEM for GPC with Crumbed Rubber waste Aggregate (Zone 2)
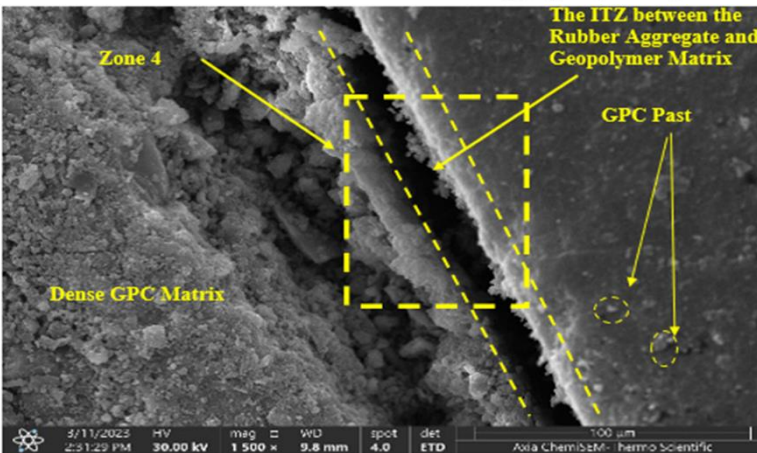
d- SEM for GPC with Crumbed Rubber waste Aggregate (Zone 3)
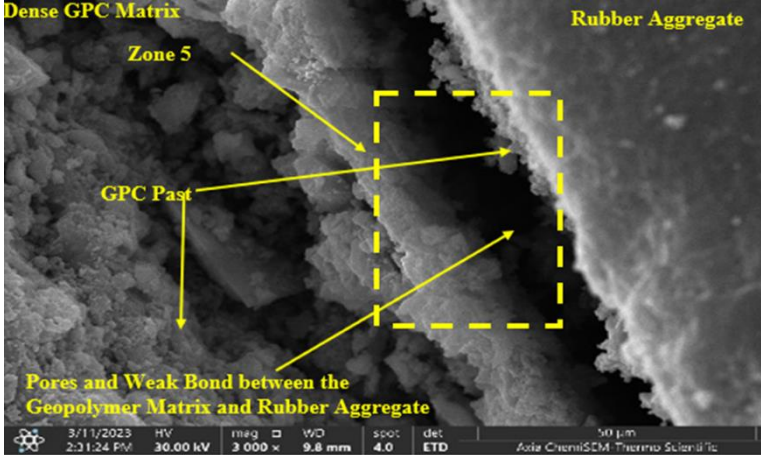
e- SEM for GPC with Crumbed Rubber waste Aggregate (Zone 4)
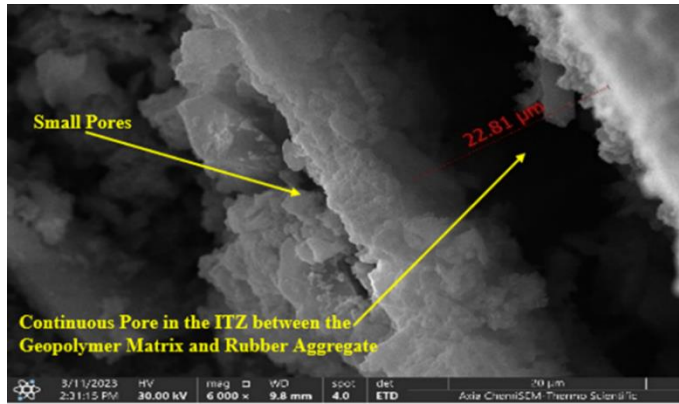
f- SEM for GPC with Crumbed Rubber waste Aggregate (Zone 5)

Fig. 11. (a-f) SEM images for GPC containing 10% crumbed rubber waste aggregate with different magnifications
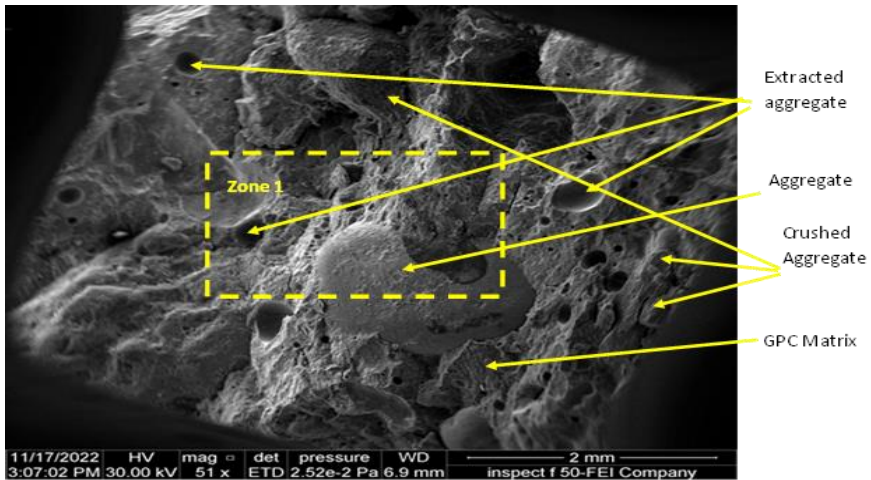
a-SEM for GPC with natural coarse aggregate
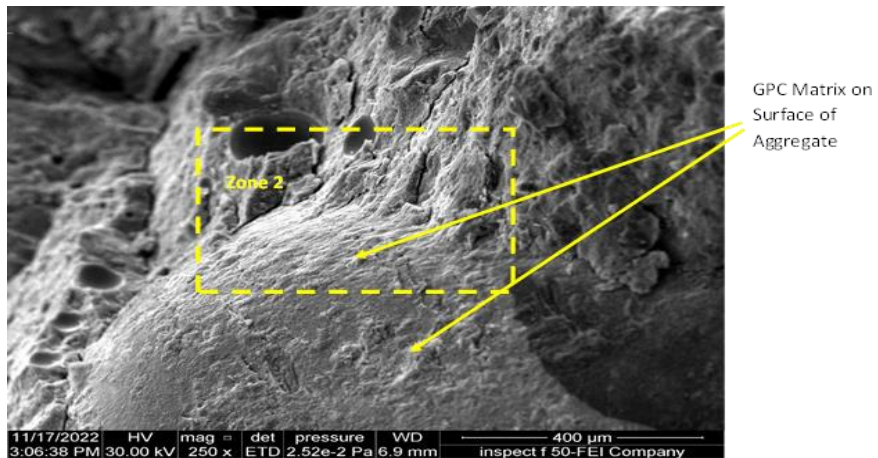
b- SEM image of GPC with natural coarse aggregate (Zone 1)

225
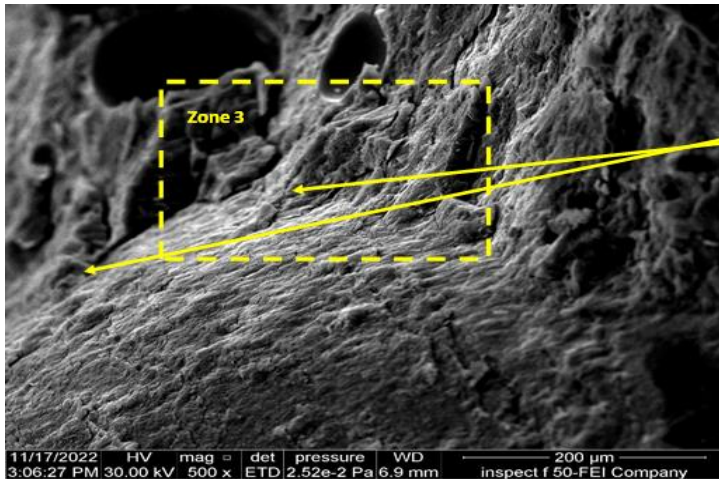
c- SEM image of GPC with natural coarse aggregate (Zone 2)
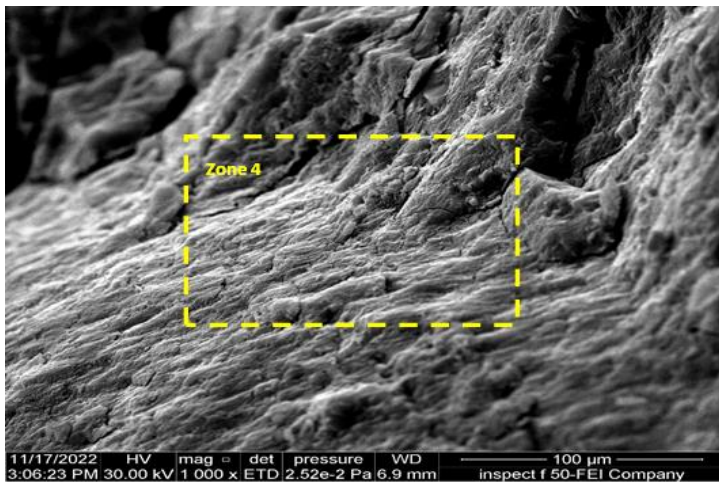
d- SEM image of GPC with natural coarse aggregate (Zone 3)
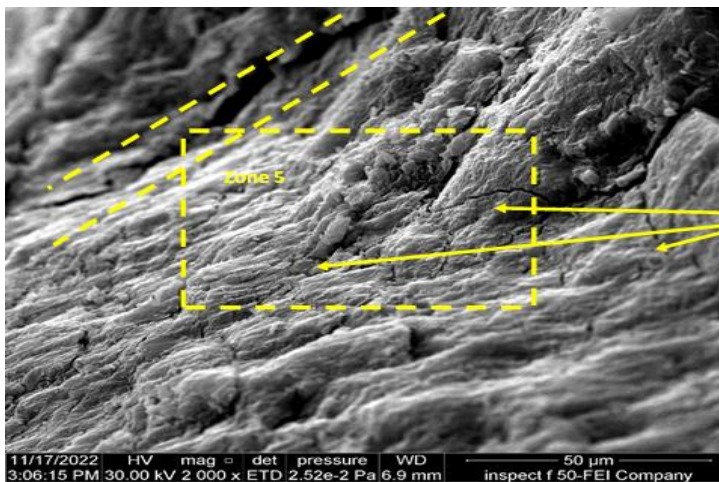
e-SEM image of GPC with natural coarse aggregate (Zone 4)
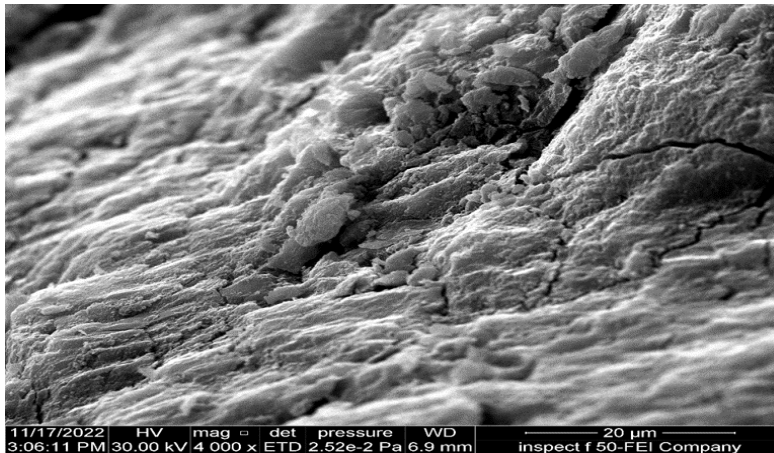
f- SEM image of GPC with natural coarse aggregate (Zone 5)

Fig. 12 (a-f) SEM images for GPC without waste aggregate with different magnifications

The interfacial transition zone (ITZ) can be observed in the geopolymer concrete with 10% rubber, while this distance is unclear in the geopolymer concrete without rubber. The lack of clarity of the ITZ of geopolymer concrete is probably due to the limited use of water in geopolymer concrete compared to cement concrete[57,59].

4. Conclusions

In addition to not utilizing cement in the concrete industry, GPC with CRWA reduces carbon dioxide emissions, energy consumption, and natural resource preservation. Furthermore, based on the findings and experimental work reported in this study, the following conclusions may be drawn:

- The fresh and dry densities of modified metakaolin-based GPC decreased when natural coarse aggregate was replaced with crumb rubber waste. This will be beneficial in reducing the weight of concrete (dead load) on the load-bearing concrete members, which is reflected positively in the design of concrete sections.
- Using coarse aggregates from rubber waste substantially reduces the compressive strength of geopolymer concrete. The compressive strength of geopolymer concrete specimens containing 10, 20, and 25% rubber waste coarse aggregate decreases by 38.6%, 44.6%, and 52.6%, respectively, compared to concrete specimens without rubber waste. In addition to reducing splitting and flexural strengths, the maximum reductions in splitting and flexural strengths are 21.2% and 16.5% for geopolymer concrete specimens containing 25% CRWA, respectively. Despite the decrease in the mechanical properties, geopolymer concrete produced in this investigation with 10% and 20% crumbed rubber waste aggregate (CRWA) can be used in different structural applications with compressive strengths of 35.6 MPa and 32 MPa, respectively. Geopolymer concrete with 25% CRWA can be used for non-structural purposes.
- The inclusion of rubber waste as coarse aggregate in geopolymer concrete increases the water absorption of geopolymer concrete compared with the reference GPC without wastes. However, the average water penetration depth was less than 50 mm (11–18 mm) for all of the tested geopolymer concrete specimens. This means that the geopolymer concrete is considered to be impermeable.

- The thermal conductivity and ultrasonic pulse velocity decrease significantly as the rubber waste aggregate content increases.
- The microscopic images for geopolymer concrete containing crumbed rubber waste aggregate enhance the experimental results obtained in this study in terms of strength reduction, thermal conductivity reduction, and the increase in water absorption and permeability.

Acknowledgements

References

[1] Al-Obediy NF. Some properties of polymer modified sustainable concrete. MS.c Thesis, University of Technology, Baghdad, Iraq 2016.

[2] ACI-523. Guide for cellular concretes above 50 lb/ft3 (800 kg/m3). 2014.

[3] Davidovits J. Properties of geopolymer cements. Conference: First International Conference Alkaline Cements and ConcretesAt: Kiev, Ukraine. 1994:131-149.

[4] Wallah S, Rangan BV. Low-calcium fly ash-based geopolymer concrete: long-term properties. Curtin University of Technology Perth, Australia 2006:1-107.

[5] Palomo A, Grutzeck M, Blanco M. Alkali-activated fly ashes: a cement for the future. Cement and Concrete Research 1999; 29:1323-1329. https://doi.org/10.1016/S0008-8846(98)00243-9

[6] Shen W, Shan L, Zhang T, Ma H, Cai Z, Shi H. Investigation on polymer-rubber aggregate modified porous concrete. Construction and Building Materials 2013; 38:667-674. https://doi.org/10.1016/j.conbuildmat.2012.09.006

[7] Aly A, El-Feky M, Kohail M, El-Sayed. Performance of geopolymer concrete containing recycled rubber. Construction and Building Materials 2019; 207:136-144. https://doi.org/10.1016/j.conbuildmat.2019.02.121

[8] Kurek I. The use of rubber granules from tire recycling as geopolymers filler - search. Conference, Cracow University of Technology, Faculty of Mechanical Engineering, Institute of Materials Engineering, Warszawska 24, 31-155 Cracow, Poland. 2017:1-6.

[9] Yeluri SC, Yadav N. Mechanical properties of rubber aggregates based geopolymer concrete - a review. IOP Conference Series: Materials Science and Engineering 2020; 989:1-12. https://doi.org/10.1088/1757-899X/989/1/012014

[10] Ahmed MF. Properties of Geopolymer Concrete Containing Waste Materials. 2020.

[11] Al-Shathr B, Al-Attar T, Hasan Z. Optimization of geopolymer concrete based on local Iraqi metakaolin. The 2nd International Conference of Buildings, Construction and Environmental Engineering, Beirut, Lebanon. 2015:97-100.

[12] AL-Swaidawi A. Performance of geopolymer concrete exposed to waste accumulation in oil refineries. Civil Engineering Department University of Technology PHD Thesis, Baghdad, Iraq 2022.

[13] Hasan Z. Manufacturing and studying properties of geopolymer concrete produced by using local materials. 2016.

[14] Yun-Ming L, Cheng-Yong H, Al-Bakri MM, Hussin K. Structure and properties of clay-based geopolymer cements: a review. Progress in Materials Science 2016; 83:595-629. https://doi.org/10.1016/j.pmatsci.2016.08.002

[15] Liu Z, LiuShao NN, Huang TY, Qin JF, Wang DM, Yang Y. Effect of SiO2/Na2O mole ratio on the properties of foam geopolymers fabricated from circulating fluidized bed fly ash. International Journal of Minerals, Metallurgy and Materials 2014; 21:620-626. https://doi.org/10.1007/s12613-014-0950-5

[16] ASTM - C618-22. Standard specification for coal fly ash and raw or calcined natural pozzolan for use in concrete. American Society for Testing and Materials, Annual Book: West Conshohocken, PA, USA 2022.

[17] Iraqi-Specification-No. 45. Aggregate from natural sources for concrete and construction. Central Organization Iraq 2016.

[18] DCP. Data sheet for flocrete SP33. https://www.dcp-int.com/iq/en/products/flocrete-sp33.

[19] ASTM-C494M-17. Standard specification for chemical admixtures for concrete. American Society for Testing and Materials, Annual Book: West Conshohocken, PA, USA 2017.

[20] Sika-Company. Silica fume. https://www.sika.com/

[21] ASTM-C1240. Standard specification for silica fume used in cementitious mixtures. American Society for Testing and Materials, Annual Book: West Conshohocken, PA, USA 2020.

[22] Xue G, Cao M. Effect of modified rubber particles mixing amount on properties of cement mortar. Advances in Civil Engineering 2017; 5:1-6. https://doi.org/10.1155/2017/8643839

[23] Segre N, Monteiro PJ, Sposito G. Surface characterization of recycled tire rubber to be used in cement paste matrix. Journal of Colloid and Interface Science 2002; 248:521-523. https://doi.org/10.1006/jcis.2002.8217

[24] Siddique R, Kadri E. Properties of high-volume fly ash concrete reinforced with natural fibres. Leonardo Journal of Sciences 2012; 21:83-98.

[25] ASTM - C29M-15. Standard test method for bulk density ("unit weight") and voids in aggregate. American Society for Testing and Materials, Annual Book: West Conshohocken, PA, USA 2015.

[26] ASTM-C127-15. Standard test method for density, relative density (specific gravity), and absorption of coarse aggregate. American Society for Testing and Materials, Annual Book: West Conshohocken, PA, USA 2015.

[27] Hadi M, Farhan N, Sheikh M. Design of geopolymer concrete with GGBFS at ambient curing condition using Taguchi met1. Hadi M, Farhan N, Sheikh M. Design of geopolymer concrete with GGBFS at ambient curing condition using Taguchi method. Constr Build Mater. 2017;140:424-31. hod. Construction and Building Materials 2017; 140:424-431. https://doi.org/10.1016/j.conbuildmat.2017.02.131

[28] Mehta A, Siddique R, Singh B, Aggoun S, Łagód G, Barnat-Hunek D. Influence of various parameters on strength and absorption properties of fly ash based geopolymer concrete designed by Taguchi method. Construction and Building Materials 2017; 150:817-824. https://doi.org/10.1016/j.conbuildmat.2017.06.066

[29] ASTM-C143. Standard test method for slump of hydraulic cement concrete. American Society for Testing and Materials, Annual Book: West Conshohocken, PA, USA 2015.

[30] Alsaif A, Koutas L, Bernal S, Guadagnini M, Pilakoutas K. Mechanical performance of steel fibre reinforced rubberised concrete for flexible concrete pavements. Construction and Building Materials 2018; 172:533-543. https://doi.org/10.1016/j.conbuildmat.2018.04.010

[31] Su H, Yang J, Ling TC, Ghataora G, Dirar S. Properties of concrete prepared with waste tyre rubber particles of uniform and varying sizes. Journal of Cleaner Production 2015; 91:288-296. https://doi.org/10.1016/j.jclepro.2014.12.022

[32] ASTM-C138. Standard test method for density (unit weight), yield, and air content (gravimetric) of concrete. American Society for Testing and Materials, Annual Book: West Conshohocken, PA, USA 2015.

[33] Khaloo A, Dehestani M, Rahmatabadi P. Mechanical properties of concrete containing a high volume of tire-rubber particles. Waste Management 2008; 28:2472-2482. https://doi.org/10.1016/j.wasman.2008.01.015

[34] Hamidi F, Valizadeh A, Aslani F. The effect of scoria, perlite and crumb rubber aggregates on the fresh and mechanical properties of geopolymer concrete. Structures 2022; 38:895-909. https://doi.org/10.1016/j.istruc.2022.02.031

[35] Siddique R, Naik T. Properties of concrete containing scrap-tire rubber - an overview. Waste Management 2004; 24:563-569. https://doi.org/10.1016/j.wasman.2004.01.006

[36] ASTM-C642. Standard test method for density, absorption, and voids in hardened concrete. American Society for Testing and Materials, Annual Book: West Conshohocken, PA, USA 2015.

[37] Atahan AO, Yücel AÖ. Crumb rubber in concrete: static and dynamic evaluation. Construction and Building Materials 2012; 36:617-622. https://doi.org/10.1016/j.conbuildmat.2012.04.068

[38] ASTM-C597. Standard test method for pulse velocity through concrete. American Society for Testing and Materials, Annual Book: West Conshohocken, PA, USA 2015.

[39] Babafemi A, Šavija B, Paul S, Anggraini V. Engineering properties of concrete with waste recycled plastic: a review. Sustainability (Switzerland) 2018; 10:1-26. https://doi.org/10.3390/su10113875

[40] Jain A, Siddique S, Gupta T, Jain S, Sharma R, Chaudhary S. Fresh, strength, durability and microstructural properties of shredded waste plastic concrete. Iranian Journal of Science and Technology - Transactions of Civil Engineering 2019; 43:455-465. https://doi.org/10.1007/s40996-018-0178-0

[41] ASTM-C496. Standard test method for splitting tensile strength of cylindrical concrete specimens. American Society for Testing and Materials, Annual Book: West Conshohocken, PA, USA 2015.

[42] Bignozzi M, Sandrolini F. Tyre rubber waste recycling in self-compacting concrete. Cement and Concrete Research 2006; 36:735-739. https://doi.org/10.1016/j.cemconres.2005.12.011

[43] Ganjian E, Khorami M, Maghsoudi A. Scrap-tyre-rubber replacement for aggregate and filler in concrete. Construction and Building Materials 2009; 23:1828-1836. https://doi.org/10.1016/j.conbuildmat.2008.09.020

[44] ASTM-C78. Standard test method for flexural strength of concrete (using simple beam with third-point loading). American Society for Testing and Materials, Annual Book: West Conshohocken, PA, USA 2015.

[45] Yung WH, Yung LC, Hua LH. A study of the durability properties of waste tire rubber applied to self-compacting concrete. Construction and Building Materials 2013; 41:665-672. https://doi.org/10.1016/j.conbuildmat.2012.11.019

[46] Gabryś K. Experimental research on compressibility characteristics of recycled concrete aggregate: recycled tire waste mixtures. Journal of Material Cycles and Waste Management 2023:1-12. https://doi.org/10.1007/s10163-023-01694-9

[47] Wang H, Wu Y, Cheng B. Mechanical properties of alkali-activated concrete containing crumb rubber particles. Case Studies in Construction Materials 2022; 16:1-13. https://doi.org/10.1016/j.cscm.2021.e00803

[48] Azrem A, Mustafa M, Mohd C, Ahmad R, Musa L, Sheau L. The effect of different crumb rubber loading on the properties of fly ash-based geopolymer concrete. IOP Conference Series: Materials Science and Engineering 2019; 551:1-9. https://doi.org/10.1088/1757-899X/551/1/012079

[49] Neville A. Properties of concrete. Fifth edit. San Diego: Wiley; 2011.

[50] BS-EN-12390-8. Testing hardened concrete depth of penetration of water under pressure. Standard-British-Institution 2019.

[51] Khatib Z, Bayomy F. Rubberized portland cement concrete. Journal of Materials in Civil Engineering 1999; 11:206-213. https://doi.org/10.1061/(ASCE)0899-1561(1999)11:3(206)

[52] Skutnik Z, Sobolewski M, Koda E. An experimental assessment of the water permeability of concrete with a superplasticizer and admixtures. Materials 2020; 13:1-16. https://doi.org/10.3390/ma13245624

[53] Mangat P, Azari M. A theory for the free shrinkage of steel fibre reinforced cement matrices. Journal of Materials Science 1984; 19:2183-2194. https://doi.org/10.1007/BF01058094

[54] Bouguerra A, Laurent J, Goual M, Queneudec M. The measurement of the thermal conductivity of solid aggregates using the transient plane source technique. Journal of Physics D: Applied Physics 1997; 30:2900-2904. https://doi.org/10.1088/0022-3727/30/20/018

[55] ASTM-C1113. Standard test method for thermal conductivity of refractories by hot wire (platinum resistance thermometer technique). American Society for Testing and Materials, Annual Book: West Conshohocken, PA, USA 2015.

[56] Benazzouk A, Douzane O, Mezreb K, Laidoudi B, Quéneudec M. Thermal conductivity of cement composites containing rubber waste particles: experimental study and modelling. Construction and Building Materials 2008; 22:573-579. https://doi.org/10.1016/j.conbuildmat.2006.11.011

[57] Ahmad J, Zhou Z, Majdi A, Alqurashi M, Deifalla AF. Overview of Concrete Performance Made with Waste Rubber Tires: A Step toward Sustainable Concrete. Materials 2022; 15. https://doi.org/10.3390/ma15165518

[58] Al-Jaberi L, Wissam Al-Saraj ASK, Sahar AL-Serai ASJ. Scanning Electron Microscopy of Metakaolin Based Geopolymer Concrete. Journal of Physics: Conference Series 2021; 2114:012061. https://doi.org/10.1088/1742-6596/2114/1/012061

[59] Mehta P, Monteiro P. Concrete: microstructure, properties, and materials. 4th Editio. McGraw-Hill Education; 2014.

Research Article

Enhancing surface properties and corrosion resistance of API 5L X52 steel through orthogonal ball burnishing

Selma Belabend[1, a], Hamid Hamadache[1, b], Quang Phamdonhat[2, c]

[1]Research Laboratory of Advanced Technology in Mechanical Production (LRATPM), Mechanical Eng. Dept., Faculty of Technology, Badji Mokhtar-Annaba University, Algeria
[2] Sarl Ava Cristal, 12 Latham Beau Séjour, 23000 Annaba, Algeria

Article Info	Abstract
	Surface engineering involves using various technologies to modify the surface and near-surface areas of a material to enable it to perform different functions from the bulk of the material. Two primary methods of surface engineering are surface coatings and surface modification. Orthogonal ball burnishing is a process that improves certain surface integrity properties of materials through superficial plastic deformation. This study focuses on the effect of this treatment and the influence of its parameters on the physico-geometric surface characteristics of API 5L X52 steel. Burnishing tests were conducted with four main parameters: burnishing force (Py), feed rate (f), spindle speed (N), and number of passes (i). The analysis revealed an appropriate combination of burnishing parameters that led to a 98% reduction in surface roughness and a 42% increase in surface microhardness. A multi-objective optimization of roughness and microhardness after burnishing yielded optimal parameters. Furthermore, a multifactorial experimental design demonstrated that corrosion resistance increased by 318%.

1. Introduction

Deterioration of structural elements is caused by mechanical interactions, contact with other elements, exposure to aggressive environments and exposure to dynamic loads. This necessitates the modification of surface layers to enhance properties and meet high technical standards, with a particular emphasis on strength and corrosion resistance[1,2].Despite considerable efforts to ensure their safety and reliability, pipeline failures still occur. The primary mode of failure is leakage or rupture caused by cracks and defects in the pipes during their production process or corrosion during their service life. Such defects can compromise the integrity of the pipeline and pose serious safety risks[3].Failure on the outer surface of oil and gas pipelines is a significant concern [4,5]. Several studies have investigated the causes and consequences of pipeline failures Song et al[6] found that the leakage and ignition of a carbon steel pipeline were mainly due to local electrochemical corrosion. Ranjbar and Alavi Zaree [7] identified pitting corrosion as the primary failure mechanism in a micro alloyed steel pipeline, caused by the accumulation of corrosion products and water separation. Assessment of oil and gas pipeline failure in Vietnam has been studied by Dao U et al [8]. They propose a model that integrates Fault Tree Analysis (FTA) and fuzzy theory to analyze the causes of pipeline failure and evaluate the level of uncertainty using Monte Carlo simulation. The study identifies twenty-one risk factors that lead to pipeline failure, with rupture being the highest risk, followed by puncture. Corrosion has lower chances of pipeline failure but carries catastrophic

consequences. To prevent such occurrences, it is essential to ensure high-quality surface finishes for these products. In this regard, surface integrity is widely used as a quality criterion or for comparison purposes among different materials or different states of the same material. Such properties strongly depend on the quality of the surface finish. However, it has been found that regardless of the manufacturing technology (e.g., machining, heat treatment), on the one hand, the surface layers can be overloaded due to residual tensile stresses that add to the service stresses, and on the other hand, all mechanical surfaces consist of irregular pics and valleys with varying heights and spacing [9] , which can act as sites for corrosion or stress concentration. Therefore, these surfaces undergo surface finishing processes that can improve their physical-geometric properties in terms of microhardness and roughness [5-6].

One increasingly used solution in surface engineering is to integrate surface treatment operations into the production process of structural elements. Burnishing is one such surface treatment operation that is gradually being used as a finishing process to quickly generate high-quality surfaces, offering additional benefits to surface integrity [12]. The process can be easily executed without chip removal on both universal and CNC machine tools [13]. In this regard, various tool designs have emerged, ranging from simple devices to tools assisted by vibrations or ultrasonics [9-10], enabling process automation and increased production rates [16]. In all cases, the generated surface results from a controlled and carefully applied pressure using a ball or roller, without any change in volume, structure, or chemical composition of the material to impart specific physical, mechanical, and tribological properties [17]. The process provides good corrosion resistance and improved fatigue life[18]. A literature review has shown that numerous experimental studies have been conducted to identify the effects of burnishing on surface quality and surface microhardness. Surface roughness, after ball burnishing treatment, can be improved by 40% to 90%, while hardness can be increased by 5% to 160% [16,19]. A multi-objective optimization of process parameters for low plasticity burnishing on aluminum alloy AA6061T6 was performed by Thorat et al [20]. The burnishing process parameters considered were pressure, speed, ball diameter, ball material, and number of passes. Kovács et al. [21] applied Magnetic Assisted Ball Burnishing (MABB) to enhance the hardness and decrease the roughness of machined parts made of C45 steel. Through Taguchi method optimization, they discovered that the corrosion rate is greatly influenced by the burnishing speed and strategy. Al-Qawabeha et al. [22] conducted research on the influence of burnishing on A53 steel. Their study revealed that the corrosion rate decreased with an increase in applied force up to 80 N. However, exceeding this threshold force resulted in an escalation of the corrosion rate. The ball burnishing process has been extensively studied, with parameters such as speed, feed rate, burnishing force, ball diameter, and lubricant type under investigation. These parameters have been found to have significant effects on various aspects of the burnishing process, including surface roughness, residual stresses, microhardness, plastic strain, phase transformation, elastic recovery effect, ball indentation mark, and thermal behavior of the workpiece. Additionally, process parameters also influence the surface integrity of the workpiece, affecting properties such as corrosion resistance, wear resistance, fatigue life, and dimensional tolerances [23–25]. Four critical factors—burnishing force (Py), feed rate (f), spindle speed (N), and the number of passes (i)—were investigated to assess their influence on the surface roughness and microhardness of the outer surface of the pipeline material. The authors of this study based their selection burnishing parameters on well-established guidance from the existing literature[25–27].

By employing a robust combination of Taguchi L16 to analyse the effect of ball burnishing parameters on roughness and microhardness, and a comprehensive full-factorial design study was executed to meticulously evaluate the effects of burnishing parameters on corrosion resistance. Additionally, to gain deeper insights into corrosion resistance, Response Surface Methodology (RSM) was adeptly employed alongside regression

analysis. These analytical tools collectively facilitated the development of a precise linear model capable of predicting the behaviour of essential parameters, including surface roughness (Ra), microhardness (µHv), and, significantly, corrosion resistance (Rp). The incorporation of ANOVA provided essential statistical insights into the impact of these parameters on the overall performance of the material.

Furthermore, to optimize the material properties, a Desirability Function Approach (DFA) was employed. This optimization technique aimed to maximize microhardness while simultaneously minimizing surface roughness. The integration of DFA further enhanced the study's ability to fine-tune the burnishing process for superior material performance.

2. Experimental Details

2.1. Material

The material used in this study is API 5L X52 steel, which is commonly used in the oil and gas industries. It is a high yield strength low alloy steel that meets the specification requirements of the API 5L standard [28]. To perform spectral examination of the material, spectrometry (OLYMPUS optical microscope) was utilized, which resulted in the chemical composition as follows (Table 1).

Table 1. Chemical composition of API 5L X52 steel [29]

Compound	C	Mn	Si	P	S	Cu	Ni	Cr
%	0.16	1.33	0.22	0.010	0.002	0.033	0.013	0.047

The mechanical properties of the steel were assessed using tensile testing conducted at room temperature. Prismatic specimens were meticulously prepared in accordance with the ASTM A370 standard [28], ensuring precision and consistency in the testing process. A total of six tests were carried out on the steel specimens, and the subsequent analysis yielded the following average mechanical properties: the yield strength (Re) was determined to be 439.24 MPa, while the ultimate tensile strength (UTS) was measured at 575.5 MPa. Additionally, the elongation at rupture (A%) was calculated to be 35.6. The steel was subjected to six tests, and the resulting average properties were evaluated. Specifically, the initial surface condition was characterized by a roughness of Ra = 2.82 µm and a microhardness of µHv = 188 [29].

2.2. Burnishing

In order to guarantee the inclusiveness of industrial structures, samples were collected longitudinally from a pipeline. The preliminary surface preparation was conducted by employing a vertical milling machine, more precisely an HMT India Type, which was outfitted with a carbide metal end mill. To facilitate the implementation of the burnishing treatment, as per the experimental design methodology, the sample was partitioned into zones with the aid of grooves that had a width of 50 mm and a depth of 2 mm, as depicted in Figure 1[29].

The mechanical treatment of the specimens was executed through the utilization of a ball burnishing instrument on a vertical milling apparatus. To achieve this, a purpose-specific burnishing tool was designed, as illustrated in Figure 2. The system comprises a sturdy steel ball that is affixed to a shaft which glides within a hub of the tool holder. The applied force is measured with a load spring calibrated to a specific value. The burnishing system is then mounted on the spindle to be subjected to vertical displacement. The burnishing procedure begins by exerting force with the ball onto the surface of a part, thereby causing a corresponding plastic deformation on a point of the external layer. The ball is then

scanned across the entire surface in order to complete the burnishing operation[30]. In this investigation of ball burnishing of API 5L X52 steel, the mechanical surface treatment was performed on the exterior surface of the pipeline.

For this study, a bespoke static device with interchangeable heads was meticulously designed. This device is capable of treating both cylindrical and prismatic surfaces. A patent application (No.: DZ/P/2023/000830) for this apparatus was filed on 18/06/2023.
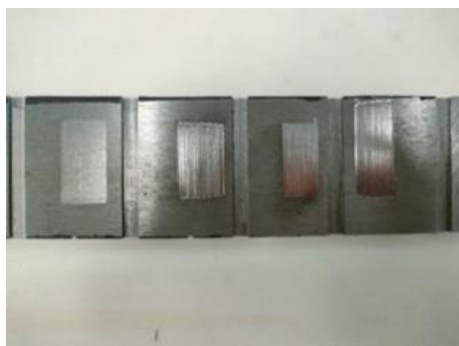
Fig. 1. Sample preparation [29]

Fig. 2. Setup photo of the burnishing operation[29]

Roughness was measured at three distinct locations on the machined surface using a Cyber Technology CT100 laser source profilometer. The measurements were repeated three times, and the average values were recorded. Microhardness of the samples was measured using a Matsuzawa MXT70 microhardness tester with a 200-gf load applied for 10 seconds. Similarly, measurements were taken at three different zones, and the average value was considered as the test result. Table 2 summarizes the test results along with the corresponding signal-to-noise (S/N) ratios.

Table 2. Taguchi Matrix of Measured Values for Ra and μHv

N°	Py	f	N	i	Ra	μHv
1	265	300	560	1	0.18	236
2	265	400	730	3	0.17	254
3	265	500	900	5	0.15	250
4	265	600	1070	7	0.13	230
5	347.5	300	730	5	0.09	239
6	347.5	400	560	7	0.07	245
7	347.5	500	1070	1	0.12	239
8	347.5	600	900	3	0.05	211
9	430	300	900	7	0.26	246
10	430	400	1070	5	0.14	229
11	430	500	560	3	0.22	267
12	430	600	730	1	0.14	211
13	512.5	300	1070	3	0.12	223
14	512.5	400	900	1	0.14	205
15	512.5	500	730	7	0.15	218
16	512.5	600	560	5	0.11	214

2.3. Corrosion Test

There are several techniques to determine corrosion rates, including electrochemical impedance spectroscopy (EIS), electrochemical linear polarization resistance (LPR), and the weight loss technique. For the electrochemical analysis, a Gamry 600+ cell controlled by a microcomputer was utilized to investigate the electrochemical properties. Corrosion tests were conducted on samples coated with acrylic resin to improve adhesion. The samples were cleaned in an ultrasonic tank and dried with acetone prior to coating. The examination specimens were arranged in a three-electrode configuration, consisting of a reference electrode, a counter electrode, and a working electrode. These specimens were then immersed in a concentrated 3.5% NaCl aqueous solution of distilled water (Fig 3). The electrochemical linear polarization resistance (LPR) technique was employed as part of this study to assess the corrosion behavior of the specimens[31,32]. The electrochemical linear polarization resistance (LPR) technique can be used for corrosion monitoring and control in various applications. It is a method that measures the resistance of a material to corrosion by applying a small potential to the material and measuring the resulting current. LPR can be used to validate the corrosion rate obtained from other methods, such as the impressed current method, and can provide a more accurate quantification of the actual mass loss rate of steel in natural environments[33–35].

Electrochemical corrosion tests were performed at room temperature. The corrosion potential (Ecorr) was set within the range of -0.8 to -0.3 mV, and the scanning rate was set at 1 mA/s. However, the immersion time of the samples in the saline solution was limited to 30 minutes to record the OCP (Open Circuit Potential) curves, while it was extended to 20 minutes for the Tafel curves. Corrosion resistance was characterized by the corrosion potential (Ecorr), corrosion current (Icorr), and the potential (β) between the cathode and anode. Such measurements were directly obtained using the GAMRY software, which controlled the electrochemical cell.

2.4. Methodology

Taguchi techniques are a strategy that uses simulation to optimize parameters and reduce
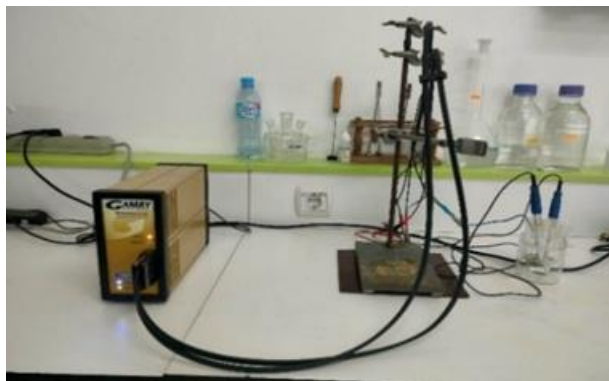
Fig. 3. Corrosion test Gamry 600+ cell [29]

solution space in various fields. To optimize the number of simulations required, they involve a sequence of experiments to narrow down the combinations of factors and levels. The Taguchi orthogonal array design matrix is used by the technique to determine the most significant factors that influence the performance parameter of interest. The analysis of variance (ANOVA) is then used to identify the contribution of each factor. Taguchi

method consists of three steps: design of experiments (DOE), signal-to-noise (S/N) ratio analysis, and optimization. In the DOE step, a set of experiments is designed to investigate the effects of several factors on the performance of the process. The experiments are designed based on orthogonal arrays, which are a set of systematically arranged test cases that allow for the efficient and effective identification of the most significant factors. Orthogonal arrays reduce the number of experiments required while ensuring that all factors are evaluated at different levels [36,37]

Table 3 shows the configuration of the burnishing parameters and their levels for roughness and microhardness tests. These parameters were combined with each other in accordance with Taguchi's orthogonal plane L16 (Table 2).

Table 3. Factors and their levels for the experiments

Burnishing Parameters	Level			
	1	2	3	4
Py	265	347.5	430	512.5
f	300	400	500	600
N	560	730	900	1070
i	1	3	5	7

The design of the experimental design was optimized by the signal-to-noise ratio (S/N). This report is widely used as an objective function to solve engineering design problems [3]. The signals adopted for this study are such as "smaller is better" for roughness (Eq. 1) and "larger is better" for microhardness (Eq. 2).

$$\eta_s = -10\,log\left(\frac{1}{n}\sum_i^n y_i^2\right) \tag{1}$$

$$\eta_l = -10\,log\left(\frac{1}{n}\sum_i^n \frac{1}{y_i^2}\right) \tag{2}$$

where, y_i: the ith result of the experiment. n: the repeated number of the ith experiment

The experimental corrosion tests were conducted using a multifactorial design of full experiments. Two burnishing parameters, Py and f, were selected for this purpose, with two levels (low and high) assigned to each parameter. The burnishing was conducted with one pass and at 900 rpm. To facilitate analysis, the factors were translated into reduced focused variables, denoted as X1 and X2. The coding scheme employed in this study utilized (-1) to represent the low levels and (+1) to represent the high levels. A series of 4 trials were conducted, during which the factor levels were systematically combined based on the prescribed design and matrix of experiments. (Table 4).

Table 4. Factors and their levels for the experiments for the corrosion test

N	Natural Value		Coded Value	
	Py	f	X1	X2
1	265	400	-1	-1
2	265	500	-1	+1
3	430	400	+1	-1
4	430	500	+1	+1

3.Results and Discussion

3.1. Effect of Burnishing on Surface Roughness and Microhardness

The effect of burnishing on Ra and µHv was evaluated through the analysis of the signal-to-noise (S/N) ratio (Table 2). Under certain conditions, burnishing resulted in a surface topography characterized by Ra values ranging from 0.05 to 0.26 µm Figure 4 and 5.

The effect of each variable on the output response (Ra and µHv) is estimated using the S/N ratio for each experiment (Table 2). However, analyzing average S/N ratio by factor levels (Table 5) reveals that the optimal burnishing conditions for roughness are provided by level 2 of the burnishing force, level 4 of the feed rate and spindle speed, and level 3 of the number of tool passes. The corresponding actual values for this combination are as follows: Py = 347.5 N, f = 600 mm/min, N = 1070 rpm, and i = 5. The most significant effects (according to the RANK) are those of Py and f.
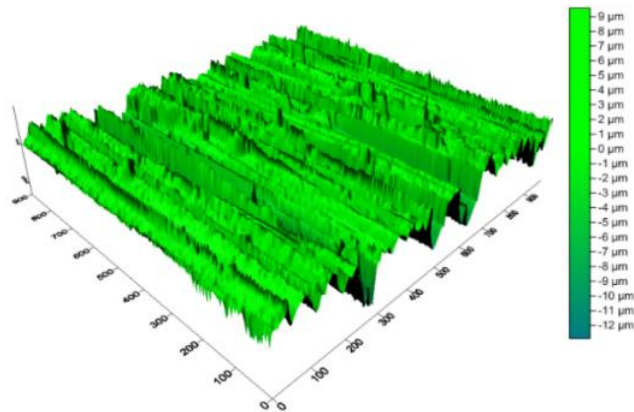
Fig. 4. Example of surface topography: before burnishing
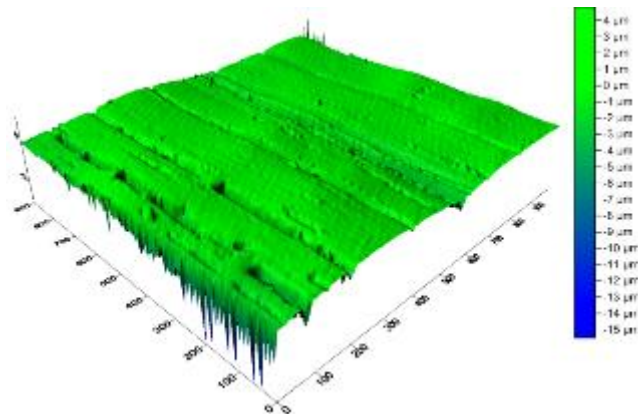
Fig. 5. Example of surface topography: after burnishing

Similarly, analyzing the S/N ratio for each level of parameters for surface microhardness reveals an optimal combination characterized by low levels of Py and spindle speed (N), level 3 of the feed rate (f), and level 2 of the number of passes (i). The corresponding actual values for this combination are as follows: Py = 265 N, f = 500 mm/min, N = 560 rpm, and i = 3. According to the Rank in Table 5, it is also observed that Py and f are the most

significant factors for microhardness. The effect of spindle speed is the least significant for both output responses.

Table 5. Average S/N Ratio by Level for Roughness (Ra) and Microhardness (µHv)

Levels	S/N Ra				S/N µHv			
	Py	f	N	i	Py	f	N	i
1	16.12	16.44	17.51	17.01	47.69	47.46	47.59	46.93
2	22.08	18.09	17.51	18.29	47.35	47.32	47.22	47.52
3	14.76	16.15	17.81	18.35	47.50	47.70	47.12	47.33
4	17.79	20.07	17.93	17.11	46.64	46.71	47.24	47.40
Delta	7.31	3.92	0.42	1.34	1.04	0.99	0.47	0.59
Rang	1	2	4	3	1	2	4	3

Figures 6 and 7 visually illustrate the primary effects of burnishing parameters on surface roughness and microhardness, respectively. In relation to both Ra and µHv, the burnishing force (Py) seems to exert a substantial influence on the signal-to-noise ratio. Regarding Ra, the second level of Py is considered the most favorable, while for µHv, the first level of Py is deemed the most desirable. Furthermore, the burnishing feed (f) also plays a significant role in both responses. When it comes to Ra, the fourth level of this parameter appears to be the most favorable, although the third level holds the greatest significance for µHv. Consequently, N (Spindle Speed) has the least significant impact on both Ra and µHv. Therefore N (Spindle Speed) has the least significant impact on both Ra and µHv. The number of passes (i) shows some influence, but it varies in its effect on the two responses.

To optimize the burnishing process and achieve the desired balance between surface roughness (with the aim of minimizing it) and microhardness (with the objective of maximizing it), a composite optimization approach known as the Desirability Function Approach (DFA) is performed. DFA is a powerful tool because it enables the simultaneous optimization of multiple factors and responses. By assigning desirability values to different levels of each parameter and response, DFA provides a comprehensive perspective on process performance [38].
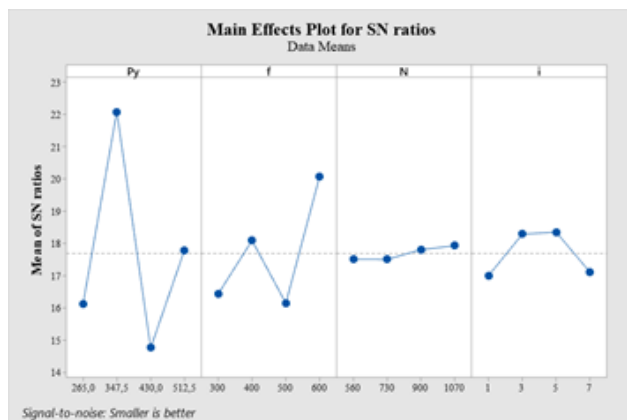
Fig. 6. Main effects of burnishing parameters Ra
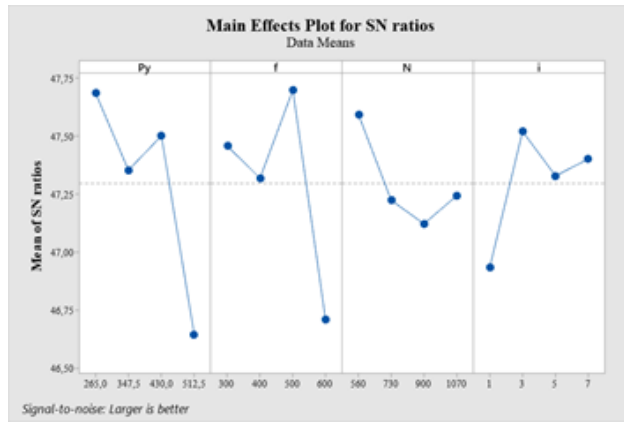
Fig. 7. Main effects of burnishing parameters µHv

3.2. ANOVA Analysis

To explore the impacts of burnishing process parameters in a quantitative manner, an Analysis of Variance (ANOVA) based on the Signal-to-Noise (S/N) ratio was utilized. An overview of the ANOVA outcomes for surface roughness is presented in Table 6, while Table 7 depicts the outcomes for microhardness. Following the ANOVA, a determination of the degree of influence of the parameters on the output was performed at a 95% confidence level via the calculation of the percentage contribution[37]. It can be observed from the ANOVA tables that burnishing force (60%) and feed rate (21%) play a significant role in minimizing surface roughness, whereas spindle speed (3%) and the number of passes (5%) do not exhibit notable effects on controlling surface roughness.

Table 6. Analysis of variance for surface roughness

Source	DF	Adj SS	Adj MS	F-Value	P-Value	Contribution %
Py	3	0.024850	0.008283	5.65	0.094	37%
f	3	0.008676	0.002892	1.97	0.296	32%
N	3	0.001247	0.000416	0.28	0.836	8%
i	3	0.001973	0.000658	0.45	0.737	12%
Error	3	0.004402	0.001467			11%
Total	15	0.041148				100%

This analysis shows that the burnishing force and feed rate are the most influential factors in reducing surface roughness, together accounting for (81%) of the variance. In contrast, spindle speed and the number of passes have minimal impact on surface roughness, contributing only (8%) in total.

Table 7. Analysis of variance for microhardness

Source	DF	Adj SS	Adj MS	F-Value	P-Value	Contribution %
Py	3	1754.4	584.8	3.54	0.163	60%
f	3	1519.9	506.6	3.07	0.191	21%
N	3	372.2	124.1	0.75	0.590	3%
i	3	562.4	187.5	1.14	0.459	5%
Error	3	495.0	165.0			11%
Total	15	4703.8				100%

ANOVA analysis for microhardness results indicates that the force applied (Py) and the feed rate (f) have a substantial impact on microhardness, contributing 37% and 32% to the variance, respectively. On the other hand, spindle speed (n) and the number of passes (i) show relatively lower contributions of 8% and 12%, respectively. The remaining unexplained variance is attributed to error, accounting for 11% of the total variance.

3.3 Regression Analysis

The regression analysis has yielded quadratic models to predict surface roughness (Eq. 3) and surface microhardness (Eq. 4) at any point within the study domain.

$$Ra = -13.83 + 0.03889 Py + 0.006061 + 0.03369\ N - 1.240\ i - 0.000049\ Py^2 - 0.000000\ f^2 - 0.000017 N^2 + 0.04531 i^2 - 0.00\ 0002\ Py \times f - 0.000005 Py \times N + 0.000135 Py \times i - 0.000020 f \times N + 0.001000 f \times i \tag{3}$$

$$\mu Hv = -1441 + 4.61\ Py + 1.197\ f + 3.152\ N - 113.5\ i - 0.00480\ Py^2 - 0.000203\ f^2 - 0.001144\ N^2 + 3.50\ i^2 - 0.000938\ Pyf - 0.001461\ Py \times N + 0.03467\ Py \times i - 0.002064\ f \times N + 0.0856\ f \times i \tag{4}$$

The obtained models accurately characterize the respective output responses, as indicated by the high coefficient of determination (R^2) values of 98.86% for surface roughness and 99.26% for microhardness. The quality of fit of the models to the experimental data is further validated by the adjusted determination coefficients (R_{aj}^2), which are approximately 91.43% and 94.44% for surface roughness and microhardness, respectively. The difference of less than 5% between these values indicates the absence of insignificant terms in the models [11].

3.4 Optimization and Validation of Results

To improve the corrosion resistance of the material post-treatment, it is imperative to find a compromise through the burnishing parameters that aim for both minimal roughness and maximum microhardness. Such an objective can be approached using the Desirability Function Approach (DFA). The considerable use of this approach is attributed to its simplicity, flexibility in weighting, and availability in the statistical software Minitab. When the responses are outside their acceptable limits (unacceptable value), the desirability is set to 0, while if the responses exactly coincide with the acceptable limits (target value), it is set to 1. Between these two values, the user has the discretion to assess, based on the responses calculated by the statistical model, the equivalent of a satisfaction percentage with respect to the set objectives. Therefore, the burnishing parameters need to be adjusted to approach the target value as closely as possible[38].

The significant utilization of this approach can be attributed to its simplicity, flexibility in weighting, and availability in statistical software. By assigning a value of +1 to the desired value (Ytarget) and a value of 0 to the unacceptable value (Yin), the desirability (di) can be expressed as follows: (Eq. 5).

$$d_i = \frac{y_i - y_{in}}{y_{target} - y_{in}} \tag{5}$$

Desirability allows for the evaluation of the level of satisfaction with regards to the established objectives, based on the responses obtained from the statistical model. Consequently, the global (composite) desirability can be expressed in the following form (Eq. 6):

$$D_i = \left[\sqrt{d_1 * d_2 * d_3 * d_4 * \ldots * d_n}\right]^{1/n} \tag{6}$$

If the value falls between 0 and 1, all the responses will be as close as possible to their target value, thus achieving the optimal compromise for the studied responses [38].
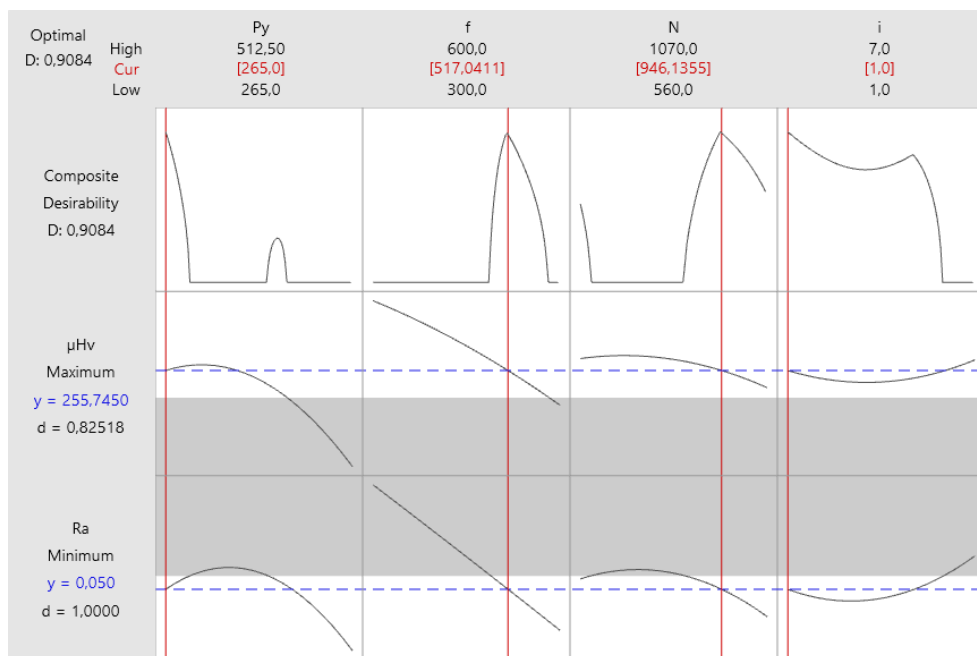
Fig. 8. Optimization graph of µHv and Ra

The results were collected and analyzed using the statistical software Minitab 19. By assigning equal weight and importance to both output responses, the burnishing regime that is expected to achieve a roughness ranging from 0.050 to 0.26 µm and a micro hardness ranging from 204.67 to 266.57 µHv is characterized by level 1 of (Py) and (i), level 2 of (f), and level 3 of (N). Validating the adjustment of this regime yields a composite desirability value of D = 0.9084. Figure 8 graphically illustrates the optimal individual adjustments of the burnishing parameters to achieve the predetermined objective. Finally, the burnishing regime derived from the DFA was experimentally evaluated for confirmation. The results are satisfactory, considering the achieved surface roughness (Ra = 0.07 µm) and microhardness (µHv = 265). These values are awfully close to those predicted by the regression models, demonstrating an improvement of 97.51% in surface roughness and a 40% increase in microhardness.

3.5. Effect of Burnishing on Corrosion Resistance

The experiments were performed on specimens in both their original machined condition and their burnished condition, utilizing various magnitudes of the burnishing force (Py) and feed rate (f) in accordance with a comprehensive, all-encompassing experimental design known as a full-factorial multifactorial design (Type 2^2) [29].The corrosion resistance was characterized by the polarization curve of API 5L X52 steel: Polarization curve of API 5L X52 steel– Tafel analysis and Open Circuit Potential (OCP) (Figure 9 and 10). Additionally, the Polarization Resistance (Rp) can be related to the corrosion current through the Stem and Geary relationship. (Eq. 7)[39]:

$$I_{corr} = \frac{1}{R_p} \times \frac{\beta a \times \beta c}{2.303(\beta a + \beta c)} \tag{7}$$
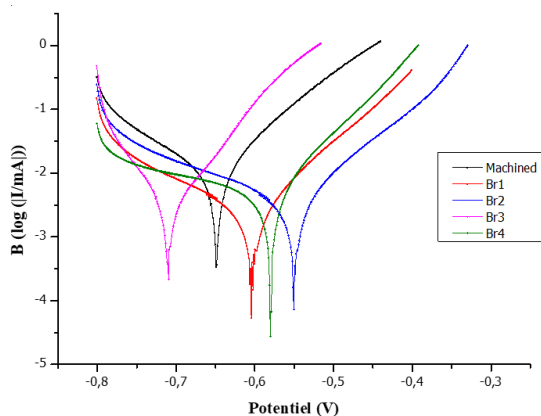
Fig. 9. Polarization curve of API 5L X52 steel– Tafel analysis [29]
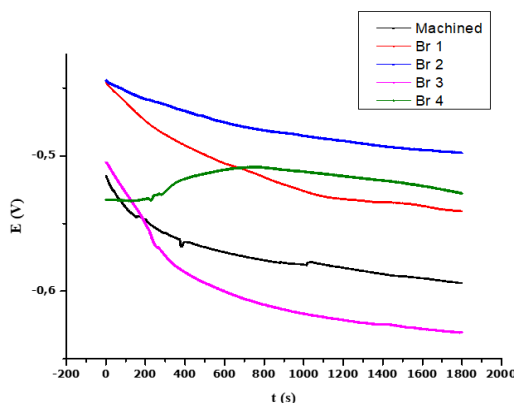
Fig. 10. Open Circuit Potential (OCP) Curve[29]

Polarization curve of API 5L X52 steel– Tafel analysis figure 9 show a rightward deviation for the burnished curves compared to the curve of the machined sample. This deviation is more pronounced for the parameters Py = 430 N and f = 500 mm/min (Br2). Table 8 presents the results of the corrosion tests conducted on samples in the machined and burnished states. Figure 10 shows the evolution of the corrosion potential for samples immersed in a saline solution with NaCl. Over time, the corrosion potential decreases regardless of the treatment. The burnished curves are located above the curve of the machined sample, with a rapid drop in the corrosion potential within the first 200 seconds. Beyond this period, the curves continue to decrease with a less steep slope, while maintaining the same trend. Except for the sample treated with a burnishing force (Py) of 430 N and feed rate (f) of 400 mm/min, the other combinations of burnishing parameters have a higher potential (E). The optimal combination to achieve the highest corrosion potential is Py = 430 N and f = 500 mm/min.

The reduction of Rp gain on X52 steel from 318 to 109% for both low and high levels of Py can be achieved by increasing the value of f. To obtain the best possible corrosion resistance, it is essential to apply burnishing on low Py and f values, which results in Rp = 14.17 Ω. The use of RSM has enabled the identification of a linear prediction model of corrosion resistance, given by equation 6, which indicates that the burnishing force has a preponderant influence compared to the feed (fig 11 and 12). Additionally, an interaction between these two parameters has been observed, emphasizing the importance of

considering both factors in the burnishing process to achieve optimal corrosion resistance. Consequently, it is recommended that further research be done to determine the optimal values of Py and f, which will lead to better corrosion resistance and overall durability of X52 steel [29].

Table 8. Electrochemical parameters of API 5L X52 steel

N°	Treatment	E_{COR} (mv)	I_{COR} (µA)	β_c (mv)	β_a (mv)	R_P (Ω)	(%)
M	Machined	-606.379	7.278	200	82.9		Ref
Br1	Br (265-400)	-603.725	1.538	132.7	84.9	14.617	318
Br2	Br (430-500)	-546.650	2.892	210.9	94.8	6.048	73
Br3	Br (430-400)	-710.564	1.824	46.5	61.1	6.285	80
Br4	Br (265- 500)	-577.445	3.644	300.6	77.0	7.304	109

$$R_p = 8.564 - 2.397X_1 - 1.88X_2 + 1.769X_1X_2 \quad [29] \tag{5}$$

It can be observed that the burnishing process has a positive effect on the corrosion resistance of API 5L X52 steel, as evidenced by the decrease in I_{CORR} and the consequent increase in Rp compared to the machined state (Table 8). The burnishing condition, characterized by Py=265 N and f=400 mm/min, offers the highest Rp value of 14.617 A with a gain of 318% in Rp. However, increasing the Py value from 265 N to 430 N reduces the Rp values, regardless of the f value. Similarly, increasing the f value also reduces the Rp gain from 318% to 109% (fig 13)[29].
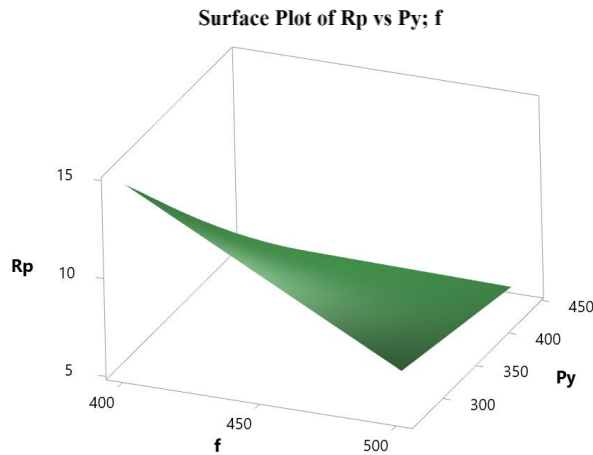
Fig. 11. Surface plot of Rp [29]
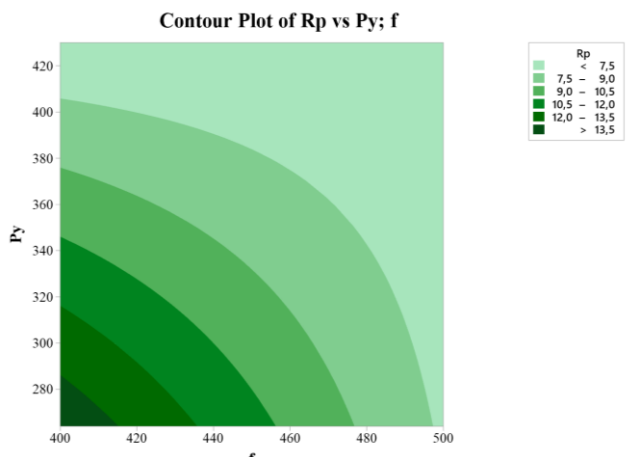
Fig. 12. Contour plot of Rp [29]
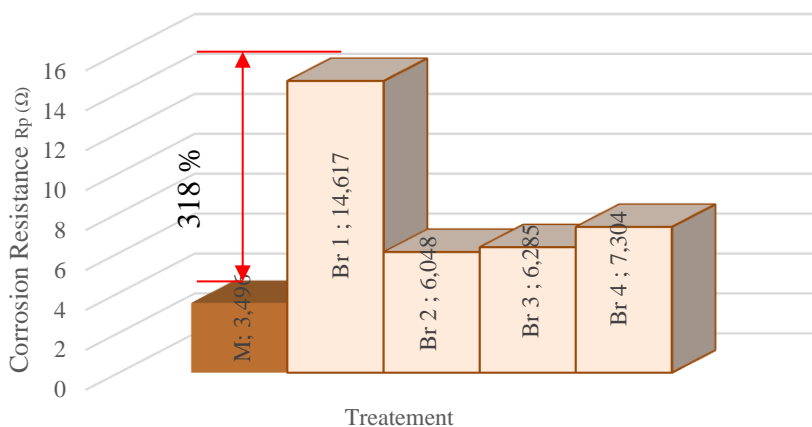
Fig. 13. Effect of burnishing parameters on corrosion resistance (Rp)

3.6. Microscopic Observations

Figure 14 and 15 present images acquired through scanning electron microscopy, offering insights into the corroded surfaces under examination. These visual representations distinctly depict variations in corrosion patterns, primarily emphasizing the contrasting effects of machining and burnishing processes on the material's surface. Specifically, these images underscore that corrosion tends to be more prominent on the machined surface, manifesting within the recesses of the machining asperities. In contrast, when the burnishing process is applied, it leads to a significant smoothing of these asperities, thereby reducing surface roughness [29]. This reduction in surface roughness, in turn, contributes to a noteworthy decrease in corrosion susceptibility. When burnishing is conducted with a force of 265 N and a feed rate of 500 mm/min, the resulting surface is the cleanest in terms of corrosion attack.
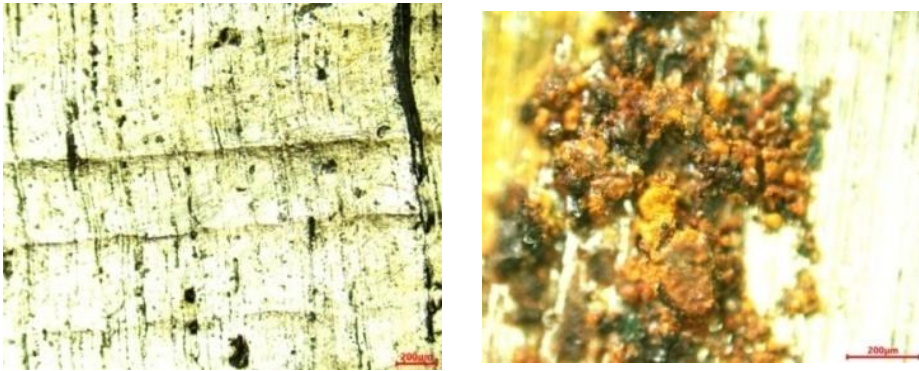
Fig. 14. Evolution of corrosion resistance (Rp) before and after corrosion tests for unburnished samples[29].
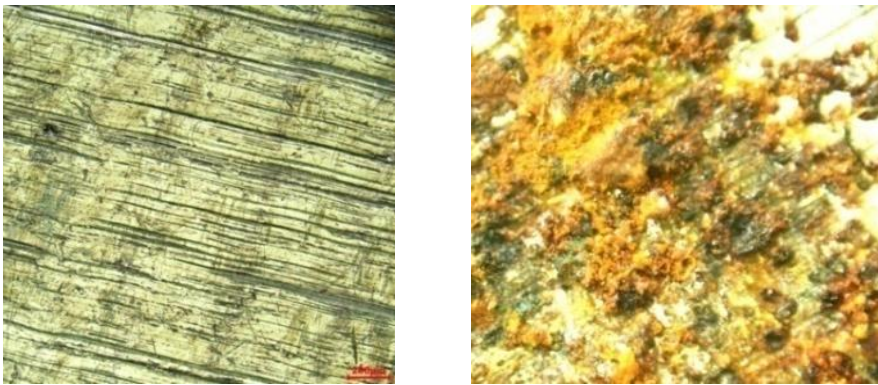
Fig. 15. Evolution of corrosion resistance (Rp) before and after corrosion tests for burnished samples[29]

5. Conclusions

After subjecting the API 5L X52 steel to ball burnishing under various conditions, the following conclusions can be drawn:

- This study focused on the mechanical surface treatment of API 5L X52 steel, emphasizing the outer surface of the pipeline. It also presented a bespoke static device capable of treating both cylindrical and prismatic surfaces, highlighting its versatility and potential impact.
- The optimal burnishing parameters for plane surface burnishing were determined by conducting the process using the Taguchi L16 experimental design, S/N analysis. The surface roughness (Ra) of the sample can be improved from approximately 0.26 to 0.05 μm using the optimal ball burnishing parameters. The Vickers microhardness of the tested sample was improved from 204.67 to 266.57 after the burnishing process.
- The use of the Taguchi experimental design allowed for accurate modelling and prediction of the roughness and microhardness responses. The obtained models showed excellent correlation with the experimental results, with appreciable determination coefficients. The utilization of Analysis of Variance (ANOVA) based

on Signal-to-Noise (S/N) ratio has provided a quantitative insight into the influence of burnishing process parameters on both surface roughness and microhardness.

- Regarding surface roughness, the ANOVA reveals that the force applied (Py) and the feed rate (f) play pivotal roles, contributing 37% and 32% to the observed variance, respectively. In contrast, spindle speed (N) and the number of passes (i) have relatively minor effects, with contributions of 8% and 12%, respectively. A portion of the remaining variance is attributed to error, comprising 11% of the total variance.

- Similarly, the ANOVA analysis for microhardness results underscore the dominant role of burnishing force (Py) and feed rate (f) in minimizing surface roughness, contributing a significant combined effect of 81%. In contrast, spindle speed (N) and the number of passes (i) exhibit limited impact, accounting for only 8% of the variance collectively. These findings emphasize the critical importance of optimizing burnishing force and feed rate to achieve desired surface roughness improvements.

- Multi-objective optimization inspired by DFA revealed the following regime: Py = 265 N; f = 500 mm/min; N = 900 rpm; and i = 1. This burnishing regime yielded a surface roughness of Ra = 0.07 μm and a microhardness of μHv = 265. These values are awfully close to those predicted by the regression models, demonstrating an improvement of 97.51% in surface roughness and a 40% increase in microhardness.

- The findings of the study indicate that ball burnishing can be deemed as a significant technique to enhance the corrosion resistance of API 5L X52 steel. Based on the outcome of the experiment, it is evident that the impact of burnishing results in a noteworthy surge of up to 318% in the corrosion resistance. Thus, it can be inferred that the implementation of ball burnishing can be an effective strategy to protect steel against corrosion.

Acknowledgement

Nomenclature

- Symbols:
- A   Elongation (%)
- Ecorr   Corrosion potential (mV)
- f   Burnishing (mm/min)
- Icorr   Corrosion current (μA)
- i   Number of passes
- N   Spindle speed (rpm)
- Py   Burnishing force (kgf)
- Re   Average yield strength (MPa)
- UTS   Ultimate tensile strength (MPa)
- Ra   Surface roughness (μm)
- μHv200   Surface Vickers Microhardness

- Rp   Polarization resistance to corrosion (ohms)
- β   Potential difference between cathode and anode
- βa   Sample polarization (mV)
- βc   Reference measurement cell polarization (mV)
- ηRa   Signal to noise Ratio for roughness
- ηµHv   Signal to noise Ratio for microhardness

Abbreviations:

- DFA   Desirability function approach
- OCP   Open circuit potential
- MABB   Magnetic Assisted Ball Burnishing
- MST   Mechanical surface treatment
- RSM   Response surface methodology
- SEM   Scanning electron microscopy
- SPD   Superficial plastic deformation
-

References

[1] Shao X. Research on the Steel for Oil and Gas Pipelines in Sour Environment. MATEC Web of Conferences, vol. 238, EDP Sciences; 2018. https://doi.org/10.1051/matecconf/201823804010

[2] Al-Janabi YT. An Overview of Corrosion in Oil and Gas Industry: Upstream, Midstream, and Downstream Sectors. 2020.

[3] Ma Q, Tian G, Zeng Y, Li R, Song H, Wang Z, et al. Pipeline in-line inspection method, instrumentation and data management. Sensors 2021;21. https://doi.org/10.3390/s21113862

[4] Shehata MF, El-Shamy AM. Hydrogen-based failure in oil and gas pipelines a review. Gas Science and Engineering 2023;115:204994. https://doi.org/10.1016/J.JGSCE.2023.204994

[5] Mahmoodian M, Li CQ. Stochastic failure analysis of defected oil and gas pipelines. Handbook of Materials Failure Analysis with Case Studies from the Oil and Gas Industry 2016:235–55. https://doi.org/10.1016/B978-0-08-100117-2.00014-5

[6] Song CL, Liu XB, Pan X, Chen QG, Wang P, Fang Y. Failure Analysis of the Leakage and Ignition of an Oil–Gas Mixture Transportation Pipeline. Journal of Failure Analysis and Prevention 2022;22. https://doi.org/10.1007/s11668-021-01279-4

[7] Ranjbar K, Alavi Zaree SR. Longitudinal fracture and water accumulation at 6 o'clock position of an API 5L X52 oil pipeline. Eng Fail Anal 2021;129. https://doi.org/10.1016/j.engfailanal.2021.105691

[8] Dao U, Sajid Z, Zhang Y. Risk Assessment of Oil and Gas Pipelines Failure in Vietnam. International Journal of Engineering and Technology 2023;15. https://doi.org/10.7763/ijet.2023.v15.1215

[9] Gharbi F, Sghaier S, Hamdi H, Benameur T. Ductility improvement of aluminum 1050A rolled sheet by a newly designed ball burnishing tool device. International Journal of Advanced Manufacturing Technology 2012;60:87–99. https://doi.org/10.1007/s00170-011-3598-6

[10] López De Lacalle LN, Lamikiz A, Muñoa J, Sánchez JA. Quality improvement of ball-end milled sculptured surfaces by ball burnishing. Int J Mach Tools Manuf 2005;45:1659–68. https://doi.org/10.1016/j.ijmachtools.2005.03.007

[11] Tadic B, Todorovic PM, Luzanin O, Miljanic D, Jeremic BM, Bogdanovic B, et al. Using specially designed high-stiffness burnishing tool to achieve high-quality surface finish.

International Journal of Advanced Manufacturing Technology 2013;67:601–11. https://doi.org/10.1007/s00170-012-4508-2

[12] Jerez-Mesa R, Travieso-Rodríguez JA, Landon Y, Dessein G, Lluma-Fuentes J, Wagner V. Comprehensive analysis of surface integrity modification of ball-end milled Ti-6Al-4V surfaces through vibration-assisted ball burnishing. J Mater Process Technol 2019;267:230–40. https://doi.org/10.1016/j.jmatprotec.2018.12.022

[13] Maximov JT, Duncheva G V., Anchev AP, Ichkova MD. Slide burnishing—review and prospects. International Journal of Advanced Manufacturing Technology 2019;104:785–801. https://doi.org/10.1007/s00170-019-03881-1

[14] Jerez-Mesa R, Travieso-Rodriguez JA, Gomez-Gras G, Lluma-Fuentes J. Development, characterization and test of an ultrasonic vibration-assisted ball burnishing tool. J Mater Process Technol 2018; 257:203–12. https://doi.org/10.1016/j.jmatprotec.2018.02.036

[15] Zhou Z yu, Yu G lei, Zheng Q yang, Ma G zheng, Ye S bin, Ding C, et al. Wear behavior of 7075-aluminum after ultrasonic-assisted surface burnishing. J Manuf Process 2020;51:1–9. https://doi.org/10.1016/j.jmapro.2020.01.026

[16] Saldaña-Robles A, De La Peña JÁD, De Jesús Balvantín-García A, Aguilera-Gómez E, Plascencia-Mora H, Saldaña-Robles N. Ball burnishing process: State of the art of a technology in development. Dyna (Spain) 2017;92:28–33. https://doi.org/10.6036/7916

[17] Tugay IO, Hosseinzadeh A, Yapici GG. Hardness and wear resistance of roller burnished 316L stainless steel. Mater Today Proc, vol. 47, Elsevier Ltd; 2021, p. 2405–9. https://doi.org/10.1016/j.matpr.2021.04.363

[18] Jayaraman N, Prevéy PS, Ravindranath R. Low Plasticity Burnishing (LPB) Treatment to Mitigate FOD and Corrosion Fatigue Damage in 17-4 PH Stainless Steel. n.d.

[19] Al-Qawabeha UF, Al-Qawabah SM. Effect of roller burnishing on pure aluminum alloyed by copper. Industrial Lubrication and Tribology 2013;65:71–7. https://doi.org/10.1108/00368791311303438

[20] Thorat SR, Thakur AG. Analysis of surface roughness and wear resistance in low plasticity burnishing process using multi-objective optimization technique. Mater Today Proc, vol. 41, Elsevier Ltd; 2019, p. 1082–8. https://doi.org/10.1016/j.matpr.2020.07.543

[21] Kovács Z. The investigation of tribological characteristics of surface improved by magnetic polishing and roller burnishing. Procedia Eng, vol. 149, 2016. https://doi.org/10.1016/j.proeng.2016.06.654

[22] Al-Qawabeha U, Al-Rawajfeh AE, Al-Shamaileh E. Influence of roller burnishing on surface properties and corrosion resistance in steel. Anti-Corrosion Methods and Materials 2009;56:261–5. https://doi.org/10.1108/00035590910989552

[23] Jawahar M, Suresh kumar J, Srikiran M, Ismail S. Experimental Investigation of Ball Burnishing Process Parameters Optimization for Al 5083 Using Taguchi Method. Lecture Notes in Mechanical Engineering, 2020. https://doi.org/10.1007/978-981-15-1124-0_17

[24] Vaishya RO, Sharma V, Mishra V, Gupta A, Dhanda M, Walia RS, et al. Mathematical Modeling and Experimental Validation of Surface Roughness in Ball Burnishing Process. Coatings 2022;12. https://doi.org/10.3390/coatings12101506

[25] Pathade HP, Gupta DrMK, Kumar DrN, Pathade MP, Wakchaure PB, Gadhave SN, et al. A Review on Surface Integrity of Ball Burnishing Process. International Journal of Research Publication and Reviews 2022. https://doi.org/10.55248/gengpi.2022.3.10.3

[26] Yadav PS, Ghatge DA. Performance Improvement of Roller Burnishing Process– A Review. IARJSET 2017;4. https://doi.org/10.17148/iarjset/ncdmete.2017.34

[27] Raza A, Kumar S. A critical review of tool design in burnishing process. Tribol Int 2022;174. https://doi.org/10.1016/j.triboint.2022.107717

[28] ASTM Standards. ASTM: A370 /ASME SA-370 Standard Test Methods and Definitions for Mechanical Testing of Steel Products1. American Society for Testing and Materials 2016.

[29] Hamadache Hamid, Belabend Selma, Phamdonhat Quang. Improved Corrosion Resistance Of Ball Burnished Api X52 Steel. The 2nd World Energy Storage Conference (WESC-2022), December 18-21, 2022, Istanbul, Turkiye, Istanbul, Turkiye: 2022.

[30] Bounouara A, Hamadache H, Amirat A. Investigation on the effect of ball burnishing on fracture toughness in spiral API X70 pipeline steel. International Journal of Advanced Manufacturing Technology 2018;94. https://doi.org/10.1007/s00170-017-1181-5.

[31] Lieth HM, Al-Sabur R, Jassim RJ, Alsahlani A. Enhancement of corrosion resistance and mechanical properties of API 5L X60 steel by heat treatments in different environments. Journal of Engineering Research (Kuwait) 2021;9:428–40. https://doi.org/10.36909/jer.14591

[32] Garcia MP, de Souza JS, Glover C, Ansell P, Williams G, Mantovani GL, et al. Global and Local Corrosion of Welded Joints of High-Strength Low-Alloy Automotive Steel. Corrosion 2021;77:562–74. https://doi.org/10.5006/3718

[33] Alraeeini AS, Nikbakht E, Ismail MC. Square Steel Tube Impressed Current Corrosion Rate in Term of Linear Polarization Resistance (LPR) Method. Lecture Notes in Civil Engineering, vol. 139 LNCE, 2021. https://doi.org/10.1007/978-981-33-6560-5_14

[34] Díaz-Jiménez V, Arellanes-Lozada P, Likhanova N V., Olivares-Xometl O, Chigo-Anota E, Lijanova I V., et al. Investigation of Sulfonium-Iodide-Based Ionic Liquids to Inhibit Corrosion of API 5L X52 Steel in Different Flow Regimes in Acid Medium. ACS Omega 2022;7:42975–93. https://doi.org/10.1021/acsomega.2c05192

[35] Nikitasari A, Astuti IM, Musabikha S, Kusumastuti R, Prifiharni S, Priyotomo G. Chasew (Anacardium Occidentale) Leaves Extract as Green Corrosion Inhibitor of API 5L X52 in Acidic Media. Trends in Sciences 2023;20. https://doi.org/10.48048/tis.2023.4733

[36] Asmare A, Al-Sabur R, Messele E. Experimental investigation of friction stir welding on 6061-t6 aluminum alloy using taguchi-based gra. Metals (Basel) 2020;10:1–21. https://doi.org/10.3390/met10111480

[37] Trembach B, Grin A, Turchanin M, Makarenko N, Markov O, Trembach I. Application of Taguchi method and ANOVA analysis for optimization of process parameters and exothermic addition (CuO-Al) introduction in the core filler during self-shielded flux-cored arc welding n.d. https://doi.org/10.1007/s00170-021-06869-y

[38] Fajdek-Bieda A. The use of the desire function analysis (DFA) of selected unit processes in chemical technology. Procedia Comput Sci, vol. 207, Elsevier B.V.; 2022, p. 810–8. https://doi.org/10.1016/j.procs.2022.09.136

[39] Han ZY, Huang XG. Stress corrosion behavior of X80 pipeline steel in the natural seawater with different dissolved oxygen contents. Frattura Ed Integrita Strutturale 2019;13:21–8. https://doi.org/10.3221/IGF-ESIS.50.03

Comparative analysis of fouling resistance prediction in shell and tube heat exchangers using advanced machine learning techniques

Kouidri Ikram[*1,a], Kaidameur Djilali[1,b], Dahmani Abdennasser[1, 2,c], Raheem Al-Sabur[3,d], Benyekhlef Ahmed[2,e], Abdel-Nasser Sharkawy[4, 5,f]

[1]*Dept. of Mechanical Eng., GIDD Industrial Engineering and Sustainable Development Laboratory, Faculty of Science and Technology, University of Relizane, Algeria*
[2]*Laboratory of Biomaterials and Transport Phenomena (LBMPT), University of Medea, Algeria*
[3] *Dept. of Mechanical Eng., College of Engineering, University of Basrah, Basrah 61001, Iraq*
[4] *Dept. of Mechanical Eng., Faculty of Engineering, South Valley University, Qena 83523, Egypt*
[5] *Dept. of Mechanical Eng., College of Engineering, Fahad Bin Sultan University, Tabuk 47721, Saudi Arabia*

Article Info	Abstract
	Heat exchangers are utilized in a vast region of the process industry for heating and cooling. Long-term operation of heat exchangers results in decreased efficiency due to many problems, such as fouling. Therefore, the object of this research paper is to use three artificial intelligence techniques (feedforward neural networks-multilayer perceptron (FNN-MLP), nonlinear autoregressive networks with exogenous inputs (NARX), and support vector machines (SVM-RBF)) for predicting the fouling resistance in the tube and the shell heat exchanger in the preheating circuit of atmospheric distillation. The results summarize the high training as well as the predictive capacity of the "FFNN-MLP" model for predicting the fouling resistance in the heat exchanger with the highest coefficient of correlation (R = 0.99961) and the lowest root-mean-squared error (nRMSE = 1.0031%) for the testing phase, where the FNN-MLP network is superior to that provided using the SVM model (R = 0.9955 and nRMSE=3.8652%). All the models of artificial networks and machine learning techniques used in the current work can be used to predict the fouling resistance in heat exchanger data with high accuracy. Despite this, the FNN-MLP model is the preferred model compared with the other proposed models, followed by the NARX model.

1. Introduction

The heat exchanger (HE) is an essential equipment widely used in considerable industrial applications such as power production, heating and refrigeration, petroleum and chemical industry, food processing, and waste heat recovery [1], [2]. Usually, around 90% of the thermal industrial operations pass in a heat exchanger at least once [3]. It ensures heat transfer occurs between two fluids at different temperatures. Also, it can transmit energy in the form of latent heat, such as in condensers and boilers, or sensible heat, such as in coolers and heaters [4]. Heat exchangers are categorized based on the principal using criteria such as transfer processes, quantity of fluids, surface compactness, construction characteristics, heat transfer methods, and flow arrangements [5]. Among various

classifications of HE, shell and tube heat types are the most often utilized in industrial applications. In this exchanger, the tubes are arranged according to different motifs [6].

In contrast, several baffles are usually added at a uniform spacing inside the shell to increase turbulence and improve heat transfer. The flow can be parallel, counter, or sometimes crossed [7]. Despite their advantages, heat exchangers' performance declines dramatically with age of exchangers, and many problems arise, especially vibration and fouling. The poor quality of the media used, especially on the tube side, can lead to increased fouling problems and decrease the exchanger's performance, even in short periods. A fouling phenomenon occurs when unwanted deposits accumulate on the heat transfer surfaces in heat exchanges over time. This phenomenon leads to operational inefficiencies and increases energy consumption. So, accurate prediction of fouling resistance is a crucial goal for many industries.

Sediments, crystals, and biological residues are familiar forms of fouling and can be extended to the products of a chemical reaction or even the combination of several of these elements. This deposit, developed on one side or both sides of the heat exchange surface, has poorer thermal conductivity than the metal comprising the exchange surface, resulting in a high increase in total resistance [8]. The fouling results are the main reason for the decrease in heat transfer coefficients, as are changes in the surface's topography and the flow's geometry. Furthermore, significant pressure reductions occur due to the constriction of flow and increased friction caused by scale development that can render a heat exchanger unusable even before the lowered thermal efficiency [9], [10]. Many aspects influence the development of fouling, including fluid composition, operating conditions, heat exchanger type and features, and fouling site [11]. As a result, considering all these variables makes it impossible to build a semi-empirical or empirical connection to predict the fouling factor precisely [12]. Accurately predicting fouling resistance is essential for optimizing heat exchanger performance, reducing downtime, and minimizing maintenance costs.

Fouling prediction is a primary goal for many researchers, and the methods that can be used for this purpose have varied. It is worth noting that experiments, computational fluid dynamics (CFD) simulations, and other traditional methods failed due to many considerations, including time, resources, and accuracy in predicting the effects of fouling. Accordingly, research institutions have turned to more appropriate patterns, such as machine learning algorithms, to predict the fouling resistance.

Rached Ben-Mansour et al. [13] explored and discussed the fouling analysis in several previous studies on various types of heat exchangers, especially those considering thermal desalination systems. Xiao Zheng et al. [14] used regression neural network (GRNN) as well as random forests (RF) algorithms to predict the coefficient of heat transfer in channels of heat exchange with the effect of bulges in many locations on HTC as input data and 143 set data. They concluded that the GRNN model is better than the RF algorithm in the heat transfer channels' prediction accuracy and generalization ability. Jyoti Prakash Panda et al. [15] modeled the heat transfer correlations for the twisted tape heat exchangers. Artificial neural network (ANN), random forest (RF), and polynomial regression are employed for surrogate modeling. The input data are the Reynolds numbers, the twist ratio, the perforation percentage, and the different numbers of the twisted tapes. This study concluded that the potential ANN is suitable for future data-driven modeling. Anurag Kumra et al. [16] used the SVM and ANN models for predicting the heat transfer rate in wire-on-tube type heat exchangers, they used the flow direction, heat transfer surfaces area, diameter, volumetric flow rate, mass flow rate, and temperature as input values. The results showed that the SVM modeling approach provides better performance and more precise results. Wen et al. [17] indicated that the vector regression machine (SVR)

approach outperformed the partial least squares (PLS) algorithm for predicting the fouling in the plate heat exchanger. They used the input data of pH, dissolved oxygen, chloride ion, iron ion, conductivity, dissolved, hardness, turbidity, alkalinity, and the total bacterial count. In the same direction, Wen Xiaoqiang et al.[18] the multi-resolution wavelet neural network (MRWNN) exceeds other neural networks according to its significance in nonlinear function approximations. Aminian and Shahhosseini [19] tried to avoid the operating conditions that accelerate fouling in pre-heat exchangers by using ANN to develop the mathematical formulation sets. Seyit Ahmet Kuzucanlı et al. [20] examined several multi-classification algorithms and compared them to predict the fouling resistance and the overall heat transfer coefficient in plate heat exchangers. They found that the Naïve Bayes algorithm was better than the decision tree algorithm and k-nearest neighbors (kNN). Sreenath Sundar et al. [21] found that using a robust algorithmic framework for deep learning non-linear functional relationships is suitable for predicting the fouling of the waste heat recovery crossflow heat exchanger. Also, they found that multiple ANNs attain more reasonable accuracy and robustness to noise. Sun Lingfang et al. [22]used the SVM and the wavelet relevance vector machine [23] to predict the fouling resistance in heat exchangers based on the statistical learning theory. They found that the SVM model indicates high prediction accuracy.

More specifically, some studies have been concerned with predicting fouling resistance in shell and tube heat types. Emad M.S. El-Said et al. [24] utilized social media optimization (SMO), k-nearest neighbors' algorithm (KNN), SVM, random vector functional link (RVFL) algorithms to predict the outlet temperature and pressure drop values, and they found that the RVFL outperformed other algorithms. Cao Shengxian et al. [25] indicated that the least squares-support vector machine (LS-SVM) and the BP neural network algorithms have better accuracies than traditional methods for predicting cooling water biofouling resistance. They considered pH, conductivity, total number of bacteria, dissolved oxygen, TN, and NH3-N as input parameters. R. Harche et al. [26] employed long-short-term memory (LSTM) and random forest (RF) to predict fouling status according to historical data in crude distillation unit preheat trains in petroleum refineries. Al-Naser et al. [27] also used LSTM and the ANN in two stages to calculate the fouling factor of the shell and tube heat exchangers using commercial software, and they found the prediction accuracy to be very high. Later, Al-Naser et al. [28] expanded their study from fouling prediction to estimating the local fouling factor using an artificial model of different fouling tactics simulations.

Providing accurate and robust results to predict fouling resistance in heat exchangers is one of the limitations in recent years when using traditional methods, where the results are far from practical reality. Therefore, researchers' growing consensus emerged regarding the need for advanced artificial intelligence (AI) models because they possess excellent capabilities, such as dealing with complex and non-linear patterns. These techniques have become the most promising comprehensive comparative analysis method. This study highlights the importance of advanced artificial intelligence models in predicting fouling resistance in shell-and-tube heat exchangers.

In the realm of heat exchanger research, there exists a notable research gap regarding the comprehensive exploration of three distinct artificial intelligence techniques, namely feedforward neural networks-multilayer perceptron (FNN-MLP), a nonlinear autoregressive model with exogenous inputs (NARX), and the support vector machine (SVM), in predicting fouling resistance. Their application to shell and tube heat exchangers has remained largely uncharted territory. This study endeavours to bridge this research gap by offering a comprehensive investigation into the prediction of fouling resistance through an extensive comparison of FNN-MLP, NARX, and SVM-RBF methods. Furthermore, we aim to present the outcomes of our research in a manner that facilitates

their practical implementation in the real world, drawing upon experimental data from a refinery in Algeria. By addressing this research gap, our work seeks to contribute significantly to resolving a longstanding industrial challenge in heat exchangers, particularly within the shell and tube configurations domain.

2. Materials and Methods

2.1. Data Acquisition and Preprocessing for Experimental Analysis

Atmospheric distillation (U100) is the basic unit of an ALGIERS refinery. It aims to split crude oil into various finished products (kerosene, diesel, fuel oil, LPG, and light and heavy solvents), which can be used for one or more treatments. For our study, we are interested in the preheating circuit of this unit when the crude oil leaves the storage bins at room temperature; it is discharged by one of three pumps of type centrifugal, P101, to the atmospheric distillation unit, then passes through two circuits of E101 battery (FED and CBA). Crude oil passes through the battery on the tube side, where it is heated with head reflux (RT), the light product mixture from the top of the C101 distillation column at tray 46. The oil then passes through electrostatic desalination by treating the water with caustic soda. This treated water is injected at the E101 heat exchanger inlet and at the desalted entrance to wash the crude oil and drive the salts present (Fig.1).
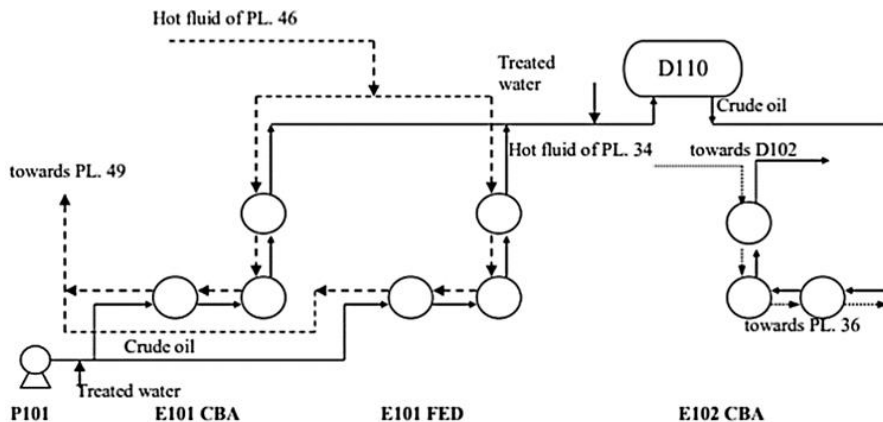
Fig. 1. Atmospheric distillation scheme (unit 100) [26]
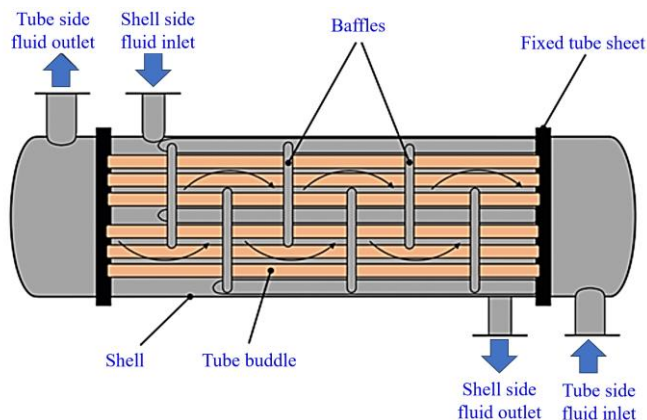
Fig. 2. Shell and tube heat exchanger

This work primarily aims to verify the performance measure of the E101 CBA heat exchanger by predicting the fouling resistance. E101CBA is a shell and tube exchanger with one pass on the shell and two on the tube sides. Fig. 2 illustrates the main parts of the shell and tube heat exchanger. Crude oil passes through the tubes while head reflux (RT) flows in the shell side. Several sensors are placed to measure flow rates and temperatures. Table 1. presents the measured variables of the E101CBA heat exchanger. Standard deviations (SD) were added to explore the process variables' variation.

Table 1. Statistical analysis for shell and tube process parameters

Side	Parameters	Unit	Min	Mean	Max	SD
Tube	Inlet Temperature (t_i)	°C	17	24	31	4.169
	Outlet Temperature (t_o)	°C	101	92	110	2.367
	Mass flux ($\dot{m}_t$)	Kg/s	23.50	34.80	46.10	6.009
Shell	Inlet Temperature (T_i)	°C	111	120.5	130	3.253
	Outlet Temperature (T_o)	°C	44	54	64	4.528
	Mass flux ($\dot{m}_s$)	Kg/s	38.98	59.54	80.104	6.560
	Fouling resistance (R_f)	m²°C/W	0.00017	0.0093	0.0017	0.003

2.2. Feed-forward Multi-layer Perceptron

The most often utilized architecture now is the multilayer-feedforward neural network, referred to as the multi-layer perceptron (MLP) network [29]. This structure comprises the hidden layer or layers, the output layer, and the input layer. A nonlinear input-output model structure can be considered this kind of network. This network passes signals from one node to each subsequent layer's nodes [30]. The multi-layer feed-forward neural network's topology is shown in Fig. 3. This picture shows how the input layer receives all the input signals and transfers them to additional neurons in the hidden layer, where the processing task is carried out. The output layer then receives the data. Synaptic weights and biases are the parameters of such a network.
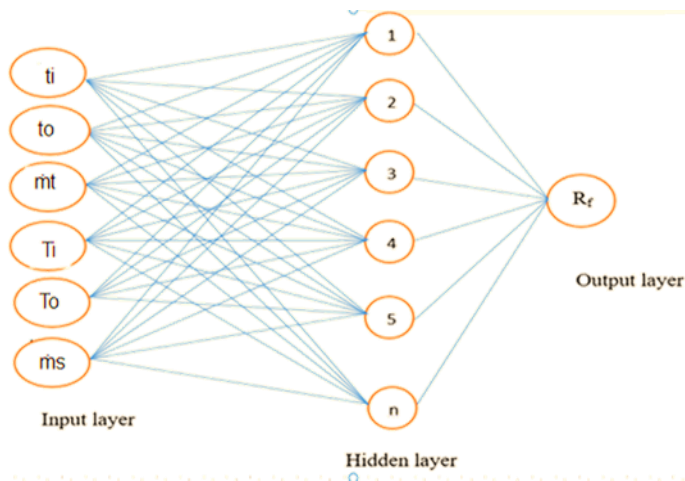
Fig. 3. Multilayer feedforward neural network's topology

The outputs of the FNN are the outcomes of the neuromorphic model. The output of the proposed MLP neural network can be given as follows [31]:

$$y_i = Qi(\sum_{j-1}^{n^i} W_j^i Z_j^i + b^i) \tag{1}$$

The activation function Qi regulates the i-th node's output within a specific range, which depends on the total incoming connections n^i, bias bi, weight Wi, and input Zi.

2.3. Nonlinear Autoregressive Models with Exogenous Inputs (NARX)

The NARX network [32], [33] is the recurrent ANN with feedback connections enclosing many network layers. This model has the well-known ARX model nonlinear generalization. In addition, it predicts the time series in a very efficient way [34], [35]. This model is used widely with nonlinear systems [36], [37]. The NARXNN model consists of three layers, as indicated in Fig. 4. The input layer consists of six parameters (mentioned before), a nonlinear hidden layer that contains the hidden neurons and its activation function of type hyperbolic tangent, tanh. In contrast, the third layer represents the nonlinear output which estimates the fouling resistance. The activation function in the output layer is the hyperbolic tangent, tanh. The vector of the input delay is [0 1], whereas the vector of the output delay is [1 2].
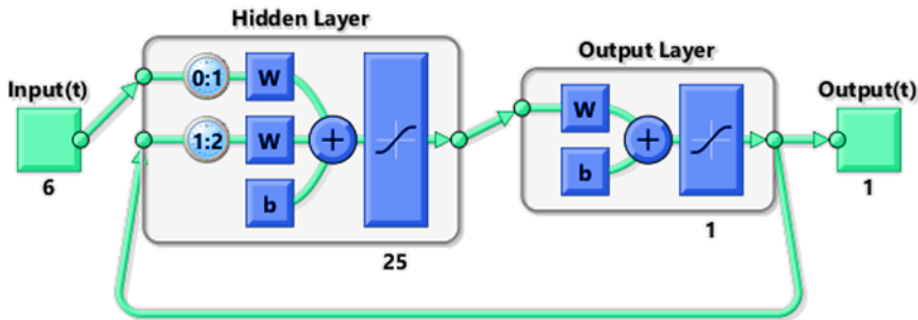
Fig. 4. The designed and proposed NARX network architecture

2.4. Support Vector Machine

The SVM technique is a collection of supervised learning strategies designed to address discrimination and regression issues [38]. Due to its capacity to handle vast amounts of data, SVM gained popularity quickly [39]. The SVM implements nonlinear class borders using some input vectors of nonlinear mapping into the high-dimensional feature space and then uses a linear model to generate a hyperplane. The Radial basis function kernel (RBF kernel) is a well-liked kernel function in support vector machine classification [40].

The output of an SVM model can be determined by solving a specific equation (2):

$$f(x_i) = \omega^T \emptyset(x_i) + b, i = 1,2, \dots, n \tag{2}$$

Where $f(x_i)$ refers to the predicted data, $\varphi(x_i)$ is the implicitly constructed nonlinear function, ω is the SVM model's weight vector, and b is the SVM model's bias. The dataset has the D-dimensional input vector $x_i \in R^D$ and the scalar output $y_i \in R$.

2.5. Assessment Performance Evaluation

Several error measures w**e**re employed to control the prediction models' precision level. These error measures include the Coefficient of Correlation (R), Mean Absolute Error

(nMAE), Root mean squared error (nRMSE), and standard prediction error (SEP). Equations that specify these errors mathematically represent the equations (3–7) [41], [42]. These error measurements make it possible to evaluate the performance of the prediction models in detail and get a good grasp of their advantages and disadvantages.

y and y' are the measured and calculated values of the fouling resistance in the tube and the shell heat exchanger; their mean values are:

$$\bar{y} = \sum_{i=1}^{N} y_i / N \quad \text{and} \quad \bar{y}' = \sum_{i=1}^{N} y_i' / N \quad \text{where N is the data number}$$

$$R = \frac{\sum_{i=1}^{n} \left(Y_{i,exp} - \overline{Y_{i,exp}} \right)\left(Y_{i,cal} - \overline{Y_{i,cal}} \right)}{\sqrt{\sum_{i=1}^{n} \left(Y_{i,exp} - \overline{Y_{i,exp}} \right)^2 \sum_{i=1}^{n} \left(Y_{i,cal} - \overline{Y_{i,cal}} \right)^2}} \tag{3}$$

The mean absolute error, MAE, as well as its normalized value, nMAE:

$$MAE = \frac{1}{n} \sum_{i=1}^{n} \left| Y_{i,cal} - Y_{i,exp} \right| \quad ; \quad nMAE = MAE/\bar{y} \tag{4}$$

The root-mean-square error, RMSE, as well as its normalized value, nRMSE:

$$RMSE = \sqrt{\frac{\sum_{i=1}^{n} \left(Y_{i,cal} - Y_{i,exp} \right)^2}{n}} \quad ; \quad nRMSE = RMSE/\bar{y} \tag{5}$$

$$SEP(\%) = \frac{RMSE}{Y_e} \times 100 \tag{6}$$

Concerning a dataset comprising n data points, where $Y_{i,exp}$, and $Y_{i,cal}$ correspond for the experimental and calculated fouling resistance values, and $\overline{Y}_{i,exp}$ represents the mean of experimental data.

3. Results and Discussion

3.1. The Database's Division's Impact

The entire database was divided into three sections to assess the performance of the three models: FFNN-MLP, SVM-RBF, and NARX. Section 1 had 174 training points (60%) and 116 for testing (40%); Section 2 had 203 points for training (70%); and Section 3 had 232 points for training (80%) and 58 for testing (20%). Table 2 presents the correlation coefficient (R) and the normalized root-mean-squared error (nRMSE) for predicting fouling resistance considering the database impact's division. The results show that the third section is the best division, giving better results than the other divisions for the test and training phases. The three models (SVM-RBF, FFNN-MLP, and NARX model) were used for predicting fouling resistance and compared with each other.

In this study, the BFGS quasi-Newton [trainbfg] was used as the training algorithm for FNN-MLP, and Levenberg-Marquardt (LM) for NARX, while the Radial basis function (RBF) was used for the radial basis function (RBF).

Table 2. Impact of the database's partition for FNN-MLP

Partitions	Database	%	nRMSE	R
1	Training: 174 points	60%	1.5970	0.99872
	Testing: 116 points	40%	1.3991	0.99904
2	Training: 203 points	70%	1.3884	0.99901
	Testing: 87 points	30%	1.3630	0.99916
3	Training: 232 points	80%	0.9694	0.99951
	Testing: 58 points	20%	1.0031	0.99961

3.2. FNN-MLP Model

The NN architecture for predicting fouling resistance was optimized using STATISTICA software, and this study uses the BFGS quasi-Newton, trainbfg, training algorithm. The optimal structure of the (FNN-MLP) model used to predict fouling resistance is the more detailed architecture presented in Table 3.

Table 3. The main structure of the developed FNN-MLP network

Training Technique	Input layer	Hidden layer		Output layer	
BFGS quasi-Newton (trainbfg)	Neurons	Neurons	Activation function	Neurons	Activation function
	06	20	Exponential	1	Sine

The agreement between experimental and calculated fouling resistance in heat exchangers obtained by the FNN-MLP model optimal is excellent, with agreed vectors about the ideal [a (the slope), (y-intercept), (correlation coefficient)] = [0.9985, 1.50750, 0.99951] in the training phase and [a, b, R] = [1.0012, -1.52666, 0.99961] in the test phase (Fig. 5).

(a)   (b)
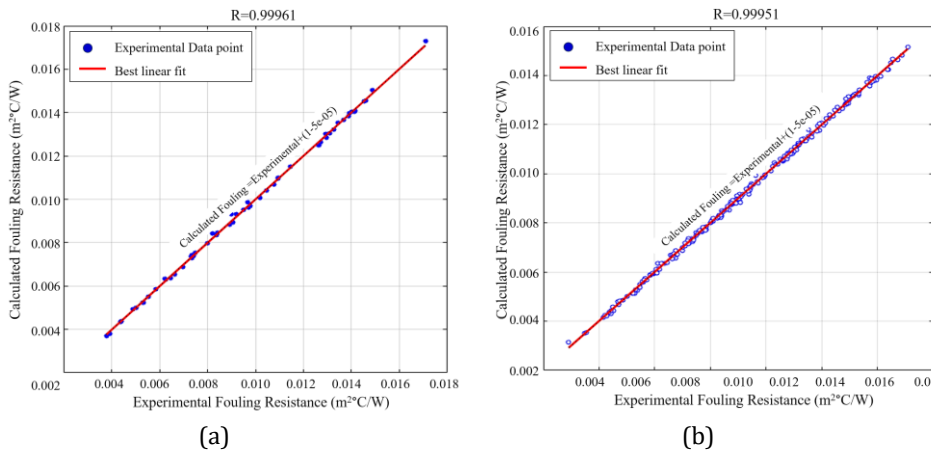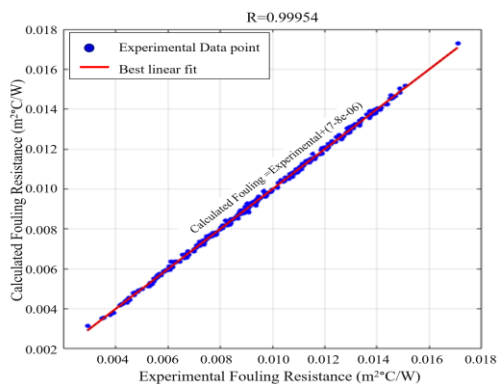
(c)

Fig. 5. FNN-MLP Model Experimental vs. calculated fouling resistance: (a) train dataset, (b) test dataset, (c) total dataset

3.3. NARX Model

The NARX neural network architecture for predicting fouling resistance was optimized using MATLAB software; this study uses the Levenberg-Marquardt (LM) training algorithm. Intel(R) Core (TM) i5-8250U CPU @ 1.60GHz processor is used for this network. The optimal structure of the NARX model used to predict fouling resistance is the more detailed structure presented in Table 4.

Table 4. Structure of the developed NARX model

Training Technique	Input layer	Hidden layer		Output layer	
the Levenberg-Marquardt (LM)	Neurons	Neurons	Activation function	Neurons	Activation function
	06	25	Hyperbolic Tangent (Tanh)	1	Hyperbolic Tangent (Tanh)

The number of layers was similar for input, hidden, and output, where it was one layer. The number of neurons in the input and hidden layers was 6 and 25, respectively, while it was 1 for the output layer.

The choice of hyperbolic tangent activation function allows the neural network models to capture complex, nonlinear relationships within the fouling resistance prediction problem. By utilizing the hyperbolic tangent activation function, the selected models can effectively comprehend and represent intricate patterns in the data, enhancing their predictive abilities.

The agreement between experimental and calculated fouling resistance in heat exchangers obtained by the optimal NARX model is excellent. The obtained regression and mean squared error (MSE) in the training and testing cases are presented in Fig. 6 and 7. The best-obtained value is 1.9318e-08 at epoch 26, a minimal value and about zero.
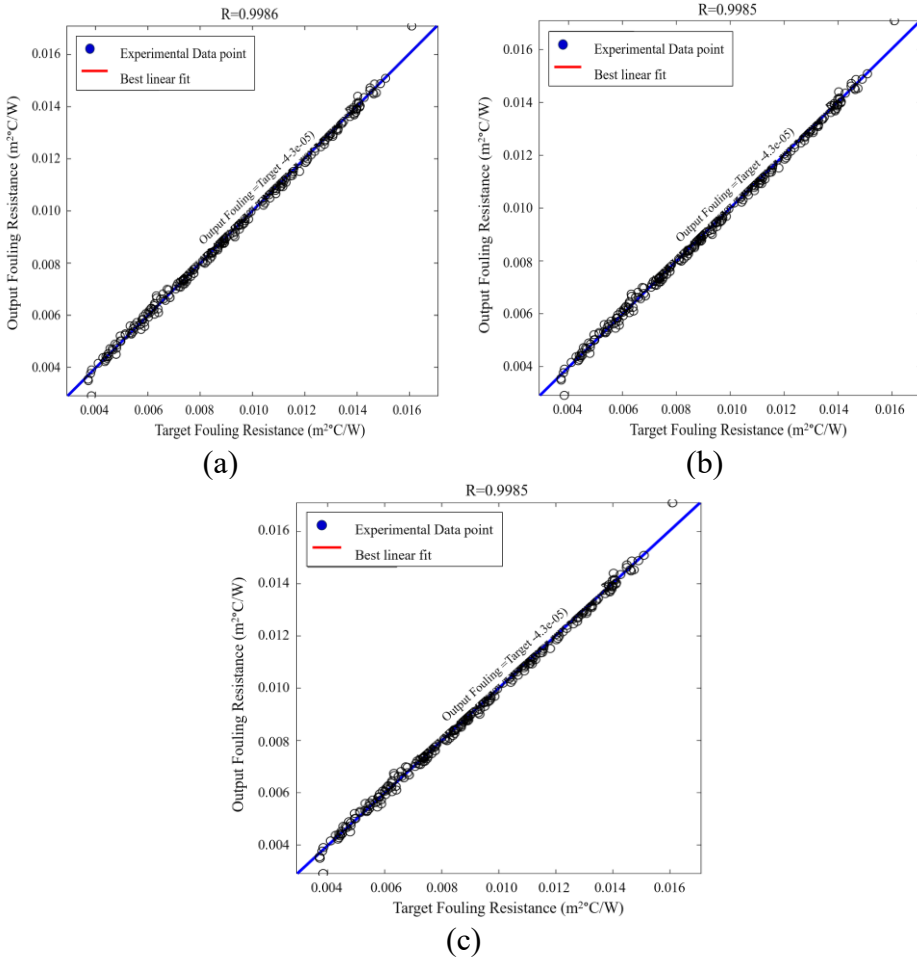
Fig. 6. NARX model Experimental vs. calculated fouling resistance: (a) train dataset, (b) test dataset, (c) total dataset
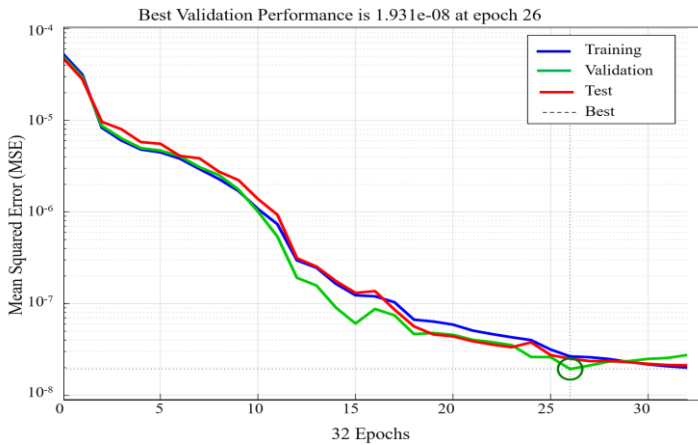
Fig. 7. MSE for the training, testing, and validation of the NARX model

The experimental fouling resistance from these Figures coincides and converges with the estimated one by the NARX neural network, where the obtained MSE is minimal and close to zero. In other words, the NARX model is an effective and perfect training method. Moreover, the experimental and the calculated fouling resistance were compared, as shown in Fig. 8. The results refer to perfect convergence and coinciding, which supports the fact that the NARX model works excellently.
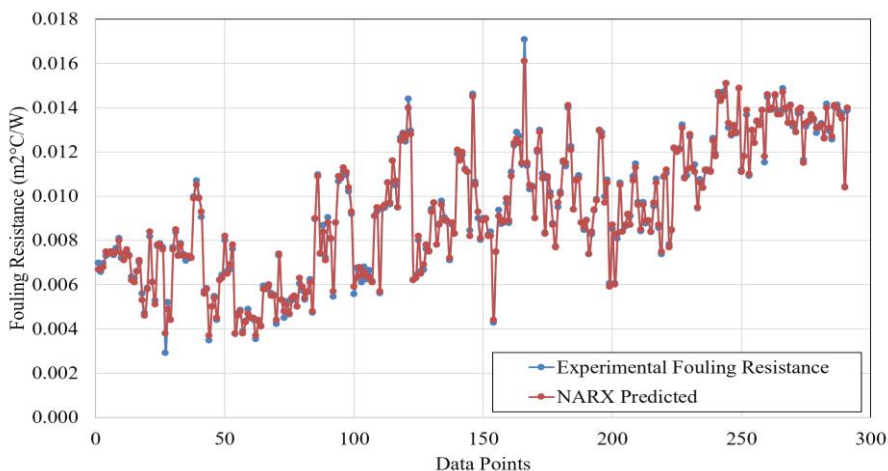
Fig. 8. Experimental fouling resistance and NARX model predicted comparison using all data

3.4. SVM-RBF Model

The SVM-RBF network gives a relationship of type nonlinear between the inputs (ti, to, ṁt, Ti, To, ṁs) and the output (fouling resistance). For the prediction of the fouling resistance in the E101CBA heat exchanger using the SVM-RBF model, the same database used in the FNN-MLP model was selected. Table 5 shows the evaluation of the SVM-RBF model in terms of the number of support vector machines (N° SV), nRMSE, and R. The nRMSE of the SVM-RBF is 3.2591 %, 3.8652 %, and 3.3871 % for training, tasting, and overall phases, respectively. The SVM-RBF model's correlation coefficients for training, testing, and overall phases are 0.99555, 0.99551, and 0.99549, respectively. These correlation indices are getting near the ideal (R = 1). In addition, the RBF-kernel function is a better choice for describing the prediction of fouling resistance.

Table 5. Evaluation of SVM-RBF model

(SVM-RBF) model	N° SV	Phase	nRMSE	R
C (10.00)	120	Training	3.2591	0.99555
nu (0.500)		Testing	3.8652	0.99551
Gamma (0.150)		Overall	3.3871	0.99549

Fig. 9 indicates a high convergence of the predicted fouling resistance to experimental sets where it is near ideal behavior (slope = 1, intercept = 0, R = 1). The correlation coefficient R and nRMSE results showed that the SVM-RBF model operated somewhat during the training and testing phases. Also, the overall phase shows the SVM-RBF model's predictive power, closely following the trend of the experimental data on fouling resistance, except in

a few instances where the differences between experimental and predicted values are notable.
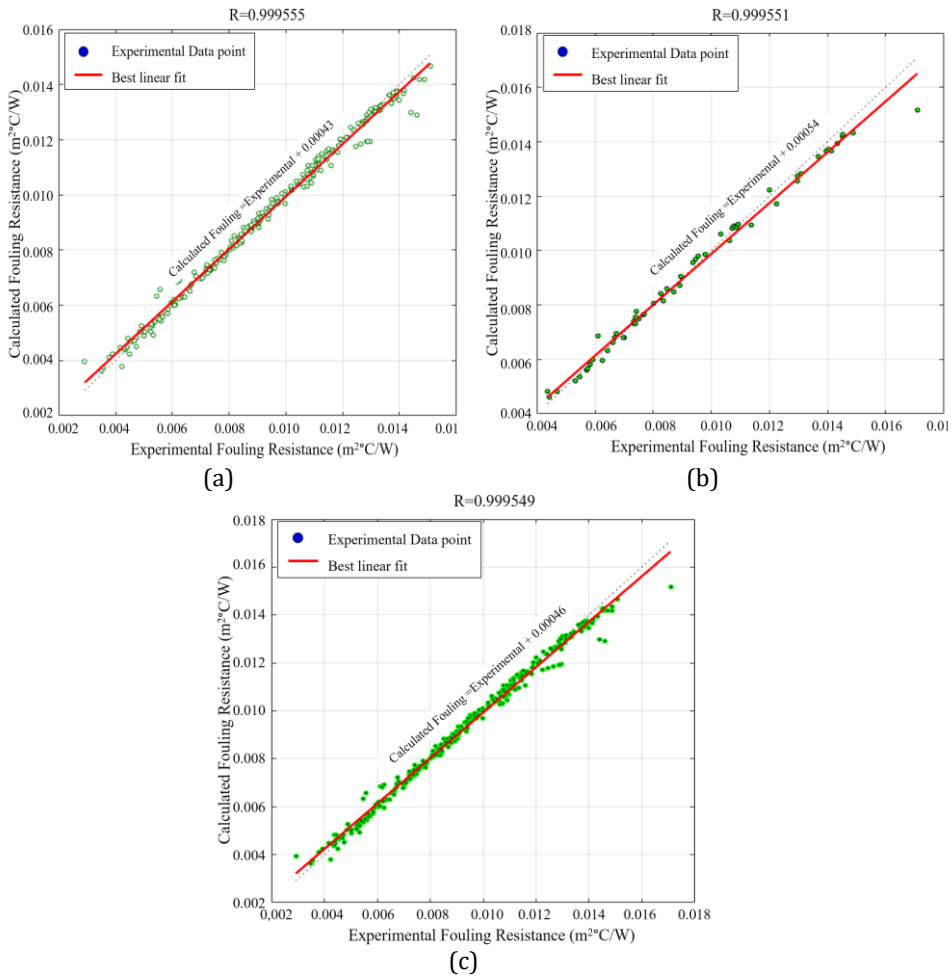
Fig. 9. SVM-RBF model Experimental vs. calculated fouling resistance: (a) train dataset, (b) test dataset, (c) total dataset

The results show that the FNN-MLP and the NARX models acquired the lowest nMAE, nRMSE, and SEP errors in the testing phase (0.7939, 1.0031, and 1.0027, respectively). It can be observed clearly in Table 6 that the FNN-MLP and the NARX-based models surpassed the SVM-RBF and RF models for predicting resistance to fouling.

Table 6. The statistical evaluation of the model's performance

Errors	FNN-MLP		NARX		SVM-RBF	
	Training	Testing	Training	Testing	Training	Testing
R	0.99951	0.99961	0.9986	0.9985	0.9956	0.9955
nMAE (%)	0.7706	0.7939	1.2589	1.2723	2.0541	2.4982
nRMSE (%)	0.9694	1.0031	1.3611	1.4231	3.2591	3.8652
SEP (%)	0.9696	1.0027	1.3508	1.4101	3.2497	3.8340

3.5. Sensitivity Analysis

A sensitivity analysis employing the "Weight" approach was used to examine the impact of the input variables (Inlet Temperature, Outlet Temperature, Mass Flow in the Tube Side and Shell Side) on the output (fouling resistance).

The "weight approach" in the sensitivity analysis was first used in the early 1990s by Garson [43] and then developed by Goh [44] to be widely used. It is usually used in experiments to give the relative significance (RI) of the input to the output of a neural network. It depends on dividing the connection's weights into the input-hidden connection's weights and the hidden-output connection's weights. Fig. 10 displays the contribution results. The most crucial variables that may affect the prediction of resistance fouling are the crude oil outlet temperature of 26.56% and the head reflux outlet temperature of 15.46%. The contributions of head reflux inlet temperature, crude oil inlet temperature, and head reflux Mass flux are not significantly different (almost the same contribution with RI = 15%), and crude oil mass flux has less effect with RI = 13%. Results of the sensitivity analysis show that all input parameters have a relative importance higher than > 12%, which explains the effect of the selected parameters on the output.
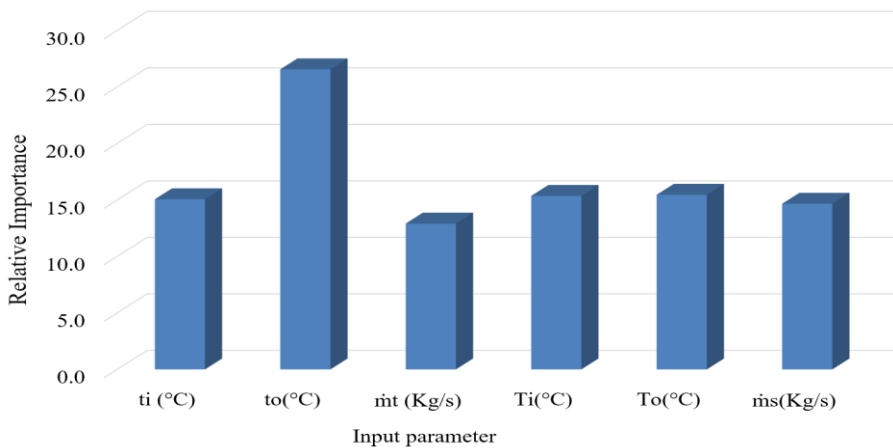
Fig. 10. Relative importance (%) of input variables on fouling resistance

3.6. Comparison with Other Models

Comparisons with similar studies are crucial to the value of scientific research and give it the value of originality. Table 7 compares a specific category of previous studies that are similar or close in their input parameters to the current study—all selected studies aimed at predicting heat exchanger fouling. The comparative study indicates that FFNN-MLP and NARX represent the most accurate and reliable models in terms of predictive values.

This superiority of the FFNN-MLP and NARX models in predicting the fouling resistance of heat exchangers can be attributed to the theoretical foundations of these two methods. Both models are mainly designed to deal with complex nonlinear relationships, especially those in which time has a significant influence. Heat exchangers depend on a complex mixture of inputs that interfere with each other, especially after a period of use. Fouling in the heat exchanger accumulate with prolonged use, especially with poor maintenance, and meads, especially on the side of the tube. Therefore, FFNN-MLP and NARX can give better results with all these nonlinear parameters.

The results obtained gave a clearer view of the prediction of fouling resistance in the atmospheric distillation (U100), which is the basic unit of an ALGIERS refinery and helped workers obtain a better performance for treating water which is injected at the E101 heat exchanger inlet.

Table 7. Predicted fouling resistance comparison with previous studies

Ref	Input variables	Prediction Variable	Model Type	Errors "R, R^2, RMSE, MAE"
Present work	Inlet and outlet temperature of crude oil, mass flow of crude oil, inlet and outlet temperature of head reflux(RT) and mass flow of (RT)	Fouling resistance	FNN-MLP	R=0.99961 nRMSE=$1.0031*10^{-2}$ nMAE= $0.7939*10^{-2}$
			NARX	R=0.9985 nRMSE=$1.4231*10^{2}$ nMAE= $1.2723*10^{-2}$
			SVM-RBF	R=0.9955 nRMSE=$3.8652*10^{2}$ nMAE= $2.4982*10^{-2}$
[45]	Fluid temperature, surface temperature, operation time, fluid density, equivalent diameter, velocity, and oxygen content.	Fouling factor	GPR	R^2=0,98770 MSE=$8,53.10^{4}$ MAE=$5,35.10^{-3}$
			SVM	R^2=0,97702 MSE=$1,65.10^{-3}$ MAE=$1,5.10^{-2}$
			Decision trees	R^2=0,98664 MSE=$9,22.10^{-4}$ MAE=$8,84.10^{-3}$
			Bagged trees	R^2=0,98484 MSE=$1,15.10^{-3}$ MAE=$1,22.10^{-2}$
			Linear regression	R^2=0,57753 MSE=$4,98.10^{-2}$ MAE=$4,65.10^{-2}$
[46]	Feed water temperature and flow rate, flue gas inlet and outlet temperatures, blower A and B air supply rates, steam flow rate and oxygen amount	Ash fouling resistance	SVM	R=0,985 MSE=0.001126
[47]	Acid inlet and outlet temperature, acid volume flow and density, steam temperature and operation time.	Fouling resistance	ANN-MLP	R^2=0,995 MSE=$4.256×10^{-6}$
[12]	Fluid and surface temperatures, dissolved oxygen concentration, equivalent diameter, operation time, density, velocity.	Fouling resistance in heat exchanger	ANN-MLP	R^2=0,9778 MSE=0.0355
[48]	Coal ash composition and structure parameters	Fouling fact or index	ANN	R^2=0,9996 MSE=0,0073 MAE= $2.308.10^{-2}$

| [1] | Acid Inlet and outlet temperatures, density, flow rate, operation time, and steam temperature. | Fouling resistance | ANN | $R^2=0,994$ MSE=2.168 $\times 10^{-11}$ RMSE=4.656$\times$ 10^{-6} |
| [49] | Input temperature and flow rate of tube side, and input temperature of shell side. | Fouling resistance | ANN | MSE= 8, 06. 10^{-2} |

4. Conclusions

Heat exchanger modelling plays a very important role in the thermal analysis of heat exchangers. Artificial intelligence methods are powerful computer models that capture and represent complex input/output relationships.

The study focused on fouling resistance prediction using conventional machine learning models such as feedforward networks multi-layer perceptron, NARX model and support vector machine radial basis function kernel (FFNN-MLP, NARX, and SVM-RBF) with supervised learning. The results indicated the fouling resistance's high train and prediction capacity with a higher correlation coefficient (R = 0.99961) and a very low root mean squared error (nRMSE = 1.0031%) for the testing phase. The prediction by FFNN-MLP correspondingly demonstrates a sound correlation between the fouling resistance experimental and predicted values, indicating that the FFNN-MLP model has superior predictive power. The analysis of sensitivity was calculated and verified that fouling resistance in heat exchanger is handled by three interactions which were arranged in dropping order: Cold-Outlet Temperature (Relative Importance RI = 26.56%), Hot-Outlet Temperature (RI = 15.46%), Hot-Inlet Temperature (RI = 54.35%), Cold-Inlet Temperature (15.09), Hot-Mass flux and Cold-Mass flux (14.65% and 12.9%, respectively). Furthermore, the study suggests that the FFNN-MLP model can be applied to predict fouling resistance in EA 101CBA heat exchangers or similar character conditions.

In future work, other neural network approaches, such as Cascaded Forward NN, Radial basis function, and recurrent neural network, can be investigated. In addition, deep learning approaches will be investigated.

References

[1] Jradi R, Marvillet C, Jeday MR. Modeling and comparative study of heat exchangers fouling in phosphoric acid concentration plant using experimental data. Heat and Mass Transfer, 2020; 56:2653-2666. https://doi.org/10.1007/s00231-020-02888-9

[2] Faes W, Lecompte S, Ahmed ZY, Van Bael J, Salenbien R, Verbeken K, De Paepe M. Corrosion and corrosion prevention in heat exchangers. Corrosion reviews, 2019; 37(2): 131-155. https://doi.org/10.1515/corrrev-2018-0054

[3] Fguiri A, Jradi R, Marvillet C, Jeday MR. Heat exchangers fouling in phosphoric acid concentration. Heat and Mass Transfer, 2020; 56:2313-2324. https://doi.org/10.1007/s00231-020-02858-1

[4] Sulaiman MA, Kuye SI, Owolabi SA. Investigation of fouling effect on overall performance of shell and tube heat exchanger in a urea fertilizer production company in Nigeria. Nigerian Journal of Technology, 2016; 35(1): 129-136. https://doi.org/10.4314/njt.v35i1.20

[5] Abbas EF, Yagoob JA, Mardan MN. Effect of tube material on the fouling resistance in the heat exchanger. In 2nd International Conference for Engineering, Technology and Sciences of Al-Kitab University, Iraq ,43-48, December, 2018. https://doi.org/10.1109/ICETS.2018.8724619

[6] Musawel RK. (2002). Simulation and fouling study of propane heat exchangers, MSc Thesis, UNIVERSITY OF BASRAH, Iraq.

[7] Abd AA, Kareem MQ, Naji SZ. Performance analysis of shell and tube heat exchanger: Parametric study. Case Studies in Thermal Engineering, 2018; 12:563-568. https://doi.org/10.1016/j.csite.2018.07.009

[8] Fguiri A, Marvillet C, Jeday MR. Estimation of fouling resistance in a phosphoric acid/steam heat exchanger using inverse method. Applied Thermal Engineering, 2021; 192:116935. https://doi.org/10.1016/j.applthermaleng.2021.116935

[9] Emani S, Ramasamy M, Shaari KZBK. Effect of shear stress on crude oil fouling in a heat exchanger tube through CFD simulations. Procedia Engineering, 2016; 148:1058-1065. https://doi.org/10.1016/j.proeng.2016.06.592

[10] Berce J, Zupančič M, Može M, Golobič I. A review of crystallization fouling in heat exchangers. Processes, 2021; 9(8):1356. https://doi.org/10.3390/pr9081356

[11] Gudmundsson O, Palsson OP, Palsson H, Lalot S. Online fouling detection of domestic hot water heat exchangers. Heat Transfer Engineering, 2016; 37(15): 1231-1241. https://doi.org/10.1080/01457632.2015.1119584

[12] Davoudi E, Vaferi B. Applying artificial neural networks for systematic estimation of degree of fouling in heat exchangers. Chemical Engineering Research and Design, 2018; 130: 138-153. https://doi.org/10.1016/j.cherd.2017.12.017

[13] Ben-Mansour R, El-Ferik S, Al-Naser M, Qureshi BA, Eltoum MAM, Abuelyamen A, Ben Mansour R. Experimental/Numerical Investigation and Prediction of Fouling in Multiphase Flow Heat Exchangers: A Review. Energies, 2023; 16(6):2812. https://doi.org/10.3390/en16062812

[14] Zheng X, Yang R, Wang Q, Yan Y, Zhang Y, Fu J, Liu Z. Comparison of GRNN and RF algorithms for predicting heat transfer coefficient in heat exchange channels with bulges. Applied Thermal Engineering, 2022; 217:119263. https://doi.org/10.1016/j.applthermaleng.2022.119263

[15] Panda JP, Kumar B, Patil AK, Kumar M, Kumar R. Machine learning assisted modeling of thermohydraulic correlations for heat exchangers with twisted tape inserts. Acta Mechanica Sinica, 2023; 39(1): 322036. https://doi.org/10.1007/s10409-022-22036-x

[16] Kumra A, Rawal N, Samui P. Prediction of heat transfer rate of a Wire-on-Tube type heat exchanger: An Artificial Intelligence approach. Procedia Engineering, 2013; 64: 74-83. https://doi.org/10.1016/j.proeng.2013.09.078

[17] Wen XQ. Study on the Methods of Predicting the Fouling Characteristics of Plate Heat Exchanger Based on Water Quality Parameters. Applied Mechanics and Materials, 2014; 459: 153-158. https://doi.org/10.4028/www.scientific.net/AMM.459.153

[18] Wen X, Miao Q, Wang J, Ju Z. A multi-resolution wavelet neural network approach for fouling resistance forecasting of a plate heat exchanger. Applied Soft Computing, 2017; 57: 177-196. https://doi.org/10.1016/j.asoc.2017.03.043

[19] Aminian J, Shahhosseini S. Neuro-based formulation to predict fouling threshold in crude preheaters. International Communications in Heat and Mass Transfer, 2009; 36(5): 525-531. https://doi.org/10.1016/j.icheatmasstransfer.2009.01.020

[20] Kuzucanlı SA, Vatansever C, Yaşar AE, Karadeniz ZH. Assessment of fouling in plate heat exchangers using classification machine learning algorithms. In CLIMA 2022 conference, Rotterdam, Netherlands, May, 2022.

[21] Sundar S, Rajagopal MC, Zha H, Kuntumalla G, Meng Y, Chang H C, Salapaka S. Fouling modeling and prediction approach for heat exchangers using deep learning. International Journal of Heat and Mass Transfer, 2020; 159: 120112. https://doi.org/10.1016/j.ijheatmasstransfer.2020.120112

[22] Sun L, Zhang Y, Zheng X, Yang S, Qin Y. Research on the fouling prediction of heat exchanger based on support vector machine. International Conference on Intelligent

Computation Technology and Automation (ICICTA), China, 240-244, October, 2008. https://doi.org/10.1109/ICICTA.2008.156

[23] Sun L, Saqi R, Xie H. Research on the fouling prediction of heat exchanger based on wavelet relevance vector machine. Advances in Neural Network Research and Applications, 2010; 37-45. https://doi.org/10.1007/978-3-642-12990-2_5

[24] El-Said EM, Abd Elaziz M, Elsheikh AH. Machine learning algorithms for improving the prediction of air injection effect on the thermohydraulic performance of shell and tube heat exchanger. Applied Thermal Engineering, 2021; 185:116471. https://doi.org/10.1016/j.applthermaleng.2020.116471

[25] Shengxian C, Yanhui Z, Jing Z, Dayu Y. Experimental study on dynamic simulation for biofouling resistance prediction by least squares support vector machine. Energy Procedia, 2012; 17: 74-78. https://doi.org/10.1016/j.egypro.2012.02.065

[26] Harche R, Mouheb A. The fouling in the crude distillation preheat train of Algerian refinery. Acta Periodica Technologica, 2022;(53):272-284. https://doi.org/10.2298/APT2253272H

[27] Al-Naser M, Al-Toum M, El-Ferik S, Mansour RB, Al-Sunni F. Heat exchanger fouling prediction using artificial intelligence. In 5th International Conference on Advances in Mechanical Engineering, Istanbul, Turkey, 17-19, December, 2019.

[28] Al-Naser M, El-Ferik S, Mansour RB, AlShammari HY, AlAmoudi A. Intelligent Prediction Approach of Fouling Location in Shell and Tube Heat Exchanger. In 10th International Conference on System Engineering and Technology (ICSET), Shah Alam, Malaysia, 139-144, November, 2020. https://doi.org/10.1109/ICSET51301.2020.9265382

[29] Luo X, Patton AD, Singh C. Real power transfer capability calculations using multi-layer feed-forward neural networks. IEEE Transactions on Power Systems, 2000; 15(2): 903-908. https://doi.org/10.1109/59.867192

[30] Tabib SS, Jalali AA. Modelling and prediction of internet time-delay by feed-forward multi-layer perceptron neural network. In Tenth International Conference on Computer Modeling and Simulation (uksim), Cambridge, United Kingdom , 611-616, April, 2008. https://doi.org/10.1109/UKSIM.2008.93

[31] Bastani D, Hamzehie ME, Davardoost F, Mazinani S, Poorbashiri A. Prediction of CO2 loading capacity of chemical absorbents using a multi-layer perceptron neural network. Fluid Phase Equilibria, 2013; 354: 6-11. https://doi.org/10.1016/j.fluid.2013.05.017

[32] Leontaritis IJ, Billings SA. Input-output parametric models for non-linear systems part I: deterministic non-linear systems. International journal of control, 1985; 41(2): 303-328. https://doi.org/10.1080/0020718508961129

[33] Boussaada Z, Curea O, Remaci A, Camblong H, Mrabet Bellaaj N. A nonlinear autoregressive exogenous (NARX) neural network model for the prediction of the daily direct solar radiation. Energies, 2018; 11(3): 620. https://doi.org/10.3390/en11030620

[34] Mohanty S, Patra PK, Sahoo SS. Prediction of global solar radiation using nonlinear auto regressive network with exogenous inputs (narx). In 39th National Systems Conference (NSC), Greater Noida, India, 1-6, December, 2015. https://doi.org/10.1109/NATSYS.2015.7489103

[35] Pisoni E, Farina M, Carnevale C, Piroddi L. Forecasting peak air pollution levels using NARX models. Engineering Applications of Artificial Intelligence, 2009; 22(4-5): 593-602. https://doi.org/10.1016/j.engappai.2009.04.002

[36] Zibafar A, Ghaffari S, Vossoughi G. Achieving transparency in series elastic actuator of sharif lower limb exoskeleton using LLNF-NARX model. In 4th International Conference on Robotics and Mechatronics (ICRoM), Iran, 398-403, October, 2016. https://doi.org/10.1109/ICRoM.2016.7886771

[37] Bouaddi S, Ahmed I. Modeling and prediction of reflectance loss in CSP plants using a nonlinear autoregressive model with exogenous inputs (NARX). International Renewable and Sustainable Energy Conference (IRSEC), Marrakach, Moroco, 706-709, November, 2016. https://doi.org/10.1109/IRSEC.2016.7984071

[38] Alabi KO, Abdulsalam SO, Ogundokun RO, Arowolo MO. (2021). Credit risk prediction in commercial bank using chi-square with SVM-RBF. In Information and Communication Technology and Applications: Third International Conference (ICTA), Minna, Nigeria, 158-169, November 24-27, 2020. https://doi.org/10.1007/978-3-030-69143-1_13

[39] Khemakhem S, Boujelbene Y. Artificial intelligence for credit risk assessment: artificial neural network and support vector machines. ACRN Oxford Journal of Finance and Risk Perspectives, 2017; 6(2):1-17.

[40] Reddy SVG, Reddy KT, Kumari VV, Varma KV. An SVM based approach to breast cancer classification using RBF and polynomial kernel functions with varying arguments. International Journal of Computer Science and Information Technologies, 2014; 5(4): 5901-5904.

[41] Amiri B, Dizène R, Dahmani K. Most relevant input parameters selection for 10-min global solar irradiation estimation on arbitrary inclined plane using neural networks. International Journal of Sustainable Energy, 2020; 39(8): 779-803. https://doi.org/10.1080/14786451.2020.1758104

[42] Dahmani A, Ammi Y, Hanini S, Redha Yaiche M, Zentou H. Prediction of Hourly Global Solar Radiation: Comparison of Neural Networks/Bootstrap Aggregating. Kemija u industriji: Časopis kemičara i kemijskih inženjera Hrvatske, 2023; 72(3-4): 201-213. https://doi.org/10.15255/KUI.2022.065

[43] Garson GD. (1991). Interpreting neural-network connection weights. AI expert, 1991; 6(4): 46-51.

[44] Goh AT. Back-propagation neural networks for modeling complex systems. Artificial intelligence in engineering, 1995; 9(3): 143-151. https://doi.org/10.1016/0954-1810(94)00011-S

[45] Hosseini S, Khandakar A, Chowdhury ME, Ayari MA, Rahman T, Chowdhury MH, Vaferi B. Novel and robust machine learning approach for estimating the fouling factor in heat exchangers. Energy Reports, 2022; 8: 8767-8776. https://doi.org/10.1016/j.egyr.2022.06.123

[46] Tong S, Zhang X, Tong Z, Wu Y, Tang, N, Zhong W. Online ash fouling prediction for boiler heating surfaces based on wavelet analysis and support vector regression. Energies, 2019;13 (1):59. https://doi.org/10.3390/en13010059

[47] Jradi R, Marvillet C, Jeday MR. Analysis and estimation of cross-flow heat exchanger fouling in phosphoric acid concentration plant using response surface methodology (RSM) and artificial neural network (ANN). Scientific Reports, 2022; 12(1): 20437. https://doi.org/10.1038/s41598-022-24689-2

[48] Tang SZ, Li MJ, Wang FL, He YL, Tao WQ. Fouling potential prediction and multi-objective optimization of a flue gas heat exchanger using neural networks and genetic algorithms. International Journal of Heat and Mass Transfe r, 2020; 152: 119488. https://doi.org/10.1016/j.ijheatmasstransfer.2020.119488

[49] Kashani MN, Aminian J, Shahhosseini S, Farrokhi M. Dynamic crude oil fouling prediction in industrial preheaters using optimized ANN based moving window technique. Chemical Engineering Research and Design, 2012; 90(7): 938-949. https://doi.org/10.1016/j.cherd.2011.10.013

Parameter optimization and surface integrity aspects in MWCNT-based nano-PMEDM process of Inconel 718

Sinthea Khatun[1,a], AKM Nurul Amin[1,b], Mamunur Rashid Mashuk[1,c], Noshin Tasnim Tuli[1,d], Ismat Jerin[1,e], M.S. Bashar[2,f], Md Jalal Uddin Rumi[3,g,*]

[1]Dept. of Industrial and Prod. Eng., Military Inst. of Science and Tech., Bangladesh
[2]Institute of Fuel Research & Development (BCSIR), Bangladesh
[3]Dept .of Aeronautical Eng., Military Institute of Science and Technology, Bangladesh

Article Info	Abstract
Article history: Received 30 May 2023 Accepted 24 Oct 2023 *Keywords:* *Inconel 718;* *NANO-PMEDM;* *MWCNT;* *Material removal rate* *Tool wear rate;* *Surface roughness;* *Response surface methodology*	This study examines the effects of Inconel 718's Nano PMEDM process parameters on Material Removal Rate (MRR), Tool Wear Rate (TWR), Surface Roughness (SR), and the integrity of surface and subsurface layers. It also examines the concentration of MWCNT nanoparticles in distilled water as a dielectric medium. Peak Current, Pulse on Time, and Powder Concentration were input variables in 20 experimental runs utilizing the Central Composite Design (CCD) of Design of Expert (DOE). To create and evaluate empirical models for MRR, TWR, and SR, response surface methodology (RSM) and ANOVA were used. According to the results of the improved RSM, the best responses for MRR, TWR, and SR are 0.012 g/min, 0.001 g/min, and 5.098 μm, respectively. These were accomplished by cutting parameters of 1.5 g/L for powder concentration, 307.967 s for pulse on time, and 19.925 Amps for peak current. GA optimization produced slightly different optimal values for MRR, TWR, and SR: 0.012 g/min, 0.003 g/min, and 5.229 μm, respectively. 20.178 Amps for Peak Current, 398.753 seconds for Pulse on Time, and 3.66 g/L for Powder Concentration were the suggested ideal cutting conditions for GA optimization. In the validation tests, both the GA-predicted outcomes and RSM-optimized values closely matched the experimental results.

1. Introduction

Inconel 718 is a high-tech structural material for crucial industrial applications because of its outstanding corrosion resistance, excellent toughness, and high-yielding strength at extreme temperatures. It has the possibilities for use in an extensive range of fields, such as developing nuclear reactors, jet engines, and turbine engines [1]. Furthermore, it is utilized in producing components for gas turbines, related components for rocket and aircraft engines (such as compressor blades), and spacecraft. Additionally, Inconel 718 has a diversity of products for the gas, oil, and chemical industries [2].

Because it can be strain-hardened while keeping a lessened thermal conductivity, Inconel 718 is a material considered difficult to machine. This is because it maintains both of these properties up to high temperatures. That's the case despite the material's significant advantages [3]. The poor thermal conductivity of the material leads to high cutting temperatures during the machining process. The thermal consequences are apparent because of the high cutting temperature and the material's poor thermal conductivity. Moreover, the material undergoes a chemical reaction that affects the cutting force and the

surface finish achieved after machining [4]. The tools get worn out faster because of the work's tendency to toughen. Because it includes hard abrasive carbide particles, excessive tool wear occurs during machining [5]. Because of all the factors covered earlier, the machining of Inconel 718 should be accomplished at minimal cutting speeds. This significantly decreases the effectiveness of the operation and pushes up the cost of production [2].

To get around the issues of poor machinability of Inconel 718, a significant number of alternative techniques and procedures, including the application of rotary tools, EDM aided by the shuddering of ultrasonic, collective electrodes, and lastly, the combination of supplements in the dielectric fluid have been tried. Introducing powder particles to the dielectric fluid of the EDM process is also referred to as PMEDM (Powder Mixed Electric Discharge Machining) process. Due to the artificial residues, the dielectric resistance was broken down more efficiently, and the machined areas had an excellent finish on the surface [6]. On the converse side, the drawbacks of electro-discharge machining are its relatively leisurely machining process and a moderate material removal rate (MRR). However, to overcome the high cost of conventional machining of difficult-to-machine materials EDM is considered an option. The new concepts of PMEDM are being looked at as potential solutions to the shortcomings of conventional EDM [7]. PMEDM improves overall machining performance over conventional EDM by adding powder particles of the right size and concentration to the dielectric medium [8]. Including metallic powder creates more intense sparks, improving the MRR. At the same time, the spark is dispersed on the powder particles, and as a result, the spark's discharge density reduces. This leads to a reduced number of cracks, holes, and gaps on the surface of the workpiece which has been constructed [9].

EDM efficiency was assessed using carbon Nanotube powders, graphite powders, and nano-sized titanium dioxide powders. The low-energy EDM technique with the CNT (Carbon Nanotube) mixed dielectric also worked. High thermal conductivity, low specific gravity, and superior mechanical and electrical qualities are all characteristics of CNTs. Single-walled carbon nanotubes (SWCNTs) and multi-walled carbon nanotubes (MWCNTs) are the two primary subcategories of CNTs. MWCNTs are more chemically and thermally stable than SWCNTs. Additionally, MWCNTs are less likely to develop oxide than SWCNTs and have greater strength and corrosion resistance [8]. A limited number of studies have been conducted on the impact that Multi-Walled Carbon Nano Tubes (MWCNT) combined with water that has been distilled to be used as a dielectric fluid has in the NANO - PMEDM process.

The literature review established that graphite and Nano TiO_2 powders were widely tested to test EDM performance. However, the effect of Multi-Walled Carbon Nano Tubes (MWCNT) mixed in distilled water as a dielectric fluid in the NANO - PMEDM process has received very little research attention.

Jadam et al. [8] investigated the effect of MWCNT powder concentration added to the dielectric media in enhancing the machining performance of Inconel 718. They varied powder concentration (0.5-1 g/L), pulse on-off time (10 µs), and peak current (2A, 4A, 6A, and 8A) as their input parameter. They found that MWCNT offers less fracture density added dielectric at 0.5 g/l concentration than 1 g/l concentration. High additive concentrations impede effective flushing and effortless debris removal. Crater enlargement results from an increase in peak current. A higher degree of material erosion from the workpiece results from an increase in average crater diameter caused by the rise in peak current. This raises the MRR. However, at MWCNT concentrations of 0.5 g/l compared to 1 g/l, increased MRR is experienced. Another study on the surface roughness and surface topography of Inconel 718 in the PMEDM process, carried out by Ahmed et al.

[10] using the input parameters powder concentration (0,2,4 g/L), Peak current (20 A, 30 A, and 40 A) and Pulse on time (200μs, 300μs, 400μs). As per their investigation, using the highest peak current for surface roughness is not advised. When the peak current increases, the surface roughness also increases. However, the surface roughness will diminish as the pulse duration increases. These studies opened up a direction to investigate the machining performance of the PMEDM process of Inconel 718 under the influence of the parameters mentioned, i.e., powder concentration, peak current, and pulse on time. These are the significant parameters that influence how the process responds.

A total of sixty 3D roughness parameters are developed in order to do a thorough roughness analysis, and they are used to define the majority of surface morphology in terms of certain functions, qualities, or applications. For the EDM Process: The best roughness parameter is S_{PD}, which measures the number of peaks per unit area following the segmentation of a surface into motifs and is calculated at an 8 mm scale. R. Deltombe used Average surface roughness i.e. Ra to measure the surface roughness of the EDM process [11]. The reason for selecting average surface roughness is regardless of the specimens' curing times; the Ra, or average roughness, values stay constant. One explanation for this phenomenon is that two surfaces with different finishing methods can have comparable average roughness (Sa) values but different roughness metrics, such as valley depth, peak curvature, interfacial area ratio, valley void volume, and peak density. This is due to the fact that surface roughness is a multi-dimensional feature and that extra factors are required to shed light on particular texture and profile aspects. Therefore, these characteristics can differ amongst surfaces even while overall roughness and height variations are comparable [12].

The Taguchi method optimizes machining and electrical and mechanical component design throughout most industrial applications. The success of the Taguchi practice is subdued by constant process variables [13]. This method confines optimization to a certain range and level of parameter values, so one may not be aware of a middle-ground combination that could enhance performance. Complex statistical methods like RSM and ANOVA are required to identify all primary relationship characteristics. Thus, the Taguchi technique can be effectively replaced by RSM [14].

RSM is one of the efficient techniques for generating mathematical models from observable data derived from the actual world [15]. This technique is particularly beneficial in circumstances in which the correlation between the inputs and outputs is nonlinear, which tends to make it challenging to figure out the optimal settings utilizing traditional statistical methods such as regression analysis. In addition, one further optimization technique known as the GA works on a population of alternative answers to generate progressively accurate approximations of the right answer that use the Principle of Darwinian (the survival of the fittest) as its cornerstone. GA is distinct from other, more conventional evolutionary algorithms in that it is not focused on locating a single optimal solution but rather on locating a population of optimal results, and it also provides the option to avoid convergent search toward less desirable solutions [16].

As EDM is the process of material removal using electrical sparks and bombardments, the surface roughness generated in the process is not comparable with that achieved in fine machining and grinding followed by polishing, as such the study on the surface roughness generated in the Nano-PMED process was not included in this study, rather an in-depth study on the composition and micro-structural properties of the EDM generated surface and sub surfaces was included in this study. The objective of the study was to identify the aftermath of the EDM bombardment at the plasma temperatures on the generated surface and sub-surfaces. SEM study, EDS analysis, and micro-hardness measurements of the

upper recast layer, the underlining heat-affected zone up to the main base material were included in this study.

Thus, this investigation looks into the machinability of Inconel 718 through the use of the Nano-PMEDM method using MWCNT as the Nano-particles and distilled water as a dielectric medium, and how the effect of MWCNT Nano-powder has on the response parameters – Material removal rate, and tool wear rate. Modeling responses to reduce MRR and TWR are the primary goal of this research. Optimization is conducted using RSM and GA.

2. Materials and Methods

2.1. Workpiece Material

As the entire purpose of the article is to deliver an appropriate configuration of the machine's settings for the NANO – PMEDM process and this research has taken into consideration a sample of the nickel-based alloy Inconel 718. The alloy's physical as well as mechanical characteristics and its chemical configurations (expressed as a percentage of total weight) are demonstrated in Tables 1 and 2, respectively.

Table 1. Physical as well as mechanical characteristics of Inconel 718

Property	Property Unit Density	Young's Modulus	Yield Tensile Strength	Ultimate Tensile Strength	Thermal Conductivity	Specific Heat Capacity	Melting Point
Unit	Kg/m³	GPa	MPa	MPa (min)	w/m°K	J/Kg°C	°C
Quantity	8190	200	1100	1375	11.4	435	1260-1336

Table 2. Chemical Configuration of Inconel 718 (wt.%)

Content	Ni	Cr	Si	Cb+Ta	Mo	Ti	Al	Co	Mn	C	Fe
Composition (Wt%)	53.8	18.2	0.09	5.26	2.96	0.94	0.44	0.3	0.064	0.028	Balanced

2.2. Powder Selection and Dielectric Fluid Preparation

2.2.1. Powder Selection

In this particular study, MWCNTs with a purity of at least 95% and a diameter of no more than 100 nm were employed, though the total length of the diameter was significantly greater than 100 nm [17]. Nano powder composed of multi-walled carbon nanotubes (MWCNT) is an elevated material that has the appearance of a cylinder and is comprised of numerous layers of carbon sheets that have been rolled up. The presence of several layers of graphene in MWCNTs and Double-walled carbon nanotubes (DWCNT) gives these nanotubes greater durability than Single-walled carbon nanotubes (SWCNT) do; for which this construction aids in their application in the field of composite material. Because of its superior mechanical, thermal, and electrical properties, it is the material of choice for use in this research. This property makes it appropriate for a broad spectrum of applications, such as energy storage, thermal management, electrical conductivity, etc. The characteristics of the particle are laid forth in Table 3.

The scanning electron microscope (SEM) image of nanoparticles is demonstrated in Fig. 1. On the other hand, the EDX particle count verifies that MWCNT powder particles are the right amount as shown in Fig. 2.
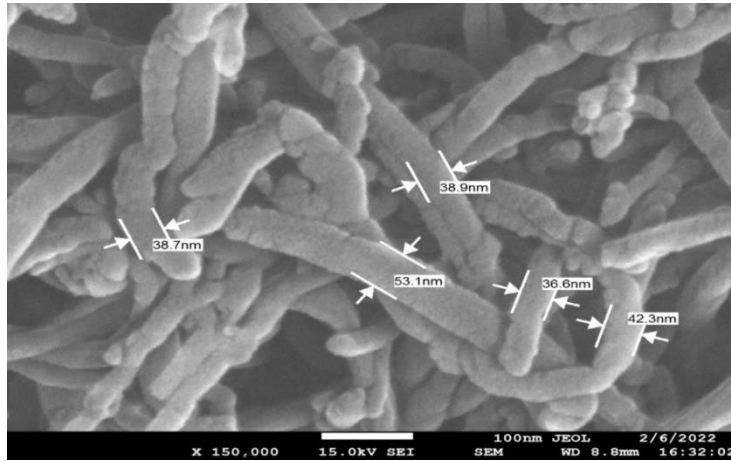
Fig. 1. SEM image of MWCNT powder particle size
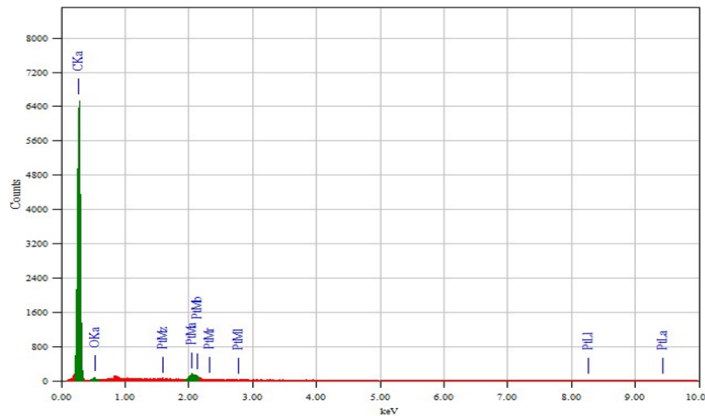
Fig. 2. EDX report for element count

Table 3. Properties of MWCNT

Property	Metallic Impurity	Length	Purity –wt%	Specific Surface Area	Average inner diameter	Number of Walls	Average Outer Diameter
Quantity	<5%	50μm	>95%	350 m²/g	5 nm	5-15	20-40 nm

2.2.2. Dielectric fluid preparation

Compared to standard dielectric media distilled water provides a lower material removal rate and results in a rough surface finish [18]. However, the incorporation of MWCNT into the distilled used as the dielectric medium causes an appreciable increase in the rate of material removal in contrast to conventional EDM without any additives. The main goal of this study is to judge how well MWCNT nanoparticles coupled with distilled water perform as a dielectric medium in the PMEDM method and assess how well they compare to the

performance of the conventional dielectric fluid. Before starting the testing, the MWCNT nanoparticles were thoroughly mixed with the distilled water using the Sonicator machine. This was to ensure there was no sedimentation during the process. In the process of producing the dielectric fluid depicted in Fig. 3, MWCNT is dissolved.
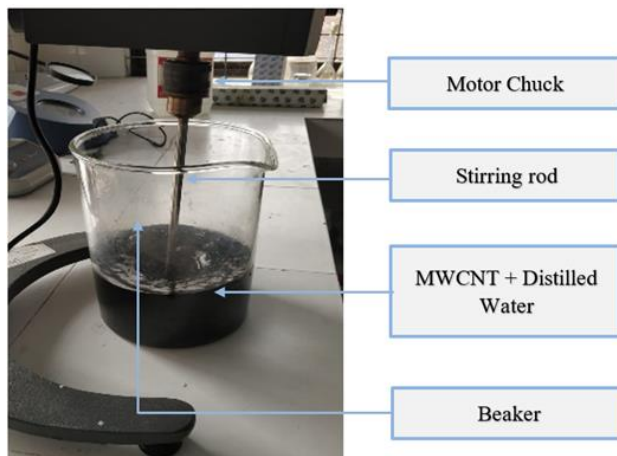
Fig. 3 Preparation of the dielectric fluid (distilled water + MWCNT)

2.3. Cutting Tool

As the experiment will be performed on an electrical discharge machine, the tool must have a high level of electrical conductivity and resistance to arc erosion at the electrode level. Copper and its alloys, graphite, and various other alloys are considered to be suitable to meet these requirements. Copper electrodes have been used in this study, as shown in Fig. 4. The diameter of the tool was maintained constant at 8 mm throughout the entire experiment. Lathe turning and facing were performed before the machining tests.

2.4. EDM Machine

The experiments were conducted on the JS EDM machine model - NCF606N (Fig. 5). A list of the machine's specifications is provided in Table 4. As shown in Fig. 6, the chamber was converted into a small box since the experiments did not require a sizable working space or EDM oil.

Table 4. EDM machine specifications

Parameter	Table dimension	X-axis travel	Y axis travel	Workpiece weight	Ram travel(z)	Max electrode weight	Machine dimension
Unit	mm	mm	mm	Kg	mm	Kg	M
Dimension	700 x 400	450	350	1000	200	120	1.47x 1.15x1.98

Table 5. Input Parameters in Central Composite Design

Name of the Parameter	Unit	Value
Pulse On Time	(µs)	150-400 µs
Peak Current	(Amp)	15-40 Amp
Powder Concentration	(g/L)	1.5-5 g/L
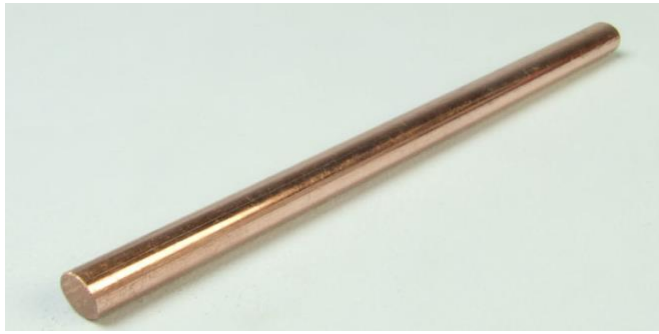
Fig. 4. Copper electrode

Fig. 5. EDM Machine
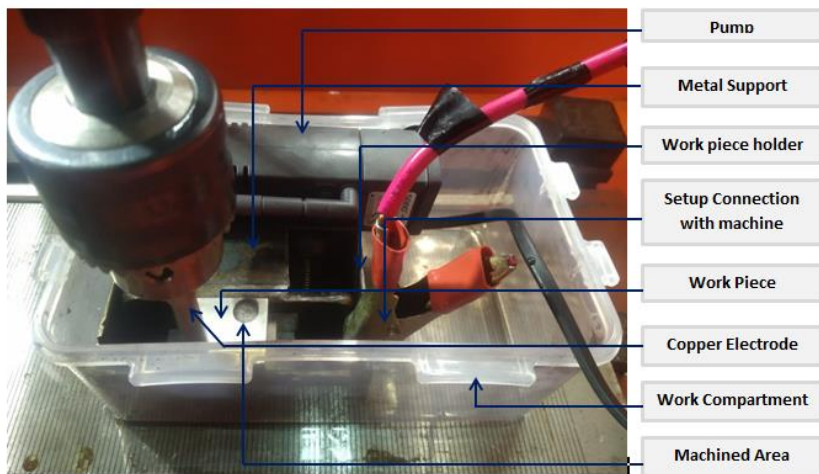
Fig. 6. Experimental setup

2.5. Experiment Design and Parameter Setting

This experiment employs the most influential factors in their appropriate ranges as identified in the prior investigations. Table 5 lists major factors and levels. The study consisted of using RSM analysis based on central composite design (CCD) to properly assess how machining parameters impacted tool wear rate and Surface roughness. The tool diameter of 8 mm and cut depth of 10 mm remain the same throughout the experiment.

3. Result and Analysis

In this study, RSM was used to develop mathematical models of MRR, TWR, and SR as functions of the vital machining factors that included Peak Current (Amp), Pulse On Time (μs), and Powder Concentration (g/L). Necessary computations for the RSM model development were conducted with the help of the Design-Expert software. The tool wear rate as well as the material removal rate was calculated in grams per minute, surface roughness was tested in micrometers as shown in Table 6. A total of 20 different experimental runs were performed under the CCD design of experiments. The influence of MWCNT fine powder was studied varying the Concentration between 1.5–5 g/L. All the electric parameters except peak current (Amp) and Pulse on Time (μs) were constant for each of the runs.

Table 6. Results of experiments on MRR, TWR, and SR in the NANO – PMEDM process

Std	Run	Factor 1	Factor 2	Factor 3	Response 1	Predicted	Response 2	Predicted	Response 3	Predicted
		A: Peak Current	B: Pulse on Time	C: Powder Concentration	MRR	MRR	SR	SR	TWR	TWR
		Amp	μs	g/L	g/min	g/min	μm	μm	g/min	g/min
4	1	40	400	1.5	0.02275	0.0226	7.309	7.32	0.00308	0.0032
7	2	15	400	5	0.00779	0.0098	6.216	6.19	0.00109	0.0011
12	3	27.5	485.224	3.25	0.01308	0.0174	8.283	8.41	0.00201	0.0019
14	4	27.5	275	6.19314	0.01291	0.0135	4.4952	4.46	0.00211	0.002
13	5	27.5	275	0.30686	0.01511	0.0155	4.6	4.58	0.00189	0.0018
10	6	48.5224	275	3.25	0.02336	0.0244	6.68	6.6	0.00501	0.0049
11	7	27.5	64.7759	3.25	0.01368	0.0117	4.903	4.73	0.00269	0.0026
9	8	6.47759	275	3.25	0.00264	0.0047	5.43	5.46	0.00085	0.0008
16	9	27.5	275	3.25	0.01343	0.0145	4.58	4.88	0.00191	0.0021
2	10	40	150	1.5	0.01486	0.0193	4.676	4.74	0.0038	0.0039
5	11	15	150	5	0.00516	0.0064	4.361	4.39	0.00119	0.0012
1	12	15	150	1.5	0.00799	0.0076	4.523	4.61	0.00109	0.0012
20	13	27.5	275	3.25	0.01274	0.0145	4.45	4.88	0.00203	0.0021
18	14	27.5	275	3.25	0.01107	0.0145	4.4689	4.88	0.00294	0.0021
19	15	27.5	275	3.25	0.01349	0.0145	5.55	4.88	0.00209	0.0021
17	16	27.5	275	3.25	0.01621	0.0145	5.595	4.88	0.002	0.0021

15	17	27.5	275	3.25	0.01147	0.0145	4.63	4.88	0.00178	0.0021
8	18	40	400	5	0.02494	0.0215	7.453	7.4	0.00329	0.0033
6	19	40	150	5	0.02567	0.0181	4.757	4.9	0.0039	0.004
3	20	15	400	1.5	0.02222	0.0109	6.592	6.49	0.00091	0.001

3.1. Model Development and Analysis of MRR

RSM was exploited to construct the model employing Design-Expert software, and ANOVA (Analysis of Variance) was suggested to assess the model's adequacy (table-7). The executed fit statistics involved selected responses of MRR found from the experiment presented in Table 6. To compare the models, fit statistics, like p values and F- values are considered.

Table 7. ANOVA of the response MRR

Source	Sum of Squares	df	Mean Square	F-value	p-value	
Model	0.0007	6	0.0001	14.65	< 0.0001	significant
A-Peak Current	0.0005	1	0.0005	59.71	< 0.0001	
B-Pulse on Time	0.0000	1	0.0000	4.95	0.0445	
C-Powder Concentration	4.626E-06	1	4.626E-06	0.5908	0.4558	
AB	0.0000	1	0.0000	1.51	0.2416	
AC	0.0001	1	0.0001	14.60	0.0021	
BC	0.0001	1	0.0001	6.53	0.0240	
Residual	0.0001	13	7.830E-06			
Lack of Fit	0.0001	8	0.0000	3.15	0.1110	not significant
Pure Error	0.0000	5	3.372E-06			
Cor Total	0.0008	19				

The Model F-value of 14.65 implies the 2FI model is significant. There is only a 0.01% chance that an F-value this large could occur due to noise. P-values less than 0.0500 indicate model terms are significant. In this case, A, B, AC, and BC are significant model terms. Values greater than 0.1000 indicate the model terms are not significant. The Lack of Fit F-value of 3.15 implies the Lack of Fit is not significant relative to the pure error. There is an 11.10% chance that a Lack of Fit F-value this large could occur due to noise. Table 8 shows the Predicted R^2 of 0.4521 is not as close to the Adjusted R^2 of 0.8117 as one might normally expect; i.e., the difference is more than 0.2. Adeq. Precision measures the signal-to-noise ratio. A ratio greater than 4 is desirable. We found a ratio of 13.103 which indicates an adequate signal.

Table 8. Fit Statistics for MRR

Std. Dev.	0.0028	R^2	0.8711
Mean	0.0145	Adjusted R^2	0.8117
C.V. %	19.26	Predicted R^2	0.4521
		Adeq Precision	13.1033

According to the fit and summary test, a 2FI model was suggested. Equation 1 was confirmed to be the fitting MRR model for Inconel-718 PMEDM:

> *MRR = - 0.001723 + 0.000120 * Peak Current + 0.000072 * Pulse on Time - 0.001908*
> ** Powder Concentration - 7.76935E-07 * Peak Current * Pulse on Time + 0.000173 ***
> *Peak Current * Powder Concentration - 0.000012 * Pulse on Time * Powder*
> *Concentration*

(1)

The factor with the coefficient has a ruling impact on the responses. In the case of MRR, powder concentration affects the response more than peak current followed by pulse on time.

3.2. Model Development and Analysis of TWR

The analysis of variance (ANOVA) was conducted to determine whether or not the model that was created by the Design-Expert software was significant by using F-values and p-values of the mode and the mode terms. This was achieved by comparing the results of the ANOVA with the research results of the Design-Expert software. The ANOVA table for this research is illustrated in Table 9.

The fact that the given model is substantial is due to its F-value, which is 50.88. An F-value of this magnitude only has a 0.01% chance of being generated by a noise level of this magnitude, taking into account all of the relevant probabilities. P-values that are lower than 0.0500 are thought to identify that the model terms being considered are significant. Here, the model terms A, B, and A2 are extremely significant. When looking at the data, values that are higher than 0.1000 demonstrate that the model terms do not have statistical significance. The fact that the F-value for lack of fit is only 0.08, which is a relatively low number, lends credence to the hypothesis that it is not statistically significant in comparison to the error.

Table 9. ANOVA for Reduced Quadratic model of TWR

Source	Sum of Squares	df	Mean Square	F-value	p-value	
Model	0.0000	6	3.734E-06	50.88	< 0.0001	significant
A-Peak Current	0.0000	1	0.0000	280.64	< 0.0001	
B-Pulse On Time	5.552E-07	1	5.552E-07	7.56	0.0165	
C-Powder Concentration	6.960E-08	1	6.960E-08	0.9482	0.3480	
AB	1.356E-07	1	1.356E-07	1.85	0.1971	
A^2	8.911E-07	1	8.911E-07	12.14	0.0040	
C^2	9.401E-08	1	9.401E-08	1.28	0.2782	
Residual	9.542E-07	13	7.340E-08			
Lack of Fit	1.094E-07	8	1.367E-08	0.0809	0.9987	not significant
Pure Error	8.448E-07	5	1.690E-07			
Cor Total	0.0000	19				

Based on the fit and summary tests, it was recommended that a quadratic model be used. The results of the analysis of the fitted tool wear rate model for Nano–PMEDM machining of Inconel 718 are presented in (Equation 2) as follows:

> *TWR = + 0.000410 + 0.000032 * Peak Current - 1.33805E-06 * Pulse On Time +*
> *0.000167 * Powder Concentration - 8.33368E-08 * Peak Current * Pulse On Time +*
> *1.61377E-06 * Peak Current^2 - 0.000025 * Powder Concentration^2*

(2)

Powder Concentration has the maximum impact on the responses of TWR than Peak Current followed by Pulse On Time as Powder Concentration has the largest coefficient (0.000167) with it.

Table 10 shows that the variance between the predicted and the observed R^2 of 0.9406 as well as the adjusted R^2 of 0.9403 is less than 0.2, indicating that the two values are reasonably comparable to one another. The signal-to-noise ratio is something that Adeq Precision measures. This is preferable to have a ratio that is higher than 4. A sufficient signal can be determined from the ratio of 25.773.

Table 10. Fit statistics

Std. Dev.	0.0003	R^2	0.9592
Mean	0.0023	Adjusted R^2	0.9403
C.V. %	11.87	Predicted R^2	0.9406
		Adeq Precision	25.7732

3.3. Model Development and Analysis of SR

Table 11 provides the results of the ANOVA for the predicted model of SR. It provides both the p-values and the F-values that were formed from the outcomes of the ANOVA for the compact quadratic model of SR eradicating the non-significant terms that had a p-value higher than 0.1. These values were generated from the findings of the ANOVA for the reduced quadratic model of SR. It seems that the model is significant given that it was calculated to have a value of 26.77 for the F-value of the model.

Table 11. ANOVA for the condensed quadratic model

Source	Sum of Squares	df	Mean Square	F-value	p-value	
Model	25.72	7	3.67	26.77	< 0.0001	significant
A-Peak Current	1.55	1	1.55	11.31	0.0056	
B-Pulse On Time	16.34	1	16.34	119.04	< 0.0001	
C-Powder Concentration	0.0175	1	0.0175	0.1277	0.7270	
AB	0.2468	1	0.2468	1.80	0.2048	
A^2	2.37	1	2.37	17.28	0.0013	
B^2	5.12	1	5.12	37.29	< 0.0001	
C^2	0.2333	1	0.2333	1.70	0.2168	
Residual	1.65	12	0.1372			
Lack of Fit	0.1804	7	0.0258	0.0879	0.9970	not significant
Pure Error	1.47	5	0.2933			
Cor Total	27.36	19				

A noise level of this magnitude would only have a 0.01% chance of producing an F-value of this proportion if the noise level were to be increased to this level. P-values for the model terms which are significantly lower than 0.0500 indicate their significance. Within the context of this particular example, the significant model terms are B, A2, and B2. The fact that the F-value for Lack of Fit is 0.09 lends credence to the notion that it does not constitute a statistically significant finding in comparison to the error. Because there is a

99.70% chance that this will be the case, a Lack of Fit F-value of this magnitude could very well be the result of noise.

With this model, one may move more easily through the design space. The fit and summary test indicated that a quadratic model would be appropriate. It was determined that (Equation 3) best represents the surface roughness model that should be used for NANO–PMEDM machining of Inconel-718;

$$SR = +7.37058 - 0.160914 * Peak\ Current - 0.015037 * Pulse\ On\ Time + 0.153404 *$$
$$Powder\ Concentration + 0.000112 * Peak\ Current * Pulse\ On\ Time + 0.002597 * \qquad (3)$$
$$Peak\ Current^2 + 0.000038 * Pulse\ On\ TIme^2 - 0.041546 * Powder\ Concentration^2$$

According to the model, Peak Current has a far greater influence on surface roughness responses than Powder Concentration or iteration, in contrast to TWR. In Contrast, the Pulse on Time has the least amount of influence on the responses when considered an individual parameter.

Table 12shows that the variation between the predicted and the observed R^2 value of 0.8961 and the adjusted R^2 value of 0.9047 is fewer than 0.2, indicating that there is reasonable agreement between the two values. Adeq Precision means signal-to-noise ratio. It is preferable to have a ratio that is higher than 4. A sufficient signal can be inferred from the ratio of 16.838.

Table 12. Fit statistics for SR

Std. Dev.	0.3705	R^2	0.9398
Mean	5.48	Adjusted R^2	0.9047
C.V. %	6.76	Predicted R^2	0.8961
		Adeq Precision	16.8377

3.4. Perturbation Plot of Machining Characteristics on MRR, TWR, and SR

In the significant range, the perturbation plot draws a parallel between the impacts of all three machining parameters and makes comparisons among them. A representation of a perturbation graph of machining parameters on surface roughness and tool wear rate may be found in Fig. 7. All three lines in the picture meet at the same position, which serves as a reference (x = 0.00). The parameters A, B, and C provide a representation of the actual cutting conditions, respectively representing Peak Current (Amp), Pulse On Time (μs), and powder Concentration (g/L). When the reference point (A = 27.5 Amp, B = 275 μs, and C= 3.25 g/L) is moved to the right or left, the graph shows that MRR, TWR, and SR either increase or decrease respectively. The lines drawn on the graph demonstrate that the MRR increases with any movement to the right or approaching +1.00 deviation from the reference point of peak current and pulse on time, however, the MRR marginally reduces with the movement of powder concentration to the right of the intersection point.

This suggests that peak current and powder concentration are critical for MRR. Yet while a drop in powder concentration raises MRR, a drop in peak current drastically lowers MRR. During Peak Current, the TWR value either rises or lowers by a large amount. The TWR decreases at a more gradual rate as both the passage of time and the Powder Concentration increase. In addition, TWR improves if any of those factors move further away from the junction point.

The perturbation plot of SR parameters demonstrates that the aspect that has the most significant effect on surface roughness is the Pulse On Time (B). When factor B (Pulse On Time) is increased from the reference point to a deviation of +1.00, the SR rises quickly.

However, the SR also falls when factor B is decreased, in a manner comparable to that of factor a (Peak Current), but at a more gradual rate. When the Powder Concentration is changed, there is a slight decrease in SR.

(a)

(b)

(c)
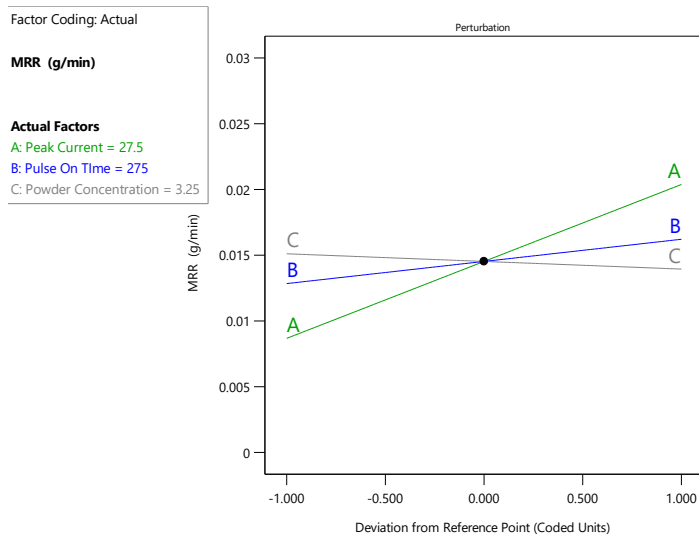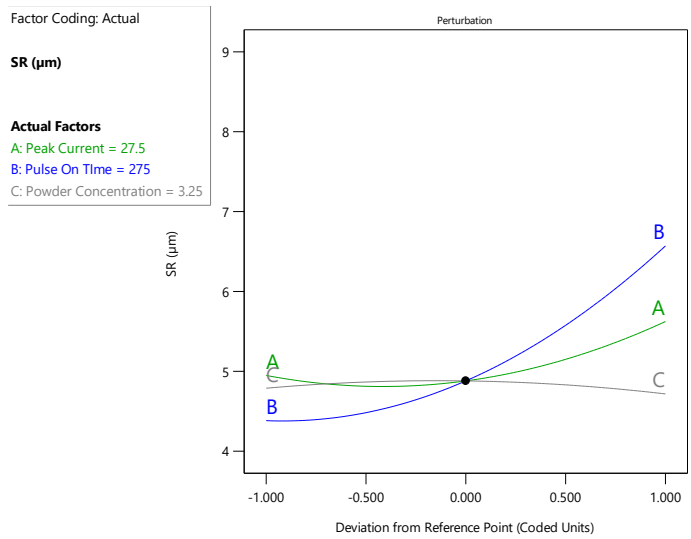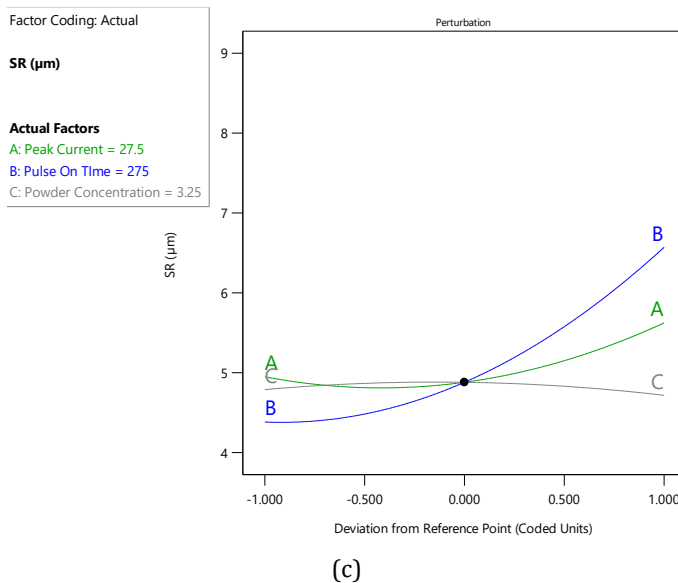
Fig. 7. Perturbation graph of (a) Material Removal Rate (MRR), (b) Tool wear rate (TWR), and (c) Surface roughness (SR)

3.5. 2D & 3D Response Surface Plot

3.5.1. Material Removal Rate (MRR)

Fig. 8 (a) and (b) respectively present the 3D and 2D plots of material removal rate as functions of Peak Current and Pulse on Time. The figures illustrate that peak current has the highest impact on Material Removal Rate. Peak current (at the range 27.5 Amp to 40 Amp) shows the maximum impact on material removal rate when powder concentration is kept constant at 3.25. Interaction between powder concentration and peak current also shows significant improvement in MRR. Increasing Pulse on time, increasing peak current, and decreasing Powder concentration provide the maximum MRR. The combination of the maximum Peak current of 40 Amp, Pulse on time of 400 μs, and minimum powder concentration of 1.5 g/L, an MRR of 0.02 g/min could be achieved. Many other combinations such as Peak current of 37.431 Amp, Pulse on time of 165.162 μs, and powder concentration of 3.865 g/L also give the maximum MRR of 0.020 g/min which indicates increasing peak current and powder concentration while lowering pule on time can result in high MRR.

Fig. 9 (a, b) presents the (a) 3D and (b) 2D graph illustrating the combined effect of powder concentration and pulse on time on MRR keeping peak current constant at 27.5 A. Varying pulse on time between 150-400 μs and pulse on time between 1.5-5 g/L while maintaining peak current fixed at 27.5 A provides a moderate MRR ranging approximately from 0.012 g/min to 0.018 g/min (Fig. 9 b).

Fig. 10 (a) 3D and (b) 2D graph represents the effect of powder concentration and peak current on MRR while the pulse on time is kept constant at 275 μs. It is clear from Fig. 10 That maximum MRR could be achieved at high peak current and moderate to high powder concentration. According to Fig. 10 b, the red zone for MRR starts at 0.02 g/min which is achieved when the peak current ranges between 35 to 40 Amp and powder concentration

from 3 to 5 g/L. And the maximum MRR achieved by the combination of peak current and powder concentration is 0.0256709 g/min.

(a)

(b)

Fig. 8. (a) 3D and (b) 2D plots of material removal rate with effect of Peak Current vs Pulse on Time using MWCNT for Powder Concentration keeping constant at the "3.25 g/L".

(a)

(b)

Fig. 9. (a) 3D and (b) 2D plots of material removal rate with effect of Powder Concentration vs Pulse on Time using MWCNT for Peak Current constant at the "27.5 A".

(a)

(b)

Fig. 10. (a) 3D and (b) 2D plots of material removal rate with effect of Powder Concentration vs Peak Current using MWCNT for Pulse On Time constant at the "275 μs".

3.5.2. Tool Wear Rate (TWR)

The influence of Peak Current and Pulse on Time on the rate of tool wear can be observed in Fig. 11, which displays 3D and 2D responses respectively. It is shown that maintaining the Powder Concentration at 3.25 g/L while reducing the Pulse On Time and increasing the Peak Current can result in the tools getting worn down more quickly. When the Powder Concentration is higher at 4.253 g/L, the Pulse on Time is amplified to 259.229 μs, and the

Peak Current is increased to 39.361 Amp respectively, the maximum tool wear of 0.004 g/min resulted. This finding is identical to the one that was obtained when the Peak Current was increased to 40 Amp, the Powder Concentration was enlarged to 5 g/L, and the Pulse on Time was reduced to 150 μs. When the Powder Concentration is held constant, the minimum TWR of 0.001 g/min that is sought can be attained with a lower Peak Current and a Pulse on Time that is higher.

(a)

(b)
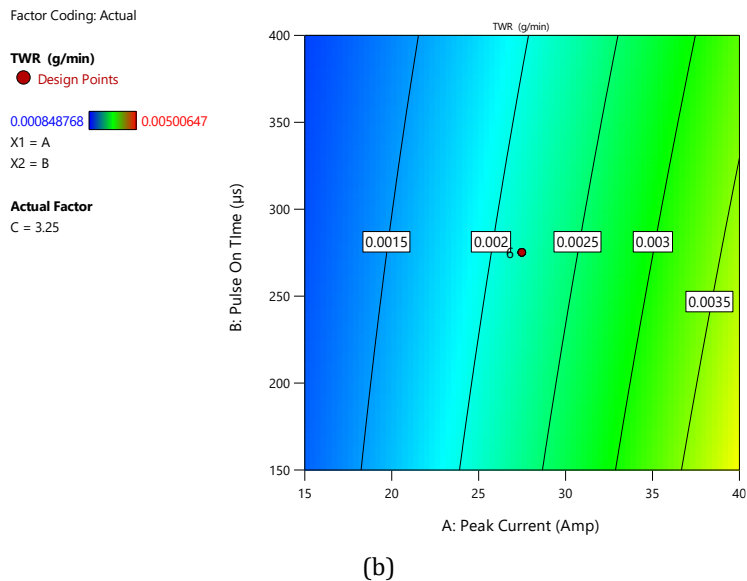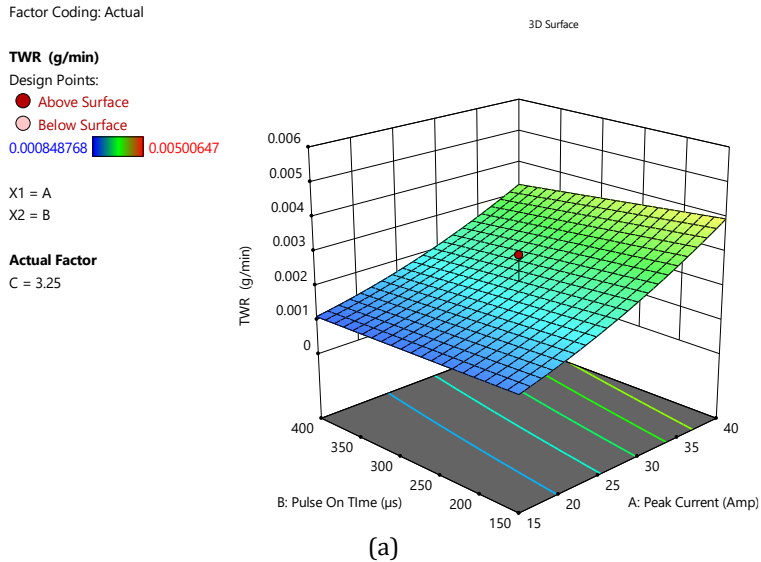
Fig. 11. (a) 3D and (b) 2D plots of Tool wear rate with the effect of Peak Current vs. Pulse on Time using MWCNT for Powder Concentration keeping constant at the "3.25 g/L".

The combined influence of powder concentration and pulse on time while maintaining the peak current constant at 27.5 A is lustrated at Fig. 12 (a) and (b). The Fig. 12 (a) explains that the combination of high pulse on time and low powder concentrations results in low

tool wear. It is evident from Fig. 12 b that the lowest tool wear that is achieved from this combination is 0.0019 g/min whereas the minimum tool wear possible for the experimental range is 0.000848768. The tool wear rate of 0.0019 g/min is attained from pulse on time ranging between 350 to 400 μs and powder concentration from 1.5 to 2 g/L.

(a)

(b)
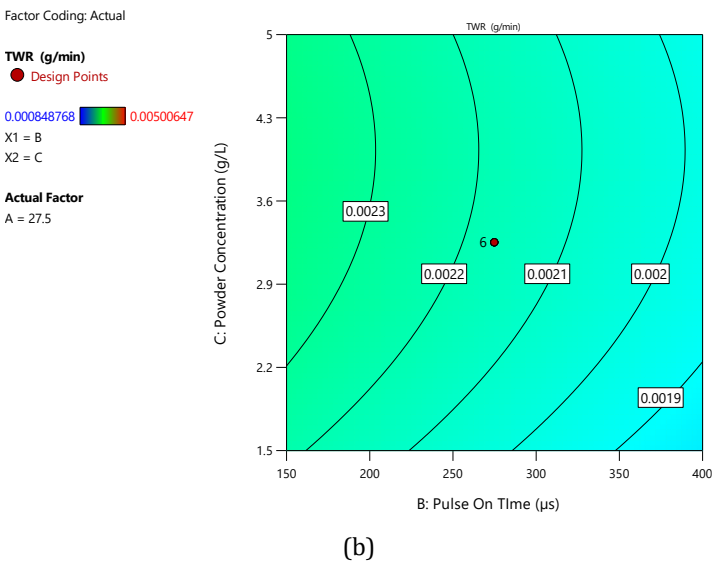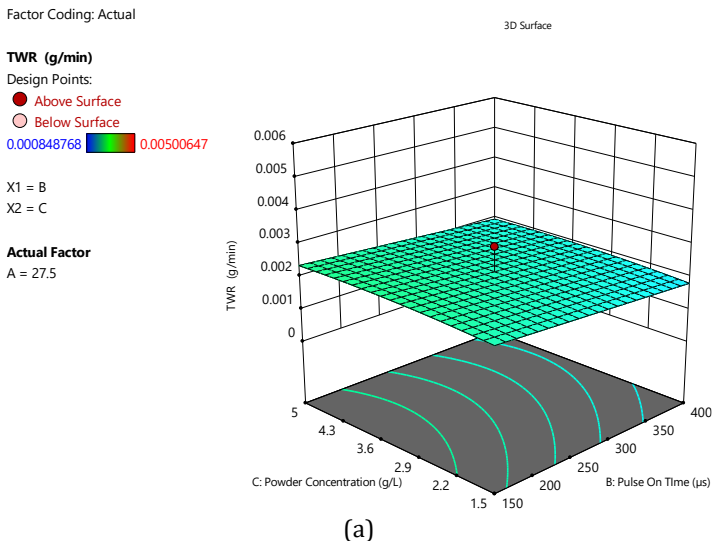
Fig. 12. (a) 3D and (b) 2D plots of tool wear rate with effect of Powder Concentration vs Pulse on Time using MWCNT for Peak Current constant at the "27.5 A"

Fig. 13 a and b illustrates that, if pulse on time is kept constant at a moderate value i.e. 275 μs and peak current along with powder concentration is varied, then minimum tool wear could be achieved at lowest peak current and average powder concentration. Fig. 13 a proves that minimum tool wear that could be achieved from the combination of powder concentration and peak current is 0.001 g/min while the lowest possible tool wear achievable for this experiment is 0.000848768 g/min. Fig. 13 b represents that the lowest

tool wear blue line which is at 0.0015g/min is achieved at 15 to 25 Amp peak current and 3 to 3.5 g/L powder concentration.

(a)

(b)
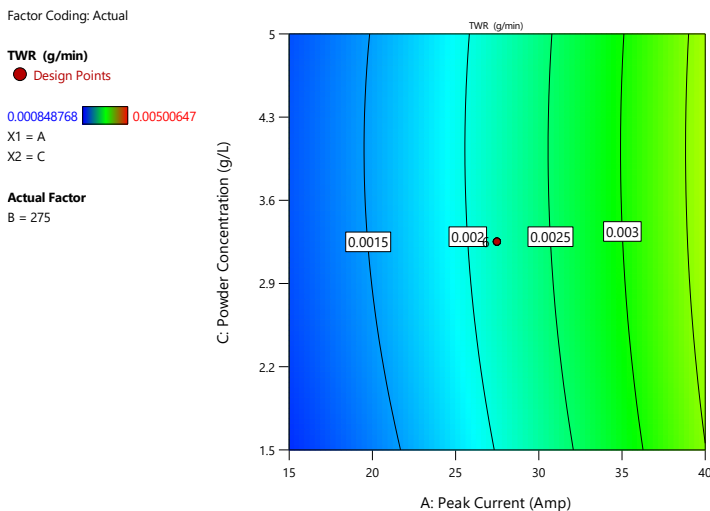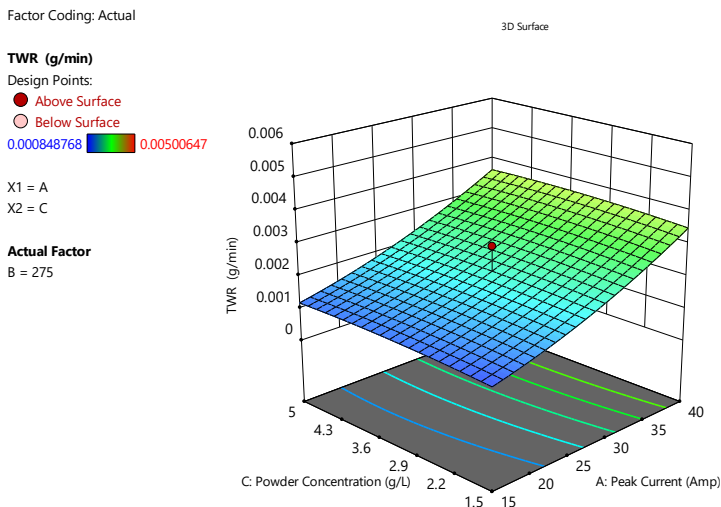
Fig. 13. (a) 3D and (b) 2D plots of tool wear rate with effect of Powder Concentration vs Peak Current using MWCNT for Pulse On Time constant at the "275 μs"

3.5.3. Surface Roughness (SR)

The result of Peak Current and Pulse on Time on Surface roughness illustrating 3D and 2D responses is represented in Fig. 14 (a, b). The figure, it demonstrates that the surface roughness is lower at the range of 15 Amp to 40 Amp of Peak Current and Pulse On Time range of 150 μs to 275μs where the third factor i.e., Powder Concentration is kept steady at 3.25 g/L. However, when Powder Concentration is increased (3.25 g/L - 3.740 g/L), and

the other factors i.e., Peak Current and Pulse on Time 22.622 Amp and 178.172 µs, the experiment showed the minimum surface roughness.

(a)

(b)
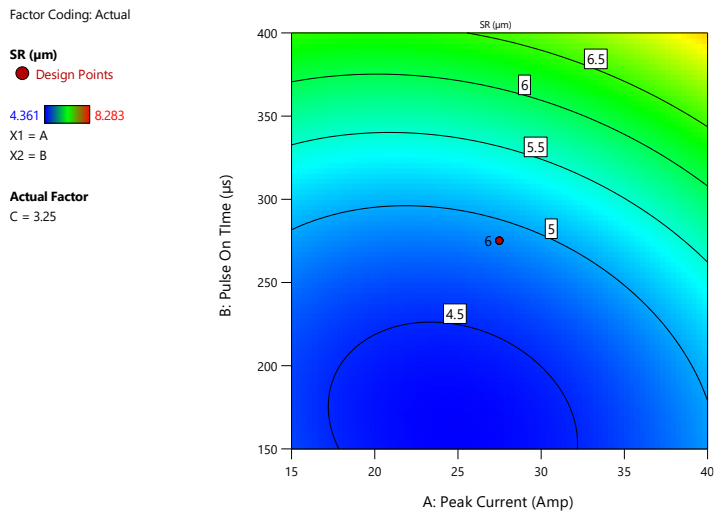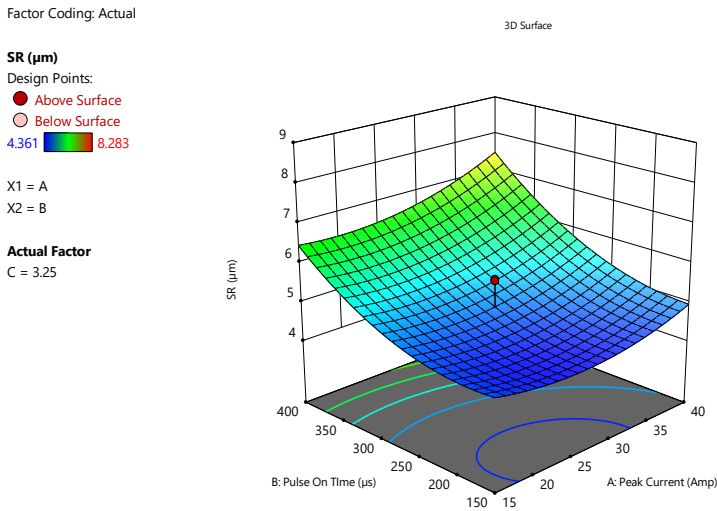
Fig. 14. (a) 3D and (b) 2D plots of Surface roughness with effect of Peak Current vs Pulse on Time using MWCNT for Powder Concentration keeping constant at the "3.25 g/L"

The influence of pulse on time and powder concentration on Surface roughness while keeping peak current fixed at 27.5 A is represented at Fig. 15 (a, b). It is illustrated at Fig. 15 (a) that the minimum surface roughness is attainable at low pulse on time and average powder concentration. The 2D graph i.e., the contour graph shows that min SR line where the roughness is 4.5µm is at the pulse on time range 150 to 250 µs.

(a)

(b)

Fig. 15. (a) 3D and (b) 2D plots of Surface roughness with effect of Powder Concentration vs Pulse on Time using MWCNT for Peak Current keeping constant at the "27.5 A"

Fig. 16 (a) and (b) is an illustration of how peak current and powder concentration affects surface roughness when pulse on time is kept constant at 275 µs. It is evident from Fig. 16 b that the lowest peak current results in the lowest surface roughness. The minimum surface roughness of 4.361 µm is attained at the lower range of peak current i.e., 15 to 30 Amp. Powder concentration has a little impact on the surface roughness value.

Factor Coding: Actual

SR (µm)
Design Points:
● Above Surface
○ Below Surface
4.361 ▮▮▮ 8.283

X1 = A
X2 = C

Actual Factor
B = 275
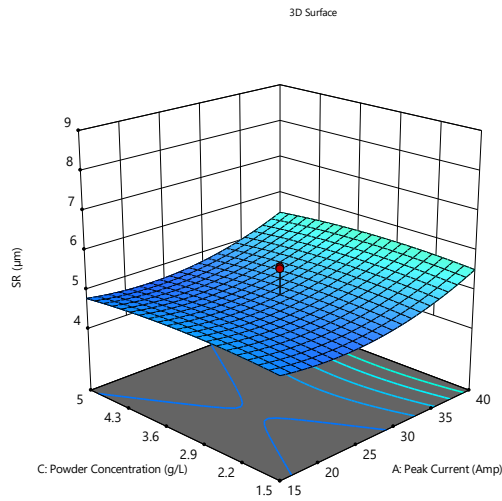
(a)

Factor Coding: Actual

SR (µm)
● Design Points

4.361 ▮▮▮ 8.283
X1 = A
X2 = C

Actual Factor
B = 275
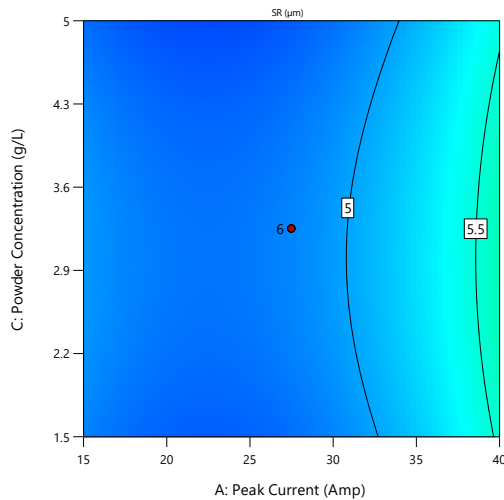
(b)

Fig. 16. (a) 3D and (b) 2D plots of Surface roughness with effect of Powder Concentration vs Peak Current using MWCNT for keeping Pulse on Time constant at the "275µs"

3.6. Optimization of the Cutting Parameters

This article applied a combined approach of optimization of response variables using the desirability function of RSM and merged models of RSM along with GA to generate optimum values of the desired combinations of output. This approach predicts the best parameter to accurately anticipate response values for every element combination in the experimental zone. The following shows the two optimization methods.

3.6.1. Optimizations of the Response Parameters by Desirability Approach

The desire function approach is quickly becoming among the most important commonly used methods for enhancing multiple response procedures in a wide variety of imposed

scientific and business fields. To construct the most accurate prediction that is even remotely possible, the optimization module will start looking for a combination of factor values that effectively meet all prerequisites for each response and component. This will allow the module to construct the most accurate model possible. This means allowing it to build the most appropriate prediction possible. DFA is a useful method for examining experiments when response needs to be optimized. The optimization of a single response identifies the impact of different input factors on response attractiveness. Prior to anything else, DFA transforms a response into a desirability function that ranges from zero to one. Desirability increases to one when the response variable approaches its aim or goal, and decreases to zero when it is outside of the acceptable range. This technique allows for the identification of the best value at which the tests should be carried out to achieve the lowest level of surface roughness and the reasonable level of tool wear value for the machining configurations that have been clarified. This guarantees that the objective for the factors is set to 'range,' while the reaction is set to 'minimum'. In this work, the target for MRR is to maximize and SR, TWR to minimize as shown at Table 13. As can be seen in Table 14, ten different solutions are ranked, and from those rankings, one solution that is deemed to be the best option is selected.

Table 13. Constraints for optimization of model

Name	Goal	Lower Limit	Upper Limit	Lower Weight	Upper Weight	Importance
A: Peak Current	is in range	15	40	1	1	3
B: Pulse On Time	is in range	150	400	1	1	3
C: Powder Concentration	is in range	1.5	5	1	1	3
MRR	maximize	0.00233779	0.0435882	1	1	5
SR	minimize	4.01	9.123	1	1	4
TWR	minimize	0.00129868	0.00230851	1	1	4

Table 14. Single response optimized solution

Number	Peak Current	Pulse On Time	Powder Concentration	MRR	SR	TWR	Desirability	
1	19.925	307.967	1.500	0.012	5.098	0.001	0.532	Selected
2	19.927	308.092	1.500	0.012	5.100	0.001	0.532	
3	19.912	307.030	1.500	0.012	5.089	0.001	0.532	
4	19.913	307.074	1.500	0.012	5.089	0.001	0.532	
5	19.944	309.309	1.500	0.012	5.112	0.001	0.532	
6	19.960	310.512	1.500	0.012	5.125	0.001	0.532	
7	19.879	304.665	1.500	0.012	5.065	0.001	0.532	
8	19.923	305.727	1.500	0.012	5.075	0.001	0.532	
9	19.867	303.754	1.500	0.012	5.056	0.001	0.532	
10	19.995	313.156	1.500	0.012	5.153	0.001	0.532	

The ideal cutting condition is a Peak Current of 19.925 Amp which indicates Peak Current should be lower, a Pulse on Time of 307.967 µs which is close to the maximum limit of Pulse on Time i.e., 400 µs and a Powder Concentration of 1.5 g/L which is the lower limit

of the range of Powder Concentration. The combination of these parameters results in an MRR of 0.012 g/min, TWR of 0.001 g/min, and SR of 5.098 μm with a desirability of 0.532, which is presented in Fig. 17.
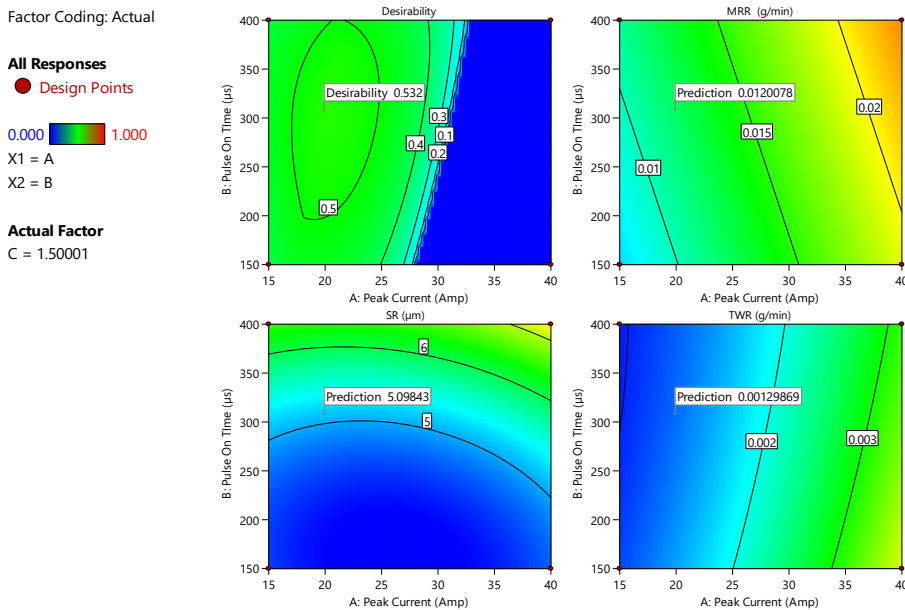
Fig. 17. Contour Graph of optimization

3.6.2. Optimization of The Response Parameters by Genetic Algorithm

Optimization of machining and current parameters in the Nano PMEDM process of INCONEL 718 is what the maximization is trying to achieve. Adjusting parameters with a numerical optimization method is efficient. Maximizing Material Removal rate, Minimizing Surface roughness and Tool wear rate needs a standard mathematical formulation:

Find: A (Peak Current), C (Powder Concentration), B (Pulse on Time)

Maximum: Material Removal Rate (A, B, C),

Objective function; - 0.001723 + 0.000120 * Peak Current + 0.000072 * Pulse on Time - 0.001908 * Powder Concentration - 7.76935E-07 * Peak Current * Pulse on Time + 0.000173 * Peak Current * Powder Concentration - 0.000012 * Pulse on Time * Powder Concentration

Minimize: Tool Wear Rate (A, B, C),

Objective function; + 0.000410 + 0.000032 * Peak Current - 1.33805E-06 * Pulse on Time + 0.000167 * Powder Concentration - 8.33368E-08 * Peak Current * Pulse on Time + 1.61377E-06 * Peak Current^2 - 0.000025 * Powder Concentration^2

Minimize: Surface roughness (A, B, C)

Objective function; +7.37058 - 0.160914 * Peak Current - 0.015037 * Pulse on Time + 0.153404 * Powder Concentration + 0.000112 * Peak Current * Pulse on Time + 0.002597 * Peak Current^2 + 0.000038 * Pulse on TIme^2 - 0.041546 * Powder Concentration^2

Subject to constrain: Ra ≤ Ra min(μm)

Within ranges: (Amin ≤ A ≤ Amax),(Cmin ≤ C ≤ Cmax),(Bmin ≤ B ≤ Bmax)

The variations of parameters to use for cutting in optimization have been selected based on the variable ranges used in the RSM model that was formed. The principles underlying natural selection and genetics are used as the basis for the Genetic Algorithm, which is an iterative search technique used for optimization. It takes its name from the genetic code, which is also its namesake [19]. The fundamentals of GA are simple and involve copying binary strings and then exchanging the binary strings that have been copied with one another. The GA method's primary selling points are the ease with which it can be utilized to perform computations and the speed with which it can do so. The GA solves the optimization problem by using an iterative process that is based on the biological evolution process that takes place in nature (Darwin's theory of survival of the fittest).
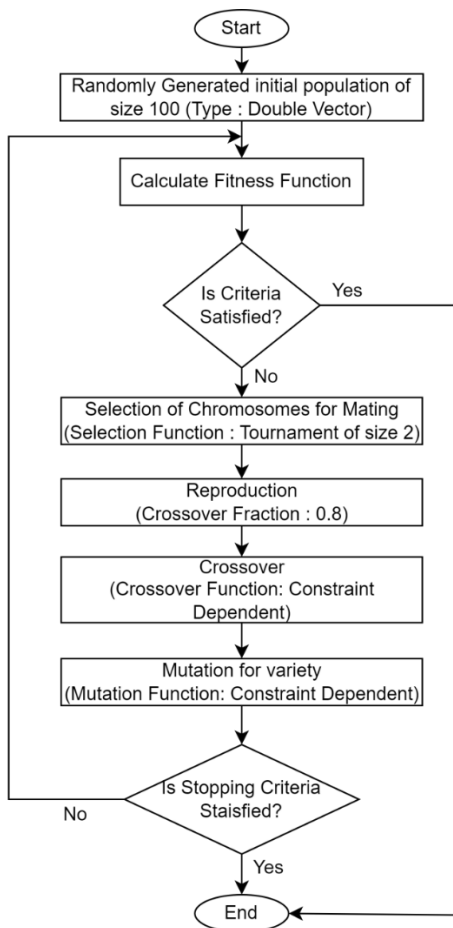
Fig. 18. Processing diagram of optimization utilizing genetic algorithm at matlab

The GA program is developed using MATLAB 2020 Toolbox for GA. The processing diagram for the GA optimization is shown at Fig. 18. GA's important parameters are population size, mutation, generations, etc. Table 15 shows the parameters. The established RSM models for MRR, SR and TWR prediction have served as optimizers for the GA. Based on objective value and constraint violation, the MATLAB GA algorithm picks chromosomes.

The most optimum parameter values used in GA as illustrated in Table 16, are Peak Current of 20.178 Amp, Pulse on Time 398.753 µs, and powder concentration of 3.66 g/L. GA

predicted optimum results for MRR, SR and TWR are 0.012 g/min, 5.229 µm and 0.003 g/min respectively.

Table 15. Genetic Algorithm parameters

Parameters	Values
Population	100
Selection	Tournament (Size = 2)
Crossover Fraction	0.8
Crossover Function	Constraint dependent
Mutation Function	Constraint dependent
Stopping Criteria	Default
Migration Direction	Forward
Creation Function	Constraint dependent

Table 16. The finest cutting condition found in GA and experimental validation for Inconel 718

Parameters	Optimized Values
Peak Current, A	20.178
Pulse on Time, B	398.753
Powder Concentration, C	3.66
MRR (g/min)	
GA prediction	0.012
SR (µm)	
GA prediction	5.229
TWR (g/min)	
GA prediction	0.003

4. Surface Characteristics

The EDM procedure adversely affects the integrity of the machined surface, as is widely known. During the sparking process in the PMEDM process, the materials in the workpiece and the tool electrode melt due to the high temperature of the spark. This is followed by a speedy re-solidification of the molten materials due to rapid cooling in the machining zone. The composition of the recast layer is of great interest to the researchers as this is the outermost layer to be exposed to the high stresses imposed on the die surfaces. This layer is supposed to contain oxides of the elements of the workpiece and the electrode materials as a result of a chemical reaction with the available oxygen inside the dielectric. The condition and composition of the HAZ are also equally important to know as this layer is going to be exposed to external loads that may be imposed on the part surface. The condition of the underlying base material and its resultant composition is also important to study as it would be a subsequent frontier to overcome the forming stresses applied to die surfaces.

SEM images of the three areas as discussed above for three selected Nano-PMEDM conditions were considered along with the EDS analysis at the three interested zones (Recast layer, HAZ, and Base metal) as indicated in Fig. 19(d). These included the 6th run (Peak Current: 48.5224 Amp, Pulse On Time: 275 µs, Powder Concentration: 3.25 g/L), as illustrated in Fig. 19 (a); 7th run (Peak Current: 27.5 Amp, Pulse On Time: 64.7759 µs, Powder Concentration: 3.25 g/L), as shown in Fig. 19 (b) and the 8th run (Peak Current: 6.47759 Amp, Pulse On Time: 275 s, Powder Concentration: 3.25 g/L) as displayed in Fig. 19 (c). The average recast layer thickness obtained after the sixth, and seventh operations are 18.5 µm and 48.2 µm respectively. The average HAZ thickness followed by the recast layer observed is 16.134 µm and 85.13 µm respectively. No discernible heat-affected zone or recast layer is present at the machined zone of the 8th run. Fig. 19 (a, b, c) makes it clear

that the recast layer is uneven in thickness and contains craters and debris. The surface of the heat-affected zone has numerous microcracks and craters. Fig. 19 (b) has more craters and unevenness than Fig. 19 (a), as well as a thicker recast layer and HAZ. Peak current and pulse on time are the variables that triggered this alteration. High peak current and pulse-on-time values provide a surface that is more uniform and has fewer craters in comparison.
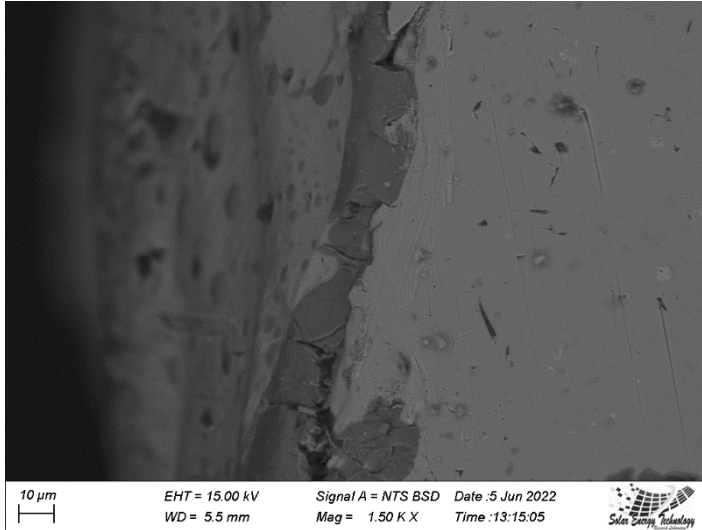
(a)
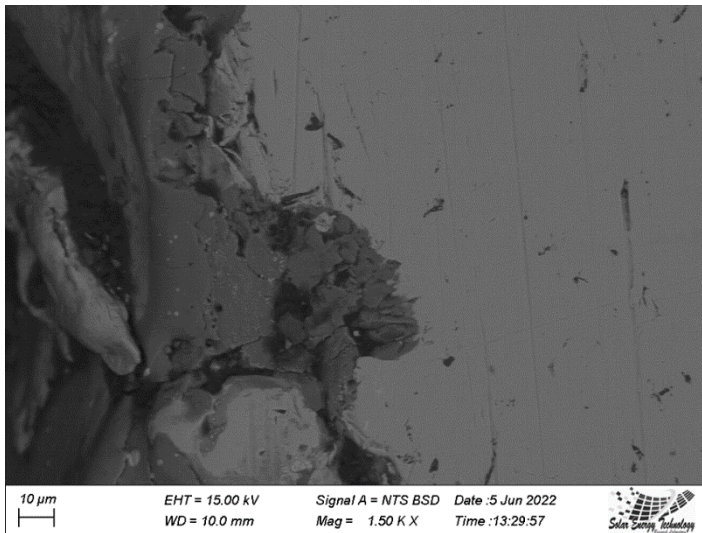
(b)
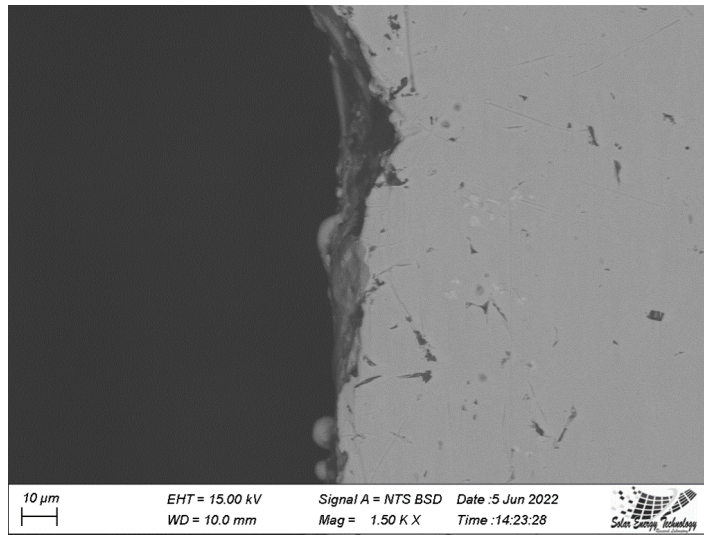
(c)
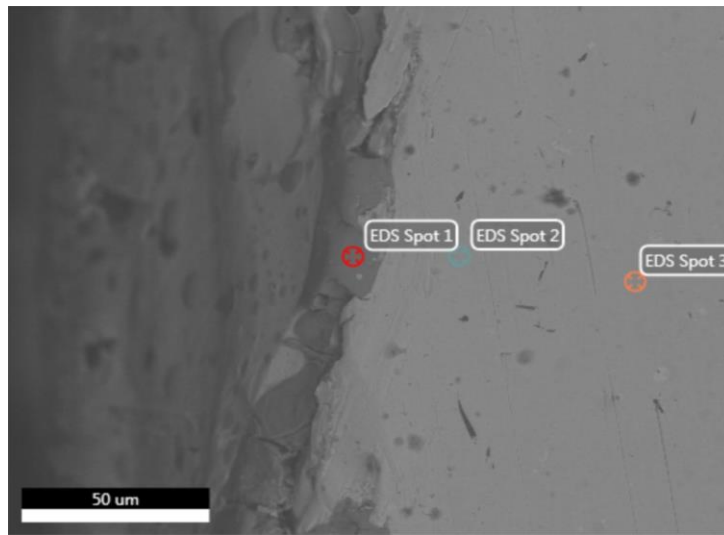
(d)

Fig. 19. SEM top view of the machined surface obtained during Nano-PMEDM machining of Inconel 718 under MWCNT for (a) sixth run, (b) seventh run, (c) eighth run, and (d) spots selected for EDS analysis
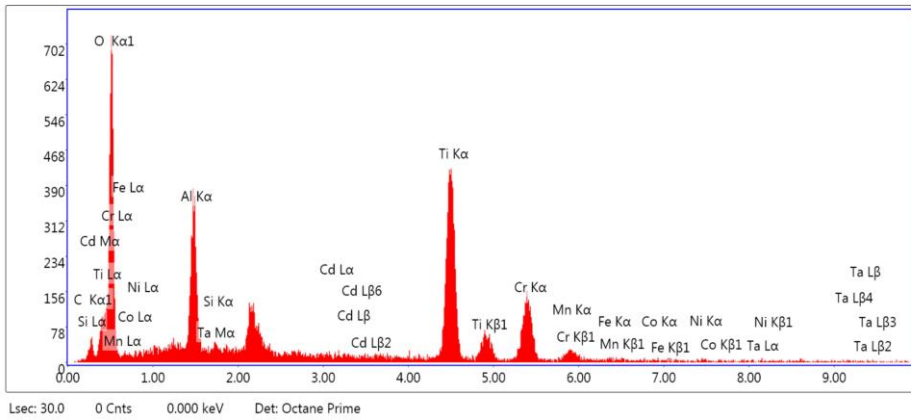
(a) EDS Spot 1, at the recast layer
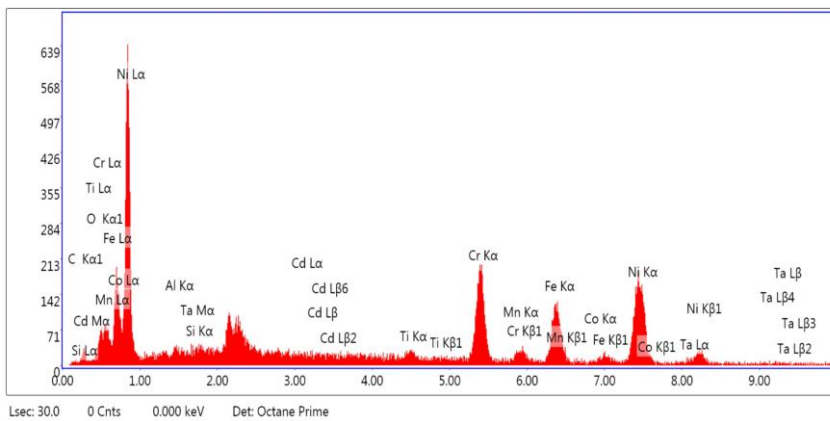
(b) EDS Spot 2, at the heat-affected zone
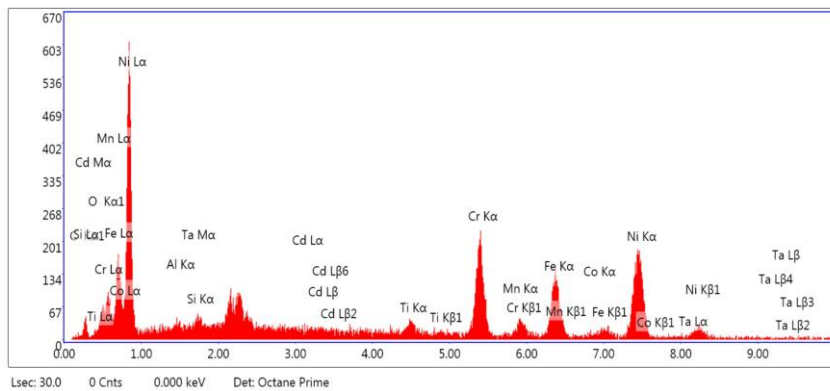
(c) EDS Spot 3, at base metal

Fig. 20. Energy Dispersive Spectrometry (EDS) microanalysis of the machined surface, obtained during Nano-PMEDM machining of Inconel 718 under MWCNT mixed with distilled water dielectric medium for 6th run

To determine the components, present in the three separate zones, three specific spots at the base metal, heat-affected zone, and recast layer were selected (Fig. 19 d). Fig. 20 (a, b, c) shows the EDS analysis image with the particle counts for run 6.

Table 17. Chemical compositions present at the recast layer, heat affected zone, and base metal for runs 6, 7, and 8

Run number	Elements	Recast Layer		Heat Affected Zone		Base Metal	
		Weight %	Atomic %	Weight %	Atomic %	Weight %	Atomic %
6	C K	4.04	8.45	3.83	15.44	4.46	17.68
	O K	37.26	58.54	0.93	2.82	0.79	2.34
	AlK	7.85	7.31	0.16	0.28	0.16	0.28
	TaM	0.14	0.02	0.22	0.06	0.39	0.10
	SiK	0.00	0.00	0.00	0.00	0.00	0.00
	CdL	0.34	0.08	0.31	0.13	0.41	0.17
	TiK	31.58	16.57	1.35	1.37	2.11	2.10
	CrK	17.37	8.40	20.20	18.82	19.81	18.16
	MnK	0.34	0.15	0.52	0.46	0.83	0.72
	FeK	0.54	0.25	18.96	16.44	19.08	16.28
	CoK	0.19	0.08	0.62	0.51	1.66	1.34
	NiK	0.36	0.15	52.90	43.66	50.28	40.81
7	C K	5.05	10.34	4.99	19.40	4.42	17.53
	O K	37.31	57.28	1.03	2.99	0.84	2.51
	AlK	9.35	8.51	0.31	0.54	0.28	0.50
	TaM	0.27	0.04	0.39	0.10	0.58	0.15
	SiK	0.00	0.00	0.00	0.00	0.00	0.00
	CdL	0.43	0.09	0.52	0.21	0.25	0.11
	TiK	34.52	17.70	1.56	1.52	1.58	1.57
	CrK	9.98	4.71	18.95	17.00	19.60	17.97
	MnK	0.82	0.37	1.13	0.96	1.06	0.92
	FeK	0.73	0.32	18.65	15.58	18.26	15.59
	CoK	0.46	0.19	1.44	1.14	1.55	1.25
	NiK	1.08	0.45	51.04	40.56	51.58	41.90
8	C K	9.89	19.42	5.99	22.64	3.63	14.69
	O K	37.49	55.26	1.06	3.01	0.92	2.80
	AlK	3.96	3.46	0.18	0.30	0.54	0.97
	TaM	1.70	0.22	0.64	0.16	0.35	0.09
	SiK	0.00	0.00	0.00	0.00	0.00	0.00
	CdL	0.39	0.08	0.44	0.18	0.42	0.18
	TiK	14.36	7.07	1.20	1.14	2.22	2.25
	CrK	29.17	13.23	18.46	16.12	20.08	18.76
	MnK	0.06	0.03	0.82	0.68	0.69	0.61
	FeK	1.95	0.82	18.19	14.78	17.96	15.63
	CoK	0.08	0.03	1.34	1.03	0.91	0.75
	NiK	0.95	0.38	51.69	39.96	52.27	43.26

The elemental composition of the Inconel alloy after being machined with various parameter settings yields an unexpected result of the atomic and weight percentages as indicated in summary Table 17. Even though Inconel is a nickel-based alloy, there is hardly any trace of Ni in the recast layer (Fig. 20 a). Just 0.36 weight percent and 0.15 atomic percent Ni are discovered at the recast layer for run number 6. Run 7 showed a 1.08 weight percentage and 0.45 atomic percentage of Ni at the recast layer. Likewise, 0.95 weight proportion and 0.38 atomic proportion of Ni are found at the recast layer after run 8.

Nevertheless, Ni is present in the heat-affected zone in the same amount as base metal as observed in all three runs. A similar finding was observed in the case of Fe. However, Ti and O are seen to be present in significant amounts at the recast layer (Fig. 20 a, showing high peaks for Ti and O). It is believed that oxygen atoms that were dissolved in distilled water during the quick cooling action were trapped at the recast layer. Oxygen may also be present as oxides formed during the bombardment process, as indicated earlier. However, the appearance of huge amounts of Ti in the recast layers is an interesting phenomenon. The copper electrode has 0.029% of Ti which might have contributed to the high amount of Ti in the recast layer. However, this phenomenon demands further study to be certain about the abnormally high presence of Ti in the recast layer. The amounts of other elements including Mn, Cr, Co, Cd, Ta, and C were the same as for the base metal. Another important development is that, while peak current and pulse on time for runs 6 and 8 were the same, material removal rate and surface roughness were found to be lower for lower peak current. There was no significantly detectable recast layer when the peak current was decreased. The Ni content increased from 0.15 atomic percent to 0.38 atomic percent and from 0.36 weight percent to 0.95 weight percent. In the area of the body impacted by heat, little cracks are seen. The recast layer thickness and disunity were raised while maintaining a middle-range peak current and increasing pulse on time.

5. Conclusion

The present research was conducted to investigate the influence of EDM parameters, such as peak current, Pulse on Time, and concentration of Nano-powder in distilled water-based dielectric on EDM response parameters – material removal rate (MRR), tool wear rate (TWR) and surface roughness (SR). The experimental investigations were conducted using the Response Surface Methodology approach. The results of the responses were developed in mathematical forms. To attain the best possible response values, RSM and GA response optimizations were employed. The following is a summary of the findings that were derived from the work:

- It was found that Peak Current, Powder Concentration and pulse on Time have a significant impact on surface roughness. A combination of Peak Current (17-20) Amp with Pulse on Time (270-350) µs and Powder Concentration (1.50-2.25) g/L was found to result in lesser SR and an optimum range of MRR and TWR.

- Development of the models of the three responses using the response surface technique and optimizing them using RSM and GA has yielded a valuable procedure for determining optimized process parameters for the Nano PMED Process.

- Maximum Material Removal Rate 0.02336g/min is achieved from 48.5224 Amp peak current, 275 µs pulse on time and 3.25 g/L powder concentration.

- Minimum Surface roughness of 4.361 µm has been found from 15 Amp peak current, 150 µs pulse on time and 5 g/L powder concentration which indicates the higher MWCNT concentration presents better surface finish.

- Minimum tool wear of 0.00085 g/min has been derived from 6.47759 Amp peak current, 275 µs pulse on time and 3.25 g/L powder concentration which is a proof that lowest peak current combined with moderate pulse on timeand powder concentration provides minimum surface roughness.

- The RSM optimization suggests that a Peak Current should be lower (19.925 Amp), Pulse on Time should be close to the maximum limit (307.967 µs), and a

Powder Concentration should be at the lower limit of the range of 1.5 g/L, for optimum of MRR 0.012 g/min, TWR (0.001 g/min) and SR (5.098 μm).

- GA optimum suggested a Peak Current of 20.178 Amp, Pulse On-Time of 398.753 μs, and Powder Concentration of 3.66 g/L for the optimum value of MRR of 0.012 g/min, TWR of 0.003 g/min and SR of 5.229 μm. However, validation tests suggest that GA provides optimized values closer to the experimental values.

- EDS investigation of the machined surface reveals a significant transfer of C and Cu elements. Cu atoms migrate onto the machined surface more readily as a result of tool wear. The amount of carbon at the machined surface is also influenced by the presence of MWCNTs in the dielectric media. Carbon content increases with increasing MWCNT concentration.

References

[1] Gong L, Su Y, Liu Y, Zhao W, Khan AM, Jamil M. Investigation on Machinability Characteristics of Inconel 718 Alloy in Cryogenic Machining Processes. Lubricants. 2023;11(2): 82. https://doi.org/10.3390/lubricants11020082

[2] Vereschaka A, Milovich F, Andreev N, Migranov M, Alexandrov I, Muranov A, et al. Specific Application Features of Ti-TiN-(Ti,Cr,Al)N, Zr-ZrN-(Zr,Mo,Al)N, and ZrHf-(Zr,Hf)N-(Zr,Hf,Cr,Mo,Al)N Multilayered Nanocomposite Coatings in End Milling of the Inconel 718 Nickel-Chromium Alloy. J Compos Sci. 2022; 6(12): 382. https://doi.org/10.3390/jcs6120382

[3] Smak K, Szablewski P, Legutko S, Krawczyk B, Miko E. Investigation of the Influence of Anti-Wear Coatings on the Surface Quality and Dimensional Accuracy during Finish Turning of the Inconel 718 Alloy. Materials (Basel). 2023;16(2) : 715. https://doi.org/10.3390/ma16020715

[4] Zhao C, Zhao Y, Zhao D, Liu Q, Meng J, Cao C, et al. Modeling and Prediction of Water-Jet-Guided Laser Cutting Depth for Inconel 718 Material Using Response Surface Methodology. Micromachines. 2023;14(2) : 234. https://doi.org/10.3390/mi14020234

[5] Sahu SK, Jadam T, Datta S, Nandi G. Effect of using SiC powder-added dielectric media during electro-discharge machining of Inconel 718 superalloys. J Brazilian Soc Mech Sci Eng [Internet]. 2018;40(7):1-19. https://doi.org/10.1007/s40430-018-1257-7

[6] Lepcha LP, Dewan PR, Phipon R. Experimental investigation for surface roughness during electrical discharge machining process of super alloy inconel 718 using silicon powder mixed dielectric. AIP Conf Proc. 2020; 2273. https://doi.org/10.1063/5.0024915

[7] Jawahar M, Sridhar Reddy C, Srinivas C. A review of performance optimization and current research in PMEDM. Mater Today Proc. 2019; 19:742-7. https://doi.org/10.1016/j.matpr.2019.08.122

[8] Jadam T, Sahu SK, Datta S, Masanta M. Powder-mixed electro-discharge machining performance of Inconel 718: effect of concentration of multi-walled carbon nanotube added to the dielectric media. Sadhana - Acad Proc Eng Sci. 2020; 45: 135. https://doi.org/10.1007/s12046-020-01378-2

[9] Abdul-Rani AM, Nanimina AM, Ginta TL, Rao TVVLN, Pedapati SR. Application of nano aluminum in modified EDM: pmedm. ARPN J Eng Appl Sci. 2016;11(20):12117-21.

[10] Ahmad S, Lajis MA, Haq RHA, Arifin AMT, Rahman MNA, Haw HF, et al. Surface roughness and surface topography of Inconel 718 in powder mixed dielectric electrical discharge machining (PMEDM). Int J Integr Eng. 2018;10(5):181-6. https://doi.org/10.30880/ijie.2018.10.05.027

[11] Deltombe R, Kubiak KJ, Bigerelle M. How to select the most relevant 3D roughness parameters of a surface. Scanning. 2014;36(1):150-60. https://doi.org/10.1002/sca.21113

[12] Kabir H, Garg N. Rapid Prediction of Cementitious Initial Sorptivity via Surface Wettability. npj Mater Degrad. 2023; 7: 52. https://doi.org/10.1038/s41529-023-00371-4

[13] Kumar A, Vivekananda K, Abhishek K. Experimental Investigation and Optimization of Process Parameter for Inconel 718 Using Wire Electrical Discharge Machining. J Adv Manuf Syst. 2019;18(3):339-62. https://doi.org/10.1142/S0219686719500185

[14] Assarzadeh S, Ghoreishi M. A dual response surface-desirability approach to process modeling and optimization of Al2O3 powder-mixed electrical discharge machining (PMEDM) parameters. Int J Adv Manuf Technol. 2013;64(9-12):1459-77. https://doi.org/10.1007/s00170-012-4115-2

[15] Anand A, Behera AK, Das SR. An overview on economic machining of hardened steels by hard turning and its process variables. Manuf Rev. 2019;6(4):1-9. https://doi.org/10.1051/mfreview/2019002

[16] Wang J, Sun Z, Dai Y, Ma S. Parametric optimization design for supercritical CO2 power cycle using genetic algorithm and artificial neural network. Appl Energy [Internet]. 2010;87(4):1317-24. https://doi.org/10.1016/j.apenergy.2009.07.017

[17] Stergioudi F, Prospathopoulos A, Farazas A, Tsirogiannis EC, Michailidis N. Mechanical Properties of AA2024 Aluminum/MWCNTs Nanocomposites Produced Using Different Powder Metallurgy Methods. Metals (Basel). 2022;12(8) : 1315. https://doi.org/10.3390/met12081315

[18] Sahu SK, Jadam T, Datta S. Performance of dielectric media (conventional EDM oil and distilled water) during machining of Inconel 825 super alloy. Mater Today Proc [Internet]. 2019;18:2679-87. https://doi.org/10.1016/j.matpr.2019.07.129

[19] Audet C, Hare W. Genetic Algorithms. Springer Ser Oper Res Financ Eng. 2017;57-73. https://doi.org/10.1007/978-3-319-68913-5_4

Research Article

Characterization and predictive modeling of thermally aged glass fiber reinforced plastic composites

Md Mijanur Rahman[*1,a], M Muzibur Rahman[2,b]

[1]Department of Mechanical and Aerospace Engineering, Oklahoma State University, U.S.A
[2]Department of Mechanical Engineering, Sonargaon University, Bangladesh

Article Info	Abstract
	Glass fiber reinforced plastics (GFRP) are exposed to thermal aging in their widespread aerospace applications. Evaluating the effect of mechanical properties due to thermal aging has remained a challenge. An experimental investigation to characterize the thermal aging effects of glass fiber epoxy composites as well as the development of a predictive modeling is presented here. Tensile test samples have been thermally aged at 50°C, 100°C, 150°C and 200°C for 30 mins, 60 mins, 90 mins and 120 mins. At higher temperatures, the samples have shown a gradually increasing brown color while emitting a burning smell. The tensile test shows that the UTS value decreases as the thermal aging temperature increases. The predictive model has been prepared by combining image processing, regression analysis and two cascaded artificial neural networks (ANNs). The model reads the photographic image of the sample and uses the color change as an identifier. Cascaded ANNs estimate the thermal aging temperature and time from the image processing program. Finally, the ANN's output is forwarded to the developed regression equation to get the estimated UTS. The predictive model's estimated UTS shows an average accuracy of 97% when compared to the experimental results.

1. Introduction

Glass fiber-reinforced plastic (GFRP) composites have seen widespread applications in the Aerospace industry [1]. In aerospace applications, GFRP composites are subjected to thermal aging at elevated temperatures, especially in UAV operations, aircraft fuselage panels, aircraft wingtips, control surfaces, bleed air ducts and inlet fan blade casing [2]. In these aerospace components, the mechanical properties of GFRP is very important to ensure safe operation during flight. The mechanical behavior of a fiber-reinforced composite basically depends on the fiber strength and modulus, the chemical stability, matrix strength and the interface bonding between the fiber/matrix to enable stress transfer [3]. Scientists and engineers are well aware of the properties of fiber reinforced polymers, but there are still a lot of questions concerning their durability and performance under harsh environmental conditions.[4].

A considerable amount of literature has been published regarding the thermal aging of GFRPs and its influence on mechanical properties. Bazli et al. [5] investigated the behavior of unidirectional, woven and chopped strand GFRP laminates subjected to impact and flexure loads at extreme temperatures. According to the findings, GFRP laminates' flexural and impact capabilities generally deteriorate as exposure time and temperature rise, and as laminate thickness decreases. Kun et al. [6] developed an epoxy glass fiber composite and performed wet and heat cycle aging tests. They found that the composites' mechanical

and dielectric properties deteriorated over time. Zuo et al. [7] performed an experiment in which the isothermal and non-isothermal crystallization behaviors of glass fiber-reinforced polyphenylene sulfide were rigorously investigated and a broad variety of widely used models were applied to this material. It was discovered that the polymer crystallizes more slowly during crystallization when it has undergone extreme age and degeneration. According to Birger et al. [8], thermal aging influences the mechanical characteristics and failure processes of graphite-fabric epoxy composites exposed to flexural stress. The authors thermally aged the samples at 170 °C for 120, 240, and 626 hours. For the longest exposure period, bare fibers were detectable due to the weakening of the fiber-matrix interface, and as thermal aging progresses, fracture transforms from ductile with more plastic deformations to brittle. Mouritz et al. [9] investigated the post-fire residual flexure strength of glass, carbon, and Kevlar-reinforced polyester, epoxy, and phenolic-based laminates. They discovered that even a little amount of fire damage resulted in a significant decrease in strength qualities, and the model used to forecast the strength properties showed a strong connection with the experimental data. Dodds et al. [10] subjected the epoxy, phenolic, and polyester GFRP panels to a high-temperature fire and compared the behavior using thermal modeling. Phenolic-based GFRP laminates were shown to be more susceptible to delamination. In addition, the thickness of the composites had a significant effect in their fire resistance.

Several researchers have also noted the color changes due to thermal aging. Zhenbo Lan et al. [11] studied the color changes and mechanical properties of glass fiber-reinforced polycarbonate (GF-PC) composites after aging at various temperatures. The experiment revealed that the brightness of the GF-PC composite is related to trends detected in their tensile strength and bending strength. Song et al. [12] investigated the impact of thermal aging on the mechanical properties of glass-reinforced PEI plate composites. They found that as the aging temperature increased from 80 to 145 C, both the tensile and flexural strengths of the GF/PEI composite samples dropped, which was also reflected in their color difference.

The glass transition temperature (Tg) is an important consideration for the thermal aging study of all FRPs. As such, several researchers have studied the effect of thermal aging at temperatures near Tg. In a study relevant to ours, Zavatta et al. [13] conducted research to determine how the strength of carbon fabric/epoxy composites changed as a result of thermal aging in air. For aging at temperatures below the glass transition temperature (Tg) of the resin, a considerable decline in strength was observed. In contrast, a fast drop in strength was found at aging temperatures exceeding Tg. Furthermore, it was determined that even brief exposure to operating temperatures over Tg might significantly reduce the load-bearing capacity of CFRP components.

For developing predictive models, researchers have also experimented with using various techniques. Gibson et al. [14] studied the raised temperature effect on the mechanical properties of woven glass fiber/polypropylene composites and suggested a 3-parameter model to define the tensile behavior and a 2-parameter model to define the compressive behavior to analyze the effects. Kim et al.[15] experimented with multiple regression analysis (MRA) and polynomial regression analysis (PRA) and ANNs, to analyze the factors affecting the tensile strength of basalt and glass fiber-reinforced polymers (FRPs). They found that ANNs could be the most efficient model for forecasting the durability of FRPs. Gayatri Vineela et al. [16] performed an experiment in which the ultimate tensile strength of hybrid short fiber composites comprised of glass fiber, carbon fiber, and epoxy resin is predicted using artificial neural network approaches. It was discovered that ANN can predict the values of tensile strength more precisely than the regression model. Mishra et al. [17] conducted an experiment to demonstrate a MATLAB-based artificial neural network (ANN)-based approach for forecasting the deflection behavior of three kinds of

beams: plain, steel-reinforced, and bamboo-reinforced beams. The findings demonstrate that the ANN is a potent and trustworthy technique for evaluating the deflection behavior of concrete beams under the studied loading circumstances. Doblies et al. [18] have developed a model to predict the mechanical properties, as well as the thermal exposure time and temperature of epoxy resin, using Fourier-transform infrared spectroscopy (FTIR)-spectroscopy, data processing, and artificial neural networks. Turco et al. [19] developed two Artificial Neural Networks (ANNs) in order to forecast the compressive (ANN1) and tensile (ANN2) strengths of natural fiber-reinforced CEBs. The correlation coefficients (R-values) for ANN1 and ANN2 were 0.97 and 0.91, respectively, demonstrating the great accuracy of their generated tools.

Summarizing the literature survey shows that, there is significant literature on the mechanical property testing of thermally aged GFRP. Also, several predictive models using multi-parameter models, regression and ANN techniques have been developed with good accuracy. It is evident that on a macroscopic level, the physical and chemical mechanisms causing a change in GFRP properties are well understood. However, the mechanical property values reported by different researchers remain in a large scatter for thermally aged GFRP. The precise physical micro-phenomena and chemical reactions, as well as how they interact, are still being researched. Again, most of the predictive models in the literature depend on testing the material and predicting the output value based on the test input parameters. This is a time-consuming process that involves disassembly, sample preparation and destructive testing. It costs a lot of money for applications in aerospace, automobile, marine and similar industries. As such, a computational method to estimate the mechanical properties of thermally aged GFRP would be very beneficial for a highly competitive and operational industry like Aerospace. However, determining the current material state and retracing the mechanical and thermal histories continue to be difficult tasks [18]. Hence, there is a research gap in further mechanical property testing of thermally aged GFRP due to the variations in results reported by researchers. Moreover, a computational method to estimate the mechanical properties of thermally aged GFRP remains largely unaddressed.

This research focuses on the characterization of mechanical properties of thermally aged glass fiber epoxy composite below and beyond the glass transition temperature (Tg). Also, a novel predictive model was developed for estimating the mechanical properties of thermally aged glass fiber reinforced plastic (GFRP) composites. The predictive model developed in this research and its exact design is completely novel and it has not been studied yet by researchers as per the literature review and best knowledge of the author. This model has the potential to save time and money by avoiding disassembly, sample preparation and destructive testing of GFRP components especially in aerospace line maintenance applications.

2. Materials and Methods

2.1. Materials Used

Commercially available high silica (SiO2 ≥ 96%) woven Glass fiber cloth of 1100 grams per square meter (GSM) weight was selected as the reinforcing element for preparing the GFRP composite material. This glass fiber cloth was purchased from Jiangnan Company and originated in Jiangsu, China. The glass fiber fabric has a thickness of 1.2 mm and a thread count of 15 for WEFT and 20 for WARP. The tensile of the woven glass fiber cloth is 86.95 MPa as per the manufacturer's specification. To create one composite slab, two layers of glass fibers were sliced into 325mm x 325mm squares. As the matrix material, Araldite AW 106 IN epoxy resin and HV 953 U hardener were used. According to the manufacturer's recommendations, a 100:80 weight ratio of resin and hardener was utilized. The viscosity

(cP) at 25°C is 50000 and 35000, respectively, while the specific gravities of the hardener and resin are 1.17 and 0.92, respectively.

As this study involves thermal aging, the elevated temperature properties of the reinforcement and the matrix were very important considerations. The glass fiber cloth can reportedly withstand operating temperatures of up to 1100°C and has a melting point of 1700°C, according to the manufacturer. The glass transition temperature (Tg) of the resin-hardener is 63°C. The Glass Transition Temperature (Tg) is one of the most important properties of any epoxy and is the temperature region where the polymer transitions from hard, glassy material to a soft, rubbery material. It is the temperature of interest for our study as our selected thermal aging temperature ranges below (50°C) and beyond (100°C, 150°C and 200°C) this temperature.

2.2. Methodology

The methodology used for this study involved 10 interrelated steps. The first 5 steps were part of the experimental work which dealt with fabrication and characterization of the GFRP. The other 5 steps were part of the computational work which dealt with predictive modeling. The step-by-step graphical methodology is shown in Figure 1 as follows.
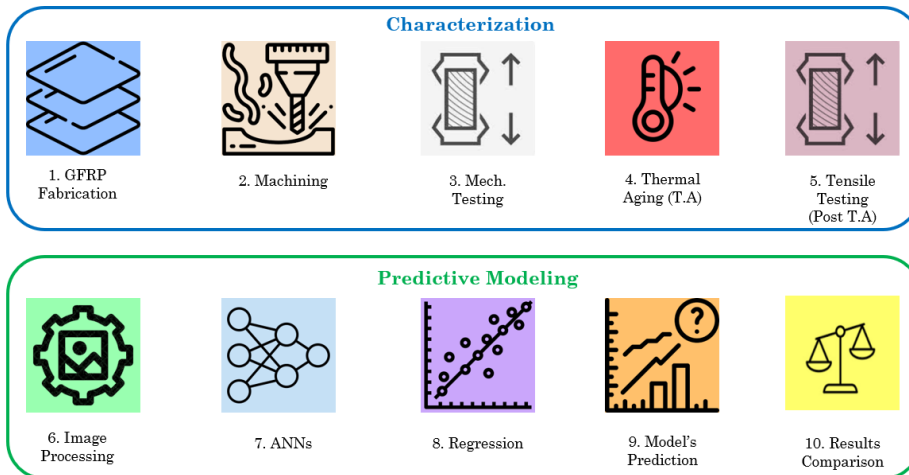
Fig. 1. Graphical methodology of this research

The details of the 10-step methodology are as follows:

- GFRP Composites were fabricated using woven and random glass fibers by hand-layup method.
- Samples for mechanical testing were prepared as per ASTM standards by mechanical cutting and laser cutting.
- These unaged samples underwent tensile test, flexural test, microhardness test and SEM imaging to find the effect of fiber orientation and machining on the mechanical properties.
- Tensile test Samples were thermally aged at different temperatures and times. Their distinct color changes at elevated temperatures were identified and photographed.
- Thermally aged Samples were mechanically tested as per ASTM standards and results including Ultimate Tensile Strength (UTS), Yield Strength, Maximum Strain, Elastic Modulus and Tangent Modulus were recorded.

- An image processing algorithm identified the color changes of the thermally aged samples (from the photos taken in step iv) and gave the most consistent Red, Green and Blue (RGB) color values as the output.
- Two ANNs were trained which took input of the RGB values and predicted the thermal aging variables (aging temperature and time) the samples underwent.
- A regression analysis was performed to correlate UTS and thermal aging variables (aging temperature and time).
- The ANN-predicted aging temperature and time were used to predict the UTS value using the regression equation developed in step viii. This was the final output of the predictive model.
- UTS from the experimental result (step v) and estimations of the predictive model (step ix) were analyzed and compared.

3. Experimental Work

3.1 Fabrication of GFRP Samples

The GFRP composite material was fabricated using the hand layup technique. A plywood mold with the dimensions of 325 mm × 325 mm x 10 mm was employed. A clear plastic release sheet was positioned at the bottom and coated with wax to make the removal procedure easier after production. To prevent air entrapment, the resin-hardener mixture was first placed in one layer and spread uniformly with a spatula. Then, one layer of the resin-hardener combination was put between two layers of glass fiber. The topmost layer was then filled with the resin-hardener combination and protected by a transparent plastic release film. Using a roller, gentle pressure was applied above the release film to release any trapped air. As soon as the topmost layer of resin-hardener was placed, the joint parts were clamped. The composite was then allowed to cure for 12 hours at room temperature under the weight of a 17 kg plywood sheet. The constructed composite slab had a 3mm thickness.
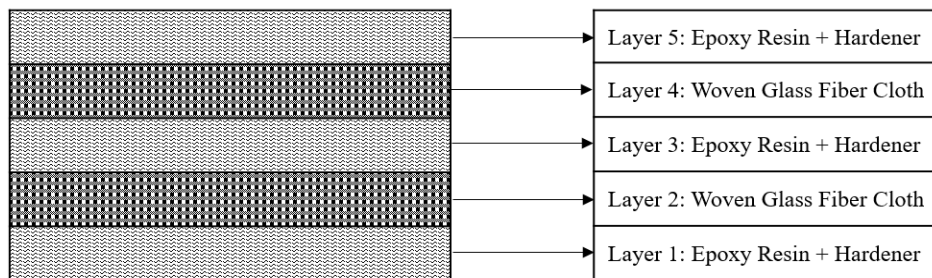
Fig 2. Arrangement of layers in fabricated GFRP composite
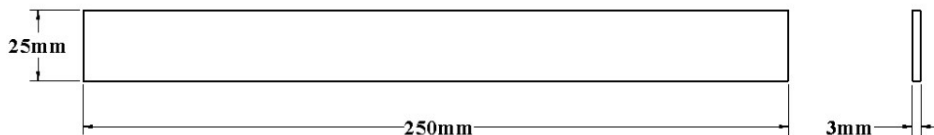
Fig 3. Solidworks drawing of tensile test sample

The configuration of the matrix and reinforcing layers of the manufactured glass fiber composite is depicted in Figure 2. Table 1 lists the components of the prepared composite

sample. The 325 mm × 325 mm x 3 mm composite slabs were mechanically cut and samples for mechanical testing were prepared. Bosch GWS 900-100 professional angle grinder with TJWELD 1.2 mm thickness cutting wheel was used to cut the samples. For tensile testing, samples were prepared as per ASTM D3039 standard. A total of 51 samples were prepared. The dimensions of the sample are shown in figure 3.

Table 1. Composition of the prepared composite sample

Material	Weight (gm)	Weight (%)
Glass Fiber Cloth	206	45
Epoxy Resin	138	30
Hardener	111	25
Total	456	100

3.2 Thermal Aging

Temperature and time were the two variables selected for the thermal aging of the samples. For thermal aging, specific temperatures and aging times were chosen considering the literature review and Tg of the epoxy. The selected thermal aging temperatures were 50°C, 100°C, 150°C and 200°C while the thermal aging time were 30 mins, 60 mins, 90 mins and 120 mins. The range of temperatures and aging time was selected based on the expected thermal conditions in Aerospace applications. Such temperatures and exposure times are frequently encountered in case of UAV operations and Air-conditioning bleed ducts of commercial aircraft.

Table 2. Sample group numbers and associated thermal aging variables

Sample group number (SGN)	Aging temperature	Aging time	Number of samples in the group
1	Unaged	Unaged	3
2	50°C	30 mins	3
3	50°C	60 mins	3
4	50°C	90 mins	3
5	50°C	120 mins	3
6	100°C	30 mins	3
7	100°C	60 mins	3
8	100°C	90 mins	3
9	100°C	120 mins	3
10	150°C	30 mins	3
11	150°C	60 mins	3
12	150°C	90 mins	3
13	150°C	120 mins	3
14	200°C	30 mins	3
15	200°C	60 mins	3
16	200°C	90 mins	3
17	200°C	120 mins	3
Total number of samples			51

Tensile testing samples were thermally aged in Carbolite Gero CWF 13/13 furnace. As per the manufacturer's specifications, this furnace can reach the maximum temperature of 1300°C in 121 minutes with a maximum continuous operating temperature of 1200°C. For each one of the thermal aging temperatures, samples were aged at all the above aging times. As such total 16 combinations of thermal aging were performed in the ovens. With the addition of the unaged samples, the total number of combinations was 17. These 17 combinations are labeled as sample group numbers (SGN). Each of the sample groups had

3 samples making a total of 51 samples for 17 groups. The sample group numbers (SGN) and associated thermal aging variables are shown in table 2.

3.3 Tensile Test

In a tensile test, a sample is subjected to controlled tension till it reaches failure. The tensile test was done as per ASTM D3039 standard. The tensile test is performed in the universal testing machine (UTM) PLS100 with a crosshead speed of 5mm/min. The flat samples are fixed between the grips of each head of the testing machine. To have a better grip on the grips of the tensile testing machine, end tabs are provided at both ends of the samples. The grip is set up in such a way that the direction of force applied to the sample is coincident with the longitudinal axis of the sample.

The Tensile test was performed for a total of 51 samples from 17 SGNs with 3 samples in each SGN. At first, 03 thermally unaged samples underwent tensile testing. From the tensile test data, max strain (%), UTS (MPa), yield strength (MPa), elastic modulus (MPa) and tangent modulus (MPa) were calculated. Afterward, 48 thermally aged samples underwent tensile testing. The average values of the 3 samples in each group were considered for the respective group. Finally, a total of 17 sets of tensile test data was obtained including UTS, Max Strain and Yield Strength. The tensile test dataset with thermal aging variables and corresponding mechanical properties is shown in table 3.

Table 3. Tensile test dataset with thermal aging variables and corresponding mechanical properties

SGN	Temperature (°C)	Time (mins)	UTS (MPa)	Max Strain (%)	Yield Strength (MPa)
1	Unaged	Unaged	85.6	6.34	25.60
2	50	30	79.33	5.52	23.83
3	50	60	71.33	5.74	20.50
4	50	90	70.00	6.30	21.47
5	50	120	72.33	5.71	21.54
6	100	30	64.00	5.64	19.33
7	100	60	58.00	5.39	17.65
8	100	90	69.00	5.59	20.67
9	100	120	61.00	4.83	18.53
10	150	30	70.33	4.37	17.00
11	150	60	56.33	4.22	17.00
12	150	90	80.67	5.02	19.00
13	150	120	62.50	5.08	19.00
14	200	30	47.00	3.71	11.90
15	200	60	63.33	4.41	18.50
16	200	90	64.67	4.06	18.50
17	200	120	58.33	3.99	17.67

4. Predictive Model

This model uses image processing, regression analysis and cascaded artificial neural networks (ANN) which were developed earlier to predict the Ultimate Tensile Strength (UTS) value with a photographic image of the sample. The model can also be customized to predict any mechanical properties with visually distinguishable identifiers dependent on thermal aging.

This model uses the color changes due to thermal aging from the photographic image as an identifier. This identifier allows it to estimate the UTS value without destructive testing. Firstly, the Image processing program reads the photographic image of the thermally aged samples and calculates the RGB color values. Two cascaded ANNs are used to estimate the thermal aging variables from the RGB color values. ANNs are used because this estimation follows a data-driven approach rather than a mathematical formulation. It involves several variables like the lighting conditions of the photo, image noise and sample precleaning which can impact the data accuracy of RGB values. With such scattered data, ANNs are found to be useful. However, the larger the dataset, the better. The regression analysis develops a mathematical equation to estimate the UTS values from the thermal aging temperature and time. This dataset in table 3 from the experimental work is used for the regression analysis. To aid the visualization of data flow between the experimental work and the predictive model, a graphical methodology has been prepared and show in Figure 4.
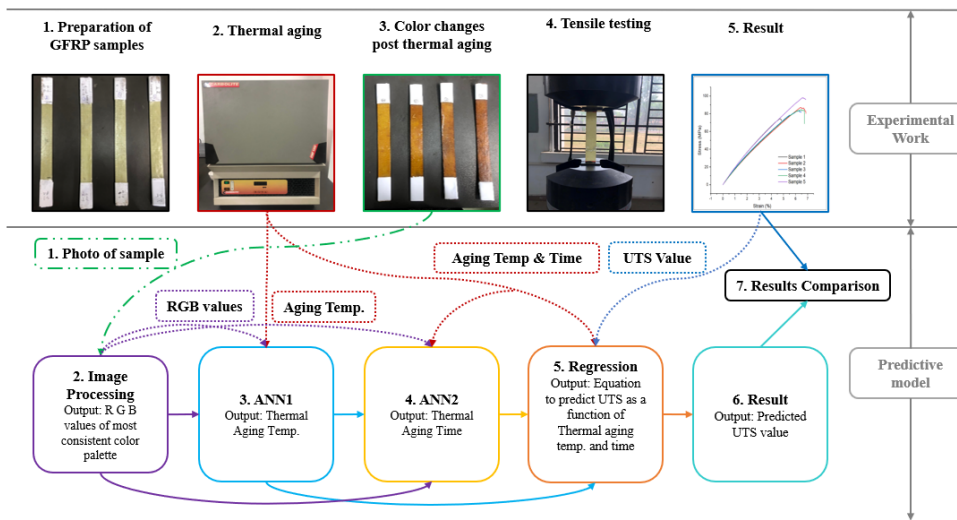
Fig. 4. Graphical methodology of the predictive model

The upper half of the figure shows the experimental work. The work process has been shown in 5 sequential steps starting from preparation of GFRP sample, thermal aging in the oven, color changes post thermal aging, tensile testing and results. Step no 2, 3 and 5 has been shown in red, green and blue color respectively. This is done to better distinguish the flow of data from these steps to the predictive model.

The lower half shows the predictive model. There are 7 sequential steps starting from the photo of the sample, image processing, ANN1, ANN2, regression, result and results comparison. 3 types of lines have been shown in the graphical methodology. Continuous lines indicate the operational phase of the predictive model. Dotted lines indicate the training phase of the predictive model. Step 1 is common for both the operational and training phase of the model. It is indicated by 'long dash dot dot' line.

4.1 Image Processing

After the thermal aging was done, it was noted that the samples were undergoing a color change at 150°C and 200°C. This started at 150°C with a very slight shade of brown color

which became more apparent at 200°C. Also, as the aging time increased, the shade of brown color became progressively darker. As such, this change of color could be used as an identifier to predict the thermal aging variables i.e., temperature and time.

To meet this purpose, A MATLAB image processing program was developed which can read and identify the color changes of the samples. SGN 10-17 were exposed to thermal aging at 150°C and 200°C. The photos of these SGN 10-17 were uploaded to the MATLAB program. To minimize the issues of lighting conditions, image noise and sample precleaning, all the samples were photographed in controlled environment with the same camera and lighting conditions. The program performed calculations and gave the most consistent value of the Red, Green and Blue color (RGB) values in a matrix form for each of the samples. The code was optimized in such a way that even if there was some slight variation of color throughout different areas of the sample, the code was able to figure out the most consistent value. The MATLAB pseudocode for the image processing algorithm is shown in Figure 5.

Step 1: Read the uploaded photo of the sample.

Step 2: Seperate the Red, Green and Blue color values for every pixel of the image in seperate matrices.

Step 3: Calculate the most consistent values of Red Green and Blue color value among all the pixels within each matrix.

Step 4: Export the results to an excel file.
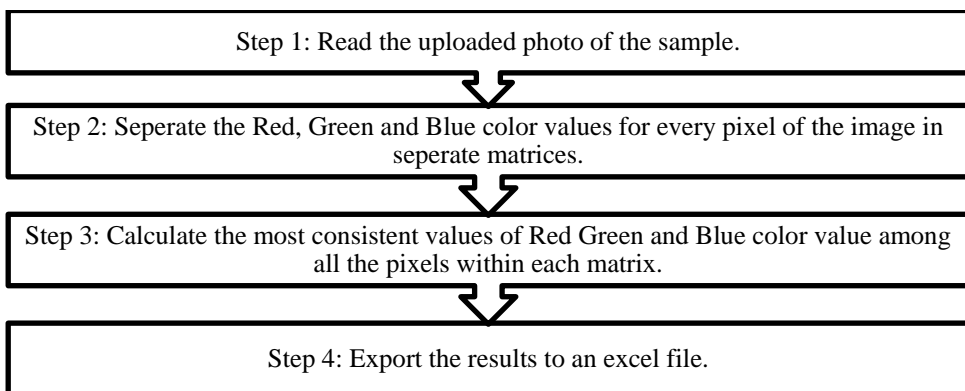
Fig. 5. MATLAB pseudocode of the image processing algorithm.

4.2 Artificial Neural Networks

Artificial Neural Networks (ANN) is a biologically-inspired computational method. It is one of many Artificial Intelligence algorithms and techniques. The ANN technique is based on a group of interconnected units or nodes called artificial neurons. The architecture of ANN consists of an input layer, one or several hidden layers and an output layer. As their name suggests, the input layer provides the input parameters to the ANN and the output layer provides the desired output. The calculations are performed by the hidden layers by means of weights and biases. The overall structure loosely models the neurons in a biological brain.

Using MATLAB, two ANNs are used in series to predict the thermal aging temperature and time. ANN1 takes 3 inputs as the RGB values and outputs the thermal aging temperature x_1. ANN2 takes 4 inputs including the same 3 previous RGB values and the output of the first ANN, x_1. The output of the second ANN is the thermal aging time x_2. Both ANNs consist of two layers including one hidden layer and one output layer. The hidden layer has 10 neurons and the output layer has 1 neuron. The transfer function of the hidden layer is chosen as tansigmoid while the transfer function of the output layer is chosen as purelin. Figure 6 shows the architecture of the two ANNs.

(a)

(b)
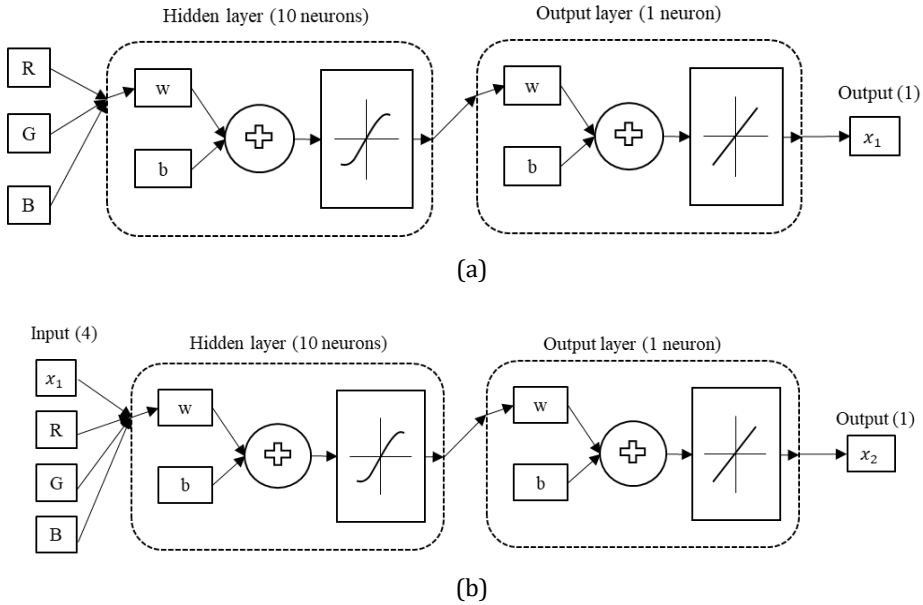
Fig. 6. The architecture of the two ANNs: (a) ANN1 (b) ANN2

Total 24 sets of thermal aging data were used for the training and testing of the two ANNs. Among the 24 sets, 19 set were used for the training and the remaining 5 sets were used for testing. Table 4 and Table 5 show the 19 sets of training data for ANN1 and ANN2 respectively.

Table 4. Training data for ANN1

Dataset No	Input (3)			Output (1)
	R	G	B	Aging Temp (x_1)
1	134	116	65	150
2	132	116	65	150
3	158	137	76	150
4	154	135	74	150
5	147	128	76	150
9	154	135	76	150
7	130	112	60	150
8	162	142	82	150
9	153	133	68	150
10	144	92	21	200
11	137	85	19	200
12	133	73	16	200
13	128	75	16	200
14	123	63	11	200
15	91	44	18	200
16	109	51	14	200
17	89	37	16	200
18	99	41	21	200
19	92	35	14	200

Table 5. Training data for ANN2

Dataset No	Input (4)				Output (1)
	R	G	B	Temp (x_1)	Aging Time (x_2)
1	134	116	65	150	30
2	132	116	65	150	30
3	158	137	76	150	60
4	154	135	74	150	60
5	147	128	76	150	90
9	154	135	76	150	90
7	130	112	60	150	90
8	162	142	82	150	120
9	153	133	68	150	120
10	144	92	21	200	30
11	137	85	19	200	30
12	133	73	16	200	60
13	128	75	16	200	60
14	123	63	11	200	60
15	91	44	18	200	90
16	109	51	14	200	90
17	89	37	16	200	90
18	99	41	21	200	120
19	92	35	14	200	120

The training performance of ANN1 and ANN2 are shown in figure 7 and figure 8 respectively.
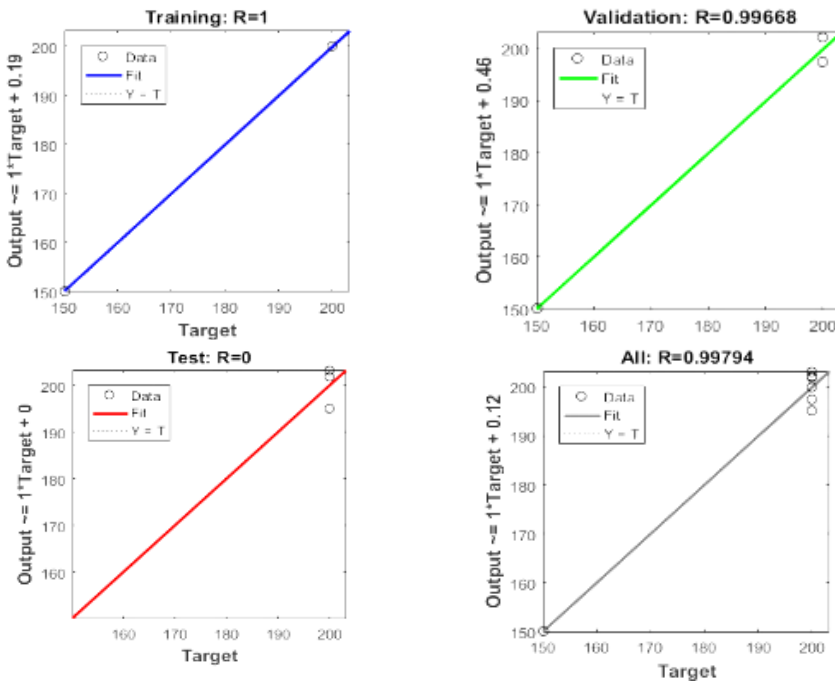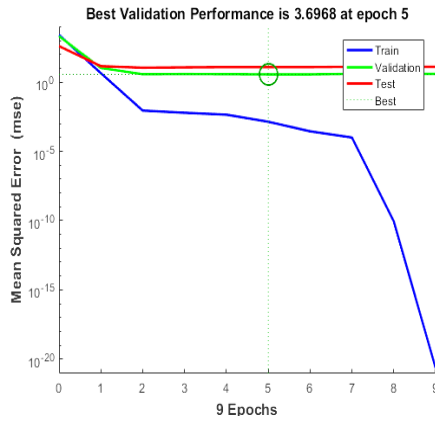
Fig. 7. Training performance of ANN1
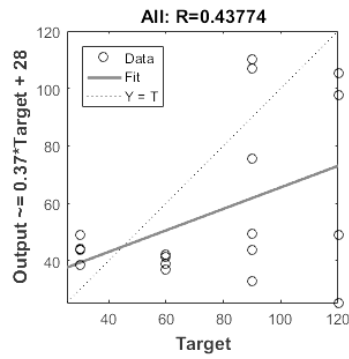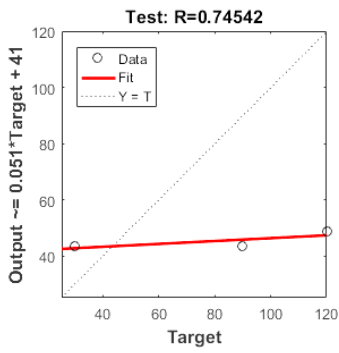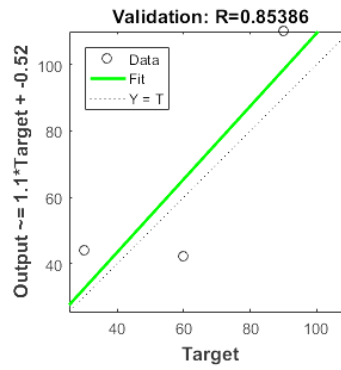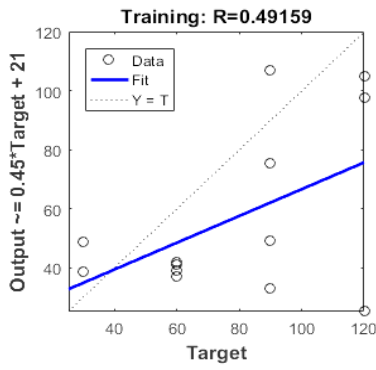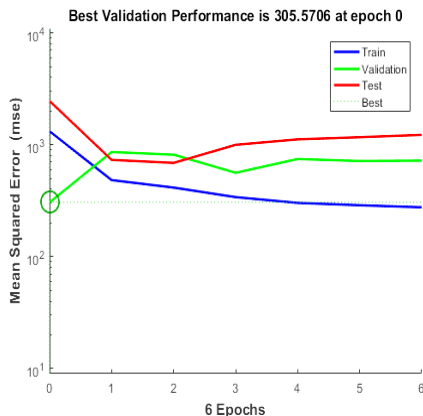
Fig 8. Training performance of ANN2

After the training of the ANNs are complete, they are tested with 5 sets of data. Table 6 and table 7 show the testing data for ANN1 and ANN2 respectively.

Table 6. Testing data for ANN1

| Dataset No | Input (3) | | | Output (1) |
	R	G	B	Temp (x_1)
1	149	130	68	150
2	149	131	70	150
3	142	121	59	150
4	130	76	17	200
5	98	34	10	200

Table 7. Testing data for ANN2

| Dataset No | Input (4) | | | | Output (1) |
	R	G	B	Temp (x_1)	Aging Time (x_2)
1	149	130	68	150	30
2	149	131	70	150	60
3	142	121	59	150	120
4	130	76	17	200	30
5	98	34	10	200	120

4.3 Regression Analysis for UTS and Max Strain

A multi-regression analysis was performed in Minitab software. The regression analysis developed an equation to estimate the UTS values from the thermal aging variables. The thermal aging temperature and time were considered as the two independent variables. UTS was the dependent variable. The two cascaded ANNs estimated the thermal aging temperature and time, which were given as input to the developed regression equation.

The tensile testing dataset of SGN 1-17 shown in Table 3 was used to perform the regression. Figure 9 shows the regression model and its various parameters.
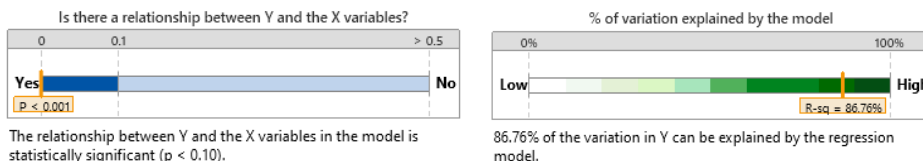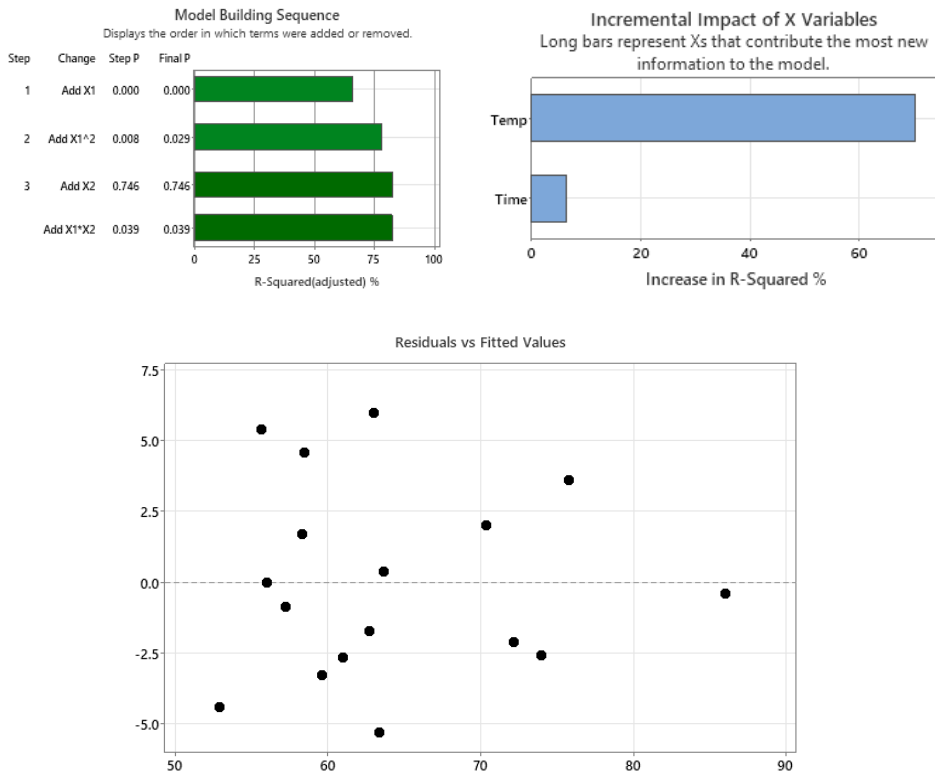
Fig. 9. The regression model and its various parameters

From the above figures, it is observed that the p-value of the regression model was less than 0.10 which indicates a strong relationship between the y and x variables. The R^2 value was 86.76% which means that 86.76% of the variation in y can be explained by the regression model. The R^2 adjusted value was found as 82.351% which indicates that most of the variables were useful in terms of generating the model. The incremental impact of x variables indicated that aging temperature had a 70.3987% impact on increasing R^2 value compared to only 6.57032% for aging time. Also, there were no residual values nor any strong curvature or clusters which would have indicated problems with the regression model. All the data points fall randomly on both sides of zero indicating a good fit.

The regression analysis found the relationship for UTS as:

$$y = 95.63 - 0.4070 \times x_1 - 0.1099 \times x_2 + 0.000900 \times x_1^2 + 0.000998 \times x_1 \times x_2 \tag{1}$$

Where, y = UTS (MPa), x_1 = Thermal aging temperature (°C) and x_2 = Thermal aging time (mins).

5. Results and Discussion

Results from the experimental work were analyzed to obtain insights about the mechanical properties of the GFRP. Also, the data from the experimental work was used to develop the predictive model. The following subsections describe the results and discussion of the experimental work and predictive model separately.

5.1. Experimental Work

Results and discussion of the experimental work are presented in this section. It is further divided into three subsections namely; Tensile Test of Unaged Samples, Thermal Aging and Tensile Test of Thermally Aged Samples.

5.1.1. Tensile Test of Unaged Samples

GFRP composites were fabricated and tensile testing samples were prepared as per ASTM D3039 standard. Figure 10 shows the mechanical properties of thermally aged GFRP samples.
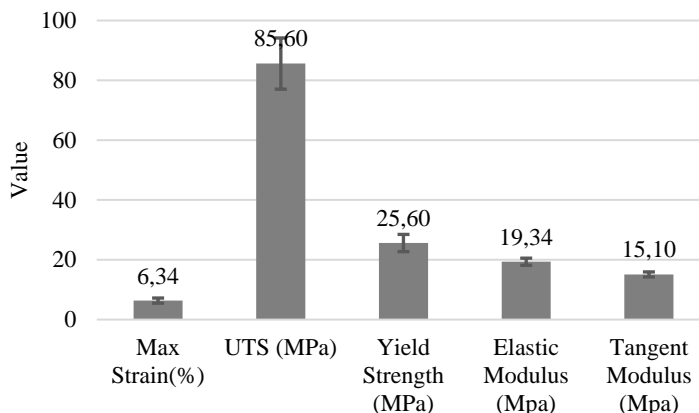
Fig. 10. Mechanical properties of thermally aged GFRP samples

From the figure, it is found that tensile testing of thermally unaged samples revealed mechanical properties UTS 85.60 MPa, Max Strain 6.34%, Yield Strength 25.60 MPa, Elastic Modulus 19.34 MPa and Tangent Modulus 15.10 MPa. It is to be noted that the UTS value of 85.60 MPa found by the tensile test is very close the UTS value of 86.95 MPa reported by the manufacturer of the glass fibers. Hence, it is apparent that during the tensile test, the glass fibers were the ultimate load-bearing member upon which the tensile strength of the GFRP was dependent.

5.1.2. Thermal Aging

During the thermal aging process at 100°C (SGN 6,7,8 and 9), very mild smoke and a burning smell were noticed. This smoke and smell effect became more noticeable at 150°C (SGN 10,11,12 and 13). At 200°C (SGN 14,15,16 and 17) the smoke and burning smell were clearly noticeable. This was expected as the glass transition temperature (Tg) of the epoxy is 63°C.

Also, at 150°C (SGN 10,11,12 and 13), the tensile test samples started to show color changes with the introduction of very slight shades of brown. At 200°C (SGN 14,15,16 and 17) this color change effect became apparent. In SGN 14, the color was light brown. As the thermal aging time increased, the brown color became progressively darker in SGN 15, 16 and 17. The color change effect due to thermal aging is shown in figure 11.

2, 3, 4 and 5 (SGN, Left to Right)   6, 7, 8 and 9 (SGN, Left to Right)
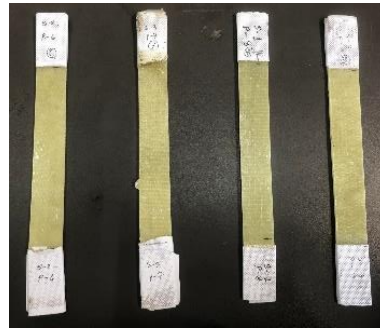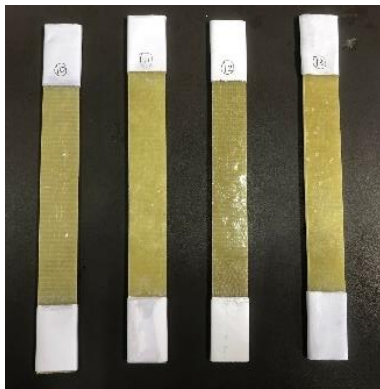
10, 11, 12 and 13 (SGN, Left to Right)   14, 15, 16 and 17 (SGN, Left to Right)
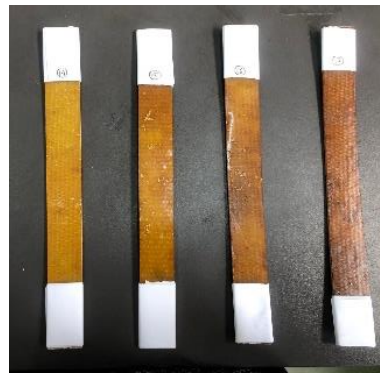
Fig 11. Color change effect due to thermal aging

The burning smell and color changes are mainly related to the oxidation process. Most notably; the carbonyl formation in the epoxy backbone due to thermo-oxidation is the cause for the color change of the material [20]. These findings agree with the existing literature. According to the literature, a higher temperature and longer exposure time typically result in a darker color. [12]. Although, the details are not fully understood yet [20], [21].

5.1.3. Tensile Test of Thermally Aged Samples.

In the present work, Ultimate Tensile Strength (UTS) is the mechanical property of interest. As such, it is analyzed with much deliberation. Figure 12 shows the change in UTS due to thermal aging. The Figure is divided into 5 separate graphs to aid the visualization of the thermal aging effect due to a fixed temperature and increasing aging time. Finally, graph 12 (e) shows the effect with all sample group numbers sequentially. The black bar in this graph represents the UTS value for unaged samples.
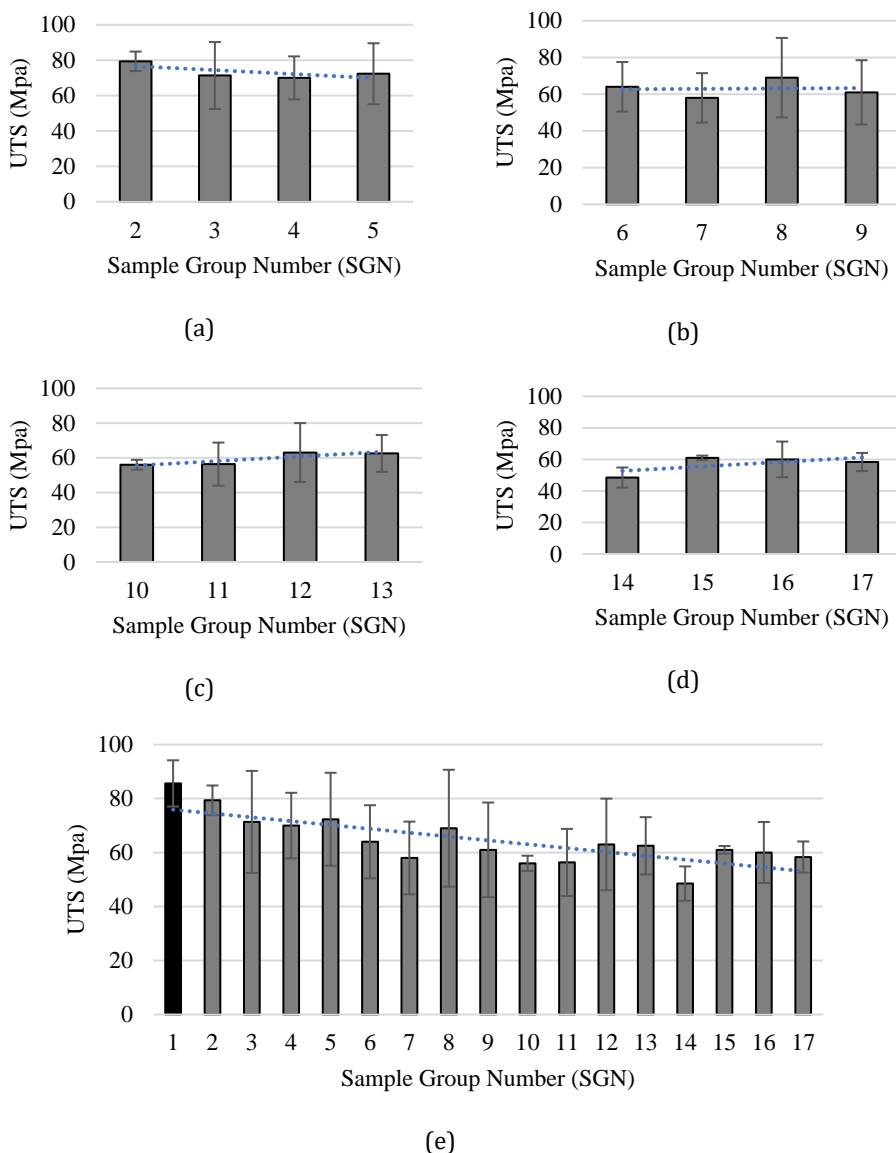
Fig. 12. Change of UTS due to thermal aging for different SGN

(a) SGN 2-5, (b) SGN 6-9, (c) SGN 10-13, (d) SGN 14-17 and (e) SGN 1-17

It is observed that for SGN 2-5 a decreasing UTS, a clear trend is observed. SGN 6-9 shows a more consistent rend with UTS values increase and decrease in an oscillating manner. For SGN 10-13 the UTS values slowly increase. For SGN 14-17, the UTS values increase initially but later reach a plateau. Finally, for graph 12(e) there is an overall trend of decreasing UTS is observed although there are noticeable variations as mentioned earlier. These variations in UTS due to different thermal aging are consistent with the literature. The initial decrease in UTS below and slightly over the Tg is expected due to the epoxy being rubbery and causing voids inside the material substrate. However, the increase in UTS at higher temperatures (SGN 11,12,13,15,16,17) is not fully understood by the author and requires further research.

Similar to UTS, Figure 13 shows the change of Max Strain due to thermal aging. The Figure is divided into 5 separate graphs to aid the visualization of the thermal aging effect due to a fixed temperature and increasing aging time. Finally, graph 13 (e) shows the effect with all sample group numbers sequentially. The black bar in this graph represents the Max Strain value for unaged samples.

(a)

(b)

(c)

(d)

(e)
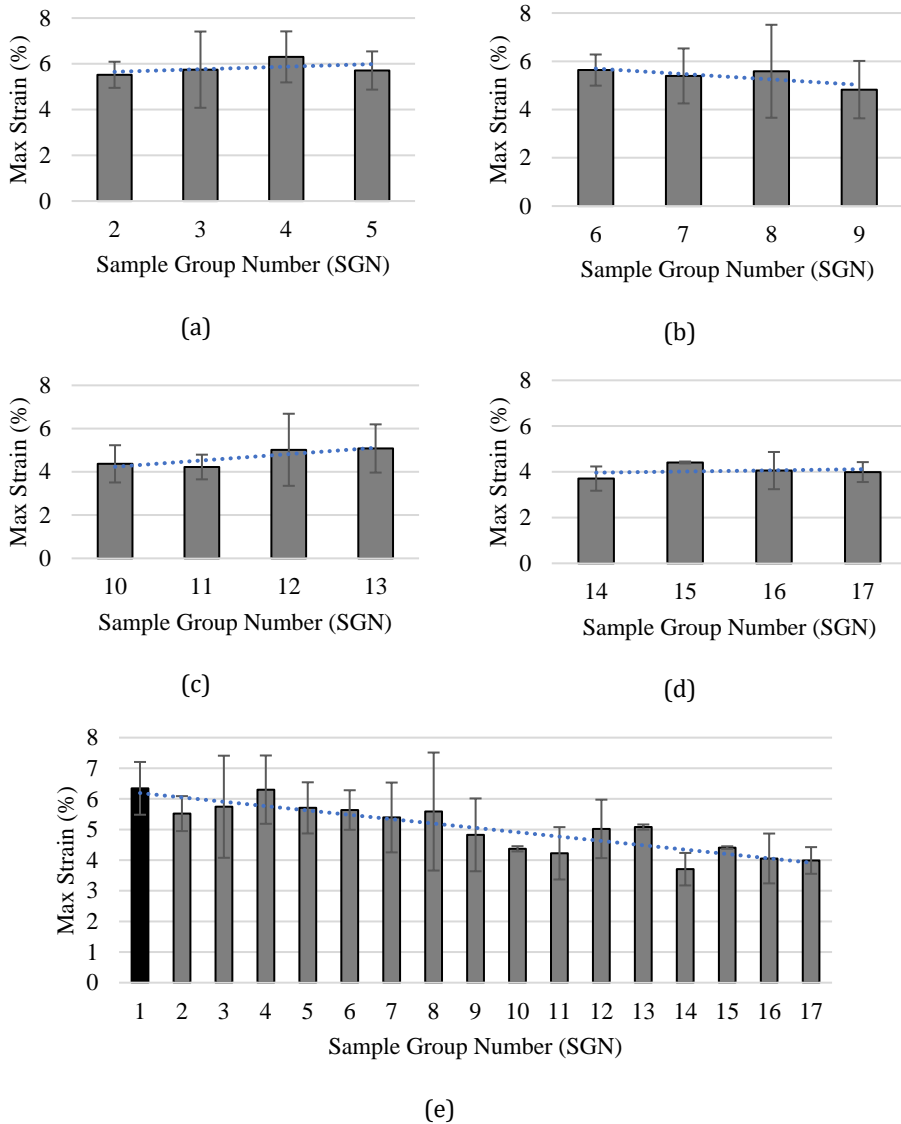
Fig. 13. Change of max strain (%) due to thermal aging for different SGN

(a) SGN 2-5, (b) SGN 6-9, (c) SGN 10-13, (d) SGN 14-17 and (e) SGN 1-17

Also, Figure 14 shows the change in Yield Strength due to thermal aging. The Figure is divided into 5 separate graphs to aid the visualization of the thermal aging effect due to a fixed temperature and increasing aging time. Finally, graph 14 (e) shows the effect with all sample group numbers sequentially. The black bar in this graph represents the Yield Strength value for unaged samples.
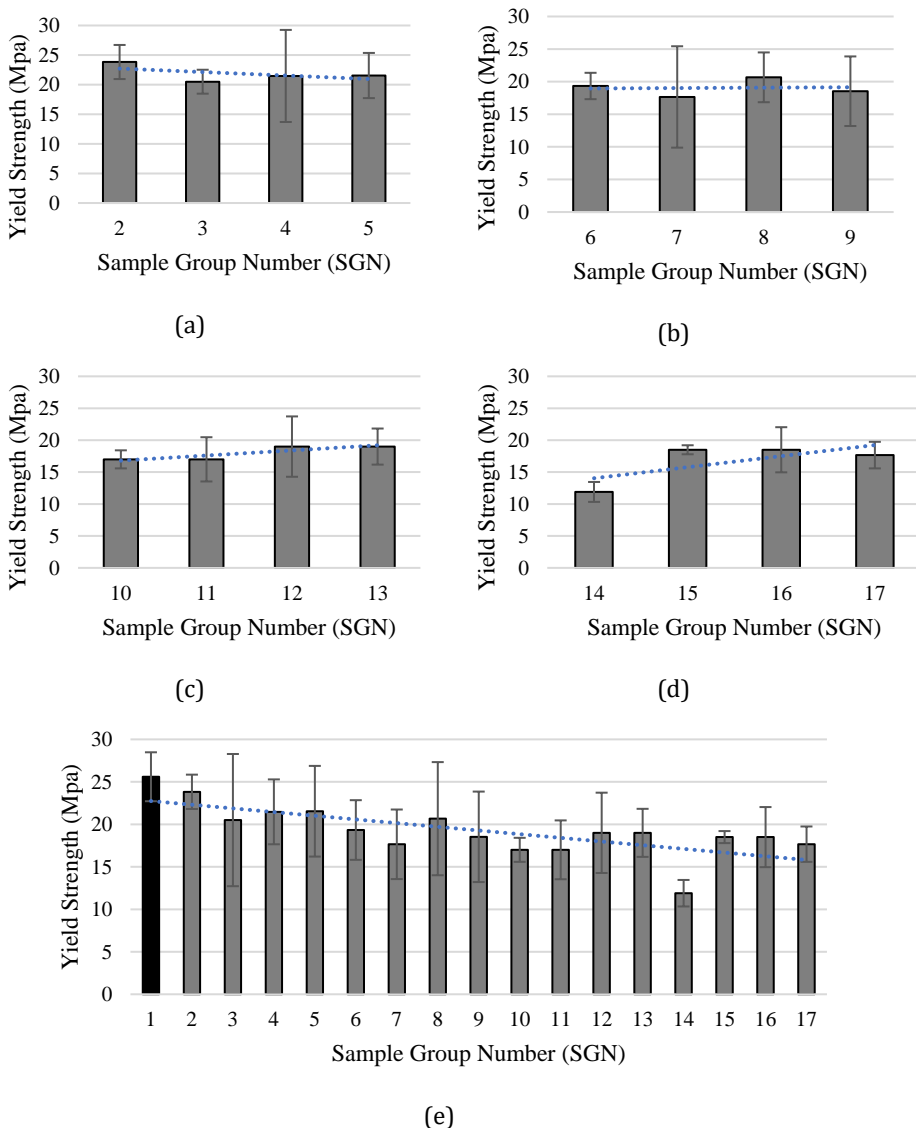
Fig. 14. Change of yield strength due to thermal aging for different SGN
(a) SGN 2-5, (b) SGN 6-9, (c) SGN 10-13, (d) SGN 14-17 and (e) SGN 1-1

As a general observation, from Figure 12 to 14, it is revealed that a gradual decrease in UTS, Max Strain and Yield strength values occurred as samples were exposed to increasingly higher temperatures during the thermal aging process. The highest value was obtained from the unaged samples while the lowest value was found from the thermally aged samples at 200°C 30 mins. The percentile decreases of UTS, Max Strain and Yield strength values were 43.34%, 41.48% and 53.52% respectively between the two extremes. The high amount of scattering in the mechanical properties after thermal aging is consistent with the literature [18].

Further analysis was performed to see variations in UTS of SGN 2 – 17, due to the variations in thermal aging temperature and time separately. Figure 15 shows the variation of UTS

due to thermal aging temperature and Figure 16 shows the variation of UTS due to thermal aging time.
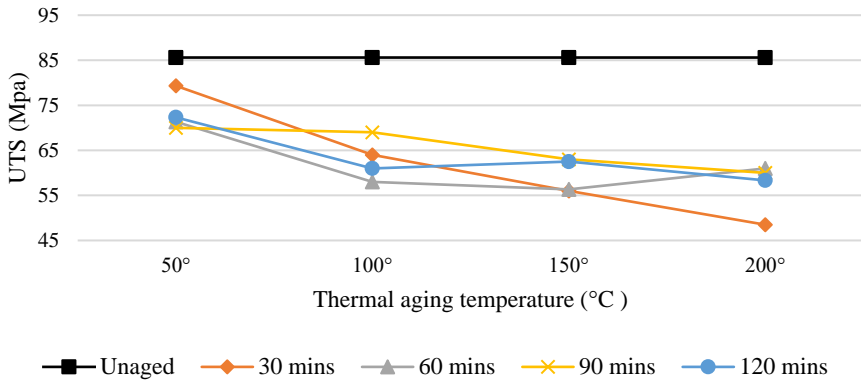
Fig. 15. Variation of UTS due to thermal aging temperature
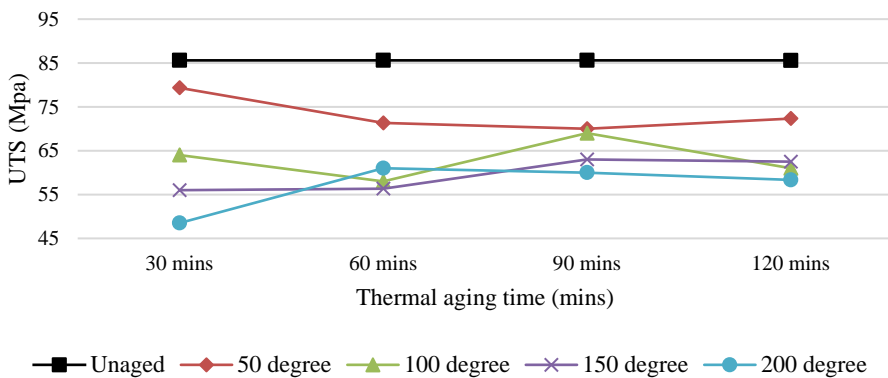
Fig 16. variation of UTS due to thermal aging time

From Figure 15, although there are some scatter and randomness in the mechanical properties after thermal aging consistent with the literature; the UTS of the thermally aged samples decreases as the thermal aging temperature increases. Generally, exposure to elevated temperatures and aging times causes the epoxy to be rubbery and develop voids inside the material substrate that lead to loss of strength [18]. However, from Figure 16, no specific trend is observed as the aging time increases for a specific temperature. In both cases, exposure to thermal aging always yields UTS values that are lower than the unaged UTS value.

Additionally, a Contour Surface plot was generated to understand the combined dependency of UTS of SGN 2 – 17 on thermal aging temperature and time. Figure 17 shows the contour plot of UTS.
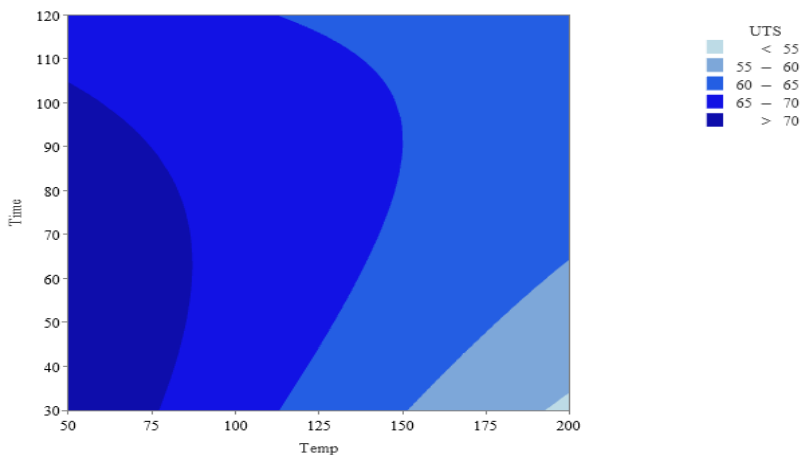
Fig 17. Contour plot of UTS

The contour plot shows the mapping of UTS values at various combinations of aging temperatures and time. In the plot, the UTS values are shown in 5 ranges which are represented by 5 shades of color. Darker shades represent higher values and lighter shades represent lower values. From the plot, the UTS decreases as temperatures reach higher values on the x-axis. However, as the aging time increases for a specific temperature in the y-axis, no trend is observed. It also affirms the previous findings that the sensitivity of UTS reduction is more dependent on the change of thermal aging temperature rather than the thermal aging time between 30 mins and 120 mins. However, existing literature suggests that a reduction of UTS can result in case of longer thermal exposures in similar temperatures [18].

5.2 The Predictive Model

Results and discussion of the predictive model are presented in this section. It is further divided into 4 subsections. In the first 3 subsections, the results and discussion of the Image processing, ANNs and Regression analysis have been presented. Finally, the performance and analysis of the complete predictive model have been presented in the fourth subsection.

5.2.1 Image Processing

The Image processing program calculated the most consistent Red Green and Blue color values of all 51 samples. Then the average of these values for 3 samples within each sample group was taken to obtain the Red Green and Blue color values for a particular sample group number. Figure 18 shows the Red Green and Blue color values for SGN 1-17.

From the above figure, it is observed that the RGB color values progressively decrease from SGN 1 to SGN 13. However, at SGN 14, when the thermal aging temperature reaches 200°C, the RGB color values decrease drastically. The overall trend of decreasing RGB color values is denoted by dotted lines for each respective color. The trend of decreasing RGB color values physically indicates the gradual darkening of color. This aligns with the observed gradually increasing brown color of the samples. Ultimately, the color reaches deep brown at SGN 17. This color change and the associated trend of RGB values agree with the color changes during thermal aging reported in Figure 11. These RGB values are used as an identifier for the ANNs.
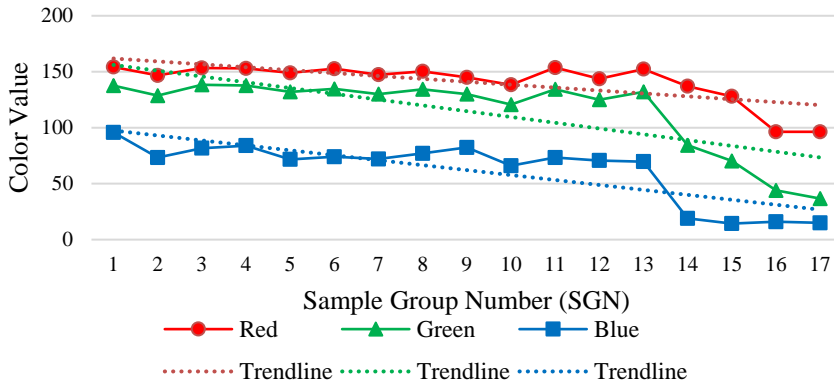
Fig. 18. Red Green and Blue color values for SGN 1-17

5.2.2. Artificial Neural Networks (ANNs)

The RGB values of the image processing program were given as input to the two cascaded ANNs to estimate the associated thermal aging temperature and time. The test performance of ANN1 and ANN2 are shown in Figure 19.

(a)   (b)
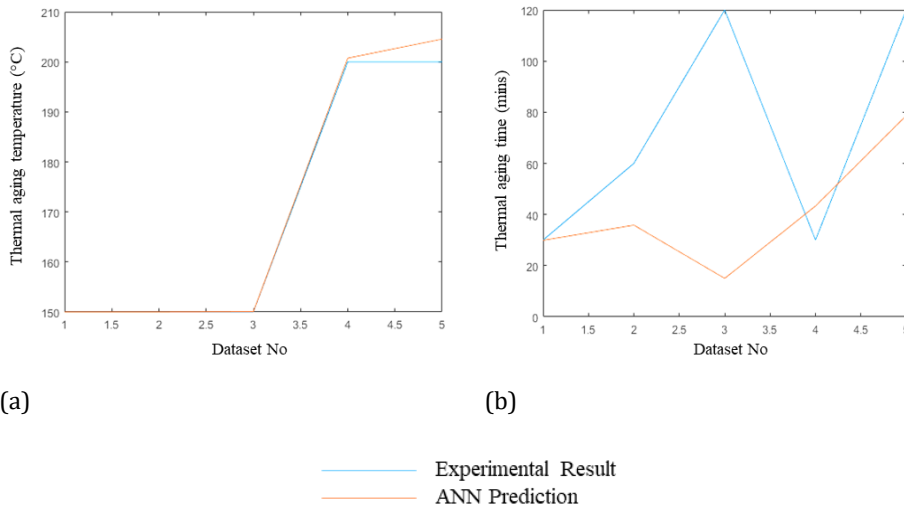
Fig 19. Testing performance of ANNs: (a) ANN1 (b) ANN2

From the above figure, it is noted that ANN1 made very accurate estimations compared to the experimental results. This is expected as per the findings and analysis of the experimental work in Figure 15. As there was a trend of declining UTS with increasing thermal aging time, ANN1 successfully followed the same. However, ANN2 predictions have high errors. This is also expected considering the experimental work in Figure 16. In this case, there were no clear trends which led to ANN2 making high errors. To achieve better results from ANN2, a much larger dataset is required,

5.2.3. Regression Analysis

A comparison was made between the results of the experimental work and the results obtained using the regression equation (1). Figure 20 shows the comparative plot of UTS values of SGN 1-17 obtained from experimental work and the regression equation.
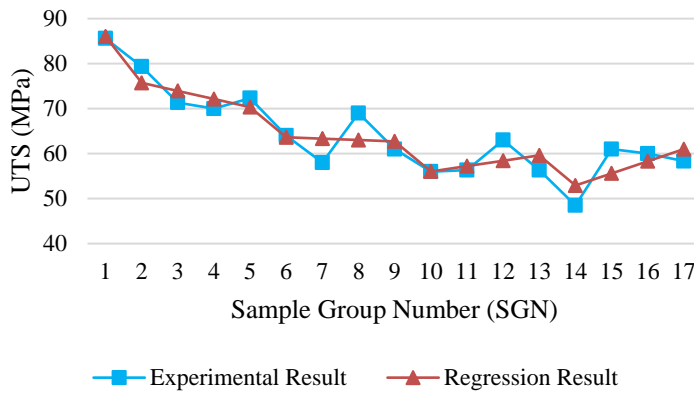
Fig. 20. Comparison of experimental and regression results for UTS

From the figure above it is seen that the UTS values obtained through the regression equation closely follow the experimental values. The average absolute error of all 17 SGN was calculated and found as 4%.

5.2.4. Performance of the predictive model

Combining the results from the Image Processing, Regression Analysis and Artificial Neural Networks; the predictive model predicted the UTS value of the thermally aged samples. The model was tested with 05 samples within SGN 10-17. Figure 21 graphically compares the experimental result and the predictive model predicted result. Table 8 shows the dataset of the experimental result and predictive model predicted result with associated errors.
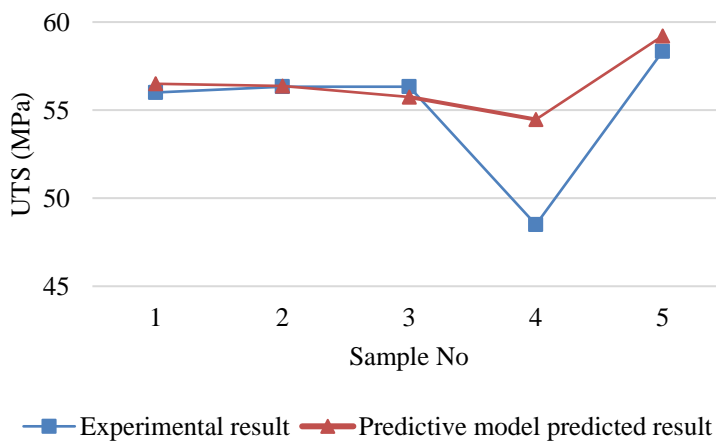
Fig. 21. Graphical comparison of experimental results and predictive model predicted results.

Table 8. The dataset of the experimental result and predictive model predicted results with associated errors.

Sample No	SGN	Temperature (°C)	Time (mins)	Experimental UTS (MPa)	Predictive Model predicted UTS (MPa)	Error (%)	Absolute Error (%)
1	10	150	30	56.00	56.50	-1%	1%
2	11	150	60	56.33	56.37	0%	0%
3	13	150	120	56.33	55.75	1%	1%
4	14	200	30	48.50	54.47	-12%	12%
5	17	200	120	58.33	59.21	-2%	2%
Average Absolute Error							3%

From the figure, it is evident that the predictive model estimated the experimental results of samples no 1, 2 and 3 with 99%, 100% and 99% accuracy. In sample no 4, the predictive model successfully followed the declining trend of the experimental result. However, the estimation had a 12% error. Again, in sample no 5, the predictive model successfully followed the rising trend of the experimental result and made an estimation with 98% accuracy. The average absolute accuracy of the predictive model is calculated as 97%.

The accuracy of the predictive model depends on the input image quality which influences the RGB values. Also, the accuracy largely depends on the regression equation as it is a best-fit equation by nature that inherently has some errors. Moreover, the predictive model is compared with experimental results which are also prone to scattering due to matrix rearrangement post-thermal aging, sample randomness and several other experimental factors.

It is seen that only in the case of sample 3, the predictive model made a noticeable error. This error may be attributed to the causes discussed above. In general, the accuracy of the predictive model can be maximized by increasing the number of experimental work samples and the ANN training dataset.

6. Conclusion

This study investigated the mechanical properties of thermally aged GFRP composites. Also, a novel predictive model was also developed consisting of image processing, regression analysis and cascaded artificial neural networks. Within the limitations of the study, the following conclusions can be made:

During thermal aging at 100°C, very mild smoke and a burning smell were noticed. This smoke and smell became more noticeable at higher temperatures. After thermal aging at 150°C, samples showed a very slight shade of brown color. At 200°C the samples became progressively dark brown as aging times increased. This gradual change of color is attributed to the oxidation process that occurs during thermal aging.

Tensile test results showed that compared to unaged samples, a general decreasing trend of UTS, Max Strain and Yield strength values were noted. However, when investigated for different ranges of temperatures separately, it became apparent that the different ranges of temperatures had fluctuations and scattering with different thermal aging times. This variation and scattering is consistent with the literature and may be attributed to several factors that require further study.

Further analysis of tensile test results reveals that, the UTS of the thermally aged samples gradually decreases as the thermal aging temperature increases up to 200°C. But no specific pattern is observed as the thermal aging time increases up to 120 mins. It is likely because the GFRP is tolerant of thermal aging time ranges selected for this study and hence did not produce any trend. A broader range of thermal aging time may be studied to explore this behavior further. However, in all cases, even the minimum exposure to thermal aging (50°C and 30 mins) reduced the UTS value below that of unaged samples. None of the thermally aged samples showed equal or higher UTS value than unaged samples.

The predictive model was developed by combining image processing, regression analysis and cascaded ANNs. The model estimated the UTS of the thermally aged GFRP with only the photographic image of the sample. The predictive model showed an average accuracy of 97% when compared to experimental results. With a sufficient dataset, this model can also be modified to predict any mechanical property that has color change as an identifier. This model has potential applications for non-destructive field testing of GFRP composites and can reduce operational costs.

Abbreviations

The following abbreviations are used in this manuscript:

ANN   Artificial Neural network

ASTM American Society for Testing and Materials,

GFRP Glass fiber reinforced plastics

RGB   Red, Green, Blue

SGN   Sample group number

UTS   Ultimate tensile strength

Reference

[1] Rao B SD, Sethi A, Das AK. Fiber laser processing of GFRP composites and multi - objective optimization of the process using response surface methodology. Journal of Composite Materials 2018;53:1459–73. https://doi.org/10.1177/0021998318805139

[2] Pavan G, Singh KK, Mahesh. Elevated thermal conditioning effect on flexural strength of GFRP laminates: An experimental and statistical approach. Materials Today Communications 2021;26:101809. https://doi.org/10.1016/j.mtcomm.2020.101809

[3] Erden S, Sever K, Seki Y, Sarikanat M. Enhancement of the mechanical properties of glass/polyester composites via matrix modification glass/polyester composite siloxane matrix modification. Fibers and Polymers 2010;11:732–7. https://doi.org/10.1007/s12221-010-0732-2

[4] Bakis CE, Bank LC, Brown VL, Cosenza E, Davalos JF, Lesko JJ, et al. Fiber-Reinforced Polymer Composites for Construction—State-of-the-Art Review. Journal of Composites for Construction 2002;6:73–87. https://doi.org/10.1061/(asce)1090-0268(2002)6:2(73)

[5] Bazli M, Ashrafi H, Jafari A, Zhao X-L, Gholipour H, Oskouei AV. Effect of thickness and reinforcement configuration on flexural and impact behaviour of GFRP laminates after exposure to elevated temperatures. Composites Part B: Engineering 2019;157:76–99. https://doi.org/10.1016/j.compositesb.2018.08.054

[6] GAO Kun, SHI Hanqiao, SUN Baogang, et al. Effects of hydro-thermal aging on properties of glass fiber/epoxy composites[J]. Acta Materiae Compositae Sinica, 2016, 33(6): 1147-1152. doi: 10.13801/j.cnki.fhclxb.20160108.001

[7] Zuo P, Tcharkhtchi A, Shirinbayan M, Fitoussi J, Bakir F. Effect of thermal aging on crystallization behaviors and dynamic mechanical properties of glass fiber reinforced polyphenylene sulfide (PPS/GF) composites. Journal of Polymer Research 2020;27. https://doi.org/10.1007/s10965-020-02051-2

[8] Birger S, Moshonov A, Kenig S. The effects of thermal and hygrothermal ageing on the failure mechanisms of graphite-fabric epoxy composites subjected to flexural loading. Composites 1989;20:341–8. https://doi.org/10.1016/0010-4361(89)90659-9

[9] Mouritz, A.P. Post-fire flexural properties of fibre-reinforced polyester, epoxy and phenolic composites. Journal of Materials Science 37, 1377–1386 (2002). https://doi.org/10.1023/A:1014520628915

[10] Dodds N, Gibson AG, Dewhurst D, Davies JM. Fire behaviour of composite laminates. Composites Part A: Applied Science and Manufacturing 2000;31:689–702. https://doi.org/10.1016/s1359-835x(00)00015-4

[11] Lan Z, Deng J, Song Y, Xu Z, Nie Y, Chen Y, et al. Color Changes and Mechanical Properties of Glass Fiber Reinforced Polycarbonate Composites after Thermal Aging. Polymers 2022;14:222. https://doi.org/10.3390/polym14020222

[12] Song Y, Deng J, Xu Z, Nie Y, Lan Z. Effect of Thermal Aging on Mechanical Properties and Color Difference of Glass Fiber/Polyetherimide (GF/PEI) Composites. Polymers 2021;14:67. https://doi.org/10.3390/polym14010067

[13] Zavatta N, Rondina F, Falaschetti MP, Donati L. Effect of Thermal Ageing on the Mechanical Strength of Carbon Fibre Reinforced Epoxy Composites. Polymers 2021;13:2006. https://doi.org/10.3390/polym13122006

[14] Gibson AG, Torres MEO, Browne TNA, Feih S, Mouritz AP. High temperature and fire behaviour of continuous glass fibre/polypropylene laminates. Composites Part A: Applied Science and Manufacturing 2010;41:1219–31. https://doi.org/10.1016/j.compositesa.2010.05.004

[15] Kim Y, Oh H. Comparison between Multiple Regression Analysis, Polynomial Regression Analysis, and an Artificial Neural Network for Tensile Strength Prediction of BFRP and GFRP. Materials 2021;14:4861. https://doi.org/10.3390/ma14174861

[16] Gayatri Vineela M, Dave A, Kiran Chaganti P. Artificial Neural Network based Prediction of Tensile Strength of Hybrid Composites. Materials Today: Proceedings 2018;5:19908–15. https://doi.org/10.1016/j.matpr.2018.06.356

[17] Mishra M, Agarwal A, Maity D. Neural-network-based approach to predict the deflection of plain, steel-reinforced, and bamboo-reinforced concrete beams from experimental data. SN Applied Sciences 2019;1. https://doi.org/10.1007/s42452-019-0622-1

[18] Doblies A, Boll B, Fiedler B. Prediction of Thermal Exposure and Mechanical Behavior of Epoxy Resin Using Artificial Neural Networks and Fourier Transform Infrared Spectroscopy. Polymers 2019;11:363. https://doi.org/10.3390/polym11020363

[19] Turco C, Funari MF, Teixeira E, Mateus R. Artificial Neural Networks to Predict the Mechanical Properties of Natural Fibre-Reinforced Compressed Earth Blocks (CEBs). Fibers 2021;9:78. https://doi.org/10.3390/fib9120078

[20] Krauklis A, Echtermeyer A. Mechanism of Yellowing: Carbonyl Formation during Hygrothermal Aging in a Common Amine Epoxy. Polymers 2018;10:1017. https://doi.org/10.3390/polym10091017

[21] Bellenger V, Verdu J. Oxidative skeleton breaking in epoxy–amine networks. Journal of Applied Polymer Science 1985;30:363–74. https://doi.org/10.1002/app.1985.070300132

Technical Note

Determination of the optimal temperature regime of plastic deformation of micro alloyed automobile wheel steels

Sergiy Sheyko[1,a], Volodymyr Tsyganov[2,b], Oleksii Hrechanyi[*1,c], Tetyana Vasilchenko[1,d], Anastasiia Hrechana[3,e]

[1]Department of Metallurgical Equipment Zaporizhzhia National University, Zaporizhzhia, Ukraine
[2]Department of Metal-Cutting Machines and Tools National University, Zaporizhzhia, Ukraine
[3]Master of Law, National Technical University of Ukraine, Kyiv, Ukraine

Article Info	Abstract
	It has been established that hot plastic deformation microalloyed steel 10HFTBch type accelerates the excretion of pearlite and causes structure refinement during subsequent cooling due to an increase of start of new phases' centers. This leads to the formation of a fine-grained dispersed two-phase structure consisting of ferrite with a high dislocation density and pearlite. It has been determined that at the optimum deformation temperature the prevailing mechanism of structure refinement is the fragmentation of austenitic and ferrite grains of a common initial orientation into misoriented subgrains (fragments) with low-angle dislocation boundaries of deformation origin. A thorough thermokinetic analysis of the course of this process made it possible to determine the optimal temperature regime for plastic deformation for this type of steel, which is 850-900 °C. Plastic deformation increases the range of of pearlite's transformation existence rates by 2.5 times, it was found that after 30% deformation at 950 °C, pearlite transformation begins at a cooling rate of 5 °C/s, and without deformation – at 2 °C/s.

1. Introduction

One of the main catalysts for the rapid development of the industrial economy sector is mechanical engineering [1]. And in this regard the automobile industry plays an important role [2]. Not only the performance of the transport as a whole, but also its efficiency depends on the reliability of the undercarriage components of trucks. One of the most critical units of trucks are wheel disks. Increasing their cargo, and hence energy efficiency [3], allows significant savings by reducing the number of trips for transporting various types of cargo [2]. And in this case, the development of new materials with special technological properties, such as specific strength [4] and impact strength [5], comes in a prominent position.

One of the ways to increase the carrying capacity of vehicles is the manufacture of rims from steels with improved characteristics. In this regard, a good alternative to conventional low-carbon steel, from which, as a rule, wheel rims of trucks are made, are micro alloyed steels, which include low-pearlite steel 10HFTBch, with the following ratio of components, %: C 0.08-0.12; Si 0.10-0.50; Mn 0.15-0.50; Cr 0.05-0,15; V 0.10-0.15; Ti 0.10-0.15; Nb 0.07-0.15; S ≤0.035; P ≤0.035; Ba 0.0005-0.0015; REM 0.001-0.010; Fe – other [6].

Studies have shown that a simultaneous increase in the strength and resistance to brittle fracture of low-alloy and ordinary low-carbon steels is possible by microalloying [7]: the introduction of micro additives (up to 0.15%) of elements, mainly IV and V groups of the periodic system [8]. The most common microalloying elements are niobium [9], titanium [10] and vanadium [11]. These elements have a high affinity with nitrogen and carbon and readily form nitrides and carbides (or carbonitrides) [12]. When heated, carbonitrides dissolve in a solid solution, and when cooled, they release as a separate dispersed phase [13]. These processes are one of the main mechanisms of steel's hardening.

Thus, in the development of 10HFTBch type steel, in addition to traditional microalloying elements, introduction of such elements as barium and rare earth metals from the group of cerium, lanthanum, praseodymium, neodymium made it possible to obtain steel with improved mechanical characteristics and increased impact strength (tensile strength 500 MPa, yield strength 440 MPa, impact strength KCU=0,80 MJ/m2) [6], while achieving equal strength of the welded joint with the base metal, as well as an increase in the impact strength of the weld and the heat-affected zone [5].

Unlike low-carbon steels, which are used for the production of wheel rims for trucks, for example, low-carbon steel 15 (tensile strength 470 MPa, yield strength 370 MPa, impact strength KCU=0.73 MJ/m^2), the proposed steel has 15-20% increased strength properties. This makes it possible not only to proportionally increase the carrying capacity of the wheels, but also to extend their survivability by about 2-2.5 times, which was confirmed by mechanical tests according to a specially developed technique in [14]. At the same time, some technological issues arise when this steel is put into mass production.

The most rational method for processing low-alloy steel is controlled rolling [15]. Distinctive features of this type of processing are: a reduced temperature of workpiece heating [16] for final rolling, a strictly regulated deformation regime, and a low temperature at the end of rolling. All this provides a sharp refinement of the austenite grain, and, consequently, the ferrite formed from it, moderate precipitation hardening, dislocation and sub grain strengthening. Microalloying with niobium and vanadium enhances the effect of controlled rolling, ultimately providing a fine austenite grain, and after a phase transformation, a fine ferrite grain, which is accompanied by a corresponding improvement in mechanical and cold-resistant properties.

With traditional rolling [17] microalloying additives increase the strength of the steel mainly due to dispersion hardening [18], and with controlled rolling or normalization (austenization with air cooling) – mainly by grain's grinding [19]. And the influence of the morphology of integral-phase layers [20] on the properties of a polycrystalline composite is covered in researches, but the process of plastic deformation [21] of micro alloyed steels with increased impact strength has not yet been fully studied and is of practical interest from the point of view of establishing the optimal temperature regime for its implementation [22].

The main raw material for the production of car wheel rims is sheet steel produced using plastic deformation methods. The proposed micro alloyed 10HFTBch steel is experimental and has not been put into mass production. This is related to the high cost of performing full-scale experiments to work out the technological modes of the proposed steel's plastic deformation to obtain a steel sheet. Therefore, simulation modeling of these processes comes to the fore. Modeling the process to establish the optimal temperatures for performing plastic deformation of a sample of the proposed micro alloyed steel will not only significantly reduce financial investments in the development of the technological process of sheet rolling, but will also speed up the process of introducing the development into production with the subsequent possibility of promptly influencing the expansion of the products' range produced from the proposed steel.

2. Materials and Methods

To study chemical reactions and phase transformations in the researched steels, occurring with the release or absorption of heat, the method of thermogravimetric analysis was applied using a Q-1500 derivatograph. To implement the modeling process, a Gleeble 3800 metallurgical process simulator, a DIL 805A/D dilatometer, and a «Setaram» plastometer were used.

The phase composition of the structural components and nonmetallic inclusions was studied by the energy-dispersive PCMA method on a JEOL JSN-6360LA raster electron microscope equipped with a JED-2300 X-ray microanalysis system.

According to the given task, experimental melting of micro alloyed steel was performed in an induction furnace with a crucible capacity of 150 kg. Melting parameters: power from the thyristor converter – 320 kW, pouring temperature of the test sample –1660 °C, the temperature was controlled by immersible W-Mo thermocouple with an accuracy of ± 10°C. Modifiers in the form of cylindrical briquettes were introduced into the melt mass after melting the charge with mechanical mixing. The duration of the melt after modifications was from 1 to 3 minutes, depending on the amount of modifier introduced. During the melting, technological samples for determination of chemical composition were selected by spectral method. Cylindrical samples with a diameter of 10 mm and length of 12 mm were received after smelting and casting, with the following mechanical characteristics of the received samples: tensile strength – 520 MPa, yield strength – 450 MPa.

3. Experimental Studies

The study of the obtained sample of steel of the 10HFTBch type by the PCMA method was carried out using a focused high-energy electron beam, which emerges from the electron gun of the microscope, is accelerated by high voltage, and is shown in Fig. 1. When hitting a sample, some of the electrons scatter, depending on the atomic number of the element and its environment in the crystal structure, and some excite the atoms of the object's substance, causing the emission of characteristic emitting. The advantage of this method is that by analyzing the energy spectrum of the emitted X-ray radiation arising from the interaction of an electron beam and atoms of a sample of the resulting steel, using an electron microscope detector, it additionally becomes possible to study its composition as well [23].

The change in the physico-mechanical properties of the sample during thermoplastic processing is a consequence of a significant restructuring of the micro- and mesostructure of the material. It is impossible to describe such processes without studying and creating appropriate models that explicitly take into account the physical causes of the evolution of the material microstructure under large deformations. Considerable attention in physical theories is given to the modification of hardening laws in connection with new experimental data obtained using high-resolution equipment and with obtaining experimental hardening curves for large plastic deformations by the plastometry method.

The dilatometric method was chosen for constructing thermokinetic diagrams. To implement the process, a DIL 805A/D dilatometer with a plastometer attachment was used. DIL 805A/D is a special dilatometer designed to determine expansion parameters under deformation conditions. Its distinguishing feature is the ability to operate at very high heating and cooling rates. This equipment has a built-in processor system that controls the operation of the generator, hydraulic system, measurement recording, gas supply, vacuum installation and security system. The dilatometer DIL 805A/D has the following main specifications:

- maximum compression force   20 кН;
- strain rate   0.001-20,0 c^{-1};
- maximum tensile force   100 кН;
- maximum temperature   1500 °C;
- heating rate   up to 4000 °C/s;
- heating method   inductive

Hot steel tests were carried out on a modern Gleeble 3800 plastometer and a dilatometer. Working parameters of the plastometer:

- temperature of the test – 20-1700 °C;
- punch speed – up to 2000 mm/s;
- degree of logarithmic deformation – ε_{com} =0.01-1.2; ε_{str} =0.01-0.15.

Model DIL 805A/D can work as a cooling and deforming dilatometer. When working with a cooling dilatometer, a cylindrical sample is inductively heated to a given temperature, and then sequentially cooled according to various (linear or exponential) schemes. Phase transformations that occur during cooling or in the isothermal regime are determined by the change in length. The beginning and end of the transformation determine the area of existence of ferrite, carbides, graphites, pearlites, bainite, martensite, and other phases.

In the study on a plastometer, samples with a diameter of d=10 mm and a height of h=12 mm were placed in a chamber, inside which air was pumped out and a vacuum was created to exclude metal oxidation. At certain intervals during loading, the yield stress and logarithmic strain were recorded. Table 1 presents the sampling parameters and limiting temperatures for thermomechanical testing of samples. The maximum heating of the central part of the studied samples, measured using thermocouples, at the moment of hot deformation was 952°C.

Table 1. Sampling parameters and limiting temperatures for testing samples

Samples	1	2	3	4	5
Temperature, °C	770	800	850	900	950
Strain rate, s^{-1}			100		
Degree of deformation, ln ε			0.01-1.2		

To predict the formation of the structure during thermomechanical treatment of low-alloy steel 10HFTBch, the features of phase transformations during continuous cooling after plastic deformation in the austenitic region below the recrystallization temperature were studied. To do this, the sample in the as-delivered state was heated to a temperature of 950 °C and plastically deformed by 30%. Next, the sample was cooled to 20°C and, in order to analyze the effect of plastic deformation on the formation of the structure, it was reheated to 950°C.

4. Results and Discussion

It has been established that the plasticity of the base metal and welded joints of two-phase steels of the 10HFTBch type used for wheel rims of vehicles is greatly affected by the hardening effect [24] caused by the appearance of quenching structures [25]. The initial structure of the studied steel can also change depending on the ratio of austenite-forming (C, N, Mn) [26] and ferrite-forming (Cr, Ti, V, Nb, Si) [27] elements [28], which is shown in Fig. 1.

(a)

(b)

(c)
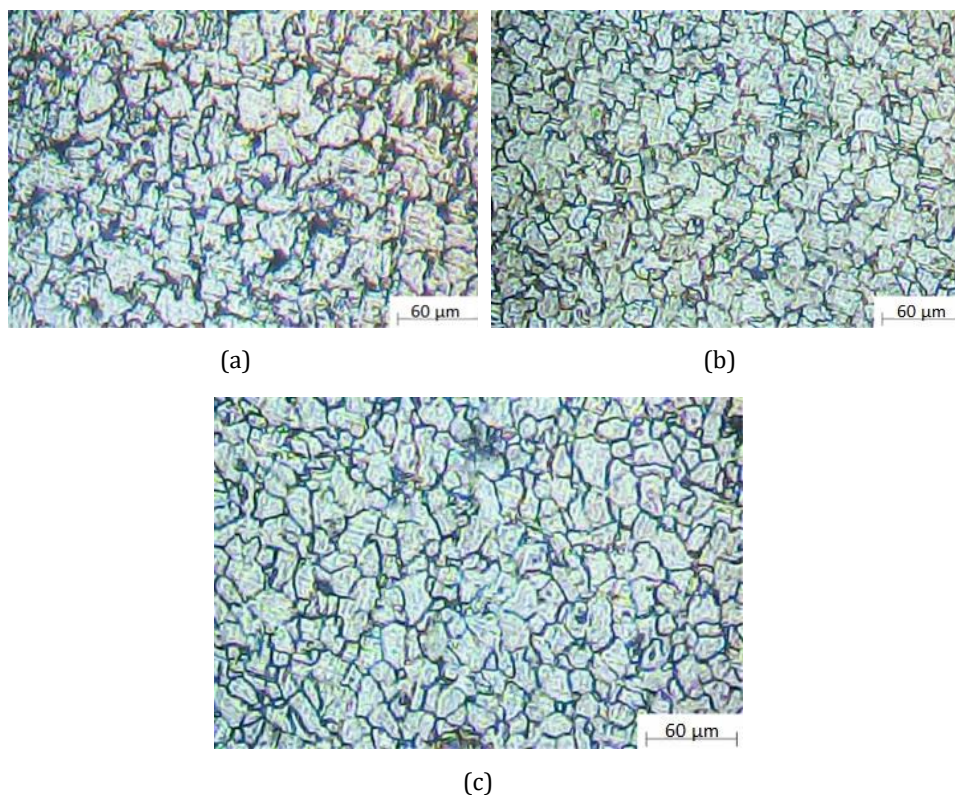
Fig. 1. The microstructure of undeformed steels of various compositions after hot deformation and heat treatment at 900 °C: a – lower, b – medium, c – upper value of the content of alloying elements

The main reason for the reduced plasticity of open cast low-carbon steels is the presence of a two-phase ferrite-martensite structure. At the same time, dispersed particles of chromium, vanadium, and titanium carbonitrides, while inhibiting the growth of ferrite and austenite grains during heat treatment, can significantly increase strength by means of dispersion strengthening.

The results of research and analysis of the structure of an undeformed 10HFTBch steel sample at various cooling rates are summarized and presented in the form of a thermokinetic diagram and are shown in Fig. 2. Under the cooling curves there are figures characterizing the average cooling rate (V, °C/s) in the temperature range from 950 to 350 °C. Analysis of the transformation shows that the γ→α transformation begins with the release of free ferrite for all the cooling rates studied. Pearlite transformation occurs at a cooling rate of 3 °C/s at temperatures ranging from 600 to 700 °C. Cooling at a rate of 3°C/s leads to the formation of a ferrite-pearlite structure consisting of 75% ferrite grains with an average size of 20 μm. Increasing the cooling rate to 20 °C/s leads to the formation of a ferrite structure, the proportion of which decreases to 50%, the size of the ferrite grain is 8 μm. A further increase in the cooling rate to 50 °C/s leads to a refinement of the structure (the size of the ferrite grain is 5 μm) and a decrease in the proportion of ferrite to 40%.

The results of studying the structure of a deformed sample of 10HFTBch steel at various cooling rates are presented in the form of a thermokinetic diagram and are shown in Fig. 3. An analysis of the transformation shows that the plastic deformation of steel at a

temperature of 950 °C has practically no effect on the temperatures at which the phase transformation of austenite into ferrite begins during continuous cooling. Only after cooling at a rate in the range from 1 to 10 °C/s hot plastic deformation affects the increase in the ferrite transformation temperature by an average of 18 °C. Preliminary plastic deformation, in the austenitic region below the recrystallization temperature, has a stronger effect on pearlite transformation at low cooling rates in the range from 0,5 to 10 °C/s.
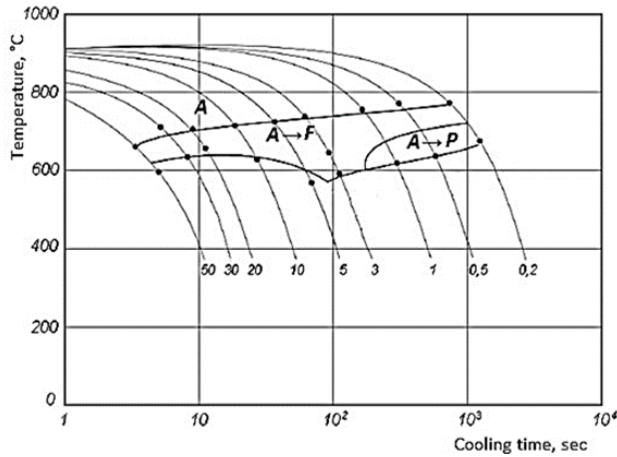
Fig. 2. Thermokinetic diagram of austenite decomposition of steel 10HFTBch during continuous cooling in a wide range of speeds: A – austenite, F – ferrite, P – perlite
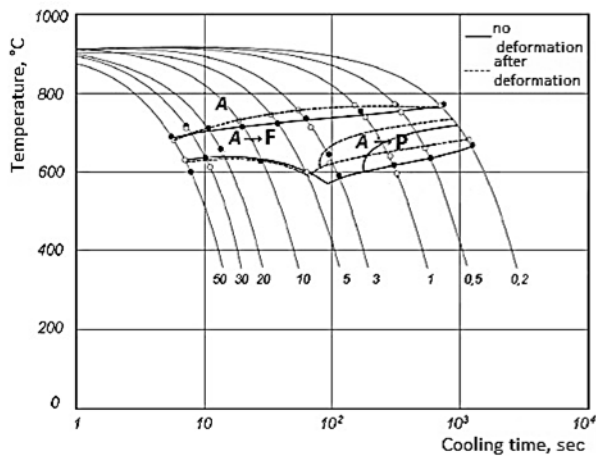
Fig. 3. Thermokinetic diagram of austenite decomposition of steel 10HFTBch during continuous cooling after plastic deformation: A – austenite, F – ferrite, P – perlite

The light dots in the diagram correspond to the onset of austenite transformation after deformation, the black dots – without deformation. The dotted curve in the diagram is the line of transformations after plastic deformation.

Thus, plastic deformation increases the speed range of existence of pearlite transformation. After deformation of 30% at 950°C, pearlite transformation begins at a

cooling rate of 5°C/s, and without deformation, at 2°C/s. Also, hot plastic deformation leads to structure refinement.

5. Conclusions

The main reason for the reduced ductility of open-melted low-carbon steels is the presence of a two-phase ferrite-martensite structure. One of the most rational ways to refine the austenite grain, and, consequently, the ferrite formed from it, is to control the parameters of plastic deformation during strip rolling, namely a strictly regulated deformation mode and a low temperature at the end of the rolling. The results of the studies show that uneven deformation during hot rolling can significantly influence the process of structure formation at the time of forming. Moreover, the grain size non-homogeneity can either increase or decrease under the influence of temperature development in the zone of intense deformation.

It has been established that with an appropriate choice of modes of thermoplastic deformation of steel of the same composition, increased strength or plastic properties can be obtained, which makes it possible to control the production of a given set of properties, and in the future, from steel of a unified chemical composition, to obtain either sheet metal of different strength category, or sheet products with different viscous-plastic properties, depending on the operating conditions.

Hot plastic deformation, which intensifies diffusion transformations, accelerates the excretion of pearlite and causes structure refinement during subsequent cooling due to an increase in the centers of nucleation of a new phase. Such a phase-forming process leads to the formation of a fine-grained dispersed two-phase structure consisting of ferrite with a high dislocation density and pearlite. An analysis of the course of this process made it possible to choose the temperature range of hot deformation for micro alloyed steel 10HFTBch, which is from 850 to 900 °C.

Abbreviations and Nomenclature

KCU, impact strength, (MJ/m^2), ε_{com}, degree of logarithmic deformation (compression); ε_{str}, degree of logarithmic deformation (stretching); d, sample diameter (mm); h, sample height (mm); V, average cooling rate, (°C/s)

References

[1] Shapurov OO. State and trends of machine-building development. Actual Problems of Economics. 2009; 3: 57-63.
[2] Shapurov OO. Essence, role and objective necessity of enterprise management improvement. Actual Problems of Economics. 2008; 8: 138-146.
[3] Tryputen M, Kuznetsov V, Kovzel M, Kovalenko V, Artemchuk V, Nadtochyi V. Minimization of the Description of Images in the Problem of Adaptive Control of Static Technological Objects. 2021 IEEE International Conference on Modern Electrical and Energy Systems (MEES), Kremenchuk, Ukraine, 2021; pp. 1-4. https://doi.org/10.1109/MEES52427.2021.9598651
[4] Belokon Y, Hrechanyi O, Vasilchenko T, Krugliak D, Bondarenko Y. Development of new composite materials based on TiN-Ni cermets during thermochemical pressing. Results in Engineering. 2022; 16: 100724. https://doi.org/10.1016/j.rineng.2022.100724
[5] Sheyko S, Tsyganov V, Hrechanyi O, Vasilchenko T, Vlasov A. Mechanical property investigation of welded joints in 10HFTBch steel for the automobile wheel production. Materials Letters: X. 2023; 17: 100181. https://doi.org/10.1016/j.mlblux.2023.100181

[6] Patent No. 105341 Ukraine, IPC C22C38 / 28 (2006.01). Low-alloyed steel. Mishchenko VG, Belikov SB, Sheyko SP, and others. Published 04/25/2014, Bull. No. 8. - 5 p.

[7] Belikov S, Shalomeev V, Tsivirko E, Aikin N, Sheyko S. Microalloyed Magnesium Alloys with High Complex of Properties. Materials Science and Technology Conference and Exhibition 2017. 1, 2017; 84-91. https://doi.org/10.7449/2017/mst_2017_84_91

[8] Fernández J, Illescas S, Guilemany JM. Effect of microalloying elements on the austenitic grain growth in a low carbon HSLA steel. Materials Letters. 2007; 61(11-12): 2389-2392. https://doi.org/10.1016/j.matlet.2006.09.021

[9] Chen C, Sun M, Chen X, Wang B, Zhou J, Jiang Z. State of the Art in Control of Inclusions and Microalloying Elements in Tire Cord Steel and Saw Wire Steel. Steel Res. Int. 2021; 93(4): 2100507. https://doi.org/10.1002/srin.202100507

[10] Wang J, Li G, Xiao A. A Bainite-Ferrite Multi-Phase Steel Strengthened by Ti-Microalloying. Mater. Trans. 2011; 52(11): 2027-2031. https://doi.org/10.2320/matertrans.M2011009

[11] Ali IHM, Moustafa IM, Farid AM, Glodowski RJ. Improvement of Low Carbon Steel Properties through V-N Microalloying. Mater. Sci. Forum. 2005; 500-501: 503-510. https://doi.org/10.4028/www.scientific.net/MSF.500-501.503

[12] Lei Y, Li T, Su MY, Li C, Wang HY, Cong T, Dai LH. Adiabatic shearing in railway wheel steel of high-speed train. Materials Letters. 2023; 134168. https://doi.org/10.1016/j.matlet.2023.134168

[13] Zhang T, Wang Y, Zhang C, Wang L, Di H, Xu W. High cycle fatigue properties and fatigue crack propagation behavior of a bainite railway axle steel. International Journal of Fatigue. 2023; 107641. https://doi.org/10.1016/j.ijfatigue.2023.107641

[14] Belodedenko S, Hanush V, Hrechanyi O. Fatigue lifetime model under a complex loading with application of the amalgamating safety indices rule. Procedia Structural Integrity. 2022; 36: 182-189. https://doi.org/10.1016/j.prostr.2022.01.022

[15] Pavlenko DV, Belokon' YO, Tkach DV. Resource-Saving technology of manufacturing of semifinished products from intermetallic γ-TiAl alloys intended for aviation engineering. Materials Science. 55(6), 2020; 908-914. https://doi.org/10.1007/s11003-020-00386-1

[16] Sereda B, Sereda D, Belokon Y. Investigation of corrosion and oxidation of γ-TiAl alloys obtained in self propagating high temperature synthesis. Materials Science and Technology Conference and Exhibition. 2015; 2: 1249-1255.

[17] Sereda B, Kruglyak I, Kovalenko A, Sereda D, Vasilchenko T. The deformation zone geometrical factors and its influence on deformation shift degree for the axial zone of rolled high bars. Metallurgical and Mining Industry. 2011; 3(7): 102-106.

[18] Belodedenko SV, Hanush VI, Hrechanyi OM. Experimental Verification of the Survivability Model Under Mixed I+II Mode Fracture for Steels of Rolling Rolls. Structural Integrity. 2022; 25: 3-12. https://doi.org/10.1007/978-3-030-91847-7_1

[19] Shejko S, Sukhomlin G, Mishchenko V, Shalomeev V, Tretiak V. Formation of the Grain Boundary Structure of Low-Alloyed Steels in the Process of Plastic Deformation. Materials Science and Technology Conference and Exhibition 2018. 2018, 1, p. 746-753. https://doi.org/10.7449/2018/MST_2018_746_753

[20] Straumal BB, Mazilkin AA, Protasova SG, Gusak AM, Bulatov MF, Straumal AB, Baretzky B. Grain Boundary Phenomena in NdFeB-based Hard Magnetic Alloys. Rev. Adv. Mater. Sci. 2014; 1 (38): 17-28.

[21] Belodedenko SV, Hanush VI, Hrechanyi OM. Experimental Verification of the Survivability Model Under Mixed I+II Mode Fracture for Steels of Rolling Rolls. Structural Integrity. 2022; 25: 3-12. https://doi.org/10.1007/978-3-030-91847-7_1

[22] Sheyko S, Mishchenko V, Matiukhin A, Bolsun O, Lavrinenkov A, Kulabneva E. Universal Equation Of Metal Resistance Dependence To Deformation On Conditions Of Thermoplastic Processing. METAL 2021 - 30th Anniversary International Conference

on Metallurgy and Materials. 2021; 329-334. https://doi.org/10.37904/metal.2021.4121

[23] Malaurent JC, Duval H, Chauvineau JP, Hainaut O, Raynal A, Dhez P. In situ X-ray multilayer reflectometry based on the energy dispersive method. Optics Communications. 2000; 173 (1-6): 255-263. https://doi.org/10.1016/S0030-4018(99)00597-0

[24] Noskov VA, Bayul KV. Research of influencing of configuration of shaping elements on the tensely-deformed state and parameters of compression of fine-fractional charge. Metallurgicheskaya i Gornorudnaya Promyshlennost. 2005; 2: 104-108.

[25] Maksymova SV, Zvolinskyy IV, Ivanchenko EV. Influence of alloying elements on solidus and liquidus. Avtomatičeskaâ svarka. 2021; 8: 24-28. https://doi.org/10.37434/as2021.08.05

[26] Ogawa K, Seki A. Modeling of Effects of Temperature and Alloying Elements on Austenite Phase Growth Rate in Duplex Stainless Steel. ISIJ Int. 2019; 59(9): 1614-1620. https://doi.org/10.2355/isijinternational.ISIJINT-2018-869

[27] Bhadeshia HKDH, Svensson LE, Gretoft B. The influence of alloying elements on the formation of allotriomorphic ferrite in low-alloy steel weld deposits. J. Mater. Sci. Lett. 1985; 4(3): 305-308.https://doi.org/10.1007/BF00719798

[28] Lee CH, Bhadeshia HKDH, Lee HC. Effect of plastic deformation on the formation of acicular ferrite. Mater. Sci. Engineering: A. 2003; 360 (1-2): 249-257. https://doi.org/10.1016/S0921-5093(03)00477-5

Research Article

Studies on mechanical performance of treated and non-treated coarse recycled concrete aggregate and its performance in concrete-an Indian case study

P.N. Ojha[a], Puneet Kaura[b], Brijesh Singh*[,c]

Centre for Construction Development & Research, National Council for Cement and Building Materials, India

Article Info	Abstract
	In India, utilization of construction & demolition (C&D) waste-based coarse recycled concrete aggregate (CRCA) for RCC work is limited up to 20% for M25 grade of concrete as codified in IS 383:2016. However, enhanced utilization is not possible until classification based on quality grading of C&D waste-based aggregate is made available. One of the possible ways to classify C&D waste-based aggregate can be routed based on specific gravity and water absorption value of the parent rock which is generally affected by the adhered mortar. In the present study, C&D waste-based coarse recycled concrete aggregate (CRCA) sourced from two different sources was studied holistically. CRCA aggregates were subjected to mechanical treatment in a Los Angeles machine and Characteristics of CRCA before and after treatment were evaluated and compared. Further, a comparative study in fresh, hardened, and durability stages was conducted on the properties of concrete made with treated and non–treated CRCA. Fresh, hardened, and durability properties of concrete made with C&DW-based CRCA investigated for the (a) Fresh properties – workability in terms of slump, and air content. (b) Hardened properties–compressive and flexural strength, modulus of elasticity, drying shrinkage (c) Durability properties –resistance to chloride (RCPT, as per ASTM C1202), resistance to carbonation as per ISO 1920 Part 12 and resistance to water penetration as per IS 516 Part2 / Section-1. From the study, it can be concluded that physical properties such as specific gravity and water absorption of CRCA can be used as a tool for the grading of C&D waste-based CRCA. Based upon fresh, hardened, and durable behavior of concrete made with CRCA, it was observed that non-treated CRCA can be used up to 40 % for a grade of concrete up to M 30 whereas treated CRCA can be used up to 100 %. This was attributed to the improvement in the ITZ.

1. Introduction

Due to the non-availability of natural resources coupled with the rise in the demand for aggregates for infrastructural projects, the use of C&DW-based aggregate can serve the purpose. In India, about 30 million tonnes per year is the average rate of C&DW generation that accounts 20% to 25 % of Municipal solid waste (MSW) [1]. By utilizing C&DW-based aggregate, the demand for natural aggregates can be reduced, which is often obtained through resource-intensive mining processes. This reduces the strain on our environment and preserves natural resources for future generations. Additionally, the use of C&DW-based aggregate helps to decrease the amount of construction and demolition waste that ends up in landfills. Furthermore, incorporating RCA in construction projects reduces the

need for energy-intensive production processes associated with traditional aggregates. However, the use of C&DW-based aggregate for construction activities is limited due to inconsistency associated with the quality of the C&DW-based aggregates that require immediate attention. Various international codes recommend the use of C&DW-based recycled concrete aggregate (RCA) up to a certain replacement level of natural aggregates for structural and non-structural applications with a cautionary note [1-5]. Recycled concrete aggregate (RCA) is generally derived from crushed concrete and primarily consists of natural aggregate with a layer of mortar attached to its surface and a certain amount of foreign materials or impurities that affects the properties of the concrete as a whole [5,6]. Unlike natural aggregates, RCA also consists of micro cracks. To date, due to its inherent characteristics, utilization of RCA has not been optimized. Some of the critical issues associated with the utilization of RCA for structural activities are addressed below. The ITZ generally refers to the transition area between the mortar and aggregate and is sometimes termed an Aggregate –paste interface [7,8]. The microstructure of the ITZ is mainly composed of crystals of calcium hydroxide, calcium silicate hydrate, and ettringite with a higher water-cement ratio than that of mortar resulting loose structure [9, 10]. With high porosity and loose microstructure, ITZ becomes the weakest link in concrete. A weak ITZ is fundamental reason for the reduced macro-mechanical properties of the concrete. RCA with a surface coated with adhered mortar layers creates two types of Interfacial Transition zones; a) old ITZ and b) new ITZ as shown in Figure 1. The old ITZ exists between the old motor and natural aggregate making the concrete microstructure more fragile due to higher porosity and cracks, thus serving as the weakest link and resulting in lower compressive strength [8, 11-13] whereas new ITZ has been defined as an interface zone between new mortar and old mortar as well as between new mortar and aggregate. Numerous studies on the microstructure of the interfacial transition zone of concrete made with RCA conclude that the strength development and durability characteristics of concrete are primarily influenced by the composition of ITZ and its thickness [12-15]. RCA generally decreases compressive strength because of higher aggregate water absorption and an inferior layer of residual mortar [16, 17]. The performance of recycled aggregate containing 50% and 100 % recycled aggregate (RA) had been studied by Olorunsogo et al. [18] who found that RA decreases the resistance of concrete against chloride ingress thus making concrete susceptible to chloride-induced corrosion.
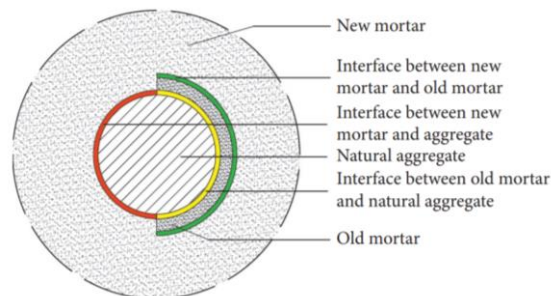
Fig. 1. Scanning electron microscope image of recycled concrete [8]

Overall durability indexes like sorptivity also increase with the addition of RA. A. Domingo et al. [19] found that concrete made with recycled aggregates has higher shrinkage strain and creep coefficient and lower modulus of elasticity in comparison to concrete made with natural aggregates. Otsuki et al. [20] investigated the influence of quality improvement techniques on RA. Properties like Vickers microhardness of ITZ including mechanical and durability performance of concrete were studied. From their study, it was observed that concrete made with recycled aggregates has lower resistance against chloride and CO_2 ingress due to the presence of old ITZ and adhered mortar. Even mechanical properties

were found to be inferior in recycled aggregate concrete. However, an improvement in mechanical and durability properties was seen in the case of treated aggregates. The test results also conclude that the quality of adhered mortar influences the characteristics of ITZ in a major way rather than its quantity. Zhang et al. [21] studied the ITZ of RCA under sulphate attack under alternate dry-wet cycles. The test results show that RCA offers lower resistance in comparison to concrete made with natural aggregate when subjected to external sulphate attack. Impurities or foreign materials present in an aggregate are those substances that result in detrimental effects on its performance in concrete. For instance, if present as a coating around the aggregates interferes with the bond characteristics, as a soft fragment can be considered as weak inclusion and may hinder the cement hydration process [22]. Excess amount of fines affects the workability of fresh concrete. Recycled concrete aggregate may contain foreign materials like metals, glass, soft fragments, clay lumps, bitumen, asphalt, filler (material finer than 75 um), ceramic material, wood, etc. [23, 24]. To avoid any damaging aftereffect due to presence of these foreign materials or impurities in RCA, it is desirable to limit their values, otherwise, their appearance will alter the concrete properties and decisively impact the long-term performance of concrete. For example, the presence of wood would generate voids [25] whereas the presence of metal like aluminum creates cracks and rock pockets within the concrete, thus diminishing its durability and mechanical properties [26]. As discussed above, the properties of concrete made with RCA are significantly affected by the adhered mortar layer. Therefore, it becomes of utmost importance to determine adhered mortar content in RCA. Since the direct estimation of adhered mortar content using techniques like Image analysis method (IAM) is time consuming and interpretation requires core-competency [27]. Therefore, eliminating techniques can be used as an indirect way for the quantification of adhere mortar content. Adhered mortar elimination from the RCA surface can be achieved through acid or mechanical treatment [28-30].

1.1. Research Significance

Fresh, hardened as well as durability properties of the concrete are chiefly influenced by the aggregate characteristics. According to the available literature, so far very limited work has been done to study these effects systematically as well as quantitatively in the case of construction & demolition (C&D) waste-based coarse recycled concrete aggregate (CRCA). In this paper, an attempt was made to study the use of C&DW based coarse recycled concrete aggregates (CRCA) available in our country for concrete production and its overall substitution level while replacing the natural aggregate. The study also investigated the impact of mechanical treatment over the characteristics of CRCA and its influence over concrete properties. The present study provides a comprehensive approach towards the utilization of C&DW- based coarse recycled concrete aggregates (CRCA) for structural work based on its physical characteristics which is presently not available in India.

2. Experimental Study

To achieve the aforementioned objectives, C&DW-based coarse recycled concrete aggregates (CRCA) from two different sources, one from the RCA plant in Delhi, India ,and the other produced through crushing of concrete samples at the laboratory were characterized for various physical and chemical parameters as per IS 383 [31] .Further, C&DW-based coarse recycled concrete aggregates (CRCA) were subjected to mechanical treatment where CRCA were exposed to more than 500 revolutions in a Los Angles abrasion test setup without any surcharge and physical properties like specific gravity ,water absorption, crushing value , abrasion value etc. were evaluated. Concrete mixes were designed at two water-to-cement ratios (0.45 and 0.65) with and without treated CRCA and detailed fresh, hardened, and durability properties of concrete were investigated. For the (a) Fresh properties – workability in terms of slump, and air content.

(b) Hardened properties – compressive and flexural strength, modulus of elasticity, drying shrinkage (c) Durability properties – drying shrinkage, resistance to chloride (RCPT, as per ASTM C1202 [32]) and chemical properties like acid & water-soluble chloride content as per IS 14959 Part 2 [33] as well as sulphate content as per IS 4032 [34]

2.1 Material Used

Portland Pozzalana Cement conforming to physical and chemical requirements of IS: 1489 Part 1(fly based) [35] was used and results are given in table 1. Natural coarse and fine aggregate conforming to IS-383 [31] was used and results are given in table 2. Fine aggregate with a water absorption value of 0.65 % and specific gravity as 2.65 has been used in the design of concrete mixes.

Table 1. Physical and chemical properties of cement

Sl.	Physical Properties	Results	Chemical properties	Results
1.	Fineness Blaine's (m2/kg)	356	Loss of Ignition (LOI) (%)	2.74
2.	Soundness by Autoclave (%)	0.06	Silica (SiO2) (%)	32.2
3.	Soundness by Le Chatelier (mm)	2	Iron Oxide (Fe2O3) (%)	3.57
4.	Setting Time Initial (minutes, min.)	155	Aluminium Oxide (Al2O3)	10.84
5.	Setting Time Initial (minutes, max.)	215	Calcium Oxide (CaO) (%)	43.42
6.	Compressive Strength, 72±1 hrs, MPa	24.55	Magnesium Oxide (MgO) (%)	1.35
7.	Compressive Strength, 168±2 hrs, MPa	32	Sulphate (SO3) (%)	2.15
8.	Compressive Strength, 672±4 hrs, MPa	43	Chloride (Cl) (%)	0.05
9.	Specific gravity	2.89	Insoluble Residue (%)	23.16

Table 3. Chemical properties of C&DW based coarse recycled concrete aggregates from RCA Plant, aggregates manufactured in laboratory

Sl. No	Characteristic	Results Obtained		
		RCA Plant, New Delhi (RCA –1)	Manufactured in lab (RCA–Lab)	Requirements of manufactured aggregate based on IS 383-2016
1	Total Alkali Content in terms of Na$_2$O equivalent, %	2.0	2.5	Maximum, 0.3%
2	Sulphate Content in terms of SO$_3$, %	0.13	0.16	Maximum 0.5%
3	Water soluble chloride Content, %	0.040	0.013	Maximum, 0.04%

C&DW-based coarse recycled concrete aggregate (CRCA): Two different sets of C&DW-based coarse recycled concrete aggregates (20mm and 10 mm), one set of aggregates from the RCA plant in Delhi, India, and another set of aggregates produced by crushing concrete samples with strength in compression around 25 MPa at laboratory and thereafter processed into different fractions were used in the study. Additionally, to study the quality grading of CRCA, two more sets of RCA samples of fractions 10 mm and 20mm were collected from RCA plant in Delhi, India. Some of the physical and chemical characteristics are given in Table 2 and Table 3 respectively.

2.2 Mix Design

The concrete mix design was carried out at two water to cement ratios i.e. 0.45 and 0.65. The natural coarse aggregates were replaced by CRCA by 20%, 40 %, and 100 % (by volume) for both set of aggregates. Naphthalene-based superplasticizer meeting IS 9103 [36] requirement was used to keep the workability in the range of 70-100 mm. Mixes were evaluated for fresh, mechanical and durability properties of concrete. The design mix was

carried out using aggregates in saturated surface dry condition under laboratory conditions of temperature of 27±2oC and relative humidity of 65±5%. The details of the design mix are given in Table 4. Demoulding of samples cast was done after 24 hours and thereafter curing was continued till test age.

Table 4. Concrete mix design

Sample ID	w/c	Mix Constituents		Recycled concrete aggregate in terms % of total aggregate (volume based)	Recycled concrete aggregate as % replacement to natural coarse aggregate (by Volume)	Dosage of Admixture % by weight of cement	Remarks
		Cement content kg/m³	Water Content kg/m³				
M1B20	0.65	280	180	60	20	0.70	
M1B40	0.65	280	180	60	40	0.70	
M1B100	0.65	280	180	60	100	0.80	
M1L20	0.65	280	180	60	20	0.70	
M1L40	0.65	280	180	60	40	0.70	
M1L100	0.65	280	180	60	100	0.70	Experimental Mixes
M2B20	0.45	378	170	65	20	1.00	
M2B40	0.45	378	170	65	40	1.00	
M2B100	0.45	378	170	65	100	1.10	
M2L20	0.45	378	170	65	20	1.00	
M2L40	0.45	378	170	65	40	1.00	
M2L100	0.45	378	170	65	100	1.00	
M1C	0.65	280	180	60	-	0.70	Control
M2C	0.45	378	170	65	-	1.00	Mix

Note: B: C&DW coarse recycled concrete aggregate obtained from RCA plant, New Delhi, Sample1, and L: C&DW coarse recycled concrete aggregate produced in laboratory by crushing concrete of around 25 MPa strength

Additionally, concrete mix design was also carried out with treated CRCA to assess their performance after the removal of adhered mortar. While doing mix design with mechanically treated C&DW-based coarse recycled concrete aggregates (CRCA), concrete mix proportioning as mentioned in table 4 including fine aggregate to coarse aggregate ratio, the dosage of admixture was kept same as that of concrete mix designed with non-treated C&DW-based CRCA. The fresh, hardened, and durability study was carried out on concrete mixes made with and without mechanically treated C&DW-based coarse recycled concrete aggregate (CRCA).

2.3 Test Conducted

The details of the hardened and durability properties studied are given in Table 5. Compressive strength and flexural strength were the two basic engineering properties tested by IS 516 Part 1/Sec1 [37] at 7, 28, and 56 days. The modulus of elasticity as well as the Poisson ratio was evaluated on a concrete cylinder (150mm (Φ) x 300mm (h)) at an age of 28 days by IS 516 Part 8 / Sec1[38]. For the determination of the Modulus of elasticity, extensometers were attached in the longitudinal directions of the concrete specimens, and the load was applied at a rate of 14 MPa/min. The basic stress (σb) equals one-ninth of the average cube compressive strength (Fc /9 MPa) was maintained for 60 seconds and strain gauge readings were measured. Thereafter, stress was increased at a constant rate of 0.20 MPa/s until the stress equals one-third of the average cube compressive strength (σa = Fc /3). The stress was maintained for 60 sec and strain gauge readings were measured. In the last, the load was reduced at the same rate as during loading to the level of the basic stress. This cycle of loading and unloading was carried out thrice and in the fourth cycle, the final reading of strains was measured. For the

determination of Poisson ratios, the loading as well as unloading cycle as mentioned for the Modulus of elasticity was kept the same, only the direction of extensometers was kept in the transverse directions of the specimens. The Modulus of elasticity (EC) and Poisson ratio (Pr) were calculated using the following equations

$$E_c = \frac{\sigma_a - \sigma_b}{\varepsilon_a - \varepsilon_b} \tag{1}$$

Where, σ_a is the upper loading stress, MPa

σ_a=F_c/3, σ_b is the basic stress=F_c/9, MPa

$$Pr = \frac{\Delta \ transverse \ strain}{\Delta \ longitudinal \ strain} \tag{2}$$

$$Pr= \frac{Transverse \ strain \ \sigma_a \ Transverse \ strain \ at \ \sigma_b}{Longitudinal \ strain \ at \ \sigma_a - Longitudinal \ strain \ at \ \sigma_b} \tag{3}$$

For the drying shrinkage test, 3 no's of concrete prism bars (75 mm x 75 mm x 300 mm) were cast as per IS 516 Part 6 [39]. The concrete specimens were cast as well as tested by the procedure given in IS 516 Part 6. After demoulding, concrete prism bars were stored in a controlled laboratory environment (Relative humidity = 65±5%, temperature = 27 ±2℃) for 7 days. After laboratory conditioning, concrete prism bars were immersed in water for up to an age of 28 days. At the age of 28 days, concrete specimens were removed from the water and initial readings were taken using a length comparator. Subsequently, concrete prism bars were placed in an oven maintained at a temperature of 50±1℃ and Relative humidity of 17±2% for 44 hours. At the end of drying, the length of each specimen was measured. This cycle of drying and measuring was repeated until a constant length was achieved. The Drying shrinkage was calculated using the following equation

$$Drying \ shrinkage(\%) = \frac{[Initial \ length \ (after \ curing) - Final \ length \ (after \ drying)]x100}{original \ effective \ gauge \ length} \tag{4}$$

A rapid chloride penetrability test was conducted in accordance with ASTM C 1202 at the age of 28 days. In this test, concrete discs (3 no's) of 100 mm diameter and 50 mm thickness were extracted from a concrete cylinder (100 mm (Φ) x 200mm (h)). The test specimen was sandwiched between two cells, one cell contained 3.0% NaCl solution and the other cell contained 0.1M NaOH solution. A 60 V DC potential difference was maintained across the ends of the test specimen for 6 hours. At the end of the test, the total charge passed was measured and an average of the three specimens was reported as the test value.

Table 5. Details of casting and test conducted

Sl.	Test and specimen type	Dimension of specimen (mm)	Test age	Test method
1	Compressive strength on Cube	150 x150 x 150	7, 28 and 56 days	IS 516 Part1 / Sec1 [37]
2	Flexural strength on beam	100 x 100 x 500	7, 28 and 56 days	IS 516 Part1 / Sec1 [37]
3	Modulus of Elasticity and Poisson Ratio on cylinder	150 (Φ) x 300 (h)	28 days	IS 516 Part 8 /Sec1 [38]
4	Drying shrinkage on beam	75 x75 x300	28 days	IS 516 Part6 [39]
5	RCPT on cylinder	100 (Φ) x 200 (h)	28 days	ASTM C1202 [32]

Table 2. Physical Properties of Natural and C&DW based coarse recycled concrete aggregates (CRCA)

S. No.	Test Conducted		Natural Aggregate		RCA Delhi Plant – Sample 1		RCA Delhi Plant–Sample 1 (after 500 Revolution treatment without charge in Los Angeles machine)		RCA Delhi Plant – Sample 2		RCA Delhi Plant–Sample 2 (after 500 Revolution treatment without charge in Los Angeles machine)		RCA Delhi Plant – Sample 3		RCA Delhi Plant–Sample 3 (after 500 Revolution treatment without charge in Los Angeles machine)		RCA lab (as crushed)		RCA lab (after 500 Revolution treatment without charge in Los Angeles machine)	
					RCA/B1/20	RCA/B1/10	RCA/B1/20/500R	RCA/B1/10/500R	RCA/B2/20	RCA/B2/10	RCA/B2/20/500R	RCA/B2/10/500R	RCA/B3/20	RCA/B3/10	RCA/B3/20/500R	RCA/B3/10/500R	RCA/lab/20	RCA/lab/10	RCA/lab/20/500R	RCA/lab/10/500R
1	Sieve results	% Passing	20 mm	10 mm	20 mm	10 mm	20 mm	10 mm	20 mm	10 mm	20 mm	10 mm	20 mm	10 mm	20 mm	10 mm	20 mm	10 mm	20 mm	10 mm
		20 mm	98	100	93	100	98	100	98	100	100	100	100	96	100	100	97	100	100	100
		10 mm	16	97	2	74	15	85	3	90	15	95	13	85	20	90	6	77	24	100
		4.75 mm	2	14	1	6	9	6	0	20	3	20	1	15	4	18	1	6	0.63	15
		2.36 mm	-	3	0	0	-	2	0	5	0	4	0	8	0	10	-	-	-	5
2	Total Deleterious content (%)		0	0	0.15	0.15	0.15	0.15	-	-	-	-	-	-	-	-	0.05	0.05	-	-
3	Specific Gravity		2.81	2.80	2.39	2.37	2.48	2.44	2.33	2.32	2.42	2.40	2.52	2.42	2.55	2.44	2.37	2.35	2.40	2.37
4	Water absorption %		0.40	0.40	4.58	4.75	3.87	3.93	5.10	5.40	4.10	4.30	3.70	3.73	3.30	3.40	4.41	4.43	4.16	4.28
5	Soundness test (Na$_2$SO$_4$),%		2.20	-	0.13	-	-	-	2.80	-	-	-	-	-	-	-	0.72	0.46	-	-
6	Abrasion value %		23.0	-	24.0	22.0	25.0	25.0	35.0	-	-	-	23.0	22.0	-	-	24.0	23.0	20.0	24.0
7	Crushing Value %		18.0	-	25.0	26.0	27.0	23.0	29.0	-	-	-	24.0	27.0	-	-	22.0	22.0	25.0	26.0
8	Impact Value %		21.0	-	20.0	17.0	20.0	20.0	25.0	-	-	-	24.0	22.0	-	-	23.0	21.0	23.0	20.0
9	Combined flakiness and Elongation Index %		19.0	-	15.8	20	18.8	18.2	17.0	-	-	-	-	-	-	-	21.3	29.6	19.6	23.3
10	Foreign Material, %		-	-	Nil	Nil	Nil	Nil	Nil	-	-	-	-	-	-	-	Nil	Nil	Nil	Nil

Note - "-" not tested

Apart from the above tests, the concrete mixes made with CRCA were also tested for pH, acid & water-soluble chloride content, and water-soluble sulphate content. The pH was measured using a pH meter. Acid and water-soluble chloride content was determined as per IS 14959 Part 2 [33] whereas water-soluble sulphate content was measured in accordance with IS 4032 [34].

3. Results and Discussion

3.1 Comparison of Physical and Chemical Characteristics of C&DW Based Coarse Recycled Concrete Aggregate (CRCA) Before and After Mechanical Treatment

Purushothaman *et al.* [28] classified various techniques as well as approaches to improve the quality of C&D waste-based concrete aggregate. It was suggested either to remove the adhered mortar in recycled concrete aggregates or to improve the quality of the adhered mortar through surface coating etc. Preliminary tests were carried out at 100, 200, and 500 revolutions in Los Angeles abrasion testing machine. It was found that mechanical treatment without any loading charge at 500 revolutions had given the best results (Table 2 & figure-2). These test results were also supported by the work done by other researchers [40]. Improvement in properties of CRCA such as specific gravity and water absorption after treatment was observed when compared with untreated CRCA.

RCA/ 20 mm Delhi plant

RCA/ 10 mm Delhi plant

RCA/ Lab/ 20 mm

RCA/Lab/ 10mm

RCA/ 20 mm Delhi plant after 500 revolutions

RCA/ 10 mm Delhi plant after 500 revolutions

RCA/ Lab/ 20 mm after 500 revolutions

RCA/Lab/ 10mm after 500 revolutions

Los Angeles Abrasion testing Machine
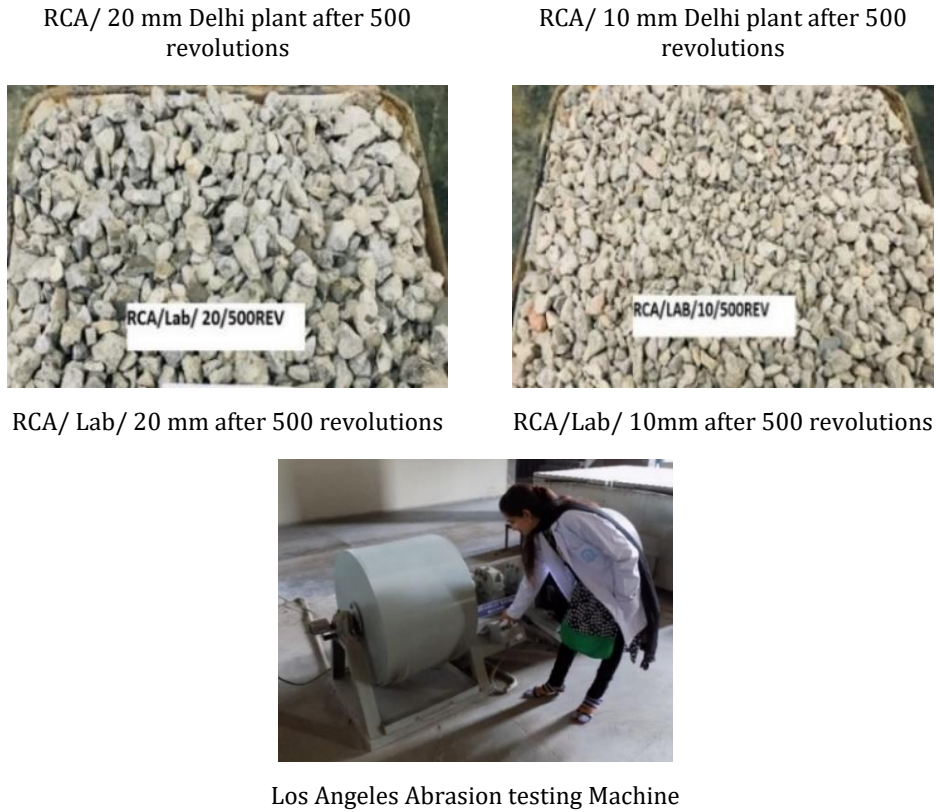
Fig. 2 C&DW based coarse recycled concrete aggregate (CRCA) from Delhi Plant as well as manufactured in Lab before and after mechanical treatment in Los Angeles abrasion testing machine

Table 6. Percentage change in specific gravity of as received and mechanically treated recycled concrete aggregate

Type of C&DW based coarse recycled aggregate	As received aggregate	Specific gravity Treated aggregate (After 500 revolution in Los Angeles machine without any charge)	Increase in specific gravity	% Increase in specific gravity over as received recycled concrete aggregate
RCA/B1/20	2.39	2.48	0.09	3.8
RCA/B1/10	2.37	2.44	0.07	3.0
RCA/B2/20	2.33	2.42	0.09	3.9
RCA/B2/10	2.32	2.40	0.08	3.4
RCA/B3/20	2.52	2.55	0.03	1.2
RCA/B3/10	2.42	2.44	0.02	0.8
RCA/lab/20	2.37	2.40	0.03	1.3
RCA/lab/10	2.35	2.37	0.02	0.9

$$\% \ Increase \ in \ specific \ gravity = \frac{(S.G.TA - S.G.AR) * 100}{S.G \ AR} \qquad (5)$$

Where, S.G.TA= specific gravity of treated recycled concrete aggregate (After 500 revolution in los Angeles machine without any charge), S.G.AR= specific gravity of as received recycled concrete aggregate

Some of the distinct qualities of C&DW-based coarse recycled concrete aggregate (CRCA) include water absorption, specific gravity /dry density, and porosity. These properties are primarily influenced by the quality as well as quantity of the adhered mortar content over

the parent aggregate. From Table 2, it was observed that the sieve gradation of CRCA fulfils the requirement of IS 383:2016. A slight refinement in the gradation was observed in the mechanically treated coarse recycled concrete aggregate (CRCA) over non- treated coarse recycled concrete aggregate (CRCA) which was found in line with the results reported by Babu et al. [40]. The total deleterious content in all the CRCA samples was found to be less than 2 % i.e. within the permissible limit as defined in IS 383:2016.

The percentage increase in specific gravity was in the range of 0.80 % to 3.4% for 10 mm aggregate, with an average increase of 2.4% in specific gravity observed for RCA from the Delhi plant, and 0.9 % for crushed RCA manufactured in a lab. For 20 mm aggregate, an increase of 1.3 % in specific gravity was observed for crushed RCA manufactured in the lab, and 3.0 % for the RCA obtained from the Delhi plant. The results of specific gravity support removal of the adhered mortar after 500 revolutions without any loading charge in the Los Angeles machine.

Table 7. Percentage Change in water absorption of as received and mechanically treated recycled concrete aggregate

Type of C&DW based coarse recycled aggregate	Water absorption (%)		Reduction in water absorption	% Reduction in water absorption over as received recycled concrete aggregate
	As received aggregate	Treated Aggregate (for more than 500 revolution without any charge in los Angeles machine)		
RCA/B1/20	4.58	3.87	0.71	15.50
RCA/B1/10	4.75	3.93	0.82	17.26
RCA/B2/20	5.10	4.10	1.00	19.61
RCA/B2/10	5.4	4.30	1.10	20.37
RCA/B3/20	3.70	3.30	0.40	10.81
RCA/B3/10	3.73	3.40	0.33	8.85
RCA/lab/20	4.41	4.16	0.25	5.67
RCA/lab/10	4.43	4.28	0.15	3.39

$$\% \, Reduction \, in \, water \, absorption = \frac{(WA.TA - WA.AR) * 100}{WA.AR} \tag{6}$$

Where, WB.TA= Water absorption of treated recycled concrete aggregate (more than 500 revolution without any charge in Los Angeles machine), WB.AR= Water absorption of as received recycled concrete aggregate

For 10 mm aggregate obtained from the RCA plant, a percentage reduction in the water absorption was found in the range of 3.39 % to 20.37%, with an average reduction of 15.50 % whereas in the case of RCA manufactured in the lab, a reduction in the water absorption was found to be 3.39%. For 20 mm aggregate, the percentage reduction in water absorption value was observed as 5.67 % for crushed RCA manufactured in lab, and 15.30% (average) for the RCA obtained from the Delhi plant. The results of water absorption also support removal of the adhered mortar after 500 revolutions without any charge in a Los Angeles machine which was found in line with the results reported by Babu et al. [40]. The abrasion, impact, and crushing value test on CRCA conforms to a maximum limit of 30 % as per IS: 383 for concrete structures subjected to wearing. The value of the combined flakiness and elongation index was between 15-25 % and it also conforms to IS: 383 requirements. From the chemical results as given in table 3, it was observed that none of the C&DW-based coarse recycled aggregates (CRCA) complied with the total alkali requirements of IS 383 because of existence of the adhered mortar whereas other chemical parameters like chloride content and sulphate content were found to be within the permissible limits.

3.2 Fresh Concrete Properties

Freshly prepared concrete was evaluated in terms of workability and air content as per IS 1199 Part 2 [41] and IS 1199 Part 4 [42] respectively. Test results of fresh concrete properties are given in table 8.

Table 8. Fresh properties – workability (slump) and air content

Sl. No.	Specimen ID	w/c ratio	Aggregate replacement %	Slump (mm)	Air content (%)	Slump (mm)	Air content (%)
				With non–mechanically treated C&DW based CRCA		With mechanically treated C&DW based CRCA	
1	M1C	0.65	-	95	1.80	-	-
2	M2C	0.45	-	100	2.00	-	-
3	M1B20	0.65	20	90	1.90	100	1.80
4	M1B40		40	85	2.10	90	2.00
5	M1B100		100	75	2.30	80	2.10
6	M2B20	0.45	20	85	2.20	95	2.00
7	M2B40		40	80	2.30	85	2.10
8	M2B100		100	70	2.50	85	2.20
9	M1L20	0.65	20	95	2.00	100	1.80
10	M1L40		40	90	2.10	90	1.90
11	M1L100		100	80	2.30	95	2.10
12	M2L20	0.45	20	85	1.90	95	1.90
13	M2L40		40	80	2.30	100	2.00
14	M2L100		100	75	2.50	90	2.20

From the earlier studies [43,44], it was established that the presence of adhered mortar in C&DW-based coarse recycled concrete aggregate (CRCA) not only leads to a loss in workability but also increases the air content value. In the present study, when natural aggregates were replaced with C&DW-based coarse recycled concrete aggregate (CRCA) at various replacement levels, a reduction in the consistency of fresh mixes was observed. This was probably due to higher water absorption of CRCA in comparison to natural aggregate. In addition to high water absorption value, its grain shape and texture as reported in past studies were also responsible for loss of workability [43, 45-48]. By using saturated surface dry recycled aggregate, the consistency of the concrete mixes made with or without C&DW-based coarse recycled concrete aggregate (CRCA) did not differ that much, and the same was supported by the test results as given in Table 8. The concrete mixes made with 100 % C&DW-based coarse recycled concrete aggregate (CRCA) showed the highest degree of workability loss. It should be noted that concrete mixes with or without mechanically treated C&DW-based coarse recycled concrete aggregate (CRCA) were designed at the same admixture dosage as that of the corresponding control mix. The air content in the concrete mixes prepared from C&DW-based coarse recycled concrete aggregate was found to be 5-25 % higher than that of the control mix. Based on the observation, it can be concluded that the admixture requirement in the concrete mixes prepared with C&DW-based coarse recycled concrete aggregate (CRCA) may be slightly higher to achieve the same level of slump as that of the control mix. In the case of concrete mixes made with treated C&DW-based coarse recycled concrete aggregate (CRCA), an improvement in the workability, as well as air content value was observed. This improvement in the fresh properties of the concrete made with treated C&DW-based coarse recycled concrete aggregate may be due to refinement in the water absorption value, due to the removal of the adhered mortar during the mechanical treatment. Such improvement in the fresh properties due to the removal of the adhered mortar was also reported by Lavado et al.[43], Poon et al. [47] and Faleschini et al . [48].

3.3 Results of Mechanical Performance in Concrete

Concrete mixes made with non-treated C&DW- based coarse recycled concrete aggregate (CRCA) and mechanically treated C&DW- based coarse recycled concrete aggregate (CRCA) were evaluated for physical parameters like compressive strength, modulus of elasticity; and Poisson ratio. The quality of aggregate in terms of its physical properties governs the strength of concrete [49, 50]. In most of the reported studies, researchers found that the addition of CRCA in concrete reduces compressive strength because of higher aggregate water absorption, and inferior quality of the adhered mortar layer [7, 51-53]. The formation of double ITZ also weaken the concrete [3-6]. On the perusal of the test results, as shown in Fig. 3 and Fig. 4, it was observed that the compressive strength of the concrete mixes made with C&DW- based coarse recycled concrete aggregate (CRCA) was significantly affected by the w/c ratio. From fig. 3, it was observed that when natural aggregate was replaced with non-treated CRCA aggregate up to 40 %, the 7-day compressive strength of concrete mixes with made non- treated C&DW coarse recycled concrete aggregate (CRCA) was slightly higher or at par in comparison to control mix whereas compressive strength of all concrete mixes made with treated C&DW coarse recycled concrete aggregate (CRCA) was higher than that of control mixes. From Fig 4., it was noticed that at 28 days, concrete mixes designed at 0.65 w/c with non- treated C&DW coarse recycled concrete aggregate (CRCA) up to 40%, compressive strength of the mixes was found comparable to that of the control mix. However, the compressive strength of concrete mixes designed at lower w/c of 0.45 with non-treated C&DW coarse recycled concrete aggregate (CRCA), irrespective of replacement percentage was lower than that of the control mix. In case of treated C&DW coarse recycled concrete aggregate (CRCA), the compressive strength of concrete mixes designed with treated CRCA up to 40 % was at par to the control mixes.

Fig. 3. Compressive strength of 7 days matured concrete mixes made with treated and non –treated C&DW-based coarse recycled concrete aggregate (CRCA

According to existing international codes and standards [3], about 20% to 60 % of the coarse recycled concrete aggregate (CRCA) is allowed to be used for structural application depending upon its properties like water absorption, specific gravity, etc. Studies reported by Tam et al. [3], Seara et al. [7,], and Silva et al. [52,53] indicate a general declining trend in the compressive strength value with the increase in the replacement level of natural aggregate with recycled concrete aggregate (RCA) due to the formation of double ITZ. However, some of the studies also report that it is possible to develop concrete with RCA with a strength equivalent to that of conventional mixes. This is possible only if the moisture condition of RCA is controlled [17]. In the present study, the moisture level of CRCA aggregates was controlled by the use of saturated surface dry recycled aggregate in concrete mix design. Based on the available data and present experimental results, it can be observed

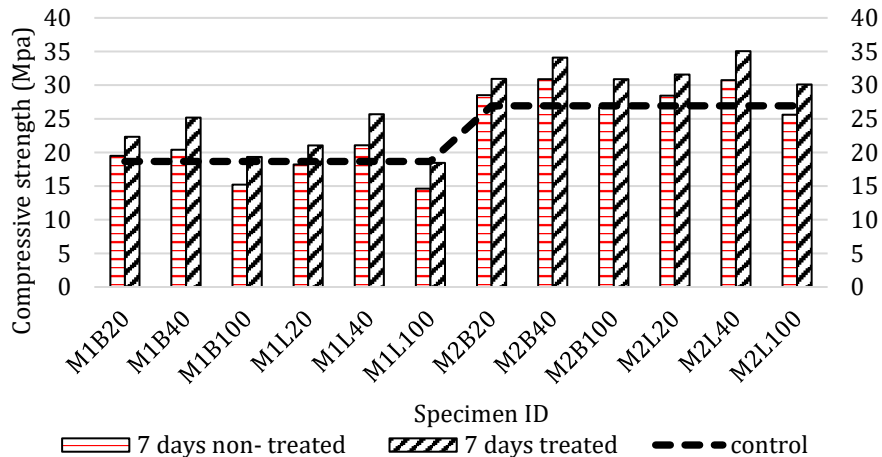that natural coarse aggregate can be replaced with coarse recycled concrete aggregate (CRCA) up to 40%.
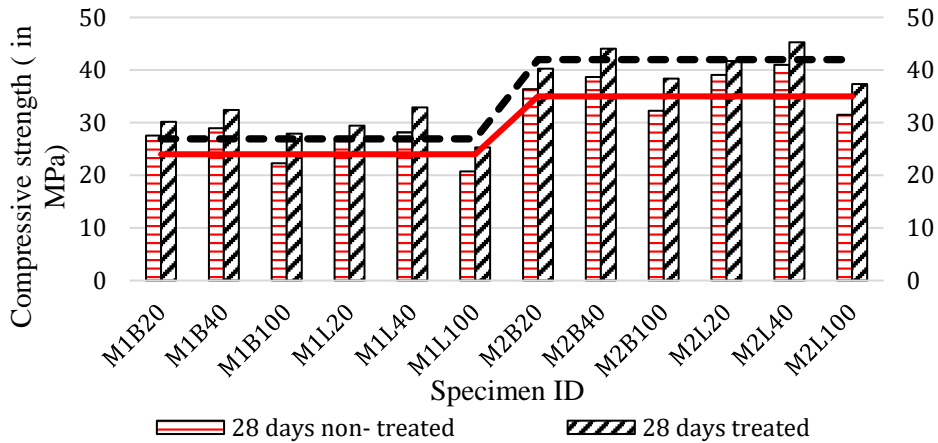
Fig. 4 Compressive strength of 28 days matured concrete mixes made with treated and non –treated C&DW-based coarse recycled concrete aggregate (CRCA)

Test results shown in Fig. 4. and Fig. 5., indicate that the quality of non-treated C&DW-based coarse recycled concrete aggregate (CRCA) obtained from the RCA plant or manufactured in the laboratory was not good enough to design concrete mixes that can perform equivalent to that of the concrete mix made with natural aggregates at lower w/c i.e. 0.45. Indeed, the strength obtained by using C&DW-based coarse recycled aggregate (CRAC) was lower in comparison to the control mix which was in line with the result reported by the various researchers [7, 51, 54]. However, concrete mixes made with C&DW coarse recycled aggregate up to 40 % can qualify the requirement to be accepted as per site condition which was in accordance with the site acceptance criteria of IS 456 [55] i.e. acceptance criteria for concrete mixes designed at 0.65 w/c which is equivalent to M20 grade of concrete and 0.45 w/c which is equivalent to M30 grade of concrete is 24 MPa and 34 MPa respectively as per IS 456(i.e. Fck +4). From Table 9, it was observed that concrete made with C&DW-based coarse recycled concrete aggregate either sourced from the RCA plant or manufactured in the laboratory by crushing concrete cube samples after treatment in Los Angeles abrasion machine shows significant improvement in strength at 7 days as well as 28 days in comparison to concrete produced from non-treated C&D waste aggregates which were in line with results reported by Purushotham et al.[28], Saravanakumar et al [56], Verma et al. [57]

From the fig. 5, it can be seen that concrete mixes designed with mechanically treated C&DW-based coarse recycled concrete aggregate at a lower w/c ratio of 0.65 can completely replace natural aggregates. However, concrete mixes designed with mechanically treated C&DW-based coarse recycled concrete aggregate at a lower w/c ratio of 0.45 can replace natural aggregates up to 40 %. Concerning the IS 456 acceptance criteria as discussed above for different grades of concrete, natural coarse aggregates can be replaced completely with mechanically treated C&DW-based coarse recycled concrete aggregates (CRCA). C&DW-based coarse recycled concrete aggregate (CRCA) after mechanical treatment will have an improved microstructure which is the result of loss in the quantity of adhered mortar. With the removal of adhere mortar possibility of the formation of double ITZ gets minimized and C&DW aggregates will act like parent rock [58]. The percentage improvement in the 28 days' strength of concrete mixes made with mechanically treated C&DW aggregates over non–treated C&DW coarse recycled concrete aggregate (CRCA) was found in the range of 6.78 % to 18.97 %, refer to Table 9 and maximum improvement in strength characteristics has been noticed in concrete mixes designed with 100 % C&DW coarse recycled concrete aggregate.

Table 9.   Percentage increase in compressive strength of concrete mixes made with mechanically treated C&DW aggregates over non –treated C&DW coarse recycled concrete aggregate

Specimen ID	M1 B20	M1 B40	M1 B100	M2 B20	M2 B40	M2 B100	M1 L20	M1 L40	M1 L100	M2 L20	M2 L40	M2 L100
At 7 days	14.52	23.49	27.15	8.52	10.36	15.77	15.53	21.83	26.2	11.04	13.98	17.62
At 28 days	9.51	12.03	25.26	10.67	13.85	18.97	9.12	16.7	22.15	6.78	10.49	18.50
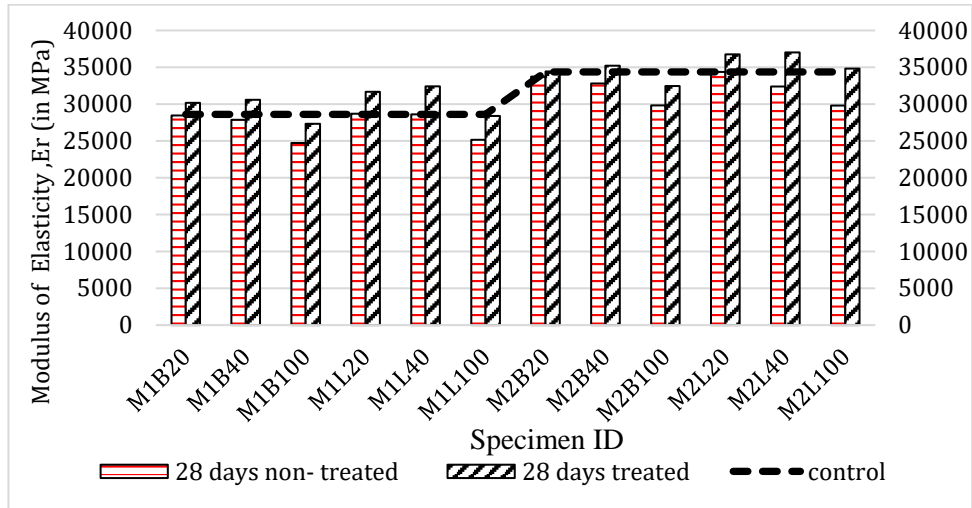
Fig. 5. Modulus of elasticity of 28 days matured concrete mixes made with mechanically treated and non –treated C&DW-based coarse recycled concrete aggregate (CRAC)

Research suggests that the modulus of elasticity of concrete was influenced by the type and amount of coarse aggregate within concrete [40, 59-66]. In fact, a 20 % reduction in the modulus of elasticity (MOE) was observed in concrete made with recycled coarse aggregate (RCA) in comparison to concrete made with natural coarse aggregate. Also, it was noteworthy to observe that up to 30 MPa strength, the difference in modulus of elasticity between recycled aggregate concrete (RCA) and conventional concrete was almost negligible, while on the other hand, for concrete with strength value more than 30 MPa, the difference between the subjected modules was increased [64-68]. The modulus of elasticity of the control mixes i.e. M1C and M2C was 28605 MPa and 34364 MPa respectively. From our study, as shown in Fig. 5, it can be observed that with the increase in the substitution level of C&DW aggregates, there was a decrease in the modulus of elasticity value. A significant reduction in MOE value in the range of 12-14 % was observed for concrete made at 100 % replacement level of natural aggregate with non –treated CRCA. However, up to 40 % replacement level of natural aggregate with non –treated CRCA, MOE values were comparable to that of the control mix. This finding was found in line with the results reported by Silva et al [69] where they had observed that replacement of the natural aggregate with recycled concrete aggregate (RCA) up to 30 % had minimal effect on the MOE value. In some of the concrete mixes made with 40 % C&DW coarse RCA i.e. M2B40, M2L40, a slight reduction in MOE value in the range of 3-5 % was observed with respect to the control mix which seems to be reasonable in comparison to 14% reduction observed. The modulus of elasticity (MOE) of concrete mixes made with treated C&DW-based coarse recycled concrete aggregates (CRCA) was found to be higher than that of control mixes. The test results of the compressive strength and MOE of concrete mixes made with or without treated C&DW-based coarse recycled concrete aggregates (CRCA) showed a constitutive relationship. The Poisson ratio test was conducted in accordance with IS 516-part 8 Section 1 on a set of concrete cylinder specimens. From Table 10, no conclusive inference was drawn from Poisson's ratio results. The Poisson ratio value of treated and non-treated C&DW coarse recycled concrete

aggregate was found to be in the range of 0.110 to 0.0127 which was in line with the reported range of 0.10-0.20 in Euro code 1992 [64-76]

Table 10. Poisson Ratio of concrete mixes made with mechanically treated and non –treated C&DW coarse recycled concrete aggregate

Specimen ID	M1 B20	M1 B40	M1 B100	M2 B20	M2 B40	M2 B100	M1 L20	M1 L40	M1 L100	M2 L20	M2 L40	M2 L100
28 days non-treated	0.113	0.110	0.115	0.105	0.109	0.107	0.12	0.128	0.121	0.124	0.121	0.112
28 days treated	0.118	0.115	0.106	0.111	0.115	0.115	0.123	0.129	0.127	0.126	0.126	0.121

3.4 Test Results of Durability Properties

The durability of concrete is a prime parameter in the service life design of concrete structures and is generally measured through performance-based tests. The concrete mixes made with non-treated C&DW-based coarse recycled concrete aggregate (CRAC) and mechanically treated C&DW-based coarse recycled concrete aggregate (CRAC) were tested for Rapid chloride penetrability test and drying shrinkage test. Since C&DW-based coarse recycled concrete aggregate (CRAC) was porous in nature due to the presence of adhered mortar. Therefore, it was expected that the permeability of such type of concrete mixes would be more than natural aggregate. The test results of RCPT are shown in Fig. 6. In general, RCPT values for the concrete made at 0.45 w/c were found to be in the category of low chloride ion penetrability class as defined in ASTM C1202 whereas concrete made at 0.65 w/c, falls in moderate category. The test results shown in Fig 6., showed that the amount of charge passed through the concrete increases in proportion to the substitution percentage of natural coarse aggregate with C&DW -based coarse recycled concrete aggregate (CRAC).

The chloride ion penetrability class of concrete made with and without mechanically treated C&DW- based coarse recycled concrete aggregate (CRAC) was found to be the same for all the replacement levels except for 100 % substitution. They also correspond to the same chloride ion penetrability class as that of control mix. However, concrete made with 100 % treated as well as non-treated C&DW-based coarse recycled concrete aggregate (CRAC) shows the least resistance against chloride ion penetration in comparison to other replacement levels and 20 % and 40 % in terms of charge passed. Even concrete mixes made with 100 % C&DW-based coarse recycled concrete aggregate perform miserably when compared to the control mixes. The performance of the concrete mixes made with treated and non-treated C&DW-based coarse recycled concrete aggregate (CRAC) up to the replacement level of 40 % against chloride ingress was comparable to that of control mixes. The reduction in the charge passed was observed in the case of concrete mixes made with mechanically treated C&DW-based coarse recycled concrete aggregate (CRAC) over concrete mixes made with non-treated C&DW-based CRAC. This reduction was found to be in the range of 6-14 % at 20 % replacement level, 19-37 % at 40 % replacement level, and 33-36 % at 100 % replacement level. It indicates with the removal of adhered mortar the quality of C&DW-based coarse recycled concrete aggregate improves and it offers better against chloride attack.

A drying shrinkage test was conducted on a hardened concrete prism bar of dimension 75x75x300 mm at 28 days in accordance with IS 516 Part6. The drying shrinkage values of control mixes M1C and M2C were 0.0250 % and 0.0182% respectively. From Table 11, it can be observed that the drying shrinkage value of hardened concrete mixes made by non-treated C&DW-based coarse recycled concrete aggregate (CRCA) was quite high in comparison to the corresponding control mix.
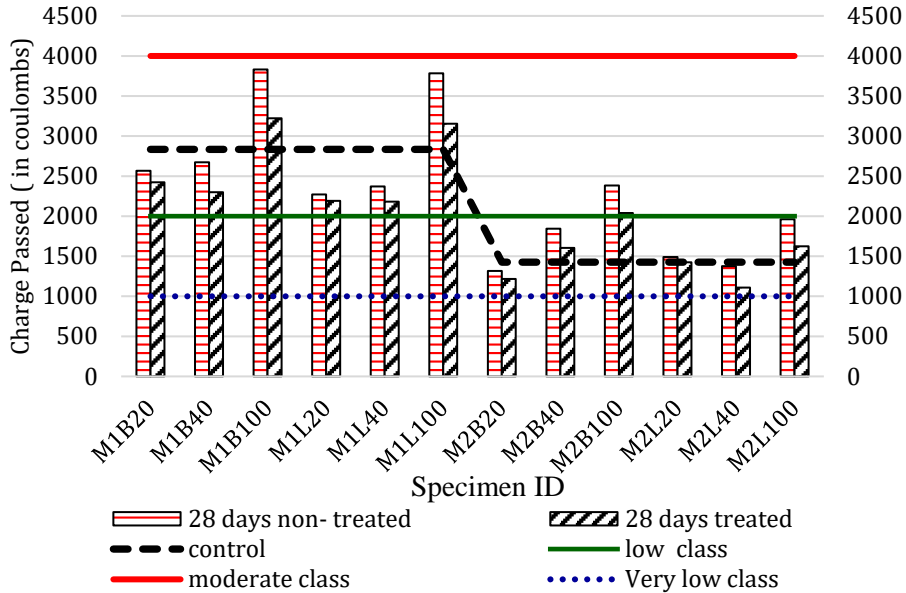
Fig. 6. Rapid chloride penetrability test (RCPT) of concrete mixes made with mechanically treated and non –treated C&DW-based coarse recycled concrete aggregate (CRAC)

Even the effect of the w/c ratio on shrinkage value was found to be quite prominent i.e. concrete mix designed at 0.45 w/c had lower shrinkage value in comparison to concrete mix designed at 0.65 w/c. The shrinkage value of concrete mixes prepared with treated and non-treated C&DW-based coarse recycled concrete aggregate (CRCA) up to a replacement level of 40 % was found to be comparable to the control mixes. At 100 % replacement level, the shrinkage percentage found to be in the range of 0.0273 % to 0.0340% which seems to be very high when compared to control mixes. However, a 4-15 % decrease in shrinkage was noticed in the case of concrete made with mechanically treated CRCA over non –treated CRCA but still shrinkage percentage was found to be high in comparison to the corresponding control mix at 100% replacement. The finding of the durability test results i.e. RCPT and drying shrinkage so obtained were in line with the study reported by various researchers [53, 77-82].

Additionally, certain concrete mixes made with non-treated C&DW-based coarse recycled concrete aggregate (CRCA) obtained from the RCA plant and manufactured in the laboratory were also tested for chemical parameters like pH, acid & water -soluble chloride content, and water-soluble sulphate content. The pH, chlorides and sulphate tests were conducted on 28 days of matured concrete samples and at various replacement levels. Table12 represents chemical results of pH, chloride, and sulphate conducted on concrete samples. The pH level at all replacement levels was observed in concrete mixes prepared with C&DW-based coarse recycled concrete aggregate (CRCA). This increase in chloride and sulphate content value may be attributed to the presence of adhered mortar which is rich in chlorides as well as sulphates.

The results of chlorides and sulphates present in the aggregates were discussed in 3.1.2. Indeed, the value of water-soluble sulphate content in concrete mixes made with non-treated C&DW-based coarse recycled concrete aggregate (CRCA) was very high in comparison to control mix but found to be within the permissible limit of 4 % by mass of cement as per IS 456 i.e. 0.86% to 3.34 % by mass of cement.

Table 11. Drying shrinkage of hardened concrete mixes made with mechanically treated and non –treated C&DW coarse recycled concrete aggregate

Specimen ID	M1 B20	M1 B40	M1 B100	M1 L20	M1 L40	M1 L100	M2 B20	M2 B40	M2 B100	M2 L20	M2 L40	M2 L100
28 days non-treated	0.0269%	0.0260%	0.0340%	0.0240%	0.0262%	0.0308%	0.0193%	0.0173%	0.0285%	0.0186%	0.0176%	0.0273%
28 days treated	0.0248%	0.0230%	0.0296%	0.0230%	0.024%	0.0269%	0.0185%	0.0156%	0.0240%	0.0174%	0.0153%	0.0230%

The acid-soluble chloride content in concrete mixes made with non-treated C&DW-based coarse recycled concrete aggregate (CRCA) was almost double in comparison to the control mixes. The value of water-soluble chloride content was found in the range of 0.480 to 0.960 kg/m^3 whereas acid soluble chloride content was found in the range of 0.816 to 1.512 kg/m^3. Various researchers have suggested chloride a threshold value between 0.9 to 1.2 kg/m^3 or 0.3% by mass of cement for the initiation of corrosion [62,63]. In the present study, concrete mixes made with non-treated C&DW based coarse recycled concrete aggregate (CRCA) exhibit a higher value than threshold value. Therefore, it is suggested to conduct a corrosion test to further examine the performance of concrete mixes made with C&DW-based coarse recycled concrete aggregate with respect to chloride-induced corrosion.

Table 12. Chemical results

Specimen ID	pH	Chlorides (in kg/m³)		Sulphates (%) by mass of cement
		Water soluble	Acid soluble	
M1C	12.26	0.480	0.572	1.03
M2C	12.35	0.408	0.592	0.95
M1B20	12.27	0.816	1.440	2.31
M1B40	12.30	0.744	1.512	2.57
M1B100	12.33	0.840	1.320	3.34
M2B20	12.29	0.960	1.152	2.03
M2B40	12.24	0.672	1.272	1.52
M2B100	12.26	0.792	1.176	1.65
M1L20	12.32	-	-	-
M1L40	12.22	-	-	-
M1L100	12.27	0.480	0.816	0.86
M2L20	12.26	0.624	1.200	0.95
M2L40	12.32	0.576	1.032	1.08
M2L100	12.35	0.635	1.215	-

Note "-" Not tested

4. Conclusion

The test results of fresh, hardened, and durability characteristics of concrete made with C&DW-based coarse recycled concrete aggregate (CRCA) either obtained from the RCA plant or manufactured at a Laboratory demolished building indicates that it is not possible to completely replace the natural coarse aggregate with CRCA for structural works. The quality of aggregate plays a significant role; therefore, it becomes prerogative to evaluate the quality of C&DW-based coarse recycled concrete aggregate before producing any type of concrete. Following are the board findings of the study

- A mechanical treatment method involving 500 revolutions in a Los Angeles machine without any charge can be used as a technique for the quality improvement of the

C&DW-based coarse recycled concrete aggregate (CRCA). From the test results, it was observed that the physical properties of the coarse recycled concrete aggregate (CRCA) such as specific gravity and water absorption improve significantly due to mechanical treatment. This was mainly due to the removal of adhered mortar

- The properties of the concrete made with non-treated C&DW-based coarse recycled concrete aggregate (CRCA) show that natural coarse aggregate can be replaced up to 40 %.
- The concrete produced with treated C&DW-based coarse recycled concrete aggregate (CRCA) had shown better mechanical as well as durability properties in comparison to non-treated C&DW-based coarse recycled concrete aggregate (CRCA) as well as control mixes. Therefore, natural coarse aggregate can be completely replaced by treated C&DW-based coarse recycled concrete aggregate (CRCA). It is mainly due to improvement in the ITZ, as coarse recycled concrete aggregate (CRCA) after treatment will lose a certain quantity of adhere mortar which is responsible for the creation of double ITZ in concrete made with C&D waste-based aggregate.

Acknowledgements

References

[1] Ministry of Housing and Urban Affairs Government of India. Draft on Circular Economy in construction and demolition waste. 2021.

[2] Pacheco-Torgal F, Tam VWY, Labrincha JA, Ding Y, de Brito J. Handbook of recycled concrete and demolition waste. Woodhead publishing limited; 2013. https://doi.org/10.1533/9780857096906

[3] Tam VW, Soomro M, Evangelista ACJ. A review of recycled aggregate in concrete applications (2000-2017). Construction and Building Materials. 2018;172:272-292. https://doi.org/10.1016/j.conbuildmat.2018.03.240

[4] Gonçalves P, Brito JD. Recycled aggregate concrete (RAC)-comparative analysis of existing specifications. Magazine of Concrete Research. 2010;62(5):339-346. https://doi.org/10.1680/macr.2008.62.5.339

[5] Malešev M, Radonjanin V, Marinković S. Recycled concrete as aggregate for structural concrete production. Sustainability. 2010;2(5):1204-1225. https://doi.org/10.3390/su2051204

[6] Meddah MS, Al-Harthy A, A Ismail M. Recycled concrete aggregates and their influences on performances of low and normal strength concretes. Buildings. 2020;10(9):167. https://doi.org/10.3390/buildings10090167

[7] Seara-Paz S, de Brito J, González-Taboada I, Martínez-Abella F, Vasco-Silva R. Recycled concrete with coarse recycled aggregate. An overview and analysis. Mater Construction. 2018;68(330):e151. https://doi.org/10.3989/mc.2018.13317

[8] Xu F, Tian B, Xu G. Influence of the ITZ Thickness on the Damage Performance of Recycled Concrete. Advances in Materials Science and Engineering. 2021. https://doi.org/10.1155/2021/6643956

[9] Scrivener KL, Crumbie AK, Laugesen P. The interfacial transition zone (ITZ) between cement paste and aggregate in concrete. Interface science. 2004;12(4):411-421. https://doi.org/10.1023/B:INTS.0000042339.92990.4c

[10] Diamond S, Huang J. The ITZ in concrete-a different view based on image analysis and SEM observations. Cement and concrete composites. 2001;23(2-3):179-188. https://doi.org/10.1016/S0958-9465(00)00065-2

[11] Kisku N, Joshi H, Ansari M, Panda SK, Nayak S, Dutta SC. A critical review and assessment for usage of recycled aggregate as sustainable construction material. Construction and building materials. 2017;131:721-740. https://doi.org/10.1016/j.conbuildmat.2016.11.029

[12] Xiao J. Recycled aggregate concrete. In Recycled aggregate concrete structures. Springer, Berlin, Heidelberg. 2018;65-98. https://doi.org/10.1007/978-3-662-53987-3_4

[13] De Juan MS, Gutiérrez PA. Study on the influence of attached mortar content on the properties of recycled concrete aggregate. Construction and building materials. 2009;23(2):872-877. https://doi.org/10.1016/j.conbuildmat.2008.04.012

[14] Kong D, Lei T, Zheng J, Ma C, Jiang J. Effect and mechanism of surface-coating pozzolanic materials around aggregate on properties and ITZ microstructure of recycled aggregate concrete. Construction and building materials. 2010;24(5):701-708. https://doi.org/10.1016/j.conbuildmat.2009.10.038

[15] Tam VW, Soomro M, Evangelista ACJ, Haddad A. Deformation and permeability of recycled aggregate concrete-A comprehensive review. Journal of Building Engineering. 2021;44:103393. https://doi.org/10.1016/j.jobe.2021.103393

[16] Silva RV, Brito JD, Dhir RK. Properties and composition of recycled aggregates from construction and demolition waste suitable for concrete production. Construction and Building Materials. 2014;65:201-217. https://doi.org/10.1016/j.conbuildmat.2014.04.117

[17] Verian KP, Ashraf W, Cao Y. Properties of recycled concrete aggregate and their influence in new concrete production. Resources, Conservation and Recycling. 2018;133:30-49. https://doi.org/10.1016/j.resconrec.2018.02.005

[18] Olorunsogo FT, Padayachee N. Performance of recycled aggregate concrete monitored by durability indexes. Cement and concrete research. 2002;32(2):179-185. https://doi.org/10.1016/S0008-8846(01)00653-6

[19] Domingo A, Lázaro C, Gayarre FL, Serrano MA, López-Colina C. Long term deformations by creep and shrinkage in recycled aggregate concrete. Materials and structures. 2010;43(8):1147-1160. https://doi.org/10.1617/s11527-009-9573-0

[20] Otsuki N, Miyazato SI, Yodsudjai W. Influence of recycled aggregate on interfacial transition zone, strength, chloride penetration, and carbonation of concrete. Journal of materials in civil engineering. 2003;15(5):443-451. https://doi.org/10.1061/(ASCE)0899-1561(2003)15:5(443)

[21] Zhang H, Ji T, Liu H. Performance evolution of recycled aggregate concrete (RAC) exposed to external sulfate attacks under full-soaking and dry-wet cycling conditions. Construction and Building Materials. 2020;248:118675. https://doi.org/10.1016/j.conbuildmat.2020.118675

[22] SP23, IS. Handbook on concrete mixes. Bureau of Indian Standards, New Delhi. 1982.

[23] Dhir RK, Brito JD, Silva RV, Lye CQ. Sustainable construction materials: recycled aggregates. Woodhead Publishing. 2019. https://doi.org/10.1016/B978-0-08-100985-7.00010-8

[24] Brito JD, Saikia N. Recycled aggregate in concrete: use of industrial, construction and demolition waste. Springer Science & Business Media. 2012.

[25] Poon CS, Chan D. The use of recycled aggregate in concrete in Hong Kong. Resources, conservation and recycling. 2007;50(3):293-305. https://doi.org/10.1016/j.resconrec.2006.06.005

[26] Park W, Noguchi T. Influence of metal impurity on recycled aggregate concrete and inspection method for aluminum impurity. Construction and Building Materials. 2013;40:1174-1183. https://doi.org/10.1016/j.conbuildmat.2012.03.009

[27] Wang Y, Liu J, Zhu P, Liu H, Wu C, Zhao J. Investigation of Adhered Mortar Content on Recycled Aggregate Using Image Analysis Method. Journal of Materials in Civil Engineering. 2021;33(9):04021225. https://doi.org/10.1061/(ASCE)MT.1943-5533.0003864

[28] Purushothaman R, Amirthavalli RR, Karan L. Influence of treatment methods on the strength and performance characteristics of recycled aggregate concrete. Journal of Materials in Civil Engineering. 2015;27(5):04014168. https://doi.org/10.1061/(ASCE)MT.1943-5533.0001128

[29] Tam VW, Tam CM, Le KN. Removal of cement mortar remains from recycled aggregate using pre-soaking approaches. Resources, Conservation and Recycling. 2007;50(1):82-101. https://doi.org/10.1016/j.resconrec.2006.05.012

[30] Shaban W, Yang J, Su H, Mo KH, Li L, Xie J. Quality improvement techniques for recycled concrete aggregate: a review. Journal of Advanced Concrete Technology. 2019;17(4):151-167. https://doi.org/10.3151/jact.17.151

[31] BIS, IS 383-2016. Specification for coarse and fine aggregates from natural sources for concrete. Bureau of Indian Standards, New Delhi. 2016.

[32] ASTM C1202 - 17a, Standard Test Method for Electrical Indication of Concrete's Ability to Resist Chloride Ion Penetration.

[33] IS: 14959 Part 2. (2001). Determination of water soluble and acid soluble chlorides in mortar and concrete-method of test. Bureau of Indian Standards, New Delhi.

[34] IS: 4032. (1988). Methods of physical tests for hydraulic cement. Bureau of Indian Standards (BIS), New Delhi, India.

[35] BIS, IS 1489 Part1 (2015). Portland Pozzolana Cement - Specification Part 1 Fly Ash Based. Bureau of Indian Standards, New Delhi.

[36] BIS, IS 9103 (1999). Specification for Concrete Admixtures. Bureau of Indian Standards, New Delhi.

[37] BIS, IS 516 Part 1/Section 1 (2021). Testing of strength of hardened concrete section 1 compressive, flexural and split tensile strength (First Revision) Bureau of Indian Standards, New Delhi.

[38] BIS, IS 516 Part 8 /Section 1 (2020). Hardened Concrete - Methods of Test -Part 8 Determination of Modulus of Elasticity Section 1 Static Modulus of Elasticity and Poisson's Ratio in Compression (First Revision). Bureau of Indian Standards, New Delhi.

[39] BIS, IS 516 Part6 (2020). Hardened Concrete -Methods of Test Part 6 Determination of Drying Shrinkage and Moisture Movement of Concrete Samples (First Revision). Bureau of Indian Standards, New Delhi.

[40] Babu VS, Mullick AK, Jain KK, Singh PK. Mechanical properties of high strength concrete with recycled aggregate-influence of processing. Indian Concrete Journal. 2014;88(5):10-26. https://doi.org/10.1080/21650373.2013.874302

[41] BIS, IS 1199 Part 2 (2018). Fresh Concrete- Methods of Sampling, Testing and Analysis Part 2 Determination of Consistency of Fresh Concrete (First Revision). Bureau of Indian Standards, New Delhi.

[42] BIS, IS 1199 Part 4 (2018). Fresh Concrete- Methods of Sampling, Testing and Analysis Part 4. Determination of Air Content of Fresh Concrete (First Revision). Bureau of Indian Standards, New Delhi.

[43] Lavado J, Bogas J, De Brito J, Hawreen A. Fresh properties of recycled aggregate concrete. Construction and Building Materials. 2020;233:117322. https://doi.org/10.1016/j.conbuildmat.2019.117322

[44] Limbachiya MC, Leelawat T, Dhir RK. RCA concrete: a study of properties in the fresh state, strength development and durability. In Sustainable Construction: Use of Recycled Concrete Aggregate: Proceedings of the International Symposium organized by the Concrete Technology Unit, University of Dundee and held at the Department of Trade and Industry Conference Centre, London, UK on 11-12 November 1998 (pp. 227-237). Thomas Telford Publishing. 1998.

[45] Silva RV, De Brito J, Dhir RK. Fresh-state performance of recycled aggregate concrete: A review. Construction and Building Materials. 2018;178:19-31. https://doi.org/10.1016/j.conbuildmat.2018.05.149

[46] Ferreira L, De Brito J, Barra M. Influence of the pre-saturation of recycled coarse concrete aggregates on concrete properties. Magazine of Concrete Research. 2011;63(8):617-627. https://doi.org/10.1680/macr.2011.63.8.617

[47] Poon CS, Kou SC, Lam L. Influence of recycled aggregate on slump and bleeding of fresh concrete. Materials and Structures. 2007;40(9):981-988. https://doi.org/10.1617/s11527-006-9192-y

[48] Faleschini F, Jiménez C, Barra M, Aponte D, Vázquez E, Pellegrino C. Rheology of fresh concretes with recycled aggregates. Construction and Building Materials. 2014;73:407-416. https://doi.org/10.1016/j.conbuildmat.2014.09.068

[49] Malešev M, Radonjanin V, Broćeta G. Properties of recycled aggregate concrete. Contemporary Materials. 2014;5(2):239-249. https://doi.org/10.7251/COMEN1402239M

[50] Shaikh FUA, Nguyen HL. Properties of concrete containing recycled construction and demolition wastes as coarse aggregates. Journal of Sustainable Cement-Based Materials. 2013;2(3-4):204-217. https://doi.org/10.1080/21650373.2013.833861

[51] McNeil K, Kang HK. Recycled Concrete Aggregates: A Review. International Journal of Concrete Structures and Materials.

[52] Silva RV, Neves R, De Brito J, Dhir RK. Carbonation behaviour of recycled aggregate concrete. Cement and Concrete Composites. 2015;62. https://doi.org/10.1016/j.cemconcomp.2015.04.017

[53] Silva RV, Neves R, De Brito J, Dhir RK. Carbonation behaviour of recycled aggregate concrete. Cem. Concr. Compos. 2015; 62: 22-32. https://doi.org/10.1016/j.cemconcomp.2015.04.017

[54] Kwan WH, Ramli M, Kam KJ, Sulieman MZ. Influence of the amount of recycled coarse aggregate in concrete design and durability properties. Construction and Building Materials. 2012;26(1):565-573. https://doi.org/10.1016/j.conbuildmat.2011.06.059

[55] BIS, IS 456 (2000). Plain and Reinforced Concrete - Code of Practice. Bureau of Indian Standards, New Delhi.

[56] Saravanakumar P, Abhiram K, Manoj B. Properties of treated recycled aggregates and its influence on concrete strength characteristics. Construction and Building Materials. 2016;111:611-617. https://doi.org/10.1016/j.conbuildmat.2016.02.064

[57] Verma A, Sarath Babu V, Arunachalam S. Influence of mixing approaches on strength and durability properties of treated recycled aggregate concrete. Structural Concrete. 2021;22:E121-E142. https://doi.org/10.1002/suco.202000221

[58] Tam VW, Soomro M, Evangelista ACJ. Quality improvement of recycled concrete aggregate by removal of residual mortar: A comprehensive review of approaches adopted. Construction and Building Materials. 2021;288:123066. https://doi.org/10.1016/j.conbuildmat.2021.123066

[59] Meddah MS, Zitouni S, Belâabes S. Effect of content and particle size distribution of coarse aggregate on the compressive strength of concrete. Construction and Building Materials. 2010;24(4):505-512. https://doi.org/10.1016/j.conbuildmat.2009.10.009

[60] Yang KH, Chung HS, Ashour AF. Influence of Type and Replacement Level of Recycled Aggregates on Concrete Properties.

[61] Standard, B. (2004). Eurocode 2: Design of concrete structures-. Part 1, 1, 230.

[62] Bentur A. Steel corrosion in concrete: fundamentals and civil engineering practice. CRC press. 1997. https://doi.org/10.1201/9781482271898

[63] Angst U, Elsener B, Larsen CK, Vennesland Ø. Critical chloride content in reinforced concrete-A review. Cement and concrete research. 2009;39(12):1122-1138. https://doi.org/10.1016/j.cemconres.2009.08.006

[64] Patel V, Singh B, Arora VV. Study on fracture behavior of high-strength concrete including the effect of steel fiber. Indian Concrete Journal. 2020;94(4):1-9.

[65] Ojha PN, Singh B, Kaura P, Singh A, Mittal P. Lightweight geopolymer fly ash sand: an alternative to fine aggregate for concrete production. Research on Engineering Structures and Materials. 2021. https://doi.org/10.17515/resm2021.257ma0205

[66] Singh B, Ojha PN, Trivedi A, Patel V, Gupta RK. High-performance fiber-reinforced concrete - for repair in spillways of concrete dams. Research on Engineering Structures and Materials. 2021. https://doi.org/10.17515/resm2022.377ma1228

[67] Singh B, Arora VV, Patel V, Experimental study on stress strain behaviour of normal and high strength unconfined concrete, Indian Concrete Journal. 2020; 94(4): 10-19

[68] Arora VV, Singh B. Durability Studies on Prestressed Concrete made with Portland Pozzolana Cement. Indian Concrete Journal. 2016;90(8). https://doi.org/10.18702/acf.2016.06.2.1.15

[69] Silva RV, De Brito J, Dhir RK. Establishing a relationship between modulus of elasticity and compressive strength of recycled aggregate concrete. Journal of Cleaner Production. 2016; 112, 2171-2186. https://doi.org/10.1016/j.jclepro.2015.10.064

[70] Ojha PN, Mittal P, Singh A, Singh B, Kaushik N. Experimental Investigations on the Use of C&D Waste as an Alternative to Natural Aggregates in Concrete. 2021;4(1):58-70.

[71] Arora VV, Singh B. Durability Studies on Prestressed Concrete made with Portland Pozzolana Cement, Indian Concrete Journal. 2016; 90(8). https://doi.org/10.18702/acf.2016.06.2.1.15

[72] Ojha PN, Singh B, Singh A, Patel V, Arora VV. Experimental study on creep and shrinkage behavior of high-strength concrete for application in high-rise buildings. Indian Concrete Journal. 2021;95(2):30-42.

[73] Ojha PN, Trivedi A, Singh B, Patel AKNSV, Gupta RK. High performance fiber reinforced concrete - for repair in spillways of concrete dams, Research on Engineering Structures and Materials, 2021. https://doi.org/10.17515/resm2021.252ma0128

[74] Arora VV, Singh B, Patel V, Trivedi A. Evaluation of modulus of elasticity for normal and high strength concrete with granite and calc-granulite aggregate. Structural Concrete. 2021 Jan; 22(S1): E-143-E-151. https://doi.org/10.1002/suco.202000023

[75] Padmini, A. K., Ramamurthy, K., & Mathews, M. S. (2009). Influence of parent concrete on the properties of recycled aggregate concrete. Construction and Building Materials, 23(2), 829-836. https://doi.org/10.1016/j.conbuildmat.2008.03.006

[76] Arora VV, Singh B, Patel V, Trivedi A. Evaluation of modulus of elasticity for normal and high-strength concrete with granite and calc-granulite aggregate. Structural Concrete. 2021;22(S1):E-143-E-151. https://doi.org/10.1002/suco.202000023

[77] Pedro D, De Brito J, Evangelista L. Influence of the use of recycled concrete aggregates from different sources on structural concrete. Construction and Building Materials. 2014;71:141-151. https://doi.org/10.1016/j.conbuildmat.2014.08.030

[78] Pedro D, De Brito J, Evangelista L. Performance of concrete made with aggregates recycled from precasting industry waste: influence of the crushing process. Materials and Structures. 2015;48(12):3965-3978. https://doi.org/10.1617/s11527-014-0456-7

[79] Mardani-Aghabaglou A, Yüksel C, Beglarigale A, Ramyar K. Improving the mechanical and durability performance of recycled concrete aggregate-bearing mortar mixtures by using binary and ternary cementitious systems. Construction and Building Materials. 2019;196:295-306. https://doi.org/10.1016/j.conbuildmat.2018.11.124

[80] Chakradhara Rao M, Bhattacharyya SK, Barai SV. Influence of field recycled coarse aggregate on properties of concrete. Materials and structures. 2011;44(1):205-220. https://doi.org/10.1617/s11527-010-9620-x

Self-healing concrete techniques and performance: A review

Ahmed H. Ghazy[*1,a], Mohamed R. Emara[2,3b], Ahmed M. Abdellah[1,c], Mohamed I.E. Attia[1,d]

¹Department of Construction and Utilities, Zagazig University, Zagazig, Egypt
²Department of Structural Engineering, Zagazig University, Zagazig, Egypt
³Department of Civil Engineering, Delta Higher Institute for Engineering & Technology, Talkha, Egypt

Article Info	Abstract
	Modern society faces the duality of rapidly expanding structure, making concrete one of the world's most traded materials. However, cement manufacturing can pollute the environment by releasing approximately one tonne of CO_2 for every tonne of cement produced. Concrete cracks can provide superior access for aggressive substances such as chlorides and sulfates, resulting in structural deterioration. So, to fix concrete cracks, different traditional methods were used, which use cement and some chemical agents that are hazardous to the environment. Because of the environmental issues and sustainability challenges associated with cement and concrete, it is preferable to reduce the amount of cement used by developing promising and unique solutions to enable quick crack healing in concrete and extend the structure's lifetime. Therefore, incorporating self-healing mechanisms into construction materials has been proposed to improve their performance and durability while reducing the need for maintenance and repair. This review assesses the performance and causes of autogenous and autonomous self-healing techniques. The autogenous technique occurs naturally due to inherent material properties, while the autonomous technique uses various healing agents, such as chemical or biological substances. Both techniques rely on forming calcium carbonate ($CaCO_3$) crystals as the principal agent for concrete healing. Previous findings showed that the autogenous technique has limited efficacy in repairing larger cracks with a width exceeding 0.3mm. In contrast, autonomous techniques have shown successful repai of cracks exceeding 2mm in width. The application of an autonomous methodology in the field of concrete has resulted in significant results, such as effectively repairing large cracks, enhancing structural integrity, and substantially decreasing permeability levels from high to exceedingly low levels.

1. Introduction

Concrete is a highly prevalent construction material worldwide, with an estimated annual production of approximately 6 million cubic meters [1]. While using concrete as a final product does not harm the environment, it is essential to note that producing concrete components has adverse effects. Specifically, the global annual consumption of Portland cement. Concrete often exhibits cracks due to excessive tensile stresses or environmental conditions [2, 3]. Accordingly, rehabilitation and maintenance of concrete structures are essential. For example, the direct cost of maintaining and repairing concrete bridges in the United States was nearly $4 billion annually [4-7]. Repairing and rehabilitating existing structures account for 50% of annual construction costs in Europe [8] and 50% in the United Kingdom [6, 9, 10].

Traditional methods, including sealing, routing, stitching, grouting, chemical injection, and carbon fiber reinforcement, have been extensively used over time. Nevertheless, these methods possess distinct disadvantages as they can be time-consuming, mainly when dealing with larger or more complex cracks. Moreover, the conventional crack healing processes may exhibit inconsistencies, which can be attributed to many factors, such as labor skill, material quality, and environmental conditions. Also, these methods often repair large cracks but are inappropriate for deep and small cracks [11]. Repairing agents can be hazardous to the environment and expensive [10]. Furthermore, the utilization of cement is required in the conventional procedure of concrete crack healing, which leads to an increase in carbon dioxide (CO_2) footprint [12]. Finally, traditional methods might require continuous maintenance and periodic reapplication of healing agents to maintain long-term efficacy.

Presently, self-healing concrete is regarded as a durable repair technique that has captured the interest of researchers [13, 14]. Self-healing concrete exhibits properties similar to the human body, whereby injuries and wounds can autonomously heal without external intervention [15]. Over the past decade, there has been a notable expansion in research related to self-healing cementitious composites. This paper aims to provide a comprehensive overview of various self-healing techniques and their respective performance. The concept of self-healing concrete, covering both autonomous and autogenous healing, was initially proposed. This review offers an in-depth review of the mechanisms by which this material achieves crack healing and the specific steps involved in the healing process. Also, the factors affecting both techniques were reviewed.

2. Self-Healing Techniques

Autogenous and autonomous are two prevalent self-healing techniques extensively employed for concrete healing. The autogenous technique aims to improve the natural mechanism of crack healing. Every concrete structure has a limited autogenous healing potential [16]. This technique includes only the material's original components due to their specific chemical structure and promotes healing under environmentally favorable systems [7]. In addition, owing to its inherent characteristics, concrete possesses micro-reservoirs containing sparsely distributed un-hydrated cement particles, which facilitate the process of self-repair [17]. The autogenous self-healing technique was initially observed about 200 years ago, in 1836 by the French Academy of Sciences [17-24]. Since the early 19th century, researchers have explored the effectiveness of this method for repairing cracks in pipes, culverts, and other water infrastructure [25-27].

On the other hand, the autonomous technique aims to modify concrete by adding various healing agents to the concrete matrix so that the crack heals autonomously after its formation [7]. In this approach, the repairing agents are pre-buried in the concrete mixture and can automatically heal cracks as they occur, saving potential costs compared to traditional methods [28].

The primary mechanism employed by both techniques to facilitate the healing of cracks involves the deposition of white crystalline calcium carbonate ($CaCO_3$) material onto the surface of the crack. This material can be generated in natural (autogenous) or artificial (autonomous) ways. In addition, $CaCO_3$ possesses a rough crystal morphology that exhibits a high propensity for surface adhesion and self-sustaining growth [29]. The subsequent sections provide a comprehensive analysis of both techniques.

3. Autogenous Self-Healing Technique

Concrete autogenous self-healing is assumed to be related to several mechanisms [30]. As per RILEM [31], autogenous self-healing can be attributed to three primary physical, chemical, or mechanical factors, as illustrated in (Fig. 1) [7, 32].
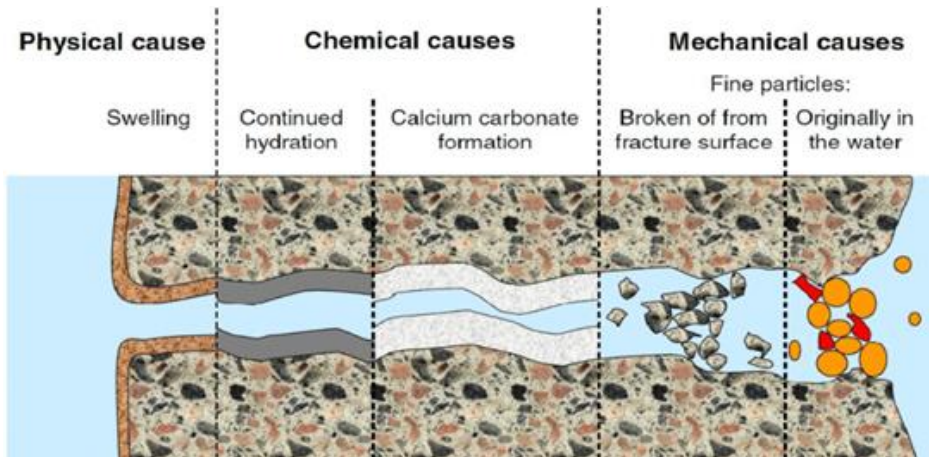
Fig. 1. Different causes of autogenous self-healing [7]

3.1. Causes of Autogenous Self-Healing Technique

3.1.1. Physical Cause

Physical cause includes the hydrated cement paste (HCP) enlargement next to the crack opening [19]. This phenomenon arises as HCP absorbs water, which goes through the space between the components of HCP, resulting in an expansion of calcium-silicate hydrate (C-S-H) gel [33]. It can be described as the volume increase due to the matrix's saturation [34].

3.1.2. Chemical Causes

The chemical causes can be divided into two mechanisms: continued hydration and calcium carbonate formation (carbonation) [18, 31].

- Continued hydration

Despite the potential impact of continued hydration on self-healing, it has not gained as much attention as the carbonation process [35]. The by-products of the continued hydration process can have twice the volume of cement [7, 36-38], filling spaces previously filled with water and causing crack healing [34]. However, if the crack width is narrow (less than 0.1 mm) and the swelling and hydration happen simultaneously, the crack may close independently. The effect decreases as the cracks get wider [7, 34].

- Carbonation

According to previous research, the carbonation effect on autogenous healing is more crucial than that of continued hydration [17, 31, 33, 36]. First, this process happens in concrete due to dissolved soluble composites moving out of the concrete matrix. Following this, the formation of $CaCO_3$ begins due to the interaction of calcium ions derived from portlandite $(Ca(OH)2)$ with carbon dioxide molecules encased in water, as shown in Eqs. (1-2) [1, 25, 39]. Finally, $CaCO_3$ appears as white crystals deposited on the surfaces of cracks.

$$CaO + H_2O \rightarrow Ca(OH)_2 \tag{1}$$

$$Ca(OH)_2 + CO_2 \rightarrow CaCO_3 + H_2O \tag{2}$$

Also, $CaCO_3$ can be formulated according to the following reactions, as shown in Eqs. (3-4) [40], depending on the reactant's temperature, concentration, and pH [7, 41, 42]. Calcium ions (Ca^{2+}) that exist in the concrete components react with carbonates (CO_3^{2-}) or bicarbonates (HCO_3^-) available in water, creating insoluble $CaCO_3$, which causes the healing of cracks [36, 40, 41].

$$Ca^{2+} + CO_3^{2-} \rightarrow CaCO_3 \qquad pH\ water > 8 \tag{3}$$

$$Ca^{2+} + HCO_3^- \rightarrow CaCO_3 + H^+ \qquad 7 < pH\ water < 8 \tag{4}$$
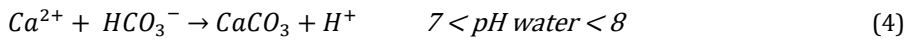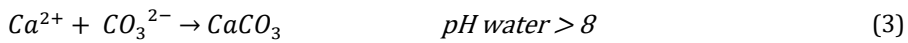
3.1.3. Mechanical Cause

This technique, also known as the self-tightening technique, does not involve any chemical reaction. Instead, it involves the obstruction of the crack by tiny particles at the crack face or the passage of small impurities through the crack [7, 32, 33], as shown in (Fig. 1).

3.2. Factors Affecting Autogenous Self-Healing Technique

Numerous parameters may affect the autogenous rate of healing, which are discussed in detail in the following sections.

3.2.1. Water/Cement Ratio

Enhancement of autogenous healing can be achieved through improving continuing hydration by increasing cement content or reducing the W/C ratio [26, 34, 43]. Theoretically, a W/C ratio of 0.22 is adequate for achieving complete hydration. However, according to sources [17, 26], approximately 30% of the cement particles present in conventional concrete have yet to undergo the hydration process. Even so, the hydrated cement particles may still include a small, slowly-hydrating, un-hydrated core, which will hydrate later [34, 44]. When unhydrated particles are contacted with external water after cracking, they hydrate, healing cracks and voids. Better and more efficient mixing processes result in fewer unhydrated cement particles reacting with air moisture [19].

3.2.2. Cement and Additives Type

Based on continued hydration, self-healing can be affected by the cement particle size [34]. The clinker content controls the amount of Ca^{2+} ions and, as a result, the matrix's capability to develop $CaCO_3$ precipitation products [45]. The influence of particle size and coarse cement mixing content on autogenous healing was investigated using ultrasonic measurements. The self-healing ratio increased with cement particle diameter for equal mixing content of coarse cement [45].

Different additives can be included in the concrete mixture, affecting the healing rate. For instance, incorporating fibers can enhance the healing processes due to their participation in reducing crack width. However, it affects workability when adding a large amount of fibers [19]. A uniformly distributed sufficient fiber content can enhance mechanical properties and tighten the crack [46, 47].

Fly ash, silica fume, and blast furnace slag are known as aluminosilicate materials, which can improve autogenous self-healing ability through a pozzolanic reaction. In alkaline conditions, silicic acid (H_4SiO_4/SH) can be formed from silicate species dissolved in pozzolanic material. Silicic acid can react with dissolved $Ca(OH)_2$ to produce C-S-H and

water [7]. These reactions can give a level of self-healing capacity due to the formation of C-S-H, according to Eqs (5-6) [7].

$$3Ca(OH)_2 + 2H_4SiO_4 \rightarrow 3Ca_2 + 2H_2SiO_4^{2-} + 4H_2O + 2OH^- \tag{5}$$

$$3Ca^{2+} + 2H_2SiO_4^{2-} + 4H_2O + 2OH^- \rightarrow 3CaO.2SiO_2.7H_2O \tag{6}$$
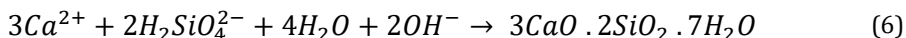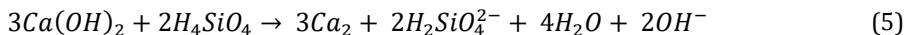
Like the C-S-H formed during the hydration of un-hydrated cement particles, the C-S-H formed during the pozzolanic process can repair small cracks. Since the pozzolanic reaction is pH-dependent, it takes much longer than cement hydration [7].

3.2.3. Water Availability During The Healing Stage

Water availability is crucial for healing since it is necessary for chemical reactions to promote $Ca(OH)_2$ dissolution from the concrete matrix next to the crack surface [7, 34, 48-50]. Several researchers found that the specimens healed through water immersion performed better than those cured through humidity chambers or air curing [34, 51]. Few investigations revealed that the self-healing phenomenon was more present in wet and dry cycles than in completely submerged conditions because of the abundance of CO_2 in the atmosphere [49, 52].

3.2.4. Concrete Age

Concrete age is vital to autogenous healing [34]. Early-aged concrete has a better healing ability than old ones due to un-hydrated cement in early-age concrete [7, 53, 54]. Also, early-age concrete can develop new C-S-H gels, which can be continued by combining the two chemical processes mentioned above. Leading to primarily $CaCO_3$ deposits for crack closure at later ages [49]. It was realized that healing efficiency diminishes with the sample's age [48, 55]. In contrast, self-healing at later ages is attributed to the formation of calcium carbonate [48].

3.2.5. Crack Width

The dimensions and patterns of cracks can influence the healing ability of concrete. [49]. By reducing the crack's width and improving the healing mechanism, larger cracks can be repaired more rapidly and efficiently. This means that the autogenous intrinsic healing potential of cement-based composites can enhanced by restricting and managing the crack width [49]. For example, for the crack width, in the first 24 hours, cracks with an effective width of less than 50 microns were reduced to 20 microns; in the following seven days, cracks with an effective width of 50 to 100 microns shrank to 20 microns. [17, 45, 55].

As mentioned in previous studies, the autogenous self-healing technique can only heal small cracks of 0.1-0.2 mm [16, 26, 31, 36, 43, 56]. However, other researchers mentioned that this technique could heal cracks up to 0.3mm in width [23, 31, 51, 57]. A high crack-healing potential of concrete structures is advantageous because it enhances the material's durability [39]. Thus, an alternative self-healing mechanism will likely be incorporated to improve the durability of such relatively cheap and environmentally sustainable concrete [25]. Moreover, the current policy seeks to reduce the cement required in a concrete mixture because its production is environmentally unfriendly due to high energy consumption and CO_2 emissions [58, 59].

4. Autonomous Self-Healing Technique

Autonomous self-healing concrete involves the incorporation of a suitable healing agent, either chemical or biological, into the concrete during its production, thereby facilitating the healing process. (Fig. 2) offers additional clarification regarding the diverse techniques employed in the process of biomineralization.
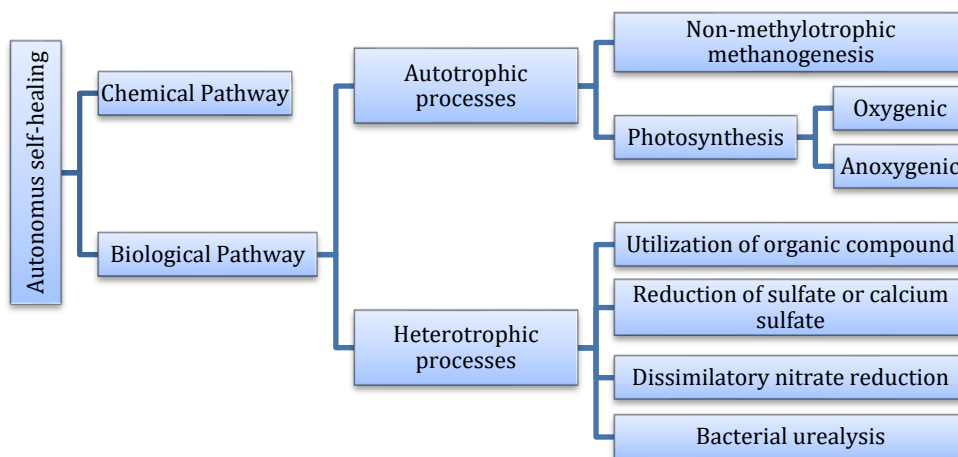
Fig. 2. Autonomous pathway processes.

4.1. Chemical Self-Healing

Chemical self-healing is an autonomous healing technique carried out by adding chemical agents to the concrete matrix during the mixing. Glue, calcium sulfoaluminate, and crystalline admixtures are the most commonly used chemical agents [34, 60]. The main drawback of this process is the possibility of achieving the healing ability before a crack formation [34]. Different scientists examined chemical agents like:

- Aqueous sodium silicate (Na_2SiO_3) reacts with $Ca(OH)_2$ from the concrete, forming C-S-H as a result, as shown in Eq. (7) [60].

$$Na_2SiO_3 + Ca(OH)_2 \rightarrow (CaO.SiO_2).H_2O + Na_2O \tag{7}$$
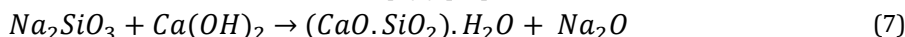
- Crystalline admixture (CA) is a distinct category of permeability-reducing admixture (PRA) [34]. Crystalline admixture reacts with tricalcium silicate ($3CaO - SiO_2$) to produce modified C-S-H and a precipitate made of calcium and water molecules as a by-product of their reaction, as shown in Eq. (8).

$$3CaO - SiO_2 + M_xR_x + H_2O \\ \rightarrow Ca_xSi_xO_xR - (H_2O)_x + M_xCaR_x - (H_2O)_x \tag{8}$$
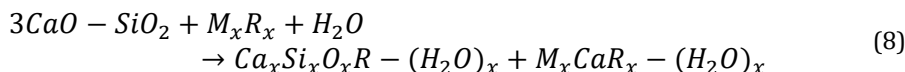
Where $3CaO - SiO_2$ is tricalcium silicate, M_xR_x is the crystalline promoter, $Ca_xSi_xO_xR - (H_2O)_x$ *is* the modified C-S-H + pore-blocking precipitate.

- Shrinkage compensators of calcium sulfoaluminates were used as self-healing agents [61, 62]. Since their expansive reaction has the potential to fill cracks, they have the potential to be self-healing agents. Compared to other mineral additions and OPC, the impact of shrinkage compensators can be visually inspected through the closure of early-age cracks of size 0.1–0.3 mm.

The best results for self-healing were obtained by combining two different admixtures, shrinkage compensators and crystalline admixtures [62]. However, it was shown that expansive admixtures respond best to adding a single mineral due to the crystals' tendency to overgrow [63].

4.2. Biological Self-Healing

In this technique, micro-organisms were chosen as healers due to their adaptability in healing cracks as a green alternative to traditional methods. This approach is known as "bacterial concrete" [4, 11, 39, 43, 64, 65]. Bacterial concrete has recently gained popularity due to its superior healing capacity, which should last for the structure's lifetime [17, 34]. The bacterial concrete technique is based on mineral-producing bacteria that deliver good results when sprayed, applied into the crack, or added to the concrete matrix [42, 65].

Bacteria make long-lasting healing possible, and this process is known as microbiologically induced calcium carbonate precipitation (MICP). MICP acts as a binder, filling cracks and binding the concrete constituents. Bio-mineralization is the basic mechanism of incorporating bacteria in concrete using different processes to produce CaCO$_3$ [56]. Generally, biomineralization can be divided into two significant processes: heterotrophic and autotrophic. Heterotrophic processes precipitate more CaCO$_3$ than autotrophic ones [66].

4.2.1. Autotrophic Processes

The autotrophic term refers to the organisms that produce complex organic compounds, such as carbohydrates, with the aid of light energy, as in photosynthesis, or chemical reactions, as in chemosynthesis. The following sections list autotrophic pathways.

- Non-methylotrophic methanogenesis

Non-methylotrophic methanogenesis is a set of micro-organisms called methanogens. This approach is more commonly observed in marine sediments. Examples of methanogens micro-organisms are those of the Methanobacterium species [67]. This type of bacteria provides methane (CH$_4$) metabolically under anaerobic conditions [67, 68]. In this process, methanogenic archaebacteria use carbon dioxide (CO$_2$) and hydrogen (H$_2$) in strict anaerobiosis to make methane (CH4), as shown in Eq. (9).

$$CO_2 + 4H_2 \rightarrow CH_4 + 2H_2O \tag{9}$$

After that, CH$_4$ is converted into bicarbonate through anaerobic oxidation with the assistance of sulfate (SO_4^{2-}), which functions as an electron acceptor, as shown in Eq. (10). Then, the produced bicarbonate (HCO_3^-) reacts with calcium ions (Ca^{2+}) resulting in $CaCO_3$ formation, as shown in Eq. (11).

$$CH_4 + SO_4^{2-} \rightarrow HCO_3^- + HS^- + H_2O \tag{10}$$

$$Ca^{2+} + HCO_3^- \rightarrow CaCO_3 + CO_2 + H_2O \tag{11}$$
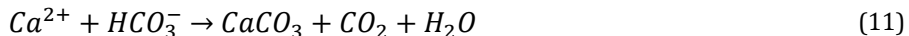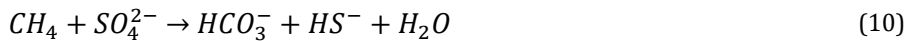
- Photosynthesis process

Photosynthetic bacteria can heal cracks through oxygenic and anoxygenic photosynthesis. In general, cyanobacteria and microalgae micro-organisms tend to display more significant activity levels in aquatic environments [69]. Different kinds of electron donors are required for oxygenic (cyanobacteria) and anoxygenic (purple bacteria) photosynthesizing organisms to produce methanal (CH_2O) successfully [68]. In the oxygenic photosynthesis, water donates electrons to produce oxygen, as shown in Eq. (12). But in anoxygenic photosynthesis, hydrogen sulfide H_2S acts as electron donor, therfore oxygen is not produced as shown in Eq. (13) [68, 70].

$$CO_2 + H_2O \xrightarrow{Oxygenic\ photosynthesis} CH_2O + O_2 \tag{12}$$

$$CO_2 + 2H_2S + H_2O \xrightarrow{Anoxygenic\ photosynthesis} CH_2O + 2S + 2H_2O \tag{13}$$
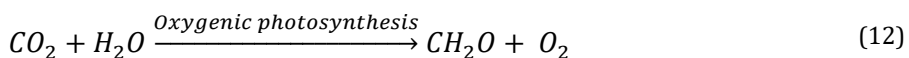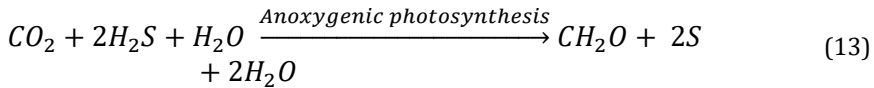
The remaining reactions are the same in both groups. CO2 is taken out of bicarbonate solutions, as shown in Eq. (14), to make carbonate compounds. This causes a concentrated rise in pH, which, as shown in Eq. (15), speeds up the creation of $CaCO_3$ when calcium ions are present, as shown in Eq. (16) [66].

$$2HCO_3^- \leftrightarrow CO_2 + CO_3^{2-} + H_2O \tag{14}$$

$$CO_3^{2-} + H_2O \leftrightarrow HCO_3^- + OH^- \tag{15}$$

$$Ca^{2+} + HCO_2^- + OH^- \rightarrow CaCO_3 + H_2O \tag{16}$$
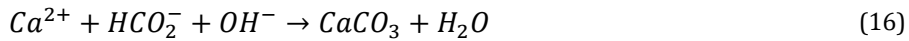
4.2.2. Heterotrophic Processes

The term heterotrophic means that micro-organisms must acquire materials and energy from an alternative source to create a substance [66]. Also, they need organic carbon to grow [56]. This process can be achieved using different methods discussed in the following sections.

- Utilization of organic compounds

Bacteria with a calcium source represent a two-component healing agent in this process. Different types of bacteria, including Anthrobacter, Rhodococcus, and Bacillus, are necessary due to their ability to facilitate the metabolic conversion of organic molecules containing calcium, such as calcium lactate, calcium acetate, or calcium formate, into $CaCO_3$ [56, 66].

The following equations show the metabolic conversion of some organic compounds in the presence of bacteria. Calcium lactate metabolic conversion is shown in Eq. (17) [10, 64]. The metabolic conversion of calcium-formate with portlandite exists in the paste matrix shown in Eq. (18) [25]. Also, calcium acetate's metabolic conversion is shown in Eqs. (19)-(20) [67]. Eventually, bacteria act as a catalyst in this process. In addition to $CaCO_3$ formation, bacteria can produce CO_2, which is trapped inside the concrete and enters a reaction similar to the carbonation process but with faster rates, as described in Eq. (2). This improves the concrete standard carbonation reaction [43].

$$CaC_6H_{10}O_6 + 6O_2 \xrightarrow{Bacteria} C_aCO_3 + 5CO_2 + 5H_2O \tag{17}$$

$$Ca(CHO_2)_2 + Ca(OH)_2 + O_2 \xrightarrow{Bacteria} 2C_aCO_3 + 2H_2O \tag{18}$$

$$CH_3COO^- + 2O_2 \xrightarrow{Bacteria} 2CO_2 + H_2O + O^- \tag{19}$$

$$Ca^{2+} + 2HCO_3^- + O_2 \xrightarrow{Bacteria} C_aCO_3 + H_2O + CO_2 \tag{20}$$
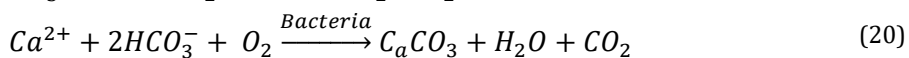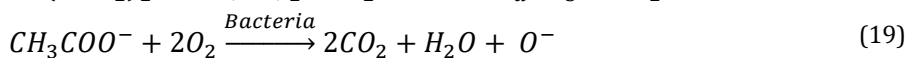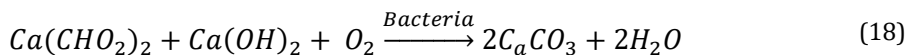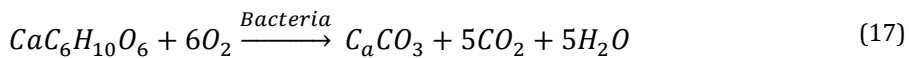
- Reduction of sulfate or calcium sulfate

In this process, the healing usually occurs under anoxic conditions using sulfate-reducing bacteria (SRB) such as (anaerobic, prokaryotes, and morphologically) [70]. The abiotic dissolution of gypsum ($CaSO_4.H_2O$) provides a media which is reach in both sulfate (SO_4^{2-}) and calcium ions (Ca^{2+}) as shown in Eq. (21). In the existence of organic matter with no oxygen, SRB can diminish sulfate (SO_4^{2-}) to hydrogen sulfide (H2S) and release bicarbonates (HCO_3^-) as shown in Eq. (22). After that, hydrogen sulphide degasses, increase the pH level leading to calcium carbonate precipitation as shown in Eq. (23) [66, 69, 70].

$$CaSO_4 . H_2O \xrightarrow{Abiotic\ dissolution} Ca^{2+} + SO_4^{2-} + 2H_2O \qquad (21)$$

$$2(CH_2O) + SO_4^{2-} \rightarrow HS^- + HCO_3^- + CO_2 + H_2O \qquad (22)$$

$$Ca^{2+} + HCO_3^- + OH^- \rightarrow CaCO_3 + H_2O \qquad (23)$$
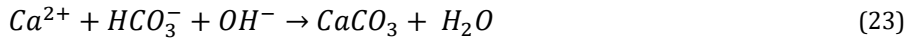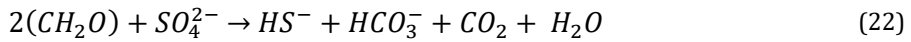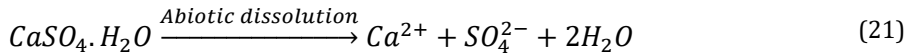
Conflicting points of view were discovered regarding utilizing the SRB strain of bacteria as a healing agent in cementitious materials. The utilization of SRB has been noted to have deleterious effects on concrete, as reported in a previous study [67]. However, other studies revealed that sulfate-reducing bacteria in concrete at different concentrations significantly improved the material's compressive, tensile, and flexural strengths. As per the findings, the utilization of this pathway is not common owing to elevated levels of sulfate [71].

- Dissimilatory nitrate reduction (Denitrification)

Calcium carbonate can be efficiently produced by utilizing nitrate-reducing bacteria, which facilitate the generation of nitrogen and carbon dioxide during the process. This process can be defined as a respiratory process that reduces nitrate to nitrite, nitric oxide, nitrous oxide, and nitrogen gas. As a result, nitrogen, carbon dioxide, and water are released in this process, as shown in Eq. (24). In addition, hydrogen ions (H+) consumption during the denitrification process increases pH levels, leading to carbonate formation, as shown in Eq. (25). Finally, calcium ions combine with carbonate to generate calcium carbonate, as shown in Eq. (26) [67].

$$NO_3^- + H^+ \xrightarrow{Denitrification} CO_2 + N_2 + H_2O \qquad (24)$$

$$CO_2 + 2OH^- \rightarrow CO_3^{2-} + H_2O \qquad (25)$$

$$Ca^{2+} + CO_3^{2-} \rightarrow CaCO_3 \qquad (26)$$
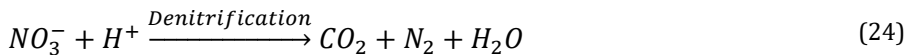
The effects of nitrate-reducing bacteria on the mechanical properties of concrete have been examined through an investigation of Diaphorobacter nitroreducens, a strain of bacteria that exhibits denitrification bacterial activity. The research findings indicated a rise in compressive strength, as evidenced by the data reported [66, 72]. The pathway in question is primarily associated with Denitobacilus, Thiobacillus, Alcaligenes, Pseudomonas, Spirilium, Achromobacteri, and Micrococcus bacterial species. Nevertheless, this methodology has not undergone comprehensive investigation, and its applicability is limited.

- Bacterial urealysis or (urea hydrolysis)

Several bacteria crucial for the environment and medicine can synthesize the enzyme urease (urea amidohydrolase) [73]. The application of urea hydrolysis as a healing agent in the autonomous self-healing mechanism of concrete was first introduced in 1995 [74]. This strain of bacteria facilitates calcite formation via a complex sequence of biochemical reactions. This bacteria is widespread because it can hydrolyze urea quickly and generate carbonate ions without using unnecessary protons [66]. According to research findings, the bacterial urease enzyme-mediated decomposition of urea is the most commonly employed healing technique in engineering applications [56, 75]. Calcium carbonate precipitation in this process is mainly affected by the amount of the enzyme urease formed by the bacteria [75].

The first step in the reaction in the presence of the bacteria catalyzes the hydrolysis of urea

($CO(NH_2)_2$), leading to the production of carbamic acid (NH_2COOH) and ammonia (NH_3), as shown in Eq. (27) [73].

$$CO(NH_2)_2 + H_2O \xrightarrow{Bacteria} NH_2COOH + NH_3 \tag{27}$$
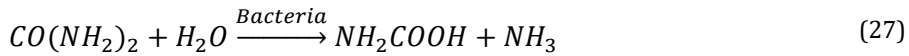
On further hydrolysis, carbamic acid spontaneously decomposes into ammonia and carbonic acid (H_2CO_3), shown in Eq. (28) [70].

$$NH_2COOH + H_2O \rightarrow NH_3 + H_2CO_3 \tag{28}$$

Carbonic acid subsequently equilibrates in water, forming bicarbonate (HCO_3^-), ammonium (NH_4^+), and hydroxide ions (OH^-) as shown in Eqs. (29)-(30).

$$H_2CO_3 \underset{\leftarrow}{\rightarrow} HCO_3^- + H^+ \tag{29}$$

$$2NH_3 + 2H_2O \underset{\leftarrow}{\rightarrow} 2NH_4^+ + 2OH^- \tag{30}$$

This reaction raises the pH level and produces carbonate ions by shifting the bicarbonate equilibrium, as shown in Eq. (31).

$$HCO_3^- + H^+ + 2NH_4^+ + 2OH^- \rightarrow CO_3^{2-} + 2NH_4^+ + 2H_2O \tag{31}$$
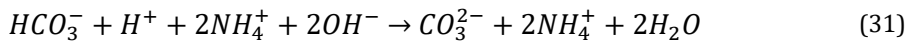
Because of their negative charge, bacterial cell walls attract cations from their surroundings, including calcium ions, which the bacteria then deposit on their surface. Nucleation of calcium carbonate crystals occurs at the cell surface as a result of Ca^{2+} reactions with carbonates CO_3^{2-}, as depicted in (Fig. 3). Finally, as indicated by Eqs. (32)-(33), an increase in carbonate concentration causes a rise in supersaturation, precipitating $CaCO_3$ around the cell in the presence of soluble calcium ions.

$$Ca^{2+} + Cell \rightarrow Cell - Ca^{2+} \tag{32}$$

$$Cell - Ca^{2+} + CO_3^{2-} \rightarrow Cell - CaCO_3^- \tag{33}$$
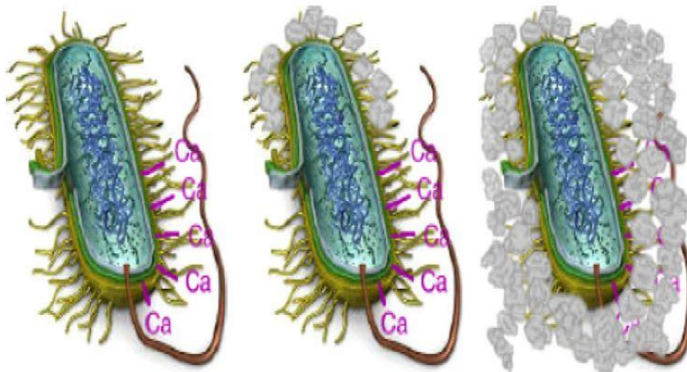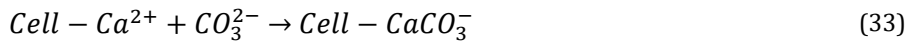
Fig. 3. $CaCO_3$ precipitation on bacteria cell wall [56]

The hydrolysis of urea has numerous potential benefits compared to the carbonate-generating approach. The hydrolysis of urea can be simply regulated, generating superior quantities of carbonate in a short period [20]. In contrast to the urease hydrolysis mechanism, the metabolic conversion of calcium lactate does not produce massive amounts of ammonia, drastically increasing the risk of reinforcement corrosion [76].

4.2.3. Factors Affecting Biological Concrete

(Fig. 4) clarifies the factors upon which the efficacy of bacterial self-healing concrete depends, which will be explained in subsequent sections.
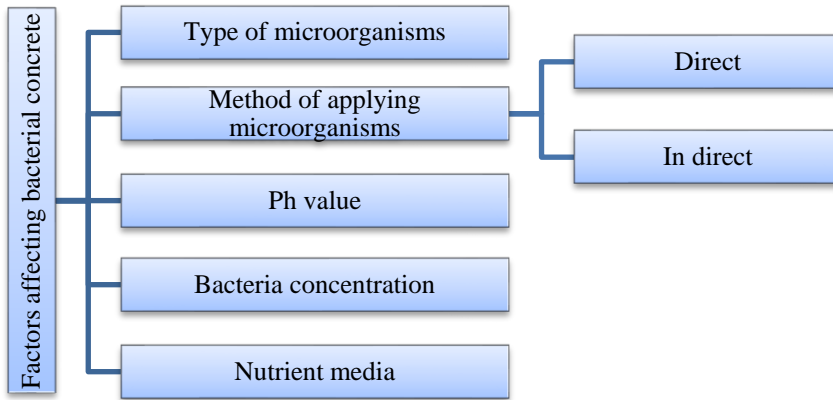
Fig. 4. Factors affecting bacterial concrete

- Type of micro-organisms

Different types of bacteria can be used in concrete, such as anaerobic and aerobic bacteria. For aerobic bacteria, using Bacillus subtilis improved compressive strength [1, 6, 10, 26, 77-84]. Using Bacillus pasteruii improved the strength and permeability of concrete [29, 85-90]. Bacillus chonii does not affect mechanical properties [25, 28, 64, 91]. Bacillus pseudofirmus did not affect compressive strength [91]. However, it was mentioned in other research that using this type of bacteria reduced compressive strength [25, 92]. Anaerobic bacteria such as E. coli did not affect strength, but Shewanella improved compressive strength [93].

- Methods of incorporating bacteria

Bacteria can be incorporated into the concrete matrix using various methods, broadly classified into direct and indirect.

In the direct method, bacteria are directly incorporated into the concrete matrix through the water of the mixing process. Unfortunately, this method reduced bacteria viability due to bacteria crushing during mixing and squeezing after concrete hardening [64, 94]. When spores were used, survivability improved, but it also changed the porosity during maturation, resulting in decreased viability and survival shortened to 1-2 months [64] or four months [64, 95]. Almost one-half of the bacterial cells were kept in a vegetative state in the matrix after 330 days with proper bacteria and nutrients [96].

The indirect method can be classified into two methods. The first method is the adsorbed method. In this method, different immobilizers were used to carry the bacteria to preserve it from the harsh environment of the concrete [97]. The immobilization technique has been reported to be effective in maintaining an efficient mineral formation capacity to incorporate bacteria in self-healing concrete over time [28]. The material used as a bacterial immobilizer must be able to immobilize bacterial spores effectively. Several trials have been conducted to develop porous bacteria immobilizers [39, 98, 99]. When the absorption factor of the immobilizer increases, the healing efficiency increases since it can

ensure adequate oxygen, water, and a growing area for bacteria after the formation of the crack. Immobilizers not only help in the survival of bacteria, but some also impact the mechanical characteristics of concrete [10]. Different immobilizers were utilized in self-healing concrete, such as iron oxide nano/microparticles and bentonite nano/microparticles [97], lightweight aggregate (LWA) and graphite nanoplatelets (GNP) [10], zeolite powder [100], and expanded clay particles [64]. Different recycled materials were used, such as recycled brick aggregate [83], recycled concrete aggregate [82], recycled rubber particles [99], and fired clay waste [101].

The second method is encapsulating the bacterial spores by adding them to capsules. These capsules are made of specific substances like glass, poly, and melamine. The encapsulation method was reported to be better than the direct method [56]. On the other hand, the complex procedures, professional equipment demand, and relatively high cost are the main drawbacks of the encapsulated method [99]. Also, due to issues with workability and strength, the capsules' amount is typically limited to 2% by the weight of the concrete [19]. As illustrated in (Fig. 5), the repair begins when the capsule is broken due to the crack initiation and propagation through it, releasing the healing agent, which can be chemicals or micro-organisms, filling the crack and preventing it from spreading further [32, 94].
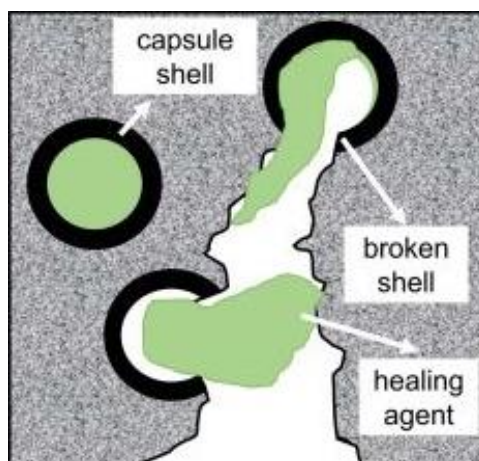
Fig. 5. Encapsulated method healing technique [19].

The inadequate design of the entire encapsulation system may allow the crack to develop around the capsule rather than penetrating it. The shell thickness also affects the performance of capsulated bacteria; using too thick shells prevents shell rupture while using thin shells allows the healing agent to be released while mixing [102]. When large-size capsules with diameters ranging from 400 to 600 μm were used, only around 8.6 % of the capsules broke, while the remainder were moved out of the matrix, dropping voids. When smaller capsules (50–200 μm) were used, approximately 34% were ruptured [103].

- pH value

The pH of the media influences the growth and survival of bacteria. Each microbial species possesses a definite pH to help grow. The activity of bacteria decreases significantly with increasing pH value as metabolic and biomineralization activities decrease as the pH value increases [91]. Cement's high pH (between 10 and 13) makes bacterial growth in an unfavorable environment [70]. Therefore, the rise in pH is a key problem that faces bacterial concrete.

- Bacteria Concentration

Cell concentration can affect the mechanical characteristics of concrete [78]. Many researchers have investigated the impact of various concentrations and observed the optimum concentration. For example, 10^5 cells/ml of mixing water was the optimum cell concentration, resulting in the best mechanical properties using Shewanella and Bacillus Subtilis micro-organisms [4, 11, 39, 43, 64, 65, 86]. Findings suggest that the hypothesis positing a correlation between the increase of bacterial concentration and the improvement of compressive strength is not entirely accurate, as evidenced by the reduction of compressive strength by 10% when Bacillus pseudofirmus was utilized at a cell concentration of 10^8 cells/ml [25, 84].

- Nutrient media

Healing ability can be influenced by various factors associated with nutrient media. The presence of this substance can enhance the formation of the healing compounds required for crack closure and promote the growth of bacterial spores [39].

The selection of such materials is critical because they must function well with concrete and not promote deterioration. In general, materials that are common to retard the setting of concrete, such as chlorides and sulfate, should be avoided. Researchers have used different nutrient media combined with organic compounds such as urea, yeast extract, sodium, protein, sugar, buffer solution, calcium lactate, and calcium acetate for metabolic pathways.

Sugars, like glucose and dextrose, have a more significant delaying influence when added after mixing the water and the cement [104]. Sugars' retarding effect is augmented when increasing sugar content. A sugar content of 0.1% by cement weight can delay hardening [105]. Using sodium as a nutrient medium was preferable [95, 106]. In addition, using sodium citrate has been shown to affect the setting and hardening of concrete [106].

Proteins, such as peptone and tryptone, were evaluated [26, 64, 84]. Strength was reduced when using 1% peptone of cement content [64]. Using large amounts of calcium lactate can postpone the setting time, decreasing the concrete's strength at an early age. Calcium lactate was the most used nutrient [10, 25, 43, 64, 89, 92] with different percentages. It was observed that 1% and 0.5% of cement content give better results than 5 and 10 % in compressive strength.

Yeast extract and calcium acetate have been used as nutrient media to study their effect on concrete mechanical properties [64, 95, 107]. They found that using yeast extract and calcium acetate by 1% of cement weight reduced the compressive strength by half [64]. However, 0.5% or less of cement weight does not affect the compressive strength when using yeast extract [95, 107].

A small amount of urea (0.5% of cement weight) does not impact concrete properties or bacteria. However, 4% urea of cement weight could delay the hydration [94].

5. Self-Healing Concrete Performance

5.1. Structural Properties

Bacterial concrete's structural properties can be affected by a number of variables, such as the bacteria used and their concentration, the type of nutrient media employed, and the presence of admixtures or additives. In order to design safe, durable, and efficient concrete buildings, it is crucial to understand and optimize these properties. Table 1 shows the results of past research on mechanical properties (compressive and flexural strength) after 28 days.

Table 1. Summary of mechanical properties past research

Reference	Bacteria type	Concentration	Insertion method	Nutrient	Compressive strength	Flexural strength
[85]	B. pasteruii	-	Indirect	-	↑ 35%	-
[78]	B. subtilis	10^6	Direct	-	↑ 28%	-
		10^7 & 10^4			↓ 9%	
[86]	B. pasteurii	10^5	Direct	Silica fume (10%)	↑ 14%	-
		10^7			↓ 6%	
[87]	B. pasteurii	-	Direct	-	↑ 30%	↑ 12%
[77]	B. subtilis & B. megaterium	10^8	Direct	Calcium lactate (0.5%)	↑ 16%	-
[26]	B. subtilis	10^3	Direct	Peptone	↑ 5%	-
		10^5			↑ 42%	
[89]	B. subtilis	10^9	Direct	Calcium lactate (10%)	↓ 21%	-
[10]	B. subtilis	10^8	LWA	Calcium lactate (5.6%)	↑ 12%	-
			GNP		↑ 9%	
[80]	B. subtilis	10^3	Direct	-	↑ 13%	-
		10^6			↑ 21%	
[90]	B. Sphaericus	-	Flyash 10%	-	↑ 69%	↑ 110%
	B. pasteurii				↑ 37%	↑ 27%
[97]	Bacillus subtilis	10^8	Direct	Calcium lactate (1%)	↑ 9%	-
			Iron oxide		↑ 21%	
			Bentonite		Slight increase	
[99]	Sporosarcina pasteurii	10^{13}	Small rubber particles	Calcium acetate (2%)	Slight increase	-
			Large rubber particles		↑ 16%	

5.2. Microstructure

In order to investigate the morphology and microstructure of concrete, a variety of tests can be conducted, such as (scanning electron microscope (SEM), x-ray diffraction (XRD), and Energy dispersive x-ray spectroscopy (EDS)). Several microstructure tests are commonly performed on bacterial and ordinary concrete to examine the formation and distribution of calcium carbonate crystals and the overall influence of bacterial activity on the microstructure of the concrete matrix. The results obtained from these experiments contribute to assessing the efficacy and long-term resilience of self-healing concrete as a self-repairing substance. Table 2 presents a comprehensive overview of researchers' various testing methodologies to investigate the microstructural aspect. The table also provides a summary of the findings obtained from these investigations.

Table 2. Summary of microstructure tests and research findings

Tests	Reference	Objective	Main findings
SEM	[17, 83, 108, 109]	Evaluate the changes in concrete microstructure after the self-healing process.	The control samples showed small quantities of $CaCO_3$ crystals, in contrast to the bacterial concrete mixtures.
	[6]	SEM analysis was performed on the strain solution precipitates that formed during MICP.	Samples of chemical and bacterial concrete both revealed polygonal calcium precipitation.
	[96]	Investigate the effect of air-entraining admixtures on the bacterial concrete.	The morphology of calcium carbonate is affected when air-entraining admixture is used.
	[82]	Examine the available evidence for any indications of biomineralizations.	Bacterial activity within concrete structures has been demonstrated through the formation of orthorhombic crystals.
	[43, 68, 110]	Examine the presence of bacterial activity in the healed cracks.	Bacterial activity can potentially be indicated by Neddele and bouquet $CaCO_3$ precipitation shapes.
	[97, 111, 112]	Study the effect of bacteria in concrete using the indirect method (Immobilization technique)	SEM images were obtained to examine the distribution of Bacillus subtilis spores in nutrition broth within the chosen immobilizer.
	[67, 113-115]	Study the healing products' morphology, crystal phases, and chemical composition.	The results of SEM imaging on samples of varying ages do not show significant differences in the size, shape, and distribution of the crystals.
XRD	[6, 82, 83, 97]	Study the precipitated material resulting from bacterial activity is $CaCO_3$.	$CaCO_3$ was found in the healed area with C-S-H, confirming both self-healing techniques.
	[111]	Examine the hypothesis of the continued hydration and bacterial activity.	The finding supports the hypothesis that sodium silicate underwent a reaction with the pre-existing $Ca(OH)_2$, resulting in the formation of additional C-S-H gel.
EDS	[82, 84, 114]	Examine the presence of the $CaCO_3$ compounds in the healed cracks.	Calcium, oxygen, and carbon were found in the healed areas, confirming $CaCO_3$ preceptations.

5.3. Durability

The concept of "concrete durability" relates to the ability of concrete structures to withstand various environmental and operational circumstances without significant degradation or loss of functionality over an extended duration. This section will examine various factors that contribute to the durability of concrete. Several researchers have indicated that incorporating self-healing concrete can effectively improve durability. Table 3 provides a comprehensive overview of various research investigations related to the durability of concrete.

Table 3. Summary of research investigations on concrete durability studies.

Durability aspect	Bacteria type	Reference	Objectives	Main findings
Porosity	Micrococcus - B. subtilis	[116]	Investigate the effectiveness of the treatment using calcinogenic bacteria.	Capillary water absorption tests showed that calcinogenic bacteria reduced porosity by 60%.
	B. sphaericus	[117]	Investigate the impact of surface porosity on treatment efficacy.	The degree of porosity affects the water absorption.
	B. megaterim - B. cereus - Lysinibacillus	[118]	Examine how FA and different bacteria types affect biomineralization.	The porosity decreased by 24-31% due to void filling and pore-clogging caused by $CaCO_3$ precipitation.
	B. sphaericus	[115]	Examine how bacteria affect mortar porosity.	The porosity was reduced by 50% using bacteria.
	B. megaterim	[119]	Reviewing the future direction of the bacterial concrete.	Bacterial concrete reduced the porosity by 31%.
	B. cereus	[120]	Investigate the effect of bacteria immobilized in metakaolin.	The process of MICP resulted in a decrease in the porosity of mortars at all ages.
	B. subtilis	[81]	Evaluate how bacteria improve shotcrete.	The compressive strength increases as porosity decreases.
	B. subtilis	[121]	Investigate the performance of bacteria on concrete.	Using B. subtilis reduced the porosity by 70%.
Water absorption	B. sphaericus	[117]	Investigate the impact of surface porosity on treatment efficacy.	Water absorption was reduced by 65 to 90% due to $CaCO_3$ deposition.
	Sporoscarcina pasteurii	[86]	Investigate the impact of bacteria on the concrete matrix.	This bacteria strain reduced water absorption four times.
	-	[111]	Investigate the effect of sodium silicate on concrete performance.	The solution reduced the capillary water absorption by approximately 50%.
	Ureolytic bacterium	[122]	Examine the effect of bacteria with baghouse filter dust.	Adding bacteria strain reduced the water absorption.
	Sporosarcina pasteurii	[123]	Investigate the effect of bacteria on water absorption.	The maximum reduction in water absorption over control samples was 80–85%.
	B. megaterim	[124]	Investigate the effect of bacteria on concrete performance.	Water absorption was reduced by 5.25 and 7.35% after 7 and 28 days, respectively.

-	[125]	Investigate bacteria effect on durability studies.	It was found that the water absorption was decreased in all bacterial mixtures.
Chloride permeability	Bacillus Paseturii	[86]	Investigate the impact of Sporosarcina pasteurii bacteria on the concrete matrix.	Using this strain of bacteria reduced chloride permeability from Low to Very Low.
	Bacillus sp. CT-5	[126]	Examine how Bacillus sp. bacteria affect durability.	Using bacteria reduced the chloride ion permeability from (3177C) to (975.3C).
	B. Sphaericus	[119]	Explore bacterial concrete uses and methods.	The chloride permeability class was decreased from Moderate to Low.
	B. Pseudofirmus	[92]	Explore how bacteria can improve concrete durability.	The chloride permeability class was decreased from Moderate to Low.
	B. Subtilis	[121]	Study the effect of Bacillus subtilis strain on the concrete.	The chloride permeability class was decreased from Moderate to Very Low.

6. Summary and Conclusions

This study has identified two approaches to self-healing concrete (autogenous and autonomous) and the influence of utilizing bacterial concrete. Autonomous self-healing was found to be more effective than autogenous self-healing. Bacterial concrete exhibits notable outcomes in terms of permeability and strength due to the presence of bacteria. Based on the current research, bacterial concrete is becoming known as an environmentally friendly alternative. At some point, it will improve the longevity of the materials used in construction.

- After 28 days, it has been observed that approximately 30% of the cement particles present in conventional concrete remain unhydrated. Even though, the hydrated cement particles can have an inner core that remains incompletely hydrated, requiring further hydration over time. This phenomenon plays an essential part in improving the autogenous self-healing mechanism.
- Fly ash and silica fume are two examples of pozzolanas that have a beneficial effect on autogenous healing because of their delayed reaction with calcium hydroxide. However, using excessive amounts of FA can decrease compressive strength.
- Calcium hydroxide and calcium carbonate formation exhibit superior autogenous self-healing properties compared to calcium-silicate-hydrate (C-S-H).
- The use of bacteria in self-healing concrete can prevent steel corrosion, reduce permeability, and enhance mechanical properties, making it more durable and substantial.
- Autonomous self-healing concrete has resistance to freeze-thaw and high carbonation, which can help decrease the porosity and permeability.
- There is no relation between compressive strength and bacterial concentration.
- Eurocode 2 is the first code to allow the use of capsules in applying bacterial concrete.
- The characteristics of microbial precipitation can be affected by several aspects, including calcium concentration, pH value, dissolved inorganic carbon concentration, and nucleation sites.

- The efficacy of the indirect approach was found to enhance healing ability to a greater extent than the direct method. This is attributed to the prolonged viability of bacteria achieved through the indirect approach.
- The particle size of immobilizers influences the rate of healing. Since, particles with a larger size exhibit superior performance due to their ability to seal cracks effectively. Moreover, it has been observed that larger particles possess a greater ability to immobilize bacteria compared to smaller particles.
- It is preferable to use small capsules rather than larger ones since large capsules can rupture while mixing or hardening.
- Water, gas, and chloride permeability can be considered self-healing indicators.
- Nutrients are an essential parameter that aids bacteria to survive and help in self-healing concrete. In addition, the negative impacts of nutrients can be controlled.
- The most familiar cause of self-healing in both techniques is the precipitation of calcium carbonate crystals ($CaCO_3$) in the crack.

7. Future Recommendations

Several suggestions are made for future research. These suggestions are not meant to be exhaustive, but they do cover much ground and could include (but are not limited to) the following:

- Conducting further studies to explain better the adverse effect of using different immobilizers for bacterial concrete and its effect on mechanical properties.
- Studying the effect of different strains and higher concentrations of bacteria, alternative feeding agents, and various immobilization techniques on concrete.
- Future research should investigate the feasibility of implementing self-healing mechanisms in structures submerged in marine environments.
- Conducting experiments on larger models or prototypes is crucial in facilitating this novel technique's widespread acceptance and implementation.
- In order to assess the economic viability of incorporating a bio additive in concrete, particularly in the context of construction materials, it is imperative to conduct feasibility studies.
- The implementation of standardized protocols is recommended for evaluating the compatibility of bacteria with construction materials, specifically in determining the optimal bacterial concentration to be incorporated into concrete and the corresponding water-to-cement ratio for different applications.

References

[1] Nguyen TH, Ghorbel E, Fares H, Cousture A. Bacterial self-healing of concrete and durability assessment. Cement and Concrete Composites. 2019;104:103-340. https://doi.org/10.1016/j.cemconcomp.2019.103340

[2] Mildenhall HS, Northcott G. A manual for the maintenance and repair of concrete roads. Transportation research board; 1986.

[3] Mahmoodi S, Sadeghian P, editors. Self-healing concrete: a review of recent research developments and existing research gaps. 7th International Conference on Engineering Mechanics and Materials; 2019; Canada: Canadian Society for Civil Engineering (CSCE).

[4] Guadalupe M, Sierra-Beltran JH, Schlangen E. Characterization of sustainable bio-based mortar for concrete repair. Construction and Building Materials. 2014;67:344-52. https://doi.org/10.1016/j.conbuildmat.2014.01.012

[5] Koch GH, Brongers MP, Thompson NG, Virmani YP, Payer JH. Corrosion cost and preventive strategies in the United States. United States. Federal Highway Administration; 2002. Contract No.: FHWA-RD-01-156,, R315-01.

[6] Feng J, Chen B, Sun W, Wang Y. Microbial induced calcium carbonate precipitation study using Bacillus subtilis with application to self-healing concrete preparation and characterization. Construction and Building Materials. 2021;280:122460. https://doi.org/10.1016/j.conbuildmat.2021.122460

[7] De Rooij M, Van Tittelboom K, De Belie N, Schlangen E. Self-healing phenomena in cement-Based materials. Spizizen J, editor: Springer; 2013. https://doi.org/10.1007/978-94-007-6624-2

[8] Hilloulin B, Van Tittelboom K, Gruyaert E, De Belie N, Loukili A. Design of polymeric capsules for self-healing concrete. Cement and Concrete Composites. 2015;55:298-307. https://doi.org/10.1016/j.cemconcomp.2014.09.022

[9] Van Breugel K, editor Is there a market for self-healing cement-based materials. Proceedings of the first international conference on self-healing materials; 2007.

[10] Khaliq W, Ehsan MB. Crack healing in concrete using various bio influenced self-healing techniques. Construction and Building Materials. 2016;102:349-57. https://doi.org/10.1016/j.conbuildmat.2015.11.006

[11] Sierra-Beltran MG, Jonkers HM, Schlangen E. Characterization of sustainable bio-based mortar for concrete repair. Construction and Building Materials. 2014;67:344-52. https://doi.org/10.1016/j.conbuildmat.2014.01.012

[12] Worrell E, Price L, Martin N, Hendriks C, Meida LO. Carbon dioxide emissions from the global cement industry. Annual review of Energy and the Environment. 2001;26(1):303-29. https://doi.org/10.1146/annurev.energy.26.1.303

[13] White SR, Sottos NR, Geubelle PH, Moore JS, Kessler MR, Sriram S, et al. Autonomic healing of polymer composites. Nature. 2001;409(6822):794-7. https://doi.org/10.1038/35057232

[14] White S, Sottos N, Geubelle P, Moore J, Kessler M, Sriram S, et al. Correction: autonomic healing of polymer composites. Nature. 2002;415(6873):817. https://doi.org/10.1038/415817a

[15] Igarashi S, Kunieda M, Nishiwaki T, editors. Research activity of JCI technical committee TC-075B: Autogenous healing in cementitious materials. Proceedings of 4th International Conference on Construction Materials: Performance, Innovations and Structural Implications; 2009.

[16] Žáková H, Pazderka J, Rácová Z, Ryparová P. Effect of bacteria bacillus pseudofirmus and fungus trichoderma reesei on self-healing ability of concrete Acta Polytechnica CTU Proceedings. 2019;21:42-5. https://doi.org/10.14311/APP.2019.21.0042

[17] Van Der Zwaag S. Self-healing materials: an alternative approach to 20 centuries of material science2007.

[18] Ramm W, Biscoping M. Autogenous healing and reinforcement corrosion of water-penetrated separation cracks in reinforced concrete. Nuclear Engineering and Design. 1998;179(2):191-200. https://doi.org/10.1016/S0029-5493(97)00266-5

[19] Rajczakowska M, Habermehl-Cwirzen K, Hedlund H, Cwirzen A. Autogenous Self-Healing: A Better Solution for Concrete. Journal of Materials in Civil Engineering. 2019;31(9). https://doi.org/10.1061/(ASCE)MT.1943-5533.0002764

[20] Reinhardt H-W, Jooss M. Permeability and self-healing of cracked concrete as a function of temperature and crack width. Cement and Concrete Research. 2003;33(7):981-5. https://doi.org/10.1016/S0008-8846(02)01099-2

[21] Neville A. Autogenous healing-a concrete miracle? Concrete international. 2002;24(11):76-82.

[22] Aldea C-M, Song W-J, Popovics JS, Shah SP. Extent of healing of cracked normal strength concrete. Journal of materials in civil engineering. 2000;12(1):92-6. https://doi.org/10.1061/(ASCE)0899-1561(2000)12:1(92)

[23] Erşan YÇ, Hernandez-Sanabria E, Boon N, de Belie N. Enhanced crack closure performance of microbial mortar through nitrate reduction. Cement and Concrete Composites. 2016;70:159-70. https://doi.org/10.1016/j.cemconcomp.2016.04.001

[24] Lauer KR, editor Autogenous healing of cement paste. Journal Proceedings; 1956.

[25] Jonkers HM, Schlangen E. Development of a bacteria-based self healing concrete. Tailor Made Concrete Structures. 2008;1:425-30. https://doi.org/10.1201/9781439828410.ch72

[26] Meera C, Subha V. Strength and durability assessment of bacteria based self-healing concrete. IOSR Journal of Mechanical and Civil Engineering. 2016:1-7.

[27] Wu M, Johannesson B, Geiker M. A review: Self-healing in cementitious materials and engineered cementitious composite as a self-healing material. Construction and Building Materials. 2012;28(1):571-83. https://doi.org/10.1016/j.conbuildmat.2011.08.086

[28] Zhang J, Liu Y, Feng T, Zhou M, Zhao L, Zhou A, et al. Immobilizing bacteria in expanded perlite for the crack self-healing in concrete. Construction and Building Materials. 2017;148:610-7. https://doi.org/10.1016/j.conbuildmat.2017.05.021

[29] Ramakrishnan V, Panchalan RK, Bang SS, City R, editors. Improvement of concrete durability by bacterial mineral precipitation. Proc ICF; 2005: Citeseer.

[30] Hearn N, Morley C. Self-sealing property of concrete-Experimental evidence. Materials and Structures. 1997;30(7):404-11. https://doi.org/10.1007/BF02498563

[31] Van Tittelboom K, De Belie N. Self-Healing in Cementitious Materials-A Review. Materials 2013;6(6):2182-217. https://doi.org/10.3390/ma6062182

[32] Toader TP, Mircea AC. Self-Healing Concrete Mix-Design Based on Engineered Cementitious Composites Principles. Proceedings. 2020;63(1). https://doi.org/10.3390/proceedings2020063005

[33] Ter Heide N. Crack healing in hydrating concrete [Master Thesis]. Delft university: Delft University of Technology; 2005.

[34] Roig Flores M. Self-healing concrete: efficiency evaluation and enhancement with crystalline admixtures [PhD thesis]. Spain: Universitat Politècnica de València; 2018.

[35] Hearn N. Self-sealing, autogenous healing and continued hydration: What is the difference? Materials and Structures. 1998;31(8):563-7. https://doi.org/10.1007/BF02481539

[36] Edvardsen C. Water permeability and autogenous healing of cracks in concrete. Innovation in concrete structures: Design and construction: Thomas Telford Publishing; 1999. p. 473-87.

[37] Neville AM. Properties of Concrete. 7th ed: Longman London; 2011. 444 p.

[38] Pisters H. Einwirkung von angreifenden Wässern auf Beton. Angewandte Chemie. 1963;75(19):938. https://doi.org/10.1002/ange.19630751927

[39] Palin D, Jonkers HM, Wiktor V. Autogenous healing of sea-water exposed mortar: Quantification through a simple and rapid permeability test. Cement and Concrete Research. 2016;84:1-7. https://doi.org/10.1016/j.cemconres.2016.02.011

[40] Roy R. Bacteria-based self-healing mortar with bio-plastic healing agents: Comparative analysis on quantification and characterization of self-healing by various experimental techniques [Master thesis]. Royal Institute of Technology (KTH): KTH School of ABE; 2020.

[41] Muhsin MH, AbdElzahra IH. Studying the combination effect of additives and micro steel fibers on cracks of self-healing concrete. Journal of Engineering. 2016;22(1):49-67. https://doi.org/10.31026/j.eng.2016.01.04

[42] Snoeck D, Van Tittelboom K, Steuperaert S, Dubruel P, De Belie N. Self-healing cementitious materials by the combination of microfibres and superabsorbent polymers. Journal of Intelligent Material Systems and Structures. 2012;25(1):13-24. https://doi.org/10.1177/1045389X12438623

[43] Jonkers HM. Bacteria-based self-healing concrete. HERON. 2011;56:1-12.

[44] Scrivener KL. The development of microstructure during the hydration of Portland cement: Imperial College London (University of London); 1984.

[45] Li ZQ, Zhou ZH, Xu DY, Yu JH. Influence of cement coarse particle on the self-healing ability of concrete based on ultrasonic method. Advanced Materials Research. 2011;177:526-9. https://doi.org/10.4028/www.scientific.net/AMR.177.526

[46] Li M, Li VC. Rheology, fiber dispersion, and robust properties of engineered cementitious composites. Materials and Structures. 2013;46(3):405-20. https://doi.org/10.1617/s11527-012-9909-z

[47] Kuder KG, Ozyurt N, Mu EB, Shah SP. Rheology of fiber-reinforced cementitious materials. Cement and Concrete Research. 2007;37(2):191-9. https://doi.org/10.1016/j.cemconres.2006.10.015

[48] Meharie MG, Kaluli JW, Abiero-Gariy Z, Kumar ND. Factors affecting the self-healing efficiency of cracked concrete structures. American Journal of Applied Scientific Research. 2017;3(6):80-6. https://doi.org/10.11648/j.ajasr.20170306.12

[49] De Belie N, Gruyaert E, Al-Tabbaa A, Antonaci P, Baera C, Bajare D, et al. A review of self-healing concrete for damage management of structures. Advanced materials interfaces. 2018;5(17):1800074. https://doi.org/10.1002/admi.201800074

[50] Stanaszek-Tomal E. Bacterial concrete as a sustainable building material? Sustainability. 2020;12(2):696. https://doi.org/10.3390/su12020696

[51] Roig-Flores M, Serna P. Concrete Early-Age Crack Closing by Autogenous Healing. Sustainability. 2020;12(11). https://doi.org/10.3390/su12114476

[52] Danish A, Mosaberpanah MA, Salim MU. Past and present techniques of self-healing in cementitious materials: A critical review on efficiency of implemented treatments. Journal of Materials Research and Technology. 2020;9(3):6883-99. https://doi.org/10.1016/j.jmrt.2020.04.053

[53] Huang H, Ye G, Damidot D. Characterization and quantification of self-healing behaviors of microcracks due to further hydration in cement paste. Cement and Concrete Research. 2013;52:71-81. https://doi.org/10.1016/j.cemconres.2013.05.003

[54] Qian S, Zhou J, Schlangen E. Influence of curing condition and precracking time on the self-healing behavior of engineered cementitious composites. Cement and Concrete Composites. 2010;32(9):686-93. https://doi.org/10.1016/j.cemconcomp.2010.07.015

[55] Clear C. The effects of autogenous healing upon the leakage of water through cracks in concrete. Transportation research board: Transport Research Laboratory; 1985. Report No.: 00451338.

[56] Vijay K, Murmu M, Deo SV. Bacteria based self healing concrete - A review. Construction and Building Materials. 2017;152:1008-14. https://doi.org/10.1016/j.conbuildmat.2017.07.040

[57] He J, Shi X. Developing an abiotic capsule-based self-healing system for cementitious materials: The state of knowledge. Construction and Building Materials. 2017;156:1096-113. https://doi.org/10.1016/j.conbuildmat.2017.09.041

[58] Gerilla G, Teknomo K, Hokao K. An environmental assessment of wood and steel reinforced concrete housing construction. Building and Environment. 2007;42(7):2778-84. https://doi.org/10.1016/j.buildenv.2006.07.021

[59] Mora EP. Life cycle, sustainability and the transcendent quality of building materials. Building and Environment. 2007;42(3):1329-34. https://doi.org/10.1016/j.buildenv.2005.11.004

[60] Bhattacharyya T. Self healing in concrete materials [Master thesis]. University of Rhode Island: Rhode Island; 2012.

[61] Jaroenratanapirom D, Sahamitmongkol R. Self-crack closing ability of mortar with different additives. Journal of Metals, Materials and Minerals. 2011;21(1).

[62] Sisomphon K, Copuroglu O, Koenders E. Self-healing of surface cracks in mortars with expansive additive and crystalline additive. Cement and Concrete Composites. 2012;34(4):566-74. https://doi.org/10.1016/j.cemconcomp.2012.01.005

[63] Jiang Z, Li W, Yuan Z. Influence of mineral additives and environmental conditions on the self-healing capabilities of cementitious materials. Cement and Concrete Composites. 2015;57:116-27. https://doi.org/10.1016/j.cemconcomp.2014.11.014

[64] Jonkers HM, Thijssen A, Muyzer G, Copuroglu O, Schlangen E. Application of bacteria as self-healing agent for the development of sustainable concrete. Ecological Engineering. 2010;36(2):230-5. https://doi.org/10.1016/j.ecoleng.2008.12.036

[65] Ramachandran SK, Ramakrishnan V, Bang SS. Remediation of concrete using micro-organisms. ACI Materials Journal. 2001;98(1):3-9. https://doi.org/10.14359/10154

[66] Li L, Zheng Q, Li Z, Ashour A, Han B. Bacterial technology-enabled cementitious composites: A review. Composite structures. 2019;225:111170. https://doi.org/10.1016/j.compstruct.2019.111170

[67] Nodehi M, Ozbakkaloglu T, Gholampour A. A systematic review of bacteria-based self-healing concrete: Biomineralization, mechanical, and durability properties. Journal of Building Engineering. 2022;49:104038. https://doi.org/10.1016/j.jobe.2022.104038

[68] Seifan M, Samani AK, Berenjian A. Bioconcrete: next generation of self-healing concrete. Applied microbiology and biotechnology. 2016;100(6):2591-602. https://doi.org/10.1007/s00253-016-7316-z

[69] Whiffin VS. Microbial CaCO3 precipitation for the production of biocement [PhD thesis]: Murdoch University; 2004.

[70] Achal V, Mukherjee A. A review of microbial precipitation for sustainable construction. Construction and Building Materials. 2015;93:1224-35. https://doi.org/10.1016/j.conbuildmat.2015.04.051

[71] Tambunan T, Juki MI, Othman N, editors. Mechanical properties of sulphate reduction bacteria on the durability of concrete in chloride condition. International Conference on Sustainable Civil Engineering Structures and Construction Materials; 2019: EDP Sciences. https://doi.org/10.1051/matecconf/201925801024

[72] Erşan YÇ, Da Silva FB, Boon N, Verstraete W, De Belie N. Screening of bacteria and concrete compatible protection materials. Construction and Building Materials. 2015;88:196-203. https://doi.org/10.1016/j.conbuildmat.2015.04.027

[73] Burne RA, Chen Y-YM. Bacterial ureases in infectious diseases. Microbes and Infection. 2000;2(5):533-42. https://doi.org/10.1016/S1286-4579(00)00312-9

[74] Gollapudi U, Knutson C, Bang S, Islam M. A new method for controlling leaching through permeable channels. Chemosphere. 1995;30(4):695-705. https://doi.org/10.1016/0045-6535(94)00435-W

[75] Jagadeesha Kumar B, Prabhakara R, Pushpa H. Effect of bacterial calcite precipitation on compressive strength of mortar cubes. International Journal of Advanced Technology and Engineering Exploration. 2013;2(3):486-91.

[76] Neville AM. Properties of concrete. 6th ed: Longman London; 1995.

[77] Zahran MA, Attia M, Nasser AA. Self-healing of cracked concrete with bacterial approach. Engineering Research Journal. 2014;37(2):255-64. https://doi.org/10.21608/erjm.2014.66913

[78] Afifudin H, Hamidah MS, Noor Hana H, Kamaruddin K. Microorganism precipitation in enhancing concrete properties. Applied Mechanics and Materials. 2011;99:1157-65. https://doi.org/10.4028/www.scientific.net/AMM.99-100.1157

[79] Manikandan A, Padmavathi A. An experimental investigation on improvement of concrete serviceability by using bacterial mineral precipitation. International Journal of Research and Scientific Innovation. 2015;2(3):46-9.

[80] Sahoo KK, Arakha M, Sarkar P, Jha S. Enhancement of properties of recycled coarse aggregate concrete using bacteria. International journal of smart and nano materials. 2016;7(1):22-38. https://doi.org/10.1080/19475411.2016.1152322

[81] Kalhori H, Bagherpour R. Application of carbonate precipitating bacteria for improving properties and repairing cracks of shotcrete. Construction and Building Materials. 2017;148:249-60. https://doi.org/10.1016/j.conbuildmat.2017.05.074

[82] Khushnood RA, Qureshi ZA, Shaheen N, Ali S. Bio-mineralized self-healing recycled aggregate concrete for sustainable infrastructure. Science of the Total Environment. 2020;703:135007. https://doi.org/10.1016/j.scitotenv.2019.135007

[83] Saleem B, Hussain A, Khattak A, Khan A. Performance evaluation of bacterial self-healing rigid pavement by incorporating recycled brick aggregate. Cement and Concrete Composites. 2021;117:103914. https://doi.org/10.1016/j.cemconcomp.2020.103914

[84] Elmahdy MA, ELShami A, Yousry E-SM, Ahmad SS. Self-healing mortar using different types, content, and concentrations of bacteria to repair cracks. Frattura ed Integrita Strutturale. 2022(59).

[85] Achal V, Mukherjee A, Reddy MS. Biocalcification by Sporosarcina pasteurii using corn steep liquor as the nutrient source. Industrial Biotechnology. 2010;6(3):170-4. https://doi.org/10.1089/ind.2010.6.170

[86] Chahal N, Siddique R, Rajor A. Influence of bacteria on the compressive strength, water absorption and rapid chloride permeability of concrete incorporating silica fume. Construction and Building Materials. 2012;37:645-51. https://doi.org/10.1016/j.conbuildmat.2012.07.029

[87] Ravindranatha, Kannan N, L LM. Self-healing material bacterial concrete. International Journal of Research in Engineering and Technology. 2014;3(3):656-9. https://doi.org/10.15623/ijret.2014.0315121

[88] Goyal M, Chaitanya PK. Behaviour of Bacterial Concrete as Self-Healing Material. International Journal of Emerging Technology and Advanced Engineering. 2015;5(1):100-3.

[89] Babu NG, Siddiraju S. An experimental study on strength and fracture properties of self-healing concrete. International Journal of Civil Engineering and Technology. 2016;7(3):398-406.

[90] Jagannathan P. Studies on the mechanical properties of bacterial concrete with two bacterial species. Materials Today: Proceedings. 2018;5(2):8875-9. https://doi.org/10.1016/j.matpr.2017.12.320

[91] Jonkers HM, Schlangen E, editors. Crack repair by concrete-immobilized bacteria. Proceedings of the first international conference on self healing materials; 2007; Delft: Springer.

[92] AlBughdadi A. Assessment of performance of bio self-healing mortar using diatomaceous earth and silica fume. AUC Knowledge Fountain: American university in cairo; 2016.

[93] Ghosh P, Mandal S, Chattopadhyay B, Pal S. Use of microorganism to improve the strength of cement mortar. Cement and Concrete Research. 2005;35(10):1980-3. https://doi.org/10.1016/j.cemconres.2005.03.005

[94] Wang J, Snoeck D, Van Vlierberghe S, Verstraete W, De Belie N. Application of hydrogel encapsulated carbonate precipitating bacteria for approaching a realistic self-healing in concrete. Construction and Building Materials. 2014;68:110-9. https://doi.org/10.1016/j.conbuildmat.2014.06.018

[95] Paine K, editor Bacteria-based self-healing concrete: Effects of environment, exposure and crack size. Proceedings of the RILEM Conference on Microorganisms-Cementitious Materials Interactions; 2016; Netherlands: RILEM Publications SARL Paris, France.

[96] Bundur ZB, Amiri A, Ersan YC, Boon N, De Belie N. Impact of air entraining admixtures on biogenic calcium carbonate precipitation and bacterial viability. Cement and Concrete Research. 2017;98:44-9. https://doi.org/10.1016/j.cemconres.2017.04.005

[97] Shaheen N, Khushnood RA, Khaliq W, Murtaza H, Iqbal R, Khan MH. Synthesis and characterization of bio-immobilized nano/micro inert and reactive additives for feasibility investigation in self-healing concrete. Construction and Building Materials. 2019;226:492-506. https://doi.org/10.1016/j.conbuildmat.2019.07.202

[98] Zhang J, Wang X, Huang H, Chen S. Clustering based virtual machines placement in distributed cloud computing. Future Generation Computer Systems. 2017;66:1-10. https://doi.org/10.1016/j.future.2016.06.018

[99] Xu H, Lian J, Gao M, Fu D, Yan Y. Self-Healing Concrete Using Rubber Particles to Immobilize Bacterial Spores. Materials. 2019;12(14). https://doi.org/10.3390/ma12142313

[100] Bhaskar S, Hossain KMA, Lachemi M, Wolfaardt G, Kroukamp MO. Effect of self-healing on strength and durability of zeolite-immobilized bacterial cementitious mortar composites. Cement and Concrete Composites. 2017;82:23-33. https://doi.org/10.1016/j.cemconcomp.2017.05.013

[101] Yang J, Du Q, Bao Y. Concrete with recycled concrete aggregate and crushed clay bricks. Construction and Building Materials. 2011;25(4):1935-45. https://doi.org/10.1016/j.conbuildmat.2010.11.063

[102] Li W, Zhu X, Zhao N, Jiang Z. Preparation and properties of melamine urea-formaldehyde microcapsules for self-healing of cementitious materials. Materials. 2016;9(3):152. https://doi.org/10.3390/ma9030152

[103] Lv L, Schlangen E, Yang Z, Xing F. Micromechanical properties of a new polymeric microcapsule for self-healing cementitious materials. Materials. 2016;9(12):1025. https://doi.org/10.3390/ma9121025

[104] Khan B, Baradan B. The effect of sugar on setting-time of various types of cements. Quarterly science vision. 2002;8(1):71-8.

[105] Thomas NL, Birchall J. The retarding action of sugars on cement hydration. Cement and Concrete Research. 1983;13(6):830-42. https://doi.org/10.1016/0008-8846(83)90084-4

[106] Alazhari M, Chen X, Sharma T, Cooper R, Heath A, Paine K. Effects of bacterial self-healing agents on properties of cement mortar. Construction and Building Materials. 2016.

[107] Cunniffe J. The effects of calcium lactate on early-age concrete. University of Bath; 2013.

[108] Nijland TG, Larbi JA, van Hees RP, Lubelli B, de Rooij M, editors. Self healing phenomena in concretes and masonry mortars: a microscopic study. Proceedings of the First International Conference on Self Healing Materials; 2007: Springer

[109] Andalib R, Abd Majid MZ, Hussin MW, Ponraj M, Keyvanfar A, Mirza J, et al. Optimum concentration of Bacillus megaterium for strengthening structural concrete. Construction and Building Materials. 2016;118:180-93. https://doi.org/10.1016/j.conbuildmat.2016.04.142

[110] Huang H, Ye G, Damidot D. Effect of blast furnace slag on self-healing of microcracks in cementitious materials. Cement and Concrete Research. 2014;60:68-82. https://doi.org/10.1016/j.cemconres.2014.03.010

[111] Alghamri R, Kanellopoulos A, Al-Tabbaa A. Impregnation and encapsulation of lightweight aggregates for self-healing concrete. Construction and Building Materials. 2016;124:910-21. https://doi.org/10.1016/j.conbuildmat.2016.07.143

[112] Siddique R, Nanda V, Kadri E-H, Khan MI, Singh M, Rajor A. Influence of bacteria on compressive strength and permeation properties of concrete made with cement baghouse filter dust. Construction and Building Materials. 2016;106:461-9. https://doi.org/10.1016/j.conbuildmat.2015.12.112

[113] De Nardi C, Cecchi A, Ferrara L, Benedetti A, Cristofori D. Effect of age and level of damage on the autogenous healing of lime mortars. Composites Part B: Engineering. 2017;124:144-57. https://doi.org/10.1016/j.compositesb.2017.05.041

[114] Luo M, Qian C-x, Li R-y. Factors affecting crack repairing capacity of bacteria-based self-healing concrete. Construction and Building Materials. 2015;87:1-7. https://doi.org/10.1016/j.conbuildmat.2015.03.117

[115] Achal V, Mukerjee A, Reddy MS. Biogenic treatment improves the durability and remediates the cracks of concrete structures. Construction and Building Materials. 2013;48:1-5. https://doi.org/10.1016/j.conbuildmat.2013.06.061

[116] Tiano P, Biagiotti L, Mastromei G. Bacterial bio-mediated calcite precipitation for monumental stones conservation: methods of evaluation. Journal of microbiological methods. 1999;36(1-2):139-45. https://doi.org/10.1016/S0167-7012(99)00019-6

[117] De Muynck W, Debrouwer D, De Belie N, Verstraete W. Bacterial carbonate precipitation improves the durability of cementitious materials. Cement and concrete Research. 2008;38(7):1005-14. https://doi.org/10.1016/j.cemconres.2008.03.005

[118] Dhami NK, Mukherjee A, Reddy MS. Viability of calcifying bacterial formulations in fly ash for applications in building materials. Journal of Industrial Microbiology and Biotechnology. 2013;40(12):1403-13. https://doi.org/10.1007/s10295-013-1338-7

[119] Achal V, Mukherjee A, Kumari D, Zhang Q. Biomineralization for sustainable construction-A review of processes and applications. Earth-science reviews. 2015;148:1-17. https://doi.org/10.1016/j.earscirev.2015.05.008

[120] Li M, Zhu X, Mukherjee A, Huang M, Achal V. Biomineralization in metakaolin modified cement mortar to improve its strength with lowered cement content. Journal of Hazardous Materials. 2017;329:178-84. https://doi.org/10.1016/j.jhazmat.2017.01.035

[121] Rao MS, Reddy VS, Sasikala C. Performance of microbial concrete developed using bacillus subtilus JC3. Journal of The Institution of Engineers : Series A. 2017;98:501-10. https://doi.org/10.1007/s40030-017-0227-x

[122] Siddique R, Jameel A, Singh M, Barnat-Hunek D, Aït-Mokhtar A, Belarbi R, et al. Effect of bacteria on strength, permeation characteristics and micro-structure of silica fume concrete. Construction and Building Materials. 2017;142:92-100. https://doi.org/10.1016/j.conbuildmat.2017.03.057

[123] Thakur A, Phogat A, Singh K. Bacterial concrete and effect of different bacteria on the strength and water absorption characteristics of concrete: a review. International Journal of Civil Engineering Technology. 2016;7(5):43-56.

[124] Parashar AK, Gupta A, editors. Experimental study of the effect of bacillus megaterium bacteria on cement concrete. IOP Conference Series: Materials Science and Engineering; 2021: IOP Publishing. https://doi.org/10.1088/1757-899X/1116/1/012168

[125] Sikder A, Saha P. Effect of bacteria on performance of concrete/mortar: a review. International Journal of Recent Technology and Engineering (IJRTE). 2019;7(6):12-7.

[126] Achal V, Mukerjee A, Reddy MS. Biogenic treatment improves the durability and remediates the cracks of concrete structures. Construction and Building Materials. 2013;48:1-5. https://doi.org/10.1016/j.conbuildmat.2013.06.061

Research Article

Recycling of waste lubricating oil using ultra filtration membrane and modeling and prediction of its rheological behavior using Gauss-Newton algorithm

Afreen Nissar*[1, a], M. Hanief[1, b], Fasil Qayoom Mir[2, c]

[1]Mechanical Engineering Department, National Institute of Technology, Srinagar, India
[2]Chemical Engineering Department, National Institute of Technology, Srinagar, India

Article Info	Abstract
	In this research, ultrafiltration membrane made of Polyacrylonitrile (PAN) was employed to recover the lubricating oil from the waste oil in tandem with other treatment methods. FESEM was also used to analyze the structure of the membrane. The resultant recycled oil was monitored with Rheometer, FTIR and UV Spectrometer and it was found that the method successfully removed >90% of contaminants and heavy metals from the waste oil and improved the properties of the oil. The proposed method proved to be very economical and gave very promising results to reclaim the waste engine oil that can be re-used for various purposes. Also, the rheological behavior of engine oil is studied by a proposed mathematical model. Given that the suggested model was non-linear, the Gauss-Newton (GN) algorithm was employed to determine the ideal values for the model parameters. The experimental results obtained for virgin, waste and recycled lubricating oils from rheometer were used for validation of the model. The proposed model was compared with Reynold's exponential model based on statistical methods (co-efficient of determination (R^2) and mean square error (MSE)). It was found that that the proposed model can predict the change in viscosity with temperature with very high degree of accuracy (>99%).

1. Introduction

Lubricating oils work by acting as a separating film between two surfaces that rub against each other and thus reduce friction and wear. Lubricating oils are made up of two materials, first one being the base oil obtained from distillation of crude oil and the second component is made up of numerous additives that improve the base oil's properties and performance. These additives include friction modifiers, pour-point depressants, metallic detergents, viscosity improvers, zinc dialkyl-dithiophosphates, etc. [1]. The engine lubrication system is designed to overcome the mechanical losses of the engine and eliminate the wear products of the machine by preventing increased wear, overheating, and seizing of friction surfaces and reducing the consumption of the specified power [2]. Lubricants are highly specialized products carefully designed to perform many important functions such as starting the engine, reducing friction, protecting machinery from rust and corrosion, lubricating engine parts, and more [3]. After use, the oil deteriorates and loses its properties, so it cannot be used for its intended purpose. Lubricant properties such as TAN, ash content, metal content, moisture content, carbon residue and color scale increase while TBN decreases [4]. Waste oil has a higher viscosity than fresh oil due to

excessive evaporation of soot and sediments, oxidation products, water, or light fractions [5]. Lubricant deterioration occurs when various additives or foreign substances (metal powder, sulphur, water, carbon, ash, etc.) contaminate the oil, change its chemical composition, and affect its physical properties [6]. Because it is insoluble, stable, and high in heavy metals and other contaminants, used oil must be collected and recycled to avoid polluting the environment [7].

Disposing of used lubricating oil is a huge business that has destructive effects on both environment as well as health of any living organisms. The reason being that almost 20000-25000 barrels of used lubricating oil are collected by each state in India per month and rest of it is dumped into soil or water bodies where it affects both plants and animals. This collected oil is then sold off to industries where they burn it as low-grade oil without removing its harmful contaminants such as metal particles that are carcinogenic in nature. As the oil burns, these contaminants go up into the air and can cause major respiratory problems. A single engine oil change can contaminate huge water bodies when it is disposed of into sewer or drain. These oils are direct substitutes for heating oils and LDOs in foundries, bitumen mills, lead smelters and the battery industry.

Used lubricating oil is a high pollutant material and its impact on the environment is hazardous. The effect of the pollutants on the human health is extremely toxic as the used oil contains some of the deadly carcinogenic contaminants. Oil once used, can be cleaned of its contaminants, and recycled and reused for various purposes. Engine oil is generated from non-renewable petroleum fuels, therefore finding new sources will be more challenging in the future. Oil prices rise as supplies become scarcer. As demand has increased over the past few years, dwindling oil reserves have forced explorers to look elsewhere.

Waste oil can be converted into lubricating base oil, fuel oil, or utilized as a feedstock to create other products with economic value after being adequately cleaned and treated to eliminate pollutants [8]. Various recovery techniques have been created and employed over time based on the oil basis and contaminants. These recycling techniques include acid/clay treatment method [9,10], vacuum distillation and hydrogenation/clay treatment [11,12], solvent treatment method [13], membrane filtration technology [14], Pyrolysis using microwave heating [15], recycling using a washing agent [16], bentonite treatment method [17,18].

Studying the rheological characteristics of used engine oil is crucial for effective recycling. [19]. The study of material flow and deformation is known as rheology. Viscosity is the property of rheology that defines the measure of the resistance to deformation. Rheology especially deals with the study of liquid and soft matter [20]. Because the viscosity of the oil is essential to the engine oil's primary functions, including wear control, friction reduction, and load carrying capacity, it must constantly be at an appropriate level. The viscosity of the oil directly affects the engine oil's strength. Oil can be blended with various additives to increase its viscosity and keep it there for longer. Addition of physical contaminants, polymerization, anti-freeze, wear particles, etc. to the engine oil during its use compromises the viscosity of the oil and the oil ceases to function properly. This leads to decline in the quality of the oil and also causes further damage to the vehicle engine parts. Thus, it is important that the engine oil should be changed after regular intervals so that deterioration of engine performance is averted.

A significant reduction of oil viscosity can cause excessive wear as the oil film becomes thin, increase in friction which in turn causes excessive energy consumption and heat generation, increased particle contamination sensitivity due to reduction in oil film thickness, and failure of oil film at high temperature and high loads, or during start-up of vehicle engine. Similarly, high viscosity can also cause extreme heat generation which

causes oxidation of oil, sludge collection, cavitation and lubrication starvation as there is insufficient oil flow, excess energy consumption and poor pumpability during cold-start [21]. Engine oil displays non-Newtonian shear thinning behavior.

Viscosity is temperature dependent characteristic. To achieve better tribological performance, proper maintenance of rheological behavior with temperature is essential [22]. Engine oil must have the ideal viscosity for proper operation; it should not be too thick to pour at low temperatures, nor should it become too thin as the temperature rises so that it won't properly form an oil film between two parts as the engine temperature varies from room temperature to 150°C while in operation. If the oil is too thick, the engine must work harder, producing more heat; if the oil is too thin, there is insufficient friction, resulting in both situations in excessive wear and tear. Beyond certain temperatures, rheological properties remain unchanged showing good flow behavior.

This paper proposes the use of ultrafiltration membranes after waste oil pre-treatment as a promising method for treating lubricating oil. In addition to removing metal particles and dust from used lubricating oil, the ultrafiltration membrane process can improve the oil's flash point and fluidity. The main aim of the proposal is to find a low-cost method to recycle the oil and achieve superlative results by producing higher quality oil. The methods that have been previously used have become outdated and are very expensive in terms of capital investment and operating cost. Also, the purity level achieved is not of a good standard thus the recycled oil is used as a low-grade fuel. Distillation, clay process, and acid treatment method are commonly used processes in India. Distillation process is a high-cost technology and needs huge financial input for plant set-up, thus discouraging budding entrepreneurs to take up the challenge as this will not only prove to be a very successful business if set-up is low-cost but also will contribute a lot towards environmental pollution and health of all living organisms. Clay and acid treatment methods are old methods and do not yield high quality results. Membrane filtration is a promising technology to dispose of used lubricants as it has a higher rejection rate than other methods.

Numerous benefits of membrane filtering include great separation efficiency, simple scaling, a less environmental impact, and good product quality. Additionally, processes can be integrated with one another, such as biological waste disposal processes. [23,24]. Due to its continuous operation requirements, low power consumption, ease of adaptability, versatility, and relatively mild operating conditions when compared to traditional separation processes like distillation, evaporation, and crystallization, membrane separation technology is a rapidly developing field of science. [25]. This process, carried out at a pressure of 0.1 MPa and a temperature of 40 °C [26], enhances the treated oil's lubricating qualities by removing metal flakes, soot, and debris from used engine oil.

In this paper a mathematical model is also developed so that change in viscosity during operation of engine vehicle as an explicit function of temperature can be predicted. Throughout the operation, it is anticipated that other system parameters like shear stress, speed, torque, etc. will remain constant. Given that the suggested model was non-linear, the Gauss-Newton (GN) algorithm was employed to determine the ideal values for the model parameters. To assess the models' efficacy, the proposed and Reynold's models were contrasted with the findings of the experiment.

2. Materials

In this study used lubricating oils SAE 5W30 were obtained from different sources. The waste engine oil to be recycled was used for almost 3000 miles. The recycling process comprised of two steps; Pre-treatment and Filtration. The pre-treatment of oil was carried out by activated charcoal, activated bentonite clay, acetic acid, sodium hydroxide for neutralization and Whatman filter paper grade 1 (circular sheet, nominal thickness 180

µm, particle retention 11 µm). Ultra-filtration membrane shown in Fig. 1 was used for the separation process.
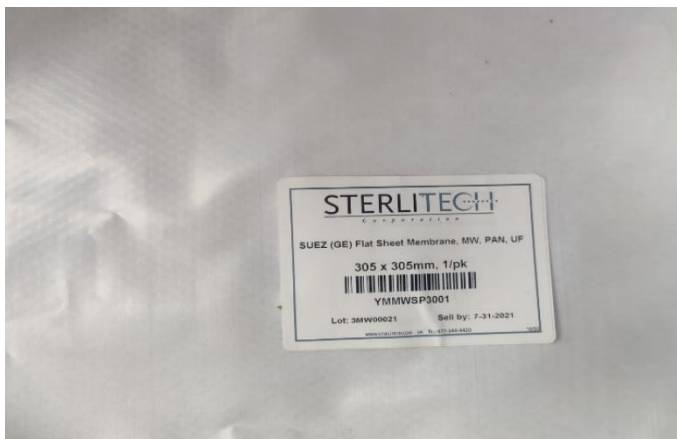
Fig. 1. Ultra-filtration membrane sheet (PAN)

2.1. Ultra-Filtration Membrane (Structural Analysis)

A flat sheet ultra-filtration membrane made of Polyacrylonitrile (PAN) with MWCO of 50 kDa was used for the separation process. Polyacrylonitrile (PAN) is a synthetic polymer with the linear formula $(C_3H_3N)_n$. Polyacrylonitrile (PAN) membranes combine superior selectivity, high flow rates and low pressures while maintaining quality and process efficiency. The unique nanofiber mesh structure combines ultra-fine pores with ample open space to facilitate fluid flow and filter out particles as small as 0.2 microns. The membrane is made by extruding ultra-thin PAN nanofibers onto a polyester substrate. The nanofibers form a dense mesh that traps particles, colloids, and bacteria larger than zero.
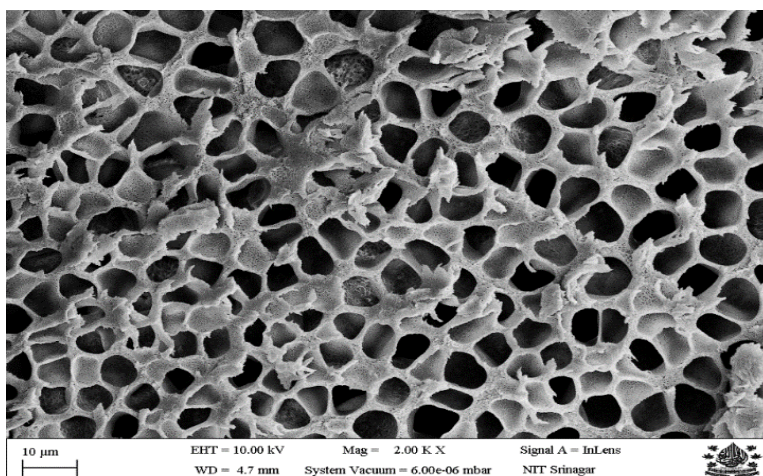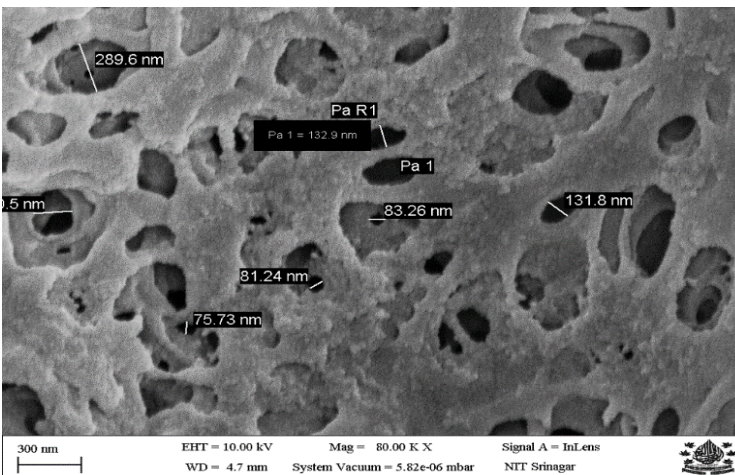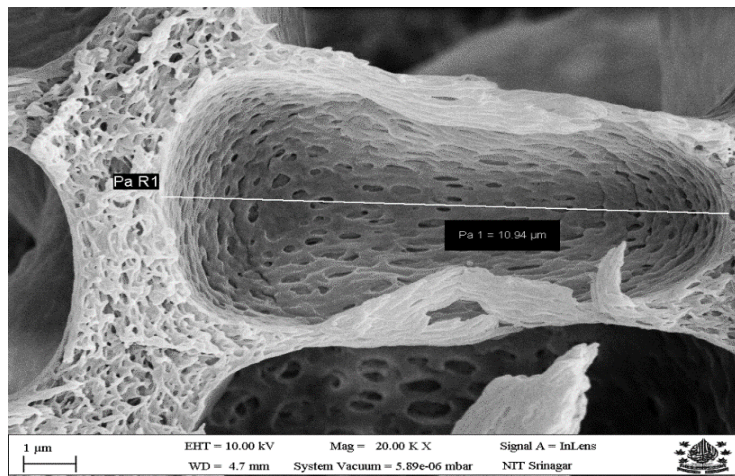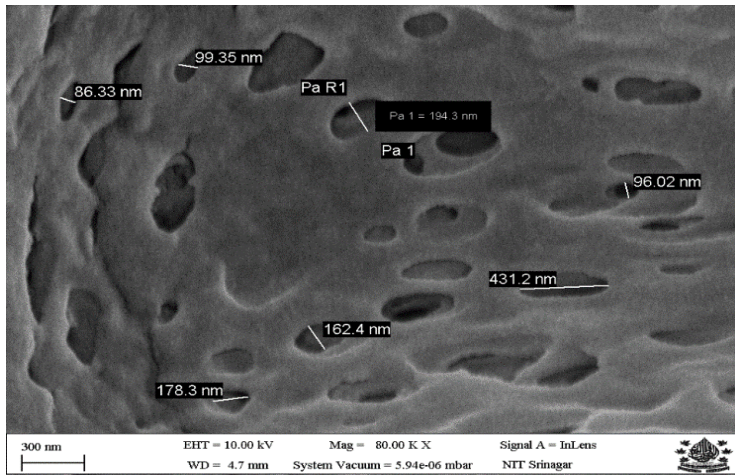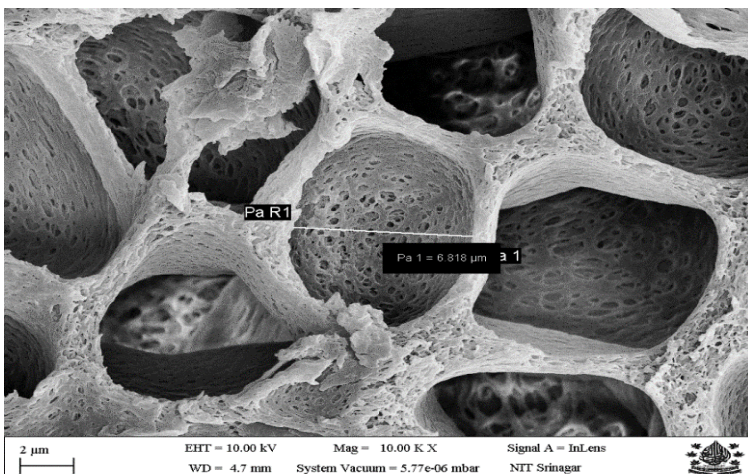
Fig. 2. FESEM images of Polyacrylonitrile UF membrane

The 2-micrometer mesh also has a relatively open structure, allowing water or aqueous solutions to pass through quickly with very little pressure. The main benefits of PAN membranes are:

- Very high flow rate
- Low pressure requirements
- Hydrophilic; no pre-wetting necessary

To analyze the structure of the membrane, FESEM (Field Emission Scanning Electron Microscopy) pictures from the surface and cross-section of the membrane are taken at various magnifications and are displayed in Fig. 2. The membrane has an asymmetrical structure made up of a porous bulk that has separate finger-like chambers contained in a porous solid matrix and a thin, thick surface layer. The surface layer is in charge of pollutant penetration or retention, whereas the pores serve as a mechanical support and let filtered oil move through. Since the heavy metal particles are removed at the pre-treatment stage, thus, the contaminants having smaller size are retained on this membrane.

3. Methodology

3.1. Pre-Treatment

The used engine oil is highly viscous due to the presence of heavy metal particles, dust, dirt, oxidation, polymerization, soot, other contaminants such as anti-freeze, etc. The particle size of these contaminants varies largely in size (20 microns and smaller). Thus, it was not possible to filter the viscous and thick oil using ultrafiltration membrane as the set-upmade of aluminum was not able to withstand the high pressure. So, pre-treatment of used oil was carried out before the ultra-filtration process. It served following purposes:

1. To decrease oil viscosity to improve the flux of membrane filtration [27].

2. To reduce the number of large particles in advance which otherwise could damage the ultrafiltration membrane.

3. To reduce the viscosity of oil sufficiently such that ultrafiltration could be carried out at mild conditions of pressure and temperature.

The stages of pre-treatment included:

1. Acid Treatment: The used lubricating oil was placed in a beaker and a magnetic stirrer was used to heat the oil to 40-50°C. During heating process acetic acid was added slowly to the oil and the mixing was done continuously for about 10 minutes.

2. Sedimentation: The oil mixed with acid was left in the container for about 24 hours and allowed to cool down. A sediment layer was formed at the bottom of the container. This oil was then filtered using Whatman filter paper shown in Fig. 4, to separate it from the sludge at the bottom of the container.

3. Bleaching: Activated charcoal and activated bentonite clay shown in Fig. 3, were added while heating the oil again to 100°C and the solution was mixed for 15 mins.

4. Neutralization: After bleaching, sodium hydroxide was added to the solution to neutralize the effects of acetic acid by reducing the pH of the oil.

5. Filtration: The solution was again allowed to settle down for 24 hours and then again filtered using Whatman filter paper.

Fig. 3. Activated charcoal and activated bentonite clay

Fig. 4. Whatman Filter Paper (Single sheet)

3.2. Membrane based filtration process

After pre-treatment process, the resultant oil obtained was less viscous and major contaminants were removed during the pre-treatment process. The oil was then allowed to undergo ultrafiltration using an experimental set-up shown in Fig. 5 designed for this purpose.
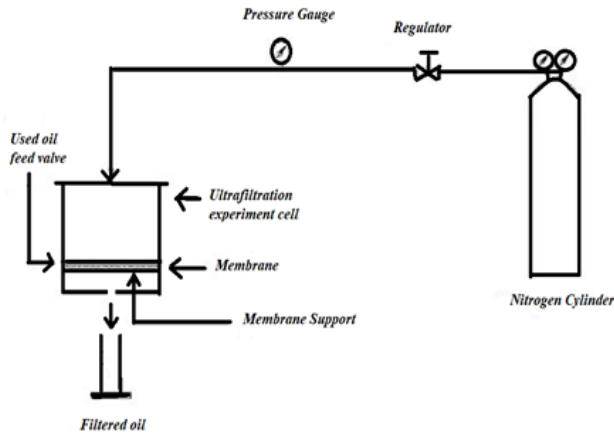
Fig. 5. Experimental set-up for ultrafiltration process

The experimental cell was fabricated from aluminum, since it is cheap and easily available. It had two compartments separated by a support for membrane. Used oil was introduced on the upper side of membrane by feed valve which was then closed. The oil was introduced at the high-pressure side where the pressure was maintained by nitrogen gas. The permeate was collected on low pressure side in a container for collection of recycled oil.

Fig. 6. Virgin, used and recycled engine oil

4. Result Analysis and Discussion

4.1. Fourier Transform Infrared Spectroscopy

Perkin-Elmer, Model Spectrum-Two (ATR Diamond) FTIR (Fourier Transform Infrared) Spectrometer was employed for characterization. The FTIR analysis method scans test materials and examines chemical characteristics using infrared light. FTIR was used to identify contaminants and functional groups in recycled, virgin and waste oil samples.

The ability of FTIR to provide a composite molecular fingerprint of engine oil makes it an extremely valuable analytical tool for condition monitoring of vehicle engines and engine oil as each constituent of oil has its own fingerprint. These constituents present a unique spectrum as they absorb radiation at that spectral location. The remaining radiation is transmitted and is shown as %Transmittance which depends on the amount of constituents present. This allows detection of all contaminants ranging from soot, nitration, oxidation to ZDDP, etc. which determines condition of the oil.
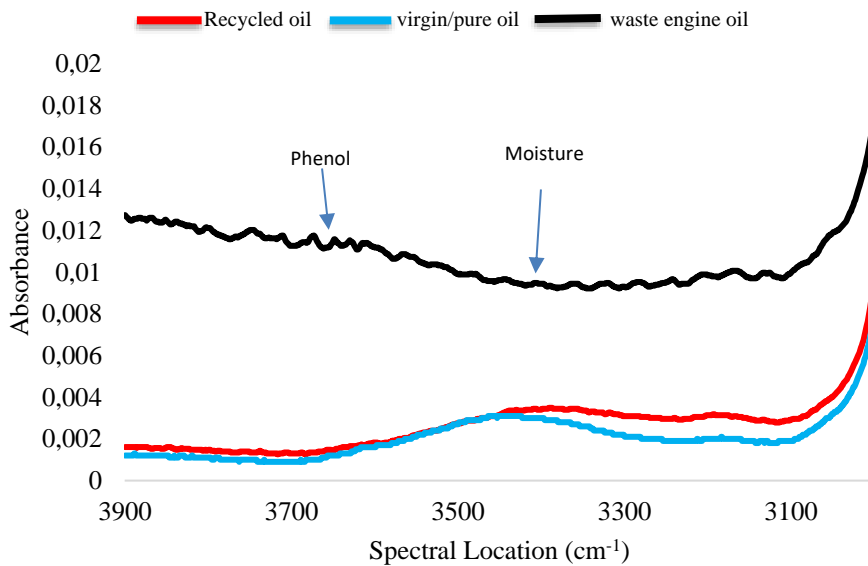
Fig. 7 FTIR of oil sample from spectral locations 4000 to 3000 cm^{-1}
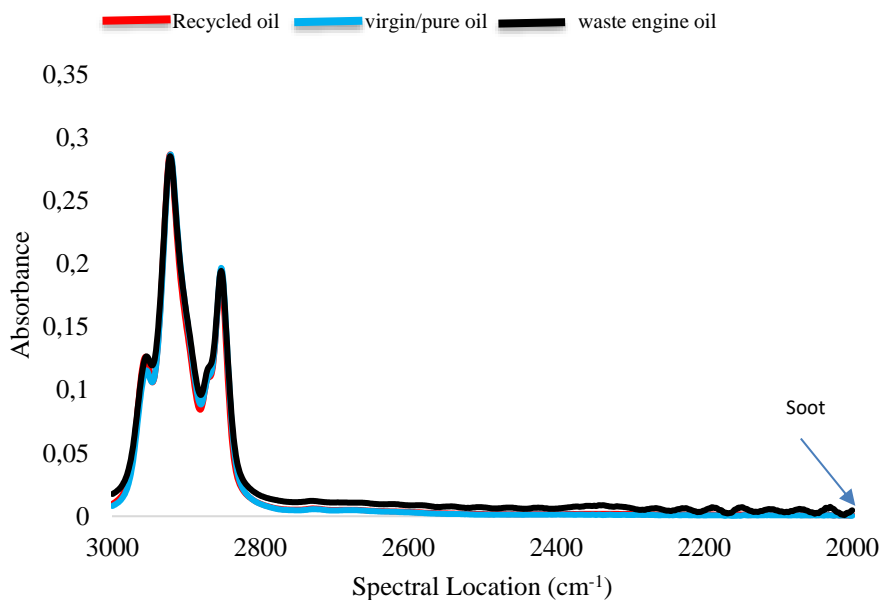
Fig. 8. FTIR of oil sample from spectral locations 3000 to 2000 cm^{-1}
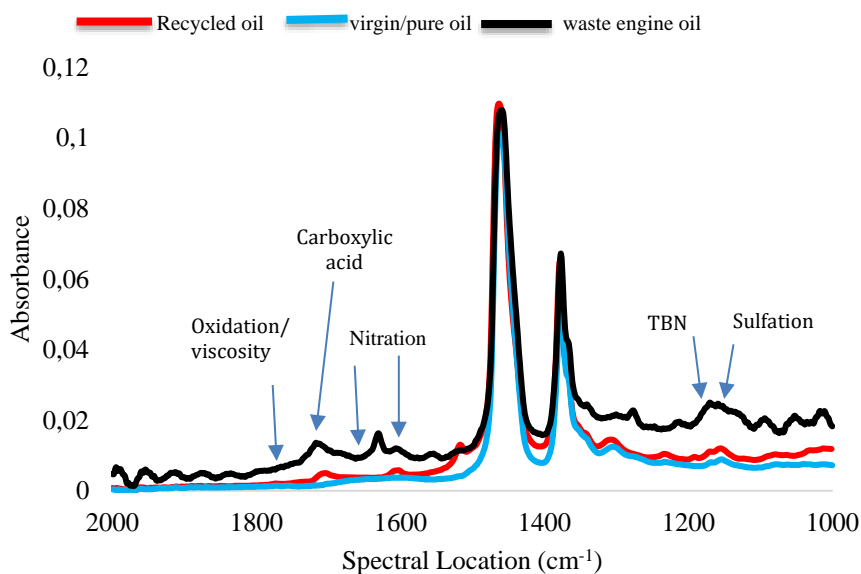
Fig. 9. FTIR of oil sample from spectral locations 2000 to 1000 cm^{-1}
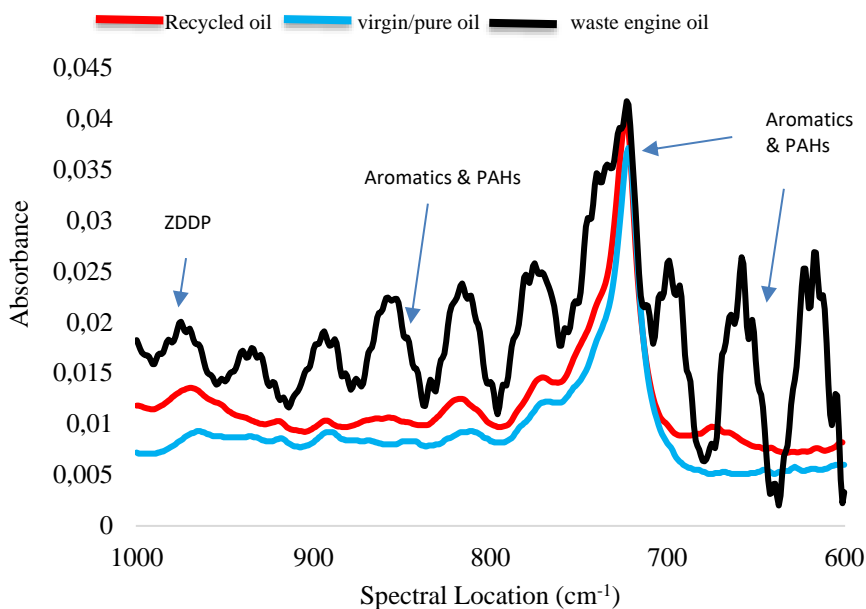
Fig. 10. FTIR of oil sample from spectral locations 1000 to 600 cm^{-1}

Table 1. Values of all oil samples' absorbances as determined by FTIR Spectroscopy

Contaminants/Functional groups	Spectral Location (cm^{-1})	Virgin oil	Used Engine Oil	Recycled oil
Phenol	3650	0.0012	0.011486	0.00143
Moisture	3400	0.003	0.00943	0.0034
Soot	2000	0.0004	0.004716	0.000782
Oxidation/Viscosity	1750	0.0013	0.007535	0.002177
Carboxylic Acid	1725	0.0014	0.011352	0.002701
Carboxylic Acid	1700	0.002	0.011396	0.00476
Nitration	1650	0.0032	0.009706	0.003707
Nitration	1600	0.0038	0.011486	0.005639
TBN	1170	0.008	0.025028	0.011129
Sulfation	1150	0.0086	0.023329	0.01153
ZDDP	980	0.0078	0.018	0.012602
Aromatics & PAHs	850	0.0083	0.019588	0.010239
Aromatics & PAHs	720	0.0365	0.0413	0.03929
Aromatics & PAHs	650	0.0052	0.016238	0.007756

The results of FTIR shown in Figs. 7-10, are depicted in form of absorbance values which are directly proportional to particular constituent quantity at certain spectral location. From the absorbance values in Table 1 it is observed that the contaminant level of recycled oil has decreased considerably when compared to that of used engine oil and the values are closer to that of virgin/pure oil thus depicting the successful removal of contaminants/ functional groups that had caused impurification of oil.

It is clear from the Table 1 that there is significant reduction in the level of contaminant after recycling. The percentage reduction in the level of the contaminants is calculated using Eq. (1).

$$\emptyset = \left[\frac{R.O - V.O}{U.O - V.O}\right] \times 100\% \tag{1}$$

Where $\emptyset$ is the Percentage reduction in the level of contaminants after recycling

R.O is the absorbance value of Recycled oil obtained from FTIR Spectroscopy

V.O is the absorbance value of Virgin/pure oil obtained from FTIR Spectroscopy

U.O is the absorbance value of Used oil obtained from FTIR Spectroscopy

The results are given in the Table 2.

Table 2. Percentage reduction in the level of contaminants after recycling

S.No.	Functional group/ Contaminant	Percentage reduction after recycling
1	Phenol	> 97%
2	Moisture	> 93%
3	Soot	> 91%
4	Oxidation/Viscosity	> 85%
5	Carboxylic Acid	> 86%
6	Nitration	> 92%
7	TBN	> 81%
8	Sulfation	> 80%
9	ZDDP	> 52%
10	Aromatics & PAHs	> 82%

The results presented in the Table 2 show that the contaminants are successfully removed from the waste engine oil and there is decrease in viscosity. There is marked improvement in the characteristics of recycled oil as the impurities are successfully removed. Also, there is a significant improvement in the color, as the color changes from pitch black of used oil to darker shade of yellow resembling the color of virgin/pure oil.

4.2. Rheological Study

An AntonPaar MCR 102 rheometer with a Peltier device for temperature control has been utilized to predict the rheological behavior of recycled, virgin and waste lubricating oils. Several experiments were conducted, including determining the fluid behavior and the relationship between viscosity and temperature at various shear rates in continuous rotation mode. Tests were conducted utilizing 50 mm parallel plate geometry. This measuring method is best suited for measuring viscosity of oils and offers quick temperature stability. The distance between two plates was kept at 0.1 mm. The rheometer

has a special TruGapTM feature. Independent of temperature and thermal expansion, TruGapTM monitors the gap and accurately adjusts the desired position. Each measurement was performed three times, and the mean was computed, in order to obtain precise data and evaluate the reliability of experimental results.

Changes in rheological parameters (viscosity, shear stress and torque) with temperature were investigated. The change in viscosity with temperature is shown in the graph in Fig. 11. We can see that the viscosity decreases with increasing temperature as the oil becomes thinner with higher temperature and the dependence is not linear. Lubricants exhibit non-Newtonian shear thinning. Lubricating oil is thick at low temperatures and becomes thinner as the temperature increases, thus decreasing the viscosity. It is pertinent to mention that the lubricating oil should not be too thick at low temperatures that makes it difficult to pump or pour, nor should it become too thin at high temperatures that its load bearing capacity is reduced. Beyond certain temperatures, rheological properties remain unchanged showing good flow behavior. Different oils show different variation in viscosity with temperature.

It has been reported that better rheological behaviour as a function of temperature leads to better tribological performance [28]. The presence of contaminants in the oil increases the viscosity and thickness of the oil. From the Fig. 11, it is observed that the viscosity of recycled oil is reduced considerably after removal of contaminants and is closer to that of virgin/pure oil and obeys Reynolds's equation given by Eq. (2):

$$\mu_o = b e^{-a T_A} \tag{2}$$

where μ_o is the dynamic viscosity at atmospheric pressure and T_A is absolute temperature. The fluidity was found to be maximum for virgin oil and least for used engine oil due to presence of contaminants. The fluidity of recycled oil is shown in Fig. 12.
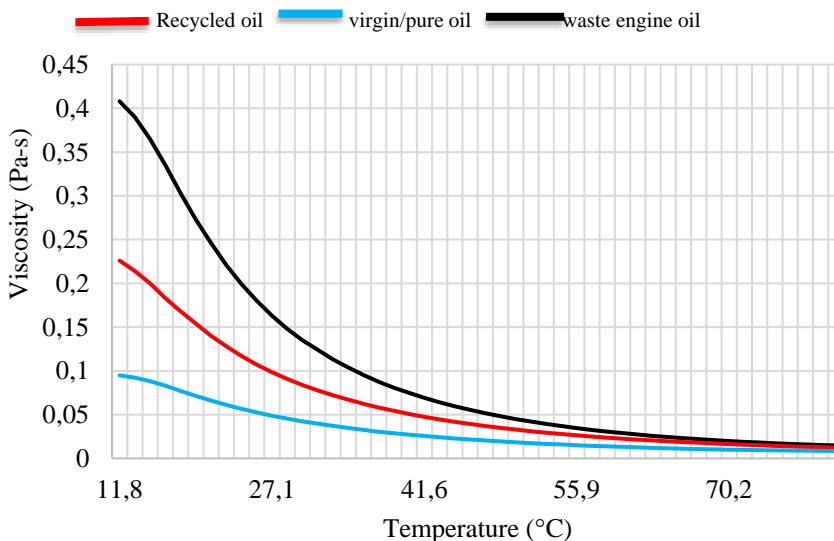

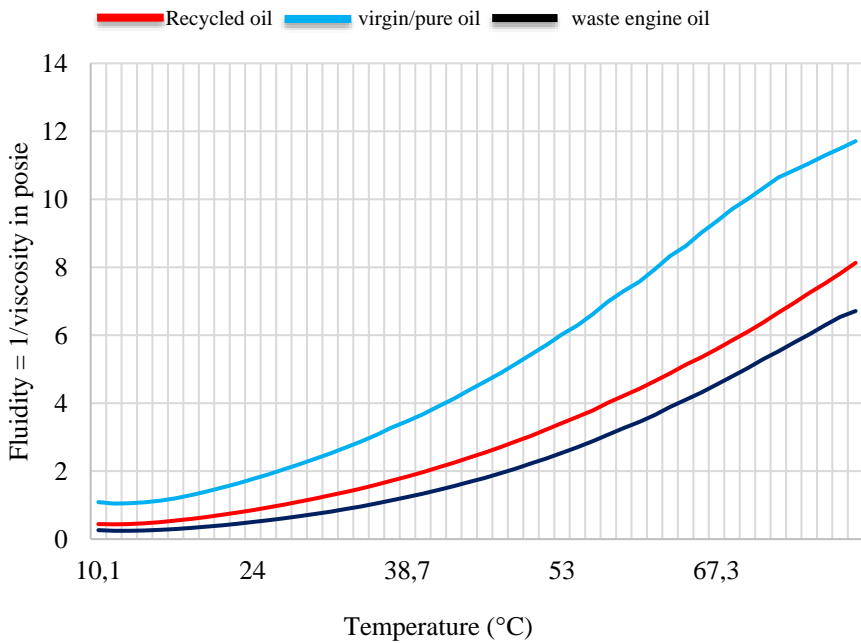Fig. 11. Effect of temperature on viscosity of oil samples

Fig. 12. Change in fluidity of oil samples with increase in temperature

4.3. UV Spectroscopy:

UV Spectroscopy is a low-cost, easy, and fast technique which is useful for identifying contaminants such as heavy metals. Many contaminants are chromophores and they absorb ultra-violet or visible light at specific wavelength. According to the Beer-Lambert law, the absorption spectrum produced by these samples at a given wavelength can be directly related to the concentration of the sample [29]. UV spectroscopy is a type of absorption spectroscopy in which light in the UV range (200-400 nm) is absorbed by molecules. Electromagnetic radiation is used in absorption spectroscopy between 190 and 800 nm and is divided into two regions. UV (190-400nm) and visible (400-800nm) region. The Beer-Lambert law, which is used in UV spectroscopy, asserts that the rate at which the intensity of a monochromatic ray decreases as a function of the thickness of the absorbing solution is proportional to the incident radiation. Moreover, the solution's concentration. Eq. (3) provides the Beer-Lambert Law's expression.

$$A = log\left(\frac{I_o}{I}\right) = ECL \tag{3}$$

where A is the absorbance, Io is the light intensity that strikes the sample cell, I is the light intensity that leaves the sample cell, C is the solute's molar concentration, L, the sample cell's length in centimeters, and E, its molar absorptivity.

The UV Spectroscopic readings of used lubricating oil and recycled oil are presented in Fig. 13. The used lubricating oil shows very small absorbance peak at around 400 nm which indicates presence of hydrocarbon chromophores with polycyclic aromatic hydrocarbons. A small peak at around 620-650 nm depicts presence of N=O in the used engine oil and its absence is seen in recycled oil after its removal. Presence of various heavy metals in used

engine oil as wear particles and their absence in recycled oil is seen at specific spectral locations.
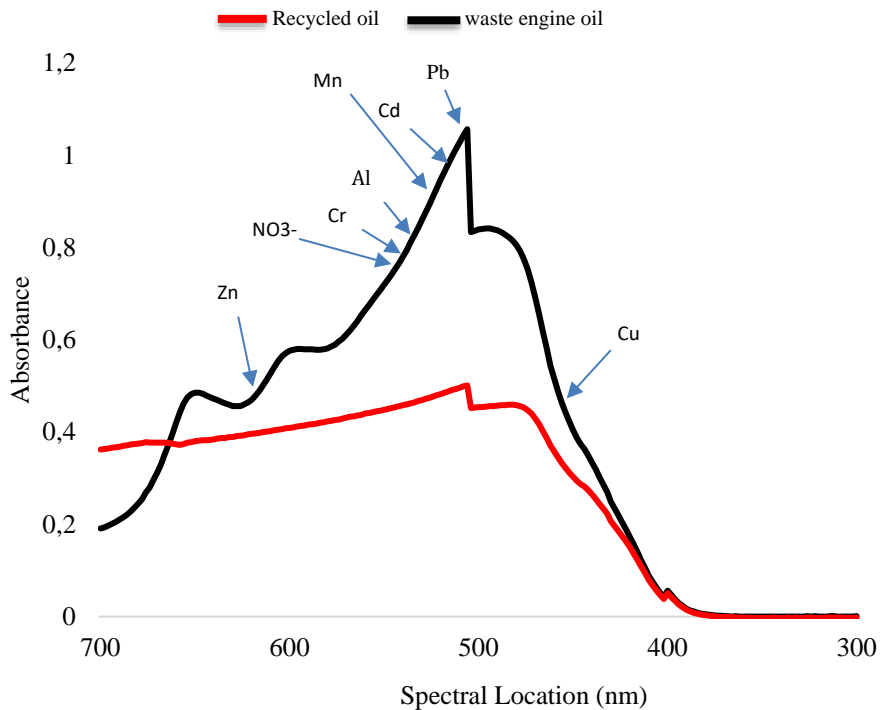
Fig. 13. Level of heavy metals in waste and recycled oil by UV Spectroscopy

4.4. Particle Size Analyzer

The AntonPaar Litesizer 500 was used to analyze the particle size distribution. This analysis is aimed to characterize nano and micro-particles in the waste and recycled oil samples.

Particle size analysis is a proven test method for oil analysis. The principle is simple: by measuring the number of particles in waste oil, the contamination ratio of the oil is known. That way, it helps to determine whether the oil is clean enough for reliable operation. Particle size analyzer test graphs in Figs. 14 and 15 clearly show decrease in the level of contaminants in the recycled oil when compared to that of used oil. It also shows the intensity of the contaminant particle size occurring in each sample.
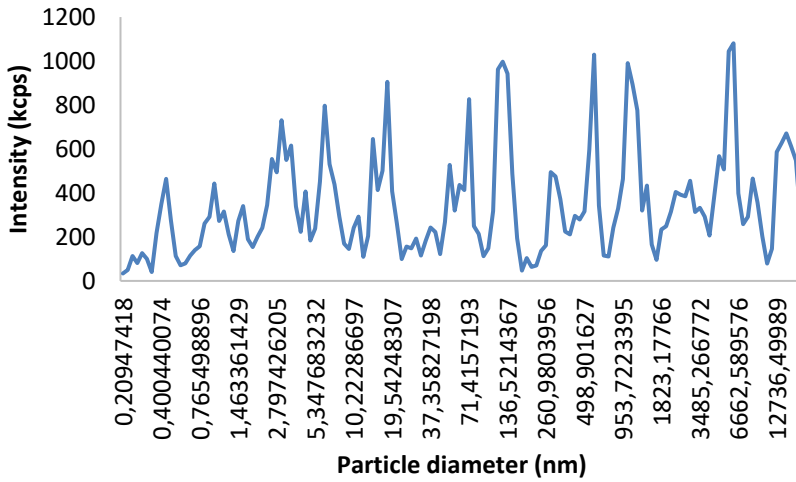
Fig. 14. Particle size distribution of Waste oil
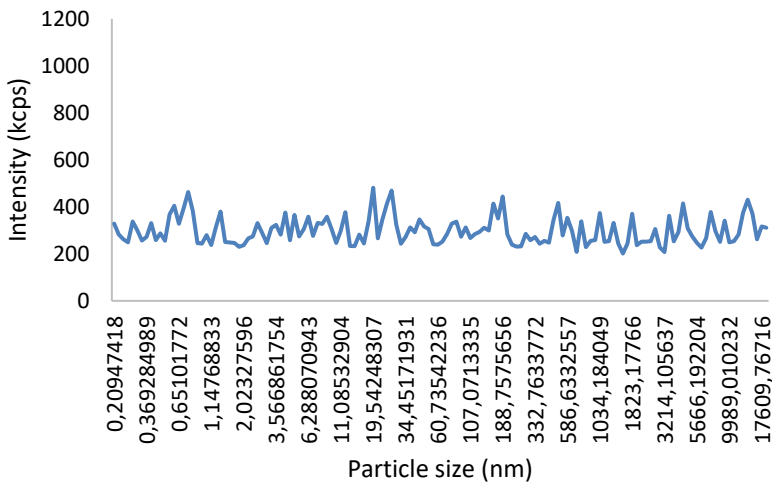
Fig. 15. Particle size distribution of Recycled oil

Modeling and Optimization Using GN Algorithm

The viscosity of liquids decreases exponentially with increase in temperature. It is observed that variation of viscosity with temperature in lubricating oils obeys Reynold's equation given by equation (2):

$$\mu o = b e^{-aT_A} \tag{4}$$

where μo is the dynamic viscosity at atmospheric pressure and T_A is absolute temperature.
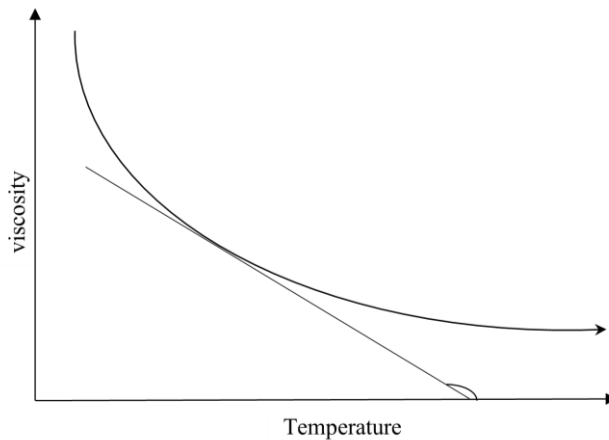
Fig. 16. Schematic representation of change of viscosity with temperature

To take non-linearity into consideration we assume,

$$-\frac{d\mu}{dT} \; \alpha \; T^n \tag{5}$$

$$-\frac{d\mu}{dT} = kT^n \tag{6}$$

Where k is the constant of proportionality

$$d\mu = -kT^n \, dT \tag{7}$$

On integration we get;

$$\mu = -\frac{kT^{n+1}}{n+1} + C \tag{8}$$

$$\mu = AT^m + C \tag{9}$$

where;

$$A = \frac{-k}{n+1} \tag{10}$$

$$m = n + 1 \tag{11}$$

Since the Eq. (9) is nonlinear and the constants cannot be determined by least square using logarithmic transformation. Eq. (9) describes the non-linear relationship between viscosity and temperature, which cannot be transformed into a linear form using a logarithmic transformation. Thus, the model parameters A, m, and C cannot be estimated using the least square technique. The Gauss-Newton technique was used to iteratively estimate the ideal values of A, m, and C. The three steps of the Gauss-Newton algorithm to estimate the model parameters are:

identifying Jacobian, Z_j calculating Forcing vector, D_j and assessing solution matrix, λ_{j+1},

where;

$$\lambda_{j+1} = [Z_j^T Z_j]^{-1}[Z_j^T]\{D_j\} \tag{12}$$

$$Z_j = \begin{Bmatrix} \left(\dfrac{\partial \mu}{\partial A}\right)_1 & \left(\dfrac{\partial \mu}{\partial m}\right)_1 & \left(\dfrac{\partial \mu}{\partial C}\right)_1 \\ \left(\dfrac{\partial \mu}{\partial A}\right)_2 & \left(\dfrac{\partial \mu}{\partial m}\right)_1 & \left(\dfrac{\partial \mu}{\partial C}\right)_1 \\ \left(\dfrac{\partial \mu}{\partial A}\right)_3 & \left(\dfrac{\partial \mu}{\partial m}\right)_1 & \left(\dfrac{\partial \mu}{\partial C}\right)_1 \\ \cdots \cdots \cdots \cdots \cdots \cdots \cdots \cdots \cdots \\ \cdots \cdots \cdots \cdots \cdots \cdots \cdots \cdots \cdots \\ \left(\dfrac{\partial \mu}{\partial A}\right)_N & \left(\dfrac{\partial \mu}{\partial m}\right)_N & \left(\dfrac{\partial \mu}{\partial C}\right)_N \end{Bmatrix}_{N\times3} \tag{13}$$

$$Z_j = \begin{Bmatrix} (T^m)_1 & (AT^m logT)_1 & 1 \\ (T^m)_2 & (AT^m logT)_1 & 1 \\ (T^m)_3 & (AT^m logT)_1 & 1 \\ \cdots \cdots \cdots \cdots \cdots \cdots \cdots \cdots \\ \cdots \cdots \cdots \cdots \cdots \cdots \cdots \cdots \\ (T^m)_N & (AT^m logT)_N & 1 \end{Bmatrix}_{N\times3} \tag{14}$$

$$D_j = \begin{Bmatrix} (S)_1 - (\mu)_1 \\ (S)_2 - (\mu)_2 \\ (S)_3 - (\mu)_3 \\ \cdots \quad \cdots \\ \cdots \quad \cdots \\ (S)_N - (\mu)_N \end{Bmatrix}_{N\times1} \tag{15}$$

where $(S)_i$, $i = 1,2,3 \ldots. N$ are the experimental viscosity values at various time intervals, and;

$$\lambda_{j+1} = \begin{Bmatrix} A \\ m \\ C \end{Bmatrix}_{3\times1} \tag{16}$$

where λ_{j+1}, $j = 1,2,3, \ldots., m$ is the matrix containing model parameters. A, m and C were initially picked at random to evaluate λ_1. The optimal values of λ_{j+1} were obtained by successive iterations using

$$\lambda_{j+1} = [Z_j^T Z_j]^{-1}[Z_j^T]\{D_j\} \tag{17}$$

The data of waste/used engine oil along with virgin and recycled/filtered oil was collected from Anton paar rheometer used for experiment and the data was used for developing the models. The results obtained from proposed model are compared with experimental data and Reynold's model in this section. MATLAB was used for programming Gauss-Newton algorithm in order to evaluate the optimal values of A, m and C and were initialized by taking arbitrary values.
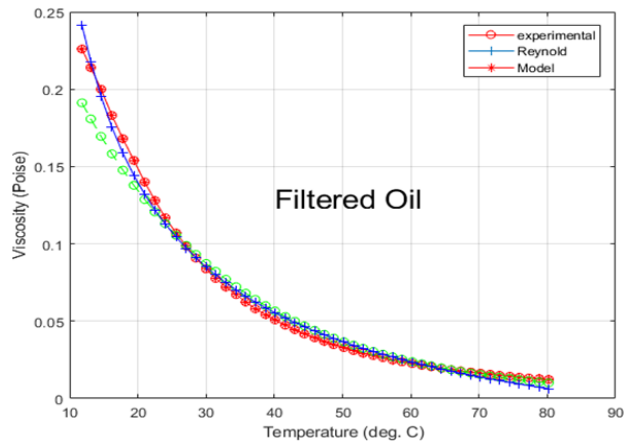
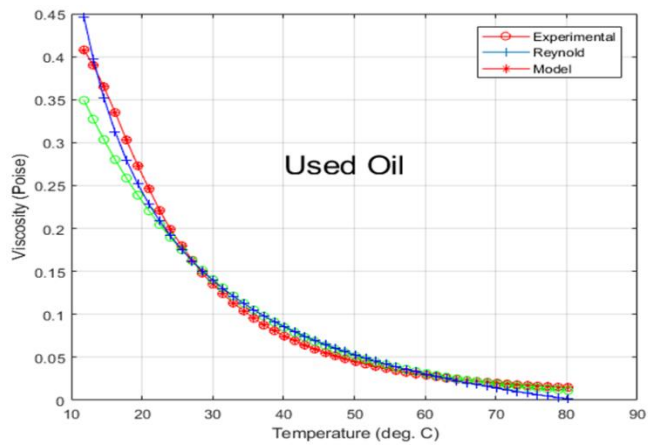Fig. 17. Change of viscosity with temperature (Filtered/Recycled oil)

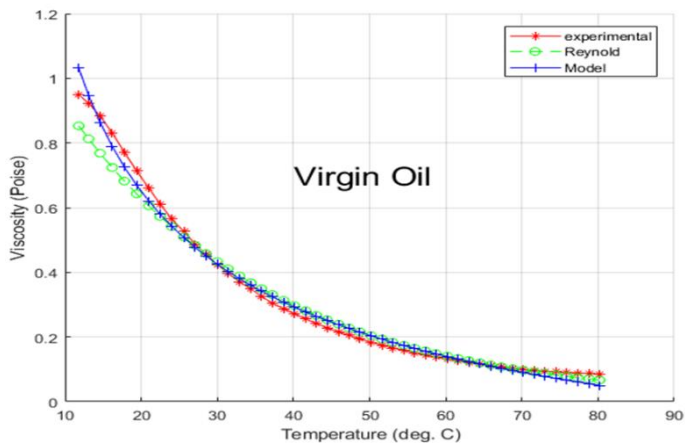Fig. 18. Change of viscosity with temperature (Used oil)

Fig. 19. Change of viscosity with temperature (Virgin oil)

Eqs. (18), (19), (20) are obtained for the results for viscosity of virgin, used and filtered/recycled oil.

$$\mu_{virgin} = -0.4620 + 5.9228T^{-0.5582} \tag{18}$$

$$\mu_{used} = -0.0973 + 4.8750T^{-0.8892} \tag{19}$$

$$\mu_{filtered} = -0.1254 + 4.1105T^{-0.7740} \tag{20}$$

Evaluation of competence of the models was estimated and presented in Table 3. From Table 3 it is obvious that in case of the proposed model there is a good correlation ($R^2 = 99.59\%$ for virgin oil), ($R^2 = 99.44\%$ for Used oil) and ($R^2 = 98.28\%$ for Filtered/recycled oil) between viscosity and temperature. The results of proposed models indicate that ≥99 % of observed variation can be explained by model's inputs.

Table 3. Statistical parameters of Reynold's model and proposed model

	R^2		MSE	
	Reynold's	Proposed	Reynold's	Proposed
Virgin oil	98.92	99.59	1.60×10^{-03}	5.82×10^{-04}
Used oil	97.76	99.44	4.09×10^{-04}	1.24×10^{-04}
Filtered oil	98.28	98.28	1.08×10^{-04}	5.41×10^{-08}

Mean squared error (MSE) of proposed model and Reynold's model in Table 3 indicates that the error between the predicted and experimental values of viscosity is very small. Therefore, the model is in good agreement with the experimental results and can be used to predict the change viscosity of the engine oil with temperature with high accuracy during the operation of the vehicle.

6. Conclusion

Proper lubrication is essential for survival and maintenance of any machinery. It not only ensures smooth operation but also increases the life of the machine by reducing friction and wear. Thus, use of lubricating oil and changing it at right time is mandatory. Also, improper disposal of waste oil causes irreversible harm to the environment and living organisms, hence finding an alternate is a necessity.

The proposed process is a very promising method to recycle the waste oil and reclaim it for further use. In this research, pre-treatment process involving acid treatment, bleaching and neutralization is followed by ultrafiltration process by Polyacrylonitrile (PAN) membrane. Following conclusions are drawn from the investigation, and the results are very promising.

- The reduction in contaminant level was found to be >93% in moisture, >91% in soot, >97% in phenol, >92% in nitration, >85% in oxidation and viscosity, >86% in carboxylic acid, >81% in Total Base Number, >80% in sulfation, >82% in Aromatics and Polycyclic Aromatic hydrocarbons and >52% in ZDDP.
- There is evident change in color and odor due to removal of contaminants.
- There is marked decrease in viscosity (from 0.0408 Pa-s of waste oil to 0.226 Pa-s of recycled oil at 11.8°C) and considerable improvement in fluidity.

- Significant reduction in levels of heavy harmful metals such as aluminum, cadmium, chromium, copper, lead, manganese, zinc, nitrate as is observed by UV Spectroscopy. In addition to above, the study can also help to investigate the condition monitoring of engine parts. The methodology adopted is environment friendly with minimal impact on ecosystem and low-cost. The resultant product is of higher quality as the method exhibits high separation efficiency. The method can find in application for other types of waste oils obtained from industries and factories which include transmission fluid, refrigeration fluid, compressor oils, metal working oils, hydraulic fluid, etc. which can provide benefit on a larger scale globally.
- Particle size analyzer test graphs clearly show decrease in the contaminant level in recycled oil.

This research also develops a mathematical model to describe the rheological behavior of recycled motor oil. It is observed that the viscosity decreases with increase in temperature as it is known that oil thins-out at higher temperature, and the relation is non-linear. The lubricants display non-Newtonian shear thinning behavior. Lubricating oil is thick at low temperatures and becomes thinner as the temperature increases, thus decreasing the viscosity. It is pertinent to mention that the lubricating oil should not be too thick at low temperatures that makes it difficult to pump or pour, nor should it become too thin at high temperatures that its load bearing capacity is reduced as the temperature in the vehicle engine varies from ambient temperature to 150°C. Beyond certain temperatures, rheological properties remain unchanged showing good flow behavior. Different oils show different variation in viscosity with temperature. Presence of contaminants in oil increase the viscosity and thickness of the oil and it is observed that the viscosity of recycled oil is reduced considerably after removal of contaminants. Gauss-Newton method use is appropriate because the suggested model is non-linear. The model equations show that under specific circumstances (Shear stress, speed, torque, etc.), the viscosity of engine oil decreases exponentially with temperature. The following results have been extracted from the study:

- Coefficient of determination, R^2 is approx. 99% for the Proposed model and approx. 98% for Reynold's model.
- The suggested model can predict the change in viscosity with temperature with an extremely high degree of accuracy, as demonstrated by Mean Squared Error.
- Additionally, there is relatively little difference in the anticipated and experimental viscosity values.

Abbreviations

Ø is the Percentage reduction in the level of contaminants after recycling

R.O is the absorbance value of Recycled oil obtained from FTIR Spectroscopy

V.O is the absorbance value of Virgin/pure oil obtained from FTIR Spectroscopy

U.O is the absorbance value of Used oil obtained from FTIR Spectroscopy

μ_o is the dynamic viscosity at atmospheric pressure

T_A is absolute temperature

A is the absorbance

I_o the intensity of light incident upon the sample cell

I the intensity of light leaving the sample cell

C the molar concentration of the solute

L the length of the sample cell (cm)

E the molar absorptivity

References

[1] Fontana A, Braekman-Danheux C, Jung CG. Fuel Process Technology, 1996, 48, 107-113. https://doi.org/10.1016/S0378-3820(96)01032-6

[2] Cock VR. Laboratory Handbook for Mineral Oil and Organic Oil Analysis. Academy Press, London, 1998, 111-113.

[3] Idumeh J. Lubecon Laboratory Handbook for Engine Oil Analysis. Lubecon Blending Company, Ilorin., 2000, 3-11.

[4] Danane F, Ahmia A, Bakiri A, Lalaoui N. Experimental regeneration process of used motor oils. Reveu des Energies Renouvelables, 2014, 17(2), 345-352.

[5] Garry MC, Bowman J. FT-IR analysis of used lubricating oils-general considerations. Thermo Fisher Sci, 2007.

[6] Diphare MJ, Muzenda E, Pilusa J, Mollagee M. A Comparison of Waste Lubricating Oil Treatment Techniques. 2nd International Conference on Environment, Agriculture and Food Sciences (ICEAFS'2013), August 25-26, 2013, Kuala Lampur, Malaysia, 106-109.

[7] Andrews L. Compendium of Recycling and Destruction Technologies for Waste Oils. United Nations Environment Programme, 2008.

[8] Bridjanian H, Sattarin M. Modern recovery methods in used oil re-refining. Petroleum & Coal, 2006, 48(1), 40-43.

[9] Regional Activity Centre for Cleaner Production (RAC/CP) Mediterranean Action Plan. Possibilities for the recycling and reuse of used oils, 2000.

[10] Ahamad MT, Chadra Sekhar BP, Mohan PN, Joshi KS, Sree TDR. Recycling and Analysis of Spent Engine Oil. International Journal of Scientific & Engineering Research. 2015; 6(11): 711-715.

[11] Rincon J, Canizares P. Waste oil recycling using mixtures of polar solvents. Ind Eng Chem Res, 2005, 7854-7859. https://doi.org/10.1021/ie0580452

[12] Osman DI, Attia SI, Taman AR. Recycling of used engine oil by different solvent. Egyptian Journal of Petroleum 27, 2018, 221-225. https://doi.org/10.1016/j.ejpe.2017.05.010

[13] Boadu KO, Joel OF, Essumang DK, Evbuomwan BO. A Review of Methods for Removal of Contaminants in Used Lubricating Oil. Chemical Science International Journal, 2019, 26(4), 1-11. https://doi.org/10.9734/CSJI/2019/v26i430101

[14] Henry M. Re-refining and recycling of used lubricating oil and natural resource conservation in Ghana. ARPN Journal of Engineering and Applied Sciences, 2015, vol. 10, 797-801.

[15] Lam SS, Russell AD, Chase HA. Pyrolysis Using Microwave Heating: A Sustainable Process for Recycling Used Car Engine Oil. Ind Eng Chem Res, 2010, 10845-10851. https://doi.org/10.1021/ie100458f

[16] Hamawand I, Yusaf T, Rafat S. Recycling of Waste Engine Oils Using a New Washing Agent. Energies, 2013, 6(2), 1023-1049. https://doi.org/10.3390/en6021023

[17] Akpomie KG, Dawodu FA. Potential of a low-cost bentonite for heavy metal abstraction from binary component system. Beni-Suef University Journal of Basic and Applied Sciences, 2015, 4(1), 1-13. https://doi.org/10.1016/j.bjbas.2015.02.002

[18] Dragne M, Pop E, Covaliu CI, Matei E, Pişă I. Experiments in use of bentonite for energy recovery of used oils. E3S Web of Conferences, 2019, 112: 1-6. https://doi.org/10.1051/e3sconf/201911204009

[19] Mamdouh T Ghannam, Mohamed YE Selim, Mona AM Khedr, Noor AG Bin Taleb, Norah R Kaalan. Investigation of the rheological properties of waste and pure lube oils. Fuel,

2021, Volume 298, 120774, ISSN 0016-2361. https://doi.org/10.1016/j.fuel.2021.120774

[20] Aurélie Taguet. Rheological characterization of compatibilized polymer blends. In: Ajitha AR, Sabu Thomas, editors. Compatibilization of Polymer Blends. Elsevier, 2020, 453-487, ISBN 9780128160060. https://doi.org/10.1016/B978-0-12-816006-0.00016-5

[21] Oil Viscosity - How It's Measured and Reported. Noria Corporation.

[22] Yadav AK, Mishra G, Yadav R. Synthesis and ultrasonic characterization of nanofluid containing silver nanoparticles. Material Science an Indian Journal, 2009, 5(3), 237-242.

[23] Sepehri A, Sarrafzadeh MH. Effect of nitrifiers community on fouling mitigation and nitrification efficiency in a membrane bioreactor. Chem Eng Processing-Process Intensif, 2018, 128, 10-18. https://doi.org/10.1016/j.cep.2018.04.006

[24] Fathali D, Mehrabadi AR, Mirabi M, Ali Mohammadi M. Investigation on nitrogen removal performance of an enhanced post-anoxic membrane bioreactor using disintegrated sludge as a carbon source: an experimental study. J Environ Chem Eng, 2019, 7(6), 103445. https://doi.org/10.1016/j.jece.2019.103445

[25] Cao Y, Yan F, Li J, Liang X, He B. Used lubricating oil recycling using a membrane filtration: Analysis of efficiency, structural and composing. Desalination and Water Treatment, 2009, 11:1-3, 73-80. https://doi.org/10.5004/dwt.2009.845

[26] Martins J. The extraction of used lubricating oil using ternary organic solvents, 1997.

[27] Mohammadi T, Safavi MA. Application of Taguchi method in optimization of desalination by vacuum membrane distillation. Desalination, 2009, 249(1), 83-89. https://doi.org/10.1016/j.desal.2009.01.017

[28] Yadav AK, Mishra G, Yadav R. Synthesis and ultrasonic characterization of nanofluid containing silver nanoparticles. Material Science, An Indian Journal, 2009, 5(3), 237-242.

[29] Niamh Nic Daeid. Forensic Sciences | Systematic Drug Identification. In: Encyclopedia of Analytical Science (Third Edition). Academic Press, 2019, 75-80, ISBN 9780081019849.

Friction stir-welding of AZ31B Mg and 6061-T6 Al alloys optimization using Box-Behnken design (BBD) and Artificial Neural network (ANN)

Dame Alemayehu Efa[1a], Endalkachew Mosisa Gutema*[1b], Hirpa G. Lemu[2c], Mahesh Gopal[1d]

[1]Dept. of Mechanical Eng., College of Eng. and Technology, Wollega University, Nekemte, Ethiopia
[2]Dept. of Mechanical and Structural Eng. and Materials Science, Faculty of Science and Technology, University of Stavanger, N-4036 Stavanger, Norway

Article Info	Abstract
	The primary goal of the study is to optimize the welding parameters using Friction Stir Welding (FSW) to join AZ31B Mg and AA 6061 alloys considering input parameters such as rotational speed, welding speed, shoulder-to-pin diameter ratio and plunge force and output parameters as peak temperature. The simulation experiment is carried out using COMSOL Multiphysics® 6.0 Software. The simulation experiment is designed using the Box-Behnken design (BBD) of Response Surface Methodology (RSM) and mathematical models were developed. The Analysis of Variance (ANOVA) is used to assess the features of the performance effectiveness of the parameters. Both direct and indirect interaction effects are investigated; the results indicate that the rotational speed is the most influential parameter when compared to other factors; as rotational speed increases consequently; there is an increase in temperature. Finally, the Artificial Neural Network was trained and tested in MATLAB software to optimize the parameters. The validation was performed to predict the minimal predicted temperature value. The confirmatory tests reveal that the predicted results are extremely close to the experimental values from the simulation.

1. Introduction

The joining of dissimilar metals is a challenge by the conventional joining process due to the physical, thermal, mechanical and chemical properties of different materials and also the welding of dissimilar metals at low melting temperatures, and high thermal conductivity, which are difficult to weld using conventional welding techniques. FSW is the solid-state joining technique in which the materials are joined without melting the workpiece. Heat is generated in the FSW process as a result of thermo-mechanical deformation and relative motion between the tool and workpiece. The material flow plasticized behind the tool as a result of the rotating tool's forward translation motion along the joint line under axial pressure and heat transfer at the plate's edge. The dissimilar metals like magnesium, aluminum, steel, copper and titanium are joined using the FSW process.

The simulation experiment using FEM techniques was conducted to study the thermal phenomenon during the welding of dissimilar metals of AZ31B-H24 Magnesium alloys and Aluminum 6061-T6 to predict peak temperature using the FSW process. The results indicate that peak temperature was more reliant on shoulder diameter and tool traverse speed than on tool rotation speed. The peak temperature is directly proportional to tool rotation speed and

shoulder diameter and inversely proportional to tool traverse speed [1]. The microstructure and mechanical characteristics of magnesium alloys to Aluminum alloy 6061-T6 of the FSW specimens were studied using elemental analysis. The elemental analysis of the AZ91D to 6061-T6 Al weld reveals that the Al and Mg distributions are more uniform in the FSW zone [2]. The research in (3) provides valuable insight into the welding and softening behavior of Al 6061-T6 and Mg AZ31B dissimilar alloys in FSW. It demonstrates that softening occurs throughout the FSW Al 6061-T6 alloy owing to the dissolving of the strengthening precipitates: In contrast, it occurs mostly within the stir zone due to localized textural differences in the FSW Mg AZ31B alloy.

The processing parameters on the microstructure and mechanical characteristics of FSW joints of AZ31B Magnesium alloy and 6061-T6 Aluminum alloy are examined by (4) concluded that the optimum joint quality is achieved at 1600 rpm of rotational speed and 500 mm/min of translational speed. AZ31B magnesium and Al6061-T6 Aluminum were used in the FSW process. Detailed microstructural research was done to determine the composition of the intermetallic phases generated in the stirring zone and their effect on micro hardness and overall mechanical properties of the weld [5]. The studies were carried out to examine the effects of tool rotational speeds on the microstructure, hardness, and tensile characteristics of 6061-T6 Aluminum and AZ31B magnesium alloys. The findings revealed that rotational speeds influence the parameters and tensile characteristics increased and subsequently declined as welding speed increased. The maximum tensile strength was 137 MPa at a welding speed of 60 mm/min [6]. The purpose of the study was to investigate the microstructural and corrosion behavior of FSW joints between a 6061 Al and AZ31 Mg with a zirconium interlayer. The Zr interlayer prevented the formation of Al-Mg intermetallic compounds due to its synergetic actions of chemical alteration and thermal resistance [7]. The influence of tool offset on the microstructure and characteristics of AA6061/AZ31B Aluminum alloys was investigated in FSW. The results revealed that increasing the tool offset had a substantial influence on the microstructure, mechanical characteristics, and micro-hardness, with the joint strength reaching a maximum of 107 MPA when the offset reached 1.5mm [8]. The FSW experiment was performed to weld AA 6061-T6 and AZ31B alloys, with the welding parameters. The results show that at 400 rpm to 700 rpm of tool rotation speed, the average micro hardness value in the nugget zone first increases then decreases, and the micro hardness value within the stir zone is greater than the base metal, with the highest value being equal to twice of the base metal [9]. FSW was utilized to join incompatible AA6061-T6 alloys to AZ31B-H24 alloys while taking into account process characteristics such as rotating speed, welding speed, tool plunge depth, and tool pin shape. The results demonstrate that the M7 joint has the maximum tensile strength of 88.2 MPa and the lowest of 18.95 MPa in the M3 weld [10]. The butt joint was designed to weld 5A06 Al and AZ31B Mg alloys with 20 mm thickness using FSW and concluded that the highest hardness was 289 HV on the IMC layer of the Mg side interface, and the nanoindentation tests revealed that the nano hardness of the $Al_{12}Mg_{17}$ layer and Al_3Mg_2 layer was 5.39 GPa and 4.18 GPa, respectively [11]. The experiment was carried out with dissimilar metals AA 6061 and Mg AZ31B. The author demonstrated that the FSW joint has much higher strength and concluded that the weld line offset from the center was responsible for the deposition of larger concentrations of magnesium, which minimizes the Inter Metallic compounds and so enables a higher tensile strength of 39MPa [12]. FSW is used to join Aluminum Al-6062 and magnesium AZ31B, using spindle speed and welding speed as process parameters. As stated by the author, the welded joint strength of the Aluminum-Magnesium joint is 110% more than that of the magnesium-magnesium joint at maximum UTS, spindle speed and welding speed of 100rpm and 50mm/min with magnesium on the advancing side [13]. The microstructural and mechanical properties of the Refill Friction Stir Spot Welding process were examined utilizing AZ31B/AA6061 dissimilar joint. The results revealed that joining metals yielded higher static shear strength and concluded that welds with a tool rotational speed of 1400 rpm have a maximum static shear strength of 3.6 KN and when the rotating speed of the tool exceeds 1400

rpm, the static shear strength of the joints decreases [14]. The author [15] discussed the development of medium-thick AA6061 Al/AZ31B Mg dissimilar alloys during submerged friction stir welding and concluded that the ultimate tensile strength of dissimilar metal of Aluminum alloy 6061 and magnesium AZ31B was increased to 171 MPa and the strength of magnesium-magnesium AZ31B is approximately 71.3%. The computational fluid dynamics-based simulation experiment was done by [16] to investigate the mixing process and material flow in the FSW of AA6061-T6 and AZ31B mg alloys. Based on the simulation results, the material mixing is unstable throughout the FSW process, resulting in a fluctuant component distribution along the longitudinal direction in the joint's stir zone. The study used a statistical design of trials to explore the impact of tool positioning factors on peak temperature in dissimilar friction stir welding of the Aluminum alloys AA6061-T6 and AA7075-T6. The findings demonstrated that the plunge depth, tilt angle, and tool offset all had a significant influence on the peak temperature and tool offset. The greatest process temperature was created at a tilt angle of 1.8 degrees, and it declined for values less and greater than this angle. Peak temperature values were lowest in samples with greater tilt angles [17].

The ANSYS FLUENT software was employed to model 3D material flow variations during FSW utilizing varied pin profiles to reduce simulation time and increase simulation result dependability [18]. The investigation process was carried out by [19] to study the impact of the traverse and rotational velocities of the noncontact shoulder tool of the friction stir joining (FSJ) process of polyamide 6 (PA6) polymer and suggests that the material velocity raised at higher rotational speed and lesser transverse velocity and in the stir zone. The author [20] investigated the influence of tensile, impact, corrosion testing, fracture, and statistical and cost analysis on dissimilar junctions built of AA6061, AZ31B, and AZ91D. The results show that AZ91 and AZ31B have the highest tensile strength, whereas AA6061 and AZ91 have the highest yield strength. The friction stir welding (FSW) procedure was used to weld dissimilar alloys of magnesium and steel in order to analyze the heat changes, material flow, and mechanical characteristics during the process. The author [21] concludes that increasing the number of shoulders increases the frictional generation of heat.

In summary, the preceding research investigation primarily considered the effect of process parameters such as tool rotational speed, welding speed, and shoulder-to-pin diameter ratio on temperature obtained during FSW using the combination of various metals. Furthermore, these investigations sought to comprehend and characterize intermetallic phases, the effects of process factors on microstructural features, the evaluation of joint strength, the simulation of material mixing during welding, and techniques to enhance tool position in FSW.

However, despite extensive literature review, there is limited research available considering rotational speed, welding speed, shoulder-to-pin diameter ratio and Plunge force to measure the peak temperature during FSW welding and no studies compare the joining of AZ31B and AA 6061 material using FEA using COMSOL Multiphysics® 6.0 Software. This study aims to address the gap by providing an in-depth investigation of the FSW process of both materials and makes a contribution to the discipline by filling in gaps in the literature. The simulation design was carried out using Response Surface Methodology (RSM) and optimization was done using an Artificial Neural Network (ANN) to analyze the parameters influencing the welding of dissimilar metals 6061-T6 Al alloys and AZ31B Mg alloys. Thus the experiment was carried out to overcome the above mentioned challenges and solve the critical issues for the industry professionals to shorten total manufacturing time.

2. Mathematical Model

In this FSW modeling the following assumptions are made by the authors:

- The frictional heat is generated at the interface of the workpiece/shoulder.

- The flow of heat stopped after the workspace melting temperature become equal to local temperatures.
- The tool pin thread can be neglected as the pin is cylindrical.

The complicated process of the FSW process becomes simpler while moving the tool in the coordinate system. The heat transfer control equation for the work piece in a moving coordinate system with a positive x-direction moving tool is given by the equation 1 [22].

$$\frac{\partial(\rho cT)}{\partial t} = \frac{\partial}{\partial_x}\left(\lambda_x \frac{\partial T}{\partial_x}\right) + \frac{\partial}{\partial_y}\left(\lambda_y \frac{\partial T}{\partial_y}\right) + \frac{\partial}{\partial_z}\left(\lambda_z \frac{\partial T}{\partial_z}\right) + W_v \frac{\partial}{\partial_x}(\rho C_p T) \tag{1}$$

Heat is considered at the interface of the pin/work piece and shoulder/work piece in this model. Heat is generated in the pin through material shearing, threaded surface friction and friction on the pin itself is illustrated in equation 2. [24], [22].

$$Q_{pin} = \frac{2\mu K \pi r_p t_w r_p}{\sqrt{3(1+\mu^2)}} + 2\pi r_p t_w K\tau \frac{V_m}{\sqrt{3}} + \frac{4F_p \mu V_m}{\pi} \cos\theta \tag{2}$$

$$\theta = 90^o \text{-} \lambda_T \text{-} tan^{-1}(\mu), \ V_{rp} = \frac{\sin\theta}{\sin(18^o - \theta - \lambda)} v_p, \ V_m = \frac{\sin\lambda}{\sin(18^o - \theta - \lambda)} v_p \ and, \ V_p = r_p \omega$$

The heat flux per unit area (W/m^2) function of distance r from the shoulder's center axis is defined as shown in equation 3. [1], [25].

$$q_s(r,T) = \begin{cases} \left(\frac{\mu F_n}{A_s}\right) \omega r; \ T < T_{melt} \\ 0 \qquad ; \ T \geq T_{melt} \end{cases} \tag{3}$$

The boundary condition of heat flux at the interface of the shoulder/work piece is given by the author as illustrated in equation 4. [22].

$$K\frac{\partial T}{\partial n} \Big/_\Gamma = q_i \tag{4}$$

The boundary condition of heat flux at the interface of the pin work piece is illustrated in equation 5. [22].

$$K\frac{\partial T}{\partial n} \Big/_\Gamma = q_p \tag{5}$$

The convective boundary condition of the surfaces of the work piece is exposed to the environment as shown in equation 6. [26], [22], [24].

$$K\frac{\partial T}{\partial n} \Big/_\Gamma = h\,(T - T_o) \tag{6}$$

2.1. Simulation Model

The simulation model is composed of 6061-T6 Aluminum and AZ31B Magnesium alloy plates as shown in Fig.1. The dimension of the plate for each material is 400 mm x 250 mm x 25 mm with infinite domains on both sides of the x-direction. During the FSW process, relative motion developed on the advancing and retreating sides, with the advancing side having the same direction of linear and rotational motion and the retreating side having the opposite direction of linear and rotational motion. The temperature on the advancing side is higher than on the retreating side because there is more shearing action as a positive velocity component on the advancing side, and it does not affect magnesium since its melting temperature is lower than that of aluminum [27]. The experiment was conducted using magnesium alloy on the advancing side since aluminum alloy has a higher yield strength than magnesium alloy [4].

The lower process temperature and defect-free weld zone can be obtained by placing the harder material with a higher melting temperature on the advancing side [28], [5]. As a result, in this investigation, magnesium was placed on the retreating side (RS), whereas aluminum was placed on the advancing side (AS). The plate's heat transfer with conductive and convective

terms in the welding tool and the coordinate system was fixed and shown by equation 7. [1], [25].

$$\nabla \cdot (-\lambda \nabla T) = Q - \rho C_p W_V \cdot \nabla T \qquad (7)$$

Due to the surface-to-ambient radiation and natural convection, the aluminum and magnesium plates lose their heat on their lower and upper surfaces and the heat flux equation corresponds to those surfaces given in equations 8, 9. [1], [29], [25].

$$q_{up} = h_{up}(To - T) + \varepsilon\sigma(T_a^4 - T^4) \qquad (8)$$

$$q_{low} = h_{low}(To - T) + \varepsilon\sigma(T_a^4 - T^4) \qquad (9)$$
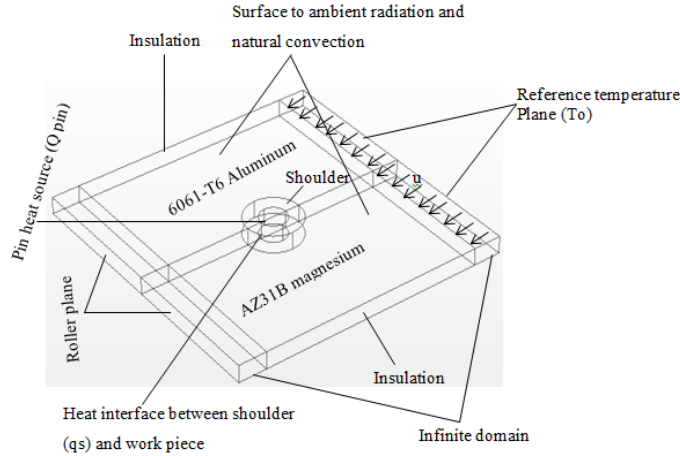
Fig. 1. Friction stir welding model geometry

The temperature is equilibrium through surface ambient radiation and natural convection with the temperature at infinity due to the infinite domain being modeled on the left side. The convective heat transfer coefficient maximum value ranges between 5 to 25 W/(m^2·K) [28]. Therefore, the coefficient of heat transfer in this study is h_{low}= 6.25 W/ (m^2·K) and h_{up} = 12.25 W/ (m^2·K).

Equation 10 shows the simulation's initial condition [29], [26]

$$T(x, y, z, 0) = T_i \qquad (10)$$

The governing equations consist of the energy equation, continuity equation and momentum equation are given in equations 11, 12, and 13. [16].

$$\nabla \cdot (\rho \vec{v}) + \frac{\partial \rho}{\partial t} = 0 \qquad (11)$$

$$\frac{\partial(\rho\vec{v})}{\partial t} + \nabla \cdot (\rho\vec{v}\vec{v}) = -\nabla P + \nabla \cdot [\mu_{mix}(\nabla\vec{v} + \nabla\vec{v}^T)] \qquad (12)$$

$$\frac{\partial(\rho H_{mix})}{\partial t} + \nabla \cdot (\rho\vec{v} H) = \nabla \cdot (\lambda \nabla T) + S_v \qquad (13)$$

According to the volume of fraction model, the two alloys of materials volume fraction is given by:

$$\phi_{mix} = \alpha_{Al}\phi_{Al} + \alpha_{Mg}\phi_{Mg} \qquad (14)$$

The aluminum's volume fraction is calculated as:

$$\frac{\partial(\alpha_{Al}\rho_{Al})}{\partial t} + \nabla \cdot (\alpha_{Al}\rho_{Al}\vec{v}_{Al}) = \dot{m}_{Mg,Al} - \dot{m}_{Al,Mg} \qquad (15)$$

The Magnesium's volume fraction is given by:

$$\alpha_{Mg} = 1 - \alpha_{Al} \tag{16}$$

As the work piece temperature was increased to the maximum value, the coefficient of friction is minimum and then approached zero. The coefficient of friction is about 0.2 at room temperature of the aluminum work piece [27]. Since the melting temperature of aluminum and magnesium is nearer to each other and the temperature is at ambient temperature (25℃) of the workpiece thus the friction coefficient was considered as 0.18 for this simulation experiment.

2.2. Meshed model

Free quadrilateral, triangular and swept (to distribute mesh in all bodies of material) are applied in the meshing of the 3D model as illustrated in Fig. 2. The meshed model obtained values of 5838 elements and 8439 mesh vertices.
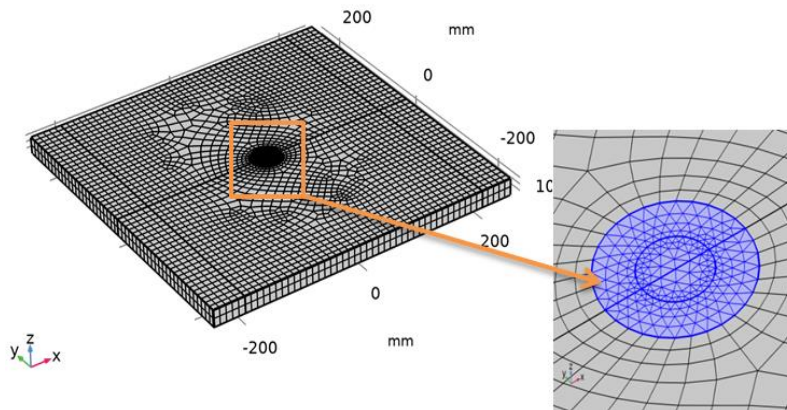
Fig. 2. Meshed model

3. Design of Simulation

The RSM method is used to determine the practical relationship between the response and the independent variables. Equation 17 shows the process variable function that indicates the response peak temperature (T_P) [30].

$$T_R = \Phi\,(R_n, W_v, S_p, F_n) + e_{ui} \tag{17}$$

When the mathematical form Φ is unknown, it is possible to accurately approximate this function within the experimental region by using polynomials stated as processing parameters variables.

The Design Expert-V13 software is utilized to design the simulation experiment while the Box-Behnken Design (BBD) of Response surface methodology (RSM) is used to create the simulation experimental design as per the procedure given by the author [31]. The author [32] reviewed the RSM methodology to measure the behaviour of the tensile strength in the friction stir welding process considering welding speed, tool rotational speed, axial load, and geometry of the tool. The experimental program consisted of four-factors and three levels which are given standard codes (-1, 0, and +1) as shown in Table. 1 [33]. The three levels (-1, 0, and +1) are also assigned for BBD methodology and Table 2 shows the 29 runs of simulation experimental sets of the actual state. The dissimilar metals of 6061-T6 Al alloys and AZ31B Mg alloys are welded using the FSW process and the input parameters are tool rotation speed, welding speed,

shoulder-to-pin diameter ratio and plunge force and output parameter as peak temperature are considered in this study and are selected based on the suggestions by (1), [10], [13], [14], [27], [29] and the factorial level ranges are selected by the guidelines given by [34]. The chemical and mechanical properties of AZ31B and 6061-T6 alloys are shown in Tables 3 and 4. The simulation experiment is conducted using COMSOL Multiphysics® 6.0 software and the output from for first run is illustrated in Fig. 3. The second-order mathematical quadratic model consists of 29 sets of experiments that estimate the process parameter's linear, quadratic, and interaction effects. The analysis of variance method is used to study both the performance characteristics of the welding operations and the interaction effect of all parameters. The Artificial Neural network heuristic methodology is coded, trained, and tested in MATLAB for the optimum cutting parameter leading to minimizing peak temperature.

Table 1. Process parameters and their levels

Sl. No	FSW parameters	Factorial levels		
		-1	0	+1
1	Tool rotational speed (rpm)	700	800	900
2	Welding speed(mm/min)	60	70	80
3	Shoulder-to-pin diameter ratio	2.5	3.0	3.5
4	Plunge force(N)	6,000	7,000	8,000

Table 2. Simulation values with responses

SI. No	R_n	W_v	S_p	F_n	Output Responses		
					T_P - Simulation	T_P-Predicted by RSM	T_P-Predicted by ANN
	rpm	mm/min	-	N	$T_{P(SIM)}$ (K)	$T_{P(RSM)}$ (K)	$T_{P(ANN)}$ (K)
1	700	60	3	7000	676.3	676.17	676.06
2	800	60	3.5	7000	749.8	748.84	747.60
3	800	70	3	7000	734.22	734.00	732.99
4	800	70	3	7000	736.22	734.00	734.90
5	700	70	2.5	7000	687.99	688.85	685.05
6	900	70	3	8000	783.32	782.63	781.46
7	800	70	3	7000	735.53	734.00	733.93
8	800	70	3	7000	734.92	734.00	732.99
9	800	70	3.5	8000	755.95	756.03	755.88
10	700	70	3.5	7000	693.99	695.23	690.32
11	900	60	3	7000	779.94	779.04	777.12
12	800	80	3	6000	706.52	707.80	702.06
13	700	70	3	6000	689.32	689.20	685.22
14	900	70	2.5	7000	760.80	761.87	757.19
15	800	70	3.5	6000	740.33	739.15	737.24
16	900	80	3	7000	741.20	739.83	738.17
17	900	70	3.5	7000	769.54	770.99	765.53
18	900	70	3	6000	750.76	751.21	748.50
19	700	80	3	7000	694.51	693.92	690.94
20	800	80	2.5	7000	730.22	730.37	724.17
21	800	80	3	8000	753.76	754.92	750.52
22	800	70	3	7000	729.12	734.00	723.99
23	700	70	3	8000	697.12	695.86	694.00

24	800	60	3	8000	736.55	737.57	730.47
25	800	60	3	6000	745.47	746.61	741.42
26	800	70	2.5	6000	730.82	729.24	724.81
27	800	70	2.5	8000	750.76	750.44	745.71
28	800	60	2.5	7000	734.52	734.35	730.13
29	800	80	3.5	7000	732.01	731.37	730.70

Table 3. Chemical Composition of AZ31B and 6061-T6 Alloys

Alloy	Al %	Mg %	Zn %	Mn %	Si %	Fe %	Cu %
Al 6061-T6	Balance	1.11	0.022	0.034	0.565	0.45	0.233
AZ31B Mg	2.95	Balance	0.912	0.31	0.006	0.004	0.002

Table 4. Mechanical properties of AZ31B and 6061-T6 Alloys

Alloy	Density (kg/m^3)	Elastic modulus (GPa)	Yield strength (MPa)	Maximum tensile strength (MPa)	Elongation (%)
Al 6061-T6	2660	70	288	334	13
AZ31B Mg	1738	45	169	297	8
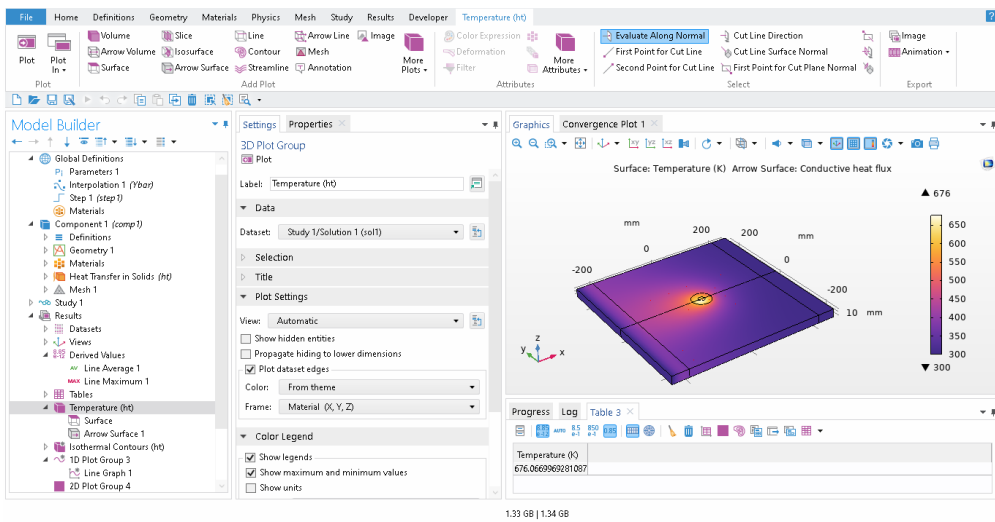
Fig. 3. COMSOL Multiphysics® 6.0 Software simulation model builder

3.1. Peak Temperature Prediction Using a Response Surface Model

The relationship between the y response area and the x process variable for a typical form of a quadratic polynomial is explained by the authors [35].

$$Y = \beta_0 + \beta_1 x_1 + \beta_2 x_2 + \beta_3 x_3 + \beta_{11} x_{12} + \beta_{22} x_{22} + \beta_{12} x_1 \tag{18}$$

The DESIGN EXPERT V13 software analyzes the observed simulation reading accurately. A second-order quadratic model was constructed to forecast peak temperature, and an analysis of variance was utilized to prove the model's significance. Table 5 illustrates the coefficients of determination.

Table 5. The determination coefficient

Source	Seq. p-value	Lack of Fit (LF) p-value	Adjusted (Adj) R^2	Predicted (Pred) R^2	
Linear	< 0.0001	0.0059	0.8359	0.7804	
2FI	0.0053	0.0185	0.9136	0.8194	
Quadratic	< 0.0001	0.9580	0.9950	0.9918	Suggested
Cubic	0.9989	0.4372	0.9894	0.8863	Aliased

The coefficient of determination for determining the precision and accuracy of the model in the DOE is based on statistical analysis such as the R-squared of predictable output from input variables and the adjusted R-squared of the modified R-squared for the predictor's number in the model. Both the R-squared and adjusted R-squared determination coefficients range from 0 to 1. The values of these parameters are close to 1 or 100%, indicating a higher suggested regression model and higher model adaptation accuracy [17].

Table 6 shows the results of the ANOVA study performed to predict the peak temperature. The software suggested a quadratic model to represent the relationship between peak temperature and FSW parameters.

Table 6. ANOVA analysis of peak temperature

Source	Sum of Squares (SS)	df	Mean Square (MS)	F-value	p-value	
Model	21142.44	14	1510.17	395.26	< 0.0001	significant
R_n -Rotational Speed	16600.87	1	16600.87	4344.92	< 0.0001	
W_v -Welding Speed	345.18	1	345.18	90.34	< 0.0001	
S_p -Shoulder-pin diameter ratio	180.27	1	180.27	47.18	< 0.0001	
F_n - Plunge Force	1087.56	1	1087.56	284.65	< 0.0001	
$R_n W_v$	810.83	1	810.83	212.22	< 0.0001	
$R_n S_p$	1.88	1	1.88	0.4912	0.4949	
$R_n F_n$	153.26	1	153.26	40.11	< 0.0001	
$W_v S_p$	45.50	1	45.50	11.91	0.0039	
$W_v F_n$	788.49	1	788.49	206.37	< 0.0001	
$S_p F_n$	4.67	1	4.67	1.22	0.2878	
R_n^2	570.88	1	570.88	149.42	< 0.0001	
W_v^2	36.75	1	36.75	9.62	0.0078	
S_p^2	137.92	1	137.92	36.10	< 0.0001	
F_n^2	169.03	1	169.03	44.24	< 0.0001	
Residual	53.49	14	3.82			
Lack of Fit (LF)	21.51	10	2.15	0.2691	0.9580	not significant
Pure Error (PE)	31.98	4	7.99			
Cor Total (CT)	21195.93	28				

The model's F-value of 395.26 indicates that it is significant. An F-value of this size might be 0.01 percent due to noise. Significant model terms have p-values less than 0.0500. In this case, R_n, W_v, S_p, F_n, $R_n W_v$, $R_n F_n$, $W_v S_p$, $W_v F_n$, R_n^2, W_v^2, S_p^2 and F_n^2 are key model terms in this scenario.

The values above 0.1000, the model terms are insignificant. The rotating speed of the tool has a greater impact on the output.

The regression equation created by Design-Expert software V13 is revealed below.

Peak Temperature (T_P)

$$= +166.36900 + 2.39519R_n + 6.38140W_v - 51.53933S_p \quad 0.20327F_n - (0.01424)R_n * W_v + (0.01370)R_n * S_p + (0.00006)R_n * F_n - (0.67450)W_v * S_p + (0.00140)W_v * F_n - (0.00216)S_p * F_n - (0.00094)R_n^2 - (0.02380)W_v^2 + (18.44433)S_p^2 + (5.10483E - 06)F_n^2.$$

The F-value for Lack of Fit of 0.27 indicates that the Fit is not significant in comparison to the pure error. A significant Lack of Fit F-value owing to noise has a 95.80% chance of occurring.

4. Results and Discussions

Aluminum (660.3°C) and magnesium (650°C) have almost identical melting temperatures, due to this heat being equally distributed across both materials; so the joining provides an excellent outcome. The peak temperature results are predicted using RSM optimization techniques.

4.1. RSM Interaction Effect Analysis

4.1.1. Interaction Effect of Rotational Speed vs Welding Speed Over Peak Temperature

The interaction effect of process parameters on the peak temperature (T_P) is discussed below. Fig. 4(a) shows the interaction plot between rotational speed (R_n) and welding speed (W_v) with respect to peak temperature. The figure shows that the rotational speed increases consistently, and the peak temperature increases. This is owing to the fact that fewer materials were employed in the formation of the weld, which enhanced the material's flowability and lowered the forward resistance. When welding speed increases, the peak temperature decreased. As welding speed increases the frictional dissipation energy decreases thus temperature decreases The higher rotational speed causes to increase in heat energy due to friction and then a higher temperature is developed and the same report is done from the experimental investigation as reported in the [26], [27], [36].

4.1.2. Interaction Effect Welding Speed vs Axial Force Over Peak Temperature

From Fig. 4(b) it is observed as the axial force increases consistently, the peak temperature also increases but when welding speed decreases the peak temperature decreased. The plastic and friction increased as the plunge force increased and then a higher plunge force leads to penetrating material thus increasing penetration force caused to increase in maximum temperature [29], [26].

4.1.3. Interaction Effect Tool Rotational Speed Vs Axial Force Over Peak Temperature

The tool rotational speed and axial force were increased; the peak temperature is also increased as shown in Fig. 4. (c, e). This is due to the temperature being directly proportional to the rotational speed of the tool. An increase in the tool rotational speed of the tool leads to an increase in temperature. As the plunge force increased more material penetrates and then the friction dissipation energy increases thus more temperature is generated [26]. This result is supported by the experimental results of [36].

4.1.4. Interaction Effect Shoulder-To-Pin Diameter Ratio Vs Welding Speed Vs Axial Force Over Peak Temperature

As the shoulder-to-pin diameter ratio increased the peak temperature increased as shown in Fig 4. (d, f). The shoulder-to-pin diameter ratio increases the temperature of the weld zone increases due to the higher area subjected to friction that caused to higher generation of heat [1], [37]. The observed vs. predicted values with data points split by 45° line as illustrated in Fig. 4(g).
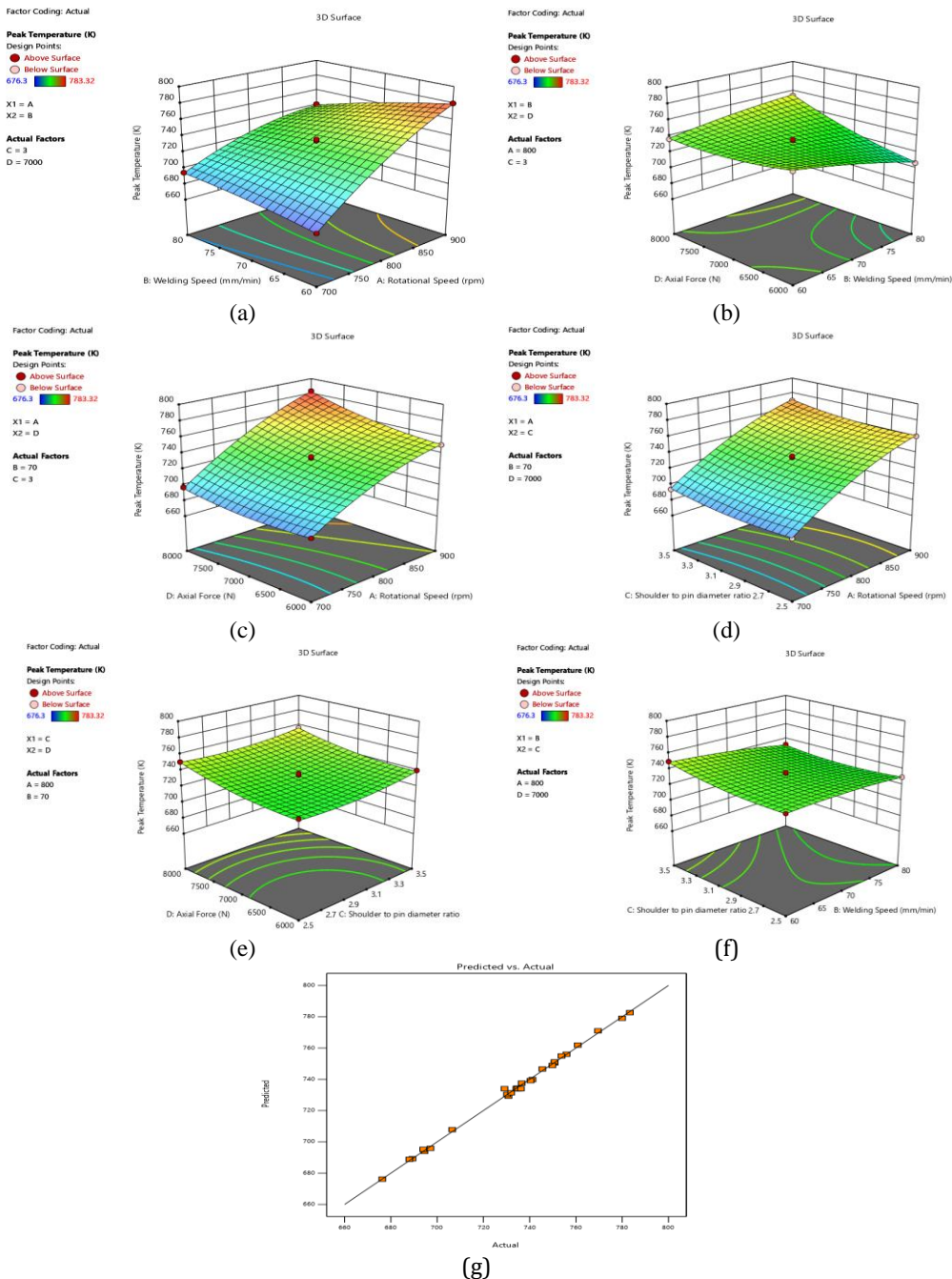
Fig. 4. 3D plot (Interaction) effect in terms of peak temperature of (a) R_n vs.W_v, (b) W_v vs. F_n, (c) R_n vs. F_n, (d) R_n vs. S_p (e) S_p vs. F_n, (f) W_v vs. S_p, and (g) 2D plot of actual vs. predicted values

5. Artificial Neural Network

The artificial network is also called a neural network are the heart of deep learning algorithm and a subset of machine learning and used to improve the quality of mechanical research [38], [39]. The learning algorithm is being developed through ANN. Unsupervised learning and supervised learning are the two categories. The input and output in supervised are trained using the data. When operating in unsupervised mode, result data is not immediately available. Instead, additional input data, referred to as clusters, must be entered [30], [40]. It is composed of three neurons layers Input layer that consists of all input values, a hidden layer that processes hidden data and an output layer that is displayed based on input values and weight values. The outcome of the ANN architecture using MATLAB software used to predict peak temperature (T_P). Input, hidden, and output layers make up the network's three layers. To study the friction, stir welding parameters, the link between the input layers and the output layers is provided by the hidden layer, and the input and output layers are represented as nodes as shown in Fig. 5. The number of neurons in the input and output layers is decided based on the structure of the problem's ANN architecture level [38]. Table 7 shows the network parameter's optimal values. Four neurons are received via the input layer whereas the output has one neuron.
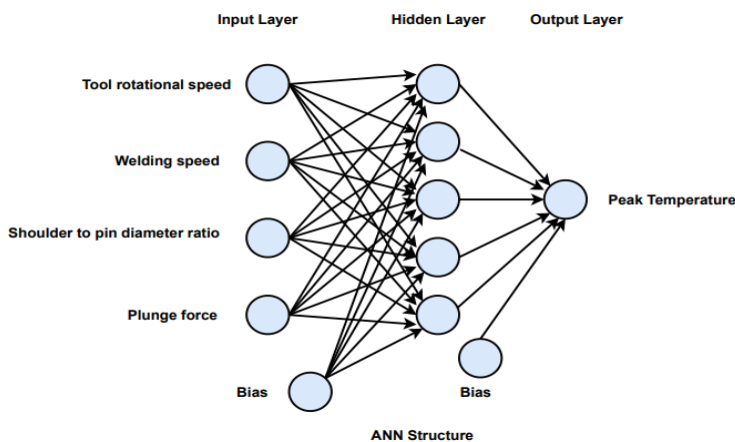
Fig. 5. ANN Structure of FSW parameters

Table 7. The ANN parameter optimum values

SI. No	Parameter	Values
1	Input layer	1
2	Input layer unit	4
3	Hidden layer	1
4	Hidden layer unit	5
5	Output layer	1
6	Output layer unit	1
7	Epochs	1000
8	Algorithm	Back propagation
9	Learning rule	Gradient descent rule

The use of Artificial Neural Networks (ANN) in welding process prediction reduces the dependable on traditional statistical methods due to their ability to excel at pattern recognition

in large datasets, thus minimizing the need for costly physical experiments while efficiently determining optimal parameter combinations and predictable welding conditions.

This study employs the neural network back propagation network technique. Input parameters include tool rotating speed, welding speed, shoulder-to-pin diameter ratio, and axial force, while output parameters include peak temperature. The prediction of peak temperature in ANN is accomplished by 1000 iterations using MATLAB software. The major procedures included developing a regression equation for performance validation of simulation data, calculating projected value, and training the algorithm.
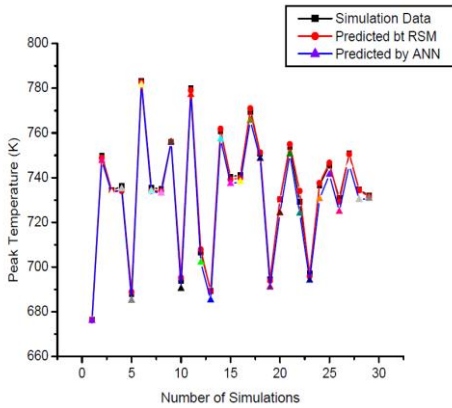
Fig.6 Comparison relationship of simulation ($T_{P(SIM)}$), RSM ($T_{P(RSM)}$) and ANN ($T_{P(ANN)}$)
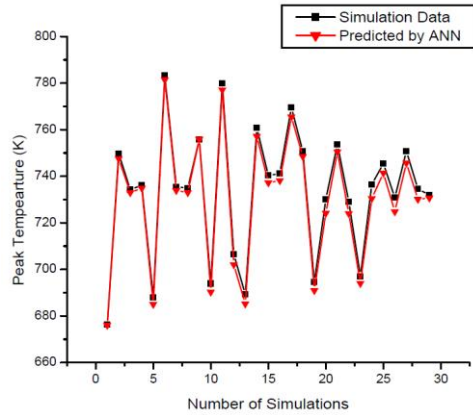
Fig.7 Comparison relationship of simulation ($T_{P(SIM)}$) and ANN ($T_{P(ANN)}$)
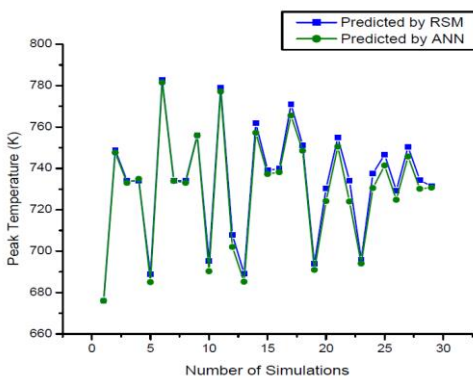
Fig. 8. Comparison of RSM ($T_{P(RSM)}$) and $T_{P(ANN)}$)
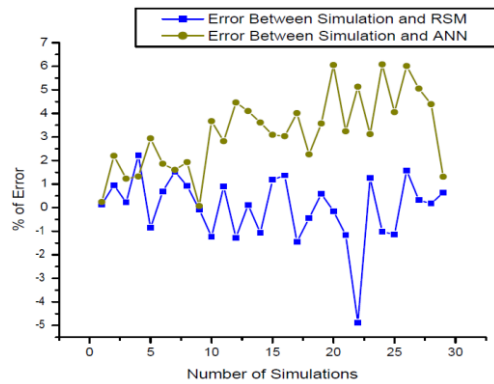
Fig.9 Error Percentage ($T_{P(RSM)}$ vs ($T_{P(ANN)}$).

Fig. 6 displays the results of the simulation, RSM, and trained ANN data. This graph demonstrates that the simulation, Design Expert software-derived RSM result, and ANN result are close to their output values. Fig. 7 displays the results of the simulation and trained ANN data. This graph demonstrates that assessments are true to their values and that experimental results achieved by utilizing ANN are quite near. Fig. 8 displays the RSM and ANN error percentages above the experimental value. The error percentage between the simulation to RSM and ANN is shown in Fig. 9. The RSM results have a higher standard deviation than the ANN projected values. It was effective in training the ANN to perform better predictions than RSM.

6. Validation of The Model

Table 2 shows the predicted experimental simulation result ($T_{P(RSM)}$) of a regression model developed using BBD by the RSM of DOE. The first 20 data sets are chosen from the 29 datasets acquired to train the ANN model; the remaining 9 data sets are chosen for testing. The ANN predicted optimum conditions were further validated with physical simulation measurements. Table 8 shows the results of the error comparison of predicted (ANN) and simulation results. An average prediction error is 0.0672017 and a maximum prediction error is 0.178959. The percentage of error is found to be within ±2 % which shows the validity of the model. The result obtained from ANN has an excellent agreement with the simulation results.

Table 8. Error Comparison of predicted (ANN) and simulation result.

SI. No	R_n	W_v	S_p	F_n	Output Responses		Error %
					Temperature - Simulation	Predicted by ANN	
	rpm	mm/min	-	N	$T_{P\,(SIM)}$ (K)	$T_{P\,(ANN)}$ (K)	
21	800	80	3	8000	753.76	753.52	0.03184
22	800	70	3	7000	729.12	728.99	0.01783
23	700	70	3	8000	697.12	696.00	0.160661
24	800	60	3	8000	736.55	736.47	0.010861
25	800	60	3	6000	745.47	745.42	0.006707
26	800	70	2.5	6000	730.82	729.81	0.138201
27	800	70	2.5	8000	750.76	750.71	0.00666
28	800	60	2.5	7000	734.52	734.13	0.053096
29	800	80	3.5	7000	732.01	730.70	0.178959
% of error							0.0672017

7. Conclusion

The Design Expert-V13 software package is employed to design BBD and used to create a second-order mathematical model to predict peak temperature in friction stir welding of dissimilar alloy metals AZ31B Mg and 6061-T6 Al with varying tool rotational speed, welding speed, shoulder-to-pin diameter ratio, and plunge force as input parameters. The simulation is carried out using the COMSOL Multiphysics® 6.0 Software. The two-stage attempt has been carried out to forecast peak temperature using surface response methodology and optimization is done using artificial neural networks. The results are fairly useful to achieve predictable process parameters and predictable peak temperature.

- The model generated by RSM is capable of providing accurate projected peak temperature values that are similar to the actual values obtained in the simulation experiments. The ANOVA was used to check the adequacy levels with a confidence level of 95 %.
- The direct and interaction impacts were discussed, and it is revealed that rotational speed has the greatest effect as compared to other parameters. From the result, the rotating speed rises, the temperature also increases. It is clear from this study that the best minimum peak temperature (T_P) values attained at Tool rotational speed (R_n) of 700 rpm, welding speed (W_v) of 60 mm/min, shoulder-to-pin diameter ratio (S_p) of 3 and plunge force (F_n) of 7000 N.
- Finally, the peak temperature was optimized using an Artificial Neural Network (ANN). The ANN predicts minimal peak temperature and the percentage of error is

less than 2% error percentage. The confirmatory test shows that the ANN and simulation results are extremely close to each other.

Acknowledgment

Abbreviations

SI. No	Name	Description	Units
1	α_{Al}	Volume fraction of Al alloy in the mixture	-
2	α_{Mg}	Volume fraction of Mg alloy in the mixture	-
3	A_s	Shoulder's surface area	m^2
4	β_0	constant	-
5	$\beta_1, \beta_2, \beta_3$	linear term coefficient	-
6	β_{11}, β_{22}	quadratic term coefficient	-
7	β_{12}	interaction term coefficient	-
8	C_p	Specific heat capacity	J/kg. K
9	ε	Surface emissivity	W/m^2
10	e_u	Residual	-
11	F_n	Plunge force	N
12	F_p	Translation force	N
13	∇	Gradient operator	-
14	$\partial T / \partial n$	Temperature gradient normal to the boundary	K/m
15	h	Coefficient of convection	W/m^2. K
16	H_{mix}:	Enthalpy of the material mixture	J/kg
17	h_{up}, h_{low}	Upper and lower surface convective heat transfer coefficient	W/m^2.K
18	i_u	Reflects the level of the ith factor in the uth observation	-
19	λ	Thermal conductivity	W/m.K
20	$\lambda_x, \lambda_y, \lambda_z$	Thermal conductivity in x, y and z direction	W/m.K
21	μ	Coefficient of friction	-
22	λ_T	Thread's helix angle	rad
23	μ_{mix}	Viscosity of the mixture property of the material	N.s/m^2
24	$\dot{m}_{Al,Mg}$	Mass flow rate of aluminum into magnesium	kg/s
25	$\dot{m}_{Mg,Al}$	Mass flow rate of magnesium into aluminum	kg/s
26	n	Direction vector normal for boundary Γ	-
27	P	Pressure	Pa
28	ρ	Density	kg/m^3
29	ρ_{Al}	Density of Al alloy	kg/m^3
30	ϕAl and ϕMg	Material properties of Al and Mg alloys	-
31	ϕ_{mix}	Mixture material property	-
32	q_p	Heat generated at tool pin/work piece interface	J
33	q_i	Heat generated at tool shoulder/work piece interface	J
34	q_s	Shoulder's heat flux	W/m^2
35	Φ	Response surface	-
36	R_n	Tool rotational speed	m/s
37	r_p	Pin radius	mm
38	τ	Material's shear stress	MPa
39	S_p	Shoulder-to-pin diameter ratio	-
40	S_v	Volumetric heat source	J/m^3
41	σ	Stefan-Boltzmann constant	W/m^2.K^4

42	T	Temperature	K
43	T_a	Ambient temperature	K
44	T_o	Reference temperature	K
45	T_P	Peak Temperature	K
46	T_R	Temperature rise	K
47	T (x, y, z, 0)	Temperature (K) at Coordinates (x, y, z) when t = 0	K
48	t_w	Work piece thickness	mm
49	u	Number of observations in the factorial experiment	-
50	$\vec{v}$	Velocity vector	m/s
51	$\vec{v}Al$	Velocity vector of Aluminium	m/s
52	W_v	Welding speed	m/s
53	ω	Tool's angular velocity	rad/s

References

[1] Vignesh RV, Padmanaban R, Arivarasu M, Thirumalini S, Gokulachandran J, Ram MSSS. Numerical modelling of thermal phenomenon in friction stir welding of aluminum plates. IOP Conf Ser Mater Sci Eng. 2016;149(1). https://doi.org/10.1088/1757-899X/149/1/012208

[2] Somasekharan AC, Murr LE. Fundamental studies of the friction-stir welding of magnesium alloys to 6061-T6 Aluminum. Magnes Technol. 2004;3:31-6.

[3] Woo W, Choo H. Softening behaviour of friction stir welded Al 6061-T6 and Mg AZ31B alloys. Sci Technol Weld Join. 2011;16(3):267-72. https://doi.org/10.1179/1362171811Y.0000000016

[4] Dorbane A, Mansoor B, Ayoub G, Shunmugasamy VC, Imad A. Mechanical, microstructural and fracture properties of dissimilar welds produced by friction stir welding of AZ31B and Al6061. Mater Sci Eng A [Internet]. 2016;651:720-33. https://doi.org/10.1016/j.msea.2015.11.019

[5] Mansoor B, Dorbane A, Ayoub G, Imad A. Friction stir welding of AZ31B magnesium alloy with 6061-T6 Aluminum alloy: Influence of processing parameters on microstructure and mechanical properties. Frict Stir Weld Process VIII. 2016;259-66. https://doi.org/10.1007/978-3-319-48173-9_28

[6] Wu B, Liu J, Song Q, Lv Z, Bai W. Controllability of joint integrity and mechanical properties of friction stir welded 6061-T6 Aluminum and AZ31B magnesium alloys based on stationary shoulder. High Temp Mater Process. 2019;38(2019):557-66. https://doi.org/10.1515/htmp-2019-0001

[7] Zheng Y, Pan X, Ma Y, Liu S, Zang L, Chen Y. Microstructure and corrosion behavior of friction stir-welded 6061 Al/AZ31 Mg joints with a Zr interlayer. Materials (Basel). 2019;12(7). https://doi.org/10.3390/ma12071115

[8] Liu H, Chen Y, Yao Z LF. Effect of Tool Offset on the Microstructure and Properties of AA6061/AZ31B Friction Stir Welding Joints. Metals (Basel). 2020;10:1-9. https://doi.org/10.3390/met10040546

[9] Kumar U, Prajapati A, Acharya U, Medhi T, Saha Roy B, Saha SC. Welding condition & microstructure of friction stir welded AA 6061-T6 and AZ31B. Mater Today Proc [Internet]. 2019;46:9484-9. https://doi.org/10.1016/j.matpr.2020.03.242

[10] Saldaña-Garcés R, Hernández-García D, García-Vázquez F, Gutiérrez-Castañeda EJ, Verdera D, Deaquino-Lara R. Friction stir welding of dissimilar aa6061-t6 to az31b-h24 alloys. Soldag e Insp. 2020;25:1-14. https://doi.org/10.1590/0104-9224/si25.25

[11] Xu Y, Ke L, Ouyang S, Mao Y, Niu P. Precipitation behavior of intermetallic compounds and their effect on mechanical properties of thick plate friction stir welded Al/Mg joint. J Manuf Process [Internet]. 2021;64(December 2020):1059-69. https://doi.org/10.1016/j.jmapro.2020.12.068

[12] Rajesh Jesudoss Hynes N, Vivek Prabhu M, Shenbaga Velu P, Kumar R, Tharmaraj R, Farooq MU, et al. An experimental insight of friction stir welding of dissimilar AA 6061/Mg AZ 31 B joints. Proc Inst Mech Eng Part B J Eng Manuf. 2022;236(6-7):787-97. https://doi.org/10.1177/09544054211043474

[13] Mughal MP, Nawaz A, Raza SF. Friction Stir Welding of Magnesium AZ31B and Aluminum Al-6062. Adv Transdiscipl Eng. 2022;25:135-42. https://doi.org/10.3233/ATDE220580

[14] Sarila V, Koneru HP, Cheepu M, Chigilipalli BK, Kantumuchu VC, Shanmugam M. Microstructural and Mechanical Properties of AZ31B to AA6061 Dissimilar Joints Fabricated by Refill Friction Stir Spot Welding. J Manuf Mater Process. 2022;6(5). https://doi.org/10.3390/jmmp6050095

[15] Huang T, Zhang Z, Liu J, Chen S, Xie Y, Meng X, et al. Interface Formation of Medium-Thick AA6061 Al/AZ31B Mg Dissimilar Submerged Friction Stir Welding Joints. Materials (Basel). 2022;15(16). https://doi.org/10.3390/ma15165520

[16] Yang C, Shi Q, Chen G. A Simulation Study on Material Flow and Mixing Mechanism in Dissimilar Friction Stir Welding of AA6061 and AZ31 Alloys [Internet]. Springer Nature Switzerland; 2023. 227-236. https://doi.org/10.1007/978-3-031-22661-8_21

[17] Ghiasvand A, Suksatan W, Tomków J, Rogalski G, Derazkola HA. Investigation of the Effects of Tool Positioning Factors on Peak Temperature in Dissimilar Friction Stir Welding of AA6061-T6 and AA7075-T6 Aluminum Alloys. Materials (Basel). 2022;15(3). https://doi.org/10.3390/ma15030702

[18] Khalaf HI, Al-Sabur R, Demiral M, Tomków J, Łabanowski J, Abdullah ME, Aghajani Derazkola H. The Effects of Pin Profile on HDPE Thermomechanical Phenomena during FSW. Polymers. 2022; 14(21): 4632. https://doi.org/10.3390/polym14214632

[19] Al-Sabur R, Khalaf HI, Świerczyńska A, Rogalski G, Derazkola HA. Effects of noncontact shoulder tool velocities on friction stir joining of polyamide 6 (PA6). Materials. 2022; 15(12): 4214. https://doi.org/10.3390/ma15124214

[20] Sidhu RS, Kumar R, Kumar R, Goel P, Singh S, Pimenov DY, Giasin K, Adamczuk K. Joining of Dissimilar Al and Mg Metal Alloys by Friction Stir Welding. Materials. 2022; 15(17): 5901. https://doi.org/10.3390/ma15175901

[21] Khalaf HI, Al-Sabur R, Derazkola, HA. Effect of number of tool shoulders on the quality of steel to magnesium alloy dissimilar friction stir welds. Archives of Civil and Mechanical Engineering. 2023; 23(2):125. https://doi.org/10.1007/s43452-023-00673-z

[22] Song M, Kovacevic R. Thermal modeling of friction stir welding in a moving coordinate system and its validation. Int J Mach Tools Manuf. 2003;43(6):605-15. https://doi.org/10.1016/S0890-6955(03)00022-1

[23] Chikh A, Serier, Al-Sabur R, Siddiquee AN, Gangil N. Thermal modeling of tool-work interface during friction stir welding process. Russian Journal of Non-Ferrous Metals. 2022; 63(6): 690-700. https://doi.org/10.3103/S1067821222060049

[24] Colegrove P. 3 Dimensional Flow and Thermal Modelling of the Friction Stir Welding Process. 2nd Int Symp Frict Stir Weld. 2000;(January):1-11.

[25] Tayo OA, Laseinde TO, Mashinini M. Finite-element modeling of thermo-mechanical phenomena in friction stir welding of AISI 4340 steel. Proc Int Conf Ind Eng Oper Manag. 2019;1215-21.

[26] Aziz SB, Dewan MW, Huggett DJ, Wahab MA, Okeil AM, Liao TW. Impact of Friction Stir Welding (FSW) process parameters on thermal modeling and heat generation of aluminum alloy joints. Acta Metall Sin (English Lett. 2016;29(9):869-83. https://doi.org/10.1007/s40195-016-0466-2

[27] Meyghani B, Awang M. Developing a Finite Element Model for Thermal Analysis of Friction Stir Welding (FSW) Using Hyperworks. Lect Notes Mech Eng. 2020;619-28. https://doi.org/10.1007/978-981-13-8297-0_64

[28] Al-Badour F, Merah N, Shuaib A, Bazoune A. Thermo-mechanical finite element model of friction stir welding of dissimilar alloys. Int J Adv Manuf Technol. 2014;72(5-8):607-17. https://doi.org/10.1007/s00170-014-5680-3

[29] Lemi MT, Gutema EM, Gopal M. Modeling and simulation of friction stir welding process for AA6061-T6 aluminum alloy using finite element method. Eng Solid Mech. 2022;10(2):139-52. https://doi.org/10.5267/j.esm.2022.2.001

[30] Gopal M. Prediction of surface roughness in turning of duplex stainless steel (DSS) using response surface methodology (RSM) and artificial neural network (ANN). Mater Today Proc [Internet]. 2020;47:6704-11. https://doi.org/10.1016/j.matpr.2021.05.118

[31] Harachai K, Prasomthong, S. Investigation of the optimal parameters for butt joints in a friction stir welding (FSW) process with dissimilar aluminum alloys. Materials Research Express, 2023, 10(2), p.026514. https://doi.org/10.1088/2053-1591/acbb54

[32] Al-Sabur R. Tensile strength prediction of aluminum alloys welded by FSW using response surface methodology-Comparative review. Materials Today: Proceedings, 2021 45, pp.4504-4510. https://doi.org/10.1016/j.matpr.2020.12.1001

[33] Box GE DN. Empirical model-building and response surfaces. John Wiley & Sons; 1987.

[34] Hoyos E, Serna, MC. Basic tool design guidelines for friction stir welding of aluminum alloys. Metals. 2021; 11(12), p.2042. https://doi.org/10.3390/met11122042

[35] Gutema EM, Gopal M, Lemu HG. Temperature Optimization by Using Response Surface Methodology and Desirability Analysis of Aluminum 6061. Materials (Basel). 2022;15(17). https://doi.org/10.3390/ma15175892

[36] Tang W, Guo X, McClure JC, Murr LE, Nunes A. Heat input and temperature distribution in friction stir welding. J Mater Process Manuf Sci. 1998;7(2):163-72. https://doi.org/10.1106/55TF-PF2G-JBH2-1Q2B

[37] Akbari M, Aliha MRM, Keshavarz SME, Bonyadi A. Effect of tool parameters on mechanical properties, temperature, and force generation during FSW. Proc Inst Mech Eng Part L J Mater Des Appl. 2019;233(6):1033-43. https://doi.org/10.1177/1464420716681591

[38] Uday KN, Rajamurugan G. Analysis of tensile strength on friction stir welded Al 6061 composite reinforced with B4C and Cr2O3 using RSM and ANN. Eng Res Express. 2023;5(1):0-15. https://doi.org/10.1088/2631-8695/acb6d1

[39] Mahajan L, Bhagat S. An artificial neural network for the prediction of the strength of supplementary cementitious concrete. Res Eng Struct Mater. 2022;8(2):421-30. https://doi.org/10.17515/resm2022.341st0918tn

[40] Asiltürk I, Çunkaş M. Modeling and prediction of surface roughness in turning operations using artificial neural network and multiple regression method. Expert Syst Appl. 2011;38(5):5826-32. https://doi.org/10.1016/j.eswa.2010.11.041

Research on

Engineering

Structures

Materials

Scopus®

DRJI

TÜBİTAK
ULAKBİM

ProQuest®

cross ref

Google Scholar

Universal Impact Factor
Scientifically derived Journal Impact Factor

SIS
Scientific Indexing Services

Journal Seeker
Research Bible

CiteFactor
Academic Scientific Journals

EZB Elektronische Zeitschriftenbibliothek

Open Academic Journals Index

GIF
GLOBAL IMPACT FACTOR

ASOS indeks

Cosmos

Publication Forum

INFOBASE INDEX

ROOTINDEXING
JOURNAL ABSTRACTING AND INDEXING SERVICE

Scope Database
Journal Indexing & Citation Analysis